

Transactions of the ASME®

FLUIDS ENGINEERING DIVISION

Technical Editor
DEMETRI P. TELIONIS (1999)

Executive Secretary
PAT WHITE (1999)
Assistants to the Editor
N. W. SCHAEFFLER
J. E. POWELL
Calendar Editor
M. F. ACKERSON

Associate Technical Editors

P. R. BANDYOPADHYAY (1997)
S. BANERJEE (1999)
P. W. BEARMAN (1998)
M. N. DHAUBHADEL (1999)
J. EATON (1999)
F. GIRALT (1997)
J. A. C. HUMPHREY (1997)
F. HUSSAIN (1998)
J. KATZ (1998)
B. SCHIAVELLO (1999)
O. SIMONIN (1998)
P. M. SOCKOL (1998)
M. W. SINDIR (1997)
M. SOMMERFELD (1999)
M. S. TRIANTAFYLLOU (1998)

BOARD ON COMMUNICATIONS

Chairman and Vice-President
R. MATES

OFFICERS OF THE ASME

President, **R. J. GOLDSTEIN**

Exec. Director
D. L. BELDEN

Treasurer
J. A. MASON

PUBLISHING STAFF

Managing Director, Engineering
CHARLES W. BEARDSLEY

Director, Technical Publishing
PHILIP DI VIETRO

Managing Editor, Technical Publishing
CYNTHIA B. CLARK

Managing Editor, Transactions
CORNELIA MONAHAN

Production Assistant
MARISOL ANDINO

Journal of Fluids Engineering

Published Quarterly by The American Society of Mechanical Engineers

VOLUME 119 • NUMBER 2 • JUNE 1997

- 233 Review—The Transient Equation of Motion for Particles, Bubbles, and Droplets
E. E. Michaelides
- 248 Status of Large Eddy Simulation: Results of a Workshop
W. Rodi, J. H. Ferziger, M. Breuer, and M. Pourquié
- 263 Experimental Study of Turbulent Concentration Flow Field in the Wake of a Bluff Body
R. Balachandar, Vincent H. Chu, and Jianbo Zhang
- 271 The Case of the Singing Vortex
B. Maines and R. E. A. Arndt
- 277 Turbulent Wall-Pressure Fluctuations: A New Model for Off-Axis Cross-Spectral Density
B. A. Singer
- 281 Wavenumber Spectra of High Magnitude Wall Pressure Events in a Numerically Simulated Turbulent Boundary Layer
B. M. Abraham and W. L. Keith
- 289 The Use of Pattern Recognition and Proper Orthogonal Decomposition in Identifying the Structure of Fully-Developed Free Turbulence
G. A. Kopp, J. A. Ferré, and Francesc Giralt
- 297 Aero-Thermodynamic Loss Analysis in Cases of Normal Shock Wave-Turbulent Shear Layer Interaction
J. K. Kaldellis
- 304 Near-Wall Modeling of Plane Turbulent Wall Jets
G. Gerodimos and R. M. C. So
- 314 Strongly-Coupled Multigrid Method for 3-D Incompressible Flows Using Near-Wall Turbulence Closures
F. B. Lin and F. Sotiropoulos
- 325 A Reynolds Stress Function for Wall Layers
R. L. Panton
- 331 Assessment of Artificial Dissipation Models for Three-Dimensional Incompressible Flow Solutions
F. B. Lin and F. Sotiropoulos
- 341 A Finite-Element Study of Newtonian and Power-Law Fluids in Conical Channel Flow
S. H. Garrioch and D. F. James
- 347 An Experimental Investigation Into the Breakdown of Low Reynolds Number Pulsed Flows at a Pipe Orifice
P. S. Addison, D. A. Irvine, A. H. C. Chan, and K. J. Williams
- 354 Transient Fluid-Structure Interaction in a Control Valve
Tienfuan Kerh, J. J. Lee, and L. C. Wellford
- 360 Design of Homologous Ram Pumps
Brian Young
- 366 Fluid Force Moment on a Centrifugal Impeller Shroud in Precessing Motion
Yoshinobu Tsujimoto, Yoshiki Yoshida, Hideo Ohashi, Norihiro Teramoto, and Shin Ishizaki
- 372 Navier-Stokes Simulations of a Novel Viscous Pump
M. C. Sharatchandra, Mihir Sen, and Mohamed Gad-el-Hak
- 383 LDV Measurements of Spatially Periodic Flows Over a Detached Solid-Rib Array
Tong-Miin Liou, Chih-Ping Yang, and Hsin-Li Lee
- 390 Axisymmetric Inertial Oscillations in Transient Rotating Flows in a Cylinder
Jae Won Kim and Jae Min Hyun
- 397 A Numerical Study on Motion of a Sphere Coated With a Thin Liquid Film at Intermediate Reynolds Numbers
S. Kawano and H. Hashimoto
- 404 Experimental Determination of Permeability and Inertia Coefficients of Mechanically Compressed Aluminum Porous Matrices
B. V. Antohe, J. L. Lage, D. C. Price, and R. M. Weber
- 413 Tip Vortex Formation and Cavitation
B. H. Maines and R. E. A. Arndt

(Contents continued on p. 262)

Transactions of the ASME, Journal of Fluids Engineering (ISSN 0098-2202) is published quarterly (Mar., June, Sept., Dec.) for \$185.00 per year by The American Society of Mechanical Engineers, 345 East 47th Street, New York, NY 10017. Periodicals postage paid at New York, NY and additional mailing offices.

POSTMASTER: Send address changes to Transactions of the ASME, Journal of Fluids Engineering, c/o THE AMERICAN SOCIETY OF MECHANICAL ENGINEERS, 22 Law Drive, Box 2300, Fairfield, NJ 07007-2300.

CHANGES OF ADDRESS must be received at Society headquarters seven weeks before they are to be effective. Please send old label and new address.

PRICES: To members, \$40.00, annually; to nonmembers, \$185.00. Add \$30.00 for postage to countries outside the United States and Canada.

STATEMENT from By-Laws. The Society shall not be responsible for statements or opinions advanced in papers or . . . printed in its publications (B7.1, Par. 3).

COPYRIGHT © 1997 by The American Society of Mechanical Engineers. Authorization to photocopy material for internal or personal use under circumstances not falling within the fair use provisions of the Copyright Act is granted by ASME to libraries and other users registered with the Copyright Clearance Center (CCC).

Transactional Reporting Service provided that the base fee of \$3.00 per article is paid directly to CCC, 27 Congress St., Salem, MA 01970. Request for special permission or bulk copying should be addressed to Reprints/Permission Department.

INDEXED by Applied Mechanics Reviews and Engineering Information, Inc. Canadian Goods & Services Tax Registration #126148048.

(Contents continued)

- 420 Numerical Modeling of the Thermodynamic Effects of Cavitation
Manish Deshpande, Jinzhang Feng, and Charles L. Merkle
- 428 Ensemble-Average Equations of a Particulate Mixture
L. M. Liljegren
- 435 Simulation of Chaotic Particle Motion in Particle-Laden Jetflow and Application to Abrasive Waterjet Machining
Z. Yong and R. Kovacevic
- 443 The Rise of Bubbles in a Vertical Shear Flow
E. A. Ervin and G. Tryggvason

Technical Briefs

- 450 Time-Dependent Vortex Breakdown in a Cylinder With a Rotating Lid
Kazuyuki Fujimura, Hide S. Koyama, and Jae Min Hyun
- 453 Flow Characteristics of a Bluff Body Cut From a Circular Cylinder
S. Aiba and H. Watanabe
- 454 A Design Method for Contractions With Square End Sections
Fuh-Min Fang
- 458 Turbulence Modification in the Limiting Cases of Heavy- and Tracer-Particles
D. I. Graham
- 460 A Short Comparison of Damping Functions of Standard Low-Reynolds-Number k - ϵ Models
A. N. Rousseau, L. D. Albright, and K. E. Torrance
- 463 Simultaneous Velocity and Temperature Patterns in the Far Region of a Turbulent Cylinder Wake
A. Vernet, G. A. Kopp, J. A. Ferré, and F. Giralt
- 466 The Response of a Turbulent Boundary Layer to a Square Groove
B. R. Pearson, R. Elavarasan, and R. A. Antonia
- 469 Effect of Roughness Aspect Ratio on the "Bursting" Period in a Fully Turbulent Channel Flow
L. Labraga, A. Mazouz, S. Demare, and C. Tournier
- 471 The Effect of Induced Swirl on Mixing
D. W. Guillaume and J. C. LaRue
- 473 Air Venting in Pressure Die Casting
G. Bar-Meir, E. R. G. Eckert, and R. J. Goldstein
- 476 Stability of Various Molecular Dynamics Algorithms
Akira Satoh
- 480 Flow Over Tube Banks—A Visualization Study
J. W. Hoyt and R. H. J. Sellin
- 484 Fluids Engineering Calendar

Announcements and Special Notices

- 270 Transactions Change of Address Form
- 313 Subscription Notice
- 330 Announcement—ICMF'98—Lyon
- 487 Call for Symposium Papers—1998 Fluids Engineering Summer Meeting
- 491 Call for Forum Papers—1998 Fluids Engineering Summer Meeting
- 495 Statement of Numerical Accuracy
- 495 Statement of Experimental Uncertainty
- 495 Access to the Electronic JFE
- 495 Submission of Papers

Review—The Transient Equation of Motion for Particles, Bubbles, and Droplets

E. E. Michaelides

Associate Dean for Research;
School of Engineering
and Center for Bioenvironmental Research,
Tulane University,
New Orleans, LA 70118-5674

The development, form, and engineering applications of the transient equation of motion of rigid particles, bubbles, and droplets are presented. Some of the early work on the equation of motion, as well as recent advances, are exposed. Particular emphasis is placed on the semiempirical forms of the equation, which are widely used in engineering practice. The creeping flow assumption, on which most of the known applications are based, is critically examined and its limitations are pointed out. Recent results on particle flow, which include the effect of the advection of a downstream wake and are applicable to finite (but small) Reynolds numbers are also presented. The form of the history (Basset) term is discussed, in the light of recent work and its effect on the integrated results of the equation of motion is examined. Recommendations are given on the appearance, importance, and significance of the history and added mass terms for those who may use the semiempirical form of the transient equation of spheres in a differential or integrated form.

Introduction

Myriads of scientific and engineering papers have used in the past thirty years an equation of motion for particles, droplets, or bubbles. In their vast majority, these papers use a semiempirical form of the equation of motion, which emanates from the early work of Stokes, Boussinesq, and Basset and is supplemented with empirical data of the more recent past (1960's and 1970's). A single article, that of Maxey and Riley (1983), seems to be the dominant source of the form of the equation of motion for most recent articles on the subject. Their article essentially clarified the work of the early researchers on the subject and pointed out some of the complexities in the derivation and use of the equation of motion at zero Reynolds numbers. Recent analytical studies by Sano (1981), Lovaletti and Brady (1993) and others provided the scientific community with an equation of motion for the arbitrary rectilinear motion of a sphere, valid at small but finite Reynolds numbers. These analytical expressions are very complex in their form and very cumbersome to be used in repetitive calculations. For this reason the use of the semiempirical and simpler expressions still dominates the literature on multiphase flows.

In the last five years, two other review articles have appeared in this journal, which are pertinent to solid particles and droplets. Both of these articles emanate from the Freeman Scholar Lecture series of the ASME. Sirignano's (1993) work pertains to sprays and deals with the dynamics and interactions of droplets, as well as the heat and mass transfer from them. The second one by Stock (1996) treats mainly the dispersion of particles in gases and the interactions of particles with turbulence. In both articles, the equation of motion of particles or droplets appears in several of its forms, which are essentially semiempirical. The articles, however, focus on their specific applications and do not elaborate on the significance, usefulness, and implications of the several terms of the equation of motion or on how and when these terms should be used.

This review article focuses on the equation of motion of particles, bubbles, or droplets *per se* and avoids lengthy presentations of particular applications or of numerical implementa-

tions. It aims at the sorting, exposition, and explanation of the diverse forms of the equation of motion of particles, which have appeared in the literature, the significance of the various terms in these expressions and their usefulness to many engineering applications. Its goals are: (a) to expose some of the details of the derivations and, hence, the limitations of the various forms of the equation of motion of particles, bubbles, and droplets to the scientist or engineer who uses this equation, (b) to present the significance of the various terms of the equation of motion for several cases of practical interest, and (c) to give some recommendations on when some of these terms should be used in practice and when it is convenient and advantageous to neglect them, especially when repetitive calculations are performed.

Historical Background

It is rather remarkable that the first work on the transient equation of motion of a particle appeared almost two decades before the development and wide acceptance of what we now call the "Navier-Stokes equations." Poisson (1831) examined the potential sinusoidal flow past a rigid sphere. His calculations revealed what we now call the "added mass term" in the equation of motion, and he correctly predicted that the added mass coefficient is $\frac{1}{2}$. Green (1833) independently obtained a solution for the potential flow of a rigid ellipse in an infinite fluid and pointed out the added mass component. A few decades later, Clebsch (1856) completed the work of Green by examining the effect of the rotation of the ellipse in a nonviscous fluid.

The practical interest of the early researchers appears to have been the motion of pendula in air and the development of more accurate clocks. The scientific work on the equation of motion of spheres and ellipses appears to be complementary to the technology related to the construction of timepieces for, among other reasons, the determination of the geographical longitude. The catalyst for these technological advances in England was the "Longitude Prize" (Sobel, 1995). Stokes (1851) seems to have had the same application in mind when he developed his theory on the unsteady sinusoidal motion of a sphere in a viscous fluid. He obtained his results as solutions to what are now widely known as the "Stokes equations." The Stokes equations for particle motion are essentially the Navier-Stokes equations, without the nonlinear inertia terms. In a strict sense, the Stokes equations are only valid in the limit of zero Reynolds number

Contributed by the Fluids Engineering Division for publication in the JOURNAL OF FLUIDS ENGINEERING. Manuscript received by the Fluids Engineering Division October 6, 1995; revised manuscript received March 11, 1997. Associate Technical Editor: D. P. Telionis.

of the sphere, a number based on the relative velocity of the sphere. This type of flow is characterized by the more modern term "creeping flow." The term implies that the object may move very slowly inside the viscous fluid. Another result of Stokes' (1845) pioneering work is the formulation of the steady-state equation of motion of a sphere in a viscous fluid and the expression for the steady-state drag coefficient, which now bears his name (Stokes drag law). The Stokes drag coefficient is most often written in terms of the quantity we now call "Reynolds number"¹ ($c_D = 24/\text{Re}$).

About thirty years after Stokes, Boussinesq (1885a and 1885b) developed the mathematical framework and the expression for the unsteady motion of a solid sphere, starting from rest, inside an infinite, viscous, and quiescent fluid. In his work, the velocity of the sphere is an arbitrary function of time, while in earlier works the velocity was always prescribed, usually as sinusoidal. The underlying assumption is the omission of the inertia (advection) terms. Hence, the results apply to creeping flows, and the theory is correct in the limit $\text{Re} \rightarrow 0$. The steady-state drag term, the added mass term, and the history integral term (which represents the effect of the diffusion of vorticity around the sphere) appear prominently in Boussinesq's expressions of the hydrodynamic forces exerted by the fluid. Three years later, Basset (1888a, 1888b), apparently unaware of the work by Boussinesq, derived independently the unsteady equation of motion of a sphere under the same creeping flow conditions. The final expressions of the last two authors for the hydrodynamic force acting on a solid sphere are identical. Given the chronological precedence of Boussinesq's work, it is ironic that the history term of the hydrodynamic force has since been called by many researchers the "Basset force" or the "Basset integral." Even when the Basset-Boussinesq-Oseen (BBO) formulation is mentioned, reference is made to a later work of Boussinesq, and not to his original (1885) papers.

An attempt to relax the creeping flow assumption was made by Whitehead (1889) shortly after the book by Basset was published. He used Stokes' method and attempted to improve upon the latter's work by obtaining higher-order approximations to the flow when Re is small but finite. His method is equivalent to an expansion in terms of the Reynolds numbers. However, it does not yield valid results, because it fails to satisfy completely the boundary conditions far from the sphere. This deficiency was pointed out by Oseen (1910). Oseen (1913) is also credited, among other advances, with the improved prediction of the drag coefficient at finite Reynolds numbers [$c_D = 24(1$

$+ \frac{3}{8} \text{Re})/\text{Re}$]. His student Faxén (1922) improved on the equation of motion of a particle by including terms due to the nonuniform fluid velocity field (the so-called "Faxén terms").

An account of the earlier work on the hydrodynamic forces and the transient equation of motion of a solid sphere may be found in some of the older treatises such as the ones by Lamb (1932), Dryden et al. (1956), Oseen (1927), and Villat (1943). Since the problem of the transient flow with particles is important and intriguing from the scientific as well as the engineering point of view, several researchers contributed to it during the more recent past. In the following sections the latter contributions will be examined, as they influenced the form of the equation of motion and its applications. It must be pointed out that in a short survey, such as this one, it is impossible to present every study on the equation of motion. The ones presented here have significantly contributed to the development of the form of the equation of motion from the scientific point of view, or have profoundly influenced the engineering applications.

The Early Form of the Equation of Motion

The Boussinesq/Basset expression for the transient hydrodynamic force (the prevalent name at the time was "fluid resistance") exerted by an infinite, quiescent fluid on a sphere, initially at rest, is as follows:

$$F = 6\pi\alpha\mu_f V + \frac{m_f}{2} \frac{dV}{dt} + 6\alpha^2 \sqrt{\pi\rho_f\mu_f} \int_0^t \frac{d\tau}{\sqrt{t-\tau}} d\tau \quad (1)$$

where $V(t)$ is the arbitrary velocity of the sphere. In this case, the three terms of Eq. (1) appear as three independent components of the hydrodynamic force. For this reason, several researchers have considered each term as a separate entity and named them the steady-state drag force, the added mass force, and the history integral force (or the Basset force, according to some).

Among the relatively recent researchers to use the transient equation of motion for a specific application was Tchen (1947) who performed calculations on the turbulent diffusion of particles. His main contribution is the development of the equation of motion of a spherical, rigid particle inside a fluid with a time-dependent velocity field (all previous studies assumed a quiescent fluid). He used this equation of motion to calculate the dispersion of particles in a turbulent flow field. It is rather unfortunate that he overlooked the fact that, when the particle does not start from rest, the history term must be complemented by a term proportional to $V_0/t^{1/2}$, where V_0 is the relative veloc-

¹ The term "Reynolds number" was not used by the early authors. Since this quantity is extensively used in the current literature, it is more convenient to present all the results in terms Re .

Nomenclature

A = vector defined in Eq. (14)
 Ac = acceleration number
 b = variable defining a step velocity change
 c_1 = coefficient for the Stokesian drag
 D_x = dispersion coefficient
 erf = error function
 f = function defined in Eq. (8)
 F = force
 H = Heavyside function
 m = mass
 P = pressure
 Re = Reynolds number of sphere
 s = Laplace transform variable
 Sl = Strouhal number
 t = time

u = fluid velocity
 V = particle velocity
 w = dimensionless frequency
 w_i = relative velocity
 α = radius of particle
 β = slip coefficient
 γ = parameter equal to $1/(1 + \frac{1}{2}\Delta_A\phi)$
 Γ = velocity shear
 δ = Dirac delta
 Δ_A = coefficient for added mass
 Δ_H = coefficient for history (Basset) term
 κ = ratio μ_s/μ_f
 λ = dimensionless variable in Laplace domain (Eq. (7))
 μ = dynamic viscosity

ν = kinematic viscosity
 ρ = density
 σ = dimensionless coefficient related to surface slip ($\mu_f/\beta\alpha$)
 τ = dummy variable for time
 τ_s = characteristic time of sphere
 ϕ = ratio ρ_f/ρ_s
 ω = dimensional frequency

Subscripts

0 = initial
 f = fluid
 j, j = Laplacian
 s = particle

Superscripts

' = derivative

ity of the sphere at the inception of motion. This omission was carried over in several subsequent studies, which used Tchen's equation of motion, and especially those pertinent to the turbulent diffusion of particles (e.g., Corssin and Lumley, 1957; Hjelmfelt and Mockros, 1966; Hinze, 1971). The missing part of the history term was pointed out in the study of turbulent dispersion coefficients by Reeks and McKee (1984).

Equation (1), or a simpler form of it, is often used in Lagrangian computations of the motion and trajectory of a sphere. Among the work currently in progress is the attempt to include the proper transient form of the hydrodynamic interaction between a sphere and the surrounding fluid in Eulerian descriptions of two-phase flows. The work by Sangani et al. (1991) is typical of this trend and includes representations of the steady-state drag, the added mass and the history terms, in a continuum description of liquid-gas flows.

Semiempirical Equations

Most practical applications of the motion of particles in viscous fluids occur at finite relative velocity between the particle and the surrounding fluid. However, the expression for the transient hydrodynamic force exerted by the fluid on a particle as derived by Boussinesq and Basset is, strictly speaking, accurate at zero relative velocity. For this reason, experimental results obtained at finite Reynolds numbers (e.g., terminal velocities of spheres in a gravitational field) did not agree well with calculations that used Eq. (1) as the hydrodynamic force. To compensate for this discrepancy, there has been a strong tendency to use empirical factors for some or for all the three terms of Eq. (1) in order to make the results derived from the modified empirical equation agree with experimental data at finite relative velocities. This practice has spawned several semiempirical equations, which are now commonly used in engineering applications. In order to obtain the empirical factors, several experimental methods were devised and rather detailed experiments were performed in the last thirty-five years.

In the early days of the development of these semiempirical equations, the experiments and the resulting empirical coefficients pertained to the steady-state drag component only. Thus, the early experimentalists measured the terminal velocity of spheres in fluids and, hence, determined a dimensionless empirical coefficient, usually as a function of the Reynolds number. They generally used the expression $\frac{1}{2}c_D\pi\rho_f\alpha^2V^2$ as the starting point for the force exerted by the steady-state drag at finite velocities and derived expressions for the drag coefficient c_D in terms of the Reynolds number of the flow. When $c_D = 24/\text{Re}$ this expression reduces to Stokes' drag $6\pi\alpha\mu_fV$. This coincidence has prompted some to offer an alternative form for the expression for the steady-state drag at finite Reynolds numbers and to write the drag force in terms of the Stokes drag as $(6\pi\alpha\mu_fV)*f$, where f is a dimensionless empirical factor, which depends on the Reynolds number. However, there is a methodological contradiction with this expression, especially when the term in parenthesis is explicitly identified as the Stokes drag: the term in parenthesis was derived and *ipso facto* is only accurate at zero relative velocity, while the factor f is a function of the Reynolds number and, hence, of the relative velocity. This apparent methodological contradiction does not pose any practical problems for the users of the derived expressions, if one realizes that the expression $(6\pi\alpha\mu_fV)*f$ may also be derived from the original expression $\frac{1}{2}c_D\pi\rho_f\alpha^2V^2$, which stems from sound scientific arguments pertaining to finite velocities and is methodologically correct, simply by substituting $c_D = 24f/\text{Re}$.

The use of the empirical factors for the steady-state drag is widespread. The early treatises by Wallis (1969), Govier and Aziz (1971), Clift et al. (1978), and Soo (1967, revised in 1990) include the most commonly used of these empirical equations. Regarding the unsteady behavior of spheres, Baird et al.

(1967) recognized that the Reynolds number may not be the only relevant variable and included the effect of the Strouhal number on the drag coefficient. Clamen and Gauvin (1969) defined and determined experimentally the effect of "the turbulence number" on the steady-state drag coefficient. The modification of the steady-state drag by all these coefficients improved dramatically the accuracy of the unsteady flow calculations conducted within the range of validity of the empirical coefficients. The result (and also the advantage) of using these empirical coefficients was to bring the "theory" (that is the semiempirical expressions) in agreement with experimental results. It must be pointed out that, even though most of the early empirical coefficients were determined from steady-state experiments, their use in transient cases was, and still is, very common.

Odar and Hamilton (1964) extended the application of the empirical coefficients to include the added mass and history terms. They introduced two additional coefficients to account for the remaining two parts of the hydrodynamic force, the added mass term and the history, or "Basset" term. According to their hypothesis, each term of Eq. (1) must be multiplied by a factor (c_1 , Δ_A and Δ_H) to account for the finite relative velocity of the particle. Thus, the resulting expression is:

$$F = c_1(6\pi\alpha\mu_fV) + \Delta_A\left(m_f\frac{dV}{dt}\right) + \Delta_H\left(\alpha^2\sqrt{\pi\rho_f\mu_f}\int_0^t\frac{dV}{\sqrt{t-\tau}}d\tau\right) \quad (2)$$

Early experiments by Odar and Hamilton (1964) suggest that the coefficient of the steady-state drag term, c_1 , is a function of the Reynolds number and those of the added mass (Δ_A) and the history term (Δ_H) are functions of the acceleration number, Ac . The two dimensionless numbers are defined as follows:

$$\text{Re} = \frac{2\alpha\rho_f|U-V|}{\mu_f}, \quad \text{Ac} = \frac{|U-V|^2}{2\alpha\left|\frac{dV}{dt}\right|} \quad (3)$$

where U is the fluid velocity. The explicit expressions for the empirical coefficients suggested by Odar and Hamilton are:

$$\Delta_A = 1.05 - \frac{0.066}{0.12 + \text{Ac}^2} \quad \text{and} \quad \Delta_H = 2.88 + \frac{3.12}{(1 + \text{Ac})^3}, \quad (4)$$

while for c_1 they originally used a table. It was found that the empirical expression $c_1 = 1 + 0.15 \text{Re}^{0.667}$ (Rowe, 1961) yields fairly accurate results for the steady-state drag coefficient. This expression appears to be very accurate and is used today widely, especially in flows of heavy particles.

The use of the three independent empirical coefficients implicitly assumes that the three parts of the hydrodynamic force are independent. It seems that this hypothesis was reinforced by the fact that the three terms of Eq. (1) were considered as distinct forces and given separate names in the past. However, the hydrodynamic resistance of a fluid is a unique entity, which only manifests itself in the form of (1) in the very narrow case of a rigid sphere starting from rest in a quiescent fluid at zero Reynolds number. It has been recently shown that any departure from these conditions significantly alters the form of the hydrodynamic force. Because of this, the theoretical justification for the use of the form of expression (2) in many practical applications is questionable.

Regardless of its precarious theoretical grounds, the general practice of separating the transient force into three independent components and using the empirical values for c_1 , Δ_A , and Δ_H was crowned with success and became very popular in engineering calculations. The reason for this is the close agreement of the calculations with experimentally observed quantities. The agreement is due to the fact that the semiempirical equation has a sound experimental basis and has always been used to determine the total hydrodynamic force, and not any of its three parts. It must be recalled that there was never (and it is not possible to conduct) an independent experimental determination and subsequent verification of all the three individual terms of the semiempirical equation. The pertinent experiments, from which the empirical coefficients emanate, determined the total hydrodynamic force on the sphere at various instances. Then, by a series of assumptions and deductions, the experimentalists estimated the three parts of Eq. (2) and, hence, calculated the three coefficients. For verification of the derived expressions, the resulting equation was used as a single entity to always calculate the total hydrodynamic force and then to compare the results with other experiments, similar to the ones from which the force was determined. For this reason, it would have been astonishing if close agreement between experiment and "theory" were not obtained. It appears that this fortuitous agreement is the only reason why the semiempirical expression is still used in various forms, especially in engineering calculations. The derived results for the total hydrodynamic force are trusted by many because they have a sound empirical basis.

In a series of calculations on the motion of particles using Eqs. (2) to (4), Odar (1966) "verified" the agreement of the results with his new experimental data. The agreement was found to be remarkable, and Odar (1968) extended the method of empirical coefficients to include the effect of the curvature of the particle's path. He introduced two more empirical coefficients (χ and λ) in combination with Δ_H and Δ_A , respectively, in order to account for the curvature of the trajectory of a sphere. He also presented a diagram for their variation with the path curvature. In addition to the limitations mentioned above, this method implicitly makes the (highly questionable) assumption that the curvature of the path independently affects the three components of the force. Because of this and of the complexity of the resulting expression, this method has not been used extensively by others. However, the general practice of introducing novel coefficients for any departure from the original conditions of derivation of (1) still persists.

Among the early proponents of the semiempirical form of the equation of motion are Al-taweel and Carley (1971a) who performed their own experiments for the determination of the coefficients. The same team (Al-taweel and Carley, 1971b) subsequently used these coefficients to calculate the behavior of spheres in pulsating fluids and to determine under what conditions the history terms were significant. Schoneborn (1975) also used the semiempirical expression to verify the experimentally observed retardation of spheres in oscillating fluids.

There is not widespread agreement on the validity of correlations shown in Eq. (4). The experiments by Karanfilian and Kotas (1978), suggest constant values for Δ_A and Δ_H (0.5 and 6, respectively) and attribute the effect of the acceleration number solely to the coefficient c_1 [$c_1 = c_{1s}(1 + Ac^{-1})^{1.2}$], where c_{1s} is the value of the steady-state drag coefficient. Similarly, Temkin and Mehta (1982) suggested that the unsteadiness of the flow affects only c_1 (although they recommend a different correlation for it). On the other hand, Tsuji et al. (1991) in an extensive experimental study confirmed the expressions by Odar and Hamilton (1964) and concluded that the accuracy of their correlations as given in (4) extends to Reynolds numbers up to 16,000 for gas-solid flows. Two recent studies by Linteris et al. (1991) and Vojir and Michaelides (1994) used the expres-

sions for the semiempirical coefficients as presented in (4) in order to determine the relative significance of the three terms. Although a definitive study on the correlations for the semiempirical coefficients has not been made, the expressions given in Eq. (4) have been verified by many researchers, have been widely used with success, and are considered the most accurate.

Among the several applications of the semiempirical equations one may include those which are preponderant in heavy-particle flows, with particle to fluid density ratios more than 1000. These studies typically use correct dimensional arguments to eliminate the history and, sometimes, the added mass term. The researchers use an empirical equation for the steady-state drag to account for the interaction between the particle(s) and the fluid. The experimental study by Rowe (1961) is typical of such studies, and yielded the widely used empirical correlation for the steady-state drag coefficient

$$c_D = 24(1 + 0.15 \text{Re}^{0.667})/\text{Re}.$$

Numerous researchers have used the empirical expressions to successfully model the interaction between the fluid and a particle from the early days until very recently (Hughes and Gilliland, 1952; Crowe et al., 1977; Wang and Stock, 1994; Stock et al., 1993; Stock et al., 1995). In a comparative study, Michaelides (1988) investigated the effect of several empirical steady-state drag coefficients on the velocity and distance travelled (an integral quantity) by a particle and found an insignificant effect, provided that very small differences were used in the numerical calculations. This is an indication that all these semiempirical expressions are practically equivalent, because they stem from a set of empirical observations.

It is evident (and calculations have verified it in the last thirty years) that using empirical coefficients with the rigorously derived expression for creeping flows is a convenient way to ensure that experiments and "theory" will match. Regardless of the questions raised as to the theoretical validity of Eqs. (2) through (4), it should not be forgotten that the calculated force emanates from experimental data. Therefore, all calculations for the total force exerted by the fluid, but not necessarily for each of the three parts of this force, have an experimental basis, and will lead to the right results and conclusions, when used properly (i.e., within the range of validity of the original data). This is the main advantage of the semiempirical equation and the reason why it is so widespread in engineering practice today. While using any semiempirical equation, one has only to ensure that the range of validity of the coefficients (in terms of Re and Ac) covers the range of the calculations.

Equations of Viscous Spheres (Droplets and Bubbles) in a Fluid of Different Viscosity

Although Eq. (1) applies to a solid sphere, early researchers have used it extensively in studies pertaining to the transient motion of bubbles and droplets. This practice is recommended in Hughes and Gilliland (1952), who also give an account of some of the early theoretical works and applications of droplet motion. Many of the studies of the 1960's and 1970's on the heat transfer and evaporation of droplets also use the rigid particle equation of motion (Hill et al., 1963; Hubbard et al., 1975; Moore and Sieverding, 1975). Gyarmathy's (1982) review is typical of this practice. It essentially treats the droplets in the same way as small particles, which may evaporate.

The case of a viscous sphere (bubble or droplet) differs from that of a solid sphere in the following aspects: (a) there is an internal velocity field, which must be considered; (b) the velocity of the whole sphere is not the same as that of the center of the sphere; (c) the shear stresses of the two fluids at the interface of the sphere must balance; and (d) the ratio of sphere to fluid densities is often much less than the density ratio of solid/air flows. These differences lead to important deviations in the

boundary conditions of the Navier-Stokes equations from which (1) emanates.

Sy et al. (1970) conducted the first detailed study on the creeping flow of a solid sphere (infinite internal viscosity) and a bubble (zero internal viscosity). Their result for the solid sphere is equivalent to that of Boussinesq/Basset. One year later, Sy and Lightfoot (1971) extended the results to spheres of finite viscosity and Konoplin (1971), using the last two studies, rushed to proclaim an analogy in the equations for heat and momentum transfer. It is rather unfortunate, however, that Sy and Lightfoot (1971) combined a dimensional boundary condition with the dimensionless governing equations. This has led to erroneous results when the viscosity ratio of the sphere to the fluid is finite. The correct formulation of the problem and its solution was first presented

$$\overline{F}_i = -6\pi\alpha\mu_f[\overline{v}_i(s) - \overline{u}_i(\tilde{Y}(t), s)] \left\{ \frac{\lambda_f^2}{9} + \lambda_f + 1 - \frac{(\lambda_f + 1)^2[\lambda_s^3 - \lambda_s^2 \tanh(\lambda_s) - 2f(\lambda_s)]\kappa\sigma + f(\lambda_s)}{[1 + \sigma(\lambda_f + 3)][\lambda_s^3 - \lambda_s^2 \tanh(\lambda_s) - 2f(\lambda_s)]\kappa + (\lambda_f + 3)f(\lambda_s)} \right\} \quad (6)$$

by Chisnell (1987). Apart from using the correct boundary conditions, Chisnell also pointed out that the problem of the motion of a viscous sphere inside a fluid of different viscosity has two time scales, which are related to the diffusion of vorticity in the two fluids (that of the sphere and that of the external fluid). He managed to derive an accurate (albeit complicated) expression, in the Laplace domain, for the velocity of a viscous sphere in a gravitational field. This expression cannot be analytically transformed in the time domain, but Chisnell obtained its asymptotic behavior at short and long times. He also asserted that the drop remains spherical as long as the motion may be described by the Stokes equations.

It appears that Chisnell's work was not immediately and adequately noticed, because some works were published afterwards using the original erroneous formulation of the problem (Kim and Karila, 1991, Yang and Leal, 1991). The matter was revisited more recently by Galindo and Gerbeth (1993), Lovalenti and Brady (1993a), and Michaelides and Feng (1995). The last three studies extended Chisnell's work and presented the appropriate formulation and solution to the problem of an accelerating viscous sphere under creeping flow conditions.

The work of Michaelides and Feng (1995) and also Feng and Michaelides (1995) is the most recent and most general on the equation of motion of a viscous sphere at $Re \rightarrow 0$. Apart from considering the differences in the viscosities of the inside and outside fluids, they also considered the possibility of slip between the sphere and the fluid. Slip may occur in the cases when the diameter of the sphere is comparable in magnitude with the mean free path of the molecules of the surrounding fluid. Slip has been observed in materials processing studies, where nanoclusters are formed (Leung and Crowe, 1993), as well as in the motion of aerosol particles in the upper part of the atmosphere. It must be pointed out, that the case of slip at the surface of a rigid sphere was first contemplated by Basset (1888a), who formulated the appropriate boundary conditions to account for it, and that Happel and Brenner (1963) obtained analytically the steady-state solution of a sphere moving with slip.

It must be recognized that an analytical expression of the equation of motion of a viscous sphere inside a fluid of different viscosity cannot be obtained analytically in the time domain. This occurs because the problem has two time scales, and the resulting equations are too complex to yield analytical solutions, even in the limit $Re \rightarrow 0$. However, an analytical expression for the total hydrodynamic force in the Laplace (or Fourier) domain may be obtained using standard methods of analysis. Michaelides and Feng (1995) have obtained as-

ymptotic expressions for the total force on a viscous sphere at short and long times from the commencement of motion. Their equation of motion in a stationary frame of reference $Ox_1x_2x_3$ is as follows:

$$m_s \frac{dv_i}{dt} = (m_s - m_f)g_i + m_f \left. \frac{Du_i}{Dt} \right|_{v(t)} + F_i, \quad (5)$$

where $v_i(t)$ is the (arbitrary) velocity of the center of the viscous sphere, located at $Y(t)$, $u_i(x_i, t)$ is the velocity of the fluid and F_i is the hydrodynamic force exerted by the flow field, due to the disturbance created by the particle. The following expression for the disturbance force F_i has been obtained in the Laplace domain:

The overbar denotes the Laplace transform of a function; κ is the ratio of the dynamic viscosities ($\kappa = \mu_s/\mu_f$) and σ is a dimensionless parameter related to the slip coefficient ($\sigma = \mu_f/\beta\alpha$). The slip coefficient, β , is equal to the shear stress on the surface of the particle divided by the slip velocity at the surface of the sphere. This coefficient is the same as the one defined by Basset (1888a) and Happel and Brenner (1963). The parameters λ_f and λ_s are the two dimensionless length scales of the fluid and the viscous sphere in the Laplace domain:

$$\lambda_f = \sqrt{\frac{s\alpha^2}{\nu_f}} \quad \text{and} \quad \lambda_s = \sqrt{\frac{s\alpha^2}{\nu_s}} \quad (7)$$

The function f of Eq. (6) is defined by the following expression:

$$f(\xi) = (\xi^2 + 3) \tanh(\xi) - 3\xi. \quad (8)$$

Equations (5) through (8) represent the most general case of a spherical particle, bubble, or droplet motion to be encountered under creeping-flow conditions. It is no surprise that the equations are complex and that a general analytical solution in the time-domain is unfeasible. However, all practical cases may be modeled as special cases of (6). For example, when the interfacial slip is zero ($\sigma = 0$), the resulting expression is the same as the one derived by Galindo and Gerbeth (1993) or Lovalenti and Brady (1993a). When the sphere viscosity is infinite, the resulting expression is the one for a rigid sphere, and when the internal viscosity is zero, Eqs. (5) and (6) yield the equation of motion of a bubble.

Even at zero slip, an analytical expression for the hydrodynamic force exerted on a viscous sphere may only be obtained in the Laplace domain. Remarkably, the cases of infinite slip coefficient (which corresponds to $\sigma = 0$, or $\beta\alpha \gg \mu_f$) and of an inviscid sphere ($0 = \mu_s \ll \mu_f$) are equivalent and result in the same equation of motion. The Laplace transform of the hydrodynamic force for the latter case was obtained by Morrison and Stewart (1976) in an implicit form (through an integrodifferential equation) while Eq. (6) yields this force in an explicit form (Michaelides and Feng, 1995). It must be pointed out that in the case of an inviscid sphere moving in a viscous fluid, the steady-state drag is two thirds that of a solid sphere ($4\pi\mu_f\alpha V$).

A glance at Eq. (6) confirms that the three terms of the equation for a solid-sphere (added mass, history, and steady-state drag) are also part of the equation of the viscous sphere. These three terms ensue from the first three terms in the curly brackets ($\lambda_f^2/9$, λ_f , and 1, respectively). However, Eq. (6) also possesses the last residual term, whose physical significance is difficult to determine, and may not be categorized as easily as the other three terms. The presence of this term, and the fact

that Eq. (6) may be rearranged so as to obscure or even eliminate any of the three originally known terms, leads to the firm conclusion that the three terms of the Boussinesq/Basset expression are not independent forces.

One must note, on the subject of the motion of viscous spheres, the short bibliographical note by Pozrikides (1994) who points out, among other things, the contributions to the equation of motion by two Russian authors. In the field of applied research, the work by Sirignano (1993) and his coworkers (Silverman and Sirignano, 1994; Chiang and Sirignano, 1993; and Chiang et al., 1992) has contributed useful empirical correlations on the steady-state drag as well as the heat transfer and mass transfer coefficients. This work confirms that, at the very high droplet to fluid density ratios, one may perform accurate calculations by using only the empirical expressions for the steady-state part of the drag coefficient. Comer and Kleinstreuer (1995) extended these results and presented values of the drag coefficients for nonspherical particles and droplets. The common part of the last studies is that the expressions for the empirical coefficients emanate from numerical, rather than experimental studies.

Recent Developments on the Creeping Flow Equations of Motion

Equations of motion based on the creeping flow assumption or on the semiempirical modifications of the Basset/Boussinesq expression are still considered fairly accurate representations of the actual motion of particles, and are being extensively used in practice. Even with the knowledge that the equations for droplets or bubbles are fundamentally different, several researchers are still using with confidence equations such as (1) and (2), or corollaries of them. Of the more recent developments on this subject, Maxey and Riley (1983) presented a detailed derivation of the creeping flow equation of motion. In their derivation, they clearly stated the pertinent assumptions and clarified several intricate theoretical parts, which were not fully apparent in the past literature. The final equation they obtained (or a simplified version of it) has been extensively used in the last fourteen years. For this reason it is repeated here:

$$\begin{aligned}
 m_s \frac{dV_i}{dt} + \frac{1}{2} m_f \frac{d}{dt} \left(V_i - u_i - \frac{\alpha^2}{10} u_{i,jj} \right) \\
 + 6\pi\alpha\mu_f \left(V_i - u_i - \frac{\alpha^2}{6} u_{i,jj} \right) \\
 + \frac{6\pi\alpha^2\mu_f}{\sqrt{\pi\nu_f}} \int_0^t \frac{d}{d\tau} \left(V_i - u_i - \frac{\alpha^2}{6} u_{i,jj} \right) \frac{d\tau}{\sqrt{t-\tau}} \\
 = (m_p - m_f)g_i + m_f \frac{Du_i}{Dt} \quad (9)
 \end{aligned}$$

The Laplacian operator is denoted by the repeated index jj , and the derivative D/Dt is a total derivative following the particle. All the spatial derivatives are evaluated at the center of the sphere [which is at $Y_i(t)$]. The corrections to the relative velocity, which are due to the nonuniformity of the external field, are proportional to $u_{i,jj}$ and are sometimes called the "Faxén terms." In a subsequent derivation, Auton et al. (1988) showed that the first two terms of the added mass term should be $0.5m_f(dV_i/dt - Du_i/Dt)$. However, in the limit of zero Reynolds number this difference is not easily discernible. It must be pointed out that Eq. (9) pertains to a rigid sphere starting from rest, while Eqs. (5) to (8) are extensions, which include viscous

spheres (droplets and bubbles) as well as the possibility of slip at the interface.

In the case when the sphere is introduced in the fluid with a finite initial relative velocity, $w_{i0} [=V_i(0) - u_i(0)]$, there is an appendage to the history term, equal to $-6\pi\alpha\mu_f w_{i0}(\pi\nu t)^{-1/2}$. This term should be added to the end of the left-hand side of Eq. (9) as pointed out in Maxey (1987a). The extension arises from the fact that, when the solid sphere is introduced at a velocity different from the local fluid velocity, the disturbance would create a strong thin vorticity layer, which will result in an infinite initial drag. Although this initial force is infinite instantaneously, its effect on the particle velocity is finite, since the two-part history term is integrable (Michaelides, 1992). It must be pointed out that, while a finite initial velocity w_{i0} is mathematically plausible, the physical process of instantaneously introducing a solid sphere (and the associated disturbance field) in the fluid at $t = 0$ is impossible to achieve in practice. Real processes of particle introduction in fluid streams are achieved by mechanical injection devices, which modify the local velocity field of the fluid and exert an initial impulse on particles over a small, but finite time duration.

The work of Maxey and Riley (1983) exposed and rectified some of the omissions and errors of previous studies on the equation of motion of a rigid sphere. It also highlighted the assumptions used in the derivation of the creeping flow equation and made other researchers more aware of its limitations. Since 1983, several others realized the severity of the assumptions and began to question the justification of some of the previous uses of equations of particle motion. The first profound criticism of such expressions was put forward by Reeks and McKee (1984): While calculating the dispersion of particles, they found that the inclusion of the history term (their "Basset term") resulted in the (unreasonable) conclusion that the effect of the initial velocity of a particle on the distance traveled does not fade out at very long times. Thus, it appeared that the particles always retained the memory of their initial velocity, regardless of the viscosity of the fluid. This creates a paradox, because the dissipation due to the viscosity of the fluid is expected to eventually eradicate any memory of the initial velocity. The paradox would not have occurred if the history term decayed at a rate faster than $t^{-1/2}$.

Another shortcoming of the creeping flow equation of a sphere is its incompatibility with the experimentally observed phenomenon of lateral migration due to transverse lift. Leal (1992) gives a simple and convincing argument on this inconsistency. The case of the lift forces will be briefly examined in a later section of this manuscript.

Lawrence and Weinbaum (1986 and 1988) conducted a study on a rigid spheroid of revolution under creeping flow conditions. They used the method of decomposition of the outside velocity field and a second-order expansion for the eccentricity of the spheroid. As expected, they found that the eccentricity resulted in pertinent expansions for the added mass, history, and steady-state terms. What was unexpected in their study was the presence of an additional history term, which is entirely due to the eccentricity. This term is absent in the case of the sphere. It is also remarkable that the drag force contributed by the last term is frequency dependent. The study by Lawrence and Weinbaum raises questions on the applicability of equations such as (1) or (2) for nonspherical particles. In particular, it challenges the common practice of using the concept of an "equivalent diameter" to account for the shape of irregular solid particles.

Gavze's (1990) general mathematical work examines the tensors associated with the motion of a rigid particle of arbitrary shape and their symmetry properties. This work yields three terms, which may be associated with the added mass, the steady-state drag, and the history term. However, their form is a great deal more complex than that of Eqs. (1) and (2). This has added to the skepticism regarding the universal applicability of these equations in their prevailing forms.

The work on viscous spheres, which was mentioned in the previous section, also reinforced the arguments on the limitations of the original Boussinesq/Basset expression and on the early semiempirical equations to accurately model the unsteady motion of droplets and bubbles. It became apparent that the three terms of the transient hydrodynamic force are not independent components, but rather, the manifestation of a more complex functional in the very simple case of a solid sphere. Hence, attention was focused to new theories and to expressions emanating from more realistic assumptions. These led to the search for expressions, which in some way include the advective terms of the Navier-Stokes equations.

Equations for Finite Reynolds Numbers

Since the early studies by Stokes, Boussinesq, and Basset pertain to the development of the equation of motion in the limit of zero relative velocity, it was not long after their publication that the first studies appeared on the forces exerted by the fluid on a sphere at finite Reynolds numbers. Although the first attempts were for the steady-state problem, it is worth mentioning them because their final results have been extensively used in transient problems (under an implicit or explicit quasi-steady assumption). Whitehead (1889) made the first attempt at this problem. However, his method (an extension of Stokes' method) was unsuccessful because it did not exactly satisfy the boundary conditions at infinity. This led to a faulty result, which is sometimes referred to as "Whitehead's paradox." The paradox was resolved by Oseen (1910), who recognized that a singular asymptotic analysis is necessary for the solution of the problem. He identified two regions for the problem of the flow around the sphere at finite Reynolds numbers: (a) The inside region, where the advective term has a negligible effect on the momentum transport and where the problem may be adequately described by the so-called "Stokes equations:"

$$-\nabla^2 P + \mu \nabla^2 \tilde{u} = 0, \quad \nabla \cdot \tilde{u} = 0, \quad (10)$$

and (b) the outer region, where the advective term contributes significantly to the momentum transport and cannot be neglected. In this region, the flow should be described by a set of equations, which are sometimes called the "Oseen equations:"

$$-\nabla^2 P + \mu \nabla^2 \tilde{u} = \rho \tilde{V} \cdot \nabla \tilde{u}, \quad \nabla \cdot \tilde{u} = 0 \quad (11)$$

The difference between the Oseen equations and Stokes equations is the advective term. The boundary between the two regions defined by Oseen is at a distance equal to αRe^{-1} from the center of the sphere. This radius has been referred to by many as "the Oseen distance."

Oseen (1913, 1927) did not compute the velocity field around the sphere. His singular perturbation analysis yielded an improvement to the Stokes expression for the steady-state drag force, which is: $F = 6\pi\alpha\mu_f V(1 + 3 \text{Re}/8)$. The last term in the parenthesis is a correction to the Stokes drag, and is often referred to as "the Oseen correction." This correction represents a considerable practical improvement over Stokes' original expression. An experimental study by Maxworthy (1965) verified that the Oseen correction is more accurate than other empirical formulae up to $\text{Re} = 0.45$.

The velocity field around a solid sphere and a cylinder at steady-state was first calculated by Proudman and Pearson (1957) to $O(\text{Re})$. The two devised a technique to solve the singular perturbation problem that is associated with the two regions around the sphere. They essentially expanded the stream function in suitable polynomials, locally valid in the inner and outer regions of the flow. This enabled them to extend Oseen's result and, thus, calculate the steady-state drag coefficient to $O(\text{Re}^2)$. Brenner and Cox (1963) and Cox (1965) used the same technique and extended the theory to the case of a solid particle of arbitrary shape and to derive expressions for the drag

coefficient of such a particle. Riley (1968) discussed the inner and outer expansion of the velocity field for an oscillating sphere in a viscous fluid and pointed out some of the implicit assumptions used by previous researchers in conjunction with this problem.

Ockendon (1968) tackled the problem of the time-dependent motion of a sphere in a viscous fluid. He considered, however, only one time scale for the motion and proved that an asymptotic expansion in Re becomes invalid at long times. Therefore, the problem must be posed in terms of at least two time scales. He proved that the transient drag is considerably different from the steady-state drag in the asymptotic case, when the time scale of the particle is very long in comparison to that of the fluid. Ten years later, Bentwich and Miloh (1978) used a matched asymptotic expansion to calculate the transient force on a solid sphere, whose velocity undergoes a step temperature change, as well as of the velocity field around a solid sphere, on which a constant force is suddenly applied. Sano (1981) showed that the procedure used in the last study was incomplete. He succeeded in deriving the unsteady drag on a solid sphere in a quiescent fluid, which undergoes a step change in its velocity, $VH(t)$, correct to $O(\text{Re}^2)$. His dimensionless solution for the transient hydrodynamic force acting on the solid sphere is:

$$F(t) = 6\pi\alpha\mu_f V \left\langle H(t) + \frac{1}{3} \delta(t) + \frac{1}{\sqrt{\pi t}} + \frac{3}{8} \text{Re} \left[\left(1 + \frac{4}{\text{Re}^4 t^2} \right) \text{erf} \left(\frac{1}{2} \text{Re} t^{1/2} \right) + \frac{2}{(\pi t)^{1/2} \text{Re}} \left(1 - \frac{2}{\text{Re}^2 t} \right) \exp \left(-\frac{\text{Re}^2 t}{4} \right) - \frac{8}{3(\pi t)^{1/2} \text{Re}} \right] + \frac{9}{40} \text{Re}^2 \ln \text{Re} \right\rangle + O(\text{Re}^2) \quad (12)$$

Time in the last equation is made dimensionless by the quantity α^2/ν_f . The expression in the square brackets results from the contribution of the outer field and is a consequence of the use of the advective terms in the Oseen equations. For this reason, it has been referred to as the "Oseen contribution" (Lovalenti and Brady, 1993).

It must be pointed out that the last term of the Oseen contribution cancels the $(\pi t)^{-1/2}$ term of what may in analogy be called the "Boussinesq/Basset contribution." The remaining transient terms decay as follows:

$$t^{-2} \text{erf}(t^{1/2}) \sim t^{-3/2} \text{ (for } t < 1) \text{ or } \sim t^{-2} (t > 3)$$

$$t^{-1/2} \exp(-\frac{1}{4} \text{Re}^2 t)$$

and

$$t^{-1} \exp(-\frac{1}{4} \text{Re}^2 t)$$

The fact that the transients at long times decay faster than the conventional $t^{-1/2}$ rate, yields a satisfactory answer to the problem posed by Reeks and McKee (1984), which was discussed in the previous section: Under all the above rates, the particle trajectory in the viscous fluid will not retain any memory of the initial velocity at long times.

Mei, Lawrence, and Adrian (1991) conducted a numerical study on the motion of a rigid particle for $0 < \text{Re} < 50$ when the freestream velocity fluctuates with a small amplitude. Their numerical results indicate that, in the low frequency limit, the hydrodynamic force decays faster than the conventional $t^{-1/2}$ rate. Shortly thereafter, Mei and Adrian (1992) obtained an analytical solution for the motion at very low frequencies (SI

$\ll \text{Re} < 1$). A modified history term was obtained with an integration kernel, which at long times decays as t^{-2} .

The method used by Sano (1981) was followed by Lovalenti and Brady (1993b), who extended the previous results to derive the equation of motion of a particle when the fluid velocity is an arbitrary function of time. They derived a general expression for the hydrodynamic force on the particle, in terms of the Reynolds and Strouhal numbers. As with Sano's solution, the solution by Lovalenti and Brady is also valid for finite but small Reynolds numbers ($0 < \text{Re} < 1$). The same authors also confirmed the fact that the unsteady terms of the equation of motion decay much faster when the advection terms are retained. In the case of a sphere settling in a stagnant fluid, their equation reduces to the following expression:

$$F = -6\pi\mu_f\alpha\mathbf{V}(t) - \frac{2}{3}\pi\alpha\mu_f\text{Re}\text{Sl}\frac{dV}{dt} - \frac{6\mu_f\alpha V(t)}{t^{1/2}}(\pi\text{Re}\text{Sl})^{1/2} - \frac{9}{4}\mu_f\alpha(\pi\text{Re}\text{Sl})^{1/2}\int_0^t\frac{2}{(t-s)^{3/2}}\left[\frac{2}{3}V(t) - \left[\frac{1}{A^2}\left[\frac{\pi^{1/2}}{2A}\text{erf}(A) - \exp(-A^2)\right]\right]V(s)\right]ds \quad (13)$$

where the vector \mathbf{A} is given as

$$\dot{\mathbf{A}} = \frac{\text{Re}}{2}\sqrt{\frac{t-s}{\text{Re}\text{Sl}}}\int_s^t\dot{\mathbf{V}}(q)dq \quad (14)$$

In the manuscript by Lovalenti and Brady (1993b), there is a remarkable appendix by Hinch (1993) who presents simple arguments and asymptotic methods to explain the solutions obtained. Hinch reduces the effect of the Oseen contribution (that is, of the advection terms) to the action of sources and sinks associated with the presence of a wake behind the particle. His arguments are very simple to follow and are summarized here:

According to Hinch (1993) the velocity decay in the steady wake behind the spherical particle is:

$$U - u = \frac{3U\alpha}{2z}\exp\left(-\frac{U(x^2 + y^2)}{4z\nu_f}\right) \quad (15)$$

The momentum and mass deficits, due to this wake, are $6\pi\mu_f\alpha V$ and $6\pi\mu_f\alpha$ respectively. Therefore, during the process of start-up from rest, the wake is formed, diffuses downstream and the particle creates an additional force equal to

$$6\pi\mu_f\alpha\frac{3\alpha\nu_f}{2U^2t^2}\sim t^{-2} \quad (16)$$

During a stopping process, there is already a downstream wake, which diffuses cylindrically in the outer fluid. With no wake upstream, the particle experiences an additional force equal to

$$-6\pi\mu_f\alpha\frac{3\alpha}{4t}\sim t^{-1} \quad (17)$$

During a step increase of the velocity from V_0 to V_n , there are two wakes, the "old" and the "new," with the same total mass deficit $6\pi\mu_f\alpha$, the same width $(\nu t)^{1/2}$ but different false origins. Their combined effect on the particle reduces to a velocity disturbance, which is due to the exponentially small diffusion of vorticity. There is "an interesting competition" between the decay from the spatial variation and the growth from spreading with the age of the wake. If $V_0 > \frac{1}{2}V_n$, then the spatial decay predominates, while, if $V_0 < \frac{1}{2}V_n$, the temporal growth predomi-

nates. Thus, for a small velocity increase ($V_0/V_n = b$) the additional force is:

$$6\pi\mu_f\alpha\frac{3(1-b)}{8\pi^{1/2}(2-b)}t^{-5/2}\exp(-b^2t) \quad (18)$$

while, for a large velocity increase, this additional force becomes:

$$6\pi\mu_f\alpha\frac{3}{32(1-b)^2}t^{-2}\exp[-4b(1-b)t] \quad (19)$$

It is of interest to note that in all the asymptotic expressions, the transients decay faster than the original rate of $t^{-1/2}$. Hence, the memory of any initial velocity of the particle fades completely at long times.

The asymptotic behavior of the unsteady drag has also been the subject of a few very recent theoretical papers by Mei (1994) for an oscillating sphere, Lawrence and Mei (1995) for the motion induced by an impulse, and Lovalenti and Brady (1995) for an abrupt change of the velocity of the sphere.

It must be pointed out in conclusion, that the Boussinesq/Basset theory and the resulting expressions are exactly the same in the acceleration and the deceleration of a particle. Thus, the expressions are kinematically, but of course not thermodynamically, reversible with the reversal of the particle motion. Apparently, the inclusion of the advective terms brings kinematic irreversibilities in the forces and the motion of a particle. These effects are associated with the presence and advection of the wake downstream the sphere. For this reason, the form of the hydrodynamic force during a decelerating motion is substantially different from that of an accelerating motion. The transient force in both cases is nonlinear and has a strong dependence on the magnitude, as well as the direction, of the particle velocity. This observation, and the recent analytical results, may cast doubts on the semiempirical equation as well as on the form of the empirical coefficients (Eqs. (2) through (4)), since the latter are exactly the same for acceleration and deceleration. However, one must recall that the semiempirical equations emanate from experimental data at relatively high Reynolds numbers. This leads to the conclusion that the kinematic irreversibilities associated with the wake are either very weak to have been measured during the experiments, or they act on a particle at times much shorter than the characteristic times of the measurements. In the first case, the kinematic irreversibilities would not be significant at all, while in the second they would not be significant at relatively long durations of particle motion.

Lift Forces on a Small Sphere

Whereas the subject of this review article is mainly the rectilinear equation of motion, it would have been a serious omission not to mention, at least briefly, the effect of the transverse lift on a particle in rotating or shear flows. The lift plays an important role in the processes of lateral dispersion and migration of particles. This occurs because the lift force is one of the determining factors in 2-D and 3-D simulations of particle trajectories with any kind of transverse motion.

The solution of the Stokes or Oseen equations with flow shear or rotation is a very demanding task. For this reason, all the pertinent solutions of the equation of motion, which were mentioned above, essentially neglect both the effects of flow shear and rotation on the particles. Actually, one may prove that the presence of lift and lateral migration is inconsistent with the creeping flow equations, which are strictly for the rectilinear motion of a sphere (Leal, 1992).

The interest on the transverse lift acting on a particle can be traced to the time of Poiseuille (1841), who reported that blood cells keep away from the walls of capillaries. Since then, every observation on the motion of particles, droplets, or bubbles in pipe and channel flows has confirmed this early observation

and, hence, demonstrated the existence of a lateral force (Segre and Silberberg, 1962; Drew and Lahey, 1982; Tsuji et al., 1984) on particles, droplets, and bubbles moving inside boundary layers.

There are two causes for the lateral lift force on a spherical particle: The first is due to the rotation of a particle moving in a fluid with a different local translational velocity. This is usually called the "Magnus effect" (Magnus, 1861). The sphere may rotate because of collisions with a wall, interparticle collisions or, simply, because of the shear of the fluid. The second cause is the shear of the fluid itself, which may induce a lateral force on the sphere, even in the absence of rotation. This is sometimes called "the Saffman effect" (Saffman, 1965). It must be pointed out that it is impossible to calculate the spin of a sphere, without detailed knowledge of the mechanics of the particle collisions, or to even measure it accurately. For this reason, the Magnus force is usually absent in the calculations of the motion of spheres. On the other hand, the Saffman force is easily computed and studies frequently include it in two- or three-dimensional equations of motion.

Childress (1964) obtained a correction to the drag on a sphere in a rotating viscous fluid in terms of the Taylor number ($Ta = \Omega a^2 / \nu$). His work showed that one does not need the complete knowledge of the outer velocity field in order to determine the inner velocity field and, consequently, the drag force on the sphere (at least to the first order of approximation). His method was followed and expanded by Saffman (1965), who demonstrated that there is a lateral force on a sphere in shear flow, even if the sphere is not rotating. This force is equal to $(81.2\mu_r V \alpha^2 \Gamma^{1/2} / \nu^{1/2})$ where Γ is the fluid velocity gradient. Batchelor (1979) extended the result to the mass transfer from a sphere in a linear velocity field. The recent works of McLaughlin (1994) and Cherukat et al. (1994) show that the Saffman expression should be slightly modified, in order to take into account the proximity of the sphere to a wall, which is usually the cause for the shear. Michaelides (1981) used Saffman's expression of the lift force to explain the selective scaling in geothermal wells, while Wang et al. (1994) explained the behavior of drops near walls by also referring to the Saffman expression. The Saffman force has often been used as an (ad hoc) added component of the total hydrodynamic force in Lagrangian simulations of particles in nonuniform velocity fields. Although there is no strict theoretical justification for this practice, it must be recognized that the lift force becomes very important in many cases of lateral migration of particles, as for example, in the cases of particle deposition and resuspension from walls and bubble void fraction close to a wall. Because of this, in studies of the motion of particles, droplets, or bubbles inside strong shear fields, it is common practice to supplement the equation of rectilinear motion of the particle, with a transverse component, which usually emanates from the expression given by Saffman (1965). Kalio's (1993) study, which confirmed the relative importance of this force in the case of the particle deposition on walls, is typical of this practice.

Regarding rotating flows, the work by Ho and Leal (1974), and later by Vasseur and Cox (1976) sheds light on the lateral migration of particles in two-dimensional flows. A little known study by Feuillebois and Lasek (1978) reveals a history torque term (analogous to the history force term) in shear flows with particles. The review by Leal (1980) provides an overview of (among other subjects) the lateral motion of particles in non-Newtonian fluids. Recently, Auton (1987) and Auton et al. (1988) calculated the lift force on a sphere and proved that this force is made up of a rotational and an inertial component, similar to the added mass term. Also, the recent work of Stone and his coworkers (Stone, 1993; Tanzosh and Stone, 1994) contributes theoretical insights on the forces due to rotation, and links them to some practical applications. It must be pointed out, however, that the known analytical expressions of the lift force are still restricted to laminar flow, concurrent motion of

particle and fluid, linear shear and very small Reynolds numbers.

The Equation of Motion as Should Be Used in Practice

It is apparent that the unsteady hydrodynamic force acting on a particle has a complex form in the limit of zero Reynolds numbers and becomes even more complex at finite (but still very small for many practical applications) Reynolds numbers. Moreover, the exact value of the force in the last case is still unknown, because all pertinent expressions emanate from asymptotic expansions. This precludes the possibility of performing calculations with any known degree of accuracy by using the expressions derived for $0 < Re < 1$, which were introduced in the last section. Analytical expressions for the transient hydrodynamic force at $Re > 1$ (where a great deal of the engineering applications fall) are unknown to-date. From what we know so far, we can only deduce that they will greatly depend on both the Reynolds and the Strouhal numbers.

When performing engineering calculations, one needs to use an expression that is accurate enough to satisfy the precision of the overall problem, and yet simple enough to be used easily and repetitively (for example in stochastic simulations). At first glance, it appears that none of the forms of the hydrodynamic force on the particle (and to an extent the forms of the equation of motion) may be suitable for engineering applications. A moment's reflection, however, proves that relatively accurate calculations were made in the past and equipment design was successfully accomplished by using simplified equations of motion for particles, bubbles or droplets. In their vast majority, these expressions are simplified forms of the semiempirical equation, which has a sound empirical basis.

In a recent ASME *Symposium on Gas-Particle Flows* (Stock et al., 1995), there were forty-seven contributed papers, all of which used, in one way or another, expressions for the hydrodynamic force on the particles. Two invited papers in this symposium dealt directly with the influence of the transient terms. The vast majority of the contributed manuscripts pertain to the transient motion of particles. Most of the authors used the Stokes law for the drag or a simple empirical expression to model the hydrodynamic force. Several of the authors mentioned the existence of the transient terms (history and added mass). However, by using dimensional arguments or by referring to higher authority, all of these authors eventually neglected the transient terms in their calculations. In this case, the implicit assumption was made, that the particle motion may be described in a quasistatic way, and hence, the transient terms do not influence appreciably the quantities of their interest, which are usually time-averaged properties of the flow. Despite this simplification, the calculations in all the papers appear to lead to reasonable results, show agreement with experiments, and satisfy the required precision.

This practice is typical in heavy particle flows where the objective is to obtain an integrated quantity, such as the dispersion of particles, the length traveled by the particles, or the time-average velocity. In these cases, the transient terms of the force make a negligible contribution to the integrated results, because their values change signs frequently and their overall integrated effect becomes very small. In contrast, the integrated effect of the steady-state drag term is significant. Because the steady-state part is the major contributor to the final (time-averaged) result, the other transient parts may be conveniently neglected in most cases. While studying the effect of the history term on the average velocity and distance traveled by a particle in simulated transient flows, Vojir and Michaelides (1994) found ample support for this practice.

The cases of bubbly and slurry flows and where the desired result is an instantaneous and not a time-averaged quantity, are markedly different. In the case of slurry and bubbly flows, dimensional arguments suggest that the history and the added

mass terms are of comparable or higher order as the steady-state drag term. Li and Michaelides (1992) calculated that the history term accounts for about 25 percent of the instantaneous force on a sphere, when the density ratio is 2.7. This strongly recommends the inclusion of the transient terms in any equation of motion for slurries and bubbles.

Accounting for the added mass term in the equation of motion does not present any difficulties. The resulting equation is still explicit in the relative velocity of the sphere and may be solved analytically or numerically without difficulty. What complicates the solution procedure considerably, is the inclusion of the history integral term. Then the equation of motion becomes an integrodifferential equation, which is implicit in the relative or absolute velocity of the sphere. As a consequence, an iterative scheme must be adopted for the numerical solution of the equation. This results in a considerable increase of the computational time required. Especially when Lagrangian simulations of an ensemble of spheres are made, the inclusion of the history term slows the computations significantly. This is the main reason why the history term has often been conveniently neglected in many cases where other terms of lesser magnitude were included in the computations.

In order to speed up the computations, when the history term must be included, one may use an integrodifferential transformation for the equation of motion. This transforms the first-order implicit equation to a second-order equation, which is explicit in the relative velocity (Michaelides, 1992, Vojir and Michaelides, 1994). Thus, the semiempirical Eq. (2), when transformed, and written in terms of the relative velocity, $W_i = V_i - u_i$, appears in the following form:

$$\begin{aligned} \frac{d^2 W_i}{dt^2} + \gamma \left(2c_1 - \frac{9\phi\gamma\Delta_H^2}{2} \right) \frac{dW_i}{dt} + \gamma^2 c_1^2 W_i \\ = -\gamma(1-\phi) \frac{d^2 u_i}{dt^2} - \gamma^2(1-\phi) c_1 \frac{du_i}{dt} \\ + \gamma^2(1-\phi) \Delta_H \sqrt{\frac{9\phi}{2\pi}} \int_0^t \frac{d^2 u_i}{d\tau^2} \frac{d\tau}{(t-\tau)^{0.5}} \\ + \gamma \Delta_H \sqrt{\frac{9\phi}{2\pi t}} \left\langle \gamma(1-\phi) u'(0) - \gamma(1-\phi) G_i + c_1 \frac{V_{io}}{2t} \right\rangle \\ + \gamma^2(1-\phi) c_1 G_i + \gamma^2 V_{io} \frac{9\phi\Delta_H^2}{2} \delta(t) \\ + \gamma \Delta_H \sqrt{\frac{9\phi}{2\pi}} V_{io} \delta^2(t), \quad (20) \end{aligned}$$

with the following initial conditions for the velocity and acceleration:

$$\begin{aligned} W_i(0) = W_{io} \text{ and} \\ \frac{dW_i}{dt}(0) = -\gamma c_1 V_{io} - \gamma(1-\phi) u'_i(0) \\ + \gamma(1-\phi) G_i - V_{io} \gamma \Delta_H \sqrt{\frac{9\phi}{2\pi}} \delta(t) \quad (21) \end{aligned}$$

Equation (20) yields the transformed equation for the Bousinesq/Basset expression when all empirical coefficients are equal to 1. In the above two equations, V_i is the dimensionless relative velocity vector, the parameter ϕ is defined as the fluid to sphere density ratio, and the parameter γ , which is equal to $1/(1 + \frac{1}{2}\Delta_A\phi)$ includes the added mass coefficient. The time has been made dimensionless by using the characteristic time of the sphere ($\tau_s = 2\rho_s a^2/9\mu_f$) and the velocity by using the

characteristic velocity U_o . The dimensionless gravity vector is $G_i = g_i \tau_s / U_o$, where g_i is the gravitational acceleration. Because Eq. (20) is explicit in the relative velocity, an iterative numerical procedure is not needed for its solution. This has been observed to considerably reduce the required CPU time for repetitive calculations. However, care must be exercised when solving the transformed equation for $\phi > 1$, where it may become unstable. In addition, even the transformed explicit equation is computationally intensive when compared with an equation which excludes the history term. For this reason, it is always convenient and advantageous to neglect the history term, whenever, this practice can be thoroughly justified.

Recommendations

Calculations were conducted to determine the circumstances under which neglecting the history term will result in small and acceptable errors. For this purpose, we solved the semiempirical equation of motion [Eq. (2) or its transformed version, Eq. (20)] with the coefficients as in (4) in two ways: (a) by including all terms and (b) by setting $\Delta_H = 0$, thus neglecting the history term and keeping all the other terms. In both cases a simple, unidirectional, dimensionless, unsteady fluid velocity field was used: $u(t) = 1 + u'$, where u' is a random velocity field. This random field was obtained from a Gaussian distribution with standard deviation 0.1 and zero mean. Each random velocity component acts on the particle for a positive dimensionless interval, Δt , which is obtained from another Gaussian distribution. The inverse of the standard deviation of the latter distribution is an approximate measure of the dimensionless frequency, w , of the random velocity field.

The calculations were performed with the initial condition $W_{i0} = 0$. The density ratio and dimensionless standard deviation of the interaction time, Δt , were parameters in the calculations. The equation of motion was integrated and the distance traveled by the particle was calculated by a fourth-order Runge-Kutta scheme from $t = 0$ up to $t = 100\tau_s$ (for $\Delta t = 0.1$ and 1) and up to $t = 1000\tau_s$ (for $\Delta t = 10$ and 100). The trajectories of one thousand spherical particles were computed with and without taking into account the history terms. Hence, the 1-D longitudinal dispersion coefficient

$$D_x = \frac{1}{1000} \sum_{i=1}^{1000} \frac{(X_i - X_{av})^2}{X_{av}^2} \quad (22)$$

was computed, where X_i is the final position of the i th particle and X_{av} is the average distance traveled by all particles. The results for the dispersion coefficients and the percentage difference (error), resulting from the omission of the history term are shown in Figs. 1 to 4. The dimensionless interaction times, Δt of 0.1, 1, 10, and 100 correspond to approximate dimensionless frequencies, w , of 10, 1, 0.1 and 0.01, respectively. It must be pointed out that, since the dimensionless times and frequencies were obtained by dividing or multiplying by τ_s , a certain value of Δt or w denotes different dimensional frequencies for different spheres. Table A gives certain typical kinds of spheres, their characteristic times, and their actual frequencies (in Hz), which correspond to the values of the parameter Δt .

One may use Figs. 1 to 4 and Table A to determine the influence of the history term on the calculations of the dispersion coefficient, which is a time-averaged quantity. First, it is apparent that the history term is always important in the calculations, whenever $\rho_f/\rho_p > 1$. This range covers all types of bubbly flows and many types of solid-liquid flows (organic solid particles). Second, for heavy particles in air $\rho_f/\rho_p < 0.004$, the history term does not play an important role in the determination of the dispersion coefficient, even at the high range of fluid velocity frequencies. Thus, in the case of a small (0.1 mm) droplet, the error in the dispersion coefficient is less than 4 percent, even

Time standard deviation=0.1

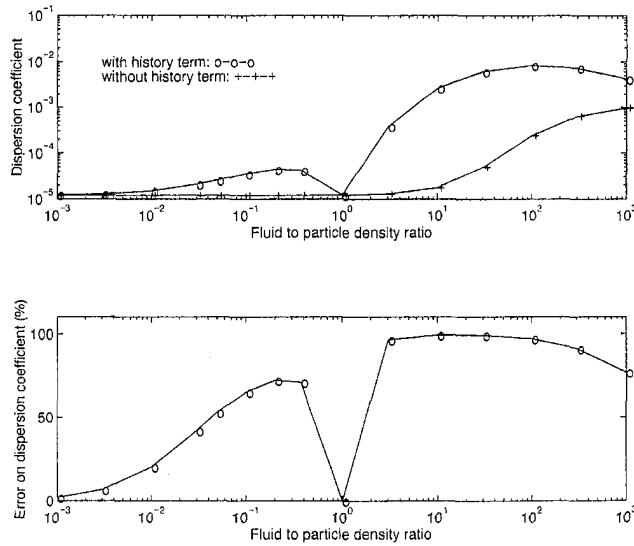


Fig. 1 Dispersion coefficient and error by neglecting the history term for fluid/particle interaction time, $\Delta t = 0.1$ ($w = 10$)

at fluid velocity frequencies of 81 Hz. Therefore, the history term may be justifiably omitted from these calculations. Third, the error in the range of density ratios $0.004 < \rho_f/\rho_p < 1$ depends very much on the type of particles and on the frequency of the fluid velocity fluctuations. The error is very low (less than 5 percent) at low frequencies, but becomes significant (more than 50 percent) at higher frequencies. In the case of a 0.1 mm sand particle in water, the error will be less than 8 percent if the fluid velocity frequencies were less than 17 Hz

Time standard deviation=10

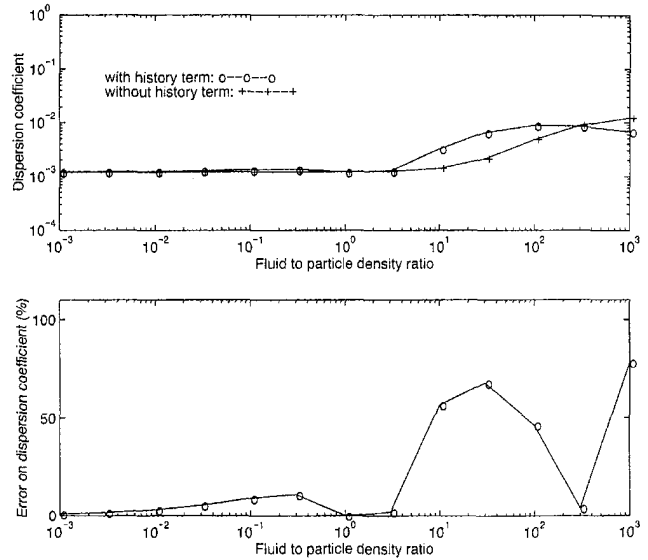


Fig. 3 Dispersion coefficient and error by neglecting the history term for fluid/particle interaction time, $\Delta t = 10$ ($w = 0.1$)

($\Delta t = 10$) and will reach almost 50 percent at frequencies of 1700 Hz.

The dispersion coefficient emanates from a time-averaged quantity, the total distance traveled. The errors shown in Figs. 1 to 4 are typical of those expected in the range of parameters covered, for the time-averaged quantities. Although, in principle, one has to determine the importance of the history terms in every application (by performing similar calculations), it is not expected that the results will differ substantially from those depicted in Figs. 1 to 4. Another deduction from our calculations

Time standard deviation=1

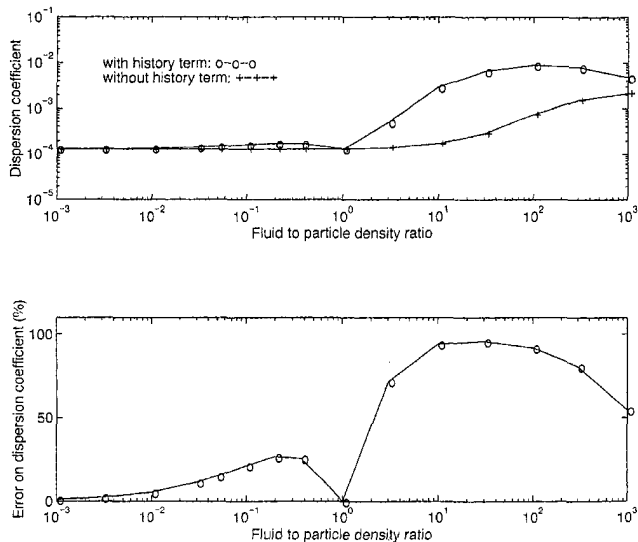


Fig. 2 Dispersion coefficient and error by neglecting the history term for fluid/particle interaction time, $\Delta t = 1$ ($w = 1$)

Time standard deviation=100

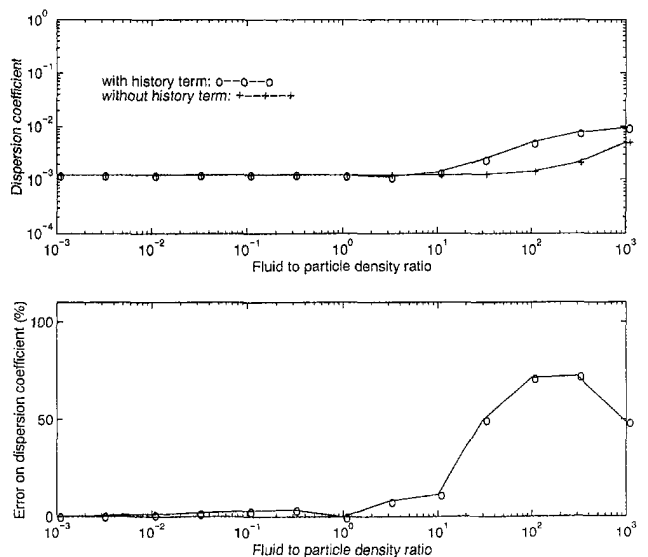


Fig. 4 Dispersion coefficient and error by neglecting the history term for fluid/particle interaction time, $\Delta t = 100$ ($w = 0.01$)

Table A Dimensional frequencies ω (Hz) in terms of Δt and w

	$\Delta t = 0.1$ $w = 10$	$\Delta t = 1$ $w = 1$	$\Delta t = 10$ $w = 0.1$	$\Delta t = 100$ $w = 0.01$
4 mm bubble in water ($\rho_f/\rho_s = 833, \tau_s = 4.26 \cdot 10^{-3}$ s)	2,343	234	23.4	2.34
1 mm bubble in water ($\rho_f/\rho_s = 833, \tau_s = 2.7 \cdot 10^{-4}$ s)	37,500	3,750	375	37.5
0.1 mm sand sphere in water ($\rho_f/\rho_s = 0.37, \tau_s = 6 \cdot 10^{-3}$ s)	1,667	167	16.7	1.67
0.1 mm droplet in air ($\rho_f/\rho_s = 0.0012, \tau_s = 0.123$ s)	81	8.1	0.81	0.081
10 μm particle in air ($\rho_f/\rho_s = 4 \cdot 10^{-4}, \tau_s = 3.7 \cdot 10^{-3}$ s)	2,700	270	27	2.7

is that the history term was always a significant fraction (more than 5 percent) of the instantaneous force on the sphere. This is especially evident in the early stages, after each random change of the fluid velocity, where it may reach 30–35 percent of the composite instantaneous force, even in the case of heavy particles ($\rho_s/\rho_f = 1000$). This indicates that, if a semiempirical expression is used, the history term should not be neglected at all in the calculations of the instantaneous force on the sphere.

In the case of heavy particle flows and especially when the variables of interest are integral quantities, the transient terms of the equation of motion are justifiably neglected. Oftentimes, the expression $c_1 = 1 + 0.15 \text{Re}^{0.667}$ is used for the steady-state drag term and the dimensionless equation of motion of a particle (in the absence of gravitational influence) becomes:

$$\frac{dV}{dt} = \frac{18\mu_f}{4\alpha^2\rho_p} (1 + 0.15 \text{Re}^{0.667})(U - V) \quad (23)$$

where U represents the uniform velocity of the fluid. It is tempting (and many authors have followed this procedure) to disregard the dependence of Re on the relative velocity ($\text{Re} = 2\alpha\rho_f|U - V|/\mu_f$) and to integrate explicitly Eq. (23), over a time step δt , to obtain:

$$V = U - (U - V_0) \exp(-f\delta t/\tau_s), \quad \text{with} \quad f = 1 + 0.15 \text{Re}^{0.667} \quad (23a)$$

It is obvious that f is considered as a constant in this integration process. Some have argued that if δt is small enough and f is updated in every step, the resulting error from expression (23a) is small. This argument notwithstanding, the above expression is not exact and will always be associated with an error. It has been proven (Michaelides, 1988) that the original Eq. (23) may be integrated exactly (over any time period t) to yield the following expression for the velocity of the particle:

$$V = V_0 + (U - V_0) \left[1 - \left[(1 + 0.15 \text{Re}_f^{0.667}) \times \exp\left(\frac{0.667t}{\tau_s}\right) - 0.15 \text{Re}_f^{0.667} \right]^{-1/0.667} \right] \quad (24)$$

where Re_f is a Reynolds number, which is based on the uniform velocity of the fluid ($\text{Re}_f = 2\alpha U\rho_f/\mu_f$). The importance of the correct integration of the simplified equation of motion on the velocity of the particle is shown in Fig. 5. This figure depicts the error in the calculation of the instantaneous velocity of a particle versus dimensionless time ($t^+ = t/\tau_s$). The fractional difference of the velocity shown is defined as the normalized difference of the (exact) results obtained from Eq. (24) with three versions of expression (23a). The solid curve represents results obtained for $\delta t/\tau_s = 1$ (the parameter f is not updated during the time of integration). The broken curve with dots represents results from Eq. (23a) when $\delta t/\tau_s = 0.1$ (f is updated ten times during the calculations). The broken line represents the fractional error in the instantaneous velocity arising from (23a) when $\delta t/\tau_s = 0.02$ (f is updated fifty times during the integration process from 0 to τ_s). It is obvious that, even in the

last case, the error in calculating the velocity of the particle at the inception of the process is more than 5 percent. The error in the calculation of the total distance traveled during the whole time interval τ_s , may be as high as 10 percent (Michaelides, 1988). Since Eq. (24) is simple to be programmed and exact, it is strongly recommended that it is used in preference to (23a) or similar expressions.

Another problem with the practical application of the equation of motion is the proximity of a particle to the wall. This subject is closely related to the studies of particle and droplet deposition, or bubble migration from walls. Studies on wall-drag reduction by a second phase (microbubbles) also fall in this category. It is well known that, to a first approximation, the steady-state drag of a sphere increases as the ratio α/y for small values of α/y , where y is the distance from the wall (Cox and Brenner, 1967). Very close to the wall (higher values of α/y) this increase is nonlinear and the drag coefficient is substantially enhanced. In this case, one must use empirical data and correlations on the modification of the drag coefficient (Happel and Brenner, 1965; Cox and Brenner, 1967; Kalio and Reeks, 1989; McLaughlin, 1994).

A more difficult problem to overcome seems to be that of the irregularly shaped particles, on which very few studies exist, either experimental or analytical. As mentioned above, the deviations from sphericity introduce complex terms in the equation of motion. The concept of an "equivalent diameter" is (at least from a theoretical point of view) inappropriate, and in the cases

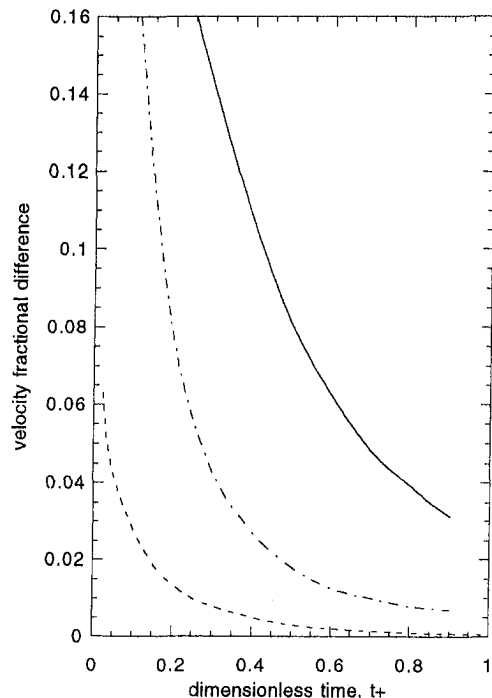


Fig. 5 Fractional error of the instantaneous velocity of a particle during the time interval [0 to τ_s]. — $\delta t = \tau_s$, - - - $\delta t = 0.1\tau_s$, - - - $\delta t = 0.02\tau_s$.

of drastic deviations from sphericity (e.g., dendritic shapes), appears to be inaccurate. A practical solution to this question may emerge from experimental work (Wiegand, 1995) on the unsteady forces in complex shaped particles, by numerical simulations for laminar flows, or by direct numerical simulations. By extensive and accurate physical or numerical experiments, empirical solutions to this problem will be found, at least for the shapes and processes of the highest practical interest.

Summary

The development of the equation of motion of particles, bubbles, and droplets has been in progress for more than one hundred and fifty years. The early works of Stokes, Boussinesq, and Basset on the creeping flow equation established the terms of the equation of motion of a sphere in the case of creeping flow as steady-state drag, history and added mass terms. Subsequent analytical work was aimed at the development of equations valid at finite Reynolds numbers. Experimental work was used to supplement the terms of the creeping flow equation with empirical coefficients and to extend the use of this equation to finite velocity differences and finite Reynolds numbers. Recent work on the subject generated analytical expressions valid for viscous spheres as well as for finite but small Reynolds numbers. The latter studies show that the history terms decay faster when fluid advection is taken into account. These studies also show that the acceleration process of a sphere is different than the deceleration process (there is a kinematic irreversibility in the equation of motion at finite Reynolds numbers). Despite the fact that an integrodifferential transformation may simplify and accelerate the calculations with the history term, it is still convenient and advantageous to neglect this term, if this practice can be justified. Calculations show that the history term may be justifiably neglected when the fluid to particle ratio is less than 0.004 (heavy particle flows). This term, as well as the added mass term should be retained when the density ratio is greater than 1. In the intermediate range, the significance of the history term depends on the characteristic frequencies of the flow, as shown in Table A. Finally, a little-known integrated form of the equation of motion is recommended to be used in the cases of heavy particles, when the history and added mass terms may be neglected.

Acknowledgments

The assistance of Dr. Feng and Messrs. Vojir and Henn in the original work and the calculations in this manuscript is very much appreciated. The original work of the author was partly supported by grants from the NSF, DOE (through the Tulane/Xavier CBR and CER) NASA-EPSCoR and LEQSF to Tulane University.

References

- Al-taweel, A. M., and Carley, J. F., 1971a, "Dynamics of Single Spheres in Pulsated Flowing Liquids: Part I. Experimental Methods and Results," *A.I.Ch.E. Symp. Ser.*, Vol. 67, No. 116, pp. 114–123.
- Al-taweel, A. M., and Carley, J. F., 1971b, "Dynamics of Single Spheres in Pulsated Flowing Liquids: Part II. Modeling and Interpretation of Results," *A.I.Ch.E. Symp. Ser.*, Vol. 67, No. 116, pp. 124–131.
- Auton, T. R., 1987, "The Lift Force on a Spherical Body in a Rotational Flow," *Journal of Fluid Mechanics*, Vol. 183, pp. 199–218.
- Auton, T. R., Hunt, J. R. C., and Prud'homme, M., 1988, "The Force Exerted on a Body in Inviscid Unsteady Non-uniform Rotational Flow," *Journal of Fluid Mechanics*, Vol. 197, pp. 241–257.
- Baird, M. H. I., Senior, M. G., and Thompson, R. J., 1967, "Terminal Velocities of Spherical Particles in a Vertically Oscillating Liquid," *Chemical Engineering Sciences*, Vol. 21, pp. 551–557.
- Basset, A. B., 1888a, *Treatise on Hydrodynamics*, Deighton Bell, London.
- Basset, A. B., 1888b, "On the Motion of a sphere in a Viscous Liquid," *Phil Transactions of the Royal Society of London*, Vol. 179, pp. 43–63.

- Batchelor, G. K., 1979, "Mass Transfer from a Particle Suspended in a Fluid with a Steady Linear Ambient Velocity Distribution," *Journal of Fluid Mechanics*, Vol. 95, p. 369.
- Bentwich, M., and Miloh, T., 1978, "The unsteady Matched Stokes-Oseen Solution for the Flow past a Sphere," *Journal of Fluid Mechanics*, Vol. 88, pp. 17–32.
- Boussinesq, 1885a, *Applications à l'étude des potentiels*, (reedition 1969) Blanchard, Paris.
- Boussinesq, 1885b, "Sur la Resistance qu' Oppose un Liquide Indefini en Repos. . ." *Comptes Rendu, Acad. Sci.*, Paris, Vol. 100, pp. 935–937.
- Brenner, H., 1963, "Forced Convection Heat and Mass Transfer at Small Peclet Numbers from a Particle of Arbitrary Shape," *Chemical Engineering Sciences*, Vol. 18, p. 109.
- Brenner, H., and Cox, 1963, "The Resistance to a Particle of Arbitrary Shape in Translational Motion at Small Reynolds Numbers," *Journal of Fluid Mechanics*, Vol. 17, pp. 561–575.
- Cherukat, P., McLaughlin, J. B., and Graham, A. L., "The Inertial Lift on a Rigid Sphere translating in a Linear shear Flow Field," *International Journal of Multiphase Flows*, Vol. 20, 339–353.
- Chiang, C. H., Raju, M. S., and Sirignano, W. A. 1992, "Numerical Analysis of Convecting, Vaporizing, Fuel Droplets with Variable Properties," *International Journal of Heat and Mass Transfer*, Vol. 35, pp. 1307–1324.
- Chiang, C. H., and Sirignano, W. A. 1993, "Interacting Convecting, Vaporizing, Fuel Droplets with Variable Properties," *International Journal of Heat and Mass Transfer*, Vol. 36.
- Childress, S., 1964, "The slow Motion of a Sphere in a Rotating Viscous Fluid," *Journal of Fluid Mechanics*, Vol. 20, pp. 305–314.
- Chisnell, R. F., 1987, "The unsteady Motion of a Drop Moving Vertically under Gravity," *Journal of Fluid Mechanics*, Vol. 176, pp. 434–464.
- Clebsch, H., 1856, "Über die Bewegung einer Ellipsoids in einer tropfbaren Flüssigkeit," *Crelle*, Vol. 52, pp. 103–121.
- Clamen, A., and Gauvin, W. H., 1969, "Effects of Turbulence on the Drag Coefficients of Spheres in a Supercritical Flow Regime," *A. I. Ch. E. Journal*, Vol. 15, pp. 184–189.
- Clift, R., Grace, J. R., and Weber, M. E., 1978, *Bubbles, Drops and Particles*, Academic Press, New York.
- Comer, J. K., and Kleinstreuer, C. 1995, "A Numerical Investigation of Laminar Flow Past Nonspherical Solids and Droplets," *ASME JOURNAL OF FLUIDS ENGINEERING*, Vol. 117, pp. 170–175.
- Corssin, S., and Lumley, J. L., 1957, "On the Equation of Motion of a Particle in a Turbulent Fluid" *Applied Scientific Research*, Section A, Vol. 6, pp. 114–116.
- Cox, R. G., 1965, "The Steady Motion of a Particle of Arbitrary Shape at Small Reynolds Numbers," *Journal of Fluid Mechanics*, Vol. 23, pp. 625–543.
- Cox, R. G., and Brenner, H., 1967, "The slow motion of a Sphere through a Viscous Fluid towards a plane Surface," *Chemical Engineering Sciences*, Vol. 22, pp. 1753–1777.
- Crowe, C. T., Sharma, M. P., and Stock, D. E., 1977, "The Particle Source-Cell (PSI-CELL) Model for Gas-Droplet Flows" *ASME JOURNAL OF FLUIDS ENGINEERING*, Vol. 99 pp. 325–332.
- Drew, D., and Lahey, R. T., 1982, "Phase Distribution Mechanisms in Turbulent Two-Phase Flow in a Circular Pipe," *Journal of Fluid Mechanics*, Vol. 117, pp. 91–106.
- Dryden, H. L., Murnaghan, F. P., and Bateman, H. 1956, *Hydrodynamics*, Dover.
- Faxén, 1922, "Der Widerstand gegen die Bewegung einer starren Kugel in einer zähen Flüssigkeit, die zwischen zwei parallelen Ebenen Wänden eingeschlossen ist" *Annalen der Physik*, Vol. 4, pp. 89–119.
- Feng, Z.-G., and Michaelides, E. E., 1995, "History Terms in the Momentum and Energy Equations of Particles," *Proceedings, 2nd Intern. Conf. on Multiphase Flows*, Kyoto.
- Feuillebois, F., and Lasek, A., 1978, "On the Rotational Historic Term in Non-Stationary Shear Flow," *Quarterly Journal of Mechanical Applied Mathematics*, Vol. 31, pp. 435–443.
- Galindo, V., and Gerbeth, G., 1993, "A Note on the Force on an Accelerating Spherical Drop at Low Reynolds Numbers," *Physics of Fluids*, Vol. 5(12), pp. 3290–3292.
- Gavze, 1990, "The Accelerated Motion of Rigid Bodies in Non-steady Stokes Flow," *International Journal of Multiphase Flow*, Vol. 16, pp. 153–166.
- Govier, G. W., and Aziz, K., 1977 (reprint), *The Flow of Complex Mixtures in Pipes*, Kruger Publ., Huntington.
- Green, G., 1833, "Researches on the Vibration of Pendulums in Fluid Media," *Transactions of Royal Society of Edinburgh*, Vol. 13, pp. 54–68.
- Gyarmathy, G., 1982, "The Spherical Droplet in Gaseous Carrier Streams: Review and Synthesis," *Multiphase Science and Technology*, Vol. 1, G. F. Hewitt, J. M. Delhaye and N. Zuber, eds., Hemisphere, Washington.
- Happel, J., and Brenner, H., 1986, *Low Reynolds Number Hydrodynamics*, Martinus Nijhoff Publ., reprint, orig. publ. 1963.
- Hill, P. G., Witting, H., and Demetri, E. P., 1963, "Condensation of Metal Vapors during Rapid Expansion," *ASME Journal of Heat Transfer*, Vol. 85, pp. 303–317.
- Hinch, E. J., 1993, "The Approach to Steady State in Oseen Flows," *Journal of Fluid Mechanics*, Vol. 256, 601–603.
- Hinze, J. O., 1971, "Turbulent Fluid and Particle Interaction," *Progress in Heat and Mass Transfer*, Vol. 6, pp. 433–452.
- Hjelmfelt, A. T., and Mockros, L. F., 1966, "Motion of Discrete Particles in a Turbulent Fluid," *Applied Scientific Research*, Vol. 16, pp. 149–161.

- Ho, B. P., and Leal, L. G., 1974, "Inertial Migration of Rigid Spheres in Two-Dimensional Unidirectional Flows," *Journal of Fluid Mechanics*, Vol. 65, pp. 365–400.
- Hubbard, G. L., Denny, V. E., and Mills, A. F., 1975, "Droplet Evaporation Effects of Transients and Variable Properties," *International Journal of Heat & Mass Transfer*, Vol. 18, pp. 1003–1008.
- Hughes, R. R., and Gilliland, E. R. 1952, "The Mechanics of Drops," *Chemical Engineering Progress*, Vol. 48, pp. 497–504.
- Kalio, G. A., and Reeks, M. W. 1989, "A Numerical Simulation of Particle Deposition in Turbulent Boundary Layers," *International Journal of Multiphase Flow*, Vol. 15, pp. 433–446.
- Kalio, G. A., 1993, "Random Walk modeling of Particle Deposition," *Gas-Solid Flows-1993*, Stock et al., eds., ASME FED, vol. 166, pp. 161–167.
- Karanfilian S. K., and Kotas, T. J., 1978, "Drag on a Sphere in Unsteady Motion in a Liquid at Rest," *Journal of Fluid Mechanics*, Vol. 87, pp. 85–96.
- Kim, S., and Karila, S. J., 1991, *Microhydrodynamics: Principles and Selected Applications*, Butterworth-Heinemann, Boston.
- Konoplin, N., 1971, "Gravitationally Induced Acceleration of Spheres in a Creeping Flow," *American Institute of Chemical Engineering Journal*, Vol. 17, pp. 1502–1503.
- Lamb, H., *Hydrodynamics*, Cambridge Univ. Press, 1932.
- Lawrence, C. J., and Weinbaum, S., 1986, "The Force on an Axisymmetric Body in Linearized Time-Dependent Motion: A New Memory Term" *Journal of Fluid Mechanics*, Vol. 171, pp. 209–218.
- Lawrence, C. J., and Weinbaum, S., 1988, "The Unsteady Force on a Body at Low Reynolds Number; the Axisymmetric Motion of a Spheroid," *Journal of Fluid Mechanics*, Vol. 189, pp. 463–498.
- Lawrence, C. J. and Mei, R. 1995, "Long-time Behavior of the Drag in Impulsive Motion," *Journal of Fluid Mechanics*, Vol. 283, pp. 307–327.
- Leal, L. G., 1980, "Particle Motions in a Viscous Fluid," *Annual Review of Fluid Mechanics*, Vol. 12, pp. 435–476.
- Leal, L. G., 1992, *Laminar Flow and Convective Transport Processes*, Butterworth-Heinemann, Boston.
- Leung, A. L., and Crowe, C. T., 1993, "Collection of Nanoclusters by Thermophoresis" *Gas-Solid Flows-1993*, D. E. Stock et al., eds., ASME, New York.
- Li, L., and Michaelides, E. E., 1992, "The Magnitude of Basset Forces in Unsteady Multiphase Flow Computations," *ASME JOURNAL OF FLUIDS ENGINEERING*, Vol. 114, pp. 352–355.
- Linteris, G. T., Libby, P. A., and Williams, F. A., 1991, "Droplet Dynamics in a Non-Uniform Field" *Combustion Science and Technology*, Vol. 80, pp. 319–335.
- Lovalenti, P. M., and Brady, J. F., 1993a, "The Force on a Bubble, Drop or Particle in Arbitrary Time-Dependent Motion at Small Reynolds Numbers," *Physics of Fluids A*, Vol. 5, pp. 2104–2116.
- Lovalenti, P. M., and Brady, J. F., 1993b, "The Hydrodynamic Force on a Rigid Particle Undergoing Arbitrary Time-Dependent Motion at Small Reynolds Numbers," *Journal of Fluid Mechanics*, Vol. 256, pp. 561–601.
- Lovalenti, P. M., and Brady, J. F., 1995, "Force on a Body in Response to an Abrupt Change in Velocity at Small but Finite Reynolds Number," *Journal of Fluid Mechanics*, Vol. 293, pp. 35–46.
- Magnus, G., 1861, "A Note on the Rotary Motion of the Liquid Jet," *Annalen der Physik und Chemie*, Vol. 63, pp. 363–365.
- Maxey M. R., and Riley, J. J., 1983, "Equation of Motion of a Small Rigid Sphere in a Non-uniform Flow" *Physics of Fluids*, Vol. 26, pp. 883–889.
- Maxey, M. R., 1987a, "The Motion of Small Spherical Particles in a Cellular Flow Field," *Physics of Fluids*, Vol. 30, pp. 1915–1928.
- Maxey, M. R., 1987b, "The gravitational Settling of Aerosol Particles in Homogeneous Turbulence and Random Flow Fields," *Journal of Fluid Mechanics*, Vol. 174, pp. 441–465.
- Maxey, M. R., 1993, "The Equation of Motion for a Small Rigid Sphere in a Nonuniform Unsteady Flow," *Gas-Solid Flows-1993*, D. E. Stock et al., eds., ASME, 1993.
- Maxworthy, T., 1965, "Accurate Measurements of a Sphere Drag at Low Reynolds Numbers," *Journal of Fluid Mechanics*, Vol. 23, pp. 369–372.
- McLaughlin, J. B., 1994, "Numerical Computation of Particles-Turbulence Interaction," *International Journal of Multiphase Flow*, Vol. 20, pp. 211–232.
- Mei, R., 1994, "Flow due to an Oscillating Sphere and an Expression for Unsteady Drag on the Sphere at Finite Reynolds Numbers," *Journal of Fluid Mechanics*, Vol. 270, pp. 133–174.
- Mei, R., Lawrence, C. J., and Adrian, R. J., 1991, "Unsteady Drag on a Sphere at Finite Reynolds Number with Small Fluctuations in the Free-Stream Velocity," *Journal of Fluid Mechanics*, Vol. 233, pp. 613–631.
- Mei, R., and Adrian, R. J., 1992, "Flow past a Sphere with an Oscillation in the Free-Stream and unsteady Drag at Finite Reynolds Number," *Journal of Fluid Mechanics*, Vol. 237, pp. 323–341.
- Michaelides, E. E., 1981, "The Effect of Magnus Force on the Deposition of the Geothermal Wells," *ASME Journal of Energy Resources Technology*, Vol. 103, p. 352–355.
- Michaelides, E. E., 1988, "On the Drag Coefficient and the Correct Integration of the Equation of Motion of Particles in Gases" *ASME JOURNAL OF FLUIDS ENGINEERING*, Vol. 110, pp. 339–342.
- Michaelides, E. E., 1992, "A Novel Way of computing the Basset Term in Unsteady Multiphase Flow Computations," *Physics of Fluids*, Vol. A4, pp. 1579–1582.
- Michaelides, E. E., and Feng, Z.-G., 1995, "The Equation of Motion of a Small Viscous Sphere in an Unsteady Flow with Interface Slip," *International Journal of Multiphase Flow*, Vol. 21, pp. 315–321.
- Michaelides, E. E., Li, L., and Lasek, A., 1992, "The Effect of Turbulence on the Phase Change of Droplets and Particles under Nonequilibrium Conditions," *International Journal of Heat and Mass Transfer*, Vol. 34, pp. 601–609.
- Moore, M. J., and Sieverding, C. H., 1976, *Two-Phase Steam Flow in Turbines and Separators*, Hemisphere, Washington.
- Morrison, F. A., and Stewart, M. B., 1976, "Small Bubble Motion in an Accelerating Fluid," *ASME Journal of Applied Mechanics*, Vol. 97, pp. 399–402.
- Ockendon, J. R., 1968, "The unsteady Motion of a Small Sphere in a Viscous Fluid," *Journal of Fluid Mechanics*, Vol. 34, pp. 229–239.
- Odar, F., and Hamilton, W. S., 1964, "Forces on a Sphere Accelerating in a Viscous Fluid," *Journal of Fluid Mechanics*, Vol. 18, pp. 302–303.
- Odar, F., 1966, "Verification of the Proposed Equation for Calculation of the Forces on a Sphere Accelerating in a viscous Fluid" *Journal of Fluid Mechanics*, Vol. 25, pp. 591–592.
- Odar, F., 1968, "Unsteady Motion of a Sphere along a Circular Path in a Viscous Fluid," *ASME Journal of Applied Mechanics*, Vol. 86, pp. 652–654.
- Oseen, C. W., 1910, "Über die Stokes'sche Formel und über eine verwandte Aufgabe in der Hydrodynamik," *Ark. Mat. Astron. Fysik*, Vol. 6, no. 29.
- Oseen, C. W., 1913, "Über den Gültigkeitsbereich der Stokesschen Widerstandsformel," *Ark. Mat. Astron. Fysik*, Vol. 9, no. 19.
- Oseen, C. W., 1927, *Hydrodynamik*, Leipzig.
- Poiseuille, J. L. M., 1841, "Recherches sur le Mouvement du Sang dans les Vein Capillaires," *Mem. de l'Acad. Roy. des Sciences*, Vol. 7, pp. 105–175.
- Poisson, S. A., 1831, "Mémoire sur les Mouvements simultanés d'un pendule et de l'air environnant," *Mem. de l'Academie des Sciences*, Paris, Vol. 9, p. 521–523.
- Pozrikides, C., 1994, "A Bibliographical Note on the Unsteady Motion of a Spherical Drop at Low Reynolds Numbers," *Physics of Fluids*, Vol. 6(9), pp. 3209–3210.
- Pozrikides, C., 1996, *Introduction to Theoretical and Computational Fluid Dynamics*, Oxford Univ. Press, Oxford.
- Proudman I., and Pearson, J. R. A., 1956 "Expansions at Small Reynolds Numbers for the Flow past a Sphere and a circular Cylinder," *Journal of Fluid Mechanics*, Vol. 2, pp. 237–262.
- Reeks, M. W., and McKee, S., 1984 "The Dispersive Effects of Basset History Forces on Particle Motion in Turbulent Flow," *Physics of Fluids*, Vol. 27, pp. 1573–1582.
- Riley, N., 1966, "On a Sphere Oscillating in a Viscous Fluid," *Quarterly Journal of Applied Mathematics*, Vol. 19, pp. 461–472.
- Rowe, P. N. 1961, "The Drag Coefficient of a Sphere," *Transactions of Institute of Chemical Engineering*, Vol. 39, pp. 175–181.
- Saffman, P. G., 1965, "The Lift on a Small Sphere in a Slow Shear Flow," *Journal of Fluid Mechanics*, Vol. 22, 385.
- Sangani, A. S., Zhang, D. Z., and Prosperetti, A., 1991, "The Added Mass, Basset and Viscous Drag Coefficients in Nondilute Bubbly Liquids Undergoing Small-Amplitude Oscillatory Motion," *Physics of Fluids*, Vol. A3, pp. 2955–2970.
- Sano, T., 1981 "Unsteady Flow past a sphere at Low Reynolds Number," *Journal of Fluid Mechanics*, Vol. 112, pp. 433–441.
- Schoneborn, P. R., 1975, "The Interaction between a single Sphere and an Oscillating Fluid," *International Journal of Multiphase Flows*, Vol. 2, pp. 307–317.
- Segre, G., and Silberberg, A., 1962, "Behavior of Macroscopic Rigid Spheres in Poiseuille Flow," *Journal of Fluid Mechanics*, Vol. 14, pp. 115–157.
- Silverman, I., and Sirignano, W. A., 1994, "Multidroplet Interaction Effects in Dense Sprays," *International Journal of Multiphase Flows*, Vol. 20, pp. 99–116.
- Sirignano, W. A., 1993, "Fluid Dynamics of Sprays," *ASME JOURNAL OF FLUIDS ENGINEERING*, Vol. 115, pp. 345–378.
- Sobel, D., 1995, *Longitude*, Penguin Books, New York.
- Soo, S. L., 1990, *Multiphase Fluid Dynamics*, Science Press, Beijing.
- Stock, D. E., 1996, "Particle Dispersion in Flowing Gases," *ASME JOURNAL OF FLUIDS ENGINEERING*, Vol. 118, pp. 4–17.
- Stock, D. E., Reeks, M. W., Tsuji, Y., Michaelides, E. E., and Gautam, M., 1993, *Gas-Particle Flows*, FED, Vol. 173, ASME, New York.
- Stock, D. E., Reeks, M. W., Tsuji, Y., Michaelides, E. E., and Gautam, M., 1995, *Gas-Particle Flows*, FED, Vol. 228, ASME, New York.
- Stokes, G. G., 1845, On the Theories of Internal Friction of the Fluids in Motion" *Transactions Cambridge Philos. Society*, Vol. 8, pp. 287–319.
- Stokes, G. G., 1851, "On the Effect of the Internal Friction of Fluids on the Motion of a Pendulum," *Transactions Cambridge Phil. Society*, 9, pp. 8–106.
- Stone, H. A., 1993, "An Interpretation of the Translation of Drops and Bubbles at High Reynolds Numbers in Terms of the Vorticity Field," *Physics of Fluids*, Vol. 10, pp. 2567–2569.
- Sy, F., Taunton, J. W., and Lightfoot, E. N., 1970, "Transient Creeping Flow around Spheres," *American Institute of Chemical Engineering Journal*, Vol. 16, pp. 386–391.
- Sy, F., and Lightfoot, 1971, "Transient Creeping Flow around Fluid Spheres," *American Institute of Chemical Engineering Journal*, Vol. 17, pp. 177–181.
- Tanzosh, J., and Stone, H. A., 1994, "Motion of rigid Particles in a Rotating Viscous Fluid: an Integral Equation Approach," *Journal of Fluid Mechanics*, Vol. 175, pp. 225–256.
- Tchen, C. M., 1947, "Mean Values and Correlation Problems Connected with the Motion of Small Particles Suspended in a Turbulent Fluid," Doctoral Dissertation, Delft, Holland.
- Temkin, S., and Mehta, H. K., 1982, "Droplet Drag in an accelerating and decelerating Flow," *Journal of Fluid Mechanics*, Vol. 116, pp. 297–313.

- Tsuji, Y., Morikawa, Y., and Shinomi, H., 1984 "LDV Measurements of Air-Solid Two-Phase Flow in a Vertical Pipe," *Journal of Fluid Mechanics*, Vol. 139, pp. 417-434.
- Tsuji, Y., Kato, N., and Tanaka, T., 1991, "Experiments on the Unsteady Drag and Wake of a Sphere at High Reynolds Numbers" *International Journal of Multiphase Flow*, Vol. 17, pp. 343-354.
- Vasseur, P., and Cox, R. G., 1976, "The Lateral Migration of Spherical Particles in Two-Dimensional shear Flow," *Journal of Fluid Mechanics*, Vol. 78, pp. 385-413.
- Villat, H., 1943, *Lecons sur les Fluides Visqueux*, Gauthier-Villars, Paris, 1943.
- Vojir, D. J., and Michaelides, E. E., 1994, "The Effect of the History Term on the motion of Rigid Spheres in a viscous Fluid," *International Journal of Multiphase Flows*, Vol. 20, pp. 547-556.
- Wallis, G. B., 1969, *One-Dimensional Two Phase Flow*, McGraw-Hill, New York.
- Wang, L. P., and Stock, D. E., 1994, "Numerical Simulation of Heavy Particle Dispersion-Scale Ratio and Flow Decay Considerations," *ASME JOURNAL OF FLUIDS ENGINEERING*, Vol. 116, pp. 154-163.
- Wang, M. R., Huang, D. Y., and Liu, Y. C., 1994, "Droplet Dynamics near the Wall in a Vertical Rectangular Duct," *ASME JOURNAL OF FLUIDS ENGINEERING*, Vol. 116, pp. 349-353.
- Whitehead, A. N., 1889, "Second Approximation to Viscous Fluid Motion. A Sphere moving steadily in a Straight Line," *Quarterly Journal of Mathematics*, Vol. 23, pp. 143-152.
- Wiegand, S. F., 1995, "The Measuring of Drag Forces acting on an Equiaxed Dendrite using Vision Tracking Technique," M.S.E. thesis, Tulane University.
- Yang, S.-M., and Leal, L. G., 1991, "A Note on Memory-Integral Contributions to the Force of an Accelerating Spherical Drop at Low Reynolds Number," *Physics of Fluids A*, Vol. 3, pp. 1822-1824.

W. Rodi

Professor,
Institut für Hydromechanik,
Universität Karlsruhe,
Karlsruhe, Germany

J. H. Ferziger

Professor,
Department of Mechanical Engineering,
Stanford University Stanford, CA 94305-
3030

M. Breuer

Researcher.

M. Pourquié

Researcher.

Institut für Hydromechanik,
Universität Karlsruhe,
Karlsruhe, Germany

Status of Large Eddy Simulation: Results of a Workshop

1 Introduction

The mixed quality of the results obtained with conventional (Reynolds averaged) turbulence models i.e., those used in conjunction with the Reynolds averaged Navier-Stokes or RANS equations, together with the continually decreasing cost of doing computations, has led to increased interest in the possibility of using large eddy simulation (LES) as a tool for prediction of practical turbulent flows. This paper is, in large part, a summary of the results presented at a conference designed to assess the current state of the art in LES for complex flows and the conclusions reached on the basis of those results.

Large eddy simulation was first applied to engineering flows by Deardorff (1970). In the early days, its application was limited to simple flows and to a small number of groups fortunate enough to have access to supercomputers. In essence, it was developed to complement laboratory experiments in the investigation of the fundamental processes that occur in relatively simple turbulent flows. When the capability of computers increased still further in the 1980s, it became possible to perform direct numerical simulations (DNS) of interesting flows and the latter became the preferred approach to fundamental studies of turbulence. More recently, the possibility of simulating more complex flows has reawakened interest in LES; interest centers on flows too difficult to treat with DNS, mainly ones in complex geometries. The decreasing cost of computing has also put the possibility of using LES into the hands of many more people.

The success that LES has had is, in the opinion of the authors, largely due to careful selection of target flows and the parameters used in the simulations. There is a danger that this success may give some people the impression that success is automatic and thus lead to over-optimism that LES is bound to be successful. This impression is, of course, not correct; a great deal of research is required before it will be known how widely the method can be used.

As with any method, there is a need for continuous assessment of the models, numerical methods, and geometrical treatments that are used in LES of complex flows. It is time to begin to perform such assessments. It was for precisely this reason that the authors coordinated a workshop designed to assess the present state of the art in LES of complex flows (Workshop on Large Eddy Simulation of Flows past Bluff Bodies). It was held in Rottach-Egern, Germany on 26–28 June 1995. The participants, all of whom were required to submit results of simulations, are listed in Tables 3, 5, and 6.

In the remainder of this paper we shall present a short overview of LES, the subgrid scale models that are used in LES, the numerical methods used, results obtained for two complex flows, and an assessment of those results.

2 A Short Overview of LES

The methods and models used in large eddy simulation have been presented in many papers. It is traditional in such papers to present the equations anew each time but, by now, the fundamental equations that are solved in LES should be familiar to most readers, making another presentation of them unnecessary. Accordingly, we shall break with tradition and not write the detailed equations here. Rather, a short description of them will be given. The reader desiring an introduction to the practice of LES is referred to articles by Ferziger (1983), Moin and Rogallo (1984), Ferziger (1996), and Breuer et al. (1996a, 1996b).

The objective of large eddy simulation is to explicitly simulate the large scales of a turbulent flow while modeling the small scales. To do so, one begins by filtering the Navier-Stokes equations to obtain an equation for the large scale motions. As stated above, these equations, which have been given in the literature many times, will not be presented here. The most important point is that the nonlinearity of the Navier-Stokes equations makes it impossible to obtain an exact closed equation for any filtered quantity. This means that a term analogous to the Reynolds stress in RANS is produced and must be modeled. For incompressible flow, the density may be normalized out and the quantity to be modeled is:

$$\tau_{ij} = \overline{u_i u_j} - \overline{u_i} \overline{u_j} \quad (1)$$

An overbarred quantity is one that has been filtered. The

Contributed by the Fluids Engineering Division for publication in the JOURNAL OF FLUIDS ENGINEERING. Manuscript received by the Fluids Engineering Division July 10, 1996; revised manuscript received January 2, 1997. Associate Technical Editor: S. P. Vanka

quantity τ_{ij} defined by Eq. (1) is called, naturally enough, the subgrid scale Reynolds stress. It represents the interactions between the large scales that we intend to simulate and the small scales that have been filtered away. In the absence of information about the small scales, an exact expression for this term is impossible to construct so models, called subgrid scale (SGS) models, are required. These are described in the following section of this paper.

It is also important to note that the filtered Navier-Stokes equations must be solved accurately in both space and time. Filtering removes the smallest scales but, in the desire to obtain the most from a simulation, one usually tries to retain as much energy in the resolved scales as possible. To accomplish this, it is necessary to leave considerable energy in the smallest resolved scales. This places a heavy demand on the accuracy of the spatial discretization method and usually means that the order of a discretization approximation is not a good measure of its accuracy. It also makes LES prone to errors that produce wiggles in the solution and aliasing errors; the latter may make a simulation unstable. Many of the simulation results presented at the conference exhibit at least a small bit of wiggly behavior, indicating that they have not used sufficient resolution.

Upwind methods are often employed to eliminate the wiggles that central difference methods are prone to produce. They accomplish this by introducing diffusion (often of order higher than two), thereby producing a smooth field. When used with sufficient resolution, upwind methods are capable of producing results as accurate as central difference methods. However, the added viscosity should be counted as part of the model and its contribution to the dissipation of energy should be measured; estimation of the effect of numerics on energy dissipation was not required in the workshop discussed herein.

3 Models

3.1 Subgrid Scale (SGS) Models. In this section we shall introduce the subgrid scale models used in the simulations. The nature of this paper demands that we sacrifice completeness in order to introduce only the models that were applied by the conference participants. We shall try to stick to this script and be as brief as possible without trivializing the subject.

By far the oldest and best known subgrid scale model is the one due to Smagorinsky (1963). It can be considered the large eddy simulation version of the well-known mixing length model of Prandtl and can be written:

$$\tau_{ij} = -2v_T \bar{S}_{ij} \quad (2)$$

where v_T is the eddy viscosity and \bar{S}_{ij} is the strain rate in the resolved velocity field. By dimensional analysis, one can demonstrate that a reasonable form for the eddy viscosity is:

$$v_T = (C_S \Delta)^2 |\bar{S}| \quad (3)$$

where $|\bar{S}|^2 = \bar{S}_{ij} \bar{S}_{ij}$ and Δ is the length scale associated with the filter i.e. it is the length that distinguishes a 'small' eddy from a 'large' one. The parameter in this expression can be computed from various theories which suggest that, for isotropic turbulence:

$$C_S \approx 0.2 \quad (4)$$

This model (with different values of the parameter) was in fact used by approximately half the participants at the conference that is the subject of this paper.

Despite its usefulness, the Smagorinsky model has significant disadvantages. It has long been known that, to obtain the proper behavior in a region close to a wall, it is necessary to introduce a rather arbitrary damping of the eddy viscosity produced by the Smagorinsky model. This modification is difficult to justify and hard to apply in complex geometries. The eddy viscosity also needs to be reduced when stratification and/or rotational

effects are present. In regions of anisotropic turbulence (which require anisotropic filters), the choice of length scale is not obvious. Finally, the Smagorinsky model is not capable of predicting laminar-turbulent transition in wall-bounded flows accurately because it dissipates too much energy too early in the simulated flow.

To improve on the Smagorinsky model one can follow the direction long used in RANS modeling and introduce one or more partial differential equations for the quantities that determine the model. This approach has been used a few times but has not met with great success. An approach that has had more success is to use the small scales of the resolved field to determine the model for the unresolved scales. One such model is the scale-similarity model of Bardina et al. (1981), which in the form most commonly used today, is:

$$\tau_{ij} = \overline{\overline{u_i u_j}} - \overline{u_i u_j} \quad (5)$$

where the double overbar means that the quantity has been filtered twice. (Double filtering gives a smoother result than single filtering.) This model does not dissipate much energy and must be combined with the Smagorinsky model to be useful. The resulting mixed model has been used quite often and with considerable success.

The final approach to be discussed in this section is not really a model at all but is better called a procedure. This is the dynamic method of Germano et al. (1991). We shall not present full details of this procedure here; only an outline is given. The interested reader is referred to the original papers for complete details. In the dynamic procedure, one uses the smallest scales of the resolved field to determine the parameters of the model. By filtering the velocity field with a filter wider than the one used in the LES one can make a kind of a priori test (Clark et al., 1979) to determine the model parameter. In the simplest version of the method, the Smagorinsky model is assumed to hold on both the original LES level and the 'test filter' level. By using an identity given by Germano et al. (1991), it is possible to find a set of equations for the parameter. In fact, there are five equations for the single parameter and they can only be satisfied in the least squares sense, an approach first suggested by Lilly (1992). The result of the dynamic procedure is a value of the model parameter that varies with position and time, sometimes in quite dramatic fashion.

The dynamic procedure with the Smagorinsky model as the base model produces large negative eddy viscosities that can make a simulation numerically unstable. A number of cures for this problem have been suggested. One is to average some of the quantities over one or more homogeneous coordinate directions (done originally by Germano et al., 1991) or time (Piomelli, 1992). Another is to simply replace any negative eddy viscosity by zero (clipping). A third is to replace the Smagorinsky model, using the mixed model as the base model; this was used (with pre-filtering to remove potential problems caused by the small scales) in one submission to the conference. All of these help in mitigating the instability but none has yet proven completely satisfactory.

3.2 Wall Models. In wall bounded flows, the only correct boundary condition at the surface is the no-slip condition. However, the turbulent flows develop very small structures near walls; this has been well-documented. As the ratio of the thickness of the viscous sublayer to the overall boundary layer decreases with Reynolds number, the problem becomes worse at high Re. These structures play a very important role in the production of turbulence and thus in determining the skin friction but resolving them is very expensive due to the large number of grid points that must be used. It would be useful to have a way to avoid the necessity of resolving them.

One can apply an artificial boundary condition at some distance from the wall. In a fully developed equilibrium flow, the logarithmic region is an obvious place to try this approach. A

number of conditions that can satisfactorily represent this region for equilibrium flows have been developed. They are designed to force the mean velocity profile to have the proper logarithmic behavior in this region. Most of these were not used in the simulations discussed in this paper so we shall not review them; the interested reader is referred to the paper of Piomelli et al. (1989). A generalized condition that allows the location at which the condition is applied to lie below the logarithmic region was given by Werner and Wengle (1989); it is based on a power law profile that is capable of giving an approximate representation of the instantaneous velocity profile throughout the inner region of the boundary layer. This condition was used in a number of the submitted simulations.

When the Reynolds number is very large, the logarithmic region and viscous sublayer cover a very small part of the boundary layer and the grid used in the simulation may be sufficiently large that the filtering process removes much of the fluctuating component of the velocity. If the boundary layer is of equilibrium type, it is reasonable to require that the instantaneous velocity profile be logarithmic. A condition of this type was suggested by Mason (1992) and is often used in LES of the atmospheric boundary layer, where it seems to perform reasonably well. This corresponds to a kind of very large eddy simulation but it is doubtful that many engineering flows qualify for such treatment. For reviews of LES of the atmospheric boundary layer, see Nieuwstadt et al. (1993) and Andren et al. (1994).

4 The Test Cases

In the past, large eddy simulation has been applied mainly to relatively simple flows including essentially all possible variations of homogeneous turbulence, simple free shear flows, channel flow, and boundary layers (including the atmospheric boundary layer), to mention a few. Most of these flows can also be treated with direct numerical simulation, at least at low enough Reynolds numbers. There have been a few attempts at simulation of complex flows with LES but they involved flows for which the results are difficult to verify in detail so we shall not say more about them here.

The ideal flows for application of LES would have the following properties:

- The Reynolds numbers should be high enough to be out of reach of DNS but not so high that the model is the dominant factor in the simulation.
- The geometry should be complex enough to render DNS infeasible but not so complex that the number of grid points needed for accurate representation of the geometry is too high.
- The physics of the flow should be relatively complex. At minimum, the flow should contain significant secondary flows, separation, or other 'extra strains' that make modeling with Reynolds averaged models difficult.
- Reliable and complete experimental measurements of the flow should exist.

In choosing test cases for the conference, we were guided by the above criteria. Since this was the first conference of this kind (the conference reported in Voke et al. (1994) was of a somewhat different type), in order to avoid having too few participants due to difficulties in generating adequate grids, we added the further constraint that the geometries should be ones for which gridding is relatively easy. In practice, we restricted our attention to flows for which the geometry could be treated with a Cartesian coordinate system.

The first case selected (designated Case A) was the flow over a square cylinder for which measurements were reported by Lyn and Rodi (1994) and Lyn et al. (1995). The Reynolds number was 22,000 and the inflow was reported to have a turbulence level of 2 percent at 4.5 cylinder widths upstream

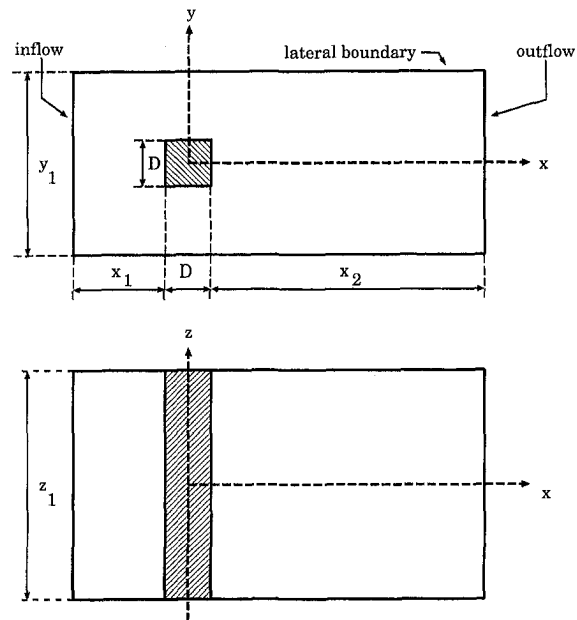


Fig. 1 The geometry of the square cylinder flow (Test Case A) indicating the definitions of the various geometric lengths

from the cylinder; no length scale information was reported for this turbulence. The experiment reported that the separation and the wake were periodic although there was some modulation of the periodicity. In addition to time-averaged quantities, the experiment reported a number of phase-averaged quantities at various locations in the flow. Selected experimental measurements of this flow will be presented below along with the simulation results.

The geometry of the flow and the corresponding parameters, including the overall domain size specified to the participants, are given in Fig. 1 and Table 1, respectively. Other than the inflow conditions, the computers were asked to apply the following conditions:

- Slip (symmetry) conditions at the lateral boundaries. The lateral size of the domain was provided in order to eliminate one variable; its value is given in Table 1.
- A choice of zero gradient or convective boundary conditions at the downstream boundary. In fact, convective conditions were used exclusively.
- A choice of no-slip boundary conditions or wall functions at the cylinder surface. All participants chose to use wall functions.

The second flow selected (designated Case B) was the flow over a cube mounted on one wall of a channel flow for which the measurements were taken from the work of Martinuzzi (1992) and Martinuzzi and Tropea (1993). The Reynolds number is 40,000 and the upstream flow is fully developed channel flow. The geometry and parameters, including the domain specifications, for this case are given in Fig. 2 and Table 2, respectively. This flow is fully turbulent everywhere and displays no obvious regularity or periodicity.

Other than fully developed channel flow at the inlet, the computers were asked to use the following conditions:

Table 1 Dimensions of the calculation domain for the square cylinder flow (Test Case A)

x_1/D	x_2/D	y_1/D	z_1/D
4.5	≥ 15.0	14.0	4.0

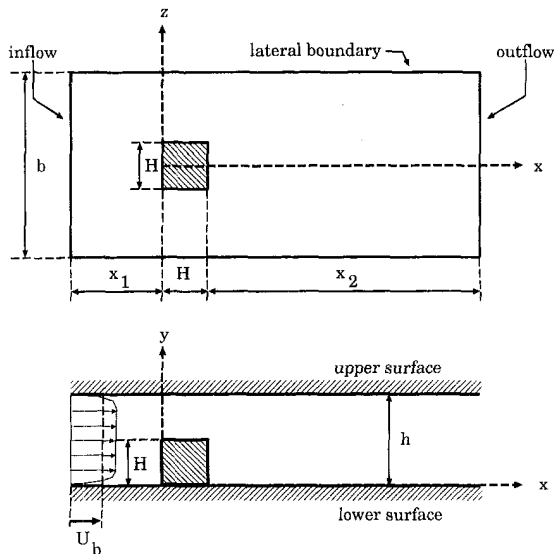


Fig. 2 The geometry of the wall-mounted cube flow (Test Case B) indicating the definitions of the various geometric lengths

- The lateral boundaries were to be treated either as slip surfaces or as periodic boundaries. The width of the domain is given in Table 2.
- A choice of zero gradient or convective boundary conditions at the downstream boundary. As in Case A, convective conditions were used exclusively.
- A choice of no-slip boundary conditions or wall functions at the cylinder surface.

Finally, in order to attempt to assess the effect of Reynolds number on the quality of an LES, a third case was added. This is the cube flow with the parameters given above but at Reynolds number 3000. This case was called B1; the high Reynolds number case was called B2. No experimental data exist for case B1.

The computers were requested to submit data to the organizers prior to the workshop in formats that were provided. Selected data were put into graphical form and given to the attendees when they registered for the meeting. Certain overall parameters (reported below) were also computed by the organizers from the provided data. The participants presented their methods but not their data at the workshop. The data presentations were made by rapporteurs, who are two of the authors of this paper (MB and MP).

5 Computational Methods

As noted, the flows chosen were ones for which Cartesian coordinate systems could be used. This was done so that grids could be generated easily. Despite this, a number of different kinds of grids were used in the calculation.

Most people used Cartesian grids; of these, most employed grid stretching but a few used uniform grids. One computer (Tamura) used two rather unusual grids for Test Case A. The first was an *O*-grid in which one set of coordinate lines encircle the cylinder. The second grid was a uniform Cartesian grid but four levels of refined grids were embedded in the main grid, principally near the surface; these grids were preselected and not created adaptively. Another group (EDF) used a finite element

Table 2 Size of the calculation domain for the wall-mounted cube flow (Test Case B)

x_1/H	x_2/H	h/H	b/H
3	≥ 6	2	7

method on a grid consisting of triangular prisms. In all cases, the number of grid points in the spanwise direction (along the cylinder axis) was much smaller than the number employed in the other two directions.

The most popular discretization method was the finite volume approach; as noted above, there was one finite element submission. Many used second order central difference approximations but some people used upwind methods; among the latter were QUICK and several third order methods.

For time advancement, the most popular method was the second order Adams-Bashforth scheme, but the Runge-Kutta, Euler, and leapfrog methods were used by some.

For the conditions at the surfaces, for Case A, about equal numbers of people used no-slip and wall functions or approximate boundary conditions; the latter were all based on the model of Werner and Wengle (1989). Although the inlet conditions for this case were specified to contain 2 percent turbulence, everyone used uniform laminar inflow conditions; the effect of this modification is difficult to assess as we note below. At the outlet, everyone used convective conditions.

For Case B1, almost everyone used similar methods—control volume methods with second-order approximations, no-slip boundary conditions, and convective outflow conditions. One unusual case used periodic boundary conditions in the streamwise direction. Two of the calculations used wall functions; the others used no-slip conditions. Other major differences are found in the subgrid scale models; the Smagorinsky, mixed, Schumann, and dynamic models were used by various computers.

The methods used in Case B2 were similar to the ones used in Case B1 but everyone applied wall functions at the surfaces.

Some of the details of the computational methods used in the simulations are given in Tables 3, 5, and 6. Computers were asked to provide a large amount of time-averaged and in Case A also phase-averaged statistical data in specified formats. Only the limited amount of results required to illustrate certain points will be included in this paper. It is the feeling of the authors that the detailed descriptions of the results belong to the authors and should be presented in their own papers.

6 Results for Case A and Their Assessment

We note again that Case A is the flow over a square cylinder. A list of submissions and the parameters and methods used is given in Table 3. Ten groups submitted a total of sixteen sets of results. As noted above, detailed discussion of the physics of these flows is reserved to papers by individual contributors.

The contributors were asked to submit the time-averaged velocity field as well as phase-averaged quantities at five different phases. This was more data than the organizers (the authors of the present paper) were able to plot so only partial results were plotted to provide the basis for discussion at the workshop. Obviously, only a much smaller selection can be presented here. Of the results, two clearly differed from the others and the experiments by so much that they were excluded from discussion (TUDELFT, EDF-FE2). Insofar as we are able to determine, the lack of quality in these results apparently derives from insufficient grid near the walls in one case and too little averaging time in the other.

An impression of the nature of the flow can be obtained from the phase-averaged streamline pictures taken from selected calculations shown in Fig. 3. The experimental streamline picture is also included. The shedding motion is qualitatively well predicted, but there are significant quantitative differences among the various calculations and with the experiment. Unfortunately, the region near the cylinder walls is not resolved in the measurements, so the computed flow behavior in this region, which contains a number of vortices, cannot be assessed.

Some important overall parameters of the flow submitted by the contributors as well as the available experimental results

Table 3 Submissions for Case A: groups, parameters and methods

Contrib./Key	Group, Affiliation	Grid	Time Scheme	Convection Scheme	Subgrid-Scale Model	C_r	Wall Damping: (a,b)	Wall Bound. Cond.	$T_{u_{in}/t_{50}}$	# of cycles
KAWAMU	H. Kawamura, N. Kawashima, Science Univ. of Tokyo, Japan	FD: 125x78x20	AB	Upwind (3rd)	—	—	—	no slip	0%	≈ 4
UMIST1	F. Archambeau, D. Laurence, EDF/LNH	FV: 140x81x13	AB	Central (2nd)	Smagorinsky	0.15	VDD: (1,1)	WF	0%	7.5
UMIST2	Chatou, France & M.A. Leschziner, UMIST, Manchester, U.K.	FV: 140x81x13	AB	Central (2nd)	Dynamic	—	—	WF	0%	4
UMIST3		FV: 140x81x13	AB	Central (2nd)	Dynamic	—	—	WF	0%	7
ILLINOIS1	G. Wang, S.P. Vanka, Univ. of Illinois at Urbana-Champaign, U.S.A.	FV: 144x128x32	AB	QUICK	Dynamic	—	—	no slip	0%	30
ILLINOIS2		FV: 176x144x32	AB	QUICK	Dynamic	—	—	no slip	0%	25
UKAHY1	M. Pourquie, M. Breuer, W. Rodi, Univ. of Karlsruhe/Inst. for Hydromechanics, Germany	FV: 169x105x20	AB	Central (2nd)	Smagorinsky	0.1	VDD: (3,0.5)	WF	0%	13
UKAHY2		FV: 146x146x20	AB	Central (2nd)	Smagorinsky	0.1	VDD: (3,0.5)	WF	0%	8
EDF-FE1	P. Miet, D. Laurence, B. Nitrosso, EDF/LNH, Chatou, France	FE: 76159	OS	Charact. M.	Smagorinsky	0.2	VDD: (1,1)	WF	0%	≈ 10
EDF-FE2		FE: 113856	OS	Charact. M.	Smagorinsky	0.065	VDD: (1,1)	WF	0%	?
TAMU1	T. Tamura, Y. Itoh, A. Takakura, Tokyo Inst. of Technology, Japan	FV: 202x100x102	EU	Upwind (3rd)	no	—	—	no slip	0%	9
TAMU2		FV: 165x113x17	EU	Upwind (3rd)	Dynamic	—	—	no slip / WF	0%	6
ONERA	K. Dang-Tran, P. Sagaut, ONERA, Chatillon, France	FV: 231x125x21	EU	mixed FE/FV	Mixed Scale	—	—	no slip	0%	8
TUDELT	B.J. Boersma, L.J.P. Timmermans, F.T.M. Nieuwstadt, Delft Univ. of Technology, The Netherlands	FV: 274x280x50	RK	Central (2nd)	Smagorinsky	0.17	VDD: (? ?)	no slip	RG: 2%	15
IIS-KOBA	T. Kobayashi, N. Fani-guchi, T. Kogaki, Inst. of Indust. Science, Univ. of Tokyo, Japan	FV: 83x63x16	AB/CN	QUICK	Smagorinsky	0.13	VDD: (1,1)	no slip	RG: 2%	12
IIS-MURA	S. Murakami, S. Iizuka, Inst. of Indust. Science, Univ. of Tokyo, A. Mochida, Y. Tamagata, Niigata Inst. of Technology, Japan	FV: 100x92x22	AB/CN	Central (2nd)	Dynamic Mixed	—	—	WF	0%	≈ 3

AB = Adams-Bashforth (2nd), CN = Crank-Nicolson, EU = Euler Scheme (1st) FD = Finite Difference, FV = Finite Volume, FE = Finite Element
 OS = Operator Splitting, RG = Random Generator, RK = Runge-Kutta (2nd), VDD = Van Driest Damping: $(1 - \exp(-y^+ / 25))^3$, WF = Wall Function

for them and RANS results to be discussed later, are given in Table 4. All submitters reported that their computed flows were periodic. We note that, with one or two exceptions, the reported values of the Strouhal number fall in a narrow range close to the experimental value. Apparently, this quantity (and others mentioned later) are not very sensitive to the parameters of the simulation. Among other things, this means that accurate prediction of the Strouhal number is not necessarily an indication of a quality simulation. This is a point to be borne in mind by future authors and reviewers. The former should present results for quantities that are hard to compute accurately; the latter should take care to determine that the simulation has been challenged sufficiently.

The results for the mean drag coefficient shown in the table display considerably more variation than do the Strouhal number results. In fact, several of the results differ by more than 20 percent from the experimental result. It appears that, in general, the simulations that used wall functions produced drag coefficients that are relatively close to the experiments while those that used no-slip conditions tend to produce high values of the drag coefficient. Possible reasons for this observation are given below.

The results for l_r , the length of the time-mean recirculation zone behind the cylinder show even greater variation, with the simulations based on no-slip boundary conditions tending to give smaller values. This is consistent with the drag coefficient results; both sets of results are consistent with the no-slip simulations having lower pressure in the base region behind the cylinder. Better values of l_r seem to be obtained in simulations with greater resolution near the surface, a point that we shall return to below.

The simulations that used wall functions had larger negative velocities close to the side walls of the cylinder; we must assume that this is a direct effect of the application of the wall functions. This increased reversed flow causes the pressure to be higher near the upstream corner so that the flow leaves the corner at a larger angle. In turn, this results in a larger recirculation region. This is an example of how all the results are tied together in this flow. Proper prediction of the wake depends very sensitively on the treatment of the flow near the cylinder.

The fluctuating side force coefficient, $C_{l,rms}$ shows more variation from simulation to simulation than any other result in the table. In general, it appears that simulations that used wall functions tended to predict lower values of these fluctuations.

Selected results for the mean velocity on the center plane of the cylinder are shown in Fig. 4; these were chosen to show the range of the results and the names of the contributors is not important. The experiment shows (somewhat surprisingly) that the velocity recovers for a while and then nearly levels off at about $0.6U_{in}$, where U_{in} is the inlet velocity. Some of the computed results show stronger recovery of the velocity than the experiment, including one that levels off and another that continues to rise. A few were low and one, a simulation by Tamura, displays nearly correct behavior although the recirculation region is a bit short.

Figure 5 shows results for the phase-averaged vertical velocity on the center plane for a particular phase; the results came from the same authors whose results were used in Fig. 4. It is clear that the agreement with each other and with the experiment is better than for the drag coefficient i.e. that this quantity and, indeed, most results concerning the vertical component of the velocity are reasonably well predicted in all simulations. We are unable to offer an explanation for this behavior but it means that the vertical velocity should not be used as a definitive indicator of the quality of a simulation.

In Fig. 6, we present the averaged pressure distribution around the cylinder along with the experimental results of Lee (1975) and Bearman and Obasaju (1982). The pressure on the upstream face is fairly well predicted but the values on the other faces show significant disagreement both with each other and with the experiments, as might be expected from the results for the separation regions. Note, too, the difference in the two sets of experimental results and oscillations in the computed results that probably indicate lack of sufficient resolution.

Finally, in Fig. 7, we show a close-up of the time-averaged streamwise velocity. The point of presenting this figure is not directly connected with the quantity plotted. Rather, it is to show that the grid distribution near the body is insufficient to resolve the region of reversed flow near the wall in most of the simulations. The maximum negative streamwise velocity occurs at the first grid point from the wall in a number of the simulations; this is a definite indicator of insufficient resolution and may explain some of the other observations. The occurrence of the maximum negative velocity at the first grid point indicates that that thickness of the reversed flow region is determined by the grid and not by the physics. More grid points should be employed in this region whether no-slip or wall-function boundary conditions are used.

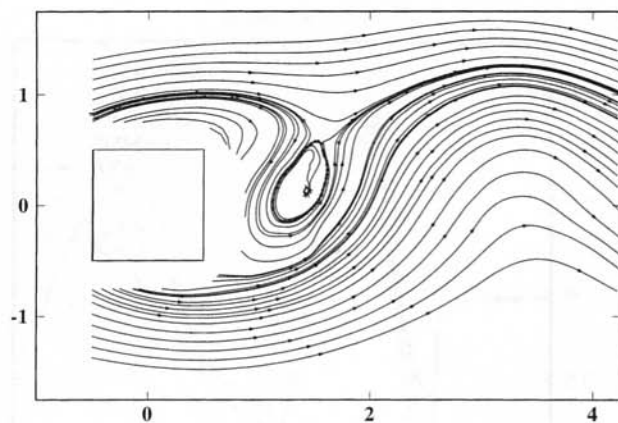


Fig. 3(a)

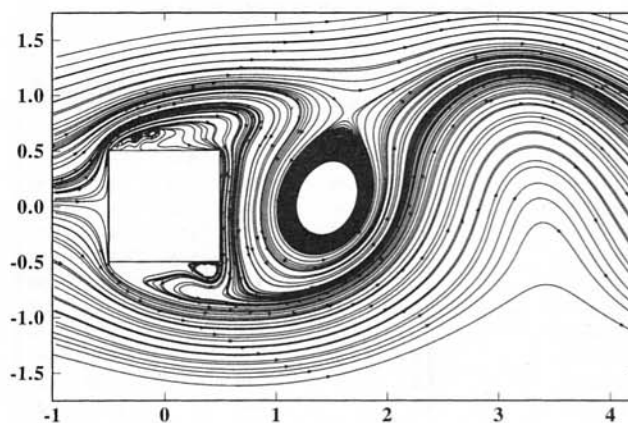


Fig. 3(b)

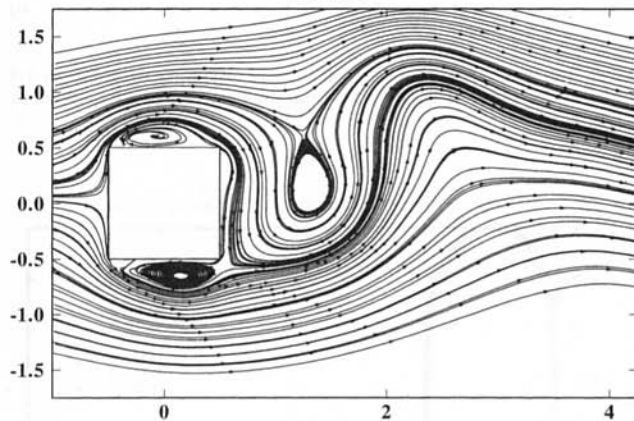


Fig. 3(c)

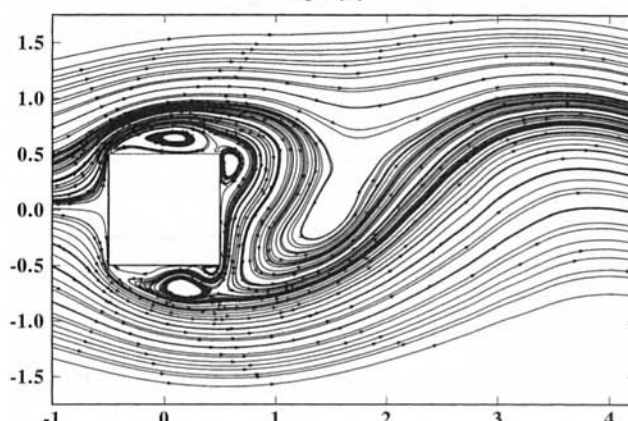


Fig. 3(d)

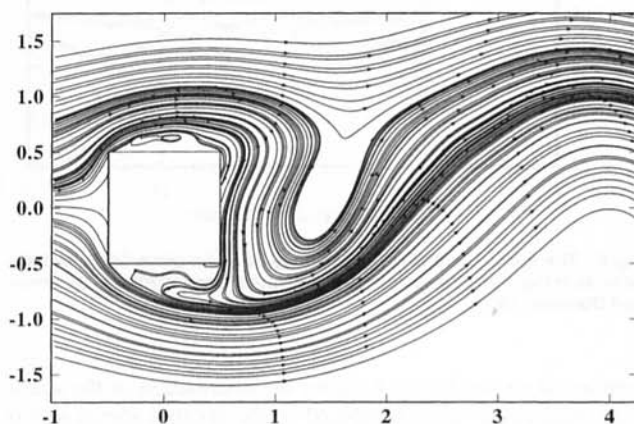


Fig. 3(e)

Fig. 3 Phase-averaged streamlines (Phase 01) from several simulations. Figure 3(a) is taken from the experiment.

It is important to recall that the inflow to the computational domain is laminar and that transition takes place in the separated shear layers on the sides of the cylinder just downstream of the front corners; this is shown by the experiments (Lyn and Rodi, 1994). It is clear that the resolution in this region (which extends some distance from the body) is not good enough to accurately capture the development and transition of the separated shear layer. Further, given the short length of travel of the reversed flow on the cylinder sides, it is certain that the reversed flows along the side walls are not fully developed turbulent boundary layers. The latter is the type of flow for which the wall functions were designed so the validity of these functions is questionable in the reverse flow regions. However, the instantaneous velocity distribution assumed in the Werner-Wengle near-wall model may be more realistic than the linear

distribution assumed when no-slip conditions are used, and this may be part of the reason why using this model leads to better prediction of the drag coefficient. The best treatment would be to use a sufficiently fine grid to resolve the near-wall flow with no-slip conditions, but this is very expensive and no one was able to perform such a simulation. It is possible that an embedded grid similar to the one used by Tamura could do the job but not enough results are available to allow one to reach a definitive conclusion on this point.

Overall, it is our judgement that no single simulation is uniformly good; significant faults can be found in every submission. It does appear, however, that one key to success is having sufficient resolution near the surface. Without it, the separated regions on the sides of the cylinder (see Fig. 3) cannot be correctly predicted and are unlikely to have the correct average thickness. This, in turn, affects the pressure distribution on the body and the size of the recirculation zone. It may also have an important effect on the velocity recovery downstream but it is difficult to address this issue on the basis of the available results.

One of the factors whose effect proved very difficult to analyze is the choice of numerical method. As already noted, a number of computers used upwind methods. Third order upwind methods create a dissipative fourth order error term that acts like an additional subgrid scale model. The QUICK scheme is similar. The simulations that used these methods tended to predict short recirculation zones; it is likely that the shortening of the recirculation zone is due, at least in part, to the diffusion added by the numerical approximation. In order to assess this, it would be useful to know the dissipation created by the numerical method; unfortunately, it was not computed and is not avail-

Table 4 Bulk coefficients for Case A

Contribution	\bar{c}_i	$c_{i,rms}$	\bar{c}_d	$c_{d,rms}$	St *	l_r
EDF-FE1	0.03	0.73	1.86	0.12	0.13	1.65
EDF-FE2	0.007	0.38	1.66	0.10	0.066	1.33
IIS-KOBA	-0.3	1.31	2.04	0.26	0.13	1.22
IIS-MURA	-	-	2.06	0.13	-	1.26
ILLINOIS1	-0.03	1.38	2.67	0.24	0.13	0.89
ILLINOIS2	-0.02	1.40	2.52	0.27	0.13	0.95
KAWAMU	-0.005	1.33	2.58	0.27	0.15	1.2
ONERA	-0.01	0.65	2.01	0.18	0.11	1.12
TUDELFT	-	-	1.96	-	0.14	2.96
UKAHY1	-0.02	1.01	2.20	0.14	0.13	1.32
UKAHY2	-0.04	1.15	2.30	0.14	0.13	1.46
UMIST1	0.	-	2.39	-	0.125	0.91
UMIST2	0.	-	2.02	-	0.09	1.21
UMIST3	0.	-	1.93	-	0.137	1.28
TAMU1	-0.03	1.37	2.28	0.20	0.13	1.15
TAMU2	-0.09	1.79	2.77	0.19	0.14	0.94
RANS results						
Bosch (1995)						
standard k- ϵ	-	-	1.637	-	0.134	2.84
KL modification	-	-	1.789	-	0.142	2.04
two-layer k- ϵ	-	-	1.719	-	0.137	2.42
two-layer with KL model	-	-	2.004	-	0.143	1.25
Franke & Rodi (1993)						
RSE model	-	-	2.150	-	0.136	0.98
two-layer RSE	-	-	2.430	-	0.159	0.98
Experiments						
Lee (1975)	-	-	2.05	0.16-0.23	-	-
Vickery (1975)	-	0.68-1.32 *	2.05	-	-	-
Cheng et al. (1992)	-	0.1-0.6 *	1.9-2.1	0.1-0.2 *	-	-
McLean et al. (1992)	-	0.7-1.4 *	1.9-2.1	0.1-0.2 *	-	-
Lyn et al. (1994, 1995)	-	-	2.1	-	0.132	1.38

*: Strouhal number estimated from peak in lift spectrum
 *: variation with degree of incoming turbulence (0 – 10%) and length scale of incoming turbulence

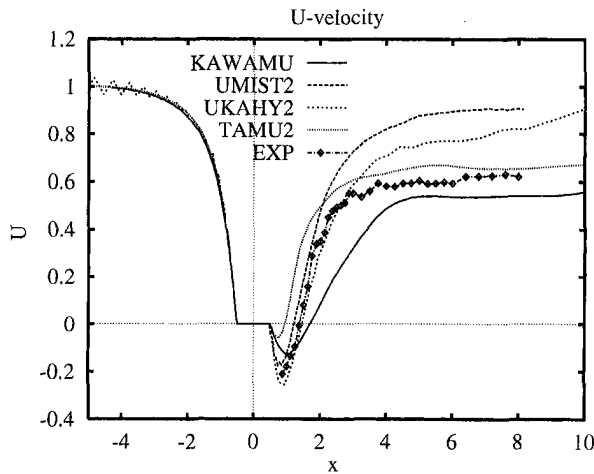


Fig. 4 The mean velocity distribution on the center plane of the cylinder from several simulations chosen to show the range of the results

able to us. It should be presented in any paper based on upwind methods and any future workshop of this type.

It appears that the simulations that used the dynamic model tended to predict longer recirculation zones and lower drag coefficients than those that used the Smagorinsky model. A figure presenting the distribution of eddy viscosity produced by the two models that was shown at the meeting indicates that the dynamic model produces a larger eddy viscosity than the Smagorinsky model in the shear layers and a smaller one almost everywhere else. This is the probably cause of the differences

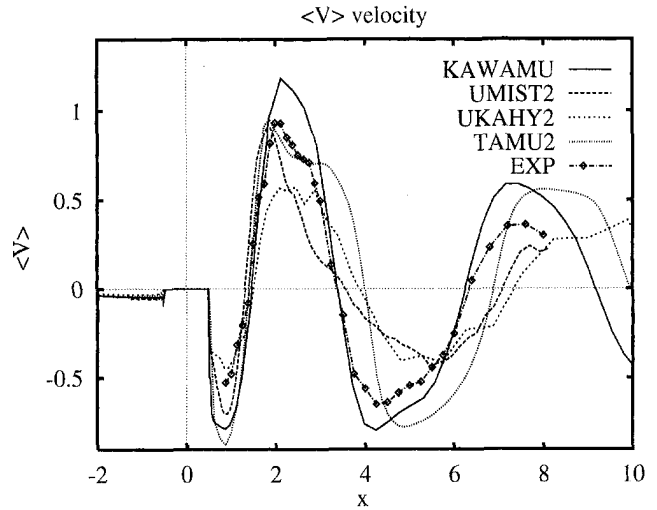


Fig. 5 The phase-averaged vertical velocity distribution (for Phase 01) on the center plane of the cylinder from the same set of simulations as in Fig. 4

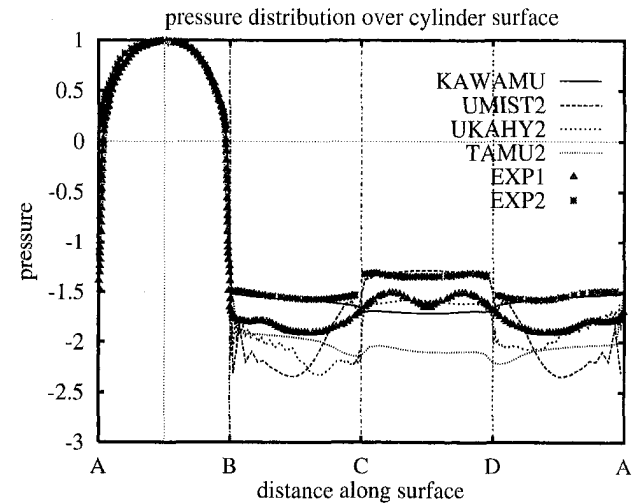


Fig. 6 The average pressure on the body from the same set of simulations as in Fig. 4 and the experimental results of Lee (1975) and Bearman and Obasaju (1982)

mentioned above. Figure 8 shows the distribution of the spanwise averaged C values computed by the dynamic model at two different instants; this is equivalent to C_x^2 of the Smagorinsky model. In the shear layers, large values of C_x^2 (of the order of 1) appear, whereas low or even negative values are observed in the other regions of the flow. In the simulations, negative values of C_x^2 were clipped by most people in order not to destabilize the numerical algorithm. It is also worth pointing out that the values of the parameter used in the simulations based on the Smagorinsky model are rather large for shear flows; most channel flow calculations have used $C_s = 0.06 - 0.10$. The larger values may be, in part, compensation for the use of the grid size as the filter width rather than the $2\Delta x$ that is widely regarded as more appropriate. This may explain some of the results found with this model.

It is also important to note that nearly all of the simulations used relatively few grid points in the spanwise (cylinder axis) direction; the spanwise extent of the domain was also quite short in most cases. Both of these factors limit the ability of the shear layers to become three dimensional. It is known from the literature that purely two dimensional simulations, for exam-

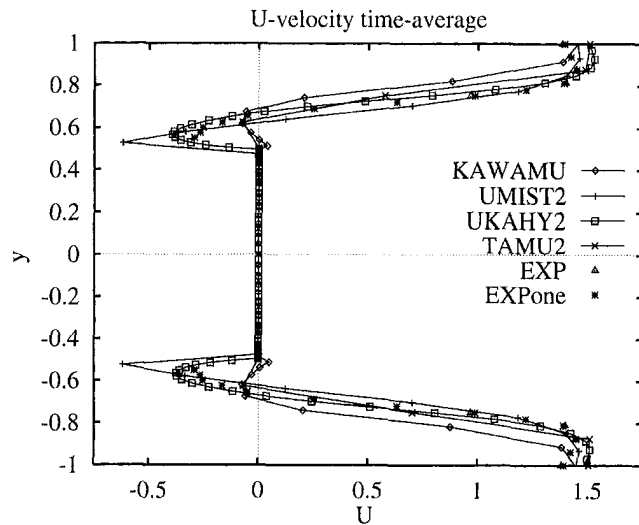


Fig. 7 Close-up of the time-averaged streamwise velocity near the body from the same set of simulations as in Fig. 4

ple, those based on vortex methods, give recirculation zones that are much too long and drag coefficients that are much too small. The experiment shows that the flow is turbulent and therefore three dimensional. Thus this factor may be another contributor to the lack of agreement with experiment demonstrated above.

To sum up, we repeat that none of the simulations was completely satisfactory. Some of the reasons for the lack of agreement with experiment are (not necessarily in order of importance): insufficient resolution near the surface, lack of turbulence in the incoming stream, numerical diffusion, insufficient grid in the spanwise direction, and insufficient width in the spanwise direction. It may be that this flow is very sensitive to small changes in various parameters (this is suggested by the variation in the experimental results). This conjecture should be verified either experimentally or by a careful series of simulations and, if true, it means that this was probably not an ideal choice for a test case.

The evaluation committee, which consisted of J. H. Ferziger, P. Moin, S. P. Vanka, and P. R. Voke, found that the results most useful in helping to discern the effects of the various factors on the simulated flow were those cases in which a single group did more than one calculation. The cases provided by a single group usually modified only a single factor (grid, model,

etc.). This allowed conclusions to be drawn about the effect of those factors. It is strongly recommended that the organizers of future meetings of this type commission particular groups to make studies in which only a single factor is modified. Many authors traditionally present only their best results in published papers. Including results obtained with other methods or parameter values (or at least describing them) would be a valuable service and should be encouraged.

It appears that the square cylinder flow is difficult to simulate in part because the inflow is basically laminar and transition takes place in the separated free shear layers on the sides of the cylinder. As suggested above, it may also be sensitive to small changes in various factors. Transitional flows are generally known to be sensitive to minor perturbations, making them difficult to simulate accurately.

7 Results for Case B and Their Assessment

We recall that Case B is the flow over a cube mounted on a wall of a channel. There are two subcases, designated B1 and B2, that have Reynolds numbers 3000 and 40,000, respectively. Four groups provided five submissions for Case B1; three groups provided four submissions for Case B2. Three of the submissions for Case B1 used no-slip boundary conditions; all of the other simulations of both cases used law of the wall type boundary conditions.

Computers were asked to provide the mean velocity field on the center plane of the flow, on a plane just above the wall to which the cube is attached, and near the surfaces of the cube and turbulence data on the center plane; from these data, streamline plots were generated. Participants were also asked for vertical profiles of various quantities at a number of locations.

This flow is not periodic but does contain a considerable amount of coherent structure, at least in the low Reynolds number case. The computers were not asked to provide any data that would permit deduction of coherent structures.

In general, the results for this flow were in better agreement with each other and with the experiments than those for Case A. This is probably due, at least in part, to the fact that the flow is everywhere fully turbulent. The similarity of the numerical methods may be another factor contributing to the agreement among the methods. The results for the two sub-cases will be presented separately.

7.1 Case B1. For Case B1, all but one of the simulations used results taken from a channel flow simulation to provide the inlet conditions. The last used periodic conditions with a period of 21 cube heights in the streamwise direction; the velocity profiles upstream of the cube in this simulation show that

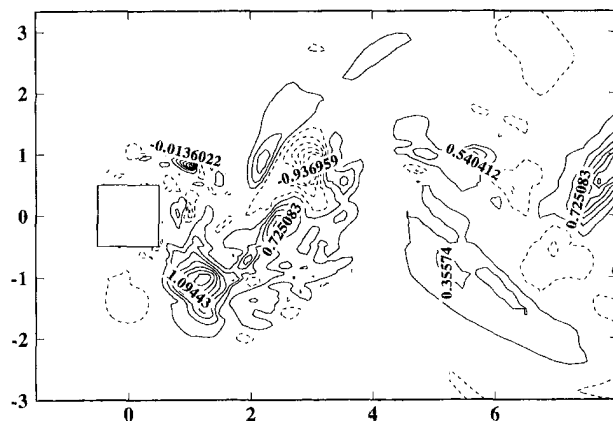


Fig. 8(a)

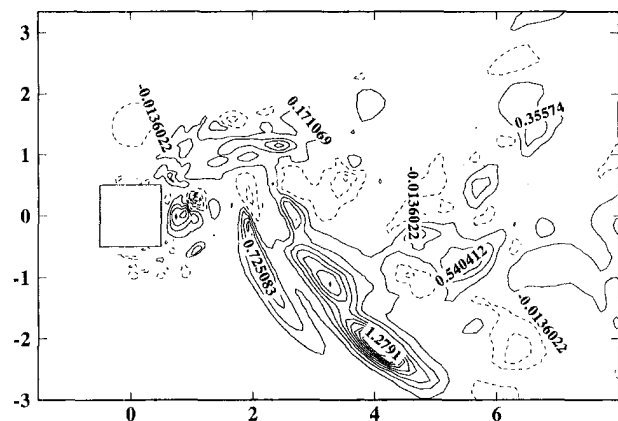


Fig. 8(b)

Fig. 8 Distribution of $C = C_2^2$; values computed by the dynamic model at two different instants, spanwise averaged values, (courtesy of S. P. Vanka, Illinois)

Table 5 Submissions for Case B1: groups, parameters and methods

Contrib./Key	Group, Affiliation	Grid	Time Scheme	Convection Scheme	Subgrid-Scale Model	C _v	Wall Damping: (a,b)	Wall Bound. Cond.	T _{averaging}
STANF	K. Shah, J.H. Ferziger, Stanford University, U.S.A.	FV: 128x64x64	CN/RK	Central (2nd)	Dynamic Mixed	-	-	no slip	75
UKAHY1	M. Breuer, M. Pourquie, W. Rodt, Univ. of Karlsruhe, Inst. for Hydromechanics, Germany	FV: 165x65x97	AB	Central (2nd)	Smagorinsky	0.1	VDD: (3,0.5)	no slip	≈ 103.5
UKAHY2	M. Breuer, M. Pourquie, W. Rodt, Univ. of Karlsruhe, Inst. for Hydromechanics, Germany	FV: 165x65x97	AB	Central (2nd)	Dynamic	-	-	no slip	≈ 200.5
UBWMI	H. Wengle, Univ. der Bundeswehr München, Germany	FV: 144x58x88	LF	Central (2nd)	Smagorinsky	0.1	no	WF	750/500
UKAST1	W. Frank, S. Kellmann, Univ. of Karlsruhe/Inst. for Fluid Mechanics, Germany	FV: 240x120x40	EU/LF	Central (2nd)	Schumann	?	?	WF (periodic b.c. in streamwise direction)	?

AB = Adams-Bashforth (2nd), CN = Crank-Nicolson, EU = Euler Scheme (1st) FV = Finite Volume, LF = Leap-Frog, RK = Runge-Kutta (2nd), VDD = Van Driest Damping: $(1 - exp(-y^+/25))^3$, WF = Wall Function

the flow is not able to recover to a fully developed channel flow state in that distance, causing the flow approaching the cube to be different from that in the other simulations. Thus, although it is bothersome to do so, it is best to do simulations with turbulent inflows with inlet conditions taken from other simulations. This submission the used periodic conditions yielded results that were noticeably different from the others and will not be discussed further. Parameters of the submitted simulations are given in Table 5.

It is unfortunate that no experimental data are available at this Reynolds number. However, the considerable similarity of the results for this flow and those for Case B2 and the agreement among the results make it reasonable to conclude that the simulations are probably fairly accurate.

Figure 9 defines the length scales that are presented in Table 7. From the table, we see that there is quite good agreement among the results; they are also quite similar to the results for Case B2 presented in Table 8 below. The major discrepancy among the results is that one simulation predicts mean flow reattachment on the roof of the cube while the others do not. In the absence of experimental data it is impossible to say with certainty which prediction is correct. However, the participant who found reattachment in this case also finds it in Case B2 and the participant who did not find reattachment and also computed Case B2 did not find it in either case. The high Reynolds number experiment showed no reattachment; from this one can infer that mean reattachment should not occur on the roof of the cube.

Note, too, that in the two simulations done by the same group, the only difference was the choice of subgrid scale model. The dynamic model produces smaller values of all the length scales presented in Table 7. The other calculation that used a dynamic model gave slightly larger length scales than this simulation; the model in the latter simulation is a modified dynamic model. It is more likely that the differences between these sets of results are due to the differences in the grid.

Figure 10 shows the streamlines of the mean flow on the centerplane of the flow. One can readily identify the heads of the horseshoe and arch vortices (upstream and downstream of the cube, respectively), the recirculation zones in front of and behind the cube that contain these vortices and small secondary separated flow regions in the up- and down-stream corners. A closer view reveals that there are some differences among the

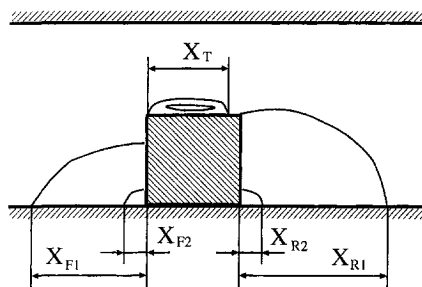


Fig. 9 Definition of length scales in the cube flow

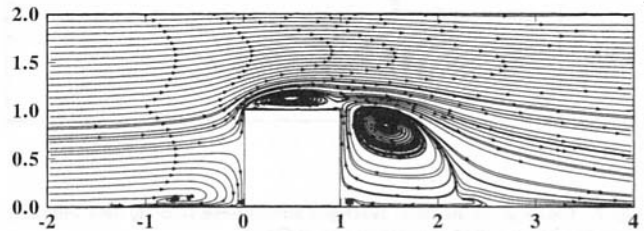


Fig. 10(a)

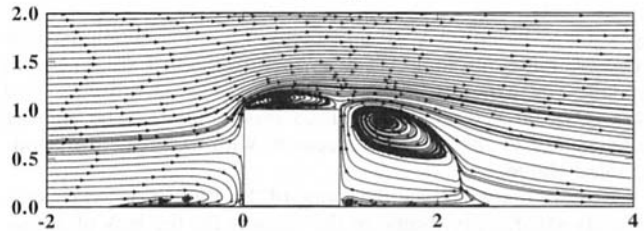


Fig. 10(b)

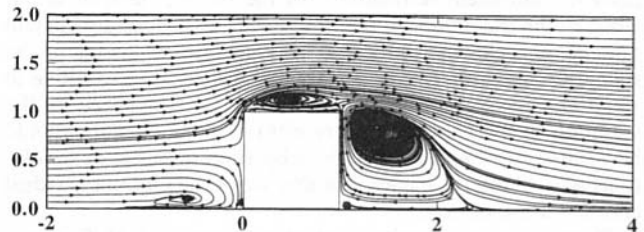


Fig. 10(c)

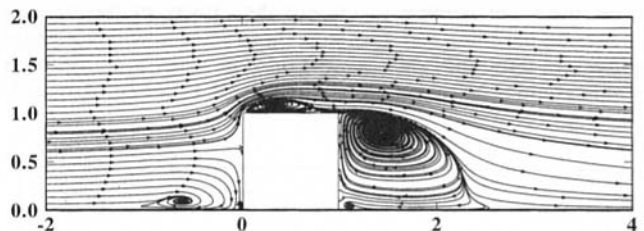


Fig. 10(d)

Fig. 10 Streamlines of the mean flow projected onto the centerline of the cube flow of Case B1

predictions with respect to the size and location of these vortices.

The surface streamlines on the floor of the channel are shown in Fig. 11. The lack of symmetry in the right part of the figure is an indication that these simulations have not been run long enough to completely stabilize the statistical averages. Unlike many other flows that have been treated with LES, this one contains almost no statistically equivalent points over which the results can be averaged. (There are equivalent points on the two sides of the symmetry plane of the cube but this hardly provides enough averaging to be worthwhile. Not performing

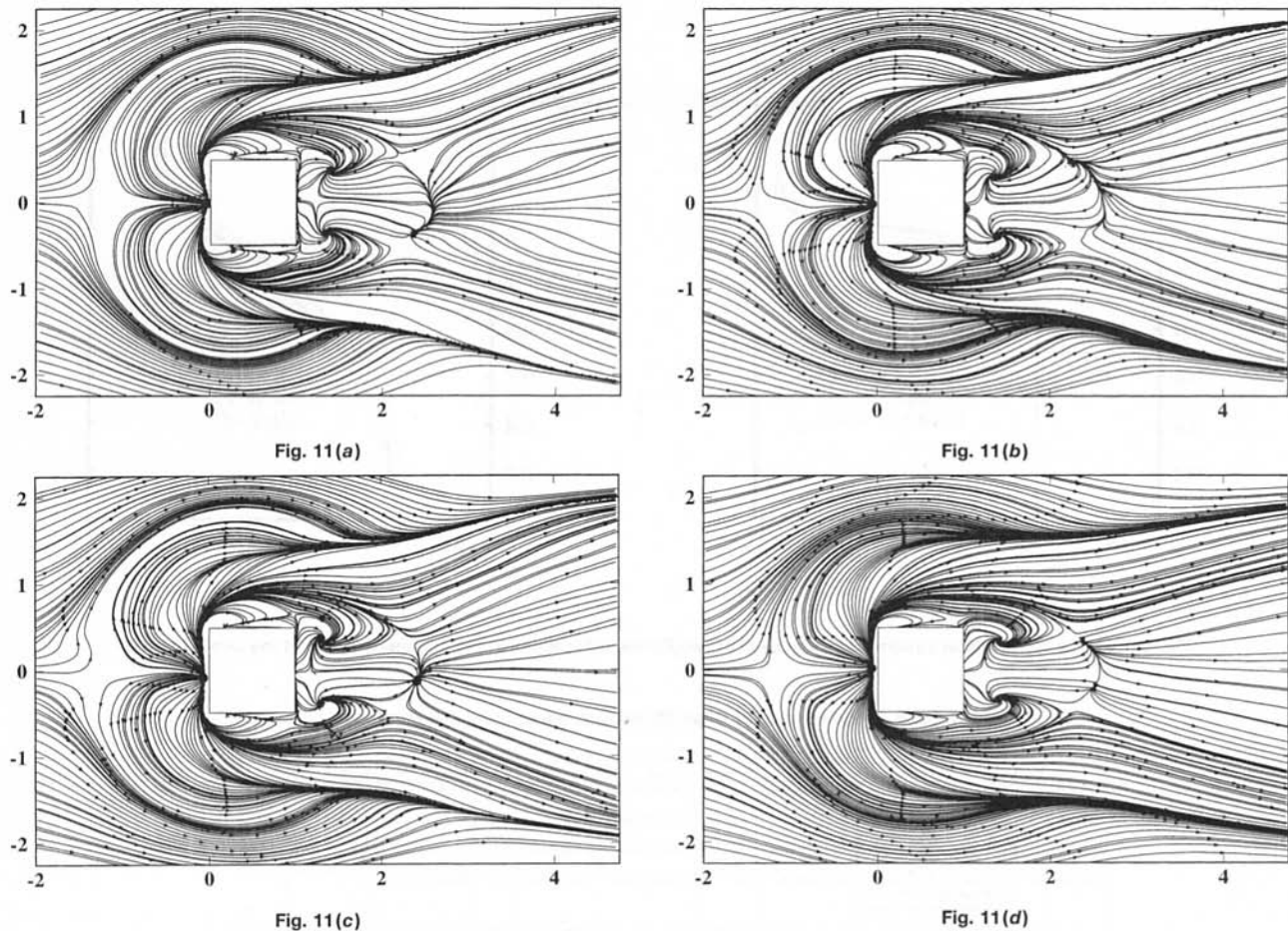


Fig. 11 Streamlines of the mean flow projected onto the floor of the channel in the cube flow of Case B1

the averaging allows symmetry to provide a measure of whether the simulation has been run long enough.)

In the surface streamline plot, one can discern the footprints of the horseshoe vortex (indicated by converging and diverging streamlines on the sides of the cube) and the arch vortex behind the cube, a forward stagnation point, and the principal reattachment line behind the cube. Some differences in the four figures are found behind the body; most of the other results submitted resemble the left part of the figure more than the right and are not shown for that reason.

The mean velocity profiles upstream of the cube (not shown here) reveal that the simulations have different mean mass fluxes (up to 6 percent variation) on the centerplane even though all cases have the same (specified) total mass flux. This is another consequence of the relatively short averaging time; the averaging times in the simulations varied between 30 and 100 D/U where D is the cube height and U is the bulk velocity at the inlet. Queries to the computers produced the response that the mass fluxes averaged over the inflow plane agreed to within about 1 percent.

The mean velocity profiles above the cube shown in Fig. 12 show no evidence that the grid resolution is causing severe problems. Note that there is also not enough evidence to support the contention that refinement of the grid would not change the results. Indeed, some of the results show small "wiggles" that are probably due to insufficient resolution. The velocity profiles in the recirculation region behind the cube (Fig. 12(b)) show fairly good agreement for a quantity that we had expected to be difficult to compute accurately.

7.2 Case B2. For Case B2, all of the simulations used the results of a channel flow simulation to provide the inlet conditions and used wall functions at the surface. A list of the parameters used in obtaining the simulation results is given in Table 6.

Table 8 gives the length scales of the simulated flows, RANS calculations to be discussed later, and the experimental values. The agreement with each other is quite good but not as good as it was in Case B1. The agreement with the experimental results is also quite good. The length, X_{F1} , locates the upstream stagnation point. Between this point and the cube, there is a very thin region of upstream moving fluid that is difficult to resolve accurately in either the experiment or the simulations so the values should be regarded with more suspicion than those for the other quantities.

For the primary reattachment length, the agreement among the simulations based on the Smagorinsky model is quite good but the one simulation that used the dynamic model, which is identical to the simulation above it in the table in every other way, predicts a shorter reattachment length. This is consistent with what was found in Case B1. Comparison of Tables 7 and 8 shows that the Reynolds number does not seem to affect the length scales (other than the location of the upstream stagnation point) very much.

The streamlines on the center plane of the flow shown in Fig. 13 demonstrate that the agreement with experiment is quite good. The most important differences are found in the head of the horseshoe vortex but this is a region where the experimental uncertainty is relatively large so it is not clear whether the simulations or experiments are more nearly correct.

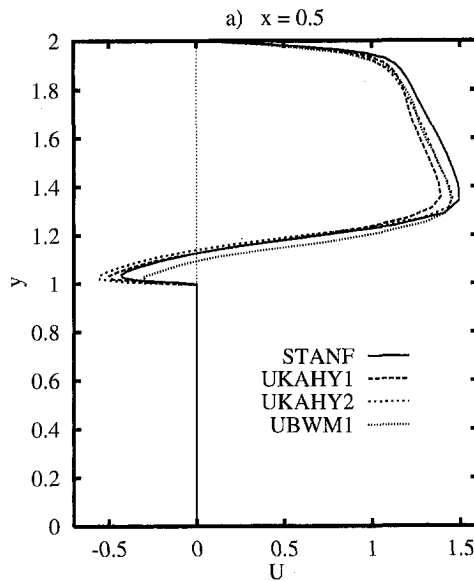


Fig. 12(a)

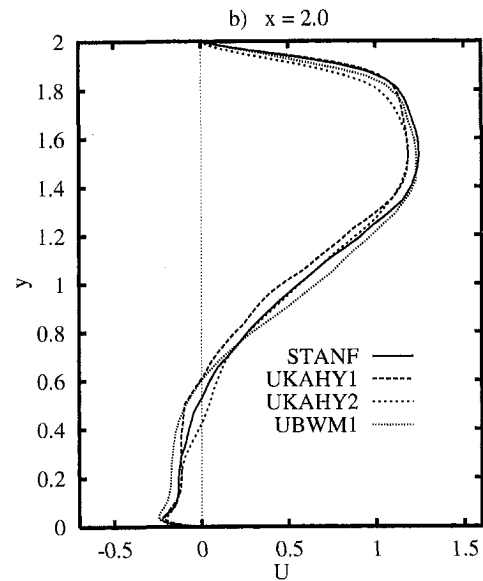


Fig. 12(b)

Fig. 12 Profile of the mean streamwise velocity U at two different locations in the symmetry plane of the cube, Case B1

Table 6 Submissions for Case B2: groups, parameters and methods

Contrib./Key	Group, Affiliation	Grid	Time Scheme	Convection Scheme	Subgrid-Scale Model	C_s	Wall Damping: (a,b)	Wall Bound. Cond.	$T_{\text{averaging}}$
UKAHY3	M. Breuer, M. Pourquie, W. Rodi, Univ. of Karlsruhe, Inst. for Hydromechanics, Germany	FV: 165x65x97	AB	Central (2nd)	Smagorinsky	0.1	VDD: (3,0.5)	WF	≈ 150.1
UKAHY4	H. Wengle, Univ. der Bundeswehr München, Germany	FV: 165x65x97	AB	Central (2nd)	Dynamic	-	-	WF	≈ 108.6
UBWM2	T. Kobayashi, N. Taniguchi, T. Kogaki, Inst. of Industrial Science, Univ. of Tokyo, Japan	FV: 144x58x88	LF	Central (2nd)	Smagorinsky	0.1	no	WF	$\approx 703/650$
IIS-KOBA	T. Kobayashi, N. Taniguchi, T. Kogaki, Inst. of Industrial Science, Univ. of Tokyo, Japan	FV: 66x36x46	RK	Central (2nd)	Smagorinsky	0.1	VDD: (1,1)	WF	10

AB = Adams-Bashforth (2nd), CN = Crank-Nicolson, EU = Euler Scheme (1st) FV = Finite Volume, LF = Leap-Frog
 RK = Runge-Kutta (2nd), VDD = Van Driest Damping: $(1 - \exp(-y^*/26))^3$, WF = Wall Function

The surface streamlines on the channel floor are shown in Fig. 14 and display all of the features described for Case B1. Indeed, the two cases are so similar that there is not much to

Table 7 Lengths for Case B1; see Fig. 9 for definitions of these length scales

Contribution/key	Separation/Reattachment Length				
	X_{F1}	X_{F2}	X_T	X_{R1}	X_{R2}
STANF	1.31	0.040	—	1.53	0.22
UKAHY1	1.39	0.059	—	1.60	0.24
UKAHY2	1.29	0.072	—	1.42	0.17
UBWM1	1.24	0.058	0.836	1.59	0.22

Table 8 Lengths for Case B2; see Fig. 9 for definitions of these length scales

Contribution/key	Separation/Reattachment Length				
	X_{F1}	X_T	X_{R1}	X_{R2}	
EXP (Martinuzzi, 1992) (Martinuzzi and Tropea, 1993)	EXP	1.040	—	1.612	?
LES	UKAHY3	1.287	—	1.696	0.265
	UKAHY4	0.998	—	1.432	0.134
	UBWM2	0.808	0.837	1.722	?
RANS (Breuer et al., 1995)	IIS-KOBA	0.835	0.814	1.652	?
	Standard $k-\epsilon$	0.651	0.432	2.182	0.021
	KL modification	0.650	—	2.728	0.020
	Two-layer $k-\epsilon$	0.950	—	2.731	0.252

add to the discussion given above. Insofar as can be determined (the experimental photograph is somewhat difficult to read), the agreement with experiment is quite good.

Two velocity profiles above and behind the cube are shown in Fig. 15. The agreement with the experimental data is satisfactory but the differences between the computed results are much larger than in Case B1 and some simulations give velocities that are much too small in the reverse-flow region. It is difficult to discern from this plot whether the boundary conditions that were used are satisfactory or not.

The results discussed above, as well as those for Case A, show that, compared to the Smagorinsky model, the dynamic model usually yields larger subgrid scale eddy viscosities in the shear layers surrounding the separated flow zones and smaller eddy viscosities in the recirculation regions themselves. This is reasonable behavior but it is difficult to demonstrate that the dynamic model actually produces better simulations than the Smagorinsky model. It does seem likely, however, since the distribution of the viscosity is more in keeping with expectations, that some version of the dynamic model will ultimately yield superior simulations.

8 Comparison With RANS Models

Test cases A and B2 have also been calculated with various RANS models by one of the organizer's groups (Franke and Rodi, 1993; Breuer et al., 1995; Bosch, 1995). For case A the unsteady two-dimensional phase-averaged equations were solved, i.e., the periodic motion was resolved, while the effect of the superimposed stochastic turbulent motion was simulated with various turbulence models for the phase-averaged Reynolds stresses. The standard $k-\epsilon$ model, a modification due to

Kato and Launder (1993) which suppresses turbulence production in the stagnation region, and a Reynolds-stress equation (RSE) model by Launder et al. (1975) were employed. In each case, either wall functions or a two-layer approach in which a one-equation model is applied in the near-wall region was used.

The Strouhal number is well predicted by most of the various RANS models, but the Kato-Launder (KL) modification produces values that are somewhat too large and the two-layer RSE model yields an excessive value (see Table 4). The mean drag coefficient is significantly underpredicted by the standard $k - \epsilon$ model, but a roughly correct value is obtained when the KL modification is used with the two-layer approach. The RSE model gives the correct value of $\overline{c_d}$ with wall functions but overpredicts it if the two-layer approach is used. This result is consistent with the significant overprediction of the length of the recirculation region by the standard $k - \epsilon$ model and its underprediction by the two-layer RSE model. There is a severe underprediction of the fluctuating energy in the former case and an overprediction in the latter. The KL modification to the $k - \epsilon$ model in combination with the two-layer approach gives overall the best prediction of the centerline velocity, especially in the near-field, but further downstream the velocity recovers faster than in the experiments. None of the RANS results is close to the measured behavior further downstream, in contrast

to at least some of the LES calculations shown in Fig. 4. If plotted on Fig. 5, the best RANS calculations would be as good as the better LES calculations. Although the total fluctuating energy is roughly correct, the stochastic part is severely underpredicted and the periodic part is overpredicted. Hence, while the RANS calculations can certainly be used for practical applications, they are not satisfactory in a more detailed view. On a VP S 600 vector computer, the $k - \epsilon$ model RANS calculations using wall functions took 2 hours and the two-layer calculations 8 hours, compared with 46 hours for the UKAHY1 LES calculations.

Case B2 was calculated with various versions of the $k - \epsilon$ model by Breuer et al. (1995): the standard model and the KL modification using wall functions, and the standard model in a two-layer approach using a one-equation model near the wall. The lengths defined in Fig. 9 predicted with these models are included in Table 8. It can be seen that all the RANS models overpredict the length of the separation zone behind the cube significantly. The standard $k - \epsilon$ model predicts early reattachment of the flow on the roof. Due to suppression of turbulence production in front of the cube, this situation is improved somewhat using the KL modification; the most realistic prediction is, however, obtained with the two-layer approach which resolves the flow on the roof better. This is also the only model in which the near-wall flow structure is close to that shown in Fig. 14; the models that use wall functions do not produce these details. Results are not available for a combination of the KL modification and the two-layer approach, but as with case A, this model version would probably give the best overall prediction (especially in the stagnation, roof, and near-wall regions), but the recirculation region would probably be too long. Hence, the velocity profiles, especially further downstream of the cube, are significantly better predicted by LES, and the turbulence quantities are in significantly better agreement with the experiments. In this case LES shows a clear superiority for which a high price has to be paid: on the VP S 600 the LES calculations (UKAHY4) took 160 hours while the RANS two-layer model calculations took 6 hours and the RANS calculations using wall functions only 15 minutes.

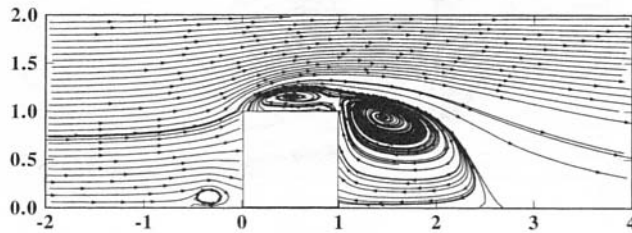


Fig. 13(a)

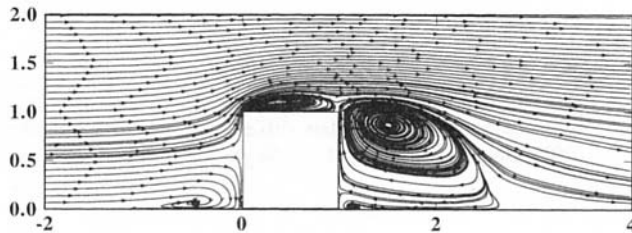


Fig. 13(b)

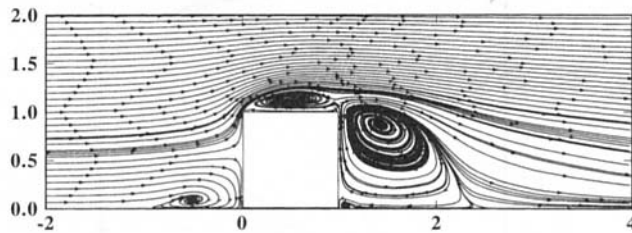


Fig. 13(c)

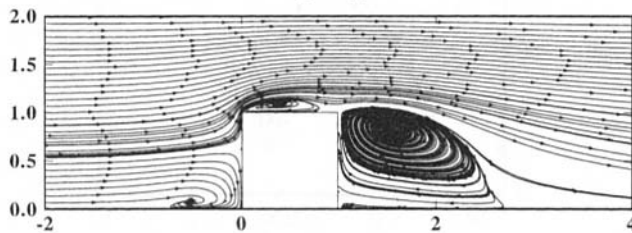


Fig. 13(d)

Fig. 13 Streamlines of the mean flow projected onto the centerline of the cube flow of Case B2

9 Conclusions

The results presented above show that LES does not automatically produce excellent results for every flow. To obtain quality results, many factors must be controlled carefully. Included among these are the following:

- *Flow:* Of the cases considered here, the cube flow was predicted much more accurately than the square cylinder flow. It appears that this is a consequence of the square cylinder flow having a transitional character and the possibility (which should be investigated) that this flow is much more sensitive to small changes in the controlling parameters. In general, it appears that transitional flows are more challenging than fully developed ones.
- *Grid:* The results are sensitive to the grid used in the simulation. It is important to resolve those regions of the flow in which the major part of the production of the turbulence and/or transition take place. This may need to be done on a kind of adaptive way in which the grid is changed after simulations are performed. Physical insight into the nature of the flow can be a considerable aid to improving the grid and should be used whenever possible and subject to examination and improvement as suggested above.
- *Boundary Conditions:* 'Law of the wall' boundary conditions can definitely reduce the cost of a simulation by something an order of magnitude. However, they do not seem to be reliable enough to be used with confidence in separated flows. It would be useful to look in detail at the

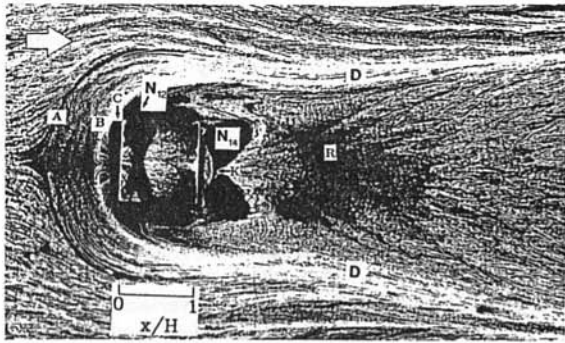


Fig. 14(a)

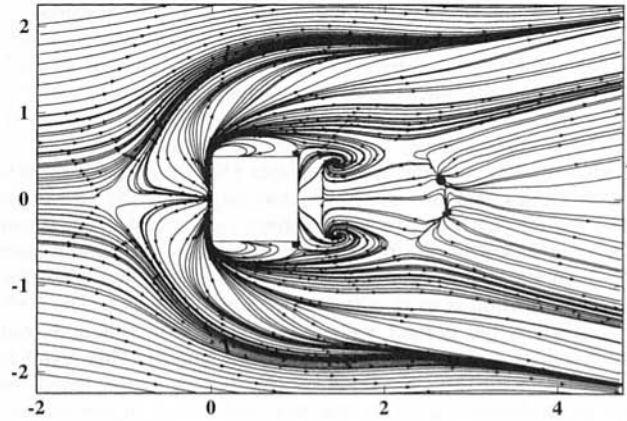


Fig. 14(b)

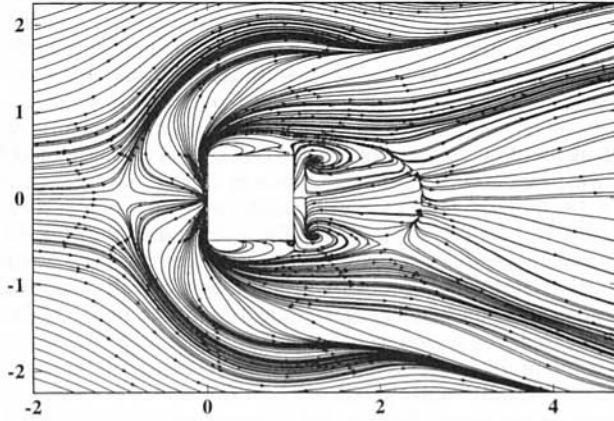


Fig. 14(c)

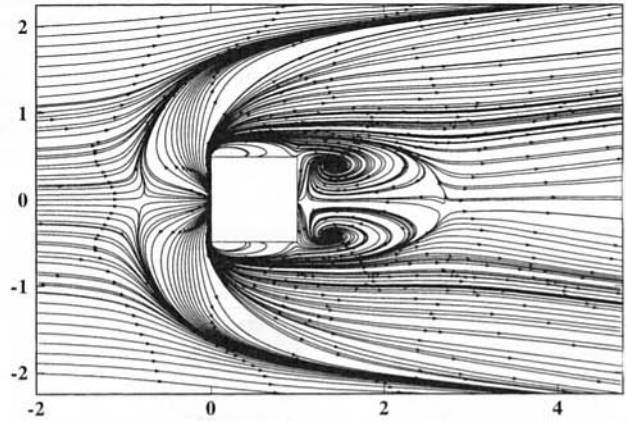


Fig. 14(d)

Fig. 14 Streamlines of the mean flow projected onto the floor of the channel in the cube flow of Case B2 along with an experimental oil-flow photograph

near wall region of the cube flow to determine why the high Reynolds number calculations are as good as they are.

- *Subgrid Scale Model:* The predictions produced by different subgrid scale models differ, and, as expected, the differences are larger at high Reynolds number. The dy-

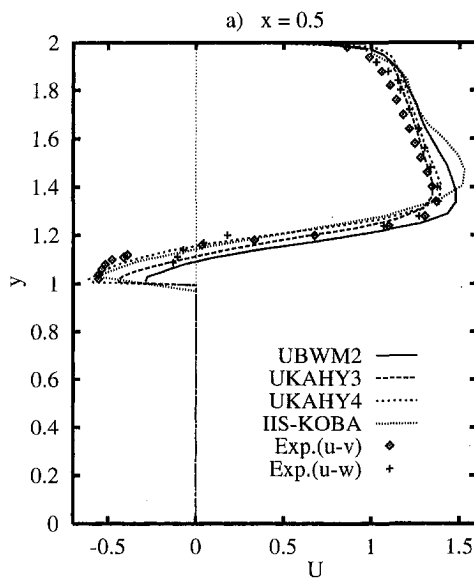


Fig. 15(a)

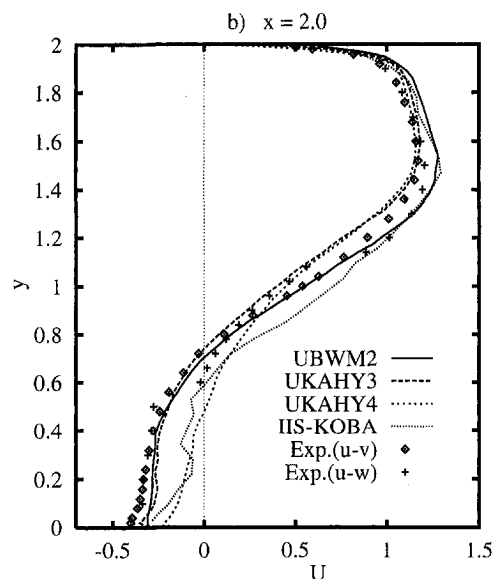


Fig. 15(b)

Fig. 15 Profile of the mean streamwise velocity U at two different locations in the symmetry plane of the cube, Case B2

dynamic model appears to produce a better spatial distribution of the subgrid scale eddy viscosity but not necessarily better overall results relative to the Smagorinsky model. We need to understand why that is and how to further improve the models.

- **Numerical Method:** The results produced by different numerical methods with similar grids certainly differ. We need to learn how to estimate the numerical errors and to determine their effects on the results, and, eventually, to learn how to control them.
- **Domain Size:** It is well-known that boundary conditions can affect the solution within a domain if the domain is not large enough. It is possible that the domain specified for the square cylinder flow is too small. There are no indications that this is the case in the cube flow.

10 Recommendations

We anticipate that there will be more workshops of this type in the future. It is natural that, in the course of a workshop of this kind, one learns things that would have made it better. We would therefore like to share some observations and make some final remarks.

Much of what was learned in terms of how the various factors affect the results was gleaned from those cases in which a single group made multiple simulations that differed in just one factor. It is therefore strongly recommended that, in future workshops of this type, one attempts to have all of the groups do one case in which all of the relevant factors are specified, and then ask them to vary one of the factors listed above in a systematic way. This would also be a useful direction for the authors of research papers to follow.

It is probably best to avoid transitional flows as they are difficult to treat with LES. Alternatively, given sufficient interest, it might be possible to have a workshop devoted entirely to this important subject.

It would be very useful to have participants present their values of eddy viscosity (assuming that type of model is used) and the dissipation produced by it. It is also important to require people who use upwind methods to report the dissipation caused by the numerical scheme.

Special attention must be devoted to the regions near solid surfaces. It is clear that many of the difficulties arise in this region. It appears that the boundary conditions intended to allow a simulation to avoid computing the wall region that exist today are not reliable.

Finally, there is a need to tackle still more complex geometries. Performing LES on unstructured grids, while it can certainly be done, still needs to be established. The one finite element submission to this workshop was not polished enough to provide as much information as one would have liked.

It is important that a workshop of this kind not become a contest in which the contributors argue about which simulation is best; the term "Olympics" that has been applied to workshops of this kind in the past is best avoided. The objective should be nothing more or less than to determine what is necessary to do the job well.

Properly chosen RANS models can simulate these flows at lower cost but also at lower accuracy. In flows in which 'significant extra strains' are present and large scale structures dominate the turbulent transport, RANS modeling will be very difficult but there is no reason to expect that LES will not be able to simulate them. Therefore the best opportunities for early application of LES will probably be to flows with complex strains and dominant large scale structures but only moderately complex geometry.

Acknowledgments

The authors are exceedingly grateful to the Max Planck Foundation which provided the primary support for the conference

that is the subject of this paper through the Alexander von Humboldt Foundation. Additional support was provided by Electricité de France and Advanced Scientific Computing (Germany) GmbH. We also need to thank the participants in the conference who generously provided their results and, especially, the other members of the evaluation committee: P. Moin, S. P. Vanka, and P. R. Voke.

References

- Andren, A., Brown, A. R., Graf, J., Mason, P. J., Moeng, C. H., Nieuwstadt, F. T. M., and Schumann, U., 1994, "Large Eddy Simulation of a Neutrally Stratified Boundary Layer," *Quarterly Journal of the Royal Meteorological Society*, Vol. 120, pp. 1457–1484.
- Bardina, J., Ferziger, J. H., and Reynolds, W. C., 1980, "Improved Subgrid Models for Large Eddy Simulation," AIAA paper 80-1357.
- Bearman, P. W., and Obasaju, E. D., 1982, "An Experimental Study of Pressure Fluctuations on Fixed and Oscillating Square Section Cylinders," *Journal of Fluid Mechanics*, Vol. 119, pp. 297–321.
- Bosch, G., 1995, Experimentelle und theoretische Untersuchung der instationären Strömung um zylindrische Strukturen, Ph.D. Thesis, University of Karlsruhe.
- Breuer, M., Lakehal, D., and Rodi, W., 1996, "Flow around a Surface Mounted Cubical Obstacle: Comparison of LES and RANS-Results," IMACS-COST Conference on Computational Fluid Dynamics, Three-Dimensional Complex Flows, Lausanne, Switzerland, Sept. 13–15, (1995), *Computation of 3D Complex Flows*, M. Deville, S. Gavrilakis and I. L. Rhyming, eds., *Notes on Numerical Fluid Mechanics*, Vol. 53, pp. 22–30, Vieweg Verlag, Braunschweig.
- Breuer, M., and Pourquie, M., 1996a, "First Experiences with LES of Flows past Bluff Bodies," *Proceedings of the 3rd International Symposium of Engineering Turbulence Modelling and Measurements*, Heraklion-Crete, Greece, May 27–29, 1996, *Engineering Turbulence Modelling and Experiments*, Vol. 3, pp. 177–186, W. Rodi and G. Bergeles, eds., Elsevier Science B.V.
- Breuer, M., and Rodi, W., 1996b, "Large-Eddy Simulation of Complex Turbulent Flows of Practical Interest," *Flow Simulation with High-Performance Computers II*, E. H. Hirschel, ed., *Notes on Numerical Fluid Mechanics*, Vol. 52, pp. 258–274, Vieweg Verlag, Braunschweig.
- Cheng, C. M., Lu, P. C., and Chen, R. H., 1992, "Wind Loads on Square Cylinder in Homogeneous Turbulent Flows," *Journal of Wind Engineering*, Vol. 41, pp. 739–749.
- Clark, R. A., Ferziger, J. H., and Reynolds, W. C., 1979, "Evaluation of Subgrid Scale Turbulence Models Using a Fully Simulated Turbulent Flow," *Journal of Fluid Mechanics*, Vol. 91, pp. 1–16.
- Deardorff, J. W., 1970, "A Numerical Study of Three-Dimensional Turbulent Channel Flow at Large Reynolds Number," *Journal of Fluid Mechanics*, Vol. 41, pp. 453–480.
- Ferziger, J. H., 1983, "Higher Level Simulations of Turbulent Flow," in: *Computational Methods for Turbulent, Transonic, and Viscous Flows*. J.-A. Essers, ed., Hemisphere.
- Ferziger, J. H., 1996, "Large Eddy Simulation," *Simulation and Modeling of Turbulent Flows*, M. Y. Hussaini and T. Gatski, eds., Cambridge University Press.
- Franke, R., and Rodi, W., 1993, "Calculation of vortex shedding past a square cylinder with various turbulence models," *Proceedings of 8th Symposium on Turbulent Shear Flows*, F. Durst et al., eds., Springer-Verlag, Berlin, pp. 189–204.
- Germano, M., Piomelli, U., Moin, P., and Cabot, W. H., 1991, "A Dynamic Subgrid Scale Eddy Viscosity Model," *Physics of Fluids A* 3 (7), pp. 1760–1765.
- Kato, M., and Launder, B. E., 1993, "The modelling of turbulent flow around stationary and vibrating square cylinders," *Proceedings of 9th Symposium on Turbulent Shear Flows*, Kyoto, pp. 10.4.1–10.4.6.
- Launder, B. E., Reece, G., and Rodi, W., 1975, "Progress in the development of a Reynolds stress turbulence closure," *Journal of Fluid Mechanics*, Vol. 68, pp. 537–566.
- Lee, B. E., 1975, "The Effect of Turbulence on the Surface Pressure Field of Square Prisms," *Journal of Fluid Mechanics*, Vol. 69, pp. 263–282.
- Lilly, D. K., 1992, "A Proposed Modification of the Germano Subgrid Scale Closure Method," *Physics of Fluids A*, Vol. 4 (3), pp. 633–635.
- Lyn, D. A., and Rodi, W., 1994, "The Flapping Shear Layer Formed by Flow Separation from the Forward Corner of a Square Cylinder," *Journal of Fluid Mechanics*, Vol. 267, pp. 353–376.
- Lyn, D. A., Einav, S., Rodi, W., and Park, J.-H., 1995, "A Laser-Doppler-Velocimetry Study of Ensemble-Averaged Characteristics of the Turbulent Near Wake of a Square Cylinder," *Journal of Fluid Mechanics*, Vol. 304, pp. 285–319.
- Martinuzzi, R., 1992, "Experimentelle Untersuchung der Umströmung wandgebundener, rechtiger, prismatischer Hindernisse," Ph.D. thesis, University of Erlangen.
- Martinuzzi, R., and Tropea, C., 1993, "The Flow around a Surface Mounted Prismatic Obstacle Placed in a Fully Developed Channel Flow," *ASME JOURNAL OF FLUIDS ENGINEERING*, Vol. 115, pp. 85–92.
- Mason, P. J., and Thompson, D. J., 1992, "Stochastic Backscatter in Large Eddy Simulation of Boundary Layers," *Journal of Fluid Mechanics*, Vol. 242, pp. 51–78.

McLean, I., and Gartshore, I., 1992, "Spanwise Correlations of Pressure on a Rigid Square Section Cylinder," *Journal of Wind Engineering*, Vol. 41, pp. 779–808.

Nieuwstadt, F. T. M., Mason, P. J., Moeng, C. H., and Schumann, U., 1992, "Large Eddy Simulation of the Convective Boundary Layer: A Comparison of Four Computer Codes," *Proceedings of 8th Symposium on Turbulent Shear Flows*, F. Durst et al., eds., Springer-Verlag, Berlin, pp. 343–367.

Piomelli, U., Ferziger, J. H., Moin, P., and Kim, J., 1989, "New Approximate Boundary Conditions for Large Eddy Simulations of Wall-Bounded Flows," *Physics of Fluids A*, Vol. 1, pp. 1061–1068.

Rogallo, R. S., and Moin, P., 1994, "Numerical Simulation of Turbulent Flows," *Annual Review of Fluid Mechanics*, Vol. 16, pp. 99–137.

Smagorinsky, J., 1963, "General Circulation Experiments with the Primitive Equations I. The Basic Experiment," *Monthly Weather Review*, Vol. 91, pp. 99–165.

Vickery, B. J., 1975, Fluctuating Lift and Drag on a Long Cylinder of Square Cross Section in a Smooth and a Turbulent Stream," *Journal of Fluid Mechanics*, Vol. 25, pp. 481–494.

Voke, P. R., Kleiser, L., and Chollet, J. P. (eds.), 1994, *Direct and Large Eddy Simulation*, Kluwer Academic Publishers.

Werner, H., and Wengle, H., 1989, "Large Eddy Simulation of Flow over a Square Rib in a Channel," *Proceedings of 7th Symposium on Turbulent Shear Flows*, Stanford University, Aug 21–23, pp. 10.2.1–10.2.6.

Experimental Study of Turbulent Concentration Flow Field in the Wake of a Bluff Body

R. Balachandar

Assistant Professor,
Department of Civil Engineering,
University of Saskatchewan,
57 Campus Drive, Saskatoon,
Canada, S7N 5A9

Vincent H. Chu

Professor.

Jianbo Zhang

Graduate Student.

Department of Civil Engineering,
McGill University,
817 Sherbrooke St. West, Montreal,
Canada, H3A 2K6

Experiments were conducted to determine the turbulent concentration field in the wake of a normal flat plate. Dye was introduced behind the plate as the tracer. The measurement of the dye concentration was carried out using an optical colorimeter in the near wake, covering a distance of five to thirty plate widths downstream of the body. The mean, r.m.s., and intermittency profiles of the concentration field were obtained at a number of cross sections. Phase averaging was also carried out to determine the structure of the large scale eddies. Typical maximum concentration levels in the core of the eddies were found to be two to four times larger than the corresponding mean values. The widths of the concentration profiles in the near wake are 1.5 to 2.5 times wider than the corresponding widths of the velocity profiles. The present dye concentration data obtained for the normal flat plate are unique and complement a small number of previous experimental investigations of the scalar field based on temperature measurements in the wake of circular cylinders.

Introduction

Turbulent wakes generated by flow past objects have been the subject of extensive investigations (Antonia, 1987; Cantwell, 1983; Cimbala, 1988; Fabris, 1979; Kiya, 1988; Perry, 1987; Roshko, 1953; Townsend, 1949; Wagnanski, 1986). Several reviews (Bearman, 1984; Berger, 1972; Marris, 1964; Sarpkaya, 1979) have also appeared on this topic. The wake generator used in many previous studies has been a circular cylinder placed normal to the flow. The flow under these conditions is subjected to severe Reynolds number effects, especially in the critical range. The location of the flow separation points shift and as a consequence, the hydrodynamic characteristics like the drag coefficient and the Strouhal number are dependent on the flow Reynolds number. Furthermore, most of the test results reported earlier deal with velocity measurements in the far wake. Flow visualization and hot wire measurements in the far wake indicate the existence of a large scale motion. These structures, though reminiscent of a Karman vortex street are nevertheless weakly organized. In this far-wake region, the velocity field has been found to be dynamically similar and can be defined by a characteristic velocity $\{U(d/x_o)^{0.5}\}$ and a characteristic length scale $\{(x_o d)^{0.5}\}$, independent of the flow Reynolds number. Here, U is the velocity upstream of the body, d is the diameter of the cylinder and x_o is the distance measured from the virtual origin.

Many earlier measurements in the near and intermediate wake, in general, indicate a qualitative confirmation of a loss of organization with increasing distance from the cylinder. Table 1 gives a comprehensive review of related studies. The visual study by Taneda (1959), revealed that the breakdown of the vortices occurred within 100 diameters from the cylinder and organized vortices reappear farther downstream. Taneda has attributed this process to a hydrodynamic instability. Several other mechanisms such as pairing or amalgamation of vortices have also been suggested to explain this process. Uberoi and Freymuth (1969), note that all regular vortices break down for $x/d > 48$. Here, x is the axial distance reckoned from the cylinder. The organization of structures in the turbulent near

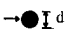
wake have been studied by Antonia (1991), Browne (1989), Hayakawa (1989), and Kiya (1988). Hayakawa (1989) studied the three-dimensional nature of the organized motions in the wake ($10 \leq x/d \leq 40$) of a circular cylinder using an array of eight X-probes. Using a similar device, Antonia (1991) addressed the contribution, the near wake structures make to the Reynolds stresses and how this contribution varies with distance from the cylinder. By obtaining the spectra of the lateral velocity fluctuations in the near wake, Browne et al. (1989) suggest that the origin of the far-wake organized motion can be traced back to the cylinder. Kiya (1988) conducted measurements at an axial location eight body widths downstream of a normal flat plate to obtain the various frequency components of the incoherent velocity fluctuations.

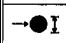
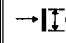
Scalar measurements like temperature have also been carried out in the far wake of circular cylinders by Antonia (1987) and LaRue (1974a, 1974b, 1974c); in the near wake by Fage (1935) and in the intermediate wake by Freymuth (1971). The structure of these wakes have been studied with regards to the spectra of temperature fluctuations. Attempts have also been made to obtain the proper scaling parameters to obtain dynamic similarity in the far wake. These studies indicate that the far wake is essentially a self preserving region. All the earlier studies dealing with scalar measurements have been carried in the wake of circular cylinders (Table 1).

The present study is concerned with the concentration flow field characteristics in the near wake of a flat plate placed normal to the flow. The fixed flow separation points at the edge of the plate ensure the independence of the flow characteristics on the Reynolds number. The study focuses on the near wake region ($0 < x/d < 30$), primarily on the measurement of a passive scalar. Concentration data are of immense usefulness in combustion studies, mixing devices and environmentally related flows. In relation to flow past objects, most of the previous data were obtained in the wake of circular cylinders. With the exception of Freymuth (1971), Antonia (1987), LaRue (1974), and Fage (1935), velocities were usually measured. However, these available concentration data are also in the wake of circular cylinders. Until now, there is no comparable tracer concentration measurement (dye or low temperatures) behind the normal flat plate. The present data not only supplement the existing information based on velocity measurements but are also useful for the purpose of turbulence model verification.

Contributed by the Fluids Engineering Division for publication in the JOURNAL OF FLUIDS ENGINEERING. Manuscript received by the Fluids Engineering Division February 18, 1995; revised manuscript received February 29, 1996. Associate Technical Editor: M. Gharib.

Table 1 Related previous studies

Body type	Reference	Measured variables and analysis technique
Circular cylinder 	Cimbala et al (1988)	Hot wire, Velocity profiles Spectra of velocity fluctuations $25 \leq x/d \leq 750, 70 < Re < 2000$
	Fabris (1979)	Temperature and velocity Conditional sampling and Intermittency ($x/d = 200, 400$)
	Freymuth et al (1971)	Temperature, Spectra ($25 \leq x/d \leq 1140, Re = 960$)
	Antonia et al (1987)	Velocity and temperature Spectra and Intermittency ($230 \leq x/d \leq 600, Re = 1190$)
	Antonia (1991)	Velocity, Reynolds stresses ($10 \leq x/d \leq 60, Re = 5600$)
	Antonia (1989)	Velocity ($x/d = 420, Re = 1170$) Spectral and phase averaging
	Browne et al (1989)	Velocity, Spectra ($6.7 \leq x/d \leq 104, Re = 1170, 5580$)
	LaRue, J.C. and Libby, P.A (1974c)	Temperature and velocity ($x/d = 400, 500, Re = 2800$) At $x/d = 400, \delta/d = 5.77$ and $\delta/d = 3.64$
	LaRue (1974b)	Temperature, Intermittency and frequency of crossing. ($x/d = 400, Re = 2800, \delta/d = 7.16$)
	Uberoi, M.S. and Freymuth, P. (1969)	Velocity, Spectra ($25 \leq x/d \leq 800, Re = 540$)
	Fige, A. and Falkner (1935)	Velocity and temperature ($x/d = 36, Re = 16900$)
	Hayakawa, M. and Hussain (1989)	Velocity, Phase averaged vorticity ($10 \leq x/d \leq 40, Re = 13000$)

Body type	Reference	Measured variables and analysis technique	
Circular cylinder 	Cantwell and Coles (1983)	Velocity Phase averaging and vorticity $0 \leq x/d \leq 8$	
	Townsend, A.A. (1949)	Velocity $500 \leq x/d \leq 950$	
	Rosliko, A. (1954)	Wake development	
	Taneda, S. (1959)	Visual observations	
	Wygnański et al (1986)	Velocity ($200 \leq x/d \leq 700$) $1360 < Re < 5800, .84 < Cd < 1.1$	
	Hussain, A. and Ramjee, V. (1976)	Velocity $4 \leq x/d \leq 12, 60 \leq Re \leq 150$	
	Kovácsnay (1949)	Velocity, Hot wire $Re = 34, 56, 2 \leq x/d \leq 100$	
	Normal flat plate 	Bradbury (1976)	Velocity - Pulsed wire ($x/d = 1, 2$)
		Perry, A.E. and Steiner (1987)	Velocity ($1 \leq x/d \leq 13$) Phase averaging, Blockage = 25%
		Kiya, M. and Matsumura (1988)	Velocity ($x/d = 8, Re = 23000, S = 0.146$)
Moss et al (1977)		Velocity ($0.5 \leq x/d \leq 2, S = 0.14$)	
Wygnański et al (1986)	Velocity ($200 \leq x/d \leq 700$) $Re = 2166, C_d = 1.82$		
Ramamurthy (1973)	Blockage effects, Vortex shedding frequency		

x = axial distance from the cylinder or plate, d = cylinder diameter or plate width, $Re = Ud/\nu$, $S = fd/U$, C_d = drag coefficient

Experimental Setup and Procedure

The wake generator used in the present study was essentially a flat plate mounted vertically, normal to the flow in a rectangular cross-section open channel (Fig. 1(a)). The channel was 0.15 m deep, 1.4 m wide and 7 m long. The straight section of the channel was preceded by a contraction and several stilling arrangements to reduce any large scale turbulence in the flow. The bluff body was mounted about 2 m downstream of the contraction. Following Fig. 1(a) 'x' refers to the coordinate measured from the body along the axis of the wake and 'y' is the lateral coordinate measured from the axial plane. The width of the body (d) was 0.10 m yielding a blockage of 7 percent. The near wake is dominated by an alternate vortex shedding mechanism and the formation of the well known Karman vortex street (Fig. 1(b)). Dye of known concentration (C_o) and flow rate (q_o) was introduced into the wake immediately behind the plate by a special dye injection device. Care was taken to see that the injected dye did not cause any large scale disturbance in the wake. To this end, various injection devices were tested and finally an inverted "T" shaped tube with several holes (diameter = 0.7 mm) drilled on either side of the "T" was adopted (Inset, Fig. 1(a)). The row of holes from which the dye issued was set in a horizontal plane at mid depth of flow.

In the present study, the dye was introduced uniformly in the wake, behind the plate at $x/d = 0$. Only a minute amount of dye was introduced in the immediate region behind the plate. Following the vortex shedding mechanism, at a given instance, all the injected dye is entrained along the shear layer forming on one edge of the plate and into the developing vortex. At the next instance, all the dye is entrained into the succeeding vortex forming on the other edge of the plate.

The dye concentration was measured by an optical colorimeter (Brinkman Instruments). The concentration time-histories were digitized online by a A/D converter and stored for further processing. Data was acquired at the rate of 64 data points per second. The colorimeter was fitted with a light filter suitable to measure blue colored dyes. Several types of blue colored dyes were tested and a type of Navy blue (Trichromatic Inc., Quebec) was found to be most suitable in terms of providing measurable concentration levels in the latter part of the near wake region ($x/d \approx 30$) and also have a low enough dye injection rate (q_o) so as not to disturb the wake. The dye concentration measurements reported herein, were conducted at mid depth of flow. However, some measurements were also conducted at one third and two thirds of the depth, to ensure uniformity of dye distribution along the depth. The maximum variation in the

Nomenclature

C = average dye concentration at any location	f = frequency of down zero crossing	y = lateral distance reckoned from the wake axis
C_o = dye concentration at point of injection	h = depth of flow	γ = intermittency factor
C_d = drag coefficient	$I(t)$ = intermittency function	δ = half wake width based on mean concentration profile
$C_{ph}(\tau)$ = time variation of concentration over a phase	M = number of digital time steps in a phase	δ_γ = half wake width based on intermittency profile
$\langle C_{ph}(\tau) \rangle$ = time variation of concentration averaged over several phases	N = number of phases	δ_{rms} = half wake width based on r.m.s. concentration profile
c' = r.m.s. concentration	t_o = first instant of down zero crossing	δ_v = half wake width based on stream-wise mean velocity profile
d = diameter of cylinder or width of the plate	q_o = dye injection rate	θ = momentum thickness
	U = freestream velocity	τ = phase
	x = axial distance reckoned from the plate	
	x_o = axial distance reckoned from the virtual origin	

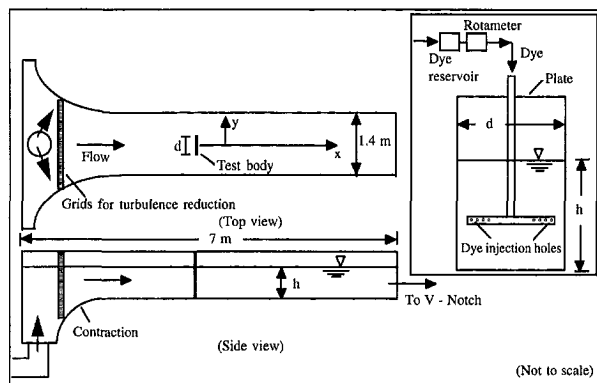
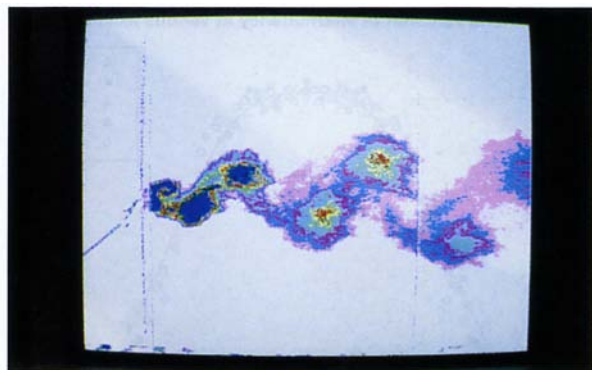


Fig. 1 (a) Experimental setup (inset: schematic of dye injection device)



Flow is from left to right

Fig. 1 (b) Digitized video image of the wake of a flat plate

mean profiles thus obtained, were less than 5 percent. The repeatability of measurements at any given section was also verified.

The distinction between the presence or absence of dye were made on the basis of instantaneous concentration fluctuations. Specifically, an intermittency function $I(t)$ was defined such that it has a value of unity in the presence of dye (turbulent) and a value of zero in the flow outside the wake (non-turbulent). The value of $I(t)$ was set equal to one when the instantaneous concentration value exceeded a particular threshold. To assist the decision on the level of the threshold, a number of plots of the concentration signal were obtained. This revealed that the fluctuations in the non-dye flow region were mostly noise and of short duration. The "hold time" procedure suggested by LaRue (1974c) and Fabris (1979) was adopted to bridge over short time periods when the signal crosses the threshold level and returns immediately so that this excursion is attributed to signal noise rather than to an extra short concentration spot. The threshold level chosen was such that there was a 1 percent change in the concentration level from the clear water reading. The hold time corresponds to 10 digital time steps. Several threshold levels were tried before adopting this value to ensure the measurement of the proper intermittency value. The average value of $I(t)$ is then defined as the intermittency factor γ . The average frequency of the up crossing (from dye to clear water) or down crossing (from clear water to dye) of the signal were also determined. To ensure that only valid crossings are accounted for, the same hold time values were adopted as that used in determining the $I(t)$ values.

Phase averaging was also carried out to study the organized motion in the near wake. This was achieved by identifying a time period (τ) from the instant of a valid down crossing to a valid up crossing. At any measurement location, after identifying the instant of first zero crossing (t_o), the variation of

concentration $C_{ph}(\tau)$ with time reckoned from t_o to $(t_o + \tau)$ is obtained. Following this, the variation of $C_{ph}(m\tau)$ with time is obtained at successive crossings. Here, m varies from 1 to N (the maximum number of phases). The average concentration over successive phases is denoted as:

$$\langle C_{ph}(\tau) \rangle = \frac{1}{N} \sum_{m=1}^{m=N} C_{ph}(m\tau)$$

Furthermore, $\tau = M\Delta t$; where M is the number of digital steps in the time period τ and $\Delta t = (\frac{1}{64})$ s. The phase averaging procedure thus involves in first identifying the value of M at a given measurement location. For a given time history, after identifying t_o , for a series of values of M , the corresponding values of $C_{ph}(\tau)$, $\langle C_{ph}(\tau) \rangle$ and the r.m.s value of $\langle C_{ph}(\tau) \rangle$ are determined. The value of M yielding the smallest r.m.s value of $\langle C_{ph}(\tau) \rangle$ is then chosen to determine τ . The minimum value signifies that the corresponding value of M yields the least random component of the r.m.s concentration for the entire time period of the presence of dye between a downward and a succeeding upward crossing and hence the most appropriate value of τ . For a given axial station (x/d), this minimum occurs in a very narrow range of M at most lateral locations (y/d) in the mid regions of the vortex. This procedure is rather unique and very easy to carry out when compared to the conventional methods of phase detection. It should be remarked that the degree of coherence of the large scale structures is expected to be very high in the near wake region. Several measurements were carried out at $x/d = 5.0, 10.0, 20.0$ and 30.0 downstream from the plate. The velocity upstream of the plate (U) was 9.22 cm/s, the water depth (h) was 5.27 cm and the dye flow rate (q_o) was 0.5 cm³/s. The Reynolds number of the flow based on the plate width was 9129.

Analysis of Results

Concentration Profiles and Half-Wake Widths. Figure 2 shows the lateral variation of the mean concentration C profiles at five axial stations downstream of the plate in the near wake region. Here,

$$C = \frac{1}{j} \sum_{i=1}^j C(i)$$

and j is the total number of digital steps in the acquired signal and $C(i)$ is the concentration at a given digital step. In the early regions of the wake, the profiles display a characteristic double peak. This can be attributed to the strongly prevalent Karman vortex street with the peak mean concentration occurring in the core region of the vortices. Visual observations indicate

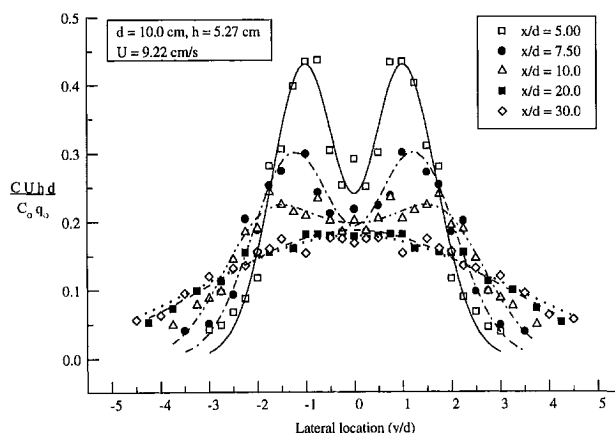


Fig. 2 Lateral variation of mean concentration at various axial stations (Uncertainty in $C = \pm 5\%$, in $y/d = \pm 2.5\%$)

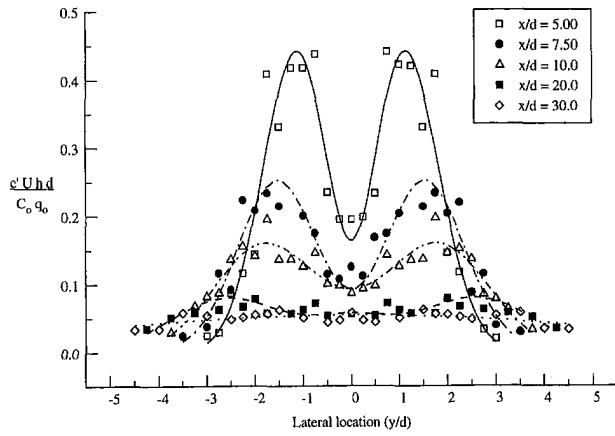


Fig. 3 Lateral variation of r.m.s. concentration at various axial stations (Uncertainty in $c' = \pm 5\%$, in $y/d = \pm 2.5\%$)

a nominally spanwise vortical structure {generally termed as ‘rolls’} connected to a succeeding roll on the other side of the wake axis by substructures called ‘ribs.’ In the early regions of the wake ($x/d \leq 10$), since the shape of the profiles appear to be preserved, one could speculate that the preferential mode of transportation of the dye is by the larger scales. As the vortex travels downstream, it entrains the surrounding fluid and the vortex increases in size. This results in the gradual fall of the peak mean concentration as indicated in Fig. 2. At larger values of x/d , the mean concentration profiles indicate a single peak as reminiscent in the far wake temperature measurements (Frey-muth, 1971, LaRue, 1974a). Equations of the form:

$$\frac{ChUd}{C_o q_o} = P_1 \exp[-(\eta/P_2 - P_3)^2] + P_1 \exp[-(\eta/P_2 + P_3)^2] - P_4 \exp[-(\eta/P_5)^2]$$

were fit through the experimental values and these are shown as lines in Fig. 2. Here, $\eta = y/d$ and the parameters P_1 to P_5 are chosen such that the fit lines have a coefficient of determination of at least 0.96. These equations were later used to determine the half-width of the wake. Similar to the mean concentration profiles, Figs. 3 and 4 show the variation of the r.m.s. (c') and maximum (C_{max}) concentration profiles, respectively. Here,

$$c' = \frac{1}{j} \sum_{i=1}^j \sqrt{[C(i) - C]^2}$$

while, C_{max} refers to the maximum value of $C(i)$ at any measur-

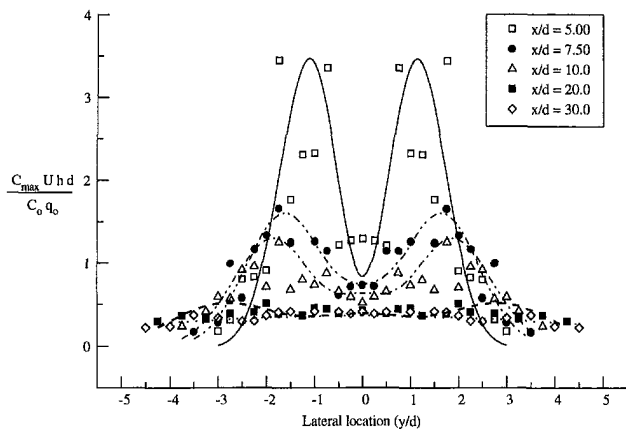


Fig. 4 Lateral variation of maximum concentration at various axial stations (Uncertainty in $C_{max} = \pm 5\%$, in $y/d = \pm 2.5\%$)

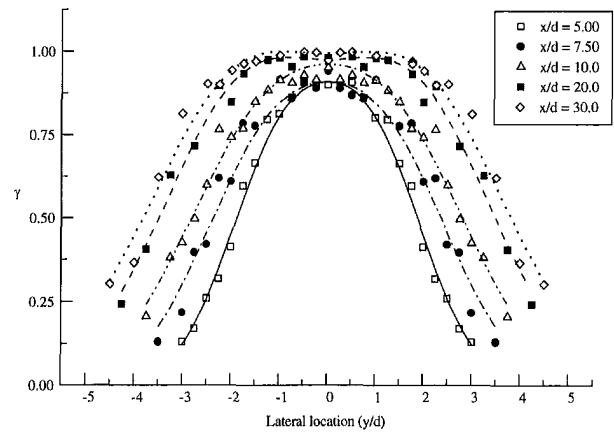


Fig. 5(a) Lateral variation of intermittency at various axial stations

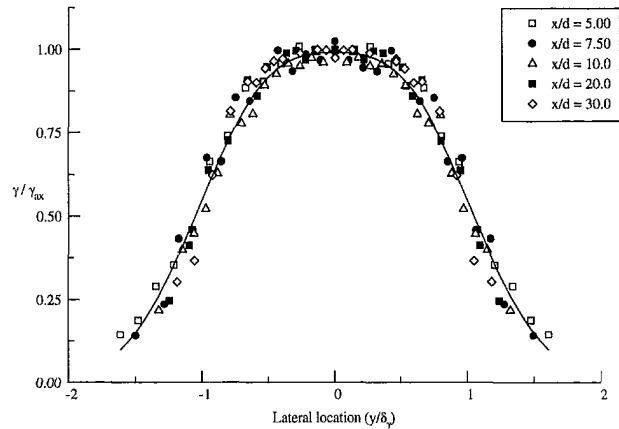


Fig. 5(b) Lateral variation of normalized intermittency at various axial stations

ing location. The r.m.s. and the maximum concentration profiles show a trend very similar to the mean concentration profiles with double peaks occurring in the early regions of the wake. While the r.m.s. concentration profiles are slightly wider than the mean concentration profiles, the maximum concentration profiles have peak values which are several times larger than the corresponding mean values. For example, at $x/d = 5.0$, the peak value in Fig. 4 is about eight times higher than that in Fig. 2. In general, at most locations, the C_{max} values are at least twice as high as the corresponding mean values. In many instances (e.g., fuel, pollutants), the value of C_{max} is major decision parameter.

Figure 5(a) shows the concentration intermittency factor profiles obtained at five different locations downstream of the test body. The peak values of the intermittency factor γ lie along the wake axis and these values approach unity as x/d increases. The profiles obtained at $x/d = 30$ typically resemble the ones obtained in the far wake temperature measurements (Antonia, 1987, LaRue, 1974). At each axial station, using the wake half-width as the length scale, one can normalize the intermittency values by the value along the wake axis (γ_{ax}). Figure 5(b) shows this plot and one notes that the data at all the axial stations collapse on to a single curve.

At any axial location, the wake half-width (δ) is defined as the point where the mean concentration is reduced to one half of the peak value as one traverses laterally from the location of the peak concentration towards the outer edge. Using Fig. 2, one can obtain the variation of δ/d with x/d (Fig. 6(a)). The wake appears to grow fairly rapidly in the regions closer to the plate. The rate of growth of the wake decreases as x/d becomes greater than 20. Also shown in Fig. 6(a) are the values of δ

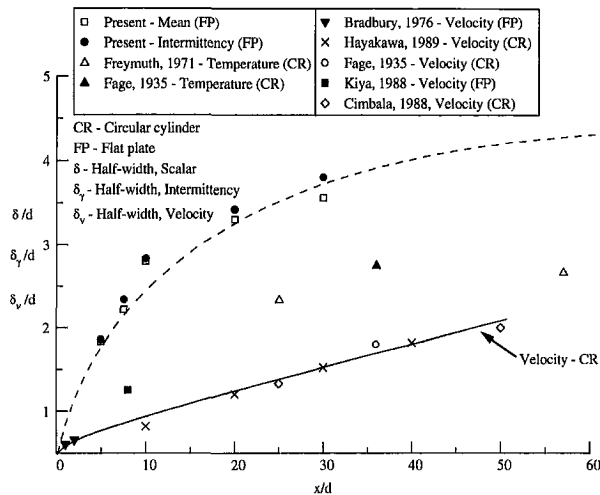


Fig. 6(a) Axial variation of wake half-width (Uncertainty in $\delta, \delta_\gamma = \pm 5\%$)

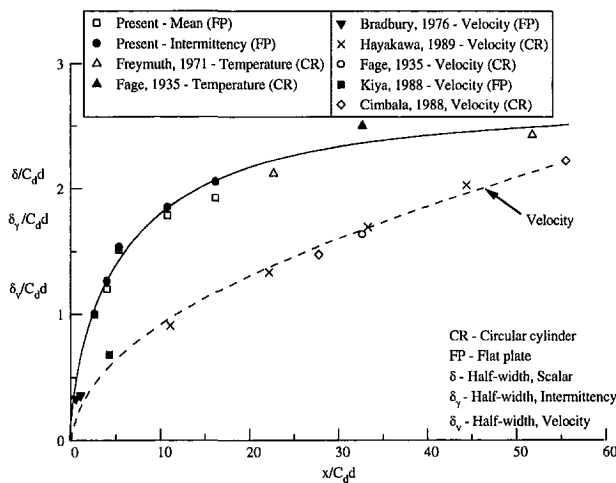


Fig. 6(b) Axial variation of normalized wake half-width (Uncertainty in $\delta = \pm 5\%$)

obtained by other investigators. The data of Freymuth (1971) and Fage (1935) were obtained using a temperature differential to mark the wake, while the widths obtained by all other investigators were evaluated using velocity profiles. The present variation of δ values based on the mean concentration profiles, are qualitatively similar but higher than previous data. This could very well be attributed to the change in the momentum length scales as the shape of the wake generators used are different. Normal flat plates have a higher drag coefficient (C_d) and hence a higher momentum thickness (θ) and consequently generate a wider wake. Following Wygnanski (1986) an effort was made in using the momentum thickness to define a characteristic length scale. Figure 6(b) shows variation of the half-wake widths normalised by $\theta (=C_d d)$. The scatter seen in Figure 6(a) seem to be fairly well absorbed for both the velocity and the scalar profiles. It should be noted that the values of C_d for the results presented have been estimated from data existing in literature (Table 1).

The value of the half-wake widths obtained using the velocity profiles (δ_v), are remarkably different from both the present set of data and other scalar measurements. The scalar profiles (concentration, temperature) indicate wake widths which are 1.5 to 2.5 times wider than those obtained by velocity measurements. A similar behavior has been noted by other investigators in the far wake (Hinze, 1959; LaRue, 1974c). However, in the far-wake, the ratio of $\delta_{\text{scalar}}/\delta_v$ is only of the order of about 1.3 ~ 1.6. The differences between δ_v and δ can be traced to the

nature of the Karman vortex street. As the vortices convect downstream, they also undergo significant rotational motion. At the outer edge of the vortices, the velocities are in the axial direction, as in the adjacent freestream. Furthermore, in the regions immediately succeeding the wake generator, the velocities in the region outside the wake are relatively high and at least 1.45 times the approaching freestream velocity (Roshko, 1954). Defining δ_v as the location where the velocity defect is reduced to one half, would therefore indicate a shorter width due to the influence of the adjacent freestream. However, in the case of an axisymmetric wake generated by a sphere, Freymuth (1973) found that the mean velocity profile was only faintly narrower than the mean temperature profile. One should note that a two-dimensional wake is more strongly organized than the wake of an axisymmetric bluff body. As noted from previous temperature measurements in the far wake (Freymuth, 1971, LaRue, 1974), the half-width increases to a value of about six diameters at 400 diameters downstream of the body.

Also defining the half wake-width as the location where γ approaches 0.50 (i.e., there is the presence of dye 50 percent of the time), one can evaluate the values of δ_γ using profiles shown in Fig. 5(a). The variation of δ_γ/d with x/d are also shown in Figs. 6(a) and 6(b). The values of half-wake widths obtained by using the intermittency factor profiles are very similar to that obtained by using the mean concentration profiles, especially in the early regions of the near wake ($x/d < 30$). It should be remarked that in earlier studies, the half-widths based on velocity intermittency profiles are 1.7 to 2 times greater than that obtained from the mean velocity profiles (Hinze, 1959; Townsend, 1949). Based on temperature measurements, LaRue (1974b) notes that δ_γ/δ was only of the order of 1.25 at $x/d = 400$.

Figure 7 shows the variation of $\delta_{rms}/C_d d$ obtained from Fig. 3 and from other previous studies (Uberoi 1969; Freymuth, 1971; Kiya, 1988). Similar to that indicated in Fig. 6(a), the values of δ_{rms}/d obtained using velocity profiles are significantly smaller than those obtained in the present study and that obtained by Freymuth (1971). However, normalization by the momentum length scale decreases the scatter. Most of the contribution to the r.m.s. values in the early regions of the wake is due to the nature of the alternate vortex shedding mechanism, i.e., it can be attributed the lateral movement of the vortices and hence to the behavior of the large scales. With increasing x/d , the Karman street is weakened and the lateral movement subsides. As a result, the rate of increase of δ_{rms}/d decreases. With increasing distance from the body, the dominant contribution to the r.m.s. values are expected to be from the smaller scales.

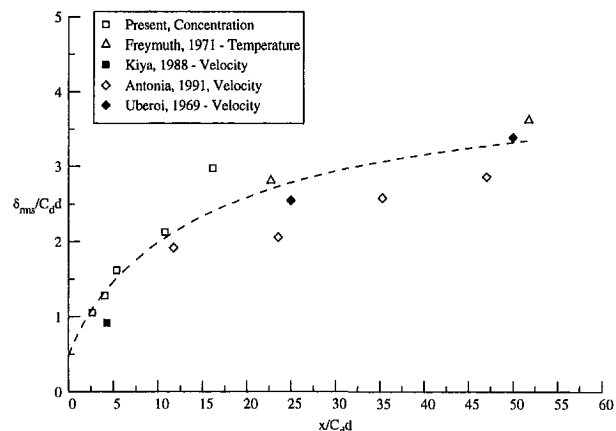


Fig. 7 Axial variation of δ_{rms}

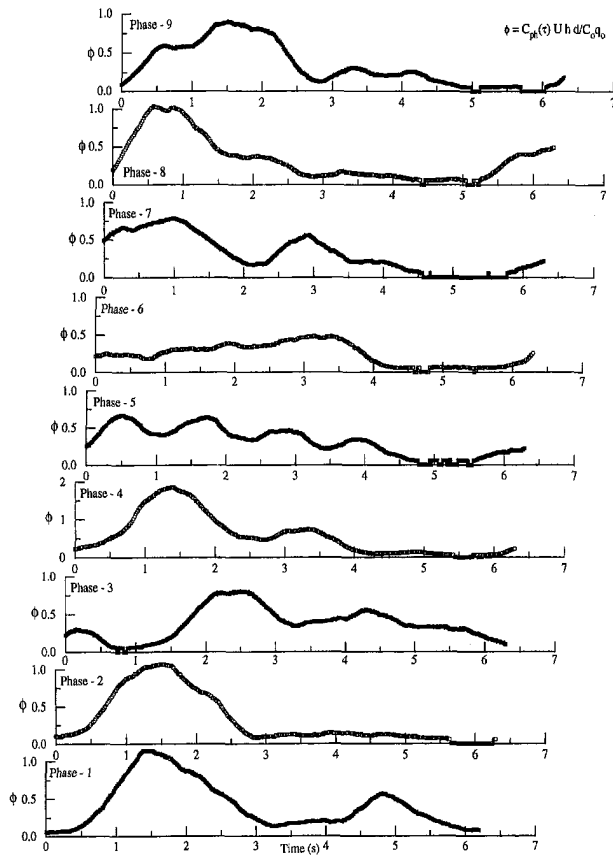


Fig. 8 Variation of concentration at several phases ($x/d = 5.0$, $y/d = 1.0$) Uncertainty in $\phi = \pm 5\%$

Phase Averaged Profiles. Using the phase detection procedure described earlier, concentration profiles at several phases were determined. Figure 8 shows a set of data obtained over nine phases at $x/d = 5.0$ and $y/d = 1.0$. One should note that though the Karman vortex shedding mechanism is fairly periodic, each one of the vortices shed are not entirely similar. For example, it is interesting to note that the concentration variation in Phase-5 is different from that noticed in Phase-1. Visually, one could also note that the lateral size of each one of the vortices also varied slightly. From a modeling point of view, a useful representation is the variation of concentration averaged across several phases. Figures 9(a) to 9(c), show a typical set of profiles in the near wake. For example, Fig. 9(a) shows the variation of $\langle C_{ph}(\tau) \rangle$ at $x/d = 5.0$ for various lateral locations. In the regions at the outer edge of the wake ($y/d = 3.0$), there is very little or no dye passing through the probe measuring volume and no distinct pattern is distinguishable. As one traverses the wake from the outer edge to the inner regions ($y/d = 1.5$), a pattern with a distinct peak begins to emerge. At this point it should be remarked that each vortex can be essentially modelled as a nearly circular Rankine vortex and has maximum concentration in the core. In this region of the wake, the connecting ribs have very little thickness in the longitudinal direction. For a given location, (say, $y/d = 1.5$), starting the concentration measurements at a point when the vortex just enters the probe measuring volume (downward zero crossing), the probe sees very little dye. As the vortex begins to move into the measuring volume, the dye concentration increases, reaches a maximum (in the core region), followed by a decrease as the vortex begins to leave the probe. The probe records clear water at the upward zero crossing. However, as one moves further into the wake, ($y/d = 1.0$), due to the presence of the rib region, the dye concentration does not decrease to zero soon after the core region. Furthermore, at $y/d = 1$, the peak

value is about twice the mean value seen in Fig. 2. As one traverses further into the wake ($y/d = 0.5$ to 0.0), the profiles indicate a double peak structure. This is due to the influence of the dye structures in the rib connecting the present vortex with the preceding vortex that is being shed. The presence of the rib structure becomes prominent around the axial region. One notices a similar pattern at section $x/d = 10.0$ (Fig. 9(b)). However, one should note that visual observations indicate that the ribs in axial sections $x/d > 5.0$, have large longitudinal widths comparable to the size of the roll. This can also be clearly seen from data presented for location $y/d = 1.0$ in Fig. 9(b). After the zero crossing is detected, the dye concentration increases for the first two seconds, followed by a decrease in the next second. However, the concentration does not decrease to zero for a significant amount of time (> 2 seconds) due to the presence of dye in the

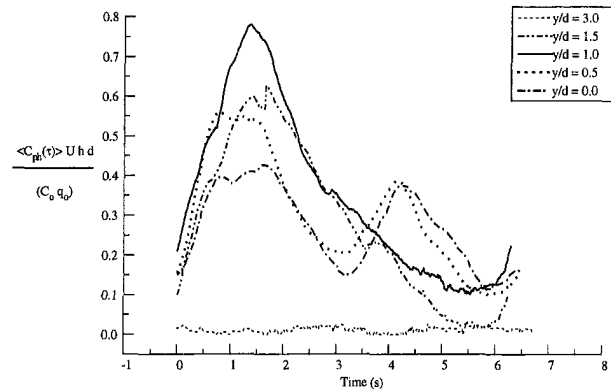


Fig. 9(a) Lateral variation of concentration averaged across several phases at $x/d = 5.0$ (Uncertainty in $\langle C_{ph}(\tau) \rangle = \pm 5\%$)

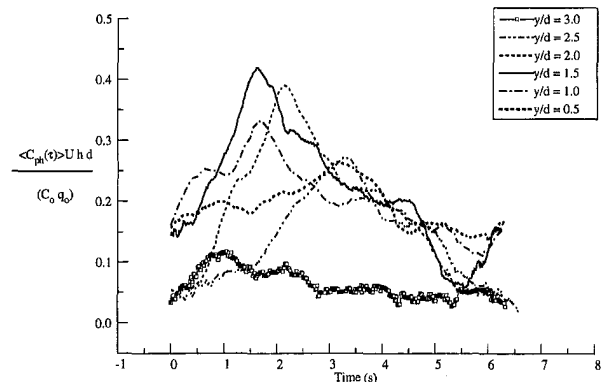


Fig. 9(b) Lateral variation of concentration averaged across several phases at $x/d = 10.0$ (Uncertainty in $\langle C_{ph}(\tau) \rangle = \pm 5\%$)

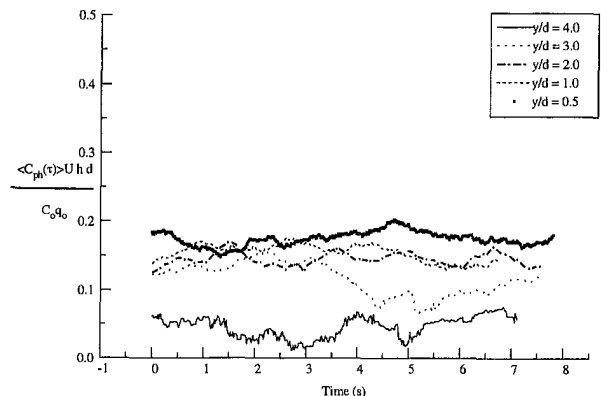


Fig. 9(c) Lateral variation of concentration averaged across several phases at $x/d = 30.0$ (Uncertainty in $\langle C_{ph}(\tau) \rangle = \pm 5\%$)

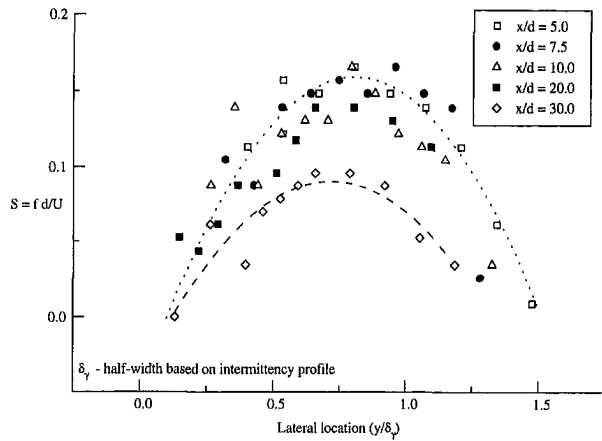


Fig. 10 Lateral variation of Strouhal number at various axial stations (Uncertainty in $S = \pm 3\%$)

rib region. The dominant structures seen in Fig. 9(a) are subsided as the vortex convects downstream as seen from Fig. 9(c).

Frequency of Crossing. Figure 10 shows the frequency of down crossings normalized by d and U for the five values of x/d . In the far-wake, a similar plot (Antonia, 1987) indicates a nearly self preserving development of the flow. In the range of x/d tested in the present study, the data obtained for the first four sections collapse fairly on to a single curve. At any of these sections, for the given blockage, the peak values of fd/U obtained in the intermittent region are comparable with the Strouhal numbers (based on frequency of vortex shedding) reported in literature (Ramamurthy, 1973; Balachandar, 1990; Kiya, 1988). The values of S noticed at the outer ($y/\delta_y > 1.2$) and inner ($y/\delta_y < 0.5$) regions of the wake are lower than that noticed in the mid region. One should note that at the outer edges, the number of crossings is reduced by the changes in the lateral size of the vortices shed. In the inner regions, the presence of the rib regions causes a reduction in the dye to clear water crossings. The data at $x/d = 30$, indicate a lower frequency. From a streamwise evolution of the lateral velocity fluctuations, Browne et al. (1989) noted that the amplitude levels at the Strouhal frequency decreased with increasing x/d and observed the presence of a secondary peak for $x/d > 30$, followed by the annihilation of the Karman frequency. Cimbalá (1988) and Wynanski (1986) note a similar behavior of the decay of the Karman vortex street for increasing distances from the wake generator. The present measurements confirm this behavior. Following Wynanski (1986), since no vortex amalgamation was visible in the present experiments, one would be inclined to think that the gradual decrease in the characteristic frequency resulting from an increase in the wavelength of the structures is caused by entrainment. It should also be pointed out that in the locations closer to the axial plane, the changes in the measurement of the crossing frequency were very high. A similar difficulty in the measurement of the crossing frequency has been noted by LaRue (1974c) in the far wake region.

Uncertainty Estimates

The following uncertainty estimates are obtained at an odds of 20:1:

Variable	Uncertainty
Velocity (U)	$\pm 4\%$
Concentration ($C(i)$)	$\pm 5\%$
Water depth (h)	± 0.5 mm
Dye flow rate (q_0)	$\pm 2.5\%$
Half-width (δ)	$\pm 5\%$

Conclusions

In the present study, flow visualization and concentration measurements were carried out in the near-wake of a normal flat plate. Such data are complimentary to a small number of previous measurements of the concentration field in the far and intermediate wake of circular cylinders. The concentration measurements, besides supplementing existing information on the wake of bluff bodies, also provide insight into the mixing of scalars like fuels, chemicals and pollutants in the early wake region. The present study indicates that maximum values of concentration occur in the core region of the vortices. The method of phase detection employed in the present study is rather unique. Phase averaged data reveal structural information and indicate that the maximum concentration levels in the core of the eddies could be several times the mean concentration. The wake spreads fairly rapidly in the early wake region. Furthermore, the half-wake widths estimated using concentration profiles have been found to be 1.5 to 2.5 times wider than previously obtained from velocity profiles. It is also observed that the length scales when suitably normalized by the momentum thickness, exhibit a nearly universal behavior. The concentration intermittency profiles can be made to collapse on to a single curve and thus bringing forth the inherent self similarity of bluff body near wakes. Observations regarding the frequency of crossing indicate that at any section ($x/d \leq 20$), the values of the Strouhal number obtained are very similar to those obtained in the previous measurements of the vortex shedding frequency. At $x/d = 30$, there is a decrease in the values of the crossing frequency, confirming earlier observations of decay of the Karman street.

References

- Antonia, R. A., 1991, "Organization in a Turbulent Near Wake," Fluid Dynamics Research, The Japan Society of Fluid Mechanics, North-Holland, Vol. 7, pp. 139–149.
- Antonia, R. A., and Britz, D., 1989, "Phase Averaging in the Turbulent Far-Wake," *Experiments in Fluids*, Springer-Verlag, Vol. 7, pp. 138–142.
- Antonia, R. A., Browne, L. W. B., and Fulachier, L., 1987, "Spectra of Velocity and Temperature Fluctuations in the Intermittent Region of a Turbulent Wake," *Physico-Chemical Hydrodynamics*, Pergamon Journals Ltd., Vol. 8, No. 2, pp. 125–135.
- Balachandar, R., 1990, "Characteristics of Separated Flows Including Cavitation Effects," Ph.D. thesis, Concordia University, Montreal, Canada.
- Bearman, P. W., 1984, "Vortex Shedding From Oscillating Bluff Bodies," *Annual Review of Fluid Mechanics*, Vol. 16, pp. 195–222.
- Berger, E., and Wille, R., 1972, "Periodic Flow Phenomena," *Annual Review of Fluid Mechanics*, Vol. 4, pp. 313–340.
- Bradbury, L. J. S., 1976, "Measurements with a Pulsed-Wire and a Hot-Wire Anemometer in the Highly Turbulent Wake of a Normal Flat Plate," *Journal of Fluid Mechanics*, Vol. 77, Part 3, pp. 473–497.
- Browne, L. W., Antonia, R. A., and Shah, D. A., 1989, "On the Origin of the Organized Motion in the Turbulent Far-Wake of a Cylinder," *Experiments in Fluids*, Springer-Verlag, Vol. 7, 475–480.
- Cantwell, B., and Coles, D., 1983, "An Experimental Study of Entrainment and Transport in the Turbulent Near Wake of a Circular Cylinder," *Journal of Fluid Mechanics*, Vol. 136, pp. 321–374.
- Cimbalá, J. N., Nagib, H. M. and Roshko, A., 1988, "Large Structure in the Far Wakes of Two-Dimensional Bluff Bodies," *Journal of Fluid Mechanics*, Vol. 190, pp. 265–298.
- Dowling, R., David, and Dimotakis, P. E., 1990, "Similarity of the Concentration Field of Gas-Phase Turbulent Jets," *Journal of Fluid Mechanics*, Vol. 218, pp. 109–141.
- Fabris, G., 1979, "Conditional Sampling Study of the Turbulent Wake of a Cylinder," *Journal of Fluid Mechanics*, Vol. 94, pp. 673–709.
- Fage, A., and Falkner, V. M., 1935, "Note on Experiments on the Temperature and Velocity in the Wake of a Heated Cylindrical Obstacle," *Proceedings of the Royal Society, London*, Vol. 135A, pp. 702–705.
- Freythuth, P., and Uberoi, M. S., 1971, "Structure of Temperature Fluctuations in the Turbulent Wake Behind a Heated Cylinder," *The Physics of Fluids*, Vol. 14, No. 12, pp. 2574–2579.
- Freythuth, P., and Uberoi, M. S., 1973, "Temperature Fluctuations in the Turbulent Wake Behind an Optically Heated Sphere," *The Physics of Fluids*, Vol. 16, pp. 161–168.
- Hayakawa, M., and Hussain, F., 1989, "Three Dimensionality of Organized Structures in a Plane Turbulent Wake," *Journal of Fluid Mechanics*, Vol. 206, pp. 375–404.
- Hinze, O., 1959, *Turbulence*, McGraw Hill, New York.

- Hussain, A., and Ramjee, V., 1976, "Periodic Wake Behind a Circular Cylinder at a Low Reynolds Number," *Aeronautical Quarterly*, Vol. 27, pp. 123–142.
- Kiya, M., and Matsumara, M., 1988, "Incoherent Turbulence Structure in the Near Wake of a Normal Plate," *Journal of Fluid Mechanics*, Vol. 190, pp. 343–356.
- Kovasznyai, 1949, "Hot-Wire Investigation of the Wake Behind Cylinders at Low Reynolds Numbers," *Proceedings of the Royal Society*, London, Vol. A 198, pp. 174–189.
- LaRue, J. C., and Libby, P. A., 1974a, "Temperature and Intermittency in the Turbulent Wake of a Heated Cylinder," *The Physics of Fluids*, Vol. 17, No. 5, May, pp. 873–878.
- LaRue, J. C. 1974b, "Detection of the Turbulent-Nonturbulent Interface in Slightly Heated Turbulent Shear Flows," *The Physics of Fluids*, Vol. 17, No. 8, August, pp. 1513–1517.
- LaRue, J. C., and Libby, P. A., 1974c, "Temperature Fluctuations in the Plane Turbulent Wake," *The Physics of Fluids*, Vol. 17, No. 11, November, pp. 1956–1967.
- Marris, A. W., 1964, "A Review on Vortex Streets, Periodic Wakes and Induced Vibration Phenomena," *ASME Journal of Basic Engineering*, pp. 185–196.
- Perry, A. E., and Steiner, T. R., 1987, "Large-Scale Vortex Structures in Turbulent Wakes Behind Bluff Bodies, Part 1. Vortex Formation Processes," *Journal of Fluid Mechanics*, Vol. 174, pp. 233–270.
- Ramamurthy, A. S., and Ng, C. P., 1973, "Effect of Blockage on Steady Force Coefficients," *Journal of Engineering Mechanics Division*, ASCE, Vol. 99, No. EM4, Aug., pp. 755–772.
- Roshko, A., 1954, "A New Hodograph for Free-Stream Line Theory," NACA TN 3169.
- Sarpkaya, T., 1979, "Vortex Induced Oscillations, A Selective Review," *ASME Journal of Applied Mechanics, Trans. ASME Series E*, Vol. 46, pp. 241–258.
- Taneda, S., 1959, "Downstream Development of Wakes Behind Cylinders," *Journal of Physical Society Japan*, Vol. 14, 843.
- Townsend, A. A., 1949, "The Fully Developed Turbulent Wake of a Circular Cylinder," *Australian Journal Science Research*, Vol. 2A, pp. 451–468.
- Uberoi, M. S., and Freymuth, P., 1969, "Spectra of Turbulence in the Wake of Circular Cylinders," *Physics of Fluids*, Vol. 12, pp. 1359–1363.
- Wynanski, I., Champagne, F., and Marasli, B., 1986, "On the Large-Scale Structures in Two-Dimensional, Small Deficit, Turbulent Wakes," *Journal of Fluid Mechanics*, Vol. 168, pp. 31–71.
-

B. Maines

Lockheed Martin Tactical Aircraft Systems,
Fort Worth, TX

R. E. A. Arndt

St. Anthony Falls Laboratory,
University of Minnesota,
Minneapolis, MN

The Case of the Singing Vortex

A relatively high amplitude, discrete tone is radiated from fully developed tip vortex cavitation under certain conditions. The phenomenon of the "singing vortex" was first reported by Higuchi et al. (1989). This study more closely examines the singing phenomenon by varying the hydrofoil cross-section, scale, angle of attack, water quality, and cavitation number in two different facilities. Noise data were collected for each condition with visual documentation using both still photography and high speed video in an effort to explain the mechanism of vortex singing. The theory of Kelvin (1880) provides a framework for correlating all the data obtained.

Introduction

This study is part of a larger investigation of tip vortex cavitation in which both the inception physics and more developed forms of cavitation are being investigated. It was found that, under certain conditions, a discrete tone was radiated when fully developed cavitation occurred, i.e. a completely vapor filled vortex core was attached to the hydrofoil. This was noted in a previous study (Higuchi et al., 1989) but was not studied extensively.

Developed cavitation in a trailing vortex has been studied in the past by Souders and Platzer (1981), Arakeri et al. (1988), and Arndt et al. (1991). The focus of these earlier studies was on the general flow features such as the vortex trajectory and the scaling of the vapor core radius with cavitation number. No mention was made of a discrete tone, presumably due to the fact that the phenomenon takes place over a very narrow range of cavitation number and is difficult to reproduce without reasonable care. However, the data reported herein have been presented at several workshops and seminars in the last two years and since that time other laboratories have been able to detect the same sound.

This study compares sound data collected in two different water tunnels in different parts of the world. A comparison is made between the results obtained in the same facility as used by Higuchi et al. (1989) and the larger water tunnel used by Arndt and Keller (1992) in Obernach, Germany. When properly normalized, the results from the two facilities agree amazingly well.

Experimental Setup

Four hydrofoils of elliptic planform with aspect ratio 3 but different cross sections were used for this study. The hydrofoil sections chosen were a NACA 66₂-415 $a = 0.8$, a modified NACA 4215 (designated herein as NACA 4215M), a NACA 16-020, and a NACA 66-012. The sectional characteristics were held constant from the root to the tip. Hence each foil had a spanwise thickness distribution that was also elliptical. Two sets of each foil were constructed. The smaller set had a root chord c_0 , of 81 mm and a half span, b , of 95 mm while for the larger set $c_0 = 129.4$ mm and $b = 152.4$ mm. The small set was utilized for cavitation testing, force measurements and observation of the bubble dynamics at the St. Anthony Falls Laboratory (SAF). The larger set was used for cavitation studies and force measurements at the Versuchsanstalt für Wasserbau in Obernach, Germany. The larger foils were also used for oil flow visualization studies at SAF. These complementary studies provide a comprehensive view of the flow in the tip region and its correlation with cavitation.

Contributed by the Fluids Engineering Division for publication in the JOURNAL OF FLUIDS ENGINEERING. Manuscript received by the Fluids Engineering Division March 6, 1996; revised manuscript received January 7, 1997. Associate Technical Editor: J. Katz.

Cavitation testing and force measurements were made in two water tunnels, one at SAF, which has a 190 mm square cross section (Arndt et al., 1991), and the other at Obernach with a 300 mm square cross section (Arndt and Keller, 1992). Oil flow visualizations were obtained in two wind tunnels, one at the Department of Aerospace Engineering at the University of Minnesota (Higuchi et al., 1987) and the second at SAF (originally an air model of the HYKAT facility, Wetzel and Arndt, 1994).

Cavitation tests were performed by fixing the angle of attack and velocity and then slowly lowering the pressure until fully developed cavitation occurred, with the vapor filled core just barely attached to the foil. Careful adjustments in either velocity or pressure were made until "singing" occurred. It was found in initial trials that the singing phenomenon was far more reproducible with the 66₂ series foil. Thus this study was concentrated on tests with this foil.

Oil flow data were obtained using a spray of fine droplets of an oil and titanium-oxide mixture (Maines and Arndt, 1993). The wind tunnel was run at the test velocity of 56 m/s ($Re \approx 485,000$). This technique highlighted the details of the boundary layer flow especially in the tip region.

Observations of cavitation were made with either conventional still photography or with high speed video. Only still photography, using a standard Nikon 6006 camera, was used for observations at SAF. A new Kodak video camera, with the possibility of framing rates as high as 40,500 fps, was used at Obernach in conjunction with still photography, also using a standard Nikon camera. Video observations were made at a framing rate of 4500 fps, which was more than adequate for observing phenomena that had a frequency less than 600 Hz. Data were collected over a range of lift coefficients, velocities and water quality in both facilities.

Radiated sound was measured in the SAF tunnel with an hydrophone positioned above the hydrofoil tip in a tank of quiescent water that was separated from the test section by a thin plate of plexiglas (Higuchi et al., 1989). The hydrofoil was mounted at the floor of the test section and the thin plexiglas plate formed the roof of the test section. A similar setup was used in Obernach, except that the hydrofoil was mounted in the roof of the test section and a single hydrophone was mounted in a tank of water that was positioned against one of the side windows of the test section. Therefore the observation angle differed by approximately 90° in the two test facilities. The significant differences in the acoustic path for measurements in the two facilities precluded comparison of amplitude data. Only frequency data were compared. A serious attempt was made to acoustically calibrate the Obernach tunnel. However, an accurate calibration procedure was not possible in the frequency range of interest, because of the complex acoustic response of the water tunnel.

Uncertainty Limits

An error analysis for the measurement of cavitation number and lift in the Obernach facility was given in Arndt and Keller

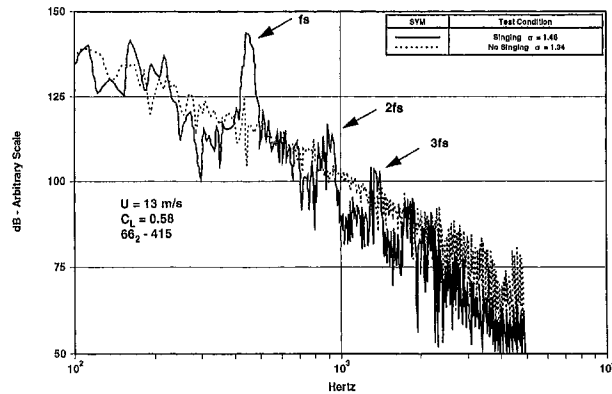


Fig. 1 Comparison of noise spectra with and without singing, $U = 13$ m/s. ($66_2 - 415$ hydrofoil in the Oberrach facility)

(1992). These measurements can be made within an accuracy of approximately 1 percent.

All the video and photographic data collected at both laboratories was reduced at SAF. A detailed discussion of the measurements made at SAF is presented in the dissertation of Maines (1995). Errors in measuring velocity were found to be less than 1 percent for velocities greater than 8 m/s. Errors in lift coefficient varied greatly with velocity but were in the range 0.2–2.2 percent in the velocity range 16 m/s to 5 m/s, the largest error occurring at the lowest velocity. The errors in cavitation number were about the same as the lift coefficient over the same velocity range, again the largest error was associated with the lowest velocity.

There is considerable difference in the errors associated with measuring core radius using still photography and video analysis. The error in analyzing the still photographs is quite good, typically less than 5 percent. Unfortunately, limitations on the spatial resolution of the video can create quite large errors (approximately 25 percent) at diameters less than 1 mm. Diameters greater than 2 mm can be resolved with error that is less than 10 percent.

Experimental Results

A sample comparison of the measured sound spectra with and without singing is shown in Fig. 1. These data were obtained in the Oberrach tunnel by holding velocity constant at 13 m/s and slowly lowering σ until singing occurred. The difference in σ for the two spectra is very small. What is apparent is that when singing occurs it shows up in the spectrum as a very intense peak of about 25 dB above the background at a discrete frequency.

The singing vortex has been observed primarily on the NACA 66_2-415 hydrofoil. Singing was achieved with the larger scale NACA 4215M at the Oberrach facility but only at very low amplitudes. Singing was not observed with the smaller scale 4215M in the SAF facility. In general, the phenomenon has the appearance of a standing wave superimposed on the surface of the hollow vortex core. Figures 2 and 3 are photographs of a cavitating core without and with singing respectively. In Fig. 2, the cavitation number has been raised just enough to suppress

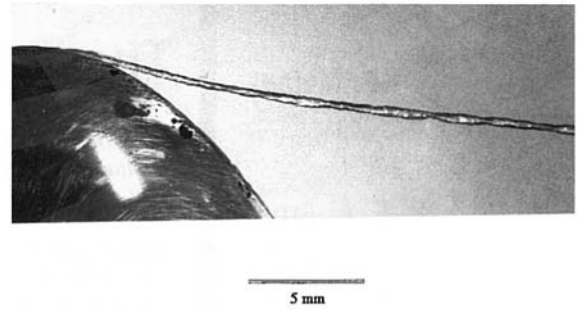


Fig. 2 Photograph of developed tip vortex cavitation without singing (NACA $66_2 - 415$)

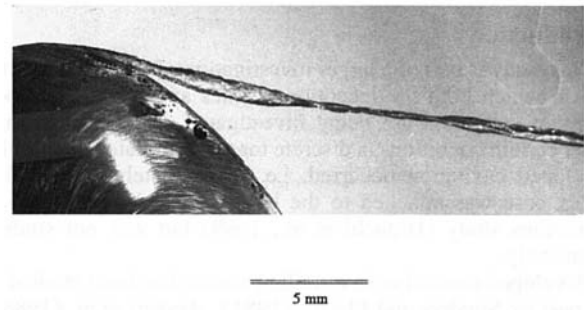


Fig. 3 Photograph of singing vortex with enlarged core near the tip (NACA $66_2 - 415$)

the singing. In Fig. 3, σ has been lowered to the point that the vortex begins to sing. Note the thickening of the core just downstream of the tip followed by a very thin core. This pattern is repeated downstream. As the oscillation progresses through one cycle, the radius of the thick portion near the tip decreases while the thin segment expands radially.

The driving mechanism for this phenomenon is still unknown. However, flow induced vibration is discounted, in agreement with Higuchi et al. (1989). The natural frequency of both sets of foils was measured using a laser vibrometer. At the SAF facility, measurements were taken with the foil outside the tunnel. Thus the measured frequency is slightly higher than it would be submerged in water. The natural frequency of the hydrofoil at the Oberrach facility was measured while submerged in the water tunnel test section under static conditions. Hydrofoil vibration was then monitored with the laser vibrometer over a wide range of flow velocity with and without cavitation and with and without singing. Under all conditions the predominant vibrational frequency was the same as that measured under static conditions. In both cases the foil natural frequency was found to be much lower than the observed singing frequencies.

Throughout the test program singing was only observed when the hollow core was attached to the tip. Thus a more likely mechanism for singing is the result of a complex interaction between the tip boundary layer and the attached cavity. High speed video observations indicate that the attached tip cavity oscillates with the same frequency as the pulsating vortex core.

Nomenclature

a = core radius, m
 b = half span, m
 c_o = root chord, m
 C_1, C_2, C_3 = constants
 C_L = lift coefficient
 f = frequency, Hertz

k = wave number, $2\pi/\lambda$, 1/m
 K_1, K'_1 = modified Bessel functions of the second kind
 N = function of ka , defined in the text
 U = freestream velocity, m/s

Γ = circulation, m^2/s
 λ = wavelength, m
 Ω = core rotational speed, radians/s
 σ = cavitation number
 σ_s = cavitation number when singing occurs



Fig. 4 Superposition photograph of the tip cavity and boundary layer characteristics

Figure 4 highlights the relationship between the tip cavity and the average boundary layer characteristics. This picture was created by superimposing a single image of a tip cavity at a cavitation number slightly higher than σ_s with a photograph of oil film streaklines taken at an equivalent condition in a wind tunnel. Note that cavity detachment correlates well with separation of the boundary layer in the tip region at this phase of the cycle.

The conditions at which singing is observed to occur are limited. For a given free-stream velocity and angle of attack, singing only occurs within a narrow band of cavitation number, $\Delta\sigma \approx \pm 0.15$ with the test condition, σ_s . While varying σ through this narrow band, the frequency of the tone is observed to decrease with decreasing sigma. In addition, the amplitude of the tone peaks at σ_s . Figure 5 is a plot of the cavitation number for singing, σ_s , versus velocity for different lift coefficients obtained in both water tunnels. Note that σ_s at a given lift coefficient remains constant with velocity. Testing in the Oberrach facility showed some variation of σ_s with velocity which may be due to water quality effects. Tests at Oberrach also indicated that water quality, i.e., air content, of the tunnel can greatly affect the cavitation number at which singing occurs. The water quality is difficult to maintain for long periods of time in this facility. The value of σ_s was relatively unaffected by water quality in the SAF facility. In general, it was found that the vortex sings most easily and with the greatest amplitude at an optimum value of lift coefficient and σ_s .

The frequency of the tone was found to vary with cavitation number around a given σ_s . In addition, the frequency also varies

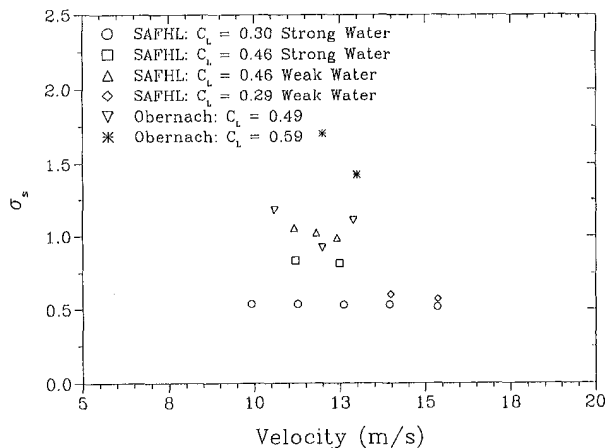


Fig. 5 Cavitation number at singing versus velocity for various conditions

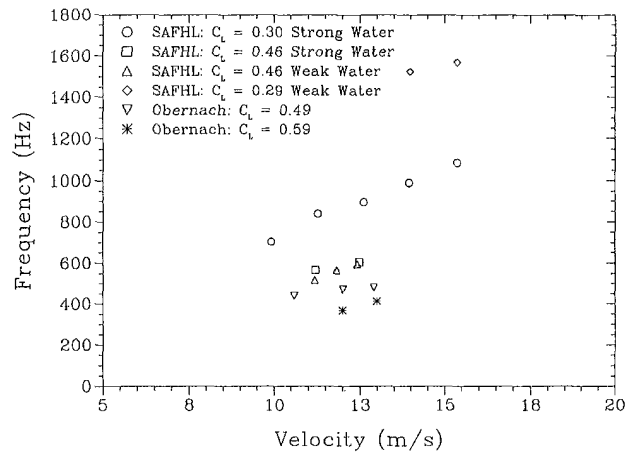


Fig. 6 Variation of singing frequency with test section velocity

with freestream velocity in a linear fashion, as noted previously by Higuchi et al. (1989). This is illustrated in Fig. 6, which is a plot of frequency versus velocity at σ_s for various conditions in both the SAF and Oberrach facilities. The frequency range in the SAF studies was approximately 650 Hz to 1600 Hz. By comparison the frequency range in the larger Oberrach tunnel was significantly lower, approximately 300 Hz to 600 Hz.

High speed video images provided a convenient method to verify the frequencies measured with the hydrophones and confirm that the noise is produced by the undulations of the vortex core. A plot of frequency measured from the video images versus that obtained with the hydrophones is shown in Fig. 7. Very good agreement is observed. As noted in Fig. 6, the frequencies measured at the Oberrach facility are consistently lower than those observed in the SAF facility. This scale effect on singing appears to be related to the radius of the cavitating core. This is confirmed by the data in Fig. 8 which contains a plot of the variation of frequency at σ_s with core radius. Clearly there is an inverse relationship between frequency and core radius. It should also be noted that core radius varies with cavitation number (see Arakeri et al., 1989) which suggests a complex relation between frequency, σ and core radius.

The final parameter measured from the video images and still photographs is the wavelength of the disturbance. Figure 9 is a graph of wavelength versus core radius. In the case of the Oberrach data, it appears that wavelength falls along two different curves. Careful analysis of the high speed video images revealed that two general types of wave oscillations exist. Both types of

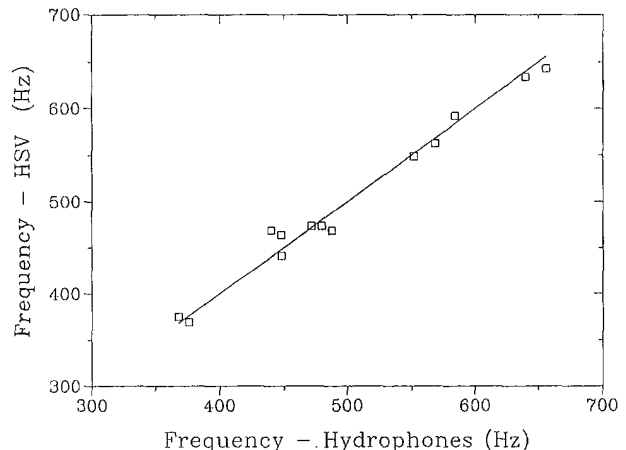


Fig. 7 Comparison of measured frequency with observed frequency in the high speed videos

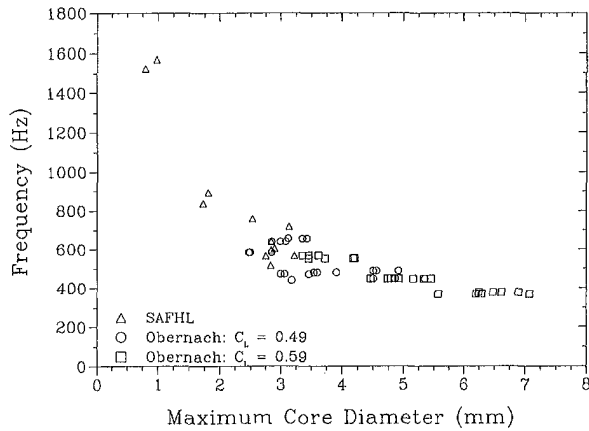


Fig. 8 Variation of singing frequency with core diameter

oscillations are possible at a given condition. However, they do not occur simultaneously. Type I oscillations are distinguished by stationary node points whereas for Type II, the nodes oscillate in the axial direction. Type I oscillations more closely resemble a standing wave. Wavelength measurements for Type II oscillations are therefore more difficult to determine and must be regarded as approximate. The SAF data have the same trend as the Obernach Type I data. However, the trend is followed in steps, rather than linearly. It is unclear at present whether the nonlinear relationship between wavelength and core radius is real or is an artifact of the experimental procedure. Since only random still photographs were available from the SAF testing, it was difficult to determine at which point in the cycle the photograph was taken. It is much easier to determine core diameter than wavelength and since diameter measurements appear to be consistent when compared to the Obernach data in Fig. 9, it is likely that the measured wavelengths from the SAF still photographs are in error.

A Proposed Correlation

The experimental observations suggest a standing wave on the surface of the hollow vortex core. Kelvin (1880) studied the wave pattern on a stationary, irrotational hollow core vortex. He found two dominate helical modes, one rotating with the same sense as the vortex and the other rotating and propagating in the opposite direction. The rotational speeds, $2\pi f$, are given by

$$\frac{2\pi f}{\Omega} = [1 \pm \sqrt{N}] \quad (1)$$

where Ω is the rotational speed of the vortex and N is a function of wave number based on core radius, $ka = 2\pi a/\lambda$, and is numerically greater than unity:

$$N = \frac{kaK_1'(ka)}{K_1(ka)} \quad (2)$$

As suggested by Keller and Escudier (1980), a standing wave is possible when the vortex is superimposed on a uniform axial flow. This can occur when the celerity of the counter-rotating mode is equal and opposite to the freestream velocity, U (negative frequency in Eq. (1)). This occurs when

$$\frac{f\lambda}{U} = 1 \quad (3)$$

In all cases tested, the condition $f\lambda/U = 1$ corresponded to Type I oscillations.

The negative root of Eq. (1) can be approximated by $C_1 ka$ or

$$\frac{2\pi fa}{U} = C_1 ka \times \left\{ \frac{\Omega a}{U} \right\} \quad (4)$$

By assuming the vortex to be irrotational, the use of the Bernoulli equation yields $(\Omega a/U) = \sqrt{\sigma}$. Using this result in combination with Eqs. (3) and (4) yields

$$\sqrt{\sigma_s} = \frac{1}{C_1}, \Rightarrow \sigma_s = \frac{1}{C_1^2} \quad (5)$$

This suggests the surprising result that a standing wave will occur at only a single value of σ . This finding is in qualitative agreement with the observation that singing only occurs over a very narrow range of cavitation number.

The assumptions leading up to Eqs. (4) and (5) imply a fixed value of lift coefficient as well. By assuming an elliptical loading of the hydrofoil and noting that $\Gamma = 2\pi\Omega a^2 = (1/2)C_L U c_o$, a relationship between lift coefficient, C_L and σ can be obtained:

$$\frac{\Gamma}{Ua} = 2\pi \left\{ \frac{\Omega a}{U} \right\} = 2\pi\sqrt{\sigma_s} \quad (7)$$

or

$$C_L = 4\pi \left(\frac{a}{c_o} \right) \sqrt{\sigma_s} \quad (8)$$

This result is also qualitatively consistent with observations, since singing is only observed over a relatively narrow range of lift coefficient as well.

Discussion

The simple theory outlined above only provides a rough framework for analysis of the data. Singing does not actually occur at a fixed value of ka and σ_s . As previously stated, a linear fit to the data in Fig. 9 corresponds to $ka = 0.5$ (assumed equal to $2\pi fa/U$). However, it was found that $2\pi fa/U$ can vary from approximately 0.25 to 0.65. The variation in ka can be correlated with variations in σ_s , as shown in Figure 10 which is a graph of $2\pi fa/U$ versus $\sigma_s^{0.5}$. This implies a slightly different dispersion relation than expressed by Eq. (4):

$$\frac{2\pi fa}{U} = C_2 \sqrt{\sigma_s} \quad (9)$$

where $C_2 \approx 0.45$.

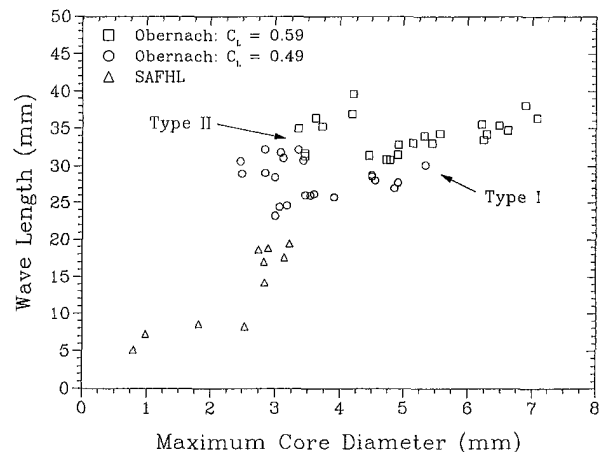


Fig. 9 Variation of wavelength with core diameter

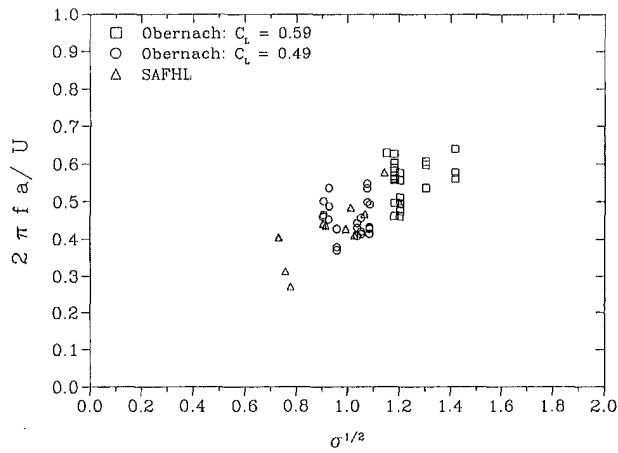


Fig. 10 Experimental dispersion relation

Equations (4) and (8) are only consistent for a fixed value of ka . As noted earlier, the Type I oscillation data can be fitted by a nearly constant value of $ka = 0.5$. If C_1 is calculated from $C_2/C_1 = ka$ and $ka \approx 0.5$, the cavitation number at which singing should occur is calculated to be $\sigma_s = 1.2$, which is in reasonable agreement with experiment. The approximate center of the cluster of the data in Fig. 10 corresponds to $ka = 0.5$ and $\sigma_s = 1.2$. Noise amplitude did vary for each data point, but could not be accurately measured in this frequency range. Had it been possible to accurately measure amplitude, it may have been possible to fit the data in Fig. 10 with iso-contours of amplitude that would be elliptical in shape with their major axes aligned at a slope of 0.45.

Kelvin's theory is actually matched by $C_1 = 0.336$, $\sigma_s = 8.85$, and $ka = 1$, which is a contradiction with the observations. However, the experimental trends are in qualitative agreement with the theory if a slightly modified dispersion relation is used with a measured value of $ka = 0.5$. This analysis clearly has limitations which could cause the observed discrepancies between theory and experiment. First, as mentioned previously, the dispersion relation in Eq. (1) is based on a linearized analysis. Observed displacements of the vortex core are on the order of twice the core radius under nonsinging conditions.

The assumption of the potential flow around the core is also questionable. Simple analytical models, e.g., Arndt and Keller (1992), indicate that potential flow can exist outside the core, but Escudier et al. (1980) suggests that a viscous layer surrounds the hollow core. In addition, it is known that a single phase vortex deviates from the simple Rankine vortex used to

model the rotational flow. Actual pressures in the core were not measured and therefore the assumption of vapor pressure may also be invalid. Unfortunately, attempts to directly measure the velocity in the liquid surrounding the vapor filled core were also not successful. In addition, the correlation with C_L is based on measured values of this parameter in noncavitating flow.

The validity of assuming noncavitating values of C_L and of assuming potential flow was investigated by Levy (1995). Using the 66₂-415 hydrofoil, the lift coefficient and core radius was measured over a wide range of σ for two values of angle of attack and velocity that bracket the conditions where singing is observed. In these experiments sigma was lowered until lift decreased. Depending on the angle of attack, the lift was found to increase by as much as 20 percent with decreasing σ before the lift decreased. Singing occurred at values of σ where the lift was equal to the noncavitating value. However, measured values of core radius did not correlate with measured values of lift coefficient as predicted by Eq. (7) in the form

$$\frac{a}{c_o} = \frac{C_L}{4\pi\sqrt{\sigma}} \quad (10)$$

This is shown in Fig. 11 in which the measured core radius in normalized form, a/c_o , is compared with the measured lift coefficient in the form $C_L/4\pi\sqrt{\sigma}$. The core radius is consistently under-predicted by this equation. Data from the Obernach experiments are in qualitative agreement with the SAF data shown in Fig. 11.

These results indirectly indicate that the Bernoulli equation is not valid which is one of the assumptions in the Kelvin theory. How inaccurate this assumption is open to debate. If the flow were irrotational, the circulation at the edge of the core would be equal to the total circulation in the vortex, i.e.,

$$\frac{2\pi\Omega a^2}{\frac{1}{2} C_L U c_o} = 1 \quad (11)$$

which was assumed in deriving Eq. (7). When the data in Fig. 11 are replotted as $(4\pi a\sqrt{\sigma}/C_L c_o) = f(\sigma/\sigma_c)$, where σ_c is the value of sigma at the lift breakpoint, it is found that $(4\pi a\sqrt{\sigma}/C_L c_o) \rightarrow 1$ as $(\sigma/\sigma_c) \rightarrow 1$. However, this occurs at values of sigma well below that for singing to occur.

Lastly, Kelvin's model was developed for an infinitely long vortex core and predicts two helical waves. In a uniform flow, when the reverse wave speed is equal to the freestream velocity, a standing wave should occur. For these experiments, a standing wave does occur for Type I oscillations but, as shown in Fig. 3, has radial undulations. This motion could be due to imprecise

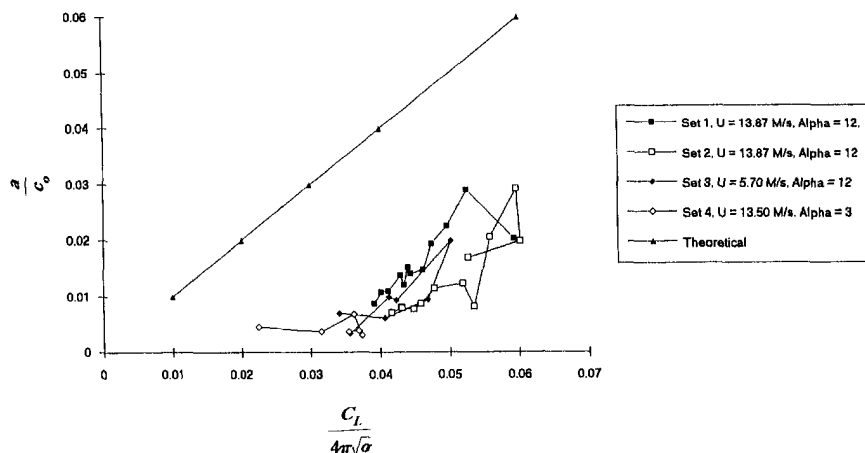


Fig. 11 Correlation of core radius with lift coefficient and σ_s

lock-in. However, it is most likely related to the fact that the experimental vortex core is not infinite but originates at the tip of the hydrofoil. Regardless of these limitations, Kelvin's dispersion relation does seem to describe the gross behavior observed experimentally.

Conclusions

Vortex singing has been observed at different facilities under varying conditions. The frequency varies inversely with the size of the hydrofoil being tested and the phenomenon is very sensitive to cavitation number. A relatively simple linear theory predicts that singing will only occur at a one fixed value of sigma that is unrealistically high and at a fixed value of lift coefficient. Experimentally, singing was observed over a range of lift coefficient and cavitation number. However, singing only occurred over a very narrow range of cavitation number for each given value of lift coefficient.

In spite of the limitations of the theory, correlation of the frequency with the measured core radius was quite good. The most likely value is $fa/U = 0.5$ at $\sigma_s \approx 1.2$. However, imprecise lock-in can occur of a range of a and σ_s given by

$$\frac{2\pi fa}{U} = 0.45 \sqrt{\sigma_s}, \quad \left[0.25 < \frac{2\pi fa}{U} < 0.65 \right] \quad (12)$$

The exact mechanism for singing is not understood. It appears that a standing wave on the vapor-liquid interface of the vortex core is in phase with sheet cavity oscillations when this phenomenon occurs.

Singing is observed most readily with the 66₂ - 415, but singing is also observed with the 4215M and 16-020 sections. Singing appears to occur more readily with the larger scale hydrofoils in Obernach.

Acknowledgments

This research is supported by the Office of Naval Research under Contract Number N/N00014-91-1239. Dr. Edwin Rood was the contract monitor. The Obernach data was collected with the collaboration of Dr. Andreas Keller and Dr. Branco Bajic. Their assistance in this project is sincerely appreciated.

References

- Arakeri, V. H., Higuchi, H. and Arndt, R. E. A. 1988, "A Model for Predicting Tip Vortex Cavitation Characteristics," *ASME JOURNAL OF FLUIDS ENGINEERING*, Vol. 110, pp. 190-193.
- Arndt, R. E. A., Arakeri, V. H. and Higuchi, H. 1991, "Some Observations of Tip Vortex Cavitation," *Journal of Fluid Mechanics*, Vol. 229, pp. 269-289.
- Arndt, R. E. A., and Keller, A. P. 1992, "Water Quality Effects on Cavitation Inception in a Trailing Vortex," *ASME JOURNAL OF FLUIDS ENGINEERING*, Vol. 114, No. 3, pp. 430-438.
- Escudier, M. P., Bornstein, J., and Zehnder, N., 1980, "Observations and LDA Measurements of Confined Turbulent Vortex Flow," *Journal of Fluid Mechanics*, Vol. 98, Part 1, pp. 49-63.
- Higuchi, H., Quadrelli, J. C., and Farrell, C. 1987, "Vortex Roll-up for an Elliptically Loaded Wing at Moderate Reynolds Number," *AIAA Journal*, Vol. 25, pp. 1537-1542.
- Higuchi, H., Arndt, R. E. A., and Rogers, M. F. 1989, "Characteristics of Tip Vortex Noise," *ASME JOURNAL OF FLUIDS ENGINEERING*, Vol. 111, No. 4, Dec., pp. 495-501.
- Keller, J. J., and Escudier, M. P., 1980, "Theory and Observations of Waves on Hollow-Core Vortices," *Journal of Fluid Mechanics*, Vol. 99, Part 3, pp. 495-511.
- Levy, M., 1995, "An Investigation of Lift Coefficient, Cavitation Number, and Core Radius" Report submitted to the Undergraduate Research Opportunities Program at the University of Minnesota
- Maines, B. H., and Arndt, R. E. A., 1993, "Viscous Effects on Tip Vortex Cavitation," *Proc. 4th Intl. Symp Cav. Inception*, ASME, N.Y., November
- Souders, W. G., and Platzer, G. P., 1981, "Tip Vortex Characteristics and Delay of Inception of a Three Dimensional Hydrofoil," *DTNSRDC*, Rpt. No. 81/007, David Taylor Res. Center, Bethesda, MD.
- Thompson, William (Lord Kelvin), 1880, "Vibrations of a Columnar Vortex," *Philosophical Magazine and Journal of Science*, Vol. X Fifth Series, July, pp. 155-169.
- Wetzel, J. M., and Arndt, R. E. A., 1994, "Hydrodynamic Design Considerations for Hydroacoustic Facilities: Parts I and II," *ASME JOURNAL OF FLUIDS ENGINEERING*, 116, June, pp. 324-337.

Turbulent Wall-Pressure Fluctuations: A New Model for Off-Axis Cross-Spectral Density

B. A. Singer

Research Engineer,
High Technology Corp.,
28 Research Drive,
Hampton, VA 23666

Models for the distribution of the wall-pressure under a turbulent boundary layer often estimate the coherence of the cross-spectral density in terms of a product of two coherence functions. One such function describes the coherence as a function of separation distance in the mean-flow direction, the other function describes the coherence in the cross-stream direction. Analysis of data from a large-eddy simulation of a turbulent boundary layer reveals that this approximation dramatically underpredicts the coherence for separation directions that are neither aligned with nor perpendicular to the mean-flow direction. These models fail even when the coherence functions in the directions parallel and perpendicular to the mean flow are known exactly. A new approach for combining the parallel and perpendicular coherence functions is presented. The new approach results in vastly improved approximations for the coherence.

1 Introduction

Reduced levels of aircraft interior cabin noise are desirable for both comfort and health-related reasons. Blake (1986) notes that a turbulent boundary layer on the fuselage at locations forward of the engines dominates the excitation of the fuselage structure. Boeing 737 flight experiments by Wilby and Gloyna (1972) confirm the importance of turbulent boundary-layer pressure fluctuations on the noise level inside the aircraft cabin. Innovative use of fuselage materials and arrangement of the frames and stringers provides some opportunity for a reduction in the amount of vibration transmitted to the interior cabin. However, in order to design such a structure, detailed information with regard to wall-pressure fluctuations in the external turbulent boundary layer is required.

Although the importance of the desired information is clear, a thorough mapping of the wall-pressure fluctuations under a turbulent boundary layer is difficult to obtain experimentally. Corcos (1963a), Schewe (1983), and Farabee and Casarella (1991) all indicate that the size of the pressure transducer influences the temporal response. Farabee and Casarella (1991) and Bull (1963) also report that the noise level and frequency range in the experimental facility must be taken into account.

Efforts to model the turbulent wall-pressure fluctuations have been hampered by the lack of an extensive and reliable database. The validity of many reasonable assumptions made in various models could not be adequately tested with available data. This situation has begun to change with the more extensive use of direct numerical simulation and large-eddy simulation (LES). Choi and Moin (1990) and Chang, Abraham, and Piomelli (1995) explored the use of these methods to obtain wall-pressure fluctuation statistics for low-Reynolds-number channel flows. More recently, Singer (1996a) performed an LES of a turbulent boundary layer with a Reynolds number based on a displacement thickness of 3500. The extensive datasets allow for a more careful evaluation of reasonable modeling assumptions. In particular, this paper will address a common assumption known as the "multiplication hypothesis" in which the coherence of the cross-spectral density for an arbitrary separation direction is formed by the product of the cross-spectral

densities for streamwise and spanwise separations, respectively. A comparison of the data from the LES with that predicted from the multiplication hypothesis will show that this assumption is inadequate. A new approach that requires no additional data will be introduced and will be shown to be more accurate than the previous model.

2 The Generic Problem

Figure 1 shows a plan view of the wall under a turbulent boundary layer. The mean flow travels in the x direction; the spanwise direction is denoted by y . The wall pressure at an arbitrary spatial location and at an arbitrary time t is $p(x, y, t)$. A second arbitrary wall-pressure is $p(x + \xi, y + \eta, t + \tau)$, where ξ and η are the separation distances in the x and y directions, respectively, and τ is a time separation between the two measurements. If the flow is homogeneous in x , y , and t , the two-point correlation depends only on the separations in space and time and can be written as a convolution integral:

$$R(\xi, \eta, \tau) = \frac{1}{L_x L_y T} \int_0^{L_x} \int_0^{L_y} \int_0^T p(x, y, t) \times p(x + \xi, y + \eta, t + \tau) dx dy dt \quad (1)$$

where L_x , L_y , and T are the domain lengths in x , y , and t . If the data are assumed to be homogeneous in all three variables, then the correlation is independent of the values of x , y , and t . In a generic flat-plate turbulent boundary layer, the homogeneity assumption is exact in y and t but only approximate in x . The growth of the boundary layer in the x direction accounts for a mild inhomogeneity; the fact that the boundary-layer growth occurs over distances that are long relative to typical correlation distances results in approximate homogeneity. In the LES of Singer (1996a), the numerical approach enforces streamwise homogeneity of the flow.

The pressure data can be investigated in the frequency domain by taking the Fourier transform of the two-point correlation,

$$\Gamma(\xi, \eta, \omega) = \mathcal{F}\{R(\xi, \eta, \tau)\} \quad (2)$$

where \mathcal{F} implies a Fourier transform. We use the standard nomenclature of the community of wall-pressure investigators and call the function $\Gamma(\xi, \eta, \omega)$ the cross-spectral density. In gen-

Contributed by the Fluids Engineering Division for publication in the JOURNAL OF FLUIDS ENGINEERING. Manuscript received by the Fluids Engineering Division April 3, 1996; revised manuscript received September 23, 1996. Associate Technical Editor: F. Hussain.

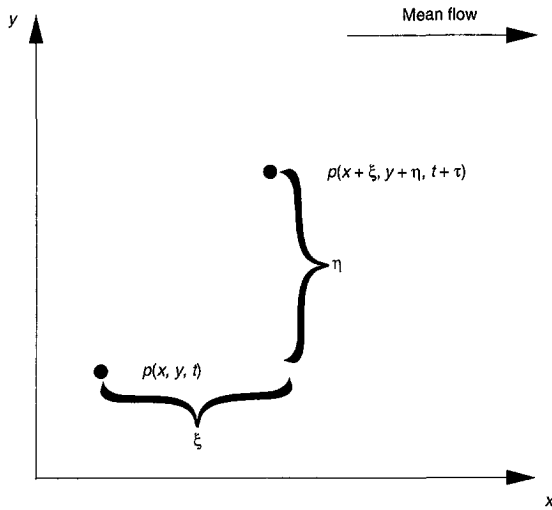


Fig. 1 Plan view of boundary layer

eral, the cross-spectral density is a complex-valued function. However, the autospectrum

$$\phi(\omega) = \Gamma(0, 0, \omega) \quad (3)$$

is strictly real. Real-valued streamwise and spanwise coherence functions, A and B , respectively, are defined as

$$A(\xi, \omega) = |\Gamma(\xi, 0, \omega)|/\phi(\omega) \quad (4)$$

and

$$B(\eta, \omega) = |\Gamma(0, \eta, \omega)|/\phi(\omega) \quad (5)$$

The coherence functions have values that vary from 0 to 1. Experimental determination of the autospectrum is a much simpler process than the determination of the full cross-spectral density function because the former only requires measurements at a single position and the latter requires a two-dimensional array of measurements. In order of decreasing availability, experiments have been performed that measure:

1. $\phi(\omega)$
2. $\Gamma(\xi, 0, \omega)$
3. $\Gamma(\xi, 0, \omega)$ and $\Gamma(0, \eta, \omega)$
4. $\Gamma(\xi, \eta, \omega)$ (usually for only a few values of η/ξ)

The recent availability of numerical simulation data can be expected to fill some of the gaps in our knowledge of the wall pressure distribution.

3 Previous Model

The model of Corcos (1963a, 1963b, 1967) has been used in various forms for more than 3 decades. The model expresses the cross-spectral density function as a product of simpler functions; that is,

$$\Gamma(\xi, \eta, \omega) = \phi(\omega)A(\xi, \omega)B(\eta, \omega) \exp(-i\alpha) \quad (6)$$

where $A(\xi, \omega)$ and $B(\eta, \omega)$ are real-valued functions that represent the coherences in the longitudinal and lateral directions, respectively, and all of the phase information is contained in α . Corcos made two important contributions with his model. The first is the general form of the cross-spectral density function as a product of simpler functions that can be individually determined (the multiplication hypothesis). The second contribution provides similarity forms for the functions $A(\xi, \omega)$ and $B(\eta, \omega)$, so that each function depends only upon a single variable. In this work, we address only the first aspect of the generalized Corcos model. In other words, does the multiplication hypothe-

sis as defined in Eq. (6) provide the proper framework for modeling the full cross-spectral density function?

4 Comparison of LES Data With Model Predictions

The LES calculation is described in detail in Singer (1996a). Briefly, the calculations were performed with a spectrally accurate LES code on a mesh of $96 \times 96 \times 64$ grid points in the streamwise, spanwise, and wall-normal directions, respectively. The wall-pressure data were divided into 11 ensembles having 50 percent overlap. Each ensemble extended over a time period T of duration $Tu_\tau/\delta^* = 5.62$, where δ^* is the displacement thickness and u_τ is the friction velocity. The cross-spectral density was computed for each ensemble and then averaged. A similar calculation was performed for a single time period on a grid with $192 \times 128 \times 64$ grid points in the coordinate directions. Both calculations produced generally similar results. Particularly important to this study are the streamwise and spanwise coherence functions A and B . In the range of frequencies resolved by both calculations, the results of both calculations agreed. The streamwise coherence function A extracted from the LES data was well fit by an exponential function having the same decay rate as that suggested by Farabee and Casarella (1991). Although the spanwise coherence function B was best fit by a modified inverse square function, a commonly used exponential function also provided a reasonable fit to the data. All of the comparisons between the two LES calculations and with available experimental data suggest that the LES data adequately reflect the features of the fluctuating wall pressure that are needed for modeling the cross-spectral density in the frequency range considered here.

For comparison of the model predictions with the LES data, we normalize the magnitude of the cross-spectral density function with the autocorrelation to obtain a coherence function

$$\gamma(\xi, \eta, \omega) \equiv |\Gamma(\xi, \eta, \omega)|/\phi(\omega) = A(\xi, \omega)B(\eta, \omega) \quad (7)$$

This work is concerned with the validity of the form of Eq. (7) and not the particular functions used to represent $\phi(\omega)$, $A(\xi, \omega)$, and $B(\eta, \omega)$; hence, the numerical values of $\phi(\omega)$, $A(\xi, \omega)$, and $B(\eta, \omega)$ will be taken directly from the LES data. Therefore, the comparison of the off-axis (both ξ and η non-zero) coherence will be the best that the multiplication hypothesis of Eq. (7) can produce.

Figure 2 shows contours of the left- and right-hand sides of Eq. (7) for a specific frequency $\omega\delta^*/u_\tau = 10.11$. The solid lines represent the values of the coherence that are determined

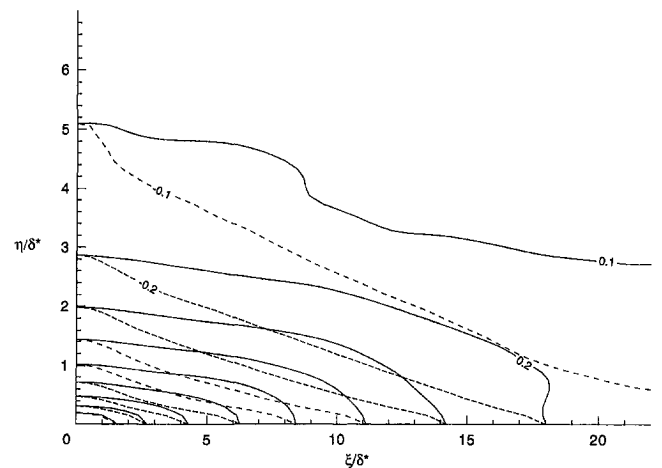


Fig. 2 Coherence contours of cross-spectral density for $\omega\delta^*/u_\tau = 10.11$. Contours are spaced with increments of 0.1. — LES data (left-hand side of Eq. (7)); - - - Results from multiplication hypothesis (right-hand side of Eq. (7)).

directly from the LES; the dashed lines represent the product $A(\xi, \omega)B(\eta, \omega)$, which traditionally has been used to model the coherence. The product formulation produces nearly straight contour lines; the contour lines of the actual coherence are curved like portions of ellipses. Even though the values of the coherence are chosen to exactly match for $\xi = 0$ and $\eta = 0$, the product formulation exhibits large errors for off-axis combinations of ξ and η . Similar problems occur at other frequencies.

5 A New Model

The elliptical shape of the contours of $\gamma(\xi, \eta, \omega)$ from the LES suggests that the coherence might be more appropriately modeled by considering $A(\xi, \omega)$ and $B(\eta, \omega)$ in a modified polar coordinate system. To develop such a coordinate system, we first seek a scaling relation for the independent variables ($\xi = s\eta$) such that the A and B curves are similarly shaped. Although the existence of a scaling relation is necessary in cases for which A and B are represented by the same functional form, an appropriate scaling relation can be found empirically, even if the optimal curve fits to A and B have different functional forms. In the general case treated here, each frequency is separately considered; hence, the scaling factor $s(\omega)$ is a function of frequency. The determination of the scaling factor for a particular frequency involves the minimization of the error

$$E(s, \omega) = \int_0^{\xi_{\text{cutoff}}} [A(\xi, \omega) - B(\xi/s, \omega)]^2 d\xi \quad (8)$$

Alternatively, the integration could be taken over η by replacing ξ with $s\eta$ in Eq. (8). The cutoff value for the integration limit must be chosen to ensure that data are available for the evaluation of both $A(\xi_{\text{cutoff}}, \omega)$ and $B(\xi_{\text{cutoff}}/s, \omega)$. An example of an optimized fit from the LES data is illustrated in Fig. 3. The value of ξ_{cutoff} was chosen to be the maximum value of ξ for which data for A were available; in the figure, $\xi_{\text{cutoff}}/\delta^* \approx 22$. In a case for which data are available for very large values of ξ , a useful value for the cutoff would be the greatest value of ξ for which the coherence $A(\xi, \omega)$ first becomes insignificant.

After the scaling function $s(\omega)$ has been obtained, radial and azimuthal coordinates are developed. The radial coordinate is

$$r = \sqrt{\xi^2 + (s\eta)^2} \quad (9)$$

and the azimuthal coordinate is

$$\theta = \arctan(s\eta/\xi) \quad (10)$$

The coherence function $\gamma(\xi, \eta, \omega)$ will be modeled in terms of $A(r, \omega)$ and $B(r/s, \omega)$. As η goes to 0, the radial coordinate r goes smoothly to ξ and the angular coordinate θ goes to 0. In

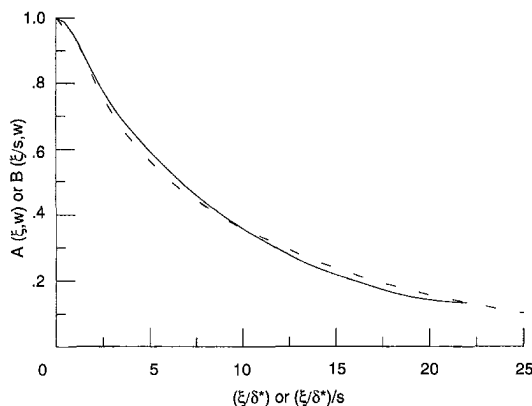


Fig. 3 Comparison of $A(\xi, \omega)$ and $B(\xi/s, \omega)$ for $\omega\delta^*/u_\tau = 10.11$. Optimized value of s is 7.86. — $A(\xi, \omega)$; ····· $B(\xi/s, \omega)$.

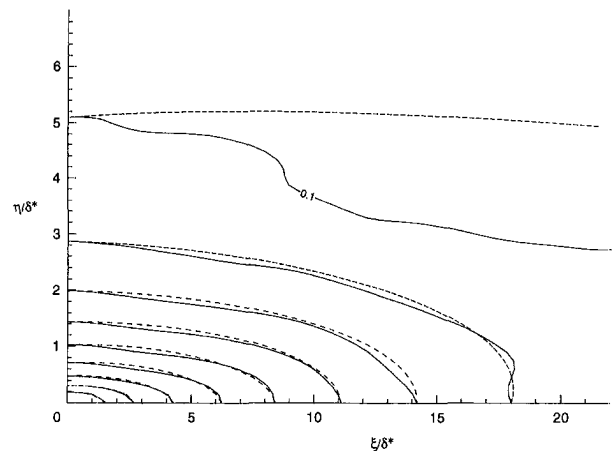


Fig. 4 Coherence contours of cross-spectral density for $\omega\delta^*/u_\tau = 10.11$. Contours are spaced with increments of 0.1. — LES data (left-hand side of Eq. (13)); - - - - New model (right-hand side of Eq. (13)).

this limit, the coherence function is best modeled as $A(r, \omega)$, that is:

$$\lim_{\eta \rightarrow 0} \gamma(\xi, \eta, \omega) = A(r, \omega) = A(\xi, \omega) \quad (11)$$

Similarly, as ξ tends to 0, the radial coordinate r tends to $s\eta$, θ goes to $\pi/2$, and

$$\lim_{\xi \rightarrow 0} \gamma(\xi, \eta, \omega) = B(r/s, \omega) = B(\eta, \omega) \quad (12)$$

If the correspondence between $A(\xi, \omega)$ and $B(\xi/s, \omega)$ were perfect, then a suitable approximation for the off-axis coherence would be a function of the radial coordinate r only. In such a circumstance, both $A(r, \omega)$ and $B(r/s, \omega)$ would be identical; either could be used to model $\gamma(\xi, \eta, \omega)$. In the more general case, only an approximate relationship exists between $A(\xi, \omega)$ and $B(\xi/s, \omega)$. In this more general case, $A(r, \omega)$ is expected to be a more accurate approximation when η is small, and $B(r/s, \omega)$ is expected to be more accurate when ξ is small. Hence, a reasonable estimate for the coherence shifts the major contribution from $A(r, \omega)$ to $B(r/s, \omega)$ as $s\eta$ increases relative to ξ . The proposed new model introduces a linear fit to represent the shifting contribution; that is,

$$\gamma(\xi, \eta, \omega) = A(r, \omega) + (B(r/s, \omega) - A(r, \omega))2\theta/\pi \quad (13)$$

Contours of the coherence predicted by the new model for $\omega\delta^*/u_\tau = 10.11$ are indicated by the dashed lines in Fig. 4. The agreement of the new model with the model used in Fig. 2. Improved agreement also exists for all other frequencies examined, some of which are illustrated in Fig. 5 of Singer (1996b).

6 Simplified Implementations

The new model for the off-axis coherence is a simple and straightforward improvement over the formulation of Eq. (7), which employs a product of the streamwise and spanwise coherences. The new model can easily be incorporated into existing computer codes with minimal programming effort. No new data are required, although new measurements of the streamwise and spanwise coherences can easily be exploited to obtain more accurate predictions. The following subsections detail simplified implementations of the new model into current algorithms that use various assumptions with regard to the form of the coherences A and B .

6.1 Coherences Depend Upon Similarity Variables. In this case $A = A(\alpha)$ and $B = B(\beta)$, where α and β are similarity variables. In the usual case $\alpha = \xi\omega/U_c$ and $\beta = \eta\omega/U_c$, where

α is related to the phase of the cross-spectral density function and U_c is the convection velocity. Because the coherences depend only on single variables, the optimal scaling parameter s is a constant and is defined by the minimization of

$$E(s) = \int_0^{\alpha_{\text{cutoff}}} [A(\alpha) - B(\alpha/s)]^2 d\alpha \quad (14)$$

where α_{cutoff} must be chosen to ensure that $A(\alpha_{\text{cutoff}})$ and $B(\alpha_{\text{cutoff}}/s)$ are defined. A reasonable choice of α_{cutoff} results in values of $A(\alpha_{\text{cutoff}})$ and $B(\alpha_{\text{cutoff}}/s)$ that are near the lower limit of significance. Greater values of α_{cutoff} cause the integral in Eq. (14) to accumulate large contributions from regions in which the coherence is small. The determination of $A(\alpha)$ and $B(\beta)$ can be performed with either algebraic expressions, function calls, or table lookups. After s has been obtained, Eqs. (9), (10), and (13) can be used instead of the product formulation (Eq. (7)).

6.2 A and B Represented by the Same Functional Form.

In this case, the scaling parameter can be found analytically. Typically, in this case, A and B are single variable functions; however, this requirement is not necessary. The scaling parameter s is chosen to make

$$A(\xi) \equiv B(\xi/s) \quad (15)$$

As an example, in the model of Efimtsov (1982):

$$A(\xi, \Lambda_\xi) = \exp(-\xi/\Lambda_\xi) \quad (16)$$

and

$$B(\eta, \Lambda_\eta) = \exp(-\eta/\Lambda_\eta) \quad (17)$$

where Λ_ξ and Λ_η are correlation lengths that depend upon the frequency and various flow parameters. In order to satisfy Eq. (15), s must be chosen so that

$$\exp(-\xi/\Lambda_\xi) = \exp(-(\xi/s)/\Lambda_\eta) \quad (18)$$

which requires

$$s = \Lambda_\xi/\Lambda_\eta \quad (19)$$

For the Efimtsov model, although s will always equal the ratio Λ_ξ/Λ_η , the specific numerical values of s will vary with the frequency and flow conditions because the values of Λ_ξ and Λ_η vary with the frequency and flow conditions. As in the previous subsections, after s has been obtained, Eqs. (9), (10), and (13) can be used instead of the product formulation (Eq. (7)). In this special case Eq. (13) reduces to

$$\gamma(\xi, \eta, \omega) = \exp(-\sqrt{(\xi/\Lambda_\xi)^2 + (\eta/\Lambda_\eta)^2}) \quad (20)$$

7 Conclusions

A large-eddy simulation database was used to evaluate the validity of the multiplication hypothesis for modeling the coher-

ence of the cross-spectral density of the wall-pressure fluctuations. Comparison with the data from the numerical simulation revealed that even under optimal conditions the use of the multiplication hypothesis predicts off-axis coherences that are badly in error. A new modeling form was introduced and shown to perform much more accurately. The new model requires no additional data than that previously used, and the implementation of the new model into existing computer codes can be readily achieved. For instances in which various simplifying assumptions with regard to the form of the streamwise and spanwise coherences have been exploited in an existing computer program, shortcuts for the inclusion of the new modeling form were discussed. Although the new modeling form works well for flat-plate boundary-layer data, its usefulness for more complex flows still must be investigated.

Acknowledgments

The author thanks Dr. Craig Streett for many useful suggestions. This work was carried in the Fluid Mechanics and Acoustics Division of NASA Langley Research Center under contract NAS1-20059.

References

- Blake, W., 1986, *Mechanics of Flow-Induced Sound and Vibration*, Vol. II, Academic Press, p. 644.
- Bull, M. K., 1963, "Properties of the Fluctuating Wall-Pressure Field of a Turbulent Boundary Layer," AGARD Report 455.
- Chang, P. A., Abraham, B. M., and Piomelli, U., 1994, "Wavenumber-Frequency Characteristics of Wall Pressure Fluctuations Computed Using Turbulence Simulations," Presented at *Symposium on Active/Passive Control of Flow-Induced Vibration and Noise: 1994 International Mechanical Engineering Congress and Exposition*.
- Choi, H. and Moin, P., 1990, "On the Space-Time Characteristics of Wall-Pressure Fluctuations," *Physics of Fluids A*, Vol. 2, pp. 1450–1460.
- Corcos, G. M., 1963a, "Resolution of Pressure in Turbulence," *The Journal of the Acoustical Society of America*, Vol. 35, pp. 192–199.
- Corcos, G. M., 1963b, "The Structure of the Turbulent Pressure Field in Boundary-Layer Flows," *Journal of Fluid Mechanics*, Vol. 18, pp. 353–378.
- Corcos, G. M., 1967, "The Resolution of Turbulent Pressures at the Wall of a Boundary Layer," *Journal of Sound and Vibration*, Vol. 6, pp. 59–70.
- Efimtsov, B. M., 1982, "Characteristics of the Field of Turbulent Wall Pressure Fluctuations at Large Reynolds Numbers," *Soviet Physics. Acoustics*, Vol. 28, pp. 289–292.
- Farabee, T. M. and Casarella, M. J., 1991, "Spectral Features of Wall Pressure Fluctuations Beneath Turbulent Boundary Layers," *Physics of Fluids A*, Vol. 3, pp. 2410–2420.
- Schewe, G., 1983, "On the Structure and Resolution of Wall-Pressure Fluctuations Associated with Turbulent Boundary-Layer Flow," *Journal of Fluid Mechanics*, Vol. 134, pp. 311–328.
- Singer, B. A., 1996a, "Large-Eddy Simulation of Turbulent Wall-Pressure Fluctuations," NASA CR-198276 February.
- Singer, B. A., 1996b, "Turbulent Wall-Pressure Fluctuations: New Model for Off-Axis Cross-Spectral Density," NASA CR-198297, March.
- Wilby, J. F. and Gloyna, F. L., 1972, "Vibration Measurements of an Airplane Fuselage Structure: 1. Turbulent Boundary Layer Excitation," *Journal of Sound and Vibration*, Vol. 25, pp. 443–466.

Wavenumber Spectra of High Magnitude Wall Pressure Events in a Numerically Simulated Turbulent Boundary Layer

B. M. Abraham
Mechanical Engineer.
Mem. ASME

W. L. Keith
Mechanical Engineer.
Mem. ASME

Submarine Sonar Department,
Naval Undersea Warfare Center,
Newport, RI 02841-1708

A method for conditionally sampling the spatial field of the wall pressure beneath a turbulent boundary layer in order to search for high magnitude events and calculate the corresponding wavenumber spectrum is presented. The high magnitude events are found using a simple peak detection algorithm at a fixed instant in time and the wavenumber spectra are calculated using discrete Fourier transforms. The frequency of occurrence for high magnitude positive events is found to be approximately the same as for high magnitude negative events. The contribution of the high magnitude events to the rms wall pressure for various trigger levels is calculated and compared with results from similar experimental studies performed in the time domain. The high magnitude events are shown to occur infrequently and to contribute significantly to the rms wall pressure. Wavenumber spectra from the high magnitude positive and negative events are calculated and compared with the unconditionally sampled spectra. The high magnitude events contain energy focused around a particular streamwise wavenumber and have high broadband spectral levels.

Introduction

Recently, Johansson et al. (1987) and Karangelen et al. (1993) have analyzed the high magnitude positive and negative wall pressure events occurring beneath a turbulent boundary layer as a function of time. They concluded that the large amplitude events are of sufficient magnitude and duration to be major contributors to the root-mean-square (rms) wall pressure. Karangelen et al. determined that the events where the pressure exceeded $3p_{rms}$ have an average duration of 14 viscous time units, occur 5 percent of the time, and contribute 49 percent to the root mean square (rms) wall pressure. Schewe (1983) noted that events exceeding $3p_{rms}$ occurred 1 percent of the time and contributed 40 percent to the total rms. Two fundamentally different approaches to gathering these statistics have been used by these investigators and their differences will be discussed in the following section.

Domaradzki et al. (1992) showed that scattering of these high magnitude events by slight imperfections in a surface coating can dramatically increase the scattered wall pressure when compared to the wall pressure measured by a flush-mounted sensor in a uniform wall. Therefore understanding the spatial structure and related wavenumber content of these high magnitude events will aid in the design of sensors that act as spatial filters to reduce noise from the turbulent boundary layer.

The objectives of this research are to identify high magnitude (positive and negative) pressure events in a turbulent boundary layer and to determine their characteristic streamwise and spanwise wavenumber content. The space-time wall pressure data from the direct numerical simulation (DNS) of fully developed turbulent channel flow by Kim et al. (1987) are used. This data set contains the fluctuating wall pressure field over a 128 by 128 spatial grid for 2564 time steps. The numerical grid and flow parameters from this investigation are listed in Table 1. With current sensor technology, sensor size and cost restrictions

prohibit an experiment that could match the spatial resolution provided by this database.

Although the simulation is for a much lower momentum thickness Reynolds number ($R_\theta = 278$) than typically encountered in most undersea and aerospace applications, the wall pressure statistics have been shown to agree reasonably well with other experimental investigations (see Choi and Moin, 1990; Keith et al., 1992). The frequency autospectrum from this simulation is compared to the experimental investigations of Schewe (1983) and Farabee and Casarella (1991). Figure 1(a) compares the spectra with a "mixed" scaling using δ and τ_w while Fig. 1(b) uses an "inner" scaling using ν and u_τ . The mixed scaling tends to scale the spectra well (over a wide range of R_θ) at lower frequencies ($\omega\delta/u_\tau < 60$) where the dominant energy is believed to be from the log-law and outer regions of the boundary layer. The inner scaling tends to collapse the higher frequency ($\omega\nu/u_\tau^2 > 1$) portions of the spectra where the primary contributors to the wall pressure are velocity fluctuations in the log-law and buffer regions. The reader is referred to Keith et al. (1992) for a more comprehensive review of spectral scalings including sensor size and Reynolds number effects.

Conditional Sampling of High Magnitude Events

The wall pressure database was searched in the spatial domain at fixed times for high magnitude events that exceeded certain threshold levels. When an event was found, the location of its peak was noted. A data subgrid was centered around this location. The nominal subgrid had a length of 32 streamwise grid points ($\pi\delta$) and a width of 32 spanwise grid points ($\pi\delta/3$). A Taylor shading window with -30 dB sidelobes and parameter $\bar{n} = 5$, where \bar{n} is essentially the number of sidelobes of level -30 dB next to the main lobe (see Streit, 1985), was applied to the data. The Taylor spatial window was used because it provides a convenient method of controlling sidelobe levels in the wavenumber domain.

Next, the two-wavenumber spectrum from the high magnitude event was calculated. After the spectrum was established, the event search continued through the remainder of the spatial

Contributed by the Fluids Engineering Division for publication in the JOURNAL OF FLUIDS ENGINEERING. Manuscript received by the Fluids Engineering Division July 11, 1995; revised manuscript received August 12, 1996. Associate Technical Editor: M. M. Sinder.

Table 1 Numerical and boundary layer parameters

Parameter	Value
Numerical grid size	128 (streamwise), 128 (spanwise)
Grid dimensions	$4\pi\delta$ (streamwise), $4\pi\delta/3$ (spanwise)
Streamwise grid spacing	$\Delta x_1 = 0.0982\delta = 17.6 \nu/u_\tau$
Spanwise grid spacing	$\Delta x_3 = 0.0327\delta = 5.9 \nu/u_\tau$
Time step of database*	$\Delta t = 0.00375\delta/u_\tau = 0.675 \nu/u_\tau^2$
Total time	$2564 \Delta t = 9.615 \delta/u_\tau = 1731 \nu/u_\tau^2$
$R_\delta = U_0\delta/\nu$	3200
$R_\theta = U_0\theta/\nu$	287
$\delta/(u_\tau)$	180
δ^*/δ	0.141
θ/δ	0.087
u_τ/U_0	0.05625
p_{rms}	$1.52\tau_w = 0.00481\rho U_0^2$

* The actual time step used in simulation was $3.75 \times 10^{-4} \delta/u_\tau$.

grid. After the grid was searched, the time was incremented 10 time steps ($0.0375\delta/u_\tau = 6.75\nu/u_\tau^2$) and the process was repeated. The engineering application of a conditional sampling method will dictate how frequently the spatial field is sampled (e.g., by the sampling frequency of an array of hydrophones). Lueptow (1993) determined that the typical duration of high magnitude events from this DNS database was $0.4\delta/u_\tau$ or $72\nu/u_\tau^2$. By advancing time less than this delay, the high magnitude events will be counted during different parts of their growth and decay cycle as long as their peak levels exceed the threshold pressure. The time delay was varied between 10 and 100 time steps (0.0375 to $0.375\delta/u_\tau$) and it will be shown to have a negligible effect on the resulting wavenumber spectra from the high magnitude events.

Figure 2 shows the character of a typical high magnitude positive event at a fixed time t_0 . The peak of this event is $6.38p_{rms}$ (or $9.7\tau_w$) and occurs at $x_1 = 9\delta$ and $x_3 = 2.55\delta$. A small region of negative pressure occurs just behind the peak in the streamwise direction. High magnitude negative events are similar in nature to the positive events, except that they are of opposite sign. Instead of a region of negative pressure behind a peak, there is typically a region of positive pressure in front of the peak. A similar relationship has been found in time series of wall pressure in the physical experiments of Schewe (1983), Johansson et al. (1987), and Karangelen et al. (1993).

The high magnitude event search was conducted for threshold pressures of 0, 3, 4, and $6p_{rms}$, where p_{rms} is the space- and time-averaged rms wall pressure (equal to $1.52\tau_w$). The absolute locations of the high magnitude positive events exceeding a threshold of $4p_{rms}$ are shown in Fig. 3. The spatial distribution of the events is essentially random in the x_1, x_3 plane. A total of 557 events was found, and thus 557 ensemble averages of the two-wavenumber spectrum were calculated. Table 2 summarizes the number of events found for the different searches and the predicted random spectral error for the two-wavenumber

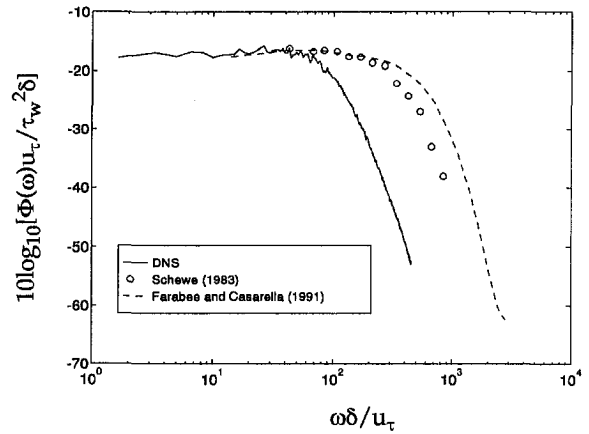


Fig. 1(a) Scaled with δ and u_τ

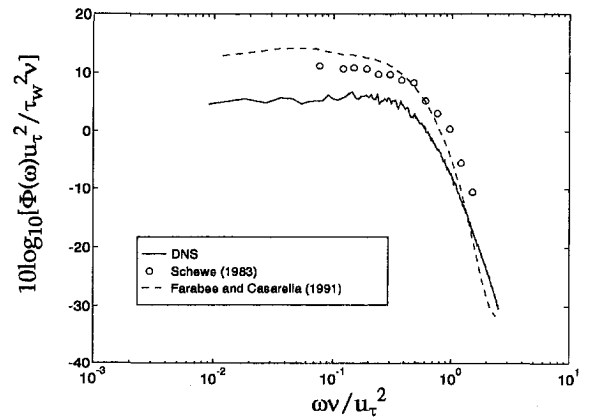


Fig. 1(b) Scaled with u_τ and ν

Fig. 1 Comparison of frequency autospectrum from Direct Numerical Simulation with experimental investigations

spectrum. The estimated random error for this spectrum is simply $\sqrt{1/N_e}$, where N_e is the number of ensemble averages. The numbers of positive and negative high magnitude events were of the same order of magnitude for a given threshold detection limit although there were slightly more negative events found than positive events. Karangelen (1993) noted the same results for conditionally sampled time series of wall pressure and Schewe (1983) noted the slight negative skewness of the wall pressure.

The DNS database was searched for positive and negative wall pressures that exceeded $p_i = 0, 1, 2, 3, 4, 5,$ and $6p_{rms}$. The contribution to the rms pressure was determined by calculating the rms pressure from these events and normalizing it by

Nomenclature

k_1, k_3 = streamwise, spanwise wavenumber (rad/m)	$W(p)$ = probability density function of the fluctuating wall pressure	ρ = fluid density (kg/m ³)
$p(x_1, x_3, t)$ = fluctuating wall pressure (Pa)	x_1, x_3 = streamwise, spanwise location (m)	τ_w = mean wall shear stress (Pa)
p_t = threshold (trigger) pressure (Pa)	δ, δ^*, θ = boundary layer, displacement, momentum thickness (m)	$\Phi(\omega)$ = frequency autospectrum (Pa ² /(rad/s))
p_{rms} = root-mean-square wall pressure (Pa)	λ = wavelength (m)	$\Phi(k_1), \Phi(k_3)$ = streamwise, spanwise wavenumber spectrum (Pa ² /(rad/m))
$R_\theta = U_0\theta/\nu$ = momentum thickness Reynolds number	ν = kinematic viscosity (m ² /s)	$\Phi(k_1, k_3)$ = two-wavenumber spectrum (Pa ² /(rad ² /m ²))
t = time (s)	ν/u_τ = viscous length scale (m)	ω = frequency (rad/s)
u_τ, U_0 = friction, freestream velocity (m/s)	ξ, η = streamwise, spanwise separation (m)	

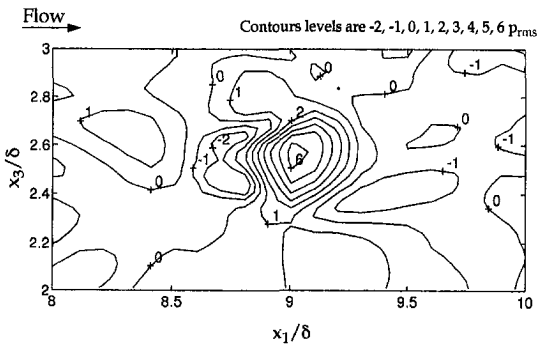


Fig. 2 Spatial field of a typical high magnitude positive wall pressure event

the rms pressure from all of the events according to the following equation:

$$\% \text{ rms} = 100 \sqrt{\frac{\sum_{n=1}^N p_i^2(n)}{\sum_{n=1}^N p^2(n)}} \quad (1)$$

where $p_r(n) = p(n)$ for $|p(n)| > p$, and $p_r(n) = 0$ for $p(n) < p$. Here N is the total number of locations in space and time that were searched (number of spatial locations multiplied by number of time steps used = 3,080,191). This method is equivalent to Schewe's (1983) method of integrating the probability density function to determine the percent time a threshold pressure is exceeded. Table 3 shows the results of the event search compared to Schewe's results for a wall pressure sensor of size $d^+ = 19$ (which has little spatial averaging). Of primary interest is that the high magnitude events (e.g., $|p| > 3p_{rms}$) contribute a statistically significant amount to the rms wall pressure (e.g., 40.9 percent) yet only occur a small percentage of the time (e.g., 1.16 percent).

Karangelen et al. (1993) noted that high magnitude wall pressure events (both positive and negative) exceeding $4p_{rms}$

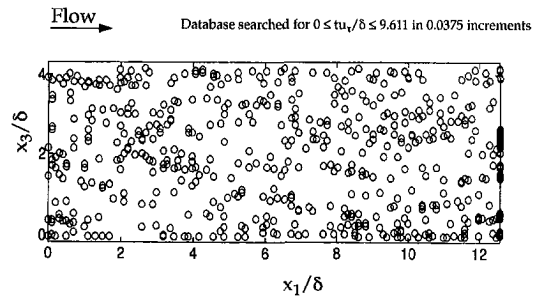


Fig. 3 Locations of high magnitude positive events exceeding $4p_{rms}$

occur 1.35 percent of the time but contribute to 31.62 percent of the rms wall pressure. The current results for the DNS database generally predict that high magnitude events occur slightly less often than shown in the results of Karangelen et al. (1993) and contribute to a slightly smaller portion of the rms wall pressure (26.7 percent for $p_i/p_{rms} = 4$). This apparent difference can be explained by examining the methods used by the different investigations.

Schewe's (1983) method and the method used in this investigation for calculating the statistics in table 3 (using the probability density function) only counts the part of the pressure events which exceed the threshold pressure p_i . Johansson et al. (1987) and Karangelen et al. (1993) calculated these statistics by identifying discrete events in the time domain and estimating a "pulse width" of the event to determine its duration and contribution to the rms wall pressure. The latter method therefore counts the pressure associated with the event and not just the pressure above the threshold. Because this investigation examined the spatial structure of the high magnitude events, a temporal pulse width was an inappropriate metric. Karangelen et al. (1993) did note, however, that their results compared favorably with Schewe's when the PDF method was used. The probability density function from the DNS database is compared with that measured by Schewe's smallest sensor ($d^+ = 19$) in Fig. 4. A Gaussian (normal) distribution is shown for reference. The

Table 2 High magnitude event search results

Threshold (trigger) pressure p_i/p_{rms}	Type of event	Number of events	Random spectral error (%)	Random spectral error (dB)
6	Positive	113	9.4	0.39
6	Negative	161	7.9	0.33
6	Both positive and negative	274	6.0	0.25
4	Positive	557	4.2	0.18
4	Negative	692	3.8	0.16
4	Both positive and negative	1249	2.8	0.12
3	Positive	1083	3.0	0.13
3	Negative	1303	2.8	0.12
3	Both positive and negative	2386	2.0	0.09

Note: For time delay of $10 \Delta t = 0.0376\delta/u_\tau = 6.75 v/u_\tau^2$ between spatial samples and 32 by 32 spatial subgrid.

Table 3 Wall pressure statistics

Threshold pressure p_i/p_{rms}	% Time for (+) events	% Time (-) events occurred	% Time (+) and (-) events occurred	% rms from (+) events	% rms from (-) events	% rms from (+) and (-) events
0	50.19 [51]	49.81 [49]	100.00 [100]	49.80	50.20	100.00
1	13.52 [13.5]	13.51 [13.5]	27.03 [27]	44.74	45.26	90.00
2	2.60 [2.30]	2.72 [2.7]	5.323 [5.0]	31.08	31.99	63.08
3	0.543 [0.4]	0.613 [0.6]	1.156 [1.0]	19.91	20.95	40.86 [40]
4	0.141 [0.1]	0.156 [0.2]	0.296 [0.3]	13.12	13.54	26.66
5	0.046	0.049	0.094	9.07	9.06	18.14
6	0.015	0.015	0.03	6.25	5.83	12.08

Note: Data in brackets [] are from Schewe (1983) for $d^+ = 19$.

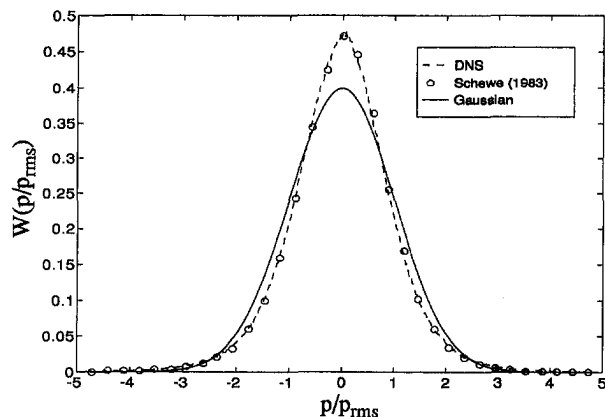


Fig. 4 Probability density function of the fluctuating wall pressure

remarkable similarity of the results attest to the agreement seen in Table 3. Above $|p/p_{rms}| > 2.6$, the “tails” of the PDF are higher than that for a Gaussian distribution. This is confirmed by the high kurtosis (flatness) of 5.2 for the DNS database.

Figure 5 shows the average spatial field from the positive wall pressure events exceeding $4p_{rms}$. This field is a composite of high magnitude positive events from different spatial locations and times that have been superimposed such that their peak pressure occurs at $\xi = \eta = 0$. The average spatial size of the event based on zero-pressure crossings is approximately 0.48δ ($86\nu/u_\tau$) in the streamwise direction. The average pressure never becomes negative in the spanwise direction at $\xi = 0$. The size of the event in the spanwise direction is also 0.48δ (or $86\nu/u_\tau$) based upon when the pressure is below $\frac{1}{10}$ th of the peak pressure.

Regions of negative pressure precede and follow the peak of the event in the streamwise direction and are consistent with the results of Lueptow (1993) and with the time-domain analyses of Karangelen et al. (1993), Johansson et al. (1987), and Schewe (1983). This effect is not seen in the spanwise direction. The regions of negative pressure are approximately the same spatial size as the high magnitude positive event. The region preceding the maximum pressure (positive ξ) has a minimum pressure of $-0.62p_{rms}$, while the region after the maximum pressure (negative ξ) reaches a minimum of $-1.12p_{rms}$.

Positive pressure peaks beneath a turbulent boundary layer have often been related to turbulent bursts (Hinze, 1975) and are thought to be from the collapse of a horseshoe vortex. A horseshoe vortex has its highest concentration of vorticity in the spanwise direction, with its tailing legs composed of counter-rotating streamwise vortices. Robinson (1991) and Snarski (1993) give reviews of the coherent structures that have been found beneath turbulent boundary layers. The horseshoe vortex model describes many of these events. Figure 6 depicts a quali-

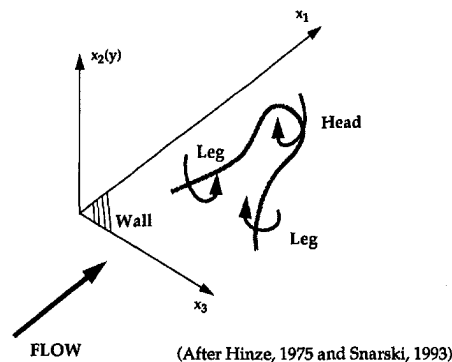


Fig. 6 Qualitative model of a horseshoe vortex

tative model of a horseshoe vortex in the boundary layer. This vortex grows until its head moves out of the boundary layer. It then becomes unstable and collapses back onto the wall, creating a high pressure burst. The negative region of wall pressure in front of the burst is from the lifting of fluid (ejection) as the horseshoe vortex lifts away from the wall. This increase in the normal fluid velocity near the wall creates a negative pressure. The negative region just behind the burst is from the legs of the horseshoe vortex, which act together to sweep fluid away from the wall.

Variable interval time averaging (VITA) techniques (see Johansson et al., 1987, and Snarski and Lueptow, 1995) have shown that the high magnitude positive wall pressure events occur when there is a sharp shear layer in the buffer region ($y^+ \approx 10$ to 15). The structure seen in the spatial field of the high magnitude wall pressure events is much bigger than this scale, however. Schewe (1983) determined the typical “wavelength” of the high magnitude events to be $145\nu/u_\tau$, or 0.25δ for an R_θ of 1400. Karangelen et al. (1993) report the typical temporal pulse width of a high magnitude event to be $10-15\nu/u_\tau^2$ with their R_θ of 3332. Assuming convection of a “frozen field” at a streamwise velocity of $0.6U_o$, the streamwise length of the high magnitude event is $199-298\nu/u_\tau$ or $0.17-0.25\delta$. These investigations span an R_θ of 278 to 3332 and all support the existence of large scale high magnitude wall pressure events.

The average wall pressure field from high magnitude negative events exceeding $-4p_{rms}$ is given in Fig. 7. The minimum average pressure is $-5.3p_{rms}$ (or $-8.0\tau_w$) while the maximum pressure of $1.18p_{rms}$ is reached just in front of the region of negative pressure. The average spatial size of the negative events is 0.49δ and 0.44δ in the streamwise and spanwise directions, respectively. Similar to the average pressure field for the high magnitude positive events, a region of opposite-sign pressure (positive in this case) is found following the high magnitude event. The average pressure level of this region is $+0.36p_{rms}$.

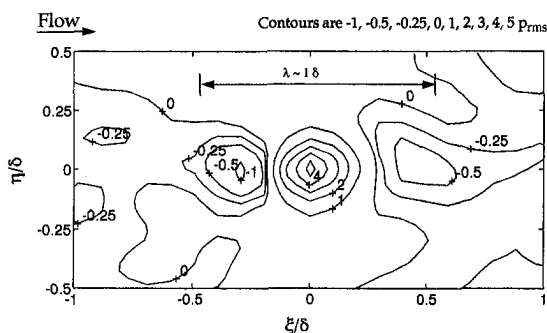


Fig. 5 Average spatial field from positive wall pressure events exceeding $4p_{rms}$

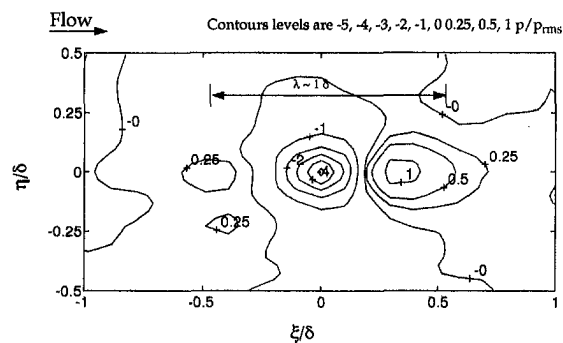


Fig. 7 Average spatial field from negative wall pressure events exceeding $-4p_{rms}$

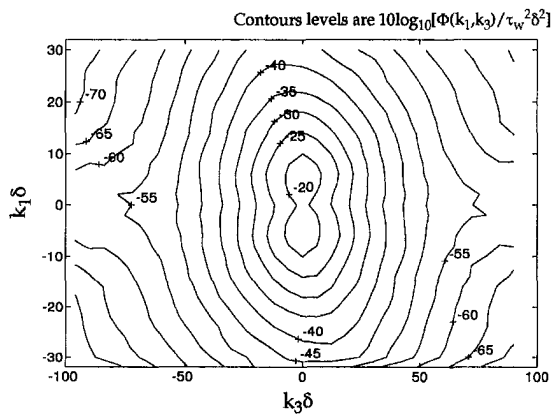


Fig. 8 Two-wavenumber spectrum from positive wall pressure events exceeding $4p_{rms}$

The negative and positive events have an asymmetry in the streamwise direction. For the positive events, the overshoot or opposite sign region preceding the maximum peak pressure is smaller than is the region after the maximum pressure. For the negative events, the overshoot region preceding the minimum peak pressure is higher in amplitude than is the region after the minimum pressure.

Negative pressure peaks found in turbulent boundary layers have been associated with sweep-type ejections. An ejection is a movement of fluid away from the wall. In addition, the ejection event has been associated with a deceleration of the streamwise velocity near the wall (Hinze, 1975). Snarks and Lueptow (1995) suggest that the negative events are part of a burst-sweep cycle near the wall which is linked to large-scale structure in the boundary layer. Because high magnitude negative events occur at least as often as positive pressure events, the importance of negative peaks is significant to the total wall pressure.

Figure 8 shows the two-wavenumber spectrum $\Phi(k_1, k_3)$ calculated from high magnitude positive-events exceeding $4p_{rms}$. The wavenumber resolution (bin width) is $2/\delta$ and $6/\delta$ for the streamwise and spanwise wavenumber, respectively, due to the reduced spatial transform size. Figure 9 shows the two-wavenumber spectrum from high magnitude negative events less than $-4p_{rms}$. Both spectra are very similar to each other, but have noticeable differences with respect to the nonconditionally sampled spectrum shown in Fig. 10. Figure 11(a) shows a comparison of $\Phi(k_1, k_3)$ from the positive events, the negative events, and the average spectrum as a function of streamwise wavenumber $k_1\delta$ at $k_3 = 0$. The maximum spectral level of Fig. 11(a) is 0.0204 (-16.9 dB), which is lower than the maximum spec-

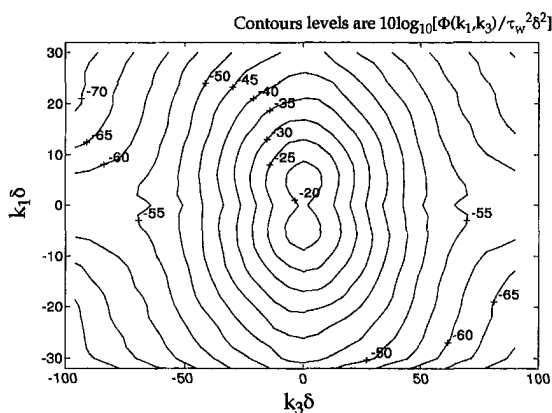


Fig. 9 Two-wavenumber spectrum from negative wall pressure events exceeding $-4p_{rms}$

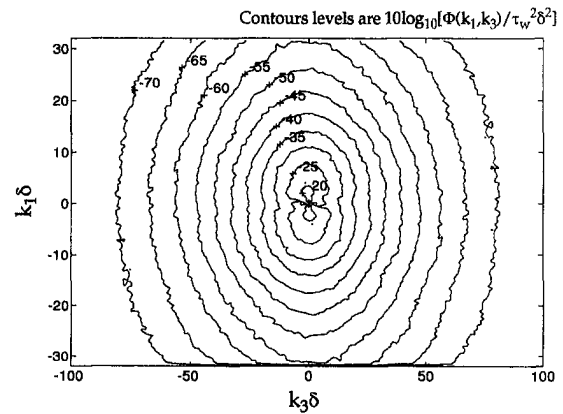


Fig. 10 Two-wavenumber spectrum from all wall pressure data

tral level from the average two-wavenumber spectrum (-13.3 dB) because the average two-wavenumber spectrum has two spikes that occur at the two-wavenumber bins centered about $k_1 = 0$. At all other wavenumbers, the spectral values from the high magnitude events are larger than those of the mean spectrum. The maximum levels occur at $k_1\delta = \pm 0.5$ for the average spectrum and ± 4.0 for the high magnitude events exceeding $4p_{rms}$. Figure 11(b) shows the same data but as a function of spanwise wavenumber $k_3\delta$ at $k_1\delta = 0$. The spectral levels of the positive and negative events are approximately the same, and are greater than the average spectral levels at all wavenumbers.

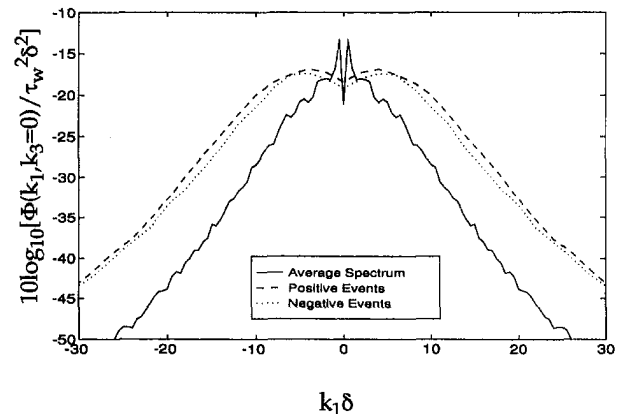


Fig. 11(a) Wavenumber cut with $k_3 = 0$

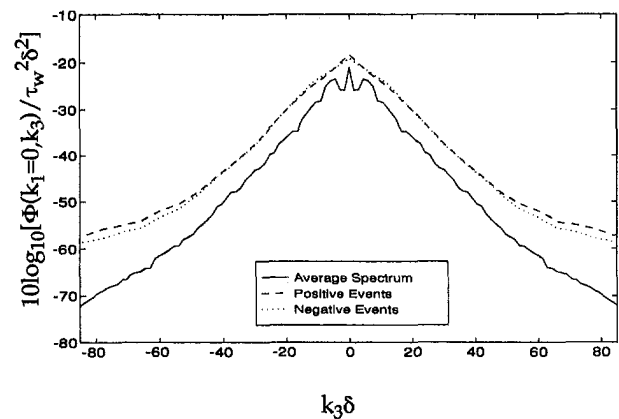


Fig. 11(b) Wavenumber cut with $k_1 = 0$

Fig. 11 Comparison of two-wavenumber spectra from high magnitude events exceeding $4p_{rms}$ with average spectrum

Figure 12 shows the streamwise and spanwise wavenumber spectra calculated from high magnitude positive, negative, and positive and negative wall pressure events exceeding $+4p_{rms}$ (or $-4p_{rms}$ for negative events) compared with the average wavenumber spectra. The streamwise wavenumber spectrum (Fig. 12(a)) was obtained by integrating the two-wavenumber spectrum over spanwise wavenumber k_3 , and the spanwise wavenumber spectrum (Fig. 12(b)) was obtained by integration over the streamwise wavenumber k_1 .

The peak spectral level in the streamwise wavenumber spectrum is -4.4 dB. Above $k_1\delta = 10$, the conditionally sampled streamwise wavenumber spectra are 11 dB higher than the average spectral levels. The maximum streamwise wavenumber spectral level occurs at $k_1\delta = 5$. The spectral magnitudes from the positive, negative, and positive and negative events are almost identical, with the positive events showing slightly (0.5 to 1 dB) higher levels about $k_1\delta = 7$. The spanwise wavenumber spectra calculated from the high magnitude positive, negative, and positive and negative wall pressure events are exactly the same within statistical error.

The streamwise wavenumber spectra from the high magnitude events contain higher energy than the average spectrum at similar streamwise wavenumbers. For example, the dominant portion (90 percent) of the energy from the wall pressure fluctuations for the high magnitude events exceeding $4p_{rms}$ is in the wavenumber range $2 < k_1\delta < 16$. A range of wavelengths associated with this range of wavenumber is $0.39 < \lambda/\delta < 3.14$ ($70 < \lambda/(\nu/u_\tau) < 565$). This range or bandwidth is $0.5 < k_1\delta < 10$ for the average spectrum. Clearly, the structure is on the order of δ in size, as seen in the average pressure fields for the positive and negative events (Figs. 5 and 7).

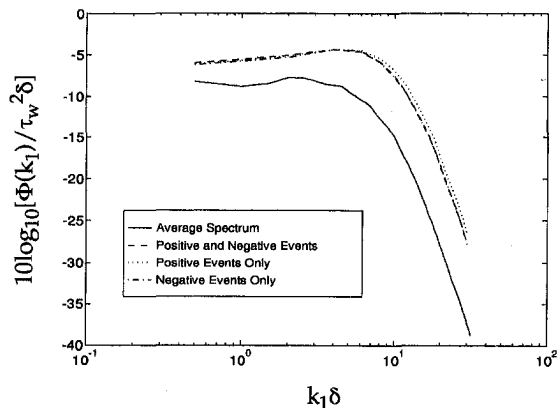


Fig. 12(a) Streamwise wavenumber spectrum

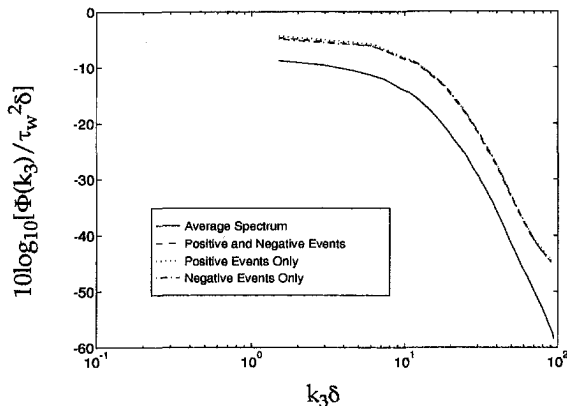


Fig. 12(b) Spanwise wavenumber spectrum

Fig. 12 Comparison of spectra from high magnitude events exceeding $4p_{rms}$ with average spectrum

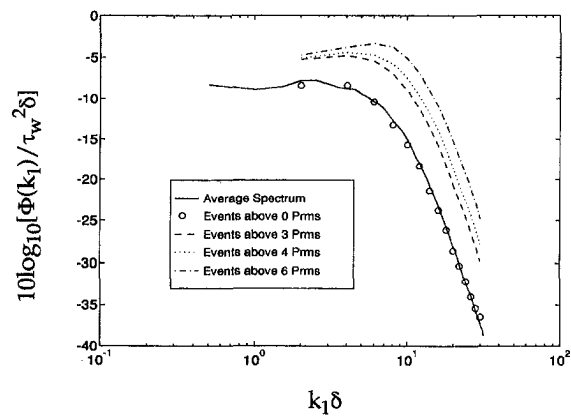


Fig. 13(a) Streamwise wavenumber spectrum

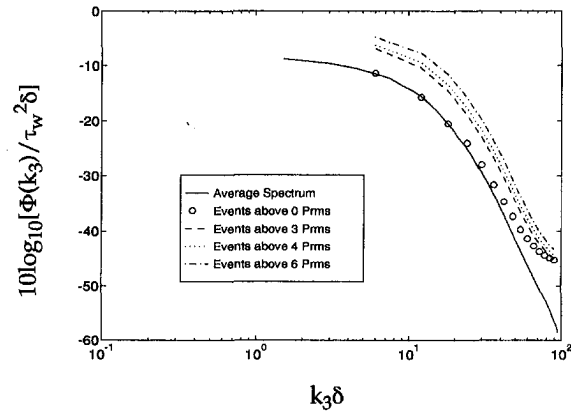


Fig. 13(b) Spanwise wavenumber spectrum

Fig. 13 Comparison of spectra from high magnitude events at various trigger levels with average spectrum

To study the effect of threshold (trigger) level on the spectra calculated from high magnitude events, the calculations were repeated with trigger levels of 6, 4, 3, and $0p_{rms}$. Both positive and negative events were considered. Figures 13(a) and 13(b) show the resulting streamwise and spanwise wavenumber spectra respectively. In general, there is a broadband (over all wavenumber) increase in spectral levels with increasing trigger level, as expected. The spectral levels do not track with the contribution of the high magnitude events to the total rms wall pressure. The conditional sampling technique only includes events above a certain threshold level in the calculation of the wavenumber spectrum. The integral of the wavenumber spectrum is the mean square power from the events, so higher trigger levels should lead to higher spectral levels. The contribution to the total rms is based on the magnitude of the events and on how often they occur.

All of the spectral calculations, except the average spectrum, used a 32 by 32 spatial grid for the calculation of the two-wavenumber spectrum and a Taylor shading window with -30 dB sidelobes. The case where the trigger level is $0p_{rms}$ shows that the average spectrum is indeed calculated when all events are considered. In Figure 13(b), however, the data for the $0p_{rms}$ trigger level does not match the average spectral data because of sidelobe leakage in the k_3 wavenumber domain. The smaller transform size used for the conditional sampling (32 by 32 grid compared with entire 128 by 128 grid) leads to higher sidelobes in the wavenumber domain.

The streamwise wavenumber spectrum shows a narrowing of the wavenumber spectrum around $k_1\delta = 7$ for the $6p_{rms}$ trigger level. The spanwise wavenumber spectra show a broadband increase in spectral level with increasing trigger level. The

Table 4 Spatial fourier transform sizes for high magnitude event search

Case #	Streamwise transform length	Spanwise transform length
1	$32\Delta x_1 = \pi\delta = 565 \nu/u_\tau$	$32\Delta x_3 = \pi\delta/3 = 188 \nu/u_\tau$
2	$24\Delta x_1 = 3\pi\delta/4 = 424 \nu/u_\tau$	$24\Delta x_3 = \pi\delta/4 = 141 \nu/u_\tau$
3	$16\Delta x_1 = \pi\delta/2 = 282 \nu/u_\tau$	$24\Delta x_3 = \pi\delta/4 = 141 \nu/u_\tau$
4	$16\Delta x_1 = \pi\delta/2 = 282 \nu/u_\tau$	$16\Delta x_3 = \pi\delta/6 = 94 \nu/u_\tau$

streamwise wavenumber at which the maximum spectral level occurs increases with increasing trigger level. The characteristic wavelength associated with this wavenumber is $\lambda = 2\pi/k_1 = 0.7\delta$ to 1.6δ ($126-288 \nu/u_\tau$). Because the spectra from high magnitude events show a clear maximum in a particular range of streamwise wavenumber, a significant portion of the energy is propagating over a fairly narrow range of wavenumbers. Since the characteristic wavelength of the event is on the order of the boundary layer thickness, the wall pressure footprint of the high magnitude events are rather large scale ($\lambda \gg \nu/u_\tau$). The average spatial size of the events shown in Figs. 5 and 7 confirm this assumption. Therefore, there is a well established correspondence between the streamwise wavenumber spectra and the spatial characteristics of the events themselves.

Next the effect of spatial transform size was investigated. For the $6p_{rms}$ trigger level, four different transform sizes in the streamwise and spanwise directions were considered. Table 4 details the transform sizes. The smallest size was based on the average spatial extent of the wall pressure events shown in Figs. 5 and 7. By reducing the transform area, only the pressure in the vicinity of the high magnitude event was considered, but resolution in wavenumber was also reduced. The streamwise and spanwise wavenumber spectra from high magnitude events exceeding $6p_{rms}$ for the four different transform areas are shown in Figs. 14(a) and 14(b), respectively. The spectral levels generally show a broadband increase with decreasing transform area, but the location of the peak spectral value in the streamwise wavenumber spectrum does not change. The increase in spectral levels is expected because the average rms wall pressure in the smaller transform areas is higher than for the larger areas. This study confirms the approach taken for conditional sampling in that the qualitative aspects of the results (e.g., energy-containing wavenumber ranges) are insensitive to the spatial transform sizes that were used.

Finally, the effect of temporal sampling delay was quantified. The spatial field was sampled at time delays of 10, 20, 50, and $100\Delta t$ (where $1\Delta t = 0.00375\delta/u_\tau$). Table 5 lists the search results for combined positive and negative events for $|p| > 4p_{rms}$. As expected, there was an inverse relationship between spatial sampling delay and the total number of events detected over the finite time available in the database. Figure 15 shows the resulting streamwise wavenumber spectra for the different search times. The only differences seen in the spectra are within the statistical error listed in Table 4, so there is not a significant effect on the wavenumber spectra by using a time delay less than that typical of the duration of a high magnitude event. This was confirmed for the other trigger levels used in the

Table 5 Search results showing effect of time delay between spatial samples

Time delay	Number of positive and negative events	Random spectral error (%)	Random spectral error (dB)
$10 \Delta t = 0.0375\delta/u_\tau = 6.75 \nu/u_\tau^2$	1249	2.8	0.12
$20 \Delta t = 0.075\delta/u_\tau = 13.5 \nu/u_\tau^2$	443	4.8	0.20
$50 \Delta t = 0.1875\delta/u_\tau = 33.75 \nu/u_\tau^2$	261	6.2	0.26
$100 \Delta t = 0.375\delta/u_\tau = 67.5 \nu/u_\tau^2$	141	8.4	0.35

Note: For $4p_{rms}$ threshold pressure and 32 by 32 spatial subgrid.

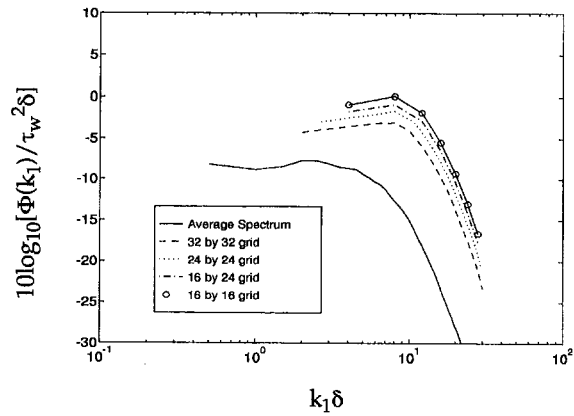


Fig. 14(a) Streamwise wavenumber spectrum

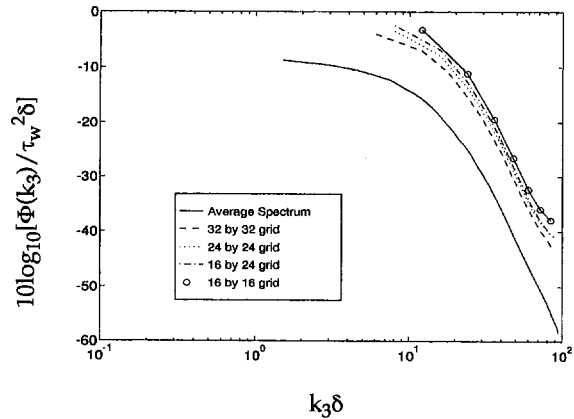


Fig. 14(b) Spanwise wavenumber spectrum

Fig. 14 Effect of spatial transform size on spectra from high magnitude positive events exceeding $4p_{rms}$

investigation and for both the streamwise and spanwise wavenumber spectra.

Conclusions

From these results for the conditionally sampled wavenumber spectra, we may come to several conclusions. The spectral levels associated with high magnitude events (positive or negative) are significantly higher than for the nonconditionally sampled (average) spectrum. The percent time that the high magnitude events occur is approximately the same for positive and negative events, and the contribution to the rms pressure is statistically significant. One may speculate that the negative and positive events are from the same process, such as the burst-sweep process, because they occur a similar percentage of time. The dominant energy in the spectra from high magnitude events occurs at higher streamwise wavenumbers than in the nonconditionally sampled spectrum. The streamwise wavenumber range or bandwidth in which most of the energy occurs narrows with increas-

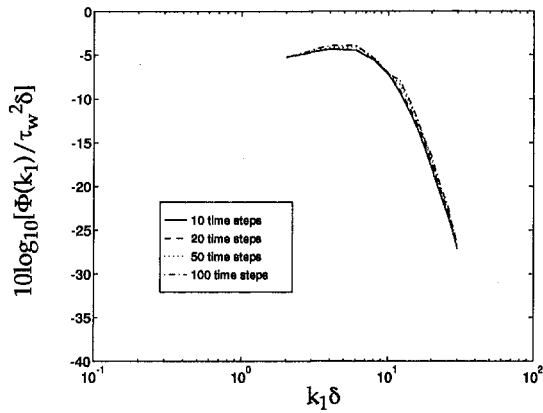


Fig. 15 Effect of temporal sampling delay on streamwise wavenumber spectrum from high magnitude events exceeding $4p_{rms}$

ing event amplitude. The wavelengths associated with this range of streamwise wavenumbers are on the order of the structure seen in the average pressure fields calculated for the high magnitude positive and negative events. Even though investigations using VITA detection show a correlation between the high magnitude wall pressure events and a velocity structure in the buffer region ($y^+ = 10$ to 15), the average spatial size of the “footprint” of the events in the $\xi-\eta$ plane from the DNS database is on the order of $\delta/2$ ($90\nu/u_\tau$). Recalling that the DNS had a low Reynolds number ($R_\theta = 278$), a series of experiments (physical or numerical) could determine if the results found for conditionally sampled spectra hold at higher Reynolds numbers. In particular, determining if the spatial structure of the high magnitude events scales with outer variables or inner variables is of interest.

Because conditionally sampled wavenumber spectra show significant differences when compared to nonconditionally sampled spectra, several implications for flow-induced noise become apparent. First, conditional sampling may be used to further study high magnitude events beneath turbulent boundary layers to learn more about the physics of the pressure-producing turbulent structures. The possibility of using active control to reduce the turbulent wall pressure seems most feasible if an indicator of the high magnitude event exists. For example, this could be a particular structure in the boundary layer that could be detected with a velocity or vorticity probe and canceled with an actuator at the wall.

Second, conditional sampling techniques could be implemented to exclude high magnitude events and thus decrease the direct-flow noise. Because the high magnitude events are of significant spatial extent, they are of engineering relevance for high Reynolds number flows. Consider a linear array of hydrophones designed to detect acoustic signals in water at 5000 Hz and below (channel spacing of 15 cm). Assuming a boundary layer thickness of 12.7 cm (5 in.) over a flat plate (e.g., the hull of a ship), the size of the high magnitude events will be on the order of the hydrophone size and little spatial filtering will occur. Therefore, data records containing the infrequently occurring high magnitude events could be discarded to effec-

tively reduce the flow-induced noise measured by the array and hence improve detection performance. Data processing methods may be able to compensate for the resulting noncontinuous data records in space and time (e.g., see Sherrill and Streit, 1987). Because very high magnitude events (e.g., $p > 4p_{rms}$) contribute to a significant portion of the rms pressure and occur relatively infrequently in time, this approach seems particularly feasible.

Lastly, the range of wavenumbers in which most of the energy from the high magnitude events propagates can aid in the design of spatial filters (see Ko and Schloemer, 1992 and Domaradzki et al., 1992) to reduce the flow-induced noise measured by a wall pressure sensor beneath a turbulent shear flow. The physical structure in which a sensor was mounted would be tuned to reject these wavenumbers while leaving the desired wavenumbers (e.g., acoustic wavenumbers) unattenuated.

Acknowledgments

The authors gratefully acknowledge the support of the Independent Research Program at the Naval Undersea Warfare Center Division, Newport, RI.

References

- Choi, H., and Moin, P., 1990, “On the Space-Time Characteristics of Wall-Pressure Fluctuations,” *Physics of Fluids A*, Vol. 2, No. 8, pp. 1450–1460.
- Domaradzki, J. A., Shah, K., and Crighton, D. G., 1992, “Scattering of Hydrodynamic Pressure Pulses by Coating Inhomogeneities,” *Journal of the Acoustical Society of America*, Vol. 92, No. 6, pp. 3302–3313.
- Farabee, T. M., and Casarella, M. J., 1991, “Spectral Features of Wall Pressure Fluctuations Beneath Turbulent Boundary Layers,” *Physics of Fluids A*, Vol. 3, No. 10, pp. 2410–2420.
- Hinze, J. O., 1975, *Turbulence*, McGraw-Hill, New York.
- Johansson, A. V., Her, J., and Haritonidis, J. H., 1987, “On the Generation of High-Amplitude Wall-Pressure Peaks in Turbulent Boundary Layers and Spots,” *Journal of Fluid Mechanics*, Vol. 175, pp. 119–142.
- Karangelen, C. C., Wilczynski, V., and Casarella, M. J., 1993, “Large Amplitude Wall Pressure Events Beneath a Turbulent Boundary Layer,” *ASME JOURNAL OF FLUIDS ENGINEERING*, Vol. 115, No. 4, pp. 653–659.
- Keith, W. L., Hurdis, D. A., and Abraham, B. M., 1992, “A Comparison of Turbulent Boundary Layer Wall Pressure Spectra,” *ASME JOURNAL OF FLUIDS ENGINEERING*, Vol. 114, No. 3, pp. 338–347.
- Kim, J., Moin, P., and Moser, R., 1987, “Turbulence Statistics in Fully Developed Channel Flow at Low Reynolds Number,” *Journal of Fluid Mechanics*, Vol. 177, pp. 133–166.
- Ko, S. H., and Schloemer, H. H., 1992, “Flow Noise Reduction Techniques for a Planar Array of Hydrophones,” *Journal of the Acoustical Society of America*, Vol. 92, No. 6, pp. 3409–3424.
- Lueptow, R. M., 1993, “Wall Pressure Events From the Direct Numerical Simulation of a Turbulent Wall-Bounded Flow,” Technical Report 10,481, Naval Undersea Warfare Center Detachment, New London, CT.
- Robinson, S. R., 1991, “The Kinematics of Turbulent Boundary Layer Structure,” Technical Memorandum 103859, National Aeronautics and Space Administration (NASA), Ames Research Center, Moffett Field, CA.
- Schewe, G. S., 1983, “On the Structure and Resolution of Wall-Pressure Fluctuations Associated With Turbulent Boundary Layer Flow,” *Journal of Fluid Mechanics*, Vol. 134, pp. 311–328.
- Sherrill, M. S., and Streit, R. L., 1987, “In Situ Optimal Reshaping of Arrays with Failed Elements,” *IEEE Journal of Oceanic Engineering*, Vol. OE-12, No. 1, pp. 155–162.
- Snarski, S. R., 1993, “Relationship Between the Fluctuating Wall Pressure and the Turbulent Structure of a Boundary Layer on a Cylinder in Axial Flow,” Technical Report 10,223, Naval Undersea Warfare Center Detachment, New London, CT.
- Snarski, S. R., and Lueptow, R. M., 1995, “Wall Pressure and coherent structures in a turbulent boundary layer on a cylinder in axial flow,” *Journal of Fluid Mechanics*, Vol. 286, pp. 137–171.
- Streit, R. L., 1985, “A Discussion of Taylor Weighting for Continuous Apertures,” Technical Memorandum 851004, Naval Undersea Warfare Center Detachment, New London, CT.

The Use of Pattern Recognition and Proper Orthogonal Decomposition in Identifying the Structure of Fully-Developed Free Turbulence

G. A. Kopp
Researcher.

J. A. Ferré
Professor.

Francesc Giralt
Professor.

Escola Tecnica Superior d'Enginyeria
Quimica,
Universitat Rovira i Virgili,
Carretera de Salou s/n,
43006 Tarragona, Spain

The eigenvectors obtained from proper orthogonal decomposition (POD) are used as the selection criteria to classify the individual events contained in data files of two-component velocity signals recorded in the non-homogeneous (vertical) and homogeneous (horizontal) planes of a fully-developed turbulent cylinder wake. This procedure uses the dominant eigenvectors from POD as initial templates to perform a pattern recognition (PR) analysis of the signals so that the individual coherent events appearing randomly in the signals can be deduced more objectively. It is found that the prototype or ensemble average of the group of events classified as the large-scale structure in the vertical plane has a circulatory motion with strong negative streamwise and outward lateral velocity fluctuations. In the horizontal plane, the average structure is a double roller with negative streamwise velocity fluctuations in its centerplane. The class of instantaneous events selected contribute significantly to the variance in the outer intermittent region, but much less in the fully turbulent core. While the first eigenvector from POD captures some of the features shown by this prototype, it is not enough to depict by itself all the characteristics shown by the ensemble average of the repetitive three-dimensional instantaneous events that occur in the fully-developed turbulent wake.

1 Introduction

There have been many techniques developed to determine the large-scale coherent structures in turbulent flows. Different features of these coherent structures have been used as the basis for their identification. For example, features such as spatial correlation functions (Grant, 1958; Lumley, 1965; Adrian and Moin, 1988), repetitive patterns (Townsend, 1979; Mumford, 1982; Ferré and Giralt, 1989), temperature gradients (Antonia, 1981), peaks in the large-scale vorticity fluctuations (Hussain, 1986), pressure fluctuations (Toyoda and Shirahama, 1994), critical points (Perry and Chong, 1987), deformation tensors (Hunt et al., 1988), quadrant analysis (Willmarth and Lu, 1972), vortices (Jeong and Hussain, 1995), and others, have been used by a variety of researchers. More recently, neural networks, in combination with a preconditioning of the velocity signal, have been used to classify repetitive events in turbulent flows (Ferre-Gine et al., 1996).

These techniques can be broadly split into two categories: correlation-tensor techniques and event-classification techniques. Proper orthogonal decomposition (POD), initially applied to turbulent flows by Lumley (1965), is the best known of the correlation-tensor techniques. It involves finding the eigenvectors and eigenvalues of the correlation tensor, which are ordered by their contribution to the variance (kinetic energy) of the data. The first eigenvector is then considered to represent the underlying large-scale structure of the particular flow (Payne and Lumley, 1967). POD has a sound mathematical basis and is widely used in fields outside of turbulence under the name Karhunen-Loève expansion (in digital image pro-

cessing, e.g., Pratt, 1978; Hall, 1979) or as principal component analysis (in multivariate statistics, e.g., Chatfield and Collins, 1980). A recent summary of the applications of the POD technique is given by Berkooz et al. (1993).

Event-classification techniques, such as VITA, conditional sampling or averaging, phase-averaging, pattern recognition (PR), etc., analyze a set of turbulent signals by searching for events that satisfy a detection or triggering criteria chosen by the researcher (e.g., Antonia, 1981; Subramanian et al., 1982). The detected events are classified as belonging to the same group, or class, and can be ensemble-averaged to depict the prototypical event of the class. When the detection criteria is related to large-scale motions, the ensemble-average represents the prototypical coherent structure. The resulting ensemble-average is analyzed for physical and statistical significance. Pattern recognition, or template matching, uses as a detection criteria a local maximum in the correlation between a template and the signals being analyzed. The difference between PR and standard conditional averaging is that the ensemble-average obtained is used as the template for the second search (or iteration), and so on, until the process converges (Mumford, 1982; Ferré and Giralt, 1989). Therefore, PR with one iteration is equivalent to conditional averaging.

A difficulty with the implementation of classification techniques is that a possible bias could be introduced when the detection or classification criterion is selected. For example, to generate acceptable results with VITA one has to compare different detection criteria and threshold levels (Subramanian et al., 1982). Once these issues are properly addressed, these techniques are able to detect specific events within the flow and to explain relevant aspects of the physics of turbulent flows (e.g., Antonia et al., 1987). On the other hand, a difficulty with the POD technique is that the dominant eigenvector may not be able to completely capture the motions of the coherent structure (Kevlahan et al., 1994).

Contributed by the Fluids Engineering Division for publication in the JOURNAL OF FLUIDS ENGINEERING. Manuscript received by the Fluids Engineering Division January 22, 1996; revised manuscript received January 29, 1997. Associate Technical Editor: M. Gharib.

There is a fundamental difference between POD and PR techniques when applied to the structural analysis of turbulent signals. The coherent structure determined by POD represents the most energetic large-scale structure found in the complete data set since the entire set is used in the analysis. On the other hand, the average structure determined by PR represents the prototypical structure of a group of individual instantaneous events selected conditionally from the turbulent flow. In developing mixing layers or wakes, where quasi-periodic large-scale motions occur, the structure deduced by either technique is similar. The first eigenvector typically captures 50–70 percent of the variance in a developing mixing layer (e.g., Delville, 1993), while the coherent motions identified with event-classification techniques account for about the same fraction of the variance (e.g., Kiyama and Matsumura, 1988). In fully-developed turbulent flows, however, the two techniques may not identify the same structures because there is no single dominant mode in the energy spectra.

The free turbulent flow analyzed here with POD and PR is the fully-developed turbulent wake. The data have been provided by R.A. Antonia at the University of Newcastle and consist of the two-component velocity fluctuations measured separately in the nonhomogeneous (vertical) and homogeneous (horizontal) planes. POD was first applied to this type of flow by Payne and Lumley (1967) who analyzed Grant's (1958) correlation data and identified a double roller structure with positive streamwise velocity fluctuations at the center. There was no evidence of spanwise vorticity at the top. On the other hand, PR analysis revealed a double roller structure with negative streamwise velocity fluctuations in the center and with spanwise vorticity at the top. This structure accounted for approximately 40 percent of the data (Giralt and Ferré, 1993) in vertical and horizontal planes. The connection between the vertical and horizontal plane measurements has been made by Vernet et al. (1997).

The aim of this paper is to combine POD and PR to reconcile the differences described above. PR is applied more objectively by using POD to produce the initial templates that PR requires to start the classification of individual instantaneous events. Also, the present analysis provides a basis for establishing a relationship between the instantaneous individual events present in the flow with the first eigenvector from POD and the class of events selected by PR. Section 2 describes the experimental details for obtaining the data used in the analysis. The dominant structural characteristics of the wake deduced by POD and PR are presented and compared in Section 3. Finally, Section 4 includes an analysis of the turbulence kinetic energy.

2 Experimental Details

The two-component velocity data used in the analysis that follows were measured in the open-return wind tunnel at the University of Newcastle. This wind tunnel has a test section $350 \times 350 \text{ mm}^2$ by 2.4 m long. Two-component velocity data were obtained in the wake of a cylinder at a Reynolds number of 1200 with the freestream velocity $U_o = 6.7 \text{ m/s}$ and the cylinder diameter $D = 2.67 \text{ mm}$. The freestream turbulence intensity was estimated to be about 0.05 percent. The cylinder aspect ratio was 131.

Antonia et al. used an array of 8 X -wires positioned at $x/D = 420$, measuring either the $u + v$ velocity components in the vertical plane or the $u + w$ velocity components in the horizontal plane, as depicted in Fig. 1. Mean velocities were subtracted from the instantaneous velocities and normalized by the freestream velocity U_o . The variables u , v , and w represent the velocity fluctuations in the streamwise (x), lateral (y), and spanwise (z) directions, respectively. In the vertical configuration the rake of probes was centered about the wake centerline. At $x/D = 420$ the spacing between adjacent probes was $\Delta y = 0.58 l_o$, where $l_o (= 12.3 \text{ mm})$ is the location where the mean velocity defect is half the maximum value. The voltage signals

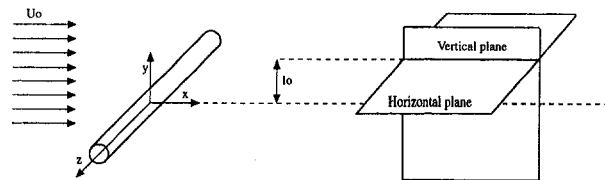


Fig. 1 Definition sketch

were sampled at 3472 Hz for 30 s. In the horizontal configuration the rake of probes was placed at the $y/l_o = 1$ with the spacing between adjacent probes being $\Delta z = 0.41 l_o$. Here, the voltage signals were sampled at 2717 Hz for 30 s. Further details about the wind tunnel and flow configuration can be found in Browne and Antonia (1986) and Antonia et al. (1987).

3 Analysis of The Experimental Data

Several points regarding the present analysis must be noted. First, velocity fluctuations only are used. Second, the flow is from left to right with the time coordinate converted into the streamwise co-ordinate using Taylor's hypothesis. Thus, $x^* = \Delta x/l_o \approx U_o \Delta t/l_o$ where Δt is the time interval between samples. The lateral and spanwise coordinates are normalized as $y^* = \Delta y/l_o$ and $z^* = \Delta z/l_o$, respectively.

3.1 Eigenvectors From Proper Orthogonal Decomposition. The POD technique involves obtaining the eigenvectors Φ_i from the velocity correlation tensor R_{ij} so that

$$\int R_{ij}(\bar{x}, \bar{x}', t, t') \Phi_j(\bar{x}', t') d\bar{x}' dt' = \lambda \Phi_i(\bar{x}, t) \quad (1)$$

where λ is the corresponding eigenvalue (i.e., the fraction of the variance accounted for by the eigenvector). Further details can be found in Lumley (1965) and Berkooz et al. (1993).

Figures 2(a) and 2(b) show the first and second eigenvectors obtained by POD in the vertical plane. The spatial and temporal extent of these eigenvectors, respectively determined by probe spacing and fixed to 8.6 ms ($\approx 4.7 l_o$), ensures that both the cross- and auto-correlations decay to zero at the extremes of the domain. The two eigenvectors in Fig. 2 account for 8 and 5 percent of the variance, while about 100 eigenvectors are required to capture 90 percent. The primary feature of the first eigenvector in Fig. 2(a) is that the streamwise and lateral velocity fluctuations are negatively correlated in the upper half of the wake, with negative u -fluctuations and positive v -fluctuations. The pattern of the first eigenvector, in this figure, is more like an outward ejection of fluid from the center of the wake. The second eigenvector (Fig. 2(b)) is a saddle point, according to the classification of Perry and Chong (1987), centered at $x^* = 0$ and $y^* = 1$. In both eigenvectors, the velocity fluctuations in the upper half of the wake are uncorrelated with those in the lower half, consistent with the cross-correlations of data. The circulatory pattern reported by Giralt and Ferré (1993), with negative (inward) lateral velocity fluctuations at the top edge, is not observed in Fig. 2(a) and barely appears at the top of Fig. 2(b).

Figures 3(a) and 3(b) show the first and second eigenvectors obtained by POD in the horizontal plane. They account for 5 and 4 percent of the variance, respectively. In this case, the primary feature of the first eigenvector (Fig. 3(a)) are the negative u -fluctuations which are much larger than the positive, with a smeared vortex at $x^* = 0$ and $z^* = 0$. Figure 3(a) yields evidence for double roller eddies with negative u -fluctuations in the centerplane as suggested by the work of Giralt and Ferré (1993). However, this double roller structure is wider than the rake of probes so that the upper roller does not appear in the plot. This is consistent with the results of Payne and Lumley (1967) but with the difference that the centerplane of the double

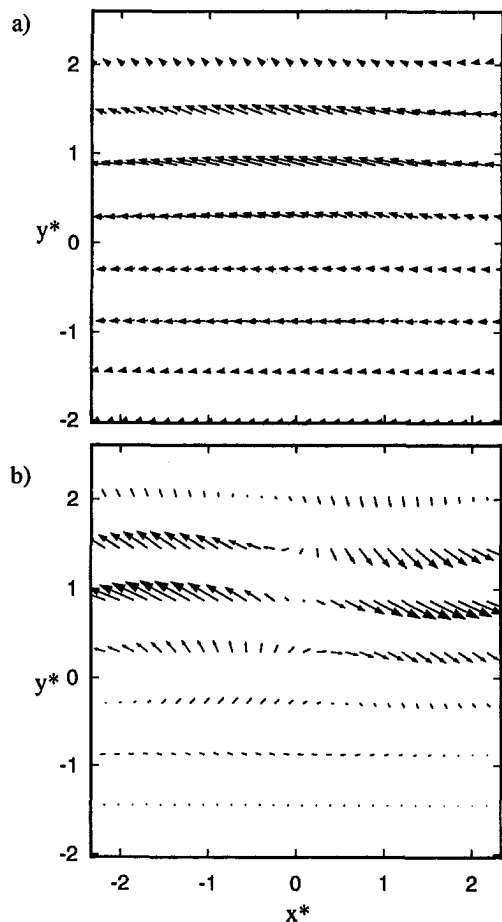


Fig. 2 The (a) first and (b) second eigenvectors in the vertical plane

roller has a deficit of momentum, rather than the excess they found. The second eigenvector in the horizontal plane (Fig. 3(b)) also shows the above features, but with the addition of a saddle point at $x^* = 0$ and $z^* = -0.8$. This saddle point is not aligned with the z -axis and is located upstream of the double roller. Vernet et al. (1997) also observed a saddle point, using temperature to conditionally classify instantaneous structures in the velocity field.

3.2 Ensemble-Averages From Pattern-Recognition.

The PR technique involves cross-correlating an initial template $a(x, y, z; t)$ with the velocity data $u(x, y, z; t + \Delta\tau)$ sampled from an experiment,

$$\gamma(\Delta\tau) = \frac{\overline{a(x, y, z; t) u(x, y, z; t + \Delta\tau)}}{a' u'} \quad (2)$$

In the present study the cross-correlation coefficient $\gamma(\Delta\tau)$ is calculated for time lags up to approximately $\Delta\tau = 30$ s.

The POD eigenvectors given in Figs. 2 and 3 have been used as initial templates for the PR analysis to eliminate possible bias introduced when the template is selected. Values of the cross-correlation coefficient, γ , larger than a threshold level identify the occurrence of individual events similar to the template. These instantaneous events can then be analyzed individually, as in Subsection 3.3, and/or ensemble-averaged to determine the prototypical structure of the instantaneous events classified. This conditional averaging procedure can be repeated until an ensemble-average equal to the penultimate ensemble-average used as template is obtained. The threshold is selected as the rms value of the cross-correlation, γ' . Further details can be found in Ferré and Giralt (1989). It should be noted that

the prototypical pattern or ensemble-average is the best projection of the group of instantaneous events classified, but not of the entire data set. Thus, this pattern does not account for the same fraction of variance as the eigenvectors from POD.

Figures 4(a) and 4(b) show the converged ensemble-averages of $\langle u \rangle / U_o + \langle v \rangle / U_o$ in the vertical plane obtained using the first and second eigenvectors given in Figs. 2(a) and 2(b) as templates. Convergence is usually attained with less than five iterations. More than one thousand instantaneous events, 1085 and 1118, contribute, respectively, to the ensemble-averages of Fig. 4. The threshold value for event selection is $\gamma' = 0.24$ for the converged template (or ensemble-average). The primary feature of both the ensemble-average in Fig. 4(a) and the first eigenvector in Fig. 2(a) is the outward v -fluctuations (i.e., positive lateral velocities), which are correlated with negative u -fluctuations. However, the ensemble-average (Fig. 4(a)) shows the additional feature of inward v -fluctuations at the upper edge of the wake, where the ejection of fluid depicted already by the first eigenvector is also accompanied by a circulatory motion. These inward motions are important with regard to the entrainment of the freestream fluid (Giralt and Ferré, 1993). This structure accounts for about 7 percent of the total variance and is also educed by the second eigenvector (Fig. 4(b)), but with its location shifted within the "data window." Figures 4(a) and 4(b) also show that there are correlated motions across the centerline of the wake with evidence of alternating modes. These modes are consistent with the conditional sampling results reported by Antonia et al. (1987). However, structures on one-side of the wake appear stronger than on the other because the corresponding instantaneous occurrence of events is not periodic.

The ensemble-averages given in Fig. 4 are similar to the pattern educed by Ferré et al. (1989) using a synthetic template of negative-to-positive u -fluctuations. (See also Fig. 2 of Giralt and Ferré, 1993, who analyzed a cylinder wake of Reynolds number 1600 with a single roller template.) Lateral alignment of the patterns was allowed in that work. Since the negative u -fluctuations are correlated with outward v -fluctuations, the slower streamwise motions in their template were sufficient to identify the instantaneous events contributing to the prototypical large-scale motions given in Fig. 4.

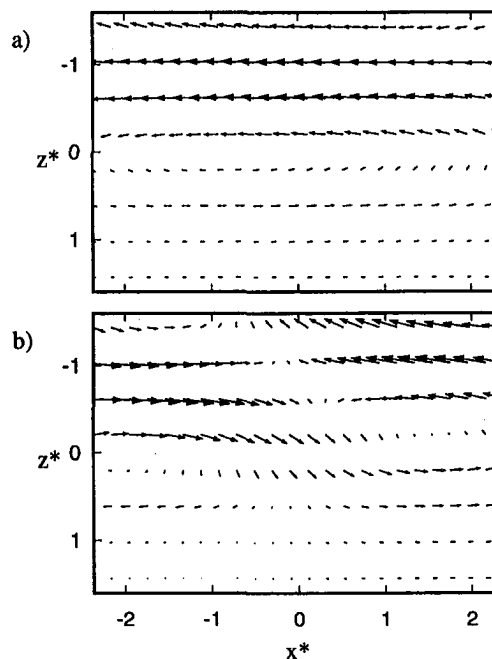


Fig. 3 The (a) first and (b) second eigenvectors in the horizontal plane

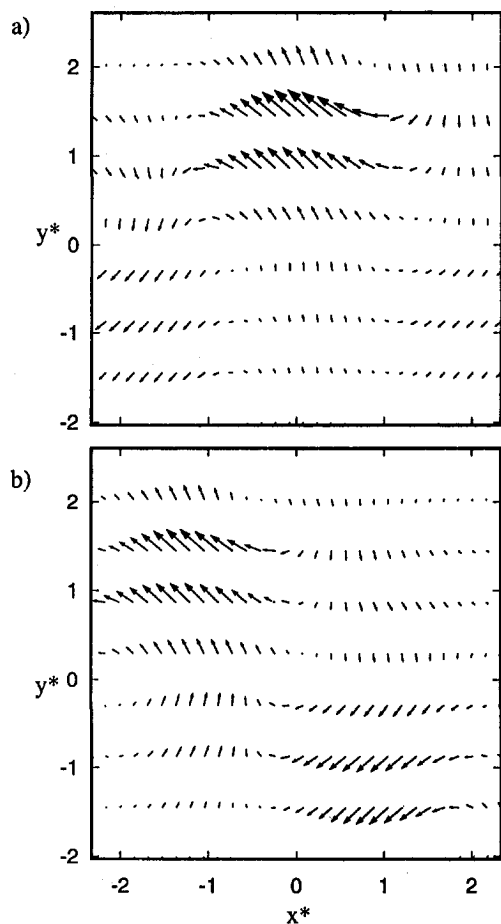


Fig. 4 The converged ensemble-average using the (a) first and (b) second eigenvectors as templates in the vertical plane

The results obtained in the horizontal plane using the first two eigenvectors (Fig. 3) as templates are presented in Figs. 5(a) and 5(b). Here, 1216 and 1613 instantaneous events contribute to the ensemble-averages of $\langle u \rangle / U_o + \langle w \rangle / U_o$. The pattern in Fig. 5(a), which accounts for 6 percent of the total variance, and the first eigenvector in Fig. 3(a) are dominated by strong negative u -fluctuations. Figure 5(a) also shows a vortex center at $x^* = -0.8, z^* = 0.2$, so that the pattern depicted has the appearance of a portion of a double roller structure. In addition, there is a saddle point at $x^* = -2$ and $z^* = -0.6$, consistent with the conditional sampling results of Vernet et al. (1997). The ensemble-average in Fig. 5(b), obtained by using the second eigenvector in Fig. 3(b) as initial template, is similar to that in Fig. 5(a) with two differences. First, there are two vortices visible, one at $x^* = 1$ and $z^* = 0$ and the other, of opposite rotation, at $x^* = -1.3$ and $z^* = 0$. Second, the u -fluctuations on either side of the saddle point are nearly equal, but with maximum values much smaller than in Fig. 5(a).

The double roller pattern found by Ferré et al. (1989) is slightly different than those obtained here (Fig. 5). These authors allowed spanwise alignment of the ensemble-average with a synthetic double roller template which was wider than the rake of probes. As a result, the ensemble-average double roller structure reported had a smeared saddle point.

Present results indicate that the template dependence of the results is weak in the vertical plane (Fig. 4). Differences are observed mainly in the location of the coherent structure within the data window and in the peak values of the ensemble-averaged velocity fluctuations. In the horizontal plane there is more template dependency as can be seen by a visual comparison of the ensemble-averages given in Figs. 5(a) and 5(b), although

the two are not inconsistent with each other. The difference is not particularly surprising because the flow in the homogeneous coordinate is not constrained like it is for the non-homogeneous coordinate. Thus, a wider range of variations in the large-eddies is expected. Nevertheless, the two figures contain the same basic structure, namely, positive u -fluctuations upstream of the centerplane of the double roller structure with negative u -fluctuations in the centerplane. There appears to be a saddle point between the positive and negative u -fluctuations. There is the additional feature of a second roller in Fig. 5(b), which may be evidence as to how the structures are grouped in the flow while advected downstream.

Finally, it is convenient to determine the characteristics and quantity of instantaneous events present in the data set that are similar to the first eigenvector. This is equivalent to determining the prototypical structure of the class of events selected during the first iteration of the pattern-recognition procedure described above, using the first eigenvector (Fig. 2(a)) as the detection criteria. Figure 6 depicts the prototype that is obtained when these conditional sampling and averaging operations are applied to the vertical plane. In this case there are 557 instantaneous events correlated with the first eigenvector. It is clearly observed that this class of events has the inward v -fluctuations like the ensemble-average of Fig. 4(a). Thus, it can be concluded that the outward motions from the core of the wake, which are similar to the first eigenvector, are generally accompanied by inward motions as well.

It is interesting to note that this ensemble-average is more similar to a linear combination of the first and second eigenvectors, with each given equal weight, than to the first alone. In fact, the correlation coefficient between the ensemble-average in Fig. 6 and this linear combination is 0.93, while that with the first eigenvector (Fig. 2(a)) is 0.81. Kevlahan et al. (1994) have already shown that POD may require more than one eigenvector to identify a given function or pattern embedded in a signal.

Figure 7 depicts the results obtained from conditional sampling the data set in the horizontal plane with the first eigenvector (Fig. 3(a)) as the detection criteria. The 777 events that contribute to this ensemble-average have, as underlying features, an incomplete double roller configuration with a saddle

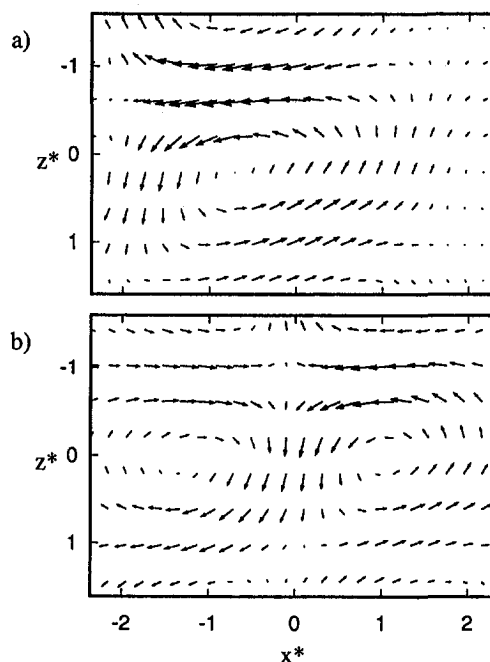


Fig. 5 The converged ensemble-average using the (a) first and (b) second eigenvectors as templates in the horizontal plane

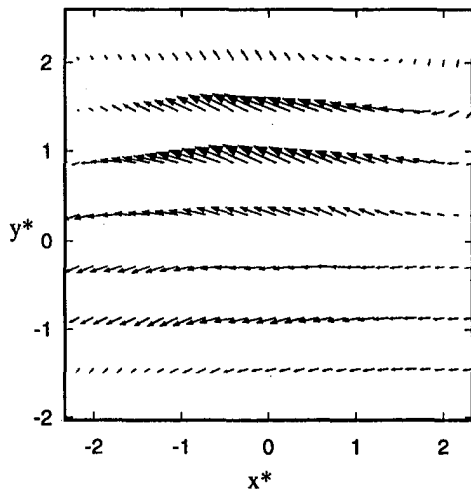


Fig. 6 The conditionally sampled ensemble-average using the first eigenvector (Fig. 2(a)) in the vertical plane as the detection criteria

point separating negative and positive u -fluctuations. In this case the conditionally sampled ensemble-average (Fig. 7) is also more similar to a linear combination of the first and second eigenvectors ($\gamma = 0.94$), with each given equal weight, than to the first alone ($\gamma = 0.68$). The fact that the saddle point is identified when searching for events highly correlated with the first eigenvector adds strength to the assertion that this is due to real features of the individual events contributing to the prototypical structure.

Some questions still remain. Does the circulatory pattern observed in the vertical plane results (Fig. 4) always occurs instantaneously when there are outward ejections of fluid from the wake center? In other words, is the underlying large-scale structure a double roller or a horseshoe-type vortex? In the group of events classified in the horizontal plane (Fig. 5), is there always a saddle point upstream of the centerplane of a double roller structure? These questions can be addressed by an analysis of the individual events classified by PR.

3.3 Analysis of the Individual Events. Clearly, there are similar features in the large-scale structures identified with POD and PR. However, it is not clear if the additional features that are observed in the PR ensemble-averages exist in each of the individual events selected or are an artifact of the averaging procedure since the thresholds used are relatively low. The use of these low thresholds has been one of the concerns expressed about PR in the literature (see Berkooz et al., 1993). In the present work the threshold is low ($\gamma' = 0.24$) in both planes due to the following factors: (i) In fully-developed free turbulence the structures are embedded in a highly random field and,

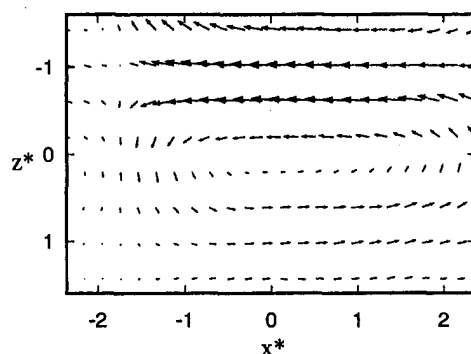


Fig. 7 The conditionally sampled ensemble-average using the first eigenvector (Figs. 3(a)) in the horizontal plane as the detection criteria

thus, they contain only a small fraction of the variance; (ii) the final ensemble-averaged structures in the vertical and horizontal planes (Figs. 4 and 5) are smaller than the data window so that correlations include velocity fluctuations that are uncorrelated with the structure; (iii) structures pertaining to the same class and contributing to the same ensemble average are present in the flow over a range of sizes, intensities, and orientations relative to the rake of probes.

To investigate the effect of the size of the data window on the correlations between the instantaneous events selected and the ensemble-averages, the previous analysis was repeated with a smaller data window. For the prototypical structure depicted in Fig. 4(a) from the vertical plane, a data window including the four X-probes for $y^* > 0$ and with a "streamwise" extent of $\Delta x^* \approx 3.5$ (or 6.3 ms) was selected. This portion of the ensemble-average was correlated with the individual events that contributed to the ensemble average in Fig. 4(a). The results are presented in Table 1, which shows how many events occur within prescribed correlation ranges. It is found that the average correlation is 0.538 while the largest number of events occur with a correlation between 0.6 and 0.7. In addition, 78 percent of the events have a correlation greater than 0.4. There are eight events which are obviously misclassified because they are negatively correlated.

Figure 8 shows five of the individual events, with different correlation coefficients, that were used to obtain the ensemble-average in the vertical plane given by Fig. 4(a). The events chosen are the first events occurring in the data set with a correlation coefficient within one of the ranges considered in Table 1. In this particular case the sequence of selected events is (a) 0.7–0.8, (b) 0.4–0.5, (c) 0.6–0.7, (d) 0.2–0.3, and (e) 0.3–0.4. Four of the five (Figs. 8(a, b, c, and e)) exhibit features similar to the ensemble-average, i.e., outward lateral velocity fluctuations correlated with negative streamwise velocity fluctuations in combination with a circulation pattern in the upper half of the wake. These events are also of the same length scale as the ensemble-average. The level of randomness in these figures is high. The instantaneous event depicted in Fig. 8(d), which has a low correlation with the prototypical pattern, seems to be misclassified although it too has some outward lateral motions with mostly negative streamwise velocity fluctuations. In this figure, the circulatory pattern is extremely weak. If it is assumed that all of the events with a correlation coefficient less than 0.3 are misclassified, then about 11 percent of the 1085 events contributing to Fig. 4(a) could be misclassified.

The smaller window used in the horizontal plane analysis has the same size as that for the vertical plane. The four X-probes chosen are those for $z^* < 0$ where the dominant negative u -fluctuations of the ensemble-average of Fig. 5(a) are located. These motions are an important feature of the coherent motions in both planes (see also Vernet et al., 1997). In this plane the

Table 1 The number of events within each correlation range using a smaller data window

Correlation range	Number of events vertical plane	Number of events horizontal plane
0.9 to 1.0	0	0
0.8 to 0.9	44	21
0.7 to 0.8	178	125
0.6 to 0.7	261	235
0.5 to 0.6	191	286
0.4 to 0.5	177	219
0.3 to 0.4	110	164
0.2 to 0.3	64	108
0.1 to 0.2	35	43
0.0 to 0.1	17	13
-0.1 to 0.0	5	1
-0.2 to -0.1	1	1
-0.3 to -0.2	2	0

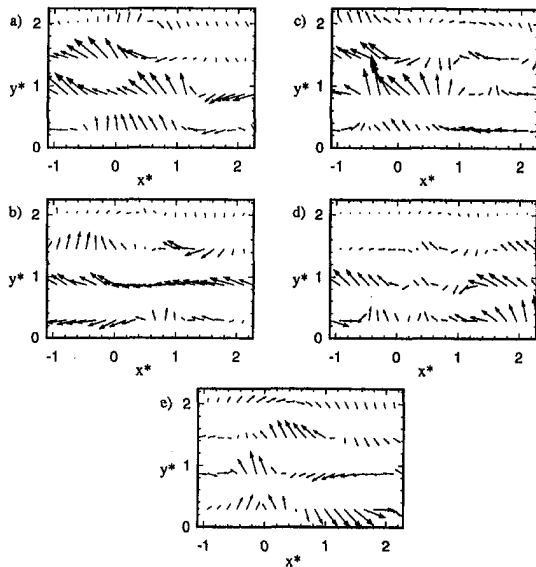


Fig. 8 The (a) second, (b) fifth, (c) ninth, (d) tenth, and (e) eleventh individual events identified with the PR technique in the vertical plane

average correlation between the smaller portion of the ensemble-average in Fig. 5(a) and the classified instantaneous events is 0.505. Table 1 shows that the correlations in the horizontal plane are lower than in the vertical plane. This is not surprising because the present horizontal plane is a homogeneous plane in the fully turbulent core of the wake. In contrast, the data windows used in the vertical plane span from the turbulent core into the intermittent region where the structures contain a larger fraction of the turbulence energy, as discussed in Section 4.

Figure 9 shows five of the individual events, with different correlation coefficients, that were used to obtain the ensemble-average in the horizontal plane given by Fig. 5(a). In this particular case the sequence of selected events is (a) 0.3–0.4, (b) 0.6–0.7, (c) 0.4–0.5, (d) 0.7–0.8, and (e) 0.2–0.3. All five events (Figs. 9(a–e)) have the characteristic negative u -fluctuations. The level of randomness is obviously high, especially upstream of the negative u -fluctuations where there is not clear evidence for saddle points. Figure 9(e), which has a low correlation with the prototypical pattern, seems to be misclassified although it too has negative u -fluctuations. In this case, it appears that the double roller structure (if it is a double roller) is twisted with regard to the z^* -axis. If it is assumed that all of

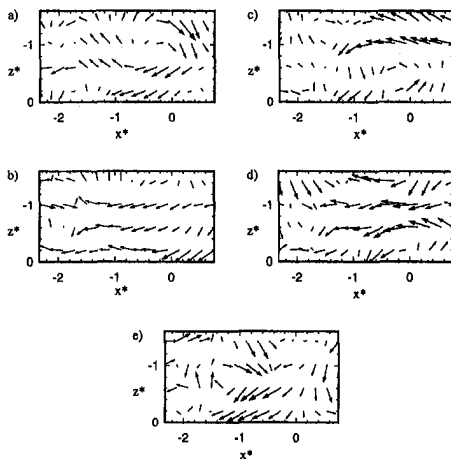


Fig. 9 The (a) first, (b) second, (c) third, (d) fourth, and (e) fourteenth individual events identified with the PR technique in the horizontal plane

the events with a correlation coefficient of less than 0.3, in this smaller data window, are misclassified then in the horizontal plane 14 percent of the 1216 events could be misclassified.

In order to further assess the probability of misclassifying events, we examined visually the first 100 events selected in the horizontal plane. For this analysis we used the full sized data windows used to obtain Fig. 5(a). We found that all of the first 100 events contained the negative u -fluctuations at roughly the correct location. However, 23 percent of these had no evidence of the vortex center or saddle point depicted in Fig. 5(a). In fact, only 42 percent of the events contained both of these features. Thus, it may be concluded that to identify vortex centers and saddle points other techniques (e.g., Perry and Chong, 1987; Jeong and Hussain, 1995; Ferre-Gine et al., 1996) may be required because critical points tend to be of a much smaller scale than the entire prototypical structure. It may be possible to identify these critical points with PR if very small templates in conjunction with high thresholds are used.

Finally, it is necessary to ascertain whether the threshold level plays any significant role in the type of structure educed and represented by the ensemble average. In other words, it is imperative to determine whether the class of events selected with a low threshold level is really a single class of instantaneous events, irrespective of the threshold chosen. A simple unambiguous way to investigate the role of the threshold level is to determine the ensemble average of the class events using a subset with a much higher threshold level. Figures 10(a) and 10(b) show the ensemble averages obtained in the vertical and horizontal planes with the events (483 and 381, respectively) pertaining to correlations higher than 0.6 in Table 1. It is clear from a visual comparison of these averages with those in Figs. 4(a) and 5(a), obtained using all events listed in Table 1 (1085 and 1216, respectively), that the effect of the threshold on the ensemble-average is minimal. In fact, the correlations between the patterns in Figs. 4(a) and 10(a), and between Figs. 5(a) and 10(b) are 0.97 and 0.95, respectively. Repeating the analy-

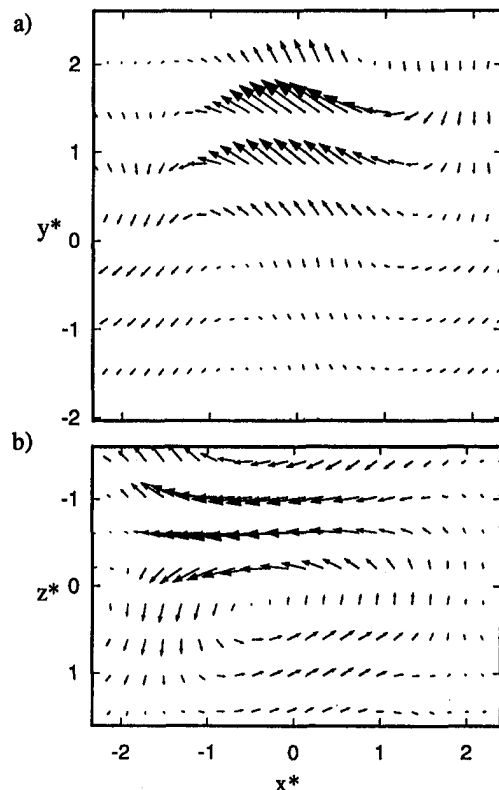


Fig. 10 The ensemble-average using the smaller data windows and a threshold of 0.6 in the (a) vertical and (b) horizontal planes

sis with the events which have correlations higher than 0.8 in Table 1 (44 and 21, in the vertical and horizontal planes respectively), it is found that the correlations between these ensemble-averaged patterns (not shown) and those in Figs. 4(a) and 5(a) are 0.96 and 0.91, respectively. Therefore, it is concluded that the two ensemble averages (Figs. 4(a) and 5(a)) obtained with PR are the prototypes of the two classes of highly coherent instantaneous events selected from the flow using the correlation, $\gamma(\Delta\tau)$. This is the reason why these ensemble averages are called "coherent" structures.

4 Turbulence Kinetic Energy

As described in Section 3, the dominant POD eigenvectors (Figs. 2(a) and 3(a)) and the PR ensemble-averages (Figs. 4 and 5) both account for a relatively small fraction of the variance. Figures 11(a, b) show how the contribution to the variance, $\langle u^2 \rangle + \langle v^2 \rangle$ and $\langle u^2 \rangle + \langle w^2 \rangle$, is distributed spatially in the vertical and horizontal planes. Figure 11(a) accounts for about 7 percent of the variance and Fig. 11(b) about 6 percent. These figures show that the majority of the variance captured by the coherent ensemble-averaged motions is due to the negative u -fluctuations and the outward v -fluctuations in the vertical plane and the negative u -fluctuations in the horizontal plane. However, the energy of these underlying motions is small, even though the group of classified instantaneous events occupies 38.5 and 35.8 percent of the flow in the vertical and horizontal planes, respectively.

The ensemble-average of the variance of the group of events, $\langle u^2 \rangle + \langle v^2 \rangle$ and $\langle u^2 \rangle + \langle w^2 \rangle$ in the vertical and horizontal planes, respectively, is calculated with the results depicted in Figs. 12(a) and 12(b). Figure 11(a), which uses the group of events selected to obtain Fig. 4(a), accounts for 44 percent of the total variance. The isocontours are similar to those for the coherent motions (Fig. 11(a)), but here the levels are significantly higher, especially in the fully turbulent core of the wake (approximately $-1 < y^* < 1$) where they are about one order of magnitude larger. This implies that there is a wide variation of the individual classified events, especially in the core of the wake. At the outer edge ($y^* > 1$), the difference

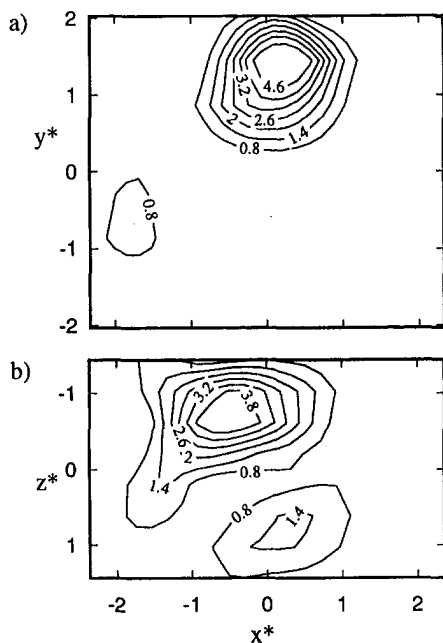


Fig. 11 The contours of (a) $\langle (u^2) + \langle v^2 \rangle / U_0^2$ from the ensemble-average of Fig. 4(a) in the vertical plane and (b) $\langle (u^2) + \langle w^2 \rangle / U_0^2$ from the ensemble-average of Fig. 5(a) in the horizontal plane. The contours have been multiplied by 10^4 .

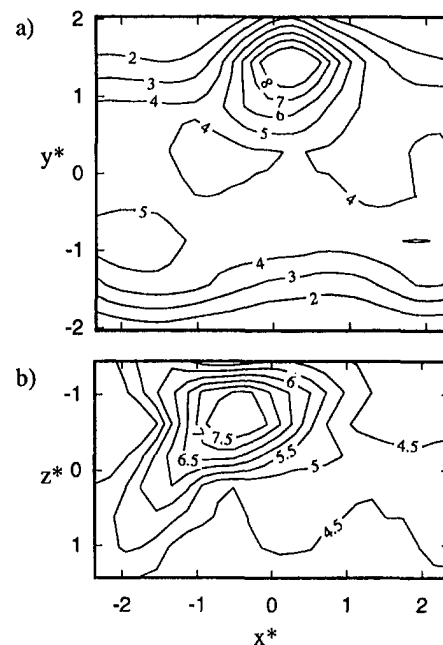


Fig. 12 The contours of (a) $\langle (u^2) + \langle v^2 \rangle / U_0^2$ from the events selected for Fig. 4(a) in the vertical plane and (b) $\langle (u^2) + \langle w^2 \rangle / U_0^2$ from the events selected for Fig. 5(a) in the horizontal plane. The contours have been multiplied by 10^4 .

between the isocontour levels in the two plots (Figs. 11(a) and 12(a)) is smaller so there must be less variation in the events selected in this region of the flow. The largest contributions to the variance are in the outer intermittent region. For example, at $y^* = 2.0$ the events educed account for 69 percent of the total variance for this location. The fraction decreases toward the fully turbulent core so that near the centerline the ensemble-average (Fig. 12(a)) contributes an amount equal to the quantity of flow averaged (38.5 percent).

Figure 12(b) shows $\langle u^2 \rangle + \langle w^2 \rangle$ obtained from the group of events selected for Fig. 5(a). It is observed that the isocontours of the variance for both the coherent motions (Fig. 11(b)) and the group of events used to obtain the coherent motions (Fig. 12(b)) are largest when the u -fluctuations are negative, consistent with the results in the vertical plane.

5 Conclusions

The eigenvectors obtained from the POD analysis of the velocity fluctuation vectors in the vertical and horizontal planes of a fully-developed turbulent wake were used as initial templates for a PR analysis. This provides an unbiased starting point for the identification of the group of events yielding the prototypical large-scale structure found in the far wake. An examination of the results shows that the dominant eigenvectors extract the most significant features of the large-scale motions in both planes. In the nonhomogeneous (vertical) plane the structure is characterized by negative u - and outward v -fluctuations while in the homogeneous (horizontal) plane a double roller structure is identified.

The eigenvectors by themselves do not reveal all the features educed by the PR analysis, however. PR reveals that the individual events connected with the outward "ejections" of fluid in the vertical plane have circulatory motions associated with them. This implies that the three-dimensional double roller structure identified by Payne and Lumley (1967) should have a circulation pattern with spanwise vorticity at the top so that the true three-dimensional structure is that of a horseshoe or Λ vortex. This double roller/horseshoe structure has negative u -fluctuations in its centerplane. The events associated with these

motions contribute significantly to the turbulence kinetic energy at the outer intermittent edges of the wake, but not in the fully turbulent core. Neither technique appears to be adequate to identify critical points in fully-developed turbulence, however.

Acknowledgments

We would like to thank Prof. R. A. Antonia for providing his experimental data. This work was financially supported by the DGICYT project PB91-0551 and NATO Grant CRG 960142, and used analytical tools developed during the DGICYT project PB93-0656-C02-01. Computer support was granted by Servei de Tecnologia Química of the Universitat Rovira i Virgili. G. A. Kopp was financially supported by NSERC Canada and the Universitat Rovira i Virgili.

References

- Adrian, R. J., and Moin, P., 1988, "Stochastic Estimation of Organized Turbulent Structure: Homogeneous Shear Flow," *Journal of Fluid Mechanics*, Vol. 190, pp. 531–559.
- Antonia, R. A., 1981, "Conditional Sampling in Turbulence Measurement," *Annual Review Fluid Mechanics*, Vol. 13, pp. 131–156.
- Antonia, R. A., Browne, L. W. B., Bisset, D. K., and Fulachier, L., 1987, "A Description of the Organized Motion in the Turbulent Far Wake of a Cylinder at Low Reynolds Number," *Journal of Fluid Mechanics*, Vol. 184, pp. 423–444.
- Berkooz, G., Holmes, P., and Lumley, J. L., 1993, "The Proper Orthogonal Decomposition in the Analysis of Turbulent Flows," *Annual Review Fluid Mechanics*, Vol. 25, pp. 539–575.
- Blackwelder, R., and Kaplan, R., 1976, "On the Wall Structure of the Turbulent Boundary Layer," *Journal of Fluid Mechanics*, Vol. 76, pp. 89–112.
- Browne, L. W. B., and Antonia, R. A., 1986, "Reynolds Shear Stress and Heat Flux Measurements in a Cylinder Wake," *Physics Fluids*, Vol. 29, pp. 709–713.
- Chatfield, C., and Collins, A. J., 1980, *Introduction to Multivariate Analysis*, Chapman and Hall, London, pp. 57–81.
- Delville, J., 1993, "Characterization of the Organization in Shear Layers Via Proper Orthogonal Decomposition," *Eddy Structure Identification in Free Turbulent Shear Flows*, Bonnet and Glauser, ed., Kluwer, Poitiers, pp. 225–237.
- Ferré, J. A., and Giralt, F., 1989, "Pattern-Recognition Analysis of the Velocity Field in Plane Turbulent Wakes," *Journal of Fluid Mechanics*, Vol. 198, pp. 27–64.
- Ferré, J. A., and Giralt, F. and Antonia, R. A., 1989, "Evidence for Double-Roller Eddies in a Turbulent Wake From Two-Component Velocity Measurements," *Proceedings 7th Symposium Turbulent Shear Flows*, pp. 24.2.1–5.
- Ferre-Gine, J., Rallo, R., Arenas, A., and Giralt, F., 1996, "Identification of Coherent Structures in Turbulent Shear Flows With a Fuzzy Artmap Neural Network," *International Journal of Neural Systems*, Vol. 7, No. 5, pp. 559–568.
- Giralt, F., and Ferre, J. A., 1993, "Structure and Flow Patterns in Turbulent Wakes," *Physics Fluids A*, Vol. 5, pp. 1783–1789.
- Grant, H. L., 1958, "The Large Eddies of Turbulent Motion," *Journal of Fluid Mechanics*, Vol. 4, pp. 149–190.
- Hall, E. L., 1979, *Computer Image Processing and Recognition*, Academic Press, New York.
- Hunt, J. C. R., Wray, A. A., and Moin, P., 1988, "Eddies, Streams, and Convergence Zones in Turbulent Flows," *Proceedings Summer Program Center Turbulence Research*, pp. 193–208.
- Hussain, A. K. M. F., 1986, "Coherent Structures and Turbulence," *Journal of Fluid Mechanics*, Vol. 173, pp. 303–356.
- Jeong, J., and Hussain, F., 1995, "On the Identification of a Vortex," *Journal of Fluid Mechanics*, Vol. 285, pp. 69–94.
- Kevlahan, N. K. -R., Hunt, J. C. R., and Vassilicos, J. C., 1994, "A Comparison of Different Analytical Techniques for Identifying Structures in Turbulence," *Applied Scientific Research*, Vol. 53, pp. 339–355.
- Kiya, M., and Matsumura, M., 1988, "Incoherent Turbulent Structure in the Near Wake of a Normal Plate," *Journal of Fluid Mechanics*, Vol. 190, pp. 343–356.
- Lumley, J. L., 1965, "The Structure of Inhomogeneous Turbulent Flows," *Proceedings International Colloquium on Atmospheric Turbulence and Radio Wave Propagation*, Moscow, pp. 166–176.
- Mumford, J. C., 1982, "The structure of the Large Eddies in Fully Developed Turbulent Shear Flow. Part 1. The Plane Jet," *Journal of Fluid Mechanics*, Vol. 118, pp. 241–268.
- Mumford, J. C., 1983, "The Structure of the Large Eddies in Fully Developed Turbulent Shear Flow. Part 2. The Plane Wake," *Journal of Fluid Mechanics*, Vol. 137, pp. 447–456.
- Payne, F. R., and Lumley, J. L., 1967, "Large Eddy Structure of the Turbulent Wake Behind a Circular Cylinder," *Physics Fluids*, Vol. 10, pp. S194–S196.
- Pratt, W. K., 1978, *Digital Image Processing*, Wiley, New York.
- Perry, A. E., and Chong, M. S., 1987, "A Description of Eddy Motions and Flow Patterns Using Critical-Point Concepts," *Annual Review Fluid Mechanics*, Vol. 19, pp. 125–155.
- Subramanian, C. S., Rajagopalan, S., Antonia, R. A., and Chambers, A. J., 1982, "Comparison of Conditional Sampling and Averaging Techniques in a Turbulent Boundary Layer," *Journal of Fluid Mechanics*, Vol. 123, pp. 335–362.
- Townsend, A. A., 1979, "Flow Patterns of Large-Eddies in a Wake and in a Boundary Layer," *Journal of Fluid Mechanics*, Vol. 95, pp. 515–537.
- Toyoda, K., and Shirahama, Y., 1994, "Eduction of Vortical Structures by Pressure Measurements in Noncircular Jets," *Applied Scientific Research*, Vol. 53, pp. 237–248.
- Vernet, A., Kopp, G. A., Ferré, J. A. and Giralt, F., 1997, "Simultaneous Velocity and Temperature Patterns in the Far Region of a Turbulent Cylinder Wake," *ASME JOURNAL OF FLUIDS ENGINEERING*, Vol. 119, published in this issue pp. 463–466.
- Willmarth, W. and Lu, S., 1972, "Structure of the Reynolds Stresses Near the Wall," *Journal of Fluid Mechanics*, Vol. 55, pp. 65–92.

Aero-Thermodynamic Loss Analysis in Cases of Normal Shock Wave-Turbulent Shear Layer Interaction

J. K. Kaldellis

Laboratory of Soft Energy Applications,
Department of Mechanical Engineering,
Technological Education Institute of
Piraeus, Pontou 58, Hellenico,
Athens, Greece 16777

Transonic-supersonic decelerating flow cases appearing in modern turbomachines are some of the most complex flow cases in fluid mechanics which also present practical interest. In the present work, a closed and coherent shock loss model is proposed based on the complete viscous flow simulation using some fast and reliable computational tools. The resulting model describes accurately the entropy rise and the total pressure loss in cases of strong shock-shear layer interaction and cancels the need to use low speed correlations modified for compressibility effects and extrapolated to transonic-supersonic flow cases. The accuracy and the reliability of the proposed shock-loss model are verified using detailed experimental data concerning various flow cases which present either flow separation or industrial interest.

1 Introduction

The development of high speed axial fans and compressors operating with supersonic relative inlet Mach numbers requires the knowledge of the performance of the machine and the flow behavior particular for transonic-supersonic operating conditions. As mentioned in previous work (Kaldellis, 1993, Kaldellis et al., 1991) the losses of transonic and supersonic flow cases are mainly either due to the entropy rise occurring through shock waves (direct shock loss) or due to viscous effects characterizing the strong flow deceleration imposed by the shock waves (indirect shock loss). For high speed compressor blading, direct and indirect shock losses constitute a major part of the overall loss (up to 70 percent) depending on inlet Mach number, inlet flow angle, and back pressure value.

The research work done up till now in the area of shock loss has followed three directions. The first one is based on empirical correlations which give satisfactory overall results, but give no details concerning the evolution of the shock losses throughout the configuration investigated (see for example Koch and Smith, 1976, Cetin et al., 1989). The second direction involves quite accurate but expensive 3-D numerical codes (Dawes, 1988, Hah and Wennerstrom, 1990) which give an enormous volume and variety of information at a significant computational cost. Since these codes are strongly influenced by turbulence modeling problems and numerical-mesh refinement shortcomings they do not present their best performance in the case of shock-shear flow interaction. Finally, the third research direction utilizes several experimental results concerning the impact of the shock waves on the complete flow pattern (Tweedt et al., 1988, Schreiber, 1986, Schofield, 1985). However, the influence of each one of the dominant flow parameters is analyzed separately, thus the resulting conclusions are strictly limited only to similar flow configurations. All the above-mentioned research directions recognize the importance of the shock induced losses and their major role in the performance of modern high speed turbomachines.

In the present work, a closed and coherent shock loss model is proposed, based on a complete viscous flow simulation using

the experience gained from the application of several advanced computational tools (Kaldellis et al., 1990; Kaldellis et al., 1991; Kaldellis, 1993) developed recently. The resulting model describes accurately the total pressure drop and the corresponding entropy rise in cases of strong shock-shear layer interaction. In this way the streamwise and spanwise distribution of the direct and indirect shock-induced losses is predicted, giving us the ability to minimize the total loss in transonic-supersonic flow cases.

For this purpose, two well-documented experimental test cases, with incoming Mach number greater than 1.40 and in presence of flow separation, are first investigated. In order to separate the shock induced losses and the pressure driven viscous losses, calculations are also made in a reference shear layer developing without interacting with the normal shock wave. Finally, the spanwise shock loss evolution throughout the supersonic rotor of a high pressure compressor stage is analyzed. Interesting conclusions drawn from the above mentioned applications are summarized in the last part of the present work.

2 Governing Equations

I. 2-D Case. For the description of the two-dimensional steady flow field of a viscous and compressible fluid the appropriate method developed by Kaldellis (1993) is applied. This method uses the complete form of the compressible integral momentum equation in the marching direction and the corresponding integral total kinetic energy equation (time averaged + turbulent kinetic energy) to calculate the basic parameters of the shock influenced boundary layer. An analytical law is also necessary to estimate the velocity distribution inside the boundary layer.

Additionally the momentum equation in the normal (to the marching) direction is used (instead of Prandtl's thin boundary layer approximation) for the calculation of the distribution of the static pressure across the shear layer. The static pressure difference, commonly neglected in previous analyses, is related to the normal to the wall Reynolds stresses and the longitudinal curvature of the external flow streamlines and takes important values especially inside the shock-shear layer interaction region. Finally, the turbulence model presented by Katramatos and Kaldellis (1991) and extended by Kaldellis (1993) for compressible flows is used to close the calculation procedure.

Contributed by the Fluids Engineering Division for publication in the JOURNAL OF FLUIDS ENGINEERING. Manuscript received by the Fluids Engineering Division February 18, 1995; revised manuscript received January 21, 1997. Associate Technical Editor: M. M. Sindir.

II 3-D Case. For the calculation of the steady, viscous and compressible flow field through a 3-D axial compressor configuration the method by Kaldellis et al. (1991), based on the circumferentially averaged form of the mass, momentum, and energy conservation equations as well as of the vorticity transport equation, is used.

More precisely, the integral form of the momentum equations in the meridional and in the peripheral direction is used in combination with the integral total kinetic energy equation to estimate the characteristics of the 3-D boundary layer. Accordingly, the transport of vorticity equation in the marching direction (written in differential form) is used to calculate the peripheral velocity component distribution across the boundary layer, while the static pressure profile is predicted by the momentum equation in the normal direction. Finally, the energy conservation equation is utilized to estimate the total enthalpy (temperature) profiles inside the boundary layer. Details concerning the development and the application of the method in several industrial configurations (high speed compressors and turbines) are given also by Kaldellis et al. (1990) and Kaldellis (1994).

III Shock-Shear Flow Interaction. An extended small disturbance theory is used for the calculation of the modified external flow field throughout the shock-shear layer or the shock-secondary flow interaction region, see also Kaldellis (1993). The theory is based on similar approximations to that of Inger and Mason (1976) and is supposed valid for Mach numbers less than 1.5. The theoretical analysis is based on Euler's equations, while details are given by Kaldellis et al. (1990) and Kaldellis (1994). It is important to mention that the real static pressure jump across the shock wave is needed as a boundary condition of the method. In order to obtain this value, a modified Rankine-Hugoniot condition is applied. The condition takes into account the area variation across the shock wave, resulting from the presence of the shear layers. The real static pressure jump " δp_r " can be expressed, in relation to the theoretical one " δp_{in} " given by the Rankine-Hugoniot condition, as a function of the displacement thickness of the two boundary layers (δ_{1w} , $\delta_{1w'}$) of the channel and the Mach number " M_{oy} " at the end of the shock-boundary layer interaction region, using the following equation (Kaldellis, 1993):

$$\frac{\delta p_r}{\delta p_{in}} = 1 - \gamma \cdot \frac{p_{ox}}{p_{oy}} \cdot \left[\frac{\frac{(\delta_{1w} + \delta_{1w'})}{H} \cdot M_{oy}^2}{1 - \left[1 + \frac{(\delta_{1w} + \delta_{1w'})}{H} \cdot M_{oy}^2 \right]} \right] \quad (1)$$

Using the proposed real static pressure value as a boundary condition, a good approximation of the pressure distribution, under which the shear layers are developing, is predicted.

3 Shock Loss Model

For the calculation of the shock induced losses one has to keep in mind that besides the entropy rise related with the

existence of the shock wave additional entropy rise takes place due to the strong flow deceleration and the possible flow separation imposed by the shock-shear flow interaction. Comparing now the shock induced entropy rise, using the inviscid flow approximation, with the real flow entropy rise, the last one is usually lower, excluding cases of fully separated shear flows. According to Calvert (1982), the shock wave-shear flow interaction has a beneficial side effect in appreciably reducing the loss of total pressure due to the shock, in comparison with any inviscid model.

The mean shock loss coefficient " ω_{SH} " is defined using the following equation:

$$\omega_{SH} = \frac{\bar{p}_{t2is} - \bar{p}_{t2}}{1/2 \cdot \rho_{\infty} \cdot u_{\infty}^2} \quad (2)$$

where the overbar indicates a mass-averaged value, i.e.,

$$\bar{p}_t = \frac{1}{\dot{m}} \cdot \int_0^{n_c} \rho \cdot u \cdot p_t \cdot dn \quad (3)$$

For the calculation of the isentropic total pressure value, see Fig. 1, Eq. (4) is valid, i.e.:

$$p_{t2is} = p_{t1} \cdot \left(1 + \frac{\Delta T_t}{T_{t1}} \right)^{(\gamma/(\gamma-1))} \quad (4)$$

where " ΔT_t " is the total temperature (enthalpy) increase in the case of a rotor blade row, and it is directly related with the energy exchange inside the rotor blade. For stationary configurations:

$$p_{t2is} = p_{t1} \quad (5)$$

and Eq. (4) is reduced to the well-known total pressure drop coefficient, see Katramatos and Kaldellis (1991), Koch and Smith (1976), etc. The corresponding real total pressure value can be computed using the isentropic relations, thus:

$$p_t = p \cdot \left[1 + (\gamma - 1) \cdot \frac{M^2}{2} \right]^{(\gamma/(\gamma-1))} \quad (6)$$

In order to separate the direct (produced by the entropy increase due to the shock) " ω_{sh} " and indirect (produced by the deceleration of the boundary layer) " ω_v " shock losses one may write that:

$$\omega_{SH} = \omega_{sh} + \omega_v \quad (7)$$

where:

$$\omega_{sh} = \frac{\bar{p}_{t2is} - \bar{p}_{t2e}}{1/2 \cdot \rho_{\infty} \cdot u_{\infty}^2} \quad (8)$$

Nomenclature

C_f = skin friction coefficient
 H = passage height
 i° = incidence angle
 M = Mach number
 \dot{m} = mass flow rate
 m = meridional distance
 n = normal distance
 p = static pressure
 p_t = total pressure
 u = velocity
 R_g = gas constant
 s = entropy

T_t = total temperature
 γ = ratio of specific heats
 δ = shear layer thickness
 δ_1 ,
 δ_2 = displacement, momentum thickness of the shear layer
 ρ = density
 ω = loss coefficient

Subscripts

e = external flow quantities
 H, T = value at hub and tip respectively

o = undisturbed external flow quantity in the shock-shear layer interaction region
 w, w' = value at the walls
 x, y = indicate the start and the end of the shock-shear layer interaction region
 ∞ = reference quantity

Superscripts

(\wedge) = initial external flow field

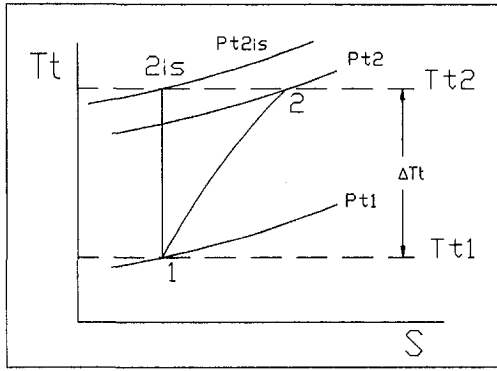


Fig. 1 T-s diagram for the definition of the shock loss coefficient

and

$$\omega_v = \frac{\bar{p}_{t_{2e}} - \bar{p}_{t_2}}{1/2 \cdot \rho_\infty \cdot u_\infty^2} \quad (9)$$

The external total pressure value " $P_{te}(n)$ " is given by Eq. (6) and can be predicted as soon as the external Mach and the static pressure distributions across the shear layer are predicted by the shock-shear flow interaction algorithm. Accordingly, the real flow total pressure value " $P_{t2}(n)$ " can also be predicted by the same equation, or equivalently as:

$$p_{t_2} = (p_{e_2} - \delta p) \cdot \left[1 + (\gamma - 1) \cdot \frac{M_{e_2}^2}{2} \cdot \left(\frac{M_2}{M_{e_2}} \right)^2 \right]^{(\gamma/(\gamma-1))}$$

$$p_{t_2} = (p_{e_2} - \delta p) \cdot \left[1 + (\gamma - 1) \frac{M_{e_2}^2}{2} \cdot \left(\frac{M_2}{M_{e_2}} \right)^2 \right]^{(\gamma/(\gamma-1))} \quad (10)$$

where the " $\delta p = p_{e_2} - p_2$ " distribution is given by the normal momentum equation and " $M/M_e(n)$ " can be predicted by the corresponding velocity profile families on the basis of the boundary layer parameters resulting from the solution of the nonlinear system of integral equations mentioned in Section 2, see also Kaldellis (1993).

For comparison purposes, the shock induced losses as they appear in nonviscous approximations can be estimated as:

$$\hat{\omega}_{SH} = \frac{\bar{p}_{t_{2is}} - \hat{p}_{t_{2e}}}{1/2 \cdot \rho_\infty \cdot u_\infty^2} \quad (11)$$

where \hat{p}_{t_e} is also given by Eq. (6), using the corresponding values of the external flow field, without taking into account the flow field modification according to shock-shear flow interaction.

The entropy rise related to the existence of the shock waves can be predicted (see also Fig. 1) using the following equation:

$$\Delta \bar{s} = -R_g \cdot \ln \left(\frac{\bar{p}_{t_2}}{\bar{p}_{t_{2is}}} \right) \quad (12)$$

once the total pressure values have been computed using Eqs. (4) and (10).

The direct and indirect shock induced entropy rise can be split using the following equations:

$$\Delta \bar{s}_{SH} = \Delta \bar{s}_{sh} + \Delta \bar{s}_v \quad (13)$$

where:

$$\Delta \bar{s}_{sh} = -R_g \cdot \ln \left(\frac{\bar{p}_{t_{2e}}}{\bar{p}_{t_{2is}}} \right) \quad (14)$$

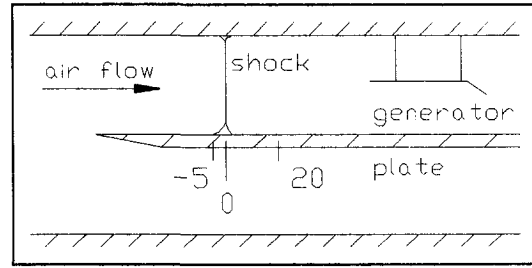


Fig. 2 Experiment of Seddon; experimental configuration

and

$$\Delta \bar{s}_v = -R_g \cdot \ln \left(\frac{\bar{p}_{t_2}}{\bar{p}_{t_{2e}}} \right) \quad (15)$$

Summarizing, the streamwise or spanwise evolution of the total pressure drop coefficient and the entropy rise can be computed once the velocity profile and the total pressure distributions are known at the desired station. In this way the analysis presented gives the additional possibility to calculate the evolution of the shock induced losses at every station throughout the configuration investigated and not only at the exit. Besides, special attention is paid to take into account the normal static pressure gradient across the shear layer and its contribution to the total pressure drop, see also Katramatos and Kaldellis (1991).

4 Comparison Between Calculations and Experiments

The above described shock loss model in conjunction with the already presented complete shock-shear flow interaction method (Kaldellis et al., 1990, Kaldellis, 1993) is used in the following to investigate the evolution of the shock induced losses for three well-documented cases which either present flow separation or have industrial interest.

I Seddon Separated Test Case ($M_e = 1.47$). The early experiment of Seddon (1960) is used as a first test case, since it is a severe experimental test (Fig. 2) with high (at least for turbomachinery applications) incoming Mach number ($M_e = 1.47$) and the appearance of flow separation.

The experimental values of Mach number are described quite realistically Fig. 3 by the results of the proposed method, al-

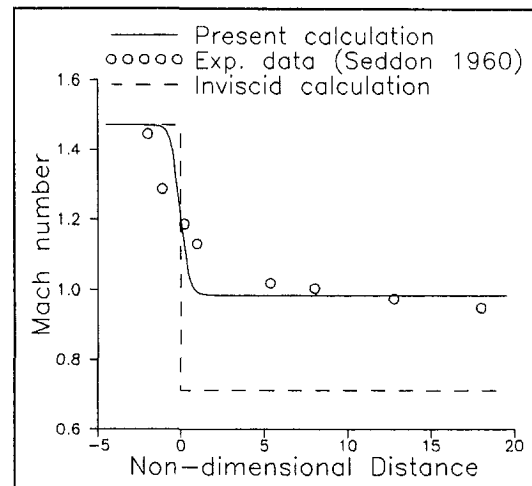


Fig. 3 Mach number distribution for the experiment of Seddon

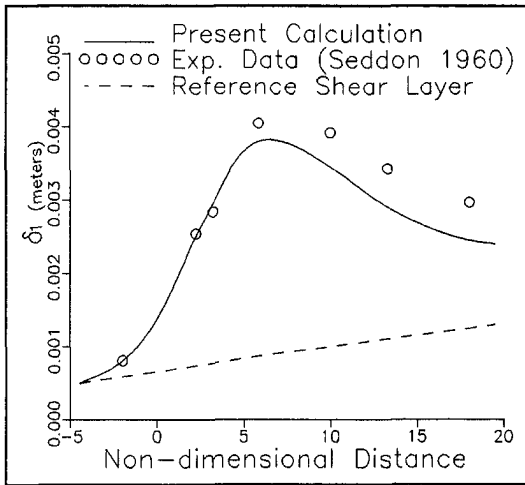


Fig. 4 Displacement thickness distribution for the experiment of Seddon

though the calculated Mach distribution at the theoretical shock position is sharper than the experimental one. This small deviation is reasonable since the small disturbance theory applied here is not strictly mathematical valid at the shock position, due to important flow changes encountered. Note that due to the strong shock-shear flow interaction the asymptotic real Mach number far downstream of the shock wave is approximately 0.93, while the corresponding inviscid value is only 0.71.

In the next two figures, 4 and 5, the predicted evolution of two main flow parameters (δ_1 , δ_2) of the shear layer are given in comparison with the experimental data. The agreement between theory and experiment can be termed good, especially for the “ δ_2 ” distribution. The above predicted shear layer parameters are used next in order to calculate the velocity profiles and finally the total pressure distribution throughout the interaction region.

For comparison purposes, the compressible shear layer method is used to calculate the characteristics of a supersonic shear layer ($M_e = 1.47$) developing on a flat plate with zero pressure gradient. This high speed shear layer will be called in the following the “reference shear layer” and its characteristic quantities (δ_1 , δ_2) are given also in Figs. 4 and 5.

The predicted, direct and indirect shock loss distributions, according to the analysis of Section Three, are given in Fig. 6 and are compared with the distribution of the total pressure drop coefficient for the reference supersonic shear layer.

As expected, a strong loss increase is encountered near the theoretical shock position, see Fig. 2, which is mainly due to

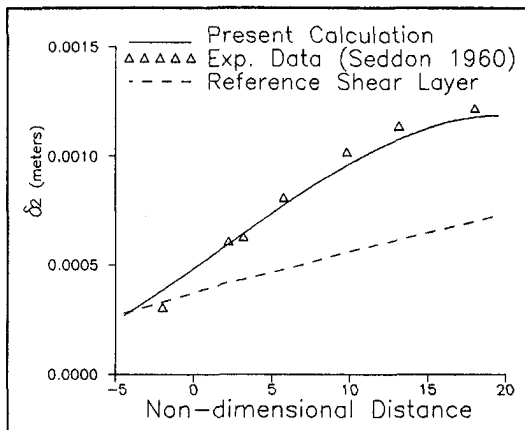


Fig. 5 Momentum thickness distribution for the experiment of Seddon

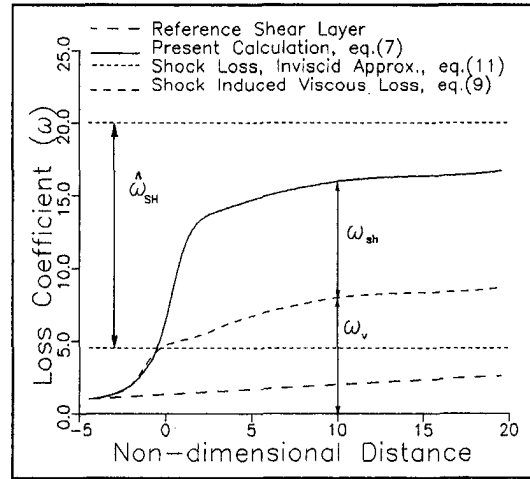


Fig. 6 Distribution of the nondimensional shock loss coefficient

the direct shock induced loss. Indirect shock induced viscous losses are responsible for the divergence between the loss distribution of the shock and the shock free shear layers before the shock position. Increased indirect shock losses are also present after the shock position and are directly related to the strong flow separation. Downstream of the interaction region the shock influenced shear layer presents a lower loss increase rate than the corresponding shock free one. In Fig. 7 the evolution of the mass averaged loss coefficient in the marching direction, predicted by Dawes (1988) for a supercritical compressor cascade, is given. The results presented are taken from a very interesting numerical study concerning the influence of the mesh refinement on the calculation results of a well known modern CFD code. The influence of the mesh coarseness on the quality of the computed results is obvious. However, for all the mesh dimensions the predicted loss profiles present a remarkable increase near the shock and a continuous loss rise downstream of the interaction region. Despite the multigrid acceleration techniques successfully used by Dawes (1988) about one week continuous run was needed on a fast Perkin Elmer 3230 computer to analyze the above mentioned test case, in addition to the enormous computer storage requirements. On the other hand, less than one hour CPU time is necessary on a 25 MHz 386 machine to analyze completely the Seddon test case using the current approach. Additionally, the proposed computational

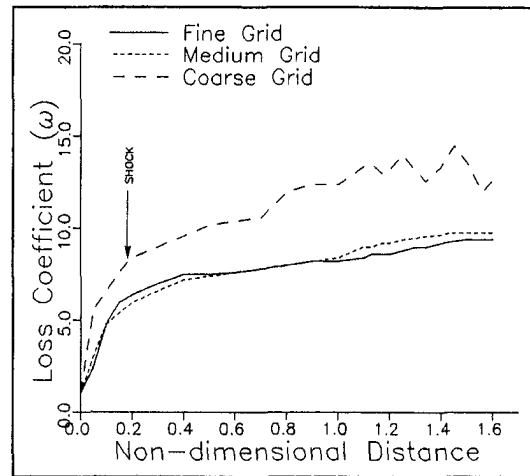


Fig. 7 Nondimensional loss coefficient for a supercritical compressor cascade, by Dawes (1988)

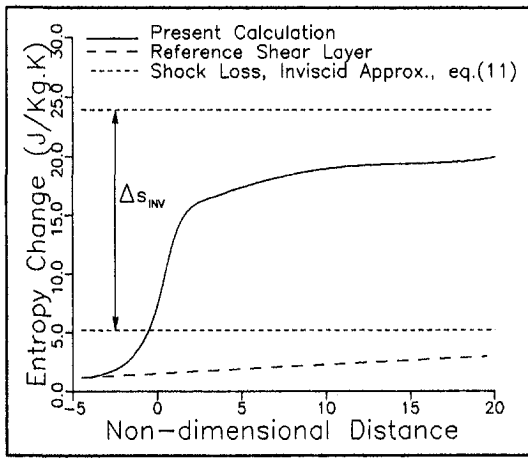


Fig. 8 Entropy changes due to the shock induced losses

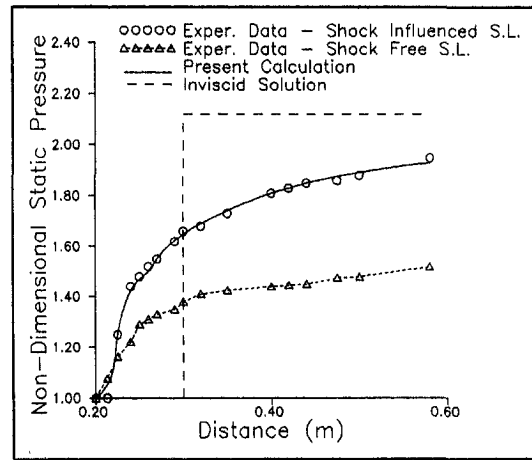


Fig. 10 Wall static pressure distribution; experiment of Schofield

algorithm is rather stable and converges rapidly, while at least second order of accuracy numerical schemes are applied for the solution of the governing equations.

Finally, the calculated shock induced entropy rise is given in Fig. 8 in comparison with the entropy rise of the shock free reference shear layer and the corresponding shock induced entropy increase computed by an inviscid approximation. Real gas effects are excluded in the calculation results, although remarkable changes of the real gas coefficients (γ , R_g , C_p) are encountered as the flow passes through the system of the shock waves. The calculated entropy distributions (see Eqs. (12)–(15)) are in accordance with the predicted total pressure drop given in Fig. 6. Therefore a sharp entropy increase is also encountered near the theoretical shock position. However, the real flow entropy increase is by 25 percent less than the corresponding one related with the shock simulation for the case of the inviscid flow approximation.

II Schofield Separated Test Case ($M_e = 1.405$). The detailed experimental data of Schofield (1985) are used next as the second test case, Fig. 9, to be analyzed. For this experimental case, besides the high incoming Mach number (≈ 1.405) and the strong flow separation, a remarkable pressure gradient was applied to the flow field additionally to the shock induced pressure jump. In order to separate the shock induced losses (direct and indirect) and the viscous losses due to the external imposed pressure gradient the same shear layer was also examined without the existence of the shock wave.

The calculated wall static pressure distribution describes satisfactorily the experimental data, Fig. 10. In the same figure the experimental static pressure distribution is also cited for the shock free shear layer. In order to diminish shock waves at the nozzle exit before the experimental region, the Mach number at the duct entrance was 0.61 for the case of the shock free shear layer, while for the shock influenced case the corresponding post-shock Mach number was 0.74. The small difference in

the Mach number values was found to be unimportant by Schofield (1985), as he compared the development of the two shear layers.

Accordingly, the computed distributions of “ δ_1 ” and “ C_f ” are given in comparison with the experimental measurements by Schofield (1985) for the shock influenced and the shock free shear layers, Fig. 11 and 12. The comparison is successful and the computed parameters are used next by the proposed shock loss model to estimate the direct and indirect shock loss distributions. The predicted total pressure drop coefficient “ ω ” for the shock influenced shear layer is given in comparison with the corresponding coefficient for the shock free shear layer, Fig. 13. From the same figure it is concluded that the total pressure drop is much greater for the pressure driven shear layer than the theoretical one, predicted using zero pressure gradient, and included also in the same figure. On the other hand, significant total pressure drop is encountered near the shock shear layer interaction region, accompanied by a remarkable viscous loss due to the flow separation. However, the total (direct and indirect) shock induced loss is 25 percent less than the corresponding “inviscid” shock induced total pressure drop. Another interesting point is that after the interaction region the total pressure seems to be almost constant despite the existing post shock pressure gradient. In comparison with the other two total pressure curves, the shock induced shear layer presents quite similar behaviour after the interaction region with the zero-pressure gradient one. Contrarily, the pressure driven shock free shear layer presents similar loss behaviour with the total pressure loss distribution given in Fig. 14. These distributions are taken from

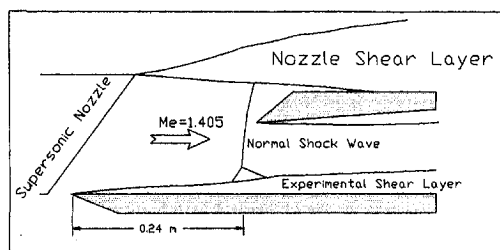


Fig. 9 Experiment of Schofield; experimental configuration

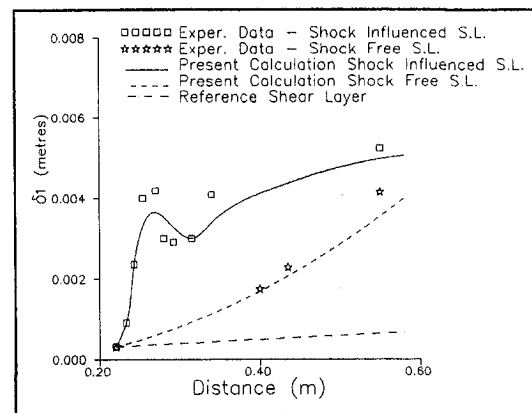


Fig. 11 Displacement thickness distribution; experiment of Schofield

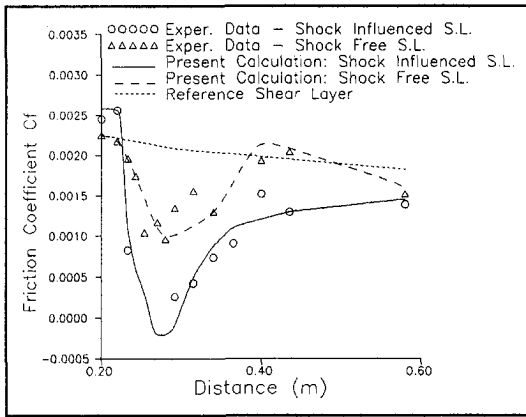


Fig. 12 Skin friction coefficient distribution; experiment of Schofield

unpublished work by the authors and concerns the distribution of the pressure loss coefficient for a subsonic compressor cascade at different incidence angles. Comparing the shock free shear layer Fig. 13 with the $i = +2^\circ$ (positive incidence angle) loss curve (see Fig. 14) one may conclude that the shock free shear layer tends to separate, a fact that is also verified by the experiments.

Using the analysis given in Section 3, the entropy distribution throughout the interaction region is also predicted. As in the previous shock-shear layer interaction case the strong entropy rise near the shock position is mainly attributed to the existing strong shock wave. Additionally entropy rise is related with the total pressure drop due to the shock induced flow separation. Although the displacement thickness at the end of the interaction region for the shock free shear layer is greater than the displacement thickness of the shock influenced one, the predicted entropy rise of the shock free shear layer is 70% less than the corresponding entropy rise of the shock influenced one. This undesirable entropy rise comes to balance in some way the much greater static pressure increase (Fig. 10) through the shock influenced shear layer, in comparison with the corresponding shock free one.

III Supersonic Rotor of an Axial High Pressure Compressor. The last test case examined concerns the spanwise distributions of the total enthalpy and the total pressure throughout the supersonic rotor of a single-stage high pressure compressor,

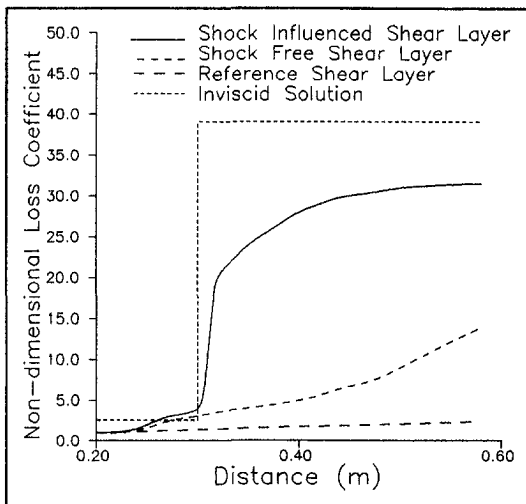


Fig. 13 Distribution of the nondimensional loss coefficient; experiment of Schofield

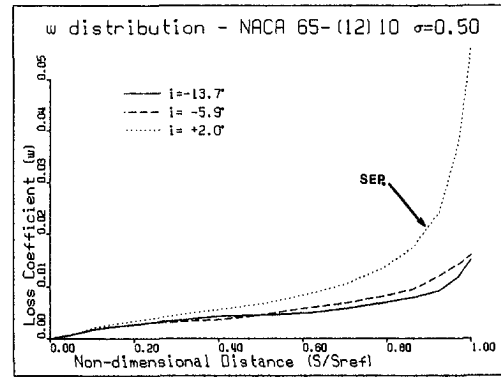


Fig. 14 Profile loss distribution for a highly loaded compressor cascade at various incidence angles

Fig. 15. The relative Mach number distribution at the rotor inlet varies from 1.32 at the tip to 1.11 at the hub and the flow field is supersonic over the full span of the leading edge of the rotor, excluding the hub and tip shear layers which include a very small subsonic part near the endwalls.

Experimental measurements and inviscid numerical calculations indicate a quasi-normal leading shock near the midchord of the rotor while the flow behind the shock is everywhere subsonic, see Goutines and Naviere (1987) and Trebinjac and Vouillarmet (1990). The strong increase of the peripheral component of the absolute velocity due to the shock-secondary flow interaction leads to an additional total enthalpy increase, especially near the tip. More precisely, the total enthalpy increase near the tip is approximately twice the corresponding one near the hub region, see Fig. 16. Additionally, the major part of the energy exchanged near the tip of the rotor is indeed exchanged inside the shock-secondary flow interaction region. In order to estimate the shock induced total pressure drop inside the rotor the theoretical analysis concerning rotor blading is utilized, taking into account the corresponding total temperature increase (ΔT_t), see also Eqs. (6) and (10). Using the complete secondary flow method developed by the authors during the last years (Kaldellis et al., 1990, Kaldellis et al., 1991) the entire secondary flow field is calculated. Comparing now the inviscid and the real total pressure distributions at the end of the interaction region, the shock induced direct and indirect (secondary losses included) losses can be predicted, see Fig. 17. In the same figure the corresponding profile losses are also drawn for comparison purposes. As can be easily seen, the shock induced losses are mainly concentrated inside the tip endwall region, since the tip shear layer is mainly influenced by the existing strong passage shock waves. Peak loss values near the hub region are mainly attributed to the strong secondary flow field inside the hub endwall shear layer. Similar spanwise evolution of rotor losses is given by Karadimas (1988) in Fig. 10 of his paper, concerning the analysis carried out for a modern transonic fan rotor. Keep in mind also that the remarkably lower loss values encountered for this fan rotor case are in accordance with the much

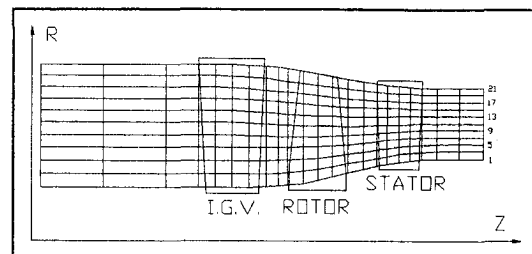


Fig. 15 Axial supersonic compressor. Meridional computational grid.

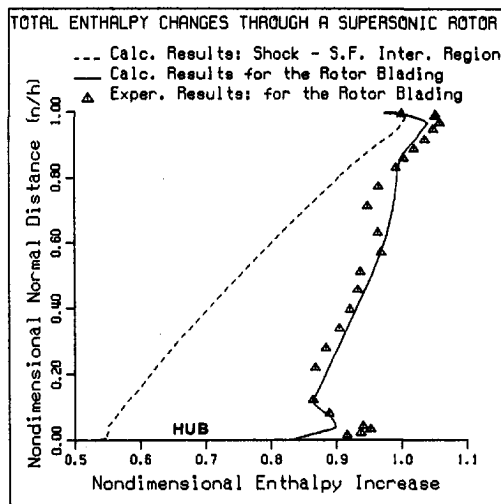


Fig. 16 Total enthalpy changes through the shock-secondary flow interaction region and the rotor blade of a supersonic axial compressor

lower loading of the fan rotor blades in comparison with the supersonic compressor case. The proposed analysis has the additional ability to present the evolution of the shock induced losses at every station along the machine. Finally, the corresponding spanwise distribution of the entropy rise across the shock wave underlines the strong increase of the entropy near the tip wall. However, in rotating blades the existence of the shock wave-boundary layer interaction not only leads to lower direct shock entropy rise in comparison with the “inviscid” shock approximation, but also leads to additional energy exchange due to the significant meridional vorticity changes resulting from the shock-secondary flow interaction.

5 Conclusions

A complete shock loss model is presented, which is based on the shock-boundary layer and shock-secondary flow methods

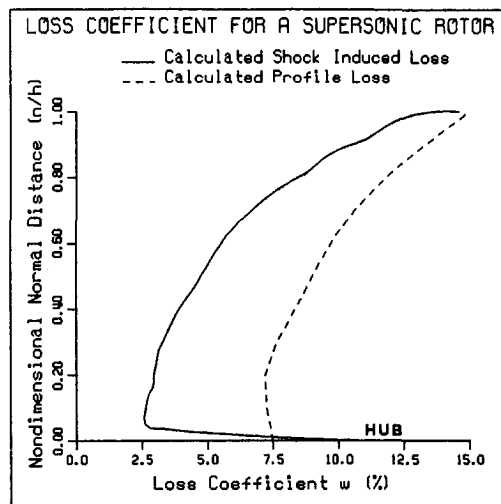


Fig. 17 Spanwise evolution of shock induced and profile losses for a high pressure supersonic rotor

developed by the authors during the last years. The proposed model distinguishes the direct and indirect shock induced losses and has the ability to present their streamwise and spanwise distribution for several configurations investigated.

The reliability and the accuracy of the proposed shock loss model is verified not only by the experiments but also by several calculation results from various well known industrial codes. However, the computational requirements of the proposed model are at least two orders of magnitude less than the corresponding ones of the above mentioned CFD codes.

The stationary and rotating flow cases analyzed present either strong flow separation or have industrial interest. Despite the high incoming Mach number values of all test cases examined both total pressure drop and entropy rise inside the shock-shear flow interaction region are realistically predicted. Thus, the proposed time-saving shock loss model cancels the need to use low speed correlations, modified for compressibility effects and then extrapolated to transonic-supersonic flow cases.

Consequently, using the presented shock loss model as a basis, a systematic analysis of the shock induced losses in transonic-supersonic compressor cascades is carried out. The experience gained will be used next for the design of high performance and minimum loss supersonic blades, a challenging domain for industrial application of the method.

References

- Calvert W. J., 1982, “An Inviscid-Viscous Interaction Treatment to Predict the Blade-to-Blade Performance of Axial Compressors with Leading Edge Normal Shock Waves,” ASME Paper 82-GT-135.
- Cetin M., Hirsch Ch., Serovy G. K., and Ucer A. S., 1989, “An Off-Design Loss and Deviation Prediction Study for Transonic Axial Compressors,” ASME Paper 89-GT-324.
- Dawes W. N., 1988, “Development of a 3D Navier-Stokes Solver for Application to All Types of Turbomachinery,” ASME Paper 88-GT-70.
- Goutines M., and Naviere H., 1987, “Conception et Essais d’un Etage de Tete d’un Compresseur HP Avance,” AGARD-CP-421, *Advanced Technology for Aero Gas Turbine Components*, Paris.
- Hah C., and Wennerstrom A. J., 1990, “Three-Dimensional Flowfields Inside a Transonic Compressor with Swept Blades,” ASME Paper 90-GT-359.
- Inger G. R., Mason W. H., 1976, “Analytical theory of transonic normal shock-boundary layer interaction,” *AIAA Journal*, Vol. 14, pp. 1266–1272.
- Kaldellis J., Douvikas D., Falchetti F., Papailiou K., 1990, “A Secondary Flow Calculation Method for One Stage Axial Transonic Flow Compressors, Including Shock-Secondary Flow Interaction,” *ASME Journal of Turbomachinery*, Vol. 112, pp. 652–668.
- Kaldellis J., Katramatos D., and Ktenidis P., 1991, “Effects of the Tip Clearance Flow Field on the Secondary Losses,” ASME Paper 91-GT-58.
- Kaldellis J., 1993, “Parametrical Investigation of the Interaction Between Turbulent Wall Shear Layers and Normal Shock Waves, Including Separation,” *ASME JOURNAL OF FLUIDS ENGINEERING*, Vol. 115, pp. 48–55.
- Kaldellis J., 1994, “Energy Exchange and Loss Prediction in Axial Turbines and Compressors,” presented at the FLOWERS’94 ASME Conference, Conference Proceeding pp. 799–811, Firenze, Italy.
- Karadimas G., 1988, “Design of High Performance Fans Using Advanced Aerodynamic Codes,” ASME Paper 88-GT-141.
- Katramatos D., and Kaldellis J., 1991, “3-D Loss Prediction Based on Secondary Flow and Blade Shear Layer Interaction,” ASME Paper 91-GT-59.
- Koch C., and Smith Jr. L. H., 1976, “Loss Sources and Magnitudes in Axial Flow Compressors,” *Trans. of ASME, Journal of Engineering for Power*, Vol. 98, pp. 411–424.
- Schofield W. H., 1985, “Turbulent-Boundary-Layer Development in an Adverse Pressure Gradient after an Interaction with a Normal Shock Wave,” *Journal of Fluid Mechanics*, Vol. 154, pp. 43–62.
- Schreiber H. A., 1986, “Experimental Investigations on Shock Losses of Transonic and Supersonic Compressor Cascades,” AGARD-CP-401, in *Transonic and Supersonic Phenomena in Turbomachines*, Munich.
- Seddon J., 1960, “The Flow Produced by Interaction of a Turbulent Boundary Layer with a Normal Shock Wave of Strength Sufficient to Cause Separation,” *RAE TM Aero 667*.
- Trebinjac I., and Vouillarmet A., 1990, “Laser Two-Focus Anemometry Investigation of the Flow Field Within a Supersonic Axial Compressor Rotor,” ASME Paper 90-GT-298.
- Tweedt T. L., Schreiber H. A., and Starken H., 1988, “Experimental Investigation of the Performance of a Supersonic Compressor Cascade,” ASME Paper 88-GT-306.

Near-Wall Modeling of Plane Turbulent Wall Jets

G. Gerodimos

Graduate Assistant,
Mechanical and Aerospace Engineering,
Arizona State University,
Tempe, AZ 85287-6106

R. M. C. So

Professor,
Mechanical Engineering Department,
The Hong Kong Polytechnic University,
Hung Hom, Kowloon, Hong Kong

In most two-dimensional simple turbulent flows, the location of zero shear usually coincides with that of vanishing mean velocity gradient. However, such is not the case for plane turbulent wall jets. This could be due to the fact that the driving potential is the jet exit momentum, which gives rise to an outer region that resembles a free jet and an inner layer that is similar to a boundary layer. The interaction of a free-jet like flow with a boundary-layer type flow distinguishes the plane wall jet from other simple flows. Consequently, in the past, two-equation turbulence models are seldom able to predict the jet spread correctly. The present study investigates the appropriateness of two-equation modeling; particularly the importance of near-wall modeling and the validity of the equilibrium turbulence assumption. An improved near-wall model and three others are analyzed and their predictions are compared with recent measurements of plane wall jets. The jet spread is calculated correctly by the improved model, which is able to replicate the mixing behavior between the outer jet-like and inner wall layer and is asymptotically consistent. Good agreement with other measured quantities is also obtained. However, other near-wall models tested are also capable of reproducing the Reynolds-number effects of plane wall jets, but their predictions of the jet spread are incorrect.

Introduction

Two-dimensional simple wall-bounded turbulent flows are defined as those where only one driving force is used to overcome the frictional force created by the presence of the wall. These flows can be further classified as external and internal. Internal simple flows are channel and pipe flows where the driving potential is the pressure gradient, and Couette flow where the driving force is the moving wall. In the case of Couette flows, viscous effects are present throughout the channel. On the other hand, the effects of viscosity are essentially negligible in the central core of channel/pipe flows. One example of an external simple flow is a flat plate boundary layer with zero pressure gradient. The driving force in this case is the external flow and viscous effects are dominant only in the inner region of the boundary layer. For this flow, the inner region consists of the viscous sublayer, the buffer layer and the log layer. The channel/pipe flows and flat plate boundary layers have been traditionally used for model validation by researchers. Couette flow, on the other hand, has not been extensively used as a validation case because most two-equation turbulence models fail to correctly predict the spatial distribution of the turbulent kinetic energy, k . In fact, the models yield a fairly constant k distribution while measurements show otherwise (Henry and Reynolds, 1984). Even higher-order models fail to capture this trend accurately (Schneider, 1989). Various reasons have been put forward to explain the discrepancies; the more important ones are the equilibrium and isotropic assumptions of two-equation models, the improper modeling of pressure diffusion in second-order models and the use of wall functions.

Another external simple flow is the plane wall jet where the jet exit momentum is the driving force. Two regions can be identified in the plane wall jet: an inner layer, which extends from the wall to the point of maximum velocity, and an outer region, which stretches from the point of velocity maximum to the jet edge. The outer region of the wall jet is similar to a plane free jet, while the inner layer has been traditionally thought of

as a boundary layer with zero pressure gradient or a Couette flow. The interaction between these two layers creates intense mixing at the interface, which can be thought of as a mixed or third region. The fact that this flow involves the interaction of a free jet and a boundary-layer type flow renders it different from other kinds of simple flows and thus relatively more difficult to model and predict. Therefore, the plane wall jet represents a challenge for turbulence models that claim to be performing well for other types of simple and complex flows. Most two-equation models can predict plane free jets and mixing layers fairly well, particularly the spreading of the jet/layer itself (Launder et al., 1972). In view of this, the correct calculations of plane wall jets rest on the ability of the models to replicate the mixed region and the inner layer.

The scaling study of Wygnanski et al. (1992) has demonstrated that the region where the law-of-the-wall applies is limited to the inner layer only. The extent of this region is much smaller than that for boundary layers and channel/pipe flows and extends to about $y^+ = yu_* / \nu = 60$ (Karlsson et al., 1992), where y is the wall normal coordinate, u_* is the friction velocity, and ν is the fluid kinematic viscosity. Also, Launder and Rodi (1983) pointed out that this region does not increase with downstream distance as in the case of boundary layers. They attributed this to the fact that the wall shear stress decreases faster than the outer region shear stress, so that the shear stress/wall shear ratio increases with downstream distance. This means that the effects of the outer region on the inner layer increase as the flow develops, thus preventing the growth of the log-law region. In fact, experiments have shown that, far enough downstream, the logarithmic region could disappear altogether depending on the flow Reynolds number. Therefore, the use of wall-functions to calculate plane wall jets is not appropriate and the near-wall region needs to be modeled. This implies that the assumptions of local equilibrium turbulence and Reynolds stress isotropy might have to be relaxed in plane wall jet modeling.

Experiments indicate that the wall jet in a stagnant surrounding is self-preserving when the local velocity and length scales are considered. These scales are given by the local maximum velocity, U_{\max} , and the jet half-width, $y_{1/2}$. The jet half-width is defined as the location where the velocity is equal to half its maximum value. Also, the $y_{\max}/y_{1/2}$ ratio has been found to be approximately 0.15, thus making the two length scales

Contributed by the Fluids Engineering Division for publication in the JOURNAL OF FLUIDS ENGINEERING. Manuscript received by the Fluids Engineering Division December 29, 1995; revised manuscript received January 13, 1996. Associate Technical Editor: F. Hussain.

Table 1 The different correcting functions and turbulent time scales adopted for the models

Model	χ	T_t	$\tilde{\epsilon}$	ξ
LS	$-2v(\partial\sqrt{k}/\partial y)^2$	k/ϵ	ϵ	$2v_t(\partial^2 U/\partial y^2)^2$
SSA	0	k/ϵ	$\tilde{\epsilon}$	$\exp\left[-\left(\frac{Re_t}{40}\right)^2\right]\left[-0.57\frac{\epsilon\tilde{\epsilon}}{k} + 0.5\frac{(\epsilon^*)^2}{k} - 2.25\frac{\epsilon}{k}P_k\right]$
YS	0	$\frac{k}{\epsilon} + \left(\frac{v}{\epsilon}\right)^{1/2}$	ϵ	$vv_t(\partial^2 U/\partial y^2)^2$
WI	0	—	—	0

interchangeable. Here, y_{max} is the location where the velocity is a maximum. The strong interaction between the outer region and the inner layer plays an important role in the development of the wall jet. An obvious effect is the location of zero shear, which is closer to the wall than the location of maximum velocity. Mathieu (1959) concluded that the shear stress at y_{max} must be of opposite sign and the same magnitude as that at the wall, if the two-dimensional momentum balance is to be satisfied. Careful experimental measurements support these findings and indicate that the ratio of the zero shear location to that of maximum velocity is approximately 0.6 (Karlsson et al., 1992). If gradient transport models are used to calculate plane wall jets, the unique characteristic of zero shear not coincident with zero mean velocity gradient cannot be predicted. Furthermore, isotropic two-equation models may not be able to predict the other characteristics because the Reynolds stresses are assumed to be linear functions of the mean velocity gradient. It remains to be seen whether some of these shortcomings of isotropic gradient transport models can be remedied by relaxing the equilibrium turbulence assumption.

A fairly complete summary of two-equation modeling of plane wall jet carried out before 1983 has been given by Launder and Rodi (1981, 1983). Since then, not much progress has been made in the modeling of plane wall jets. Even the more recent studies of Rubel and Melnik (1984) and Adeniji-Fashola and Chen (1989) are based on the assumption of wall functions. Therefore, their models also suffer the same limitations as those analysed by Launder and Rodi (1983). Two-equation models essentially assume that there is a clear cut separation of scales, hence, they cannot account for anisotropic and nonequilibrium turbulence effects. In spite of these shortcomings, the models are widely used in industrial applications because of their simplicity.

The anisotropic assumption could be partially remedied by adopting an algebraic stress model such as that proposed by Pope (1975), Speziale (1987), and Gatski and Speziale

(1993). Their proposals give rise to nonlinear relations for the Reynolds stress tensor rather than the linear ones conventionally assumed. On the other hand, the equilibrium turbulence assumption is relaxed by postulating different near-wall corrections to the governing turbulence equations (e.g., Myong and Kasagi 1990; Nagano et al., 1990; So et al., 1991; Durbin, 1991; Speziale et al., 1992; Yang and Shih, 1993; Abe et al., 1994). With the exception of Durbin (1991), most proposals invoke damping functions that depend on some or all of the following Reynolds numbers, y^+ , $Re_t = k^2/\nu\epsilon$, $Re_\epsilon = y(\nu\epsilon)^{1/4}/\nu$, and $Re_y = yk^{1/2}/\nu$, to simulate viscous effects near the wall. Here, ϵ is the dissipation rate of k . Among these Reynolds numbers, y^+ depends on u_τ , which renders the models unsuitable for free jets and flows with separation and reattachment. On the other hand, Re_ϵ and Re_y rely on y , thus, the models are not geometry independent. Only Re_t depends on local properties alone and is most suitable for use in near-wall modeling. Most models are formulated to mimic the near-wall behavior of fully-developed channel flows, whose detailed characteristics obtained through direct numerical simulations (DNS) have been reported by Kim et al. (1987). However, with the exception of So et al. (1991), not much attention has been paid to the models' asymptotic consistency in the near-wall region of other simple and complex flows. A model that can mimic the DNS data very well and yet is asymptotically consistent for simple as well as complex flows has been developed by Sarkar and So (1997). The model is found to correlate well with a wide variety of flow data, ranging from simple wall shear flows to complex flows. In spite of these recent advances, none of the near-wall models has been validated against plane wall jets.

Based on this understanding of plane wall jets, the objectives of the present investigation are clear. They can be concisely stated as: (1) to investigate the importance of near-wall modeling, (2) to critically assess four near-wall models for their ability to replicate the mixing behavior between the outer jet-like and inner wall layer, and (3) to evaluate the merits of account-

Table 2 The damping functions assumed for the different models

Model	f_1	f_2	f_μ	Wall BC
LS	1	$1.0 - 0.3 \exp(-Re_t^2)$	$\exp\left[-\frac{3.4}{(1.0 + Re_t/50)^2}\right]$	$\epsilon_w = 0$
SSA	1	1	$(1 + 3/Re_t^{3/4}) \times [1 + 80 \exp(-Re_\epsilon)] \times [1 - \exp(-Re_\epsilon/43 - Re_\epsilon^2/330)]^2$	$\epsilon_w = 2v\left(\frac{\partial\sqrt{k}}{\partial y}\right)_w^2$
YS	1	1	$[1 - \exp(-a_1Re_y - a_3Re_y^3 - a_5Re_y^5)]^{1/2}$	$\epsilon_w = 2v\left(\frac{\partial\sqrt{k}}{\partial y}\right)_w^2$
WI	$\frac{(\alpha_0 + Re_t/R_w)}{C_{\mu f_\mu}\left(1 + \frac{Re_t}{R_w}\right)}$	1	$\frac{\alpha_0^* + Re_t/R_k}{1 + Re_t/R_k}$	$\omega_1 = \frac{(2u_\tau^2)}{v\beta^*y_1^+}$

Table 3 Model constants for the different models

Model	σ_k	σ_ϵ	σ_ω	$C_{\epsilon 1}$	$C_{\epsilon 2}$	$C_{\omega 1}$	$C_{\omega 2}$	C_μ	Other
LA	1.0	1.3	—	1.44	1.92	—	—	0.090	—
SSA	1.0	1.45	—	1.5	1.83	—	—	0.096	—
YS	1.0	1.3	—	1.44	1.92	—	—	0.090	$a_1 = 1.5 \times 10^{-4}$ $a_3 = 5.0 \times 10^{-7}$ $a_5 = 1.0 \times 10^{-10}$
WI	2.0	—	2.0	—	—	5/9	3/40	1.0	$R_k = 6, R_\omega = 2.7, R_\beta = 8,$ $\alpha_0 = 0.1, \alpha_\beta^* = C_{\omega 2}/3$

ing for anisotropic effects above and beyond those due to non-equilibrium turbulence. The importance of near-wall modeling is examined by selecting several near-wall two-equation models, whose predictions of the inner region of simple flows range from incorrect to correct, to calculate plane wall jets. Next, the improvements rendered by a nonlinear Reynolds stress relation over that of a linear one is analysed. The calculations are validated against the measurements of Karlsson et al. (1992) and Karlsson (1993) at a fixed jet Reynolds number, $Re = U_j h/\nu$, and the experiments of Wygnanski et al. (1992) conducted over a fairly wide range of Re . Here, U_j is the maximum jet exit velocity and h is the slot height.

Near-Wall Two-Equation Models

Among the many near-wall two-equation models that have been proposed, the models of the $k-\epsilon$ type (e.g., Launder and Sharma, 1974; Myong and Kasagi, 1990; Nagano et al., 1990; So et al., 1991; Durbin, 1991; Yang and Shih, 1993; Abe et al., 1994; Sarkar and So, 1997), the $k-\tau$ type (Speziale et al., 1992)

and the $k-\omega$ type (Wilcox, 1994) are the most common. A critical analysis of the abilities of ten different models of these three types to replicate DNS data of simple wall-bounded shear flows at low Reynolds numbers has been carried out by Sarkar and So (1997). They have identified the models that yield incorrect and correct predictions of simple flows. According to their analysis, the models of Sarkar and So (1997) and Yang and Shih (1993), hereafter denoted as SSA and YS, respectively, seem to give uniformly good results while the models of Launder and Sharma (1974) and Wilcox (1994), designated here as LS and WI, respectively, give relatively poor predictions. Therefore, it is proposed to test these four models against plane wall jets. This choice is dictated by the desire to examine as wide a variety of models as possible. In these four models LS solves a reduced ϵ -equation, two time scales are postulated in YS, while WI considers the equation governing the transport of $\omega = \epsilon/k$, the specific dissipation rate. If the correct prediction of the inner flow is important to plane wall jet calculations, then SSA and YS are expected to yield results that correlate well with measurements.

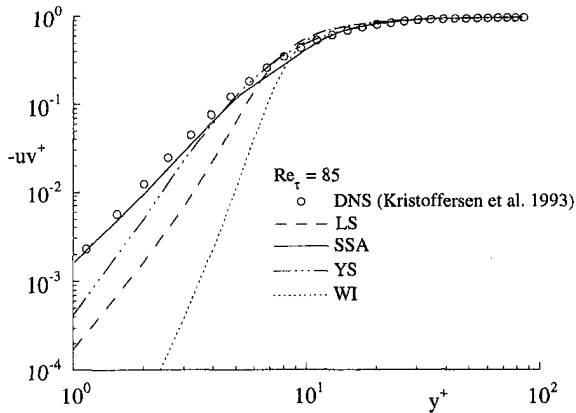


Fig. 1(a) Comparison of calculated uv^+ with DNS data in the inner region of Couette flow

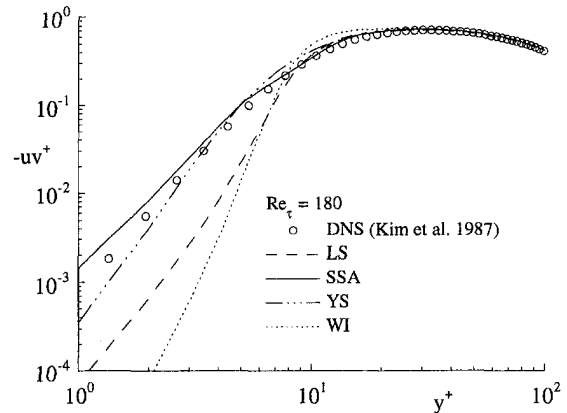


Fig. 2(a) Comparison of calculated uv^+ with DNS data in the inner region of channel flow

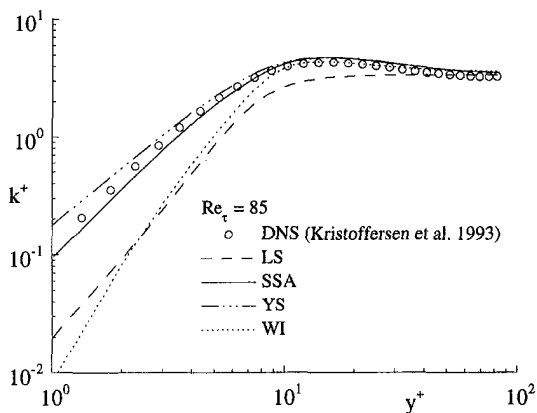


Fig. 1(b) Comparison of calculated k^+ with DNS data in the inner region of Couette flow

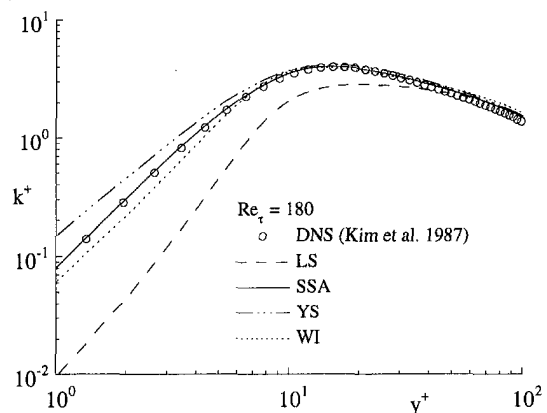


Fig. 2(b) Comparison of calculated k^+ with DNS data in the inner region of channel flow

Consider incompressible plane wall jets where the thin shear layer approximations are valid. If a Cartesian coordinate attached to the wall is chosen, the mean flow and modeled k - ϵ equations under the assumption of gradient transport can be written in Cartesian tensor form as

$$\frac{\partial U_i}{\partial x_i} = 0, \quad (1)$$

$$\frac{DU_i}{Dt} = -\frac{\partial P}{\partial x_i} + \nu \frac{\partial^2 U_i}{\partial x_j \partial x_j} - \frac{\partial \overline{u_i u_j}}{\partial x_j}, \quad (2)$$

$$\frac{Dk}{Dt} = \frac{\partial}{\partial x_j} \left[\left(\nu + \frac{v_t}{\sigma_k} \right) \frac{\partial k}{\partial x_j} \right] + P_k - \beta^* \epsilon + \chi, \quad (3)$$

$$\frac{D\epsilon}{Dt} = \frac{\partial}{\partial x_j} \left[\left(\nu + \frac{v_t}{\sigma_\epsilon} \right) \frac{\partial \epsilon}{\partial x_j} \right] + C_{\epsilon 1} f_1 \frac{1}{T_i} P_k - C_{\epsilon 2} f_2 \frac{\hat{\epsilon}}{T_i} + \xi, \quad (4)$$

where D/Dt is the material derivative, U_i is the i th component of the mean velocity, P is the mean kinematic pressure, $P_k = -\overline{u_i u_j} (\partial U_i / \partial x_j)$ is the production of k , $-\overline{u_i u_j}$ is the kinematic Reynolds stress tensor, T_i is a turbulent time scale, $\hat{\epsilon}$ is a reduced ϵ , v_t is the eddy viscosity, t is time, χ and ξ are near-wall correcting functions for the k and ϵ equations, respectively, f_1 and f_2 are damping functions and σ_k , σ_ϵ , $C_{\epsilon 1}$ and $C_{\epsilon 2}$ are model constants. Here, the overbar is used to denote time average. The governing equations for LS, SSA, and YS can all be written in the above form with $\beta^* = 1$. Therefore, their differences are in the choice for T_i , $\hat{\epsilon}$ and the specifications for χ and ξ . It should be pointed out that LS solves a reduced ϵ with its wall value subtracted out. On the other hand, SSA and YS solve for the true dissipation rate. This will be made obvious when the boundary condition for ϵ is specified.

The k -equation used in the WI model (Wilcox, 1994) is the same as that used in the k - ϵ models except for the specification of β^* . Wilcox (1994) makes use of β^* to enforce the near-wall behavior of k and ω and suggests the following expression for β^* , or

$$\beta^* = \frac{9}{100} \left[\frac{5/18 + (\text{Re}_\tau / R_\beta)^4}{1 + (\text{Re}_\tau / R_\beta)^2} \right], \quad (5)$$

where R_β is a model constant. The ω -equation is given by Wilcox (1994) as

$$\frac{D\omega}{Dt} = \frac{\partial}{\partial x_j} \left[\left(\nu + \frac{v_t}{\sigma_\omega} \right) \frac{\partial \omega}{\partial x_j} \right] + C_{\omega 1} f_1 \frac{\omega}{k} P_k - C_{\omega 2} f_2 \omega^2 + \xi, \quad (6)$$

where $\sigma_{\tau 1}$, $\sigma_{\tau 2}$, σ_ω , $C_{\omega 1}$ and $C_{\omega 2}$ are model constants and ξ is the correcting function.

Finally, $-\overline{u_i u_j}$ can be defined for all models examined here as

$$-\overline{u_i u_j} = 2\nu_t S_{ij} - \frac{2}{3} k \delta_{ij}, \quad (7)$$

where $\nu_t = C_\mu f_\mu k \psi$ is the eddy viscosity, $S_{ij} = (\partial U_i / \partial x_j + \partial U_j / \partial x_i) / 2$ is the mean strain rate, $\psi = k / \epsilon$ for all k - ϵ models and $\psi = 1 / \omega$ for the WI model, C_μ is a model constant and f_μ is a damping function. According to Wilcox (1994), the damping function f_μ introduced in ν_t renders the behavior of the WI model asymptotically correct in the very near-wall region. On the other hand, the k - ϵ models rely on ξ to replicate this near-wall behavior.

The different correcting functions and time scales used in the four models are summarized in Table 1, while Table 2 lists the damping functions assumed and Table 3 tabulates the model constants specified by the authors. In Table 1, the reduced dissipation rates $\hat{\epsilon}$ and ϵ^* used in the SSA model are given by $\hat{\epsilon} = \epsilon - 2\nu(\partial\sqrt{k}/\partial y)^2$ and $\epsilon^* = \epsilon - 2\nu k / y^2$, respectively. The cor-

recting functions and ϵ boundary conditions listed in Tables 1 and 2 are specified for thin shear layers. Other boundary conditions for the plane wall jet can be stated as $U = V = 0$, $k = 0$ at $y = 0$ and $U = 0$, $k = 0$ and $\epsilon = 0$ in the freestream for all models examined. Further clarifications of the ϵ boundary conditions listed in Table 1 are necessary. Since LS solves a reduced form of the ϵ -equation, its boundary condition is $\epsilon_w = 0$ at the wall. The boundary condition $\epsilon_w = 2\nu(\partial\sqrt{k}/\partial y)_w^2$ is assumed in the SSA and YS models. Strictly speaking, ω_w is infinite at the wall for the WI model. However, in practice, $\omega_1 = (2u_\tau^2 / \nu \beta^*) / (y_1^+)^2$ is assumed by Wilcox (1994) based on an asymptotic analysis of the ω -equation, where subscripts w and 1 are used to denote the wall and the first grid point, respectively. Note that none of the models selected has a damping function dependent on y^+ . A comparison of the calculated f_μ with the channel flow DNS data of Kim (1991) at $\text{Re}_\tau = u_\tau H / \nu = 180$ and 395 has been carried out by Sarkar and So (1997), where H is the channel half width. Their results show that the f_μ assumed in SSA yields the best correlation with data.

The above models assume gradient transport and isotropic normal stresses. Therefore, they cannot account for stress anisotropy effects. If this particular characteristic is to be captured without resorting to a full second-order modeling of the flow, anisotropic Reynolds stress tensor such as that formulated by Speziale (1987) can be considered. The expression derived by Speziale (1987) can be written as

$$-\overline{u_i u_j} = 2\nu_t S_{ij} - \frac{2}{3} k \delta_{ij} - 4 \frac{C_D v_t^2}{k} \left[S_{ik} S_{kj} - \frac{1}{3} S_{kl} S_{kl} \delta_{ij} + \hat{S}_{ij} - \frac{1}{3} \hat{S}_{kk} \delta_{ij} \right], \quad (8a)$$

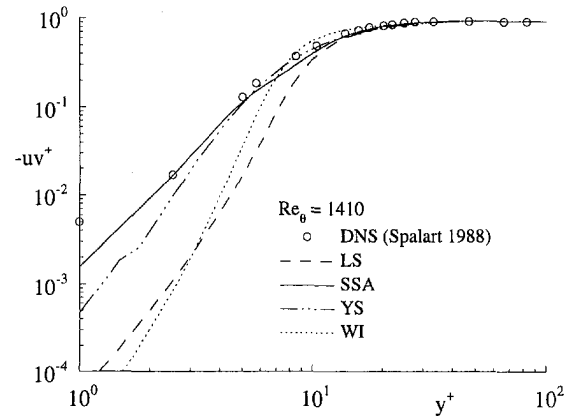


Fig. 3(a) Comparison of calculated uv^+ with DNS data in the inner region of boundary-layer flow

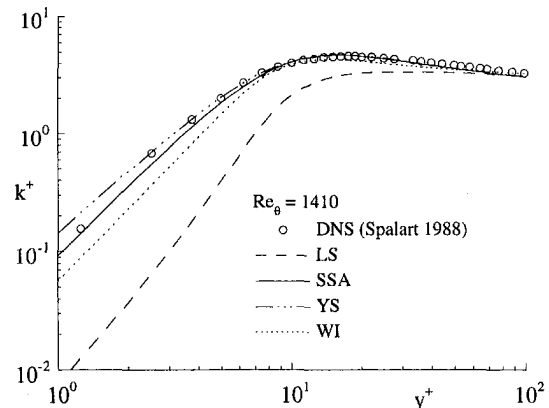


Fig. 3(b) Comparison of calculated k^+ with DNS data in the inner region of boundary-layer flow

where \tilde{S}_{ij} is the frame-indifferent Oldroyd derivative of S_{ij} and is defined as

$$\tilde{S}_{ij} = \frac{\partial S_{ij}}{\partial t} + U_k \frac{\partial S_{ij}}{\partial x_k} - \frac{\partial U_i}{\partial x_k} S_{kj} - \frac{\partial U_j}{\partial x_k} S_{ki}, \quad (8b)$$

and $C_D = 1.68$ is a dimensionless constant. Note that (7) is recovered in the limit of C_D goes to zero. Therefore, (8a) along with any modified k and ϵ equations can be used to assess the effects of nonlinear stress formulation on the calculations of plane wall jets.

However, for plane wall jets, the anisotropic Reynolds stress tensor (8) reduces to the isotropic form (7) identically. This can be easily shown to be the case. Under the assumptions of two-dimensional thin shear layers, the only non-zero shear stress is $-\overline{uv}$. As a result, δ_{ij} , \tilde{S}_{ij} and $S_{ik}S_{kj}$ are all zero and the last term on the r.h.s. of (8a) vanishes. In view of this, the anisotropic Reynolds stress tensor (8) essentially has no effect on the calculations of plane wall jets. The same conclusion can also be drawn from other anisotropic Reynolds stress tensors similar to that given by Speziale (1987). If anisotropic turbulence effects are to be accounted for, second-order modeling of the plane wall jet is necessary. From this point on, only results obtained using the isotropic Reynolds stress tensor (7) are presented and discussed below.

Results and Discussion

The models to be validated against plane wall jets are first evaluated for their performance in the predictions of other types

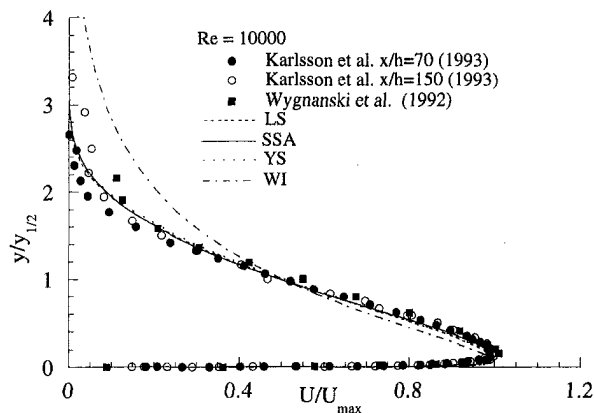


Fig. 4(a) Comparison of the calculated mean velocity with measurements of plane wall jets

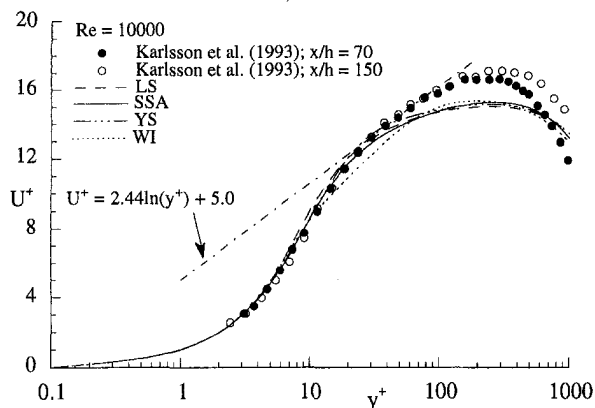


Fig. 4(b) Comparison of the calculated mean velocity with measurements in the inner region of plane wall jets

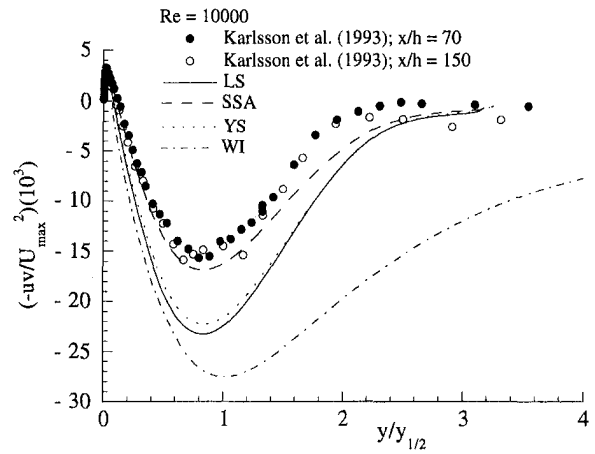


Fig. 5(a) Comparison of the calculated shear stress with measurements of plane wall jets

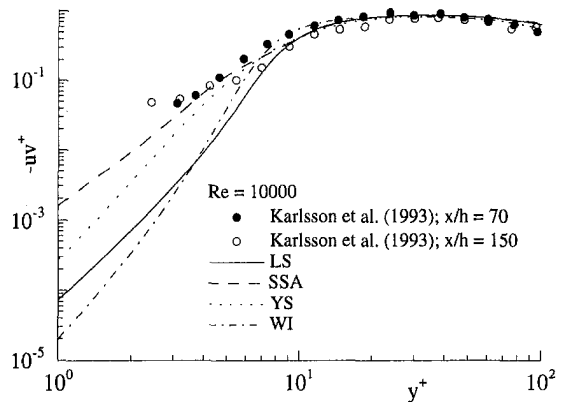


Fig. 5(b) Comparison of the calculated shear stress with measurements in the inner region of plane wall jets

of simple flows. Since the wall jet consists of two layers, an outer free-jet like region and an inner boundary-layer type flow, the models should be separately evaluated against plane free jets and simple wall-bounded flows. The latter category includes such types as channel/pipe, Couette, and boundary-layer flows. Validations of the models against wall-bounded simple flows have been carried out in detail by Sarkar and So (1997), while the calculations of plane free jets have been reported by individual researchers. Whenever such reporting is not available, the model is used to calculate a plane free jet attempted by Launder and Sharma (1974) and the results compared with their prediction. Here, the emphasis is on the jet spread rate. Once the performance of the models for the simple flows has been assessed, they are then used to calculate plane wall jets. The boundary-layer code of Wilcox (1993) is used to calculate free flows as well as flat plate boundary layers. As for the calculations of internal flows, the time marching numerical scheme of Sarkar and So (1997) is used. The interested reader is referred to these two sources for numerical details. However, it should be emphasized that the reported results are grid independent and the numerical solutions are convergent to at least 10^{-8} for the residual mass.

Plane Free Jets. The LS model is known to predict the spread of plane free jets correctly at high Reynolds numbers. Experiments give a range of 0.100–0.110 for the spread rate while the LS model predicts a value of 0.109 (Launder and Sharma, 1974). The YS and SSA models also yield the same spread rate provided the jet Reynolds numbers are high enough so that the correcting and damping functions are essentially negligible. For low-Reynolds-number flows, the correcting and

damping functions could have an adverse effect on the calculated spread rate. The low Reynolds number limit, in which this will take place, has not been investigated because the present objectives are to study wall effects rather than low-Reynolds-number effects. Besides, the outer region of the wall jets to be calculated has relatively high Reynolds number. It should be pointed out that the presence of the wall introduces both low Reynolds number and wall blocking effects. The latter contributes to an increased anisotropy of the turbulence field near the wall (Kim, 1989). On the other hand, there are no wall blocking effects present in free flows. If either the correcting or damping function depends on y^+ , the model is not suitable for free jet calculation because y^+ is entirely inappropriate for free flows. As for the WI model, Wilcox (1993) reported a spread rate range of 0.090–0.136. The actual prediction depends greatly on the freestream value specified for ω . In summary, the four models yield fairly correct predictions of the spread rate for plane free jets.

Wall-Bounded Simple Flows. A critical evaluation of the LS, SSA, YS, WI, and six other two-equation models against wall-bounded simple and complex flows has been attempted by Sarkar and So (1997). Their results show that SSA and YS yield uniformly good results for the outer region of simple flows. Therefore, there is no need to repeat the analysis here. However, since it is conjectured that plane wall jets could be predicted correctly by a two-equation model, if it is asymptotically consistent and replicates the near-wall behavior, the performance of these four models in the inner region of simple flows is examined here. Only three simple flows are considered, these are Couette, channel, and boundary-layer flows. The calculations are compared with the DNS data of Kristoffersen et

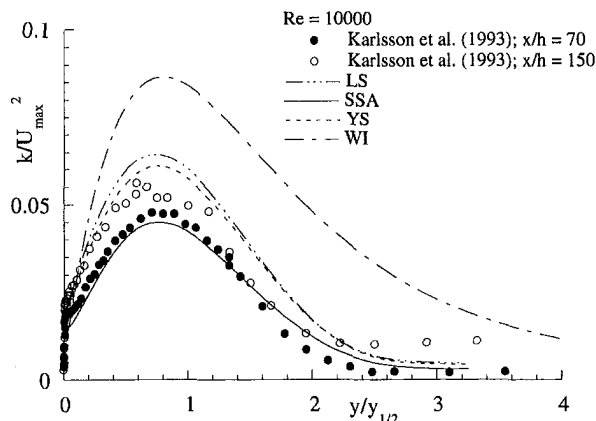


Fig. 6(a) Comparison of the calculated k^+ with measurements of plane wall jets

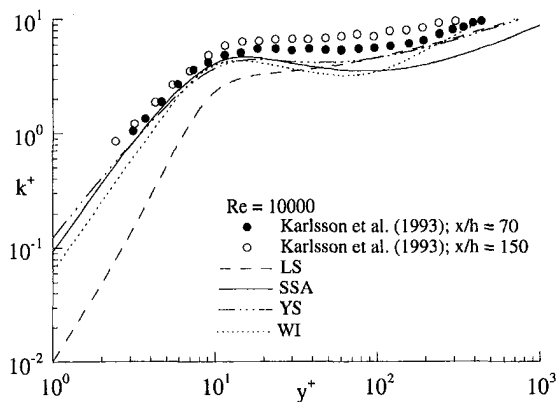


Fig. 6(b) Comparison of the calculated k^+ with measurements in the inner region of plane wall jets

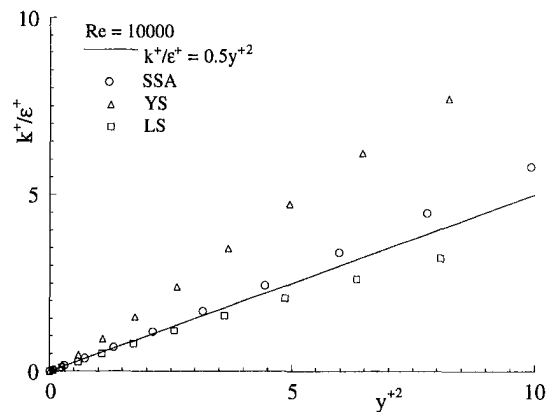


Fig. 7 A plot of k^+/ϵ^+ versus y^{+2} for the plane wall jet

al. (1993), Kim et al. (1987), and Spalart (1988) at $Re_\tau = u_\tau H/\nu = 85$ and 180 and $Re_\theta = U_\infty \theta/\nu = 1410$, respectively. Here, θ is the momentum thickness and U_∞ is the freestream velocity. The $-uv^+ = -\overline{uv}/u_\tau^2$ and $k^+ = k/u_\tau^2$ results, shown versus y^+ in log-log plots, are given in Figs. 1 to 3. Part (a) of each figure shows the $-uv^+$ results, while part (b) displays the k^+ predictions. It can be seen that all models yield a fairly correct prediction of $-uv^+$ and k^+ beyond $y^+ = 10$. However, large variations exist in the region, $0 < y^+ < 10$.

The variables, k^+ , $-uv^+$ and ϵ^+ can be expanded in terms of y^+ near a wall as

$$k^+ = a_k y^{+2} + b_k y^{+3} + \dots, \quad (9a)$$

$$\epsilon^+ = 2a_\epsilon + 4b_\epsilon y^+ + \dots, \quad (9b)$$

$$-uv^+ = a_{uv} y^{+3} + b_{uv} y^{+4} + \dots, \quad (9c)$$

where the coefficients “ a ” and “ b ” are constants. From (9a) and (9b), $k^+ \epsilon^+ / y^{+2} = 0.5$ and $\epsilon_w^+ = 2a_k$ can be determined. These results are independent of the model and represent the asymptotic behavior of k and ϵ . The analysis of Sarkar and So (1997) shows that, in all the flow cases considered, SSA and YS reproduce this behavior very well. The same is not true of LS and WI, though. Also, from (9a) and (9c), it can be seen that the slopes of the near-wall curves for k^+ and $-uv^+$ in a log-log plot are 2 and 3, respectively. Figures 1 to 3 show that SSA and YS are able to reproduce this asymptotic behavior fairly correctly, while the predictions of LS and WI are in error to different degrees. It should be pointed out that the kink noted in the $-uv^+$ prediction of YS (Fig. 3(a)) is due to the switch from viscous time scale to the Kolmogorov time scale in their modeled ϵ -equation; however, the discontinuity noted in $-uv^+$

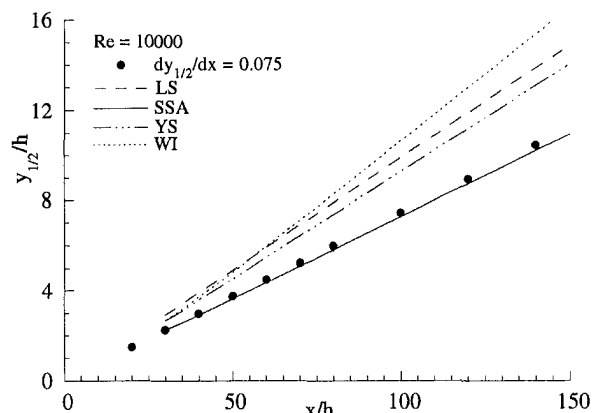


Fig. 8 Comparison of jet growth with measurements for plane wall jet

Table 4 Comparisons of calculated flow properties with data for Couette flow and plane wall jet

	Data	LS	SSA	YS	WI
κ	0.41	0.41	0.41	0.41	0.41
a_k	0.166	0.010	0.092	0.143	—
$\epsilon_w/2$	—	0.087	0.093	0.145	0
$a_{uv} \times 10^3$	1.20	0.007	1.47	0.24	—
$dy_{1/2}/dx$	0.075	0.100	0.073	0.096	0.116
$y_{max}/y_{1/2}$	0.15	0.09	0.12	0.09	0.08

does not seem to affect the calculations far away from the viscous layer. This behavior does not appear in channel and Couette flow calculations (Figs. 1(a) and 2(a)) though. From these results, it appears that SSA and YS are asymptotically consistent, while the other two models are not.

It is now clear that all four models perform well for plane free jets but only SSA and YS give a uniformly valid prediction of the near-wall behavior of wall-bounded simple flows. It remains to be seen whether this ability to reproduce the spread rate of plane free jets and the near-wall behavior of wall-bounded simple flows would enable their interactions and hence the plane wall jet to be calculated correctly.

Plane Wall Jets. The wall jets are calculated using a modified version of the boundary-layer code of Wilcox (1993). At the jet exit, a total of 282 nonuniformly distributed grids are used to cover the calculation domain. An expanding grid is used to accommodate the growth of the jet. Depending on the streamwise distance, the number of grids could be significantly larger than 282 in the downstream location. The grids are distributed so that at least 15 of them are located within $y^+ \leq 5$ and more than 40 are placed in the region $5 < y^+ < 65$. Furthermore, the distribution ensures that the first grid is placed at approximately $y^+ < 1$ even in the fully-developed region of the jet. Outlet conditions are specified by a fully-developed channel flow velocity profile and the equilibrium turbulence assumption is used to assess the distributions of k and ϵ across the jet outlet. Since the jet properties in the fully-developed region are independent of the jet outlet conditions, these specifications are appropriate for the calculations of the experiments of Karlsson et al. (1992), Karlsson (1993), and Wagnanski et al. (1992). With this grid distribution, the solutions obtained from all models tested are found to be grid independent. The experimental Re varies from 3700 to 19000. This range of Re serves to validate the ability of the models to replicate Re effects. Comparisons with the measurements of Karlsson et al. (1992) and Karlsson (1993), where Re = 10000, are presented first. This is followed by a comparison with the data of Wagnanski et al. (1992) at Re = 3700, 5000, 10000 and 19000, and an analysis of the models' ability to reproduce Re effects.

Table 5 Comparison of jet growth for four different Re

Re	$dy_{1/2}/dx$			
	LS	SSA	YS	WI
3700	0.104	0.078	0.097	0.120
5000	0.102	0.076	0.096	0.119
10000	0.100	0.073	0.096	0.116
19000	0.098	0.072	0.095	0.113

ski et al. (1992) at Re = 3700, 5000, 10000 and 19000, and an analysis of the models' ability to reproduce Re effects.

The results for the Karlsson et al. (1992) experiment are presented in Figs. 4–8. Further comparisons of the near-wall behavior derived from the measurements of Karlsson (1993) are shown in part (b) of Figs 4–6. In part (a) of these plots, U_{max} and $y_{1/2}$ are used to normalized the flow properties, while inner variables, such as y^+ , U^+ , k^+ and $-uv^+$, are used in the plots shown in part (b) of these figures. Further comparison of asymptotic consistency is given in Fig. 7, where only the calculations of LS, SSA, and YS are shown. Jet growth is compared in Fig. 8. In the near field of the jet, the flow is not fully developed. Therefore, the growth rate, $dy_{1/2}/dx$, is not linear and the results are not compared. In addition, y_{max} is determined from the calculations and listed in Table 4 for comparison with experimental data.

The three $k-\epsilon$ models essentially give identical results for U , which correlate well with the data of Karlsson et al. (1992) in the entire jet region, except near the maximum velocity location where all three models under-estimate U_{max} (Fig. 4(b)). On the other hand, the prediction of WI is not in agreement with data, particularly in the outer region and in the vicinity of the velocity maximum (Figs. 4(a) and 4(b)). Comparisons of the velocities in inner variables are shown in Fig. 4(b), where the log law, $U^+ = \kappa^{-1} \ln y^+ + 5.0$ with $\kappa = 0.41$, is also displayed. It can be seen that the data show a limited log region ($20 \leq y^+ \leq 80$) and the κ thus determined is approximately 0.41 (Karlsson, 1993). The model calculations of LS, SSA, and YS give a limited log region ($20 \leq y^+ \leq 40$), however, their extent is substantially shorter than that given by experiment. WI also predicts a limited log region, but it is displaced to $50 \leq y^+ \leq 70$. The κ 's thus determined are essentially the same as the data (Table 4). Furthermore, the intercepts obtained from these plots are different for different models; its value is, in general, lower than 5. The calculated $y_{max}/y_{1/2}$ by LS and YS is approximately the same and is in error by about 40 percent, while that given by WI is off by more than 45 percent (Table 4). On the other hand, the prediction of SSA is in error by only 20 percent. One possible explanation for this poor performance by WI could be

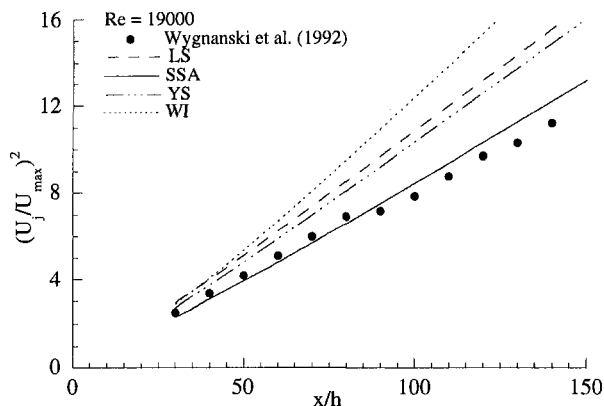


Fig. 9 Comparison of the calculated maximum velocity decay with measurements for plane wall jet

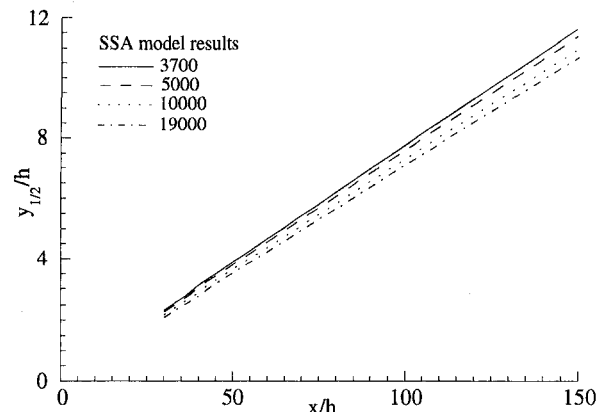


Fig. 10 Jet growth for four different Re predicted by the SSA model

Table 6 Comparison of calculated A_y , A_u , m and n with data

	Data (Narasimha et al. 1973)	Data (Wyganski et al. 1992)	LS	SSA	YS	WI
A_y	—	1.445	0.135	0.130	0.080	0.085
A_u	—	2.946	2.583	2.600	3.562	2.620
m	0.910	0.881	0.986	0.968	1.000	1.010
n	-0.506	-0.472	-0.488	-0.483	-0.483	-0.491

the incorrect calculation of the near-wall flow which, in turn, affects the outer flow.

Even though LS and YS give essentially the same U predictions as SSA, their calculations of $-\bar{uv}$ and k in the outer region differ substantially from those given by SSA (Figs. 5(a) and 6(a)). In fact, LS and YS yield the same predictions and consistently over-estimate these two quantities in the outer region of the wall jet. The predictions of WI are higher than those of LS and YS and are more than double those of SSA over most of the jet mixing region. The measurements display self-preservation at $x/h = 70$ and 150 for U and $-\bar{uv}$, but not for k . This has been observed in many experiments, and in fact the turbulence quantities may never become self-preserving (Wyganski et al., 1992). On the other hand, all four models predict self-preservation at these two locations. As far as k is concerned, the SSA results seem to agree better with data at $x/h = 70$ than at 150.

The performance of the models in the inner layer differs greatly (Figs. 5(b) and 6(b)). While the k^+ predictions of YS in the inner layer are in agreement with measurements, its calculations of $-uv^+$ are in error in this region (Fig. 5(b) and Table 4). A similar trend is also displayed by WI. On the other hand, the predictions of LS are incorrect for both properties. Only the SSA results are in good agreement with data in this region. All four models are able to predict the peak of $-uv^+$ correctly (Fig. 5(b)), while only SSA, YS, and WI manage to reproduce the first peak of k^+ . The slope of the linear region of the k^+ curves given by SSA, YS, and WI is approximately 2 (Fig. 6(b)), while only SSA gives a slope of 3 for the $-uv^+$ curve (Fig. 5(b)). These comparisons show that the ability to replicate the near-wall behavior of other simple flows correctly does not automatically carry over to the calculation of plane wall jets. This failure could be attributed to the models' inability to mimic the interactions between the outer free-jet like flow with the inner boundary-layer type flow. The mixing of these two different layers, in turn, affects the whole region, thus giving rise to the unique characteristics of the plane wall jet. The a_k 's and a_w 's obtained by curve fitting (9a) and (9c) to the calculations up to $y^+ = 5$ are compared in Table 4. It can be seen that SSA yields the least error in the predictions of these coefficients, while LS gives the most error. Both SSA and YS reproduce the relation $\epsilon_w^+ = 2a_k$ correctly. The asymptotic consistency of SSA is further supported by a plot of k^+/ϵ^+ versus y^{+2} (Fig. 7). It is obvious that only LS and SSA satisfy the requirement that $k^+/\epsilon^+ = 0.5y^{+2}$. In view of these results, it can be said that, even though YS yields good results for other simple wall-bounded flows, its predictions of plane wall jets are not as good as those deduced from SSA. This conclusion is further supported by the fact that only SSA gives a correct prediction of the jet growth (Fig. 8) and the decay of U_{max} at two different Re (Fig. 9). The other three models greatly over-estimate the growth and decay rates (Table 4 and Fig. 9).

It is obvious from the above assessment that, if plane wall jets were to be predicted correctly, the turbulence model needs to perform well for both plane free jets and simple wall-bounded flows, especially its ability to replicate the interactions between a free jet and a wall boundary layer. The failure of an otherwise valid model to replicate plane wall jet correctly could be attributed to its inability to reproduce correctly the mixing between these two vastly different shear layers. It is also clear that gradi-

ent transport is not a handicap; the only jet property that such a model cannot predict correctly is the location of zero shear. However, this drawback does not seem to have a significant effect on the predictions of other jet properties.

The ability of the models to mimic Reynolds-number effects is first assessed by using the models to calculate the four cases investigated by Wyganski et al. (1992). A summary of the jet growth rates is given in Table 5, while a sample plot of the SSA results is shown in Fig. 10. According to Thailand and Mathieu (1967), the jet growth rate should decrease by about 4 percent when Re increases by a factor of 2. The Re range investigated represents about a four-fold increase, therefore, the jet growth rate should decrease by approximately 10 percent. From Table 5, it can be seen that the calculated growth rate decreases by ~8 percent for SSA, by ~6 percent for LS and WI and by only 2 percent for YS.

Further evidence that SSA performs well can be obtained by validating the calculations against experimental data (Wyganski et al., 1992). If U_{max} , $y_{1/2}$ and x , the stream coordinate, are made dimensionless by the jet exit momentum J and v , both the growth rate of the jet and the decay rate of its maximum velocity can be shown to be correlated by

$$y_{1/2}J/v^2 = A_y[xJ/v^2]^m, \quad (10a)$$

$$U_{max}v/J = A_u[xJ/v^2]^n, \quad (10b)$$

where $A_y = 1.445$, $A_u = 1.473$, $m = 0.881$ and $n = -0.473$ are reported by Wyganski et al. (1992) for the four Re tested. It should be pointed out that the reported $A_u = 1.473$ is off by approximately a factor of 2 compared to that deduced from Fig. 5 of their paper. In view of this, the value quoted for comparison in Table 6 is based on the interpretation from their Fig. 5, or $A_u = 2.946$, rather than on 1.473. Furthermore, Narasimha et al. (1973) have reported estimates for m and n ; these are also included in Table 6 for comparison with model calculations. A comparison of the calculated $y_{1/2}J/v^2$ and $U_{max}v/J$ by SSA with data is shown in Figs. 11 and 12, respectively. Other results are similar to those given in Figs. 11 and 12, therefore, they are not shown. All model calculations can be correlated by (10a) and (10b) over the range $3700 \leq Re \leq 19000$ tested; however,

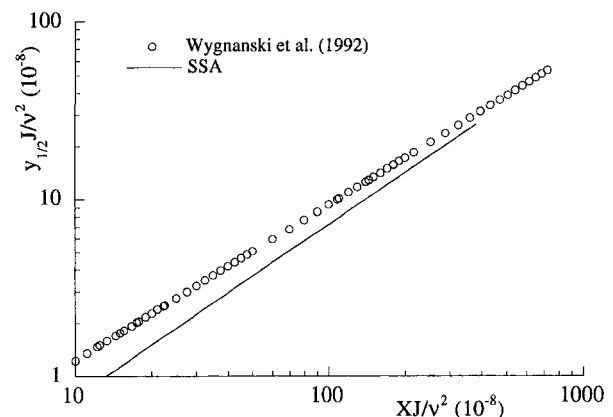


Fig. 11 A normalized plot of the jet growth for four different Re

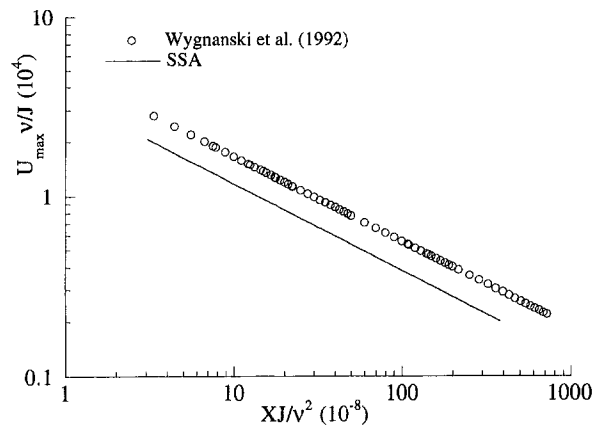


Fig. 12 A normalized plot of the maximum velocity decay for four different Re

the agreement is not as good as the other results presented above. The values of A_y , A_u , m , and n thus determined are listed in Table 6 for comparison with those given by Wynnanski et al. (1992) and Narasimha et al. (1973). The m and n deduced from all models are in better agreement with the data reported by Narasimha et al. (1973). As for A_y and A_u , the values determined from the four models are very similar. The constant A_u is in fair agreement with data, but A_y is not. According to Narasimha et al. (1973), the values of the constants greatly depend on the values of the exponents selected. In view of these results, the four models examined are able to qualitatively reproduce the Re effects of plane wall jets.

Conclusions

Since a correct calculation of plane wall jet is very much dependent on an accurate resolution of the inner layer, it is hypothesized that models that can predict plane free jets and the inner region of wall-bounded simple flows correctly could also yield reasonable results for plane wall jets. Four near-wall two-equation models among the many available are selected for critical assessment of their ability to replicate plane wall jets. Three of the four models are of the $k-\epsilon$ type and one is of the $k-\omega$ type. These models perform rather well for three different simple wall shear flows, except their abilities to predict the asymptotic behavior of such flows. Two of the models chosen (SSA and YS) replicate the near-wall properties quite well, while the other two (LS and WI) fail to different degrees. It is found that, among the four models tested, WI gives the worst prediction of plane wall jets. Not only is the mean field calculated incorrectly, the model also over-predicts $-\overline{uv}$ and k across the jet mixing region. As for LS and YS, the calculated results are essentially identical. Although they yield reasonable predictions of the mean field, their calculated $-\overline{uv}$ and k are consistently higher than the measurements over a substantial portion of the jet. Furthermore, LS, YS, and WI over-estimate the growth rate of the jet substantially. Their prediction of the inner layer behavior is in error to different degrees. Only SSA is capable of reproducing the overall jet characteristics, including near-wall asymptotes, of plane wall jets fairly correctly. Since the anisotropic Reynolds stress tensor examined reduces exactly to the isotropic tensor relation for plane wall jets, improvements in wall jet calculations can only be obtained through the use of second-order models. All four models are capable of replicating the effects of Reynolds number, at least within the Re range investigated. However, only SSA is able to reproduce the jet spread and decay of maximum velocity with fair accuracy for all Re tested.

Acknowledgments

Funding support under Grant PL0008587-AG, Knolls Atomic Power Laboratory, Schenectady, NY 12301 during the tenure of RMCS at Arizona State University is gratefully acknowledged. The grant was monitored by Dr. R. Kunz.

References

- Abe, K., Kondoh, T., and Nagano, Y., 1994, "A New Turbulence Model for Predicting Fluid Flow and Heat Transfer in Separating and Reattaching Flows—I Flow Field Calculations," *International Journal of Heat and Mass Transfer*, 37, 139–151.
- Adeniji-Fashola, A. A., and Chen, C. P., 1989, "Inlet Turbulence Intensity Level and Cross-Stream Distribution Effects on the Heat Transfer in Plane Wall Jets," *International Communication on Heat and Mass Transfer*, 16, 833–842.
- Durbin, P. A., 1991, "Near-Wall Turbulence Models Without Damping Functions," *Theoretical & Computational Fluid Dynamics*, 3, 1–13.
- Gatski, T. B., and Speziale, C. G., 1993, "On Explicit Algebraic Stress Models for Complex Turbulent Flows," *Journal of Fluid Mechanics*, 254, 59–78.
- Henry, F. S., and Reynolds, A. J., 1984, "Analytical Solution of Two Gradient-Diffusion Models Applied to Turbulent Couette flow," *ASME JOURNAL OF FLUIDS ENGINEERING*, 106, 211–216.
- Karlsson, R. I., 1993, "Near-Wall Measurements of Turbulence Structure in Boundary Layers and Wall Jets," *Near-Wall Turbulent Flows*, R. M. C. So, C. G. Speziale and B. E. Launder, eds., Elsevier, pp. 423–432.
- Karlsson, R. I., Eriksson, J., and Persson, J., 1992, "LDV Measurements in a Plane Wall Jet in a Large Enclosure," *Laser Techniques in Fluid Mechanics*, Adrian et al., eds., Springer-Verlag.
- Kim, J., Moin, P., and Moser, R. D., 1987, "Turbulence Statistics in Fully Developed Channel Flow at Low Reynolds Number," *Journal of Fluid Mechanics*, 177, 133–186.
- Kim, J., 1989, "On the Structure of Pressure Fluctuations in Simulated Turbulent Channel Flow," *Journal of Fluid Mechanics*, 205, 421–451.
- Kim, J., 1991, Private communication.
- Kristoffersen, R., Bech, K. H., and Andersson, H. I., 1993, "Numerical Study of Turbulent Plane Couette Flow at Low Reynolds Number," *Applied Scientific Research*, 51, 337–343.
- Lai, Y. G., and So, R. M. C., 1990, "On Near-Wall Turbulent Flow Modeling," *Journal of Fluid Mechanics*, 221, 641–673.
- Launder, B. E., Morse, A., Rodi, W., and Spalding, D. B., 1972, "Prediction of Free Shear Flows—A Comparison of the Performance of Six Turbulence Models," NASA SP-321, 361–426.
- Launder, B. C., Reece, G. J., and Rodi, W., 1975, "Progress in the Development of a Reynolds-Stress Turbulence Closure," *Journal of Fluid Mechanics*, 68, 537–566.
- Launder, B. E., and Sharma, B. I., 1974, "Application of the Energy Dissipation Model of Turbulence to the Calculation of Flow Near a Spinning Disc," *Letters in Heat and Mass Transfer*, 1, 131–138.
- Launder, B. E., and Rodi, W., 1981, "The Turbulent Wall Jet," *Progress in Aerospace Sciences*, 19, 81–128.
- Launder, B. E., and Rodi, W., 1983, "The Turbulent Wall Jet—Measurements and Modeling," *Annual Review of Fluid Mechanics*, 15, 429–459.
- Lee, M. J., and Kim, J., 1991, "The Structure of Turbulence in a Simulated Plane Couette Flow," *Proceedings, 8th Turbulent Shear Flows*, Technical University of Munich, Munich, Germany, Paper 5-3.
- Mathieu, J., 1959, "Contribution à l'étude aérothermique d'un jet plan évoluant en présence d'une paroi," These de Docteur ès Sciences, Université de Grenoble, Grenoble, France.
- Myong, H. K., and Kasagi, N., 1990, "A New Approach to the Improvement of the $k-\epsilon$ Turbulence Model for Wall Bounded Shear Flows," *JSME International Journal Series II*, 33, 63–72.
- Nagano, Y., and Tagawa, M., 1990, "An Improved $k-\epsilon$ Model for Boundary Layer Flows," *ASME JOURNAL OF FLUIDS ENGINEERING*, 112, 33–39.
- Narasimha, R., Narayan, K. Y., and Parthasarathy, S. P., 1973, "Parametric Analysis of Turbulent Wall Jets in Still Air," *The Aeronautical Journal*, 77, 335–352.
- Pope, S. B., 1975, "A More General Effective Viscosity Hypothesis," *Journal of Fluid Mechanics*, 72, 331–340.
- Rubel, A., and Melnik, R. E., 1984, "Jet, Wake and Wall Jet Solutions Using a $k-\epsilon$ Turbulence Model," AIAA Paper No. AIAA-84-1523.
- Sarkar, A., and So, R. M. C., 1997, "A Critical Evaluation of Near-Wall Two-Equation Models Against Direct Numerical Simulation Data," *International Journal of Heat and Fluid Flow*, to appear.
- Schneider, W., 1989, "On Reynolds Stress Transport in Turbulent Couette Flow," *Z. Flugwiss. Weltraumforsch.*, 13, 315–319.
- So, R. M. C., Zhang, H. S., and Speziale, C. G., 1991, "Near-Wall Modeling of the Dissipation-Rate Equation," *AIAA Journal*, 29, 2069–2076.
- So, R. M. C., Zhang, H. S., Gatski, T. B., and Speziale, C. G., 1994, "On Logarithmic Laws for Compressible Turbulent Boundary Layers," *AIAA Journal*, 32, 2162–2168.
- Spalart, P. R., 1988, "Direct Simulation of a Turbulent Boundary Layer up to $Re_\theta = 1410$," *Journal of Fluid Mechanics*, 187, 61–98.
- Speziale, C. G., 1987, "On Nonlinear $K-1$ and $K-\epsilon$ Models of Turbulence," *Journal of Fluid Mechanics*, 178, 459–475.

Speziale, C. G., Abid, R., and Anderson, E. C., 1992, "A Critical Evaluation of Two-Equation Models for Near Wall Turbulence," *AIAA Journal*, 30, 324–331.

Thailand, A., and Mathieu, J., 1967, "Jet Parietal," *Journal de Mecanique*, 6, 103.

Wilcox, W. C., 1993, "Turbulence Modeling for CFD," DCW Industries, Inc., La Canada, CA.

Wilcox, D. C., 1994, "Simulations of Transition with a Two-Equation Turbulence Model," *AIAA Journal*, 32, 247–255.

Wynanski, I., Katz, Y., and Horev, E., 1992, "On the Applicability of Various Scaling Laws to the Turbulent Wall Jet," *Journal of Fluid Mechanics*, 234, 669–690.

Yang, Z., and Shih, T. H., 1993, "New Time Scale Based k - ϵ Model for Near-Wall Turbulence," *AIAA Journal*, 31, 1191–1198.

Strongly-Coupled Multigrid Method for 3-D Incompressible Flows Using Near-Wall Turbulence Closures

F. B. Lin

Project Engineer,
STT Technologies Inc.,
231 Roundtree Dairy Road,
Woodbridge, Ontario L4L8B8
Canada

F. Sotiropoulos

Assistant Professor,
School of Civil and Environmental
Engineering,
Georgia Institute of Technology,
Atlanta, GA 30332

An efficient artificial compressibility algorithm is developed for solving the three-dimensional Reynolds-averaged Navier-Stokes equations in conjunction with the low-Reynolds number $k-\omega$ turbulence model (Wilcox, 1994). Two second-order accurate central-differencing schemes, with scalar and matrix-valued artificial dissipation, respectively, and a third-order accurate flux-difference splitting upwind scheme are implemented for discretizing the convective terms. The discrete equations are integrated in time using a Runge-Kutta algorithm enhanced with local time stepping, implicit residual smoothing, and V-cycle multigrid acceleration with full- and semi-coarsening capabilities. Both loosely and strongly-coupled strategies for solving the turbulence closure equations are developed and their relative efficiency is evaluated. Calculations are carried out for turbulent flow through a strongly-curved 180 deg pipe bend discretized with fine, highly-stretched and skewed meshes. It is shown that the strongly-coupled multigrid algorithm, with semi-coarsening in the transverse plane, is an efficient approach for simulating flows of practical interest with advanced near-wall turbulence closures.

Introduction

Recent work in numerical simulation of complex, three-dimensional, shear flows has clearly underscored the key role of advanced turbulence modeling for successful predictions. In a series of recent papers, Sotiropoulos and Patel (1994, 1995a, 1995b) demonstrated the inadequacy of the wall functions approach, used either in conjunction with isotropic or non-isotropic models, and established the need for careful resolution of the near-wall flow. Their work further demonstrated the necessity to account for anisotropy effects even for flows where three-dimensionality originates via the action of induced pressure gradients.

Adoption of near-wall, multi-equation models, not only increases the number of transport equations to be solved but also necessitates the use of highly-stretched, large-aspect-ratio computational meshes. Typically, at least 3 to 4 grid nodes are required within the laminar sublayer (Sotiropoulos and Patel (1994)) for meaningful predictions. For high-Reynolds-number three-dimensional simulations, however, this requirement increases rapidly the total number of grid nodes and results in computational cells with very large aspect ratios in the vicinity of the wall. Such meshes can dramatically deteriorate the convergence rate of time marching procedures—requiring several thousands of iterations for convergence—due to: (i) severe restrictions on the selection of the local time step, imposed by the very fine near-wall grid spacing; and (ii) numerical stiffness associated with the large disparity between the speeds of waves propagating parallel and normal to the wall (Buelow et al., 1993). Because of these difficulties, advanced near-wall turbulence models may be prohibitively expensive for numerous three-dimensional applications of practical interest, but yet they offer the only alternative for developing predictive CFD techniques within the Reynolds-averaged Navier-Stokes framework.

The challenge, therefore, lies in devising efficient numerical methods, for solving the mean flow and turbulence closure equations, that can effectively handle “stiff” computational meshes.

Multigrid acceleration strategies—originally developed for solving elliptic equations (Brandt, 1977) and subsequently extended to hyperbolic systems (Jameson, 1983, 1985)—offer a very promising alternative for developing such methods. Indeed, a number of very powerful multigrid methods have been recently developed and applied to simulate a wide range of three-dimensional incompressible flows. Farmer et al. (1994) proposed a finite-volume, artificial-compressibility method for simulating viscous flows past ship hulls. They employed second-order accurate central-differencing, with fourth-difference scalar artificial dissipation, for discretizing the convective terms and combined an explicit Runge-Kutta scheme with local time-stepping, implicit residual smoothing, multigrid acceleration, and grid refinement. They reported rapid convergence rates on fine computational meshes (approximately 600,000 grid nodes). A similar approach was proposed by Arnone (1994) for calculating flows through turbomachinery components. Sheng et al. (1994) combined a Newton relaxation method with multigrid acceleration to develop an efficient artificial-compressibility algorithm for external and internal flows. They reported fast convergence rates for a number of external flows past bodies of revolution—requiring 200 to 300 multigrid cycles for convergence to machine zero on meshes consisting of approximately 140,000 nodes. For complex internal flows, however, the efficiency of their method appeared to deteriorate rapidly. All these studies, focused on developing efficient numerical algorithms but overlooked the role of turbulence modeling in predicting three-dimensional flows. In fact, they all employed the algebraic model of Baldwin and Lomax (1978), due to its simplicity and computational expedience, which is not suitable for complex, nonequilibrium shear-flows (see, for example, the discussion in Sotiropoulos and Patel, 1995b). Methods for three-dimensional, incompressible flows that combine multigrid acceleration with multi-equation turbulence models have been proposed, among others, by Claus and Vanka (1990) and Cope et al. (1994),

Contributed by the Fluids Engineering Division for publication in the JOURNAL OF FLUIDS ENGINEERING. Manuscript received by the Fluids Engineering Division September 26, 1995; revised manuscript received October 7, 1996. Associate Technical Editor: S. P. Vanka.

who employed the standard $k-\epsilon$ model, and Demuren (1991), who used a seven-equation Reynolds-stress transport model for closing the mean flow equations. These studies employed SIMPLE-type approaches for achieving pressure-velocity coupling and applied multigrid acceleration only to the mean flow equations—this approach is referred to as “loosely-coupled” treatment. To avoid the resolution of the near-wall flow, all three studies adopted the wall-functions approach which not only does not suffer from the numerical difficulties associated with near-wall modeling but, most importantly, is not adequate for complex, three-dimensional flows (Sotiropoulos and Patel, 1995a). Recently, a number of efficient multigrid methods were proposed for solving compressible flow problems using near-wall, two-equation turbulence models (Martinelli and Mavriplis, 1994, Liu and Zheng, 1994). These studies reported impressive convergence rates on highly stretched meshes but were restricted to two-dimensional applications. Therefore, the effectiveness of multigrid methods for solving the mean flow equations along with near-wall turbulence models in complex, three-dimensional geometries has yet to be demonstrated.

The objective of this study is to develop an efficient, high-resolution method for simulating complex, three-dimensional flows, on fine, highly stretched and skewed computational meshes using near-wall turbulence models. The method employs the incompressible Reynolds-averaged Navier-Stokes (RANS) equations along with the low-Reynolds number $k-\omega$ turbulence closure (Wilcox, 1994) formulated in generalized curvilinear coordinates. The $k-\omega$ model is selected because, currently, it is the only available closure that does not require distance from the wall and, thus, can be readily applied to complex geometrical configurations. Pressure-velocity coupling is achieved using the artificial compressibility method of Chorin (1967). Various approaches for constructing artificial dissipation terms for the convective fluxes—central-difference with

scalar and matrix-valued artificial dissipation, and third-order accurate flux-difference splitting—are implemented and evaluated (see also Lin and Sotiropoulos, 1997). The discrete mean flow and turbulence closure equations are integrated in time in a strongly-coupled fashion using a multistage, Runge-Kutta algorithm (Jameson et al., 1981) in conjunction with local time stepping, implicit residual smoothing, and multigrid acceleration, the term strongly-coupled indicates that multigrid acceleration is applied to the momentum and turbulence closure equations simultaneously. Turbulent flow through a strongly-curved 180 deg pipe bend, for which measurements were reported by Azzola et al. (1986), is used as a test case.

The proposed algorithm is used to investigate a number of issues related to numerical accuracy, computational efficiency, and turbulence closure performance in predictions of complex shear flows. These include, assessment of: (i) the accuracy of various approaches for constructing artificial dissipation terms on highly-stretched and skewed meshes; (ii) the effect of grid coarsening strategies (full vs. semi-coarsening) on multigrid performance—the method has both full (coarsening is applied along all three directions) and semi-coarsening (coarsening is applied along selected spatial directions) capabilities; (iii) the relative efficiency of loosely and strongly-coupled approaches for solving the turbulence closure equations; and (iv) the performance of the low-Reynolds number $k-\omega$ model in a complex, three-dimensional, shear flow. The computed results indicate that the strongly-coupled, multigrid algorithm, with semi-coarsening in the transverse plane, is a very powerful method for obtaining converged (four orders of magnitude reduction of the residuals) solutions on fine, highly skewed and stretched meshes.

In the first section of this paper, the governing mean-flow and turbulence closure equations are formulated in generalized curvilinear coordinates. The second section presents a descrip-

Nomenclature

<p>A^j = Jacobian matrices ($=\partial F^j/\partial Q$)</p> <p>AD = vector containing artificial dissipation terms</p> <p>B = Jacobian matrix ($=\partial H_i/\partial Q$)</p> <p>C = vector containing convective terms</p> <p>V = vector containing diffusion terms</p> <p>C_f = skin-friction coefficient</p> <p>CFL = Courant-Friedrich-Lewis number</p> <p>D^j = artificial dissipation flux in ξ^j direction</p> <p>De = Dean number ($\equiv \text{Re} (d/R_c)^{1/2}$)</p> <p>$d$ = pipe diameter</p> <p>F^j = convective flux vector in ξ^j direction</p> <p>F^j_v = viscous flux vector in ξ^j direction</p> <p>G = production of turbulence kinetic energy</p> <p>g^{ij} = contravariant metric tensor</p> <p>H = source vector</p> <p>\mathcal{H} = implicit residual smoothing operator</p> <p>J = Jacobian of the geometric transformation</p> <p>k = turbulence kinetic energy</p> <p>L_o = reference length ($\equiv d$)</p> <p>p = nondimensional static pressure</p> <p>ϕ = forcing function</p> <p>Q = vector containing pressure, Cartesian velocity components, and turbulence quantities</p> <p>R_c = bend radius of curvature</p>	<p>Re = Reynolds number ($\equiv U_o L_o/\nu$)</p> <p>R_{ij} = mean velocity gradient tensor</p> <p>r = pipe radius</p> <p>S = arc length along pipe centerline, measured from the inlet plane</p> <p>T = restriction operator</p> <p>t = time</p> <p>U_o = reference velocity ($\equiv U_b$)</p> <p>U_b = bulk velocity</p> <p>U^j = contravariant velocity components ($j = 1, 2, 3$)</p> <p>U_θ = streamwise velocity</p> <p>U_r = radial velocity</p> <p>u_i = Cartesian velocity components ($i = 1, 2, 3$)</p> <p>V = vector containing diffusion terms</p> <p>x_i = Cartesian coordinates ($i = 1, 2, 3$)</p> <p>α, α^* = turbulence closure coefficients</p> <p>β, β^* = turbulence closure coefficients</p> <p>β_a = artificial compressibility parameter</p> <p>Δ, δ = difference operators</p> <p>ϵ = artificial dissipation coefficient ($0 < \epsilon < 1$)</p> <p>ϵ_j = implicit residual smoothing coefficient along the jth direction ($j = 1, 2, 3$)</p> <p>θ = circumferential angle measured from the start of curvature</p> <p>ν = kinematic viscosity</p>	<p>ν_t = eddy viscosity</p> <p>ξ^j = curvilinear coordinates ($j = 1, 2, 3$)</p> <p>$\xi_{x_i}^j$ = metrics of the geometric transformation ($i, j = 1, 2, 3$) ($\equiv \partial \xi^j/\partial x_i$)</p> <p>$\rho$ = fluid density</p> <p>ρ_e^j = spectral radius of A^j ($j = 1, 2, 3$)</p> <p>Ω = Von-Neumann number</p> <p>ω = specific dissipation rate</p> <p>Subscripts</p> <p>f = mean flow quantities</p> <p>h = denotes grid level</p> <p>i, j, k = indices in the ξ^1, ξ^2, ξ^3 directions</p> <p>t = turbulence quantities</p> <p>V = denotes viscous fluxes</p> <p>x_j = denotes differentiation along the x_j direction</p> <p>ξ^j = denotes differentiation along the ξ^j direction</p> <p>Superscripts</p> <p>(n) = time level</p> <p>(p) = Runge-Kutta stage</p> <p>T = transpose of a matrix</p> <p>\sim = numerically evaluated flux</p> <p>$+, -$ = denote contributions from positive and negative characteristics, respectively</p>
--	---	---

tion of the numerical method with emphasis on the spatial discretization schemes, time-stepping algorithm, and multigrid acceleration. In the third section, the flow test case along with various computational details (grid resolution, grid dependency studies, boundary conditions, etc.) are first described followed by the presentation and discussion of the computed results.

Governing Equations

Mean Flow Equations. The three-dimensional, incompressible, Reynolds-averaged Navier-Stokes (RANS) equations, nondimensionalized by the fluid density ρ , reference velocity U_o , and reference length L_o , are modified to facilitate the coupling of the velocity and pressure fields by adopting the artificial compressibility approach of Chorin (1967). Boussinesq's assumption is employed to express the Reynolds stresses in terms of the mean rate-of-strain using an isotropic eddy viscosity ν_t . The "pseudocompressible" equations are formulated in strong conservation form and transformed in curvilinear coordinates (ξ^1, ξ^2, ξ^3) . The transformed RANS equations read in compact tensor notation, where repeated indices imply summation, as follows:

$$\frac{1}{J} \frac{\partial Q_f}{\partial t} + \frac{\partial}{\partial \xi^j} (F_f^j - F_{fv}^j) = 0 \quad (1)$$

where J is the Jacobian of the geometric transformation:

$$J = \frac{\partial(\xi^1, \xi^2, \xi^3)}{\partial(x_1, x_2, x_3)} \quad (2)$$

x_i are the Cartesian coordinates, and the vectors Q_f , F_f^j , and F_{fv}^j are defined as follows:

$$Q_f = [P, u_1, u_2, u_3]^T \quad (3)$$

$$F_f^j = \frac{1}{J} [\beta_\alpha U^j, u_1 U^j + P \xi_{x_1}^j, u_2 U^j + P \xi_{x_2}^j, u_3 U^j + P \xi_{x_3}^j]^T \quad (4)$$

$$F_{fv}^j = \frac{1}{J} \left(\nu_t + \frac{1}{\text{Re}} \right) \left[0, g^{mj} \frac{\partial u_1}{\partial \xi^m} + R_{m1} \xi_{x_m}^j, g^{mj} \frac{\partial u_2}{\partial \xi^m} + R_{m2} \xi_{x_m}^j, g^{mj} \frac{\partial u_3}{\partial \xi^m} + R_{m3} \xi_{x_m}^j \right]^T \quad (5)$$

In the above equations, $P \equiv p + 2/3k$, where p is the static pressure and k is the turbulence kinetic energy (for convenience P will be referred to as the pressure), u_i are the Cartesian velocity components, $\xi_{x_j}^i$ are the metrics of the geometric transformation, U^j are the contravariant velocity components ($U^j = u_i \xi_{x_j}^i$), g^{ij} are the components of the contravariant metric tensor ($g^{ij} = \xi_{x_k}^i \xi_{x_k}^j$), and the tensor R_{ij} is defined as follows:

$$R_{ij} = \frac{\partial u_i}{\partial \xi^k} \xi_{x_j}^k \quad (6)$$

Finally, Re is the Reynolds number ($\text{Re} = U_o L_o / \nu$) and ν_t is the eddy viscosity which is expressed in terms of turbulence length and velocity scales as outlined in the subsequent section.

Turbulence Closure Equations. The isotropic, two-equation, low-Reynolds number k - ω model (Wilcox, 1994), where ω is the specific dissipation rate, is employed for turbulence closure. The model equations are transformed in generalized

curvilinear coordinates and formulated in vector form, similar to the mean flow Eqs. (1), as follows:

$$\frac{1}{J} \frac{\partial Q_t}{\partial t} + \frac{\partial}{\partial \xi^j} (F_t^j - F_{tv}^j) + H_t = 0 \quad (7)$$

where the vectors Q_t , F_t^j , F_{tv}^j , and H_t are defined as follows:

$$Q_t = [k, \omega]^T \quad (8)$$

$$F_t^j = \frac{U^j}{J} [k, \omega]^T \quad (9)$$

$$F_{tv}^j = \frac{1}{J} \left[\left(\sigma^* \nu_t + \frac{1}{\text{Re}} \right) g^{mj} \frac{\partial k}{\partial \xi^m}, \left(\sigma \nu_t + \frac{1}{\text{Re}} \right) g^{mj} \frac{\partial \omega}{\partial \xi^m} \right]^T \quad (10)$$

$$H_t = \frac{1}{J} \left[-G + \beta^* k \omega, -\alpha \frac{\omega}{k} G + \beta \omega^2 \right]^T \quad (11)$$

where the production of turbulence kinetic energy G and the eddy viscosity ν_t are given by:

$$G = \frac{1}{2} \nu_t (R_{ij} + R_{ji})^2 \quad (12)$$

$$\nu_t = \alpha^* \frac{k}{\omega} \quad (13)$$

In the above equations α , α^* , β , and β^* are closure coefficients defined as follows (Wilcox, 1994):

$$\alpha^* = \frac{\alpha_o^* + \text{Re}_t/6}{1 + \text{Re}_t/6} \quad (14a)$$

$$\alpha = \frac{5}{9} \frac{1/10 + \text{Re}_t/2.7}{1 + \text{Re}_t/2.7} (\alpha^*)^{-1} \quad (14b)$$

$$\beta^* = \frac{9}{100} \frac{5/18 + (\text{Re}_t/8)^4}{1 + (\text{Re}_t/8)^4} \quad (14c)$$

$$\beta = \frac{3}{40}, \quad \sigma = \sigma^* = \frac{1}{2}, \quad \alpha_o^* = \frac{\beta}{3} \quad (14d)$$

$$\text{Re}_t = \text{Re} \frac{k}{\omega} \quad (14e)$$

The mean flow and turbulence closure equations, Eqs. (1) and (7), respectively, can be coupled together and formulated in vector form as follows:

$$\frac{1}{J} \frac{\partial Q}{\partial t} + \frac{\partial}{\partial \xi^j} (F^j - F_{fv}^j) + H = 0 \quad (15)$$

where:

$$Q = \begin{bmatrix} Q_f \\ Q_t \end{bmatrix}, \quad F^j = \begin{bmatrix} F_f^j \\ F_t^j \end{bmatrix}, \quad F_{fv}^j = \begin{bmatrix} F_{fv}^j \\ F_{tv}^j \end{bmatrix}, \quad \text{and} \quad H = \begin{bmatrix} H_f \\ H_t \end{bmatrix} \quad (16)$$

and H_f is the zero vector of dimension four.

Numerical Method

The system of governing equations (Eq. (15)) is discretized in space using a finite volume procedure and integrated in time via a four-stage Runge-Kutta algorithm enhanced with implicit

residual smoothing, local time stepping, and multigrid acceleration. This section outlines the main features of the proposed numerical method, which include: (i) three artificial dissipation models; (ii) a coupled iterative algorithm for advancing the mean flow and turbulence closure equations in the time; (iii) and multigrid acceleration.

Spatial Discretization and Artificial Dissipation Models.

A semi-discrete approximation of Eq. (15) can be written as follows:

$$\frac{1}{J} \frac{dQ_{i,j,k}}{dt} + \frac{\tilde{F}_{i+1/2,j,k}^1 - \tilde{F}_{i-1/2,j,k}^1}{\Delta\xi^1} + \frac{(F_V^1)_{i+1/2,j,k} - (F_V^1)_{i-1/2,j,k}}{\Delta\xi^1} + \dots + H_{i,j,k} = 0 \quad (17)$$

where for clarity only derivatives in the ξ^1 direction are shown. The viscous fluxes at the cell faces $(F_V^1)_{i\pm 1/2,j,k}$, as well as the velocity derivatives at the cell centers, necessary for calculating the source terms in the turbulence closure equations (see Eq. (12)), are discretized using second-order accurate central-differencing. The convective fluxes $\tilde{F}_{i\pm 1/2,j,k}^1$, on the other hand, can be approximated in the following general manner:

$$\tilde{F}_{i\pm 1/2,j,k}^1 = \frac{1}{2}(F_{i,j,k}^1 + F_{i\pm 1,j,k}^1) + D_{i\pm 1/2,j,k}^1 \quad (18)$$

where $D_{i\pm 1/2,j,k}^1$ is an artificial dissipation flux necessary for eliminating odd-even (grid-scale) oscillations associated with the dispersive three-point central-differencing (obtained from Eq. (18) by setting $D_{i\pm 1/2,j,k}^1 = 0$). Three different approaches for constructing such dissipative flux are considered in this study: (i) third-difference scalar, nonisotropic artificial dissipation with eigenvalue scaling (CDS scheme) (Martinelli (1987), Swanson and Turkel (1987)); (ii) third-difference matrix-valued artificial dissipation (Turkel and Vatsa, 1994); and (iii) flux-difference splitting based upwind differencing (Merkle and Athavale, 1987). The former two approaches, denoted as CDS and CDM, respectively, produce central, second-order accurate discrete approximations of the convective terms with fourth-difference artificial dissipation. The third approach can be used to construct upwind and upwind-biased schemes of any order of accuracy. In the present study, a third-order accurate scheme is employed, denoted as FDS3. A detailed description of these artificial dissipation models and a comprehensive assessment of their accuracy, for three-dimensional laminar flows, can be found in Lin and Sotiropoulos (1997). Due to space considerations only a brief outline of each model is given below:

CDS scheme

$$D_{i+1/2,j,k}^1 = \epsilon \delta_{\xi^1} \{ \phi^1 \delta_{\xi^1} \delta_{\xi^1} \} \left(\frac{Q}{J} \right)_{i+1/2,j,k} \quad (19a)$$

CDM scheme

$$D_{i+1/2,j,k}^1 = \epsilon \delta_{\xi^1} \{ |A^1| \delta_{\xi^1} \delta_{\xi^1} \} Q_{i+1/2,j,k} \quad (19b)$$

FDS3 scheme

$$D_{i+1/2,j,k}^1 = -\frac{1}{6} \{ \delta_{\xi^1} [(A^1)^- \delta_{\xi^1} Q]_{i+1,j,k} + \delta_{\xi^1} [(A^1)^+ \delta_{\xi^1} Q]_{i,j,k} \} \quad (19c)$$

where: ϵ is a positive constant which controls the amount of dissipation; ϕ^1 is a scaling factor along the ξ^1 -coordinate which is proportional to the spectral radius of the Jacobian matrix $A^1 = \partial F^1 / \partial Q$; $\delta_{\xi^1} ()_{i,j,k} = ()_{i+1/2,j,k} - ()_{i-1/2,j,k}$. For more details and the definitions and precise form of the $|A^1|$, and $(A^1)^\pm$ matrices for the incompressible Navier-Stokes equations the reader is referred to Lin and Sotiropoulos (1997).

All three schemes described above are implemented for discretizing the convective terms in the mean flow equations. The turbulence closure equations, on the other hand, are discretized using only the FDS3 scheme—even when central-differencing is employed for the mean flow equations—since upwind differencing was found to enhance the robustness of the iterative procedure. Previous numerical studies using near-wall, two-equation models (Mavriplis and Martinelli, 1994, Sotiropoulos and Patel, 1995b) employed first-order upwind differencing for discretizing the convective terms in the turbulence closure equations. These studies reported that such measure was found necessary in order to eliminate oscillations in the outer part of the boundary layer, where the turbulence quantities drop sharply to their free-stream values, which may cause nonphysical eddy-viscosity values and lead to numerical instability. Despite the use of the non-monotone, third-order accurate upwind scheme, however, no such numerical difficulties were encountered in the present study. This should be attributed to the fact that the flow entering the 180 deg pipe bend, studied herein, is fully-developed and, thus, the turbulence quantities vary smoothly away from the wall. Nevertheless, the proposed method can be readily applied to flows involving developing boundary layers by employing first-order accurate differencing for the turbulence closure equations. As pointed out by Sotiropoulos and Patel (1995b) such measure is not expected to have a significant effect on the overall accuracy of the method since the turbulence closure equations are dominated by their source terms which are, in any case, discretized using second-order accurate central-differencing. One could also construct a monotone, nonoscillatory high-resolution scheme for the convective terms in the k - ω equations by incorporating nonlinear flux limiters (see, for example, Lien and Leschziner, 1994).

Strongly Coupled Runge-Kutta Algorithm. A four-stage Runge-Kutta algorithm is employed to advanced the coupled mean flow and turbulence closure equations (Eq. (15)) in time. To facilitate the description of the iterative procedure let us write the semi-discrete system of governing equations as follows:

$$\frac{1}{J} \frac{dQ}{dt} + C - V - AD + H = 0 \quad (20)$$

where C , V , AD , and H denote discrete approximations of the convective, viscous, artificial dissipation, and source terms. For reasons that are discussed below, the source term H is split into two parts, H_E and H_I , defined as follows:

$$H_E = \frac{1}{J} \left[0, 0, 0, 0, -P, -\alpha \frac{\omega}{k} P \right]^T \quad \text{and} \quad H_I = \frac{1}{J} [0, 0, 0, 0, \beta^* k \omega, \beta \omega^2]^T \quad (21)$$

so that $H = H_E + H_I$. The H_I term contains positive contributions and is treated implicitly, a measure that was found to be essential for obtaining stable solutions with the k - ω turbulence model (see also Liu and Zheng, 1994).

A four-stage Runge-Kutta algorithm, with two evaluations of the viscous and artificial dissipation terms and implicit treatment of the positive part of the source term H_I , can be written as follows (for $p = 1, 2, 3, 4$):

$$Q^{(p)} = Q^{(n)} - \gamma_p \Delta t J (C^{(p-1)} - V^{(k)} - AD^{(k)} + H_e^{(p-1)} + H_i^{(p)}) \quad (22)$$

where $Q^{(1)} \equiv Q^{(n)}$ and $Q^{(4)} \equiv Q^{(n+1)}$, n denotes the current time level, γ_p are the Runge-Kutta coefficients, Δt is the time

increment, and $k = 1$ for $p = 1, 2$ and $k = 3$ for $p = 3, 4$. The implicit part of the source term is linearized in time as follows:

$$H_i^{(p)} = H_i^{(n)} + B^{(p-1)} \Delta Q^p \quad (23)$$

where B is the Jacobian matrix $B = \partial H_i / \partial Q$:

$$B = \frac{1}{J} \begin{pmatrix} 0 & 0 & 0 & 0 & 0 & 0 \\ 0 & 0 & 0 & 0 & 0 & 0 \\ 0 & 0 & 0 & 0 & 0 & 0 \\ 0 & 0 & 0 & 0 & 0 & 0 \\ 0 & 0 & 0 & 0 & \beta^* \omega & \beta^* k \\ 0 & 0 & 0 & 0 & 0 & 2\beta \omega \end{pmatrix} \quad (24)$$

and

$$\Delta Q^p = Q^{(p)} - Q^{(n)} \quad (25)$$

Incorporating Eq. (23) into Eq. (22), the following point-implicit, Runge-Kutta algorithm is obtained (for $p = 1, 2, 3, 4$):

$$Q^{(p)} = Q^{(n)} - \gamma_p \Delta t J (I + \gamma_p \Delta t J B^{(p-1)})^{-1} R^{(p-1)} \quad (26)$$

where R is the residual vector defined as:

$$R^{(p-1)} = C^{(p-1)} - V^{(k)} - AD^{(k)} + H_E^{(p-1)} + H_i^{(n)} \quad (27)$$

The calculation of the right-hand side of Eq. (26) requires the inversion of a simple matrix (see Eq. (24)) which can be carried out analytically.

The stability limit and the robustness of the iterative algorithm, given by Eq. (26), can be further enhanced by implementing the implicit residual smoothing procedure proposed by Jameson et al. (1981). Incorporating the implicit smoothing operator in Eq. (26), and using Eq. (25), the following Runge-Kutta procedure is obtained (for $p = 1$ to 4):

$$g[\Delta Q^{(p)}] = -\gamma_p \Delta t J (I + \gamma_p \Delta t J B^{(p-1)})^{-1} R^{(p-1)} \quad (28a)$$

$$Q^{(p)} = Q^{(n)} + \Delta Q^p \quad (28b)$$

where g is the implicit residual smoothing operator defined as follows (Jameson et al., 1981):

$$g[\] = (1 - \epsilon_1 \delta_\xi^1 \xi^1) (1 - \epsilon_2 \delta_\xi^2 \xi^2) (1 - \epsilon_3 \delta_\xi^3 \xi^3) [\] \quad (29)$$

ϵ_i are positive constants of order one, and $\delta_\xi^i \xi^i$ is the three-point, central, finite-difference operator for the second derivative.

Since only steady-state solutions are of interest, local time stepping is employed to further accelerate the convergence. The value of the time increment at every grid node is calculated as follows:

$$\Delta t_{i,j,k} = \min \left\{ \frac{\text{CFL}}{\max(\rho_\xi^1, \rho_\xi^2, \rho_\xi^3)_{i,j,k}}, \text{Re} \frac{\Omega}{\max(g^{11}, g^{22}, g^{33})_{i,j,k}} \right\} \quad (30)$$

where CFL is the Courant-Friedrich-Lewis number, Ω is the Von-Neumann number, and ρ_ξ^j are the spectral radii of the Jacobian matrices A^j ($j = 1, 2, 3$).

Multigrid Acceleration Technique. A typical multigrid method applies an iterative scheme (the so-called smoother) with good smoothing properties of the high-frequency components of the error to successively coarser grids. Since coarser meshes allow the use of larger time steps, the resulting algorithm can efficiently damp the entire spectrum of error frequencies, thus, yielding rapid convergence rates. Perhaps the most attractive feature of the multigrid method is that, when properly formulated, its convergence rate does not depend on the size of the system to be solved (Hirsch, 1990). It is, therefore, especially useful for simulating three-dimensional turbulent flows

of practical interest whose accurate resolution requires the use of very fine computational grids. In the present study, the non-linear Full Approximation Scheme (FAS) proposed by Brandt (1977) is employed in conjunction with the multigrid strategy developed by Jameson (1983, 1985), for the solution of the Euler equations, and applied to the coupled system of mean flow and turbulence closure equations.

The previously described Runge-Kutta algorithm (Eqs. (28)), with coefficients: $\gamma_p = \frac{1}{4}, \frac{1}{3}, \frac{1}{2}, 1$, for $p = 1, 2, 3, 4$ respectively, is employed as the basic smoother. A series of successively coarser grids is constructed by doubling the grid spacing either along all three spatial directions (full-coarsening strategy) or along only some spatial coordinates (semi-coarsening). Starting with an estimate of the solution on the finest mesh, the flow variables are transferred (or restricted) to the coarser grid using injection, that is, a transfer operator $T_{h,2h}^s$ which picks flow variables at alternate points to define coarse grid flow data as well as the coarse grid coordinates:

$$Q_{2h}^{(n)} = T_{2h,h}^s Q_h \quad (31)$$

where the subscripts h and $2h$ denote fine and coarse mesh values, respectively. To ensure that the coarse grid solution is driven by fine mesh residuals—so that the reduced coarse-mesh accuracy does not contaminate the accuracy of the fine-mesh solution—the equations solved on the coarse mesh are modified by including a forcing term ϕ_{2h} defined as follows (Jameson, 1985):

$$\phi_{2h} = T_{2h,h}^r R_h(Q_h) - R_{2h}(Q_{2h}^{(n)}) \quad (32)$$

where $T_{h,2h}^r$ is the residual restriction operator which computes a coarse grid residual by averaging the fine-grid residuals over the 27 fine-mesh nodes surrounding a coarse-mesh node (Jameson, 1985). The solution on the coarse mesh is then advanced in time using the Runge-Kutta algorithm in conjunction with implicit residual smoothing (Eq. (28)) as follows (for $p = 1, 2, 3, 4$):

$$Q_{2h}^{(p)} = Q_{2h}^{(n)} - \gamma_p \Delta t J g^{-1} \times (I + \gamma_p \Delta t J B_{2h}^{(p-1)})^{-1} (R_{2h}^{(p-1)} + \phi_{2h}) \quad (33)$$

Once the coarsest grid is reached, the accumulated corrections are transferred (or prolonged) back to the finest grid using a series of simple trilinear interpolations on successively finer grids. On highly stretched meshes, this interpolation procedure (which is carried out in the transformed, equally-spaced, computational domain) may introduce high-frequency errors back to the fine-mesh and result in degradation of the convergence rate. To eliminate such errors, the corrections on a given coarse mesh are processed through the constant-coefficient, implicit residual smoothing operator given by Eq. (29) before using them to update the solution on the finer mesh.

A three-level V -cycle with subiterations is used in the present study for each time step on the finest mesh. One iteration is performed on the h grid, two on the $2h$ grid, and three on the $4h$ grid. Also the convective terms on all coarse meshes are discretized using first-order accurate upwind differencing. This step does not affect the fine-mesh accuracy—the formulation of the coarse-mesh equations (see Eq. (33)) guarantees that coarse-mesh corrections are driven by fine-mesh residuals—but it enhances the robustness of the overall algorithm.

The turbulence closure equations are driven primarily by their source terms. It is, therefore, essential that these terms are represented accurately on the coarse meshes in order to maintain rapid convergence rate. Obviously, the production term G defined by Eq. (12) cannot be resolved correctly on a coarse mesh since it involves velocity gradients which become very large in the vicinity of the wall. For that reason, the velocity gradient terms in Eq. (12) are computed only on the finest mesh and restricted by injection to all coarse meshes where they are kept

frozen throughout the multigrid cycle. The eddy-viscosity, however, is updated continuously at all grids at the end of every Runge-Kutta stage. This step is essential for the overall multigrid efficiency as the eddy-viscosity provides the only coupling between mean flow and turbulence closure equations.

Strongly Versus Loosely Coupled Algorithms. The algorithm outlined above is a strongly coupled solution procedure since residual smoothing and multigrid acceleration are applied simultaneously to both the mean flow and turbulence closure equations. The other alternative for simulating turbulent flows, which has been widely used in the literature (Mavriplis and Martinelli, 1994; Liu and Zheng, 1994; Demuren, 1991), is the so-called loosely-coupled approach in which multigrid acceleration is applied to the mean flow equations (Eq. (1)) while the turbulence closure equations (Eq. (7)) are solved only on the finest mesh. The four-stage Runge-Kutta procedure, used for the strongly-coupled algorithm (Eq. (28)), is also employed for the loosely-coupled variant of the method but it is applied separately to the mean flow (with $B = 0$) and turbulence closure equations (with $B = \partial H_i / \partial Q_i$). Moreover, the eddy-viscosity is updated only on the fine grid and kept frozen on all coarse meshes during the multigrid cycle. Since the mean flow equations are advanced in time at a much faster rate, due to the use of multigrid acceleration, performing only one fine-mesh iteration for the turbulence closure equations results in significant deterioration of the overall convergence rate. For that reason at the end of every multigrid cycle for the mean flow equations several fine-mesh iterations are performed on the turbulence closure equations (Liu and Zheng, 1994). Typically 3 to 4 iterations were found to produce optimal results.

It should be emphasized that the loosely-coupled approach was found to be particularly useful for obtaining a well conditioned initial guess for the strongly-coupled algorithm. The latter is sensitive to the initial guess and its implementation can lead to numerical instability during the early stages of the calculation. The loosely-coupled algorithm, on the other hand, is more robust during the initial stages and is always employed to start the computation. Typically 50 loosely-coupled multigrid cycles are carried out before the strongly-coupled procedure is activated.

Results and Discussion

Test Case and Computational Mesh. Turbulent flow through a strongly curved 180 deg pipe bend ($R_c/d = 3.375$) is selected as the test case to evaluate the efficiency and accuracy of the proposed method. This case corresponds to the experiment of Azzola et al. (1986) who reported laser-Doppler measurements of the longitudinal and circumferential mean velocity components at various streamwise sections within the bend as well as in the upstream and downstream tangents. The measurements were conducted at two Reynolds numbers, $Re = 57,400$ and $110,000$ ($Re = U_b d / \nu$, where U_b is the bulk velocity), with corresponding Dean numbers $De = 31,300$ and $59,900$, respectively. The upstream tangent extends approximately 55 pipe diameters so that the flow near the entrance of the bend is fully developed. The experimental data (Azzola et al., 1986) indicate that the strong longitudinal curvature of the bend induces an intense secondary flow—circumferential mean velocity components as high as 30 percent of the bulk velocity were recorded in the first half of the bend—which distorts the streamwise flow and results in a very complex shear flow. A rather significant feature of the measurements is the double reversal of the direction of the secondary motion that takes place in the second half of the bend, a trend which indicates the existence of two, counter-rotating, secondary motion cells in each symmetrical half section of the bend.

Calculations are carried out only for $Re = 57,400$ as this is the case for which Azzola et al. reported the most complete

set of measurements. The computational domain, curvilinear coordinates, related nomenclature, and views of the computational mesh employed in this study are shown in Fig. 1—in this as well as in all subsequently presented figures all lengths are scaled by the pipe diameter d . Note that due to the symmetry of the incoming flow, only half of the bend cross section is considered. The upstream boundary is located at $x_h = -3$ while the downstream boundary is placed at $x_h = 8$. The computational grid is generated using an algebraic grid generation method. The grid nodes are clustered near the pipe walls using the hyperbolic stretching function. Typically 3 to 4 grid nodes are located within the laminar sublayer ($n^+ = nu_\tau / \nu < 5$, where n is the normal distance from the wall, and u_τ is the shear velocity) with the first grid surface off the wall located at $n^+ \approx 1$.

The inlet velocity and turbulence quantities profiles are obtained by carrying out a separate calculation for fully-developed flow through a long circular pipe. At the exit boundary all quantities are calculated by assuming zero streamwise diffusion. On the plane of symmetry, zero gradient boundary conditions are employed for all variables except the vertical velocity component which is set equal to zero. On the solid wall, the velocity components and turbulence kinetic energy are set equal to zero while ω is calculated using the boundary condition proposed by Menter (1994). The pressure at all boundaries is computed using linear extrapolation from the interior of the solution domain.

Before proceeding with the presentation and discussion of the results it is important to emphasize the reasons why this particular test case was selected. Previous work with multigrid methods has clearly demonstrated that the performance of a multigrid algorithm is inversely proportional to flow complexity and three-dimensionality (Sheng et al., 1994). Therefore, a meaningful evaluation of the proposed algorithm should be carried out for a complex flow case which exhibits most features encountered in flows of practical interest. Yet another complicating feature of the selected test case, which makes it even more challenging for the robustness and efficiency of any numerical method, is the topology of the computational mesh which produces highly-skewed grid lines near the corners of the pipe cross-section (see Fig. 1). Finally, the flow through the bend of Azzola et al. (1986) has been previously computed by Azzola et al. (1986) and Sotiropoulos and Patel (1992), both using two-layer, $k-\epsilon$ closures. The present predictions, therefore, would gauge the performance of the $k-\omega$ model relative to two-layer $k-\epsilon$ models for a complex, three-dimensional, shear flow.

Grid Sensitivity Study. To investigate the grid sensitivity of the computed solutions, calculations are carried out on two meshes: a coarse grid with $105 \times 81 \times 41$ nodes (total of 350,000), and a fine grid with $151 \times 97 \times 49$ nodes (total of 717,703 nodes), in the ξ^1 , ξ^2 , and ξ^3 directions, respectively. All three spatial discretization schemes, CDS, CDM, and FDS3, are employed on the coarse grid while, for reasons discussed subsequently, only the latter two are used on the fine grid. The results of the grid sensitivity study are reported in terms of skin-friction ($C_f = 2u_\tau^2$) distributions (Figs. 2 and 3), plotted along the inner and outer walls of the bend on the plane of symmetry.

On the coarse mesh, Fig. 2(a), all three discretization schemes produce essentially the same qualitative skin-friction distributions, but significant quantitative differences are observed particularly along the inner wall within the bend and the downstream tangent. The CDM and FDS3 schemes produce very similar results but the CDS predictions appear to be consistently lower almost everywhere along the two walls. Along the inner wall, in particular, the CDS scheme predicts substantially lower skin-friction values within the bend and near the start of the downstream tangent. On the fine mesh, Fig. 2(b), the differences between the FDS3 and CDM predictions diminish almost entirely. This trend, which should be expected for consistent discretization schemes, suggests that the solutions obtained

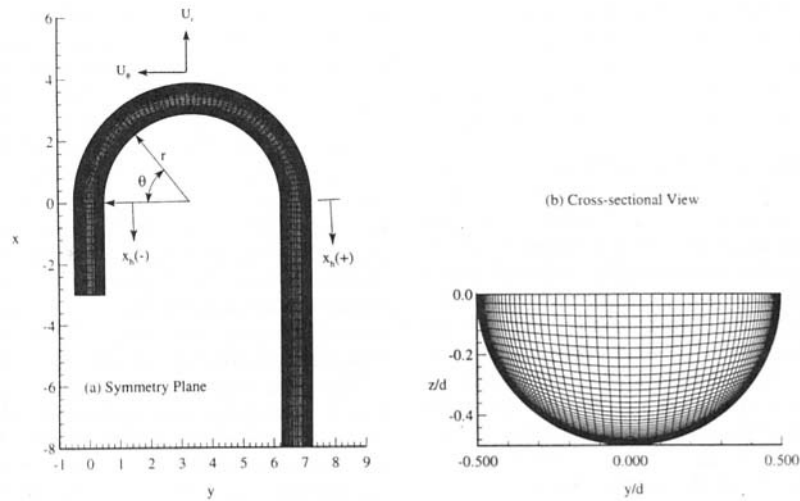
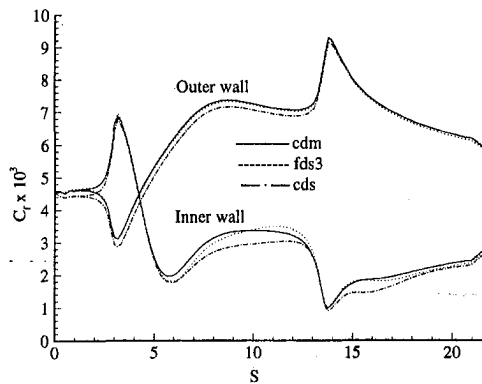


Fig. 1 Curvilinear coordinates and computational grid for the 180 deg pipe bend

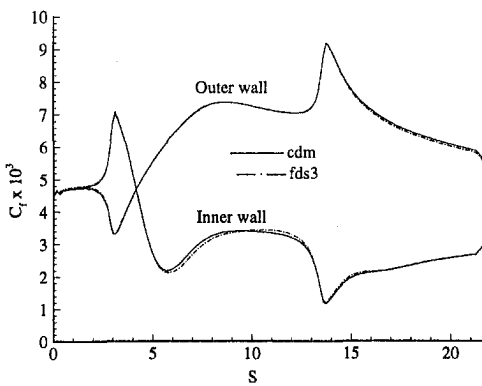
on the fine mesh are nearly grid independent, since two schemes with different truncation errors appear to converge toward the same solution. We can, therefore, consider the solution obtained on the fine mesh as the “exact” solution of the discrete equations and use it to assess the grid sensitivity of the various discretization schemes. Obviously this is not strictly true since the differences between the two fine grid solutions suggest that an even finer mesh would be necessary for establishing grid independence in a rigorous fashion. Nevertheless, the fine grid

solutions are sufficiently close (see also Fig. 3) to support such an assumption—in fact, the FDS3 and CDM fine mesh predictions differ no more than 5 percent as compared to differences as high as 12 percent on the coarse mesh.

Figure 3 shows the variation of the percentage error, between the coarse mesh skin-friction predictions and the “exact” solution, along the inner and outer walls of the bend on the plane of symmetry— $E_{C_f} = 100(C_f - C_f^*)/C_f^*$, where C_f^* denotes the “exact” solution considered to be the CDM prediction on

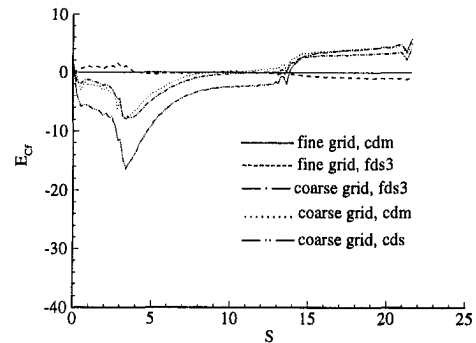


(a)

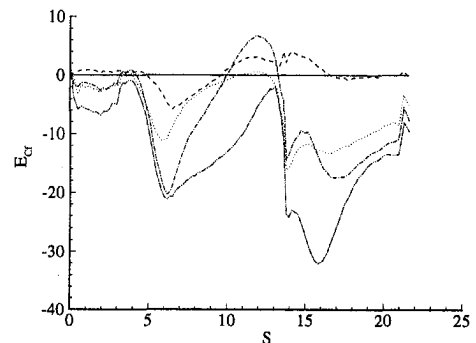


(b)

Fig. 2 Calculated C_f distributions, along the inner and outer walls, with various artificial dissipation models: (a) coarse mesh; (b) fine mesh



(a)



(b)

Fig. 3 Effect of grid refinement and artificial dissipation model on skin-friction percentage error distributions: (a) inner wall; (b) outer wall

the fine mesh. A general observation is that the skin-friction predictions along the outer wall are significantly less sensitive to grid resolution and accuracy of the spatial discretization scheme as compared to those along the inner wall. This trend should be attributed to the fact that the flow in the vicinity of the inner wall is greatly affected by the strong secondary motion whose intensity is obviously very sensitive to grid resolution. The coarse grid CDS prediction is very inaccurate with errors as high as 32 percent observed near the start of the downstream tangential along the inner wall. For that reason and to save computational resources, the CDS scheme is not pursued any further in the present study. The CDM scheme, on the other hand, appears to produce the most accurate solution on the coarse mesh. Its maximum error does not exceed 16 percent, as compared to 21 percent for the FDS3 scheme. It can be concluded, therefore, that the matrix dissipation model is, in terms of accuracy, the best choice for simulating three-dimensional flows, on highly-stretched and skewed meshes. Similar conclusions were reported by Turkel and Vatsa (1994), who compared the scalar and matrix-valued dissipation models for transonic flows past three-dimensional wings, and Lin and Sotiropoulos (1995), for laminar flow calculations. Finally, it is important to point out that the CDM and FDS3 fine grid solutions are almost identical along the outer wall of the bend (differences less than 2 percent) and within 5 percent of each other along the inner wall.

Convergence Properties and Computational Efficiency.

All calculations discussed in this section were carried out starting from the same initial conditions. The Courant-Friedrich-Lewis number, for all cases, is $CFL = 3.0$ while the Von-Neumann number is set to $\Omega = 1.5$. The pseudocompressibility parameter is set to $\beta_\alpha = 1$. The residual smoothing coefficients used to smooth fine grid residuals as well as those used during prolongation, to smooth the coarse mesh residuals before adding them to the fine mesh, are set equal to unity in all three directions. The artificial dissipation parameter ϵ , for the CDM scheme, is set equal to $\epsilon = 0.004$. Finally, the work unit, used in Figs. 6 and 7, is based on the CPU time required for one iteration of the single grid algorithm using the FDS3 scheme. The residual used in the subsequently presented figures is defined as follows:

$$\text{Average Pressure Residual} = \frac{\sum_{N=1}^{N_{\max}} |\Delta P_N^{(n)}|}{\sum_{N=1}^{N_{\max}} |\Delta P_N^{(o)}|}$$

where N_{\max} is the total number of grid nodes, (n) denotes iteration level ($n \equiv o$ denotes initial values) and $\Delta P_N^{(n)} = P_N^{(n+1)} - P_N^{(n)}$.

Figure 4 compares the convergence histories for the single and multigrid methods. The single grid algorithm is employed only in conjunction with the FDS3 scheme on the coarse mesh. The convergence of the multigrid method, on the other hand, is reported for both discretization schemes and meshes. It should be pointed out that all multigrid convergence histories shown in this figure are obtained using the strongly-coupled algorithm with coarsening applied only in the cross-plane (semi-coarsening). It is seen that regardless of discretization scheme and mesh size, the multigrid algorithm converges at approximately the same rate. Converged, to plotting scale, solutions are obtained after the residuals have dropped by approximately four orders of magnitude—this is demonstrated in Fig. 5, which shows the convergence history of the skin-friction distribution along the inner and outer walls of the bend at the plane of symmetry. This convergence level is achieved within 800 (average residual reduction rate of 0.988) and 900 (average residual reduction rate of 0.989) multigrid cycles on the coarse and fine meshes, respectively. The single grid algorithm, on the other hand, converges at a dramatically slower rate as the residual

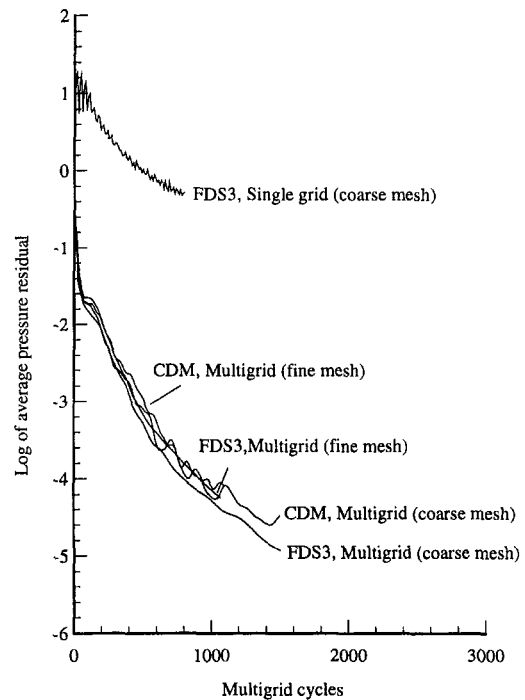


Fig. 4 Convergence histories for the single and multi-grid algorithms

drops by only 1.2 orders of magnitude after 800 time steps. Due to the excessive computational resources that would be required to reach convergence, the calculations were stopped after 800 time steps. Comparison of the solution at this point with the converged multigrid solution indicates that the single grid algorithm would require several thousands of iterations to reach steady state. This is also evident from the continuously declining slope of the single-grid convergence curve. It can be estimated from the figure, for instance, that about 3000 time steps are necessary for achieving a two-order of magnitude residual reduction. Regarding the effect of artificial dissipation on multigrid performance, it is seen that both schemes converge at similar rates but the FDS3 scheme exhibits a somewhat more monotonic (wobble-free) convergence history. In a previous study by the authors (Lin and Sotiropoulos, 1997), which assessed the relative performance of the two schemes for laminar flow through a curved duct, it was also reported that both CDM and FDS3 schemes require approximately the same number of cycles to reduce the residual by four orders of magnitude. However, the CDM scheme slowed down beyond that point never reaching machine zero which was achieved by the FDS3 scheme. Although the present calculations were not continued long enough, a similar trend is visible in Fig. 4 as the CDM scheme appears to slow down, somewhat, beyond 1000 cycles.

The effect of grid-coarsening on the efficiency of the strongly-coupled multigrid algorithm is shown in Fig. 6, which depicts the convergence histories for full- and semi-coarsening strategies using the FDS3 scheme (similar trends were observed with the CDM scheme as well). Both coarsening strategies converge at exactly the same rate during the first 800 work units. Beyond this point, however, the full-coarsening algorithm slows down significantly and requires approximately 1800 work units to reduce the residual by four orders of magnitude. Semi-coarsening, on the other hand, produces a monotonic convergence curve and requires approximately 80 percent less work to achieve convergence. It is evident, therefore, that semi-coarsening increases significantly the performance of the multigrid algorithm (see also Sheng et al., 1994). This is presumably due to the fact that for geometries such as the pipe bend considered herein, where the grid spacing in the streamwise direction is

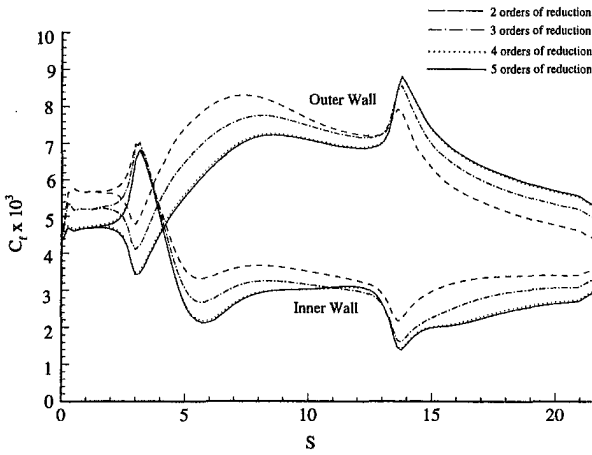


Fig. 5 Convergence of the C_f distributions along the inner and outer walls at the plane of symmetry

more or less uniform, semi-coarsening produces coarse meshes with reduced cell aspect-ratios. For the curved pipe test case, for instance, semi-coarsening yields maximum aspect ratios ranging from 163, for the coarsest grid level, to 850, for the finest grid level (the corresponding minimum aspect ratios are 1.1 and 4.2, respectively). The aspect ratios of the coarsest grid obtained via full-coarsening, on the other hand, are significantly larger ranging from 4.5 to 650.

Finally, the relative performance of the loosely and strongly-coupled (SC) procedures for solving the turbulence closure equations can be gauged from Fig. 7. The convergence histories shown in this figure have been obtained using the CDM scheme but similar results were also obtained with the FDS3 scheme. For the loosely-coupled (LC) algorithm, three iterations are carried out on the finest grid for the turbulence closure equations at the end of every multigrid cycle for the mean flow equations. The work unit used in this figure has been appropriately scaled, according to CPU time, to account for this additional computational overhead. Obviously, adopting a strongly-coupled treatment enhances the efficiency of the multigrid algorithm. With

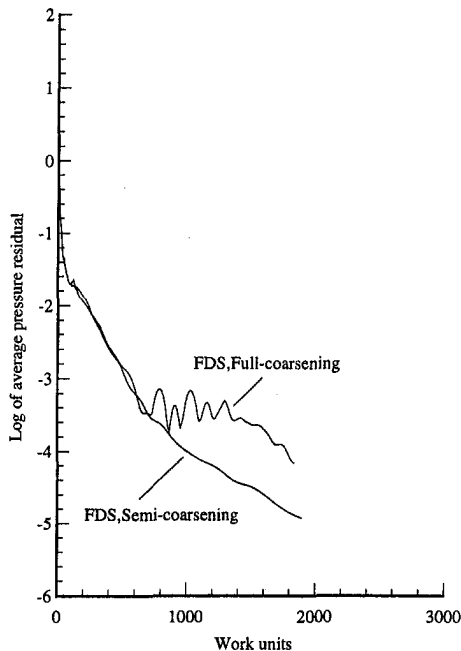


Fig. 6 Effect of grid-coarsening on multigrid performance

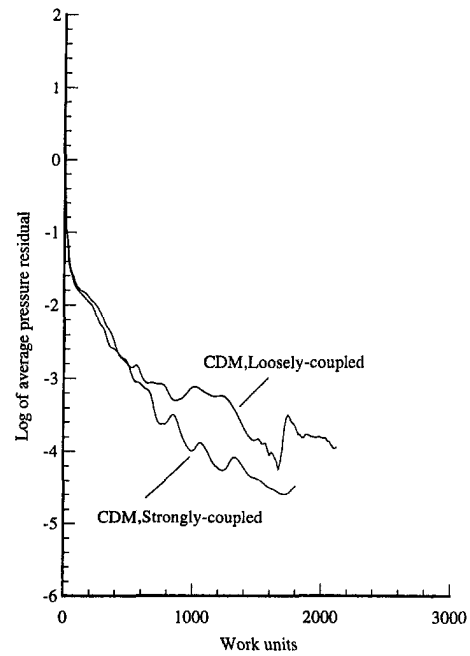


Fig. 7 Loosely versus strongly-coupled multigrid approaches for solving the turbulence closure equations

the strongly-coupled treatment convergence is achieved within 1000 work units while the loosely-coupled approach requires more than 1600 work units to reach a similar level of convergence.

Comparisons With Experimental Measurements. Figure 8 compares the calculated, on the fine mesh, and measured (Azzola et al., 1986) streamwise and circumferential mean velocity profiles at various longitudinal locations within the bend and in the upstream and downstream tangents. These profiles are plotted along the vertical radius from the pipe center to the wall. The velocity profiles obtained using the FDS3 scheme are practically indistinguishable from the CDM predictions and, thus, only the latter are included in the figure.

The predicted streamwise velocity profiles (Fig. 8(a)) are in good agreement with the measurements at all locations. An interesting feature exhibited by the measurements, and reproduced by the calculations, is the reduction of streamwise velocity in the core of the cross-section (near the center of the pipe) for $\theta > 45$ deg. This trend is associated with the pressure-

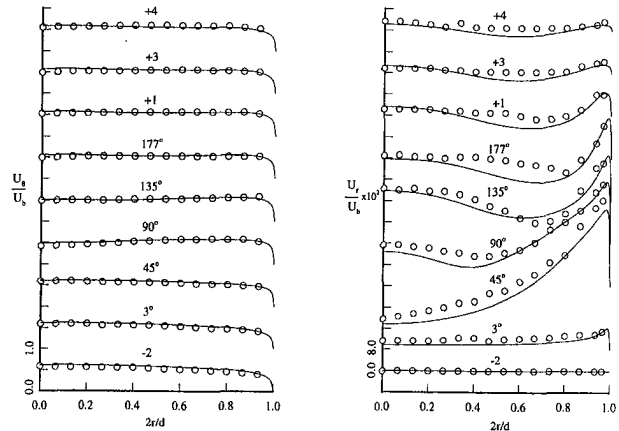
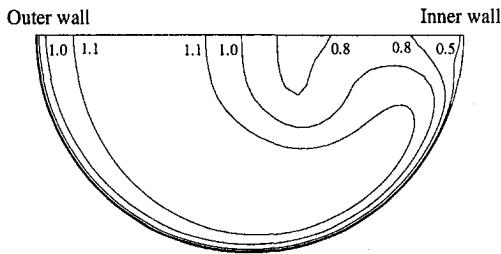


Fig. 8 Measured and calculated mean velocity profiles along the vertical radius: \circ , measurements (Azzola et al., 1986); ---, calculation (a) streamwise mean velocity; (b) circumferential mean velocity



→ 0.1

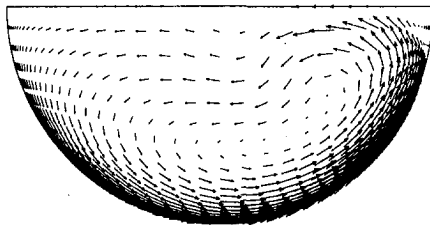
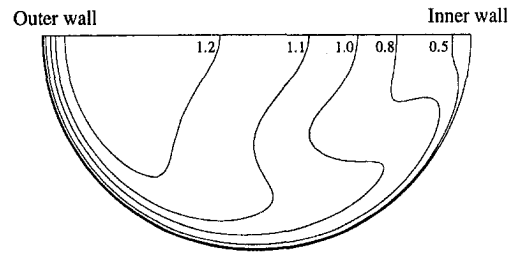


Fig. 9(a) $\theta = 90$ deg



→ 0.1

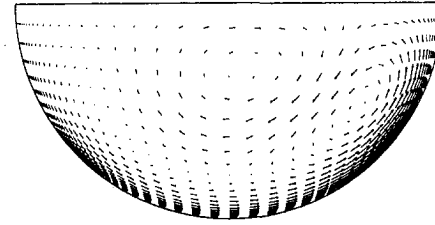
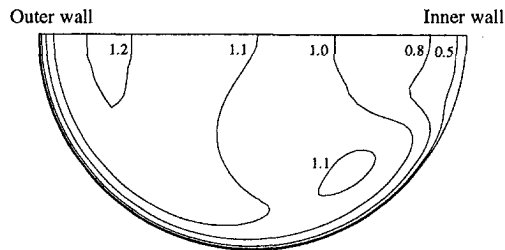


Fig. 9(c) $x_n = +3$



→ 0.1

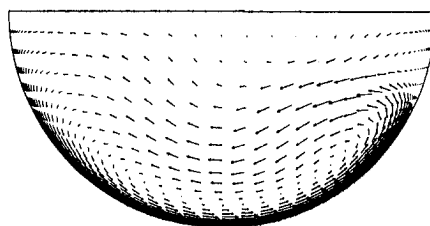


Fig. 9(b) $\theta = 177$ deg

Fig. 9 Calculated mean streamwise velocity contours and secondary flow vectors

driven secondary motion which acts to displace high-speed fluid toward the outer wall of the bend by accumulating low-speed, near-wall fluid near the inner wall. As seen in Fig. 8(b), this secondary motion is very intense with measured circumferential velocities exceeding 30 percent of the bulk flow near the wall at the $\theta = 45$ deg station. Furthermore, the measurements indicate that for $\theta > 45$ deg the secondary motion near the pipe centerline first comes to a halt (see $\theta = 90$ deg station) and eventually reverses its sign, which suggests the formation of two counter-rotating vortical cells. The calculations capture reasonably well the overall experimental trends including the sign reversal of the circumferential velocity component near the center of the flow. The most serious discrepancies are observed at the $\theta = 177$ deg station where the calculations exhibit a much larger, as compared with the measurements, region of negative circumferential velocity component.

The present predictions are broadly similar to previously reported calculations for the same test case (Azzola et al., 1986, Sotiropoulos and Patel, 1992) but exhibit a somewhat better agreement with the measurements. More specifically, the reduction of streamwise velocity near the centerline at $\theta = 90$ deg and the overall evolution of the circumferential velocity profiles between the $\theta = 90$ and 177 deg stations are captured more accurately in the present simulations. To obtain a more global picture of the predicted flowfield and facilitate a more comprehensive comparison with previous numerical results, the calculated contours of mean streamwise velocity and cross-flow vectors are plotted at three streamwise stations in Fig. 9. Similar plots can be found in Azzola et al. (1986) and Sotiropoulos and Patel (1992). In general, the present simulations indicate a greater distortion of the streamwise flow near the inner wall of the bend and higher overall velocities near the outer wall, both trends suggesting a more intense predicted secondary motion. Although the only experimental data available are these shown in Fig. 9, the improvements achieved in the prediction of both the streamwise and tangential velocity profiles suggest that the present results are somewhat closer to reality, at least in a qualitative sense, than the previously reported calculations. It is not clear, however, whether these improvements should be attributed to the $k-\omega$ turbulence closure (both previous studies employed two-layer $k-\epsilon$ models) or to the substantially finer mesh employed in the present study (717,000 grid nodes as compared to about 100,000 nodes used in Azzola et al. (1986) and 150,000 in Sotiropoulos and Patel (1992)). To resolve these issues a more comprehensive numerical study would be required which would eliminate numerical uncertainties so that the performance of the various turbulence models can be assessed fairly (Sotiropoulos and Patel, 1995b). This, however, is beyond the scope of the present work.

Summary and Conclusions

An efficient multigrid method for solving the three-dimensional RANS equations in conjunction with the low Reynolds number $k-\omega$ model is developed and validated. The method features three different spatial discretization schemes, strongly-

and loosely-coupled procedures for solving the turbulence closure equations, and has both full- and semi-coarsening capabilities. Calculations are carried out for flow through a 180 deg pipe bend and the results are compared with measurements and analyzed to assess the accuracy and efficiency of the proposed method.

The proposed strongly-coupled multigrid algorithm with semi-coarsening in the transverse plane is an efficient and robust method for obtaining solutions on the fine, highly-stretched and skewed grid employed herein. Convergence (four orders of magnitude reduction of the residuals) was achieved within approximately 800 to 900 multigrid cycles on both meshes employed. Solving the turbulence closure equations in a loosely-coupled manner, on the other hand, deteriorates the convergence rate but it is more robust during the initial stages of the iterative procedure and can, thus, be used to initialize the strongly-coupled algorithm.

The present study demonstrates that multigrid acceleration is a promising approach for simulating three-dimensional shear flows of practical interest with advanced, near-wall turbulence models. However, more work is needed to further explore the capabilities and establish the generality of the proposed algorithm by applying it to calculate a wide range of complex, three-dimensional flows. Such studies are currently underway and their results will be reported in future publications.

Regarding numerical accuracy, the matrix-valued artificial dissipation model offers the best alternative for discretizing the convective fluxes on highly-stretched and skewed meshes without significant degradation of the convergence rate. Finally, the $k-\omega$ model appears to capture most experimental trends with fair accuracy. Comparisons with previous numerical results for the same test case indicate that the present calculations are in somewhat better overall agreement with the measurements. It is not clear, however, whether these improvements should be attributed to the turbulence closure or to the substantially finer grids employed in this study.

Future work should focus on extending the proposed multigrid method to include more general turbulence models that account for turbulence anisotropy (nonlinear eddy-viscosity models or Reynolds-stress transport models). These models are necessary for accurate predictions of most three-dimensional flows and their implementation in conjunction with efficient iterative algorithms is essential for establishing them as practical engineering tools.

Acknowledgments

This work was partly supported by Grant County Public Utility District No. 2 (Ephrata, Washington) and Chellan County Public Utility District No. 1 (Wenatchee, Washington) while both authors were at the Iowa Institute of Hydraulic Research, The University of Iowa, Iowa City, Iowa. The second author also acknowledges support provided by the School of Civil and Environmental Engineering, Georgia Institute of Technology, Atlanta, Georgia. All computations were carried out on the Cray-C90 supercomputer at the San Diego Supercomputer Center.

References

Amone, A., 1994, "On the Use of Multigrid in Turbomachinery Calculations," *Proceedings of CERCA International Workshop on Solution Techniques for Large-Scale CFD Problems*, Montreal, Quebec, Canada.

- Azzola, J., Humphrey, J. A. C., Iacovides, H. and Launder, B. E., 1986, "Developing Turbulent Flow in a U-Bend of Circular Cross-Section: Measurements and Computation," *ASME JOURNAL OF FLUIDS ENGINEERING*, Vol. 108, pp. 214-226.
- Baldwin, B. S. and Lomax, H., 1978, "Thin Layer Approximation and Algebraic Model for Separated Turbulent Flows," AIAA paper 78-257.
- Brandt, A., 1977, "Multi-Level Adaptive Solutions to Boundary-Value Problems," *Mathematics of Computation*, Vol. 31, No. 138, pp. 333-390.
- Buelow, P. E. O., Venkaterwaran, S., and Merkle, C. L., 1993, "The Effect of Grid Aspect Ratio on Convergence," AIAA-93-3367, *Proceedings of 11th AIAA Computational Fluid Dynamics Conference*, July 6-9, Orlando, FL.
- Chorin, A. J., 1967, "A Numerical Method for Solving Incompressible Viscous Flow Problems," *Journal of Computational Physics*, Vol. 2, No. 1, pp. 12-26.
- Claus, R. W., and Vanka, S. P., 1990, "Multigrid Calculations of a Jet in Crossflow," AIAA Paper-90-0444.
- Cope, W. K., Wang, G., and Vanka, S. P., 1994, "A Staggered Grid Multilevel Method for the Simulation of Fluid Flow in 3-D Complex Geometries," AIAA Paper 94-0778.
- Demuren, A. O., 1991, "Multigrid Acceleration and Turbulence Models for Computations of 3D Turbulent Jets in Cross-Flow," *Int. J. Heat Mass Transfer*, Vol. 35, pp. 2783-2794.
- Farmer, J., Martinelli, L., and Jameson, A., 1994, "A Fast Multigrid Method for Solving the Non-linear Ship Wave Problem with a Free Surface," *Proceedings of Sixth International Conference on Numerical Ship Hydrodynamics*, pp. 155-172, National Academy Press, Washington, D.C.
- Hirsch, C., 1990, *Numerical Computation of Internal and External Flows*, Vol. 1, Wiley, New York.
- Jameson, A., Schmidt, W., and Turkel, E., 1981, "Numerical Solutions of the Euler Equations by Finite Volume Methods Using Runge-Kutta Time-Stepping Schemes," AIAA Paper 81-1259.
- Jameson, A., 1983, "Solution of the Euler Equations by a Multigrid Method," *Appl. Math. Comput.*, Vol. 13, 327-356.
- Jameson, A., 1985, "Multigrid Algorithms for Compressible Flow Calculations," MAE Report 1743, Princeton University, Princeton, NJ 08544.
- Lien, F. S. and Leschziner, M. A., "Modelling the Flow in a Transition Duct with a Non-Orthogonal FV Procedure and Low-Re Turbulence-Transport Models," *Advances in Computational Methods in Fluid Dynamics*, K. N. Ghia, U. Ghia, and D. Goldstein, eds., ASME FED-Vol. 196, 1994, pp. 93-106.
- Lin, F. B., and Sotiropoulos, F., 1997, "Assessment of Artificial Dissipation Models for Three-Dimensional Incompressible Flow Solutions," *ASME JOURNAL OF FLUIDS ENGINEERING*, published in this issue pp. 331-340.
- Liu, F. and Zheng, X., 1994, "A Strongly-Coupled Time-Marching Method for Solving the Navier-Stokes and $k-\omega$ Turbulence Model Equations with Multigrid," AIAA Paper 94-2389.
- Martinelli, L., 1987, "Calculations of Viscous Flows with Multigrid Methods," Ph.D. dissertation, Princeton Univ., MAE Department.
- Mavriplis, D. J., and Martinelli, L., 1994, "Multigrid Solution of Compressible Turbulent Flow on Unstructured Meshes Using a Two-Equation Model," *Int. Journal for Numerical Methods in Fluids*, Vol. 18, pp. 887-914.
- Merkle, C. L., and Athavale, M., 1987, "Time-Accurate Unsteady Incompressible Flow Algorithms Based on Artificial Compressibility," AIAA Paper 87-1137.
- Menter, F. R., 1994, "Two-Equation Eddy-Viscosity Turbulence Models for Engineering Applications," *AIAA Journal*, Vol. 18, pp. 887-914.
- Sheng, C., Taylor, L., and Whitfield, D., 1994, "An Efficient Multigrid Acceleration for Solving the 3-D Incompressible Navier-Stokes Equations in Generalized Curvilinear Coordinates," AIAA Paper 94-2335.
- Sotiropoulos, F., and Patel, V. C., 1992, "Flow in Curved Ducts of Varying Cross-Section," IIHR Report No. 358, Iowa Institute of Hydraulic Research, The Univ. of Iowa, Iowa City, Iowa 52240.
- Sotiropoulos, F., and Patel, V. C., 1994, "Prediction of Turbulent Flow Through a Transition Duct Using a Second-Moment Closure," *AIAA Journal*, Vol. 32, No. 11, pp. 2194-2204.
- Sotiropoulos, F. and Patel, V. C., 1995a, "Turbulence Anisotropy and Near-Wall Modeling in Predicting Three-Dimensional Shear-Flows," *AIAA Journal*, Vol. 33, No. 3, pp. 504-514.
- Sotiropoulos, F. and Patel, V. C., 1995b, "Application of Reynolds-Stress Transport Models to Stern and Wake Flows," *Journal of Ship Research*, Vol. 39, No. 4, pp. 263-283.
- Swanson, R. C., and Turkel, E., 1987, "Artificial Dissipation and Central Difference Schemes for the Euler and Navier-Stokes Equations," AIAA Paper 87-1107.
- Turkel, E., and Vatsa, V. N., 1994, "Effect of Artificial Viscosity on Three-Dimensional Flow Solutions," *AIAA Journal*, Vol. 32, No. 1, pp. 39-45.
- Wilcox, D. C., 1994, "Simulation of Transition with a Two-Equation Turbulence Model," *AIAA Journal*, Vol. 32, No. 2, pp. 247-255.

A Reynolds Stress Function for Wall Layers

R. L. Panton

J. H. Herring
Centennial Professor,
Mechanical Engineering Department,
University of Texas,
Austin, TX 78712
Fellow ASME

Data for the Reynolds stress near a wall are correlated by employing the theory of perturbation methods to form a composite expansion. This absorbs, to first order, the effects of Reynolds number. Published data from three experimental and three direct numerical simulations of channel flow and one experimental and two direct numerical simulations of pipe flow were examined. A single curve fits the results to within the scatter of the data. If Reynolds number effects exist, they are hidden in the scatter. A closed-form equation, with one arbitrary constant, represents the data and has the proper limiting behavior both very near and very far from the wall.

1 Introduction and Background

The Reynolds shear stress $-\langle uv \rangle$ is considered an important statistical property of turbulent wall layers because of its role in momentum transport. This paper deals with the correlation of Reynolds stress profiles and an empirical function that represents the data throughout the range of Reynolds numbers. The correlation applies for flows near equilibrium; pipe and channel flows and boundary layers with modest pressure gradients. This ‘‘law-of-the-wall’’ for the Reynolds stress is not only important in itself, but also has relevance to ‘‘wall functions’’ used in numerical modeling equations.

The Reynolds stress appears in the momentum equation. For a fully developed pipe or channel flow it is

$$-\langle uv \rangle + \nu \frac{dU}{dy} = \frac{u_*^2}{\rho} \left[1 - \frac{y}{h} \right] \quad (1)$$

It is generally accepted that turbulent wall layers have a two-layer structure. Inviscid events in the outer layer scale with the friction velocity u_* as function of the distance from the wall $Y \equiv y/h$ (h is the half width of a channel, the radius of a pipe, or the thickness of a boundary layer). In theory, the Reynolds stress profiles $-\langle uv \rangle(y)$ are treated as asymptotic expansions where the parameter is the Reynolds number $Re_* = hu_*/\nu$ (Re_* is the size of the outer region in inner region y^+ units). An outer expression, valid for some Y , $0 < Y \leq 1$ as $Re_* \Rightarrow \infty$ is symbolically

$$-\frac{\langle uv \rangle}{u_*^2} = G(Y) \quad (2)$$

In the case of channels and pipes we are fortunate in that the limit $Re_* \Rightarrow \infty$ of the momentum equation Eq. (1), written in outer variables, produces an exact relation.

$$G = 1 - Y \quad (3)$$

Equation (3) applies to pipes and channels. A different $G(Y)$ outer function would exist for boundary layers and would depend on the pressure gradient.

The inner region has the same intensity scale u_* , however, the distances scale is $y^+ \equiv yu_*/\nu$. An inner region stress law valid for some y^+ , $0 \leq y^+ < Re_*$ ($y^+ = YRe_*$) as $Re_* \Rightarrow \infty$ is

$$-\frac{\langle uv \rangle}{u_*^2} = g(y^+) \quad (4)$$

The function $g(y^+)$ obeys the inner form of Eq. (1), $g + d(U/u_*)/dy^+ = 1$, where the term containing y/h is missing. The inner and outer layers have a region of overlapping validity with a common part. By definition, the common part is

$$G_{cp} \equiv G(Y \Rightarrow 0) = g_{cp} \equiv g(y^+ \Rightarrow \infty) = 1 \quad (5)$$

Boundary layers also have the property $G(Y \Rightarrow 0) = 1$.

An obstacle in demonstrating that stress data correlates in the form of Eq. (4), $g(y^+)$, is that we must simultaneously look at small values of y^+ and large values of Re_* . A different viewpoint will overcome half of this obstacle. Consider the additive composite expansion.

$$-\frac{\langle uv \rangle(y)}{u_*^2} = g(y^+) + G(Y) - G_{cp}(Y) \quad (6)$$

This expression is valid for all values of y , $0 \leq Y \leq 1$ as $Re_* \Rightarrow \infty$. Hence, inserting Eq. (3) and Eq. (5)

$$-\frac{\langle uv \rangle(y)}{u_*^2} = g(y^+) - Y \quad \text{with} \quad Y = \frac{y^+}{Re_*} \quad (7)$$

The great advantage of Eq. (7) over Eq. (4) is that Eq. (7) is valid for all values of y^+ . Thus, in order to correlate g it is best to solve Eq. (7) than to look at Eq. (4)

$$g(y^+) = -\frac{\langle uv \rangle(y^+)}{u_*^2} \Big|_{\text{data}} + \frac{y^+}{Re_*} \quad (8)$$

A critical question is how high must Re_* be before Eq. (8) is valid?

The use of composite expansions to represent the Re_* effect on turbulent fluctuations was used in Panton (1991). This theme was continued in Panton et al. (1995) where a proper empirical relation was introduced and channel flow experiments examined. The current article extends this work to correlate results of direct numerical simulations (DNS) for channel flows and both experiments and DNS for pipe flows. The reader will also find relations between the empirical constants in the Reynolds stress function and the constants in the log law of the velocity profile. A final section compares the present work with $\langle uv \rangle$ profiles derived from the Van Driest damping function.

2 Stress Function Correlations

The correlation $g(y^+)$ has been tested by processing recent data from four sources; channel flow experiments, channel flow numerical simulations, pipe flow experiments, and pipe flow numerical simulations. The results for $g(y^+)$ by processing data

Contributed by the Fluids Engineering Division for publication in the JOURNAL OF FLUIDS ENGINEERING. Manuscript received by the Fluids Engineering Division March 1, 1996; revised manuscript received September 18, 1996. Associate Technical Editor: S. P. Vanka.

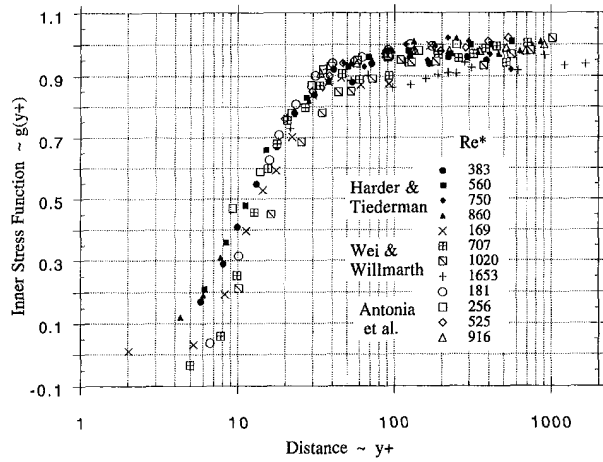


Fig. 1 Reynolds stress function over a range of Reynolds numbers from channel flow experiments

from channel flow experiments according to Eq. (8) are displayed in Fig. 1. These experiments offer the widest range of Re^* ; about a factor of ten. Admittedly, the range $Re^* = 160-1600$ is not as large as one would like. However, when Re^* is high the physical size of the inner region is too small to yield valid measurements. On Fig. 1 the data of Wei and Willmarth show the most scatter and have a tendency to be lower than the other data sets. A possible reason is that Wei and Willmarth used pressure drop measurements to compute u^* while the others found u^* by fitting Eq. (1). Because of end corrections it is common for these methods to differ by 10 percent or more. Within the scatter of the measurement one cannot discern any trend with Re^* in Fig. 1. This is true even for the lowest Reynolds numbers for which turbulence can be maintained.

Direct numerical simulations can be performed only at low values of Re^* . Results for $g(y^+)$ for seven DNS calculations of channel flow are displayed on Fig. 2. Except for the work of Kristoffersen and Andersson (1992) all results collapse together reasonably well. In order to compare DNS and experimental results, the DNS data of Kim et al. (1987) and the lowest Re^* from experiments are shown in Fig. 3. One cannot unambiguously identify any significant difference between experimental and DNS data.

In round pipes the data of Laufer (1953) is frequently quoted as direct experimental measurements for $-\langle uv \rangle$. In this regard there is an interesting situation. Schubauer (1954) analyzed the

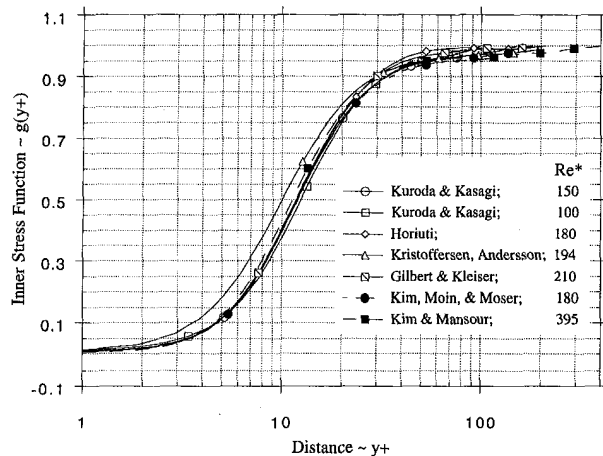


Fig. 2 Reynolds stress function from direct numerical simulations of channel flow

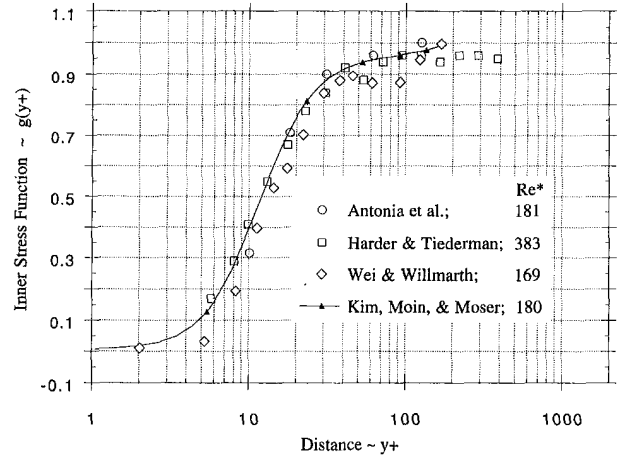


Fig. 3 Reynolds stress function at low Reynolds numbers from channel flow experiments and direct numerical simulation of KMM

pipe flow data of Laufer (1953) (this report is superseded by Laufer 1954) and used symbols which customarily indicate data points. Schubauer's graph of Laufer's data is often quoted in subsequent literature. However, in Laufer's original works there are no data points in the near wall region and the continuous line that is drawn is described in the text as the result of calculations using the measured velocity profile and Eq. (1). It would appear that Schubauer choose symbols because he wanted to compare pipe and boundary layers on the same graph and did not intend for the symbols to indicate a direct measurement of $-\langle uv \rangle$. Thus, for the low values of y^+ needed for this study Laufer's data are not direct measurements.

Experimental Reynolds stress measurements near the wall in a pipe have only recently been made. A paper to appear in the *Physics of Fluids* by Toonder and Nieuwstadt (1996), "Reynolds Number Effects in a Pipe Flow for Low and Moderate Re ," contains such data. A graph of the results processed according to Eq. (8) is given as Fig. 4. Within the scatter of the data no Reynolds number can be discerned and the curve agrees with data other sources, ie. channel flow experiments, DNS channel and DNS pipe.

There are two DNS calculations for pipes. These data, together with the channel flow data of Kim et al. (1987) for reference, are given in Fig. 5. One can see a difference in the channel and pipe results at large y^+ , however, this difference is not great in the light of the scatter on Fig. 2.

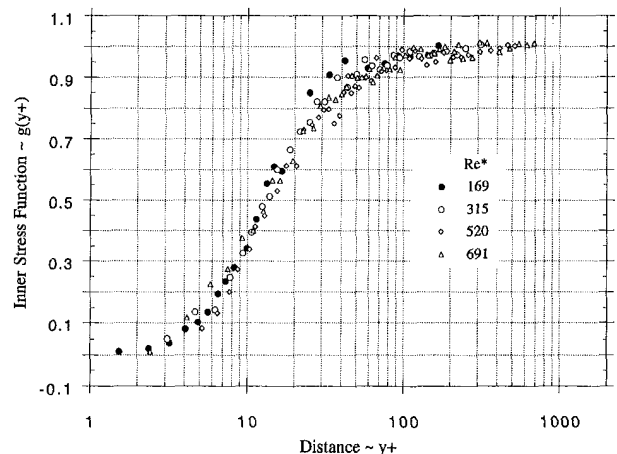


Fig. 4 Reynolds stress function from pipe flow experiments

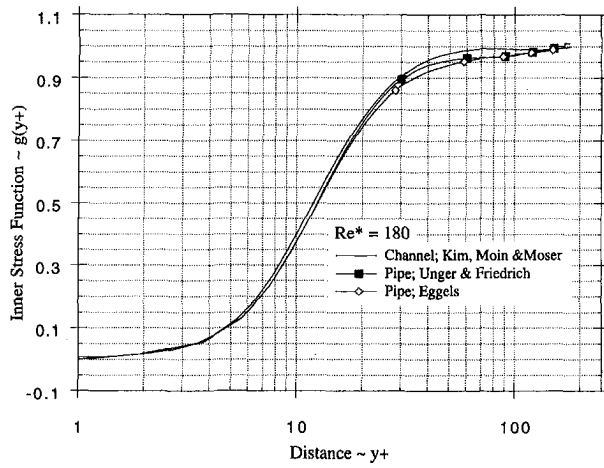


Fig. 5 Reynolds stress function from direct numerical simulations of pipe flow. Channel flow of KMM shown for reference.

The conclusion of this section is that the Reynolds stress function $g(y^+)$ is the same for pipes and channels and that major Reynolds number effects are successfully absorbed in the composite representation, Eq. (7). In principle, the law of the wall for Reynolds stress applies to any smooth wall layer—pipe, channel, or equilibrium boundary layer. Furthermore, the outer law Eq. (3) is valid for round pipes as well as for flat channels. Boundary layers have a different outer law that also depends on the pressure gradient.

$$\begin{aligned} \frac{U}{u^*} = y^+ + \frac{1}{\pi} & \left[C^+ \exp\left(\frac{-2y^+}{C^+}\right) - 4C^+ \exp\left(\frac{-y^+}{C^+}\right) - 2y^+ \right] \arctan\left(\frac{2\kappa}{\pi} y^+\right) + \frac{iC^+}{\pi} \left[-2 \exp\left(\frac{-i\pi}{2\kappa C^+}\right) Ei\left(\frac{i\pi}{2\kappa C^+} - \frac{y^+}{C^+}\right) \right. \\ & + \frac{1}{2} \exp\left(\frac{-i\pi}{2\kappa C^+}\right) Ei\left(2\left(\frac{i\pi}{2\kappa C^+} - \frac{y^+}{C^+}\right)\right) - \frac{1}{2} \exp\left(\frac{i\pi}{2\kappa C^+}\right) Ei\left(-2\left(\frac{i\pi}{2\kappa C^+} + \frac{y^+}{C^+}\right)\right) \\ & + 2 \exp\left(\frac{i\pi}{2\kappa C^+}\right) Ei\left(-\left(\frac{i\pi}{2\kappa C^+} + \frac{y^+}{C^+}\right)\right) - 4 \exp\left(\frac{i\pi}{2\kappa C^+}\right) Ei\left(-\frac{i\pi}{2\kappa C^+}\right) + 4 \exp\left(\frac{-i\pi}{2\kappa C^+}\right) Ei\left(\frac{i\pi}{2\kappa C^+}\right) \\ & \left. - \exp\left(\frac{i\pi}{2\kappa C^+}\right) Ei\left(\frac{i\pi}{\kappa C^+}\right) + \exp\left(\frac{-i\pi}{2\kappa C^+}\right) Ei\left(\frac{i\pi}{\kappa C^+}\right) \right] + \frac{1}{2\kappa} \ln\left(1 + \left(\frac{2\kappa}{\pi} y^+\right)^2\right) \end{aligned} \quad (11)$$

3 Empirical Reynolds Stress Law and Its Characteristics

It is generally accepted that a Taylor's expansion of the Reynolds stress behaves as $-\langle uv \rangle \sim y^3$ as $y \Rightarrow 0$. Since the theory of Eq. (7) applies as $Re^* \Rightarrow \infty$, $g \sim -\langle uv \rangle \sim y^3$. Another characteristic of $g(y^+)$ comes from evaluating Eq. (2) in the overlap region at high Reynolds numbers. This produces the requirement $-\langle uv \rangle \sim g \sim 1 - 1/\kappa y^+$ as $y \Rightarrow \infty$. Here κ is the von Karman constant. A stress law function that has these mathematical properties is

$$g = \frac{2}{\pi} \arctan\left(\frac{2\kappa y^+}{\pi}\right) \left[1 - \exp\left(-\frac{y^+}{C^+}\right) \right]^2 \quad (9)$$

The two adjustable constants are κ and C^+ .

It is noteworthy that at finite Reynolds number, Eq. (7) will first be in error at the extreme values of y . In the center of the channel, $Y = 1$, $y^+ = Re^*$ while $g \sim 1 - 1/\kappa y^+$, thus Eq. (7) predicts $-\langle uv \rangle(y)/u^{*2} = -1/\kappa Re^*$ rather than the correct value of zero. On the other hand, very near the wall, as $y^+ \Rightarrow$

0, $g \sim y^{+3}$ and becomes so small that the second term in Eq. (7), $Y = y^+/Re^*$ overpowers the g term. For a finite Re^* one can estimate that Eqs. (9) and (7) will predict an unrealistic negative $-\langle uv \rangle(y)/u^{*2}$ for $y^+ < \pi C^+/\sqrt{4\kappa Re^*}$. For better accuracy one would need higher order terms in the expansions Eqs. (2) and (4).

In Fig. 6 one finds a fit of Eq. (9) to the DNS data of Kim and Mansour (1995). The value $\kappa = 0.41$ was assumed and C^+ adjusted until the best fit was obtained. The DNS data is slightly lower than the fitted equation at small y^+ and also at large values where the DNS data lacks smoothness (for unknown reasons). If the trend at very low y^+ is actual, a more complex equation than Eq. (9) would be required to represent the curve accurately. Table 1 lists the values of C^+ found by fitting the various data sets (assuming $\kappa = 0.41$ in every instance). The first three sets are experimental channel flow results, the next three sets are typical channel flow DNS, and the last two sets are pipe flow DNS. The KKM and KM calculation are with the same program but for $Re^* = 180$ and 395 , respectively. One might infer that C^+ is decreasing slightly with increasing Re^* , however, the experiments, done over a much wider range of Re^* , all have larger values of C^+ . Considering the consistency of the data, one cannot find substantial conclusive differences between pipe and channel flows or between experiments and DNS.

Substituting the analytic expression Eq. (9) for g into the inner form of Eq. (1) one can integrate to obtain a relation for the mean velocity Law-of-the-Wall. For completeness the expression is given below.

$$\frac{U}{u^*} = \int_0^{y^+} (1 - g) dy^+ \quad (10)$$

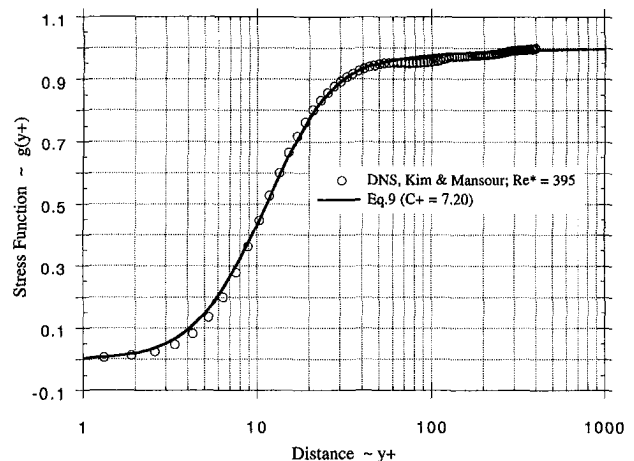


Fig. 6 Empirical Reynolds stress function, Eq. (9), fitted to direct numerical simulation of Kim and Mansour

Table 1 Fitted values of C^+ with $\kappa = 0.41$

	C^+	RMS Error
Antonia et al. (experiment-channel)	8.10	0.0051
Harder and Tiederman (experiment-channel)	7.73	0.0034
Wei and Willmarth (experiment-channel)	10.27	0.0073
Gilbert and Kleiser (DNS-channel)	7.47	0.0016
Kim, Moin, and Moser (DNS-channel)	7.85	0.0013
Kim and Mansour (DNS-channel)	7.20	0.0011
Toonder and Nieuwstadt (experiment-pipe)	9.27	0.00328
Unger and Freidrich (DNS-pipe)	7.85	0.0012
Eggels (DNS-pipe)	8.11	0.00069

Where the Exponential Integral Function is defined as

$$Ei(x) \equiv \int_{-x}^{\infty} \frac{e^{-t}}{t} dt$$

One can appreciate that often it is easier to numerically integrate Eq. (10) than to evaluate Eq. (11).

When y becomes large the velocity profile Eq. (11) must simplify to the log law

$$\frac{U}{u^*} = \frac{1}{\kappa} \ln y^+ + B \quad (12)$$

Thus, there is a relation between C^+ in Eq. (9) and B in Eq. (12). The relation was computed numerically, for various choices of κ , and parabolic fit to the curves (range $C^+ = 6-10$) yields the following approximate formula.

$$\begin{aligned} \kappa = 0.38; & B = -2.640328 + 0.953107 C^+ + 0.01579668 C^{+2} \\ \kappa = 0.39; & B = -2.547586 + 0.963875 C^+ + 0.01552454 C^{+2} \\ \kappa = 0.40; & B = -2.460446 + 0.974197 C^+ + 0.01526334 C^{+2} \\ \kappa = 0.41; & B = -2.378435 + 0.984100 C^+ + 0.01501243 C^{+2} \\ \kappa = 0.42; & B = -2.301533 + 0.993705 C^+ + 0.01476548 C^{+2} \\ \kappa = 0.43; & B = -2.229162 + 1.002988 C^+ + 0.01452478 C^{+2} \\ \kappa = 0.44; & B = -2.160774 + 1.011921 C^+ + 0.01429277 C^{+2} \end{aligned}$$

For the values recommended by Coles, $\kappa = 0.41$ and $B = 5.0$, one finds $C^+ = 6.80$. This is a little lower than the values of Table 1, however, many low Re^* layers tend to have high values of B determined from velocity. Since Eq. (9) is only an approximation for the true $g(y^+)$, one should not expect complete consistency between B found from Reynolds stress and B found from velocity profiles.

It is illustrative to plot the composite expansion Eq. (7) for $\langle uv \rangle$ using the stress function law Eq. (9). This is displayed as Fig. 7 over a range of Re^* . At $Re^* = 200$, the lowest value,

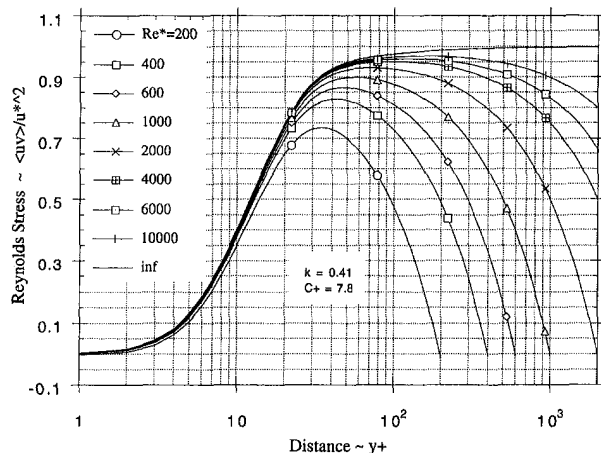


Fig. 7 Reynolds stress in inner variables as a function of Reynolds number. Behavior is computed from a composite expansion using Eq. (9).

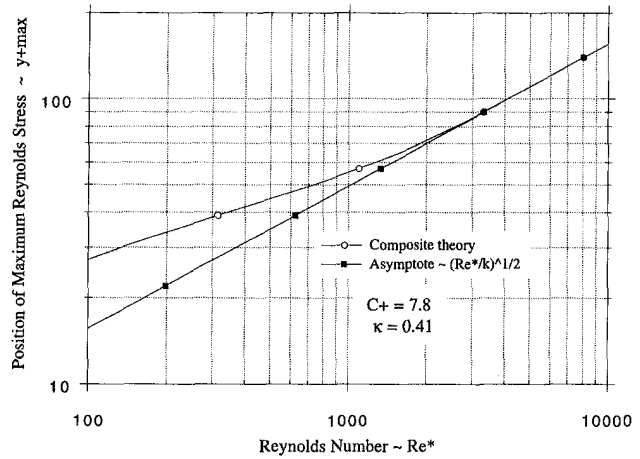


Fig. 8 Dependence of position of maximum Reynolds stress upon Reynolds number

one can observe slight Reynolds number effects down to $y^+ = 2$. The maximum of the Reynolds stress is often discussed in the literature. Figure 8 shows the value of y^+ for which the maximum occurs and Fig. 9 shows the values. In both figures the data was computed for $C^+ = 7.8$ using Eq. (9). The asymptotic results for high Reynolds numbers, Panton (1989), are also given.

$$y^+_{max} \sim \sqrt{\frac{Re^*}{\kappa}} \quad \text{as } Re^* \Rightarrow \infty \quad (13)$$

$$\frac{-\langle uv \rangle_{max}}{u^{*2}} \sim 1 - \frac{2}{\sqrt{\kappa Re^*}} \quad \text{as } Re^* \Rightarrow \infty \quad (14)$$

In both cases the asymptotic values are not closely approached until values of $Re^* > 1000-2000$. This corresponds to $y^+_{max} = 50-70$. Figures 7, 8, and 9 indicate that the movement and value of the maximum $\langle uv \rangle$ may be interpreted as a simple mixing of inner and outer layers of different sizes as Re^* changes.

4 Connection With Van Driest Formula

The computer modeling of turbulent flows near a wall is the subject of much work. A current discussion of wall functions for $k-\epsilon$ models is given by Chang et al. (1995). The ability of such functions, which contain two or more adjustable constants, to display the proper limiting behavior as $y^+ \Rightarrow 0$ and

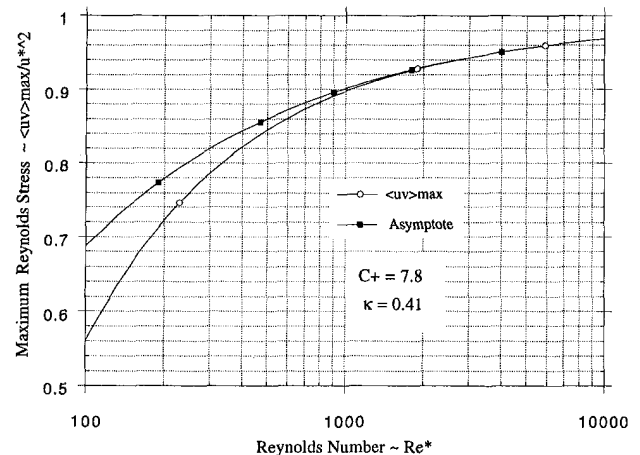


Fig. 9 Dependence maximum Reynolds stress upon Reynolds number

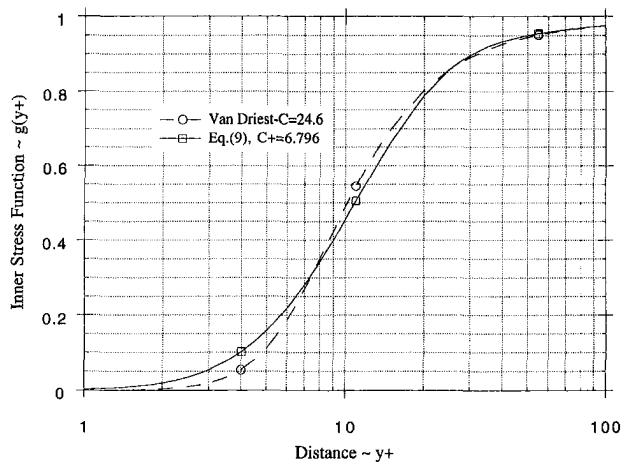


Fig. 10 Comparison of stress function law Eq. (9) and that derived from the Van Driest damping function. Constants chosen in each law to produce $B = 5.0$.

$y^+ \Rightarrow \infty$ has only recently been addressed. An early proposal for a wall function was the well-known Van Driest equation, which contains one adjustable constant, A , if the von Karman constant is considered as known. Since there is a direct connection between the Reynolds stress distribution $g(y^+)$ and the Van Driest formula, this paper would be incomplete without a short discussion of this subject.

The Van Driest wall function is an assumed relation for the mixing length.

$$l^+ = \kappa y^+ [1 - \exp(-y^+/A)] \quad (15)$$

Here l^+ is defined as the ratio turbulent eddy viscosity to molecular viscosity. The constant A is related to the additive constant in the log law by integration. The mixing length in terms of the Reynolds stress function is given by

$$l^+ = \frac{g^{1/2}}{1-g} \quad (16)$$

Combining these equations produces the relation

$$g = \frac{2l^{+2} + 1 - \sqrt{4l^{+2} + 1}}{2l^{+2}} \quad (17)$$

For some time it has been known that the Van Driest function does not have the proper behavior as $y^+ \Rightarrow 0$. Substituting Eq. (15) into Eq. (17) and evaluating as $y^+ \Rightarrow 0$ shows that the Van Driest expression for g is

$$g \sim y^{+4} \quad \text{as } y^+ \Rightarrow 0$$

Since the proper behavior is $g \sim y^{+3}$, the Van Driest law rises too slowly near zero.

A qualitative comparison of Eq. (9) and the corresponding Van Driest relation, Eq. (15) and Eq. (17), are given in Fig. 10. The constants chosen for each curve are those that will yield $\kappa = 0.41$ and $B = 5.0$. This means that the area integrals under each curve are the same. One can observe that the improper behavior of Van Driest's law near zero forces an excessively steep rise in the mid portion. The shape of the Van Driest law is not a good representation of the true g function. As a matter of interest, if one fits the VanDriest equation and Eq. (9) to the same $g(y^+)$ data, the associated value of B for the Van Driest fit will be roughly 0.5 higher than B associated with Eq. (9).

5 Summary

Composite expansions (in the sense of asymptotic expansions) display the first effects of Reynolds number on wall

turbulence. For the mean velocity the well-know law-of-the-wall added to the wake law form such a composite expansion. A composite expansion for the Reynolds stress consists of an inner function $g(y^+)$ and $-Y$ (the analog to the wake law). Data from channel flow experiments, channel flow DNS, and pipe flow DNS are well correlated when processed according to the composite expansion philosophy. Considering the scatter in the data one cannot observe Reynolds number effects even at the lowest values. This is somewhat surprising as many investigators observe a tendency for velocity profiles to have higher values of B for lower Reynolds numbers.

A simple algebraic expression with two constants, the von Karman constant κ and C^+ a constant related to B , adequately represents the inner stress function (to within the accuracy of the data). A composite expansion adequately reproduces the changes with Re^* that are observed in location and value of the maximum $-\langle uv \rangle(y^+)$. The Reynolds stress profile can also be represented by a computation employing the Van Driest law; however, the result does not have the proper shape close to the wall.

Acknowledgment

The author would like to acknowledge partial support from Grant no. N00014-94-0109, Mod. A00001, U.S. Department of the Navy, L. Patrick Purtell, grant monitor.

References

- Andersson, H. I., and Kristoffersen, R., 1992, "Statistics of Numerically Generated Turbulence," *Acta Applied Mathematics*, Vol. 26, pp. 293-314.
- Antonia, R. A., M. Teitel, J. Kim, and L. W. B. Browne, 1992, "Low Reynolds-Number Effects in a Fully Developed Turbulent Channel Flow," *Journal of Fluid Mechanics*, Vol. 236, pp. 579-605.
- Chang, K. C. Hsieh, W. D., and Chen, C. S., 1995, "A Modified Low-Reynolds Number Turbulence Model Applicable to Recirculating Flow in Pipe Expansions," *ASME JOURNAL OF FLUIDS ENGINEERING*, Vol. 117, p. 417.
- Eggels, J. G. M., Westerweel, J., Nieuwstadt, F. T. M., and Adrian, R. J., 1993, "Direct Numerical Simulation of Turbulent Pipe Flow: A Comparison Between Simulation and Experiment at Low Re-number," *Applied Science Research*, Vol. 51, pp. 319-324.
- Eggels, J. G. M., Unger, F., Weiss, M. H., Westerweel, J., Adrian, R. J., Friedrich, R., and Nieuwstadt, F. T. M., 1994, "Fully Developed Turbulent Pipe Flow: A Comparison Between Direct Numerical Simulation and Experiment," *Journal of Fluid Mechanics*, Vol. 268, pp. 175-209.
- Gilbert, N., and Kleiser, L., 1991, "Turbulence Model Testing with the Aid of Direct Numerical Simulation Results," *Proc. of 8th Symposium on Turbulent Shear Flows*, Paper 26-1, Munich, Sept. 9-11.
- Harder, K. J., and Tiederman, W. G., 1991, "Drag Reduction and Turbulent Structure in Two-dimensional Channel Flow," *Philosophical Society of the Royal Society*, Series A, Vol. 336, pp. 19-28.
- Horiuti, K., Institute of Industrial Science University of Tokyo, 7-22-1 Roppongi, Minato-ku, Tokyo 106. Private communication.
- Kasagi, N., Horiuti, K., Miyake, Y., Miyauchi, T., and Nagano, Y., 1992, "Direct Numerical Simulation Database of Turbulent Transport Phenomena," by the Ministry of Education, Science and Culture, The University of Tokyo, Bunkyo-ku, Tokyo 113: <http://www.thtlab.t.u-tokyo.ac.jp/>
- Kim, J., Moin, P., and Moser, R., 1987, "Turbulence Statistics in Fully Developed Channel Flow at Low Reynolds Number," *Journal of Fluid Mechanics*, Vol. 177, pp. 133-139.
- Kim, J., and Mansour, N., 1995, private communication.
- Kristoffersen, R., and Andersson, H. I., 1993, "Direct Simulations of Low Reynolds-Number Turbulent Flow in a Rotating Channel," *Journal of Fluid Mechanics*, Vol. 256, pp. 163-197.
- Kuroda, A., Kasagi, N., and Hirata, M., 1989, "A Direct Numerical Simulation of the Fully Developed Turbulent Channel Flow," *International Symposium on Computational Fluid Dynamics*, Nagoya, 1989, pp. 1174-1179; also in *Numerical Methods in Fluid Dynamics*, M. Yasuhara et al. eds., Vol. 2, Jap. Soc. Comp. Fluid Dyn., 1990, pp. 1012-1017.
- Kuroda, A., Kasagi, N., and Hirata, M., 1990a, "A Direct Numerical Simulation of the Turbulent Flow Between Two Parallel Walls: Turbulence Characteristics Near the Wall Without Mean Shear," *5th Symposium on Numerical Simulation of Turbulence*, IIS of the University of Tokyo, 1990, pp. 1-5.
- Kuroda, A., Kasagi, N., and Hirata, M., 1990b, "Investigation of Dynamical Effects of the Mean Shear Rate on the Wall Turbulence via Direct Numerical Simulation," *27th National Heat Transfer Symposium of Japan*, Nagoya, 1990, pp. 46-48.
- Laufer, J., 1953, "The Structure of Turbulence in Fully Developed Pipe Flow," NACA Tech. Note 2954.

- Laufer, J., 1954, "The Structure of Turbulence in Fully Developed Pipe Flow," NACA Report 1174.
- Panton, R. L., 1990, "Scaling Turbulent Wall Layers," *ASME JOURNAL OF FLUIDS ENGINEERING*, Vol. 111, No. 4, pp. 415-432.
- Panton, R. L., 1991, "The Effects of Reynolds Number on Turbulent Wall Layers," *Proceedings of the Eight Symposium on Turbulent Shear Flows*, Munich, Sept.
- Panton, R. L., Lin, Y. K., and M. Stanislas, 1995, "Turbulent Poiseuille Channel Flow Interpreted by Composite Expansions," *Proceedings of the IUTAM Conference on Asymptotic Methods for Turbulent Sh Flows*, Bochum, Germany, June, Kluwer Press, The Netherlands.
- Schubauer, G. B., 1954, "Turbulent Processes Observed in Boundary Layer and Pipe," *Physics of Fluids*, Vol. 25, pp. 188-198.
- Toonder and Nieuwstadt, 1996, "Reynolds Number Effects in a Pipe Flow for Low and Moderate Re," *Physics of Fluids*, to appear.
- Wei, T., and Willmarth, W. W., 1989, "Reynolds Number Effects on the Structure of a Turbulent Channel Flow," *Journal of Fluid Mechanics* Vol. 204, pp. 57-64.
-

Assessment of Artificial Dissipation Models for Three-Dimensional Incompressible Flow Solutions

F. B. Lin

Project Engineer,
STT Technologies Inc.,
231 Roundtree Dary Road,
Woodbridge, Ontario L4L8B8
Canada

F. Sotiropoulos

Assistant Professor,
School of Civil and
Environmental Engineering,
Georgia Institute of Technology,
Atlanta, GA 30324-0355

Various approaches for constructing artificial dissipation terms for three-dimensional artificial compressibility algorithms are presented and evaluated. Two, second-order accurate, central-differencing schemes, with explicitly added scalar and matrix-valued fourth-difference artificial dissipation, respectively, and a third-order accurate flux-difference splitting upwind scheme are implemented in a multigrid time-stepping procedure and applied to calculate laminar flow through a strongly curved duct. Extensive grid-refinement studies are carried out to investigate the grid sensitivity of each discretization approach. The calculations indicate that even the finest mesh employed, consisting of over 700,000 grid nodes, is not sufficient to establish grid independent solutions. However, all three schemes appear to converge toward the same solution as the grid spacing approaches zero. The matrix-valued dissipation scheme introduces the least amount of artificial dissipation and should be expected to yield the most accurate solutions on a given mesh. The flux-difference splitting upwind scheme, on the other hand, is more dissipative and, thus, particularly sensitive to grid resolution, but exhibits the best overall convergence characteristics on grids with large aspect ratios.

Introduction

Despite substantial advancements of the state-of-the-art and numerous reports of successful simulations, issues related to numerical accuracy and computational efficiency are still among the leading topics of Computational Fluid Dynamics (CFD) research. Questions about numerical uncertainty and code benchmarking, in particular, have recently attracted a great deal of attention as the CFD community is establishing more rigorous criteria for assessing the quality of numerical solutions that appear in the literature (Celik et al., 1993; Freitas, 1993; Ferziger, 1994). Excluding turbulence modeling, the most significant source of numerical uncertainty is that associated with the scheme employed to discretize the convective terms in the equations of motion, or more precisely, with the amount of artificial dissipation that such a discretization scheme introduces into the numerical solution. Based on the approach adopted to introduce artificial dissipation, spatial discretization schemes can be classified either as central-differencing or upwind schemes. Central-differencing schemes require the explicit addition of artificial dissipation terms to damp spurious oscillations. In such schemes, the amount of artificial dissipation is controlled manually by adjusting appropriate parameters. Upwind schemes, on the other hand, are constructed by taking into account the physical and mathematical properties of the equations of motion, namely the laws that govern the propagation of perturbations along characteristics. Such schemes contain a fixed amount of inherent artificial dissipation whose magnitude depends on the order of accuracy of the discretization.

For incompressible flow algorithms the form of artificial dissipation terms depends on the approach adopted to couple the velocity and pressure fields and satisfy the incompressibility constraint, that is whether an artificial compressibility (Chorin,

1967), or a pressure-Poisson method (Harlow and Welch, 1965) is employed. Pressure-Poisson methods, for instance, usually solve the governing equations in a segregated fashion and, therefore, artificial dissipation terms have to be constructed individually for each scalar equation. The most common discretization approach for such methods, is to employ three-point central-differencing for the divergence operator in the continuity equation, and the pressure gradient and viscous terms in the momentum equations, in conjunction with some type of upwind-differencing or central-differencing, plus explicitly added artificial dissipation, for the convective terms (Rhie and Chow, 1983; Sotiropoulos and Abdallah, 1991; Shyy et al., 1992). On nonstaggered computational meshes these methods need to introduce artificial dissipation terms—either explicitly or by the way the discrete pressure equation is constructed—in the discrete continuity equation (or equivalently in the resulting pressure-Poisson equation) in order to eliminate the well known odd-even decoupling of the pressure nodes (Rhie and Chow, 1983; Sotiropoulos and Abdallah, 1991; Tafti, 1995). Comparative studies of various discretization schemes for pressure-Poisson methods have been reported, among others, by Yeo et al. (1991), Shyy et al. (1992), and Sotiropoulos et al. (1994).

Artificial compressibility algorithms couple the pressure and velocity fields at the same level, thus, resulting to a hyperbolic system of equations which can be discretized by adopting compressible flow techniques. Central (Choi and Merkle, 1985; and Kwak et al., 1986) or upwind (Merkle and Athavale, 1987; Rogers and Kwak, 1990; and Rogers et al., 1991) discretization schemes may be constructed for the coupled system of governing equations based on the eigenvalues and eigenvectors of the Jacobian matrices of the inviscid flux vectors. To the best of our knowledge, however, a comprehensive evaluation of the various discretization strategies for artificial compressibility algorithms has yet to be carried out.

The objective of the present study is to evaluate, from the standpoint of accuracy and efficiency, the performance of spatial discretization schemes for artificial compressibility algorithms.

Contributed by the Fluids Engineering Division for publication in the JOURNAL OF FLUIDS ENGINEERING. Manuscript received by the Fluids Engineering Division April 18, 1995; revised manuscript received February 26, 1997. Associate Technical Editor: S. P. Vanka.

Three different discretization alternatives are assessed: (i) second-order accurate central-differencing with scalar, nonisotropic, artificial dissipation terms based on eigenvalue scaling (Martinelli 1987; Swanson and Turkel, 1987), denoted as CDS scheme; (ii) second-order accurate central-differencing with matrix-valued artificial dissipation terms (Turkel and Vatsa, 1994), denoted as CDM scheme; and (iii) third-order accurate flux-difference splitting upwind differencing (Merkle and Athavale, 1987) denoted as FDS3. All three schemes are implemented in an efficient Runge-Kutta time stepping procedure enhanced with implicit residual smoothing, local time stepping and multigrid convergence acceleration (Jameson, 1986; Jameson et al., 1981; Martinelli, 1987). To avoid uncertainties related to turbulence modeling, the three methods are applied to calculate three-dimensional laminar flow through a strongly curved square duct. The experiment of Humphrey et al. (1977) is selected as a test case, because it is a well documented complex flow case which has already been used by others extensively for validating incompressible flow solvers. Extensive grid refinement studies are carried out to investigate the sensitivity of each method to grid resolution. To eliminate uncertainties associated with accuracy loss on stretched meshes, all grid dependency studies are carried out on uniformly spaced grids. Calculations are also carried out on stretched meshes in order to investigate the convergence properties of the three artificial dissipation models.

In what follows, the governing equations are presented in generalized, non-orthogonal, curvilinear coordinates. This is followed by a discussion of the three artificial dissipation models and a brief description of the multigrid time-stepping algorithm. Finally, the calculated results are presented and analyzed with emphasis on grid sensitivity, accuracy, and numerical efficiency. The details of the artificial dissipation schemes are given in an appendix at the end of the paper.

Governing Equations in Generalized Curvilinear Coordinates

The three-dimensional, incompressible Navier-Stokes (NS) equations, nondimensionalized by ρ , U_o , and L_o , are modified

to facilitate the coupling of the velocity and pressure fields by adopting the artificial compressibility approach of Chorin (1967). The "pseudo-compressible" equations are formulated in strong conservation form and transformed in generalized curvilinear coordinates (ξ^1, ξ^2, ξ^3). The transformed equations read in compact tensor notation, where repeated indices imply summation, as follows:

$$\frac{1}{J} \frac{\partial Q}{\partial t} + \frac{\partial}{\partial \xi^j} (F^j - F_\nu^j) = 0 \quad (1)$$

where J is the Jacobian of the geometric transformation, and the vectors Q , F , and F_ν are defined as follows:

$$Q = [p \quad u_1 \quad u_2 \quad u_3]^T \quad (2)$$

$$F^j = \frac{1}{J} [\beta U^j \quad u_1 U^j + p \xi_{x_1}^j \quad u_2 U^j + p \xi_{x_2}^j \quad u_3 U^j + p \xi_{x_3}^j]^T \quad (3)$$

$$F_\nu^j = \frac{1}{J \text{Re}} \left[0 \quad g^{ij} \frac{\partial u_1}{\partial \xi^i} \quad g^{ij} \frac{\partial u_2}{\partial \xi^i} \quad g^{ij} \frac{\partial u_3}{\partial \xi^i} \right]^T \quad (4)$$

where, $U^j = u_i \xi_{x_j}^i$ and $g^{ij} = \xi_{x_i}^i \xi_{x_j}^j$.

Spatial Discretization and Artificial Dissipation Models

A general semi-discrete approximation of Eq. (1) can be written as follows:

$$\frac{1}{J} \left(\frac{dQ}{dt} \right)_{i,j,k} + \frac{\tilde{F}_{i+1/2,j,k}^1 - \tilde{F}_{i-1/2,j,k}^1}{\Delta \xi^1} - \frac{(\tilde{F}_\nu^1)_{i+1/2,j,k} - (\tilde{F}_\nu^1)_{i-1/2,j,k}}{\Delta \xi^1} + \dots = 0 \quad (5)$$

where, for clarity, only the terms in the ξ^1 direction are shown. In Eq. (5), the viscous fluxes at the cell faces $(\tilde{F}_\nu^1)_{i\pm 1/2,j,k}$ are

Nomenclature

A^j = Jacobian matrices ($= \partial F^j / \partial Q$, $j = 1, 2, 3$)
 C_f = skin friction
 CFL = Courant-Friedrich-Lewis number
 D^j = artificial dissipation flux in ξ^j direction ($j = 1, 2, 3$)
 De = Dean's number
 F^j = convective flux vector in ξ^j direction ($j = 1, 2, 3$)
 g^{ij} = contravariant metric tensor ($i, j = 1, 2, 3$)
 J = Jacobian of the geometric transformation ($= \partial(\xi^1, \xi^2, \xi^3) / \partial(x_1, x_2, x_3)$)
 L_o = reference length
 M_{ξ^j} = matrix whose rows are the left eigenvectors of A^j
 N = total number of grid nodes
 p = nondimensional static pressure
 Q = vector containing pressure and Cartesian velocity components
 r_i, r_o = inner and outer wall radii of curvature
 Re = Reynolds number ($= U_o L_o / \nu$)

r^* = nondimensional distance from inner wall ($= (r - r_i) / (r_o - r_i)$)
 S = arc length along the duct centerline, measured from the inlet plane
 t = time
 U_o = reference velocity
 U^j = contravariant velocity components ($j = 1, 2, 3$)
 u_i = dimensionless Cartesian velocity components ($i = 1, 2, 3$)
 x_i = Cartesian coordinates ($i = 1, 2, 3$)
 z = coordinate normal to the bottom wall of the duct
 Δ = difference operator
 Λ_{ξ^j} = diagonal matrix with entries the eigenvalues of A^j
 α = amount of near-boundary artificial dissipation ($0 < \alpha < 1$)
 β = artificial compressibility parameter
 δ = difference operator
 ϵ = amount of artificial dissipation ($0 < \epsilon < 1$)
 θ = circumferential angle measured from the start of curvature

λ_i^j = i th eigenvalue of the A^j Jacobian ($i = 1, 2, 3, 4$)
 λ_{ξ^j} = spectral radius of the Jacobian A^j
 ν = kinematic viscosity
 ξ^j = curvilinear coordinates ($j = 1, 2, 3$)
 $\xi_{x_i}^j$ = metrics of the geometric transformation ($= \partial \xi^j / \partial x_i$)
 ρ = fluid density
 ϕ^j = scaling factors for scalar dissipation ($j = 1, 2, 3$)

Subscripts

i, j, k = indices in the ξ^1, ξ^2, ξ^3 directions, respectively
 v = denotes viscous fluxes
 x_j = denotes differentiation along the x_j direction
 ξ^j = denotes differentiation along the ξ^j direction, unless indicated otherwise

Superscripts

\sim = numerically evaluated flux
 T = transpose

approximated using second-order accurate central-differencing. The inviscid fluxes $\hat{F}_{i\pm 1/2,j,k}^1$, on the other hand, can be calculated up to an arbitrary order of accuracy using the following general procedure:

$$\hat{F}_{i+1/2,j,k}^1 = \frac{1}{2}(F_{i+1,j,k}^1 + F_{i,j,k}^1) + D_{i+1/2,j,k}^1 \quad (6)$$

where $D_{i+1/2,j,k}^1$ is an artificial dissipation flux. Depending on the approach employed to construct $D_{i+1/2,j,k}^1$, Eq. (6) can produce centered, fully-upwind, or biased-upwind discretization stencils. Three different approaches for constructing such an artificial dissipation flux are examined in the present study: (i) third-difference, scalar, non-isotropic artificial dissipation with eigenvalue scaling (CDS scheme); (ii) third-difference, matrix-valued artificial dissipation (CDM scheme); and, (iii) flux-difference splitting based upwind differencing (FDS scheme). The first two approaches result in second-order accurate central-differencing schemes while the third approach may be used to construct upwind schemes of arbitrary spatial accuracy.

Scalar Dissipation With Eigenvalue Scaling. Following Swanson and Turkel (1987), nonisotropic, artificial dissipation terms can be constructed, for the incompressible flow equations, as follows:

$$D_{i+1/2,j,k}^1 = \epsilon \delta_{\xi^1} [\phi^1 \delta_{\xi^1 \xi^1}] \left(\frac{Q}{J} \right)_{i+1/2,j,k} \quad (7)$$

where

$$\delta_{\xi^1} ()_{i,j,k} = \frac{()_{i+1/2,j,k} - ()_{i-1/2,j,k}}{\Delta \xi^1} \quad (8)$$

$$\delta_{\xi^1 \xi^1} ()_{i,j,k} = \delta_{\xi^1} \delta_{\xi^1} ()_{i,j,k} \quad (9)$$

and ϵ is a positive constant which controls the amount of dissipation. The term ϕ^1 in Eq. (7) is a scaling factor along the ξ^1 -coordinate which depends on the spectral radii of the Jacobian matrices. A form similar to that proposed by Martinelli (1987) (see also Swanson and Turkel, 1987) is employed herein. The scaling factors ϕ^j are computed at the half nodes by averaging the flow variables and the metrics. This procedure is also adopted in Eqs. (11) and (13) below to evaluate Jacobian matrices at half nodes.

Near the boundaries of the computational domain, Eq. (7) can not be used since it involves grid nodes that lie outside the solution domain. For that reason, at nodes adjacent to boundaries, the second-order derivative operator in Eq. (7) is approximated as follows (Swanson and Turkel, 1987):

$$\delta_{\xi^1 \xi^1} \left(\frac{Q}{J} \right)_{1,j,k} = \delta_{\xi^1 \xi^1} \left(\frac{Q}{J} \right)_{2,j,k} \quad (10)$$

Matrix-Valued Dissipation. The matrix-valued dissipation model was recently proposed by Turkel and Vatsa (1994) for the three-dimensional, compressible, thin-layer NS equations. Employing ideas from upwind schemes, this approach replaces the scalar dissipation model, described by Eq. (7), with a matrix-valued dissipation model based on the Jacobian matrices of the inviscid flux vectors:

$$D_{i+1/2,j,k}^1 = \epsilon \delta_{\xi^1} [|A^1| \delta_{\xi^1 \xi^1}] \left(\frac{Q}{J} \right)_{i+1/2,j,k} \quad (11)$$

The absolute value of the Jacobian matrix A_1 is calculated as follows:

$$|A^1| = M_{\xi^1} |\Lambda_{\xi^1}| M_{\xi^1}^{-1} \quad (12)$$

where M_{ξ^1} is the modal matrix containing the left eigenvectors of the Jacobian A^1 , and Λ_{ξ^1} is a diagonal matrix whose entries

are the eigenvalues of A^1 . The complete form of matrix $|A^1|$ for the incompressible NS equations in generalized curvilinear coordinates is given in the Appendix. It should be noted that the entries of matrix $|A^1|$ are very complex expressions and, thus, computational implementation of eqn. (11) may result in a significant increase in CPU time over the simpler scalar model, Eq. (7). The elements of $|A^1|$ given in the Appendix have been substantially simplified, through long and tedious algebraic manipulations, so that a more efficient overall procedure may be obtained.

Flux-Difference Splitting Upwind Schemes. A third-order accurate upwind scheme is employed in the present study. It is obtained by constructing the dissipation flux as follows:

$$D_{i+1/2,j,k}^1 = \frac{1}{6} [(A^1)_{i-1/2,j,k}^+ \delta_{\xi^1} Q_{i-1/2,j,k} - (A^1)_{i+1/2,j,k}^+ \delta_{\xi^1} Q_{i+1/2,j,k} + (A^1)_{i+1/2,j,k}^- \delta_{\xi^1} Q_{i+1/2,j,k} - (A^1)_{i+3/2,j,k}^- \delta_{\xi^1} Q_{i+3/2,j,k}] \quad (13)$$

where

$$(A^1)^\pm = M_{\xi^1} \Lambda_{\xi^1}^\pm M_{\xi^1}^{-1} \quad (14)$$

The $\Lambda_{\xi^1}^+$ and $\Lambda_{\xi^1}^-$ matrices contain the positive and negative eigenvalues of A_1 , respectively (see Appendix).

Implementation of Eq. (13) requires special treatment near the boundaries as it involves points that lie outside the solution domain. Rogers and Kwak (1990) proposed to replace, at nodes adjacent to boundaries, the third-order accurate flux given by Eq. (13) with the following first order formula:

$$D_{i+1/2,j,k}^1 = -\frac{\alpha}{2} [(\Delta F^1)_{i+1/2,j,k}^+ - (\Delta F^1)_{i+1/2,j,k}^-] \quad (15)$$

where α is a positive constant ($\alpha \leq 1$). To minimize accuracy loss without any stability problems, all subsequently reported calculations are carried out with $\alpha = 0.01$. Another approach for handling near-boundary points would be to either set δQ at nodes outside the solution domain to zero or calculate them via extrapolation from the interior nodes—this is similar to the approach employed by Swanson and Turkel (1987) to construct near-boundary artificial dissipation terms for central-differencing schemes. These approaches were also evaluated in the course of the present study but produced results almost identical to these obtained using Eq. (15).

The effect of the order of accuracy of the upwind differencing was also investigated in the present study. For that reason, both a second-order accurate fully upwind scheme and a fifth-order accurate biased upwind scheme (Rogers and Kwak, 1990) were implemented and evaluated. It was found that, on a fixed computational mesh, there is a dramatic improvement in accuracy when going from a second-order to a third-order accurate scheme. The fifth-order scheme, on the other hand, was found to yield results almost identical to those obtained using the third-order accurate scheme. This is presumably due to the unavoidable reduction of global accuracy caused by the treatment of the near-boundary grid nodes. For brevity, only the results obtained with the third-order accurate scheme are presented in the subsequent sections.

Solution Procedure

A four-stage, explicit, Runge-Kutta time-stepping procedure is employed to integrate the discrete system of governing equations in time. For all three artificial dissipation models, the following coefficients are used: $\frac{1}{4}$, $\frac{1}{3}$, $\frac{1}{2}$, and 1. To save computational time, the artificial dissipation and the viscous terms are updated only at the first and third stages of the Runge-Kutta procedure. This approach is employed for all three discretization schemes. Multigrid acceleration, local time-stepping and constant-coefficient implicit residual smoothing (Jameson, 1986) are employed to accelerate the convergence rate of the iterative

procedure. The efficiency of the multigrid scheme is further enhanced using a semi-coarsening approach, which allows selective grid coarsening along some spatial directions. In the present study coarsening is applied only to (ξ^2, ξ^3) planes (see Fig. 1).

Results and Discussion

The experiment of Humphrey et al. (1977), who measured the flow through a strongly curved 90 deg square bend with fully-developed flow at the entrance of the bend, is selected as test case in the present study. The measurements were carried out at a Reynolds number $Re = 790$, based on the bulk velocity and the hydraulic diameter, with a corresponding Dean's number $De = 368$.

Four, successively finer, computational meshes are employed to investigate the grid sensitivity of each discretization scheme: (i) Grid 1, with $61 \times 41 \times 21$ nodes; (ii) Grid 2, with $61 \times 57 \times 29$ nodes; (iii) Grid 3, with $121 \times 57 \times 29$ nodes; and (iv) Grid 4, with $151 \times 97 \times 49$ nodes in the streamwise, radial, and normal directions, respectively (see Fig. 1). The corresponding streamwise spacing inside the bend is 3.0 deg for Grids 1 and 2, 1.5 deg for Grid 3, and 1.125 deg for Grid 4. To eliminate uncertainties associated with accuracy loss on stretched meshes, the grid nodes, for all four grids, are distributed uniformly in the cross-plane. It should be emphasized that Grid 4 consists of 717,000 grid nodes which makes it the finest grid to be used so far to calculate the duct of Humphrey et al. (1977). Previous calculations for this flow (Rogers et al., 1991; Yeo et al., 1991; Rosenfeld et al., 1991; Sotiropoulos et al., 1994) employed grids comparable, in terms of total number of grid nodes, to Grids 1 and 2 of the present study. Calculations are also carried out on a stretched computational mesh in order to investigate the convergence properties of the three discretization schemes on large aspect-ratio meshes. This grid, which is denoted as Grid 5, consists of $61 \times 57 \times 29$ grid nodes. The grid lines are clustered near the solid walls using a hyperbolic tangent stretching function. The minimum, near-wall grid spacing is 0.001 and the maximum grid stretching ratio is 1.35. Typical views of the computational grid on the plane of symmetry and the cross-section along with the related nomenclature are shown in Fig. 1. As the duct geometry is symmetric with respect to the z -axis and the entry velocity profile is also symmetric, only one-half of the duct is considered.

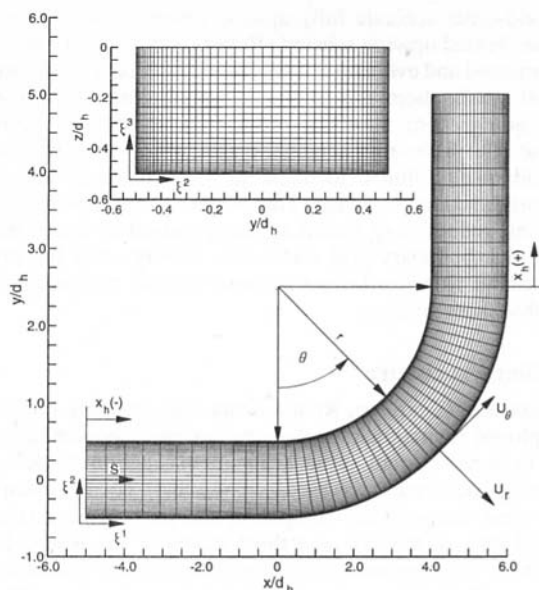


Fig. 1 Curvilinear coordinates and computational grid for a curved square duct

The computational domain starts 2.5 hydraulic diameters upstream of the bend and fully-developed flow conditions are prescribed there using the analytical solution given in White (1991). The exit boundary is located 2.5 hydraulic diameters downstream of the end of the bend. The sensitivity of the computed solutions to the location of the inflow and outflow boundaries was investigated extensively by carrying out calculations for various shorter and longer domains, and the dimensions given above were found sufficient to obtain domain-independent results.

To ensure a fair and unbiased comparison, the same set of boundary conditions are employed for all three discretization schemes. Dirichlet conditions are used for the velocity components at the inlet (analytical solution) and on the solid walls (no-slip, no-flux condition), while at the exit the three velocity components are computed by assuming zero streamwise diffusion. The pressure at the inlet, and solid boundaries is computed using linear extrapolation from within the solution domain, while at the exit is fixed to a constant level. On the symmetry plane ($z = 0$), zero gradient boundary conditions are employed for all variables, except the vertical velocity component which is set equal to zero, using three-point, backward, second-order accurate differencing to discretize the normal derivative. In order to investigate the possibility of numerical errors associated with the zero gradient condition on the plane of symmetry, calculations were also carried out for the entire duct configuration. However, no appreciable differences between the half and full duct solutions were observed.

Grid Refinement Studies. A systematic grid refinement study is carried out, using Grids 1 to 4. The results of this study are reported in terms of: (i) skin-friction distributions, plotted along the inner and outer walls on the plane of symmetry (Fig. 2); and (ii) streamwise and radial velocity profiles, plotted along the radial direction at the end of the bend ($\theta = 90$ deg) on the plane of symmetry (Figs. 3 and 4). Note that no pressure comparisons are included herein, since the pressure field was found to be fairly insensitive to grid refinement.

For all three artificial dissipation models, the skin-friction profiles, shown in Fig. 2, exhibit similar qualitative trends on all four meshes. However, quantitative differences, between the predictions obtained on the two intermediate meshes (Grids 2 and 3) and those obtained on the finest mesh (Grid 4), are observed along the outer wall of the bend. The maximum skin-friction value on the finest mesh decreases, relative to its value on Grids 2 and 3, by approximately 5 and 7 percent for the central-differencing (CDS and CDM schemes) and upwind (FDS3) schemes, respectively. These trends clearly demonstrate that in order to obtain grid converged solutions for complex three-dimensional flows very careful and systematic grid refinement studies are required. Considering, for instance, only the solutions obtained on Grids 1, 2, and 3, one could falsely conclude that Grid 3 is sufficient for establishing grid independence for all three discretization schemes. This issue is even more pronounced in the comparisons of streamwise and radial velocity profiles, shown in Figs. 3 and 4.

Figure 3 demonstrates that the velocity distribution near the inner wall of the bend is very sensitive to grid resolution. Both the CDS and CDM predictions exhibit, on all four grids, a well defined local maximum of the velocity profile at approximately $r^* = 0.2$. The level of the maximum, however, is seen to vary in an oscillatory fashion as the grid is refined. The FDS3 scheme, on the other hand, yields overall lower, as compared to the central-differencing schemes, streamwise velocities near the inner wall. In fact, on the three coarser meshes (Grids 1, 2, and 3) the velocity profile does not exhibit a local maximum but rather a plateau in the vicinity of $r^* = 0.2$. Furthermore, the results obtained on Grids 2 and 3 are almost identical, which may again create the false impression that grid independence has been achieved. Obviously, this can not be the case, as the

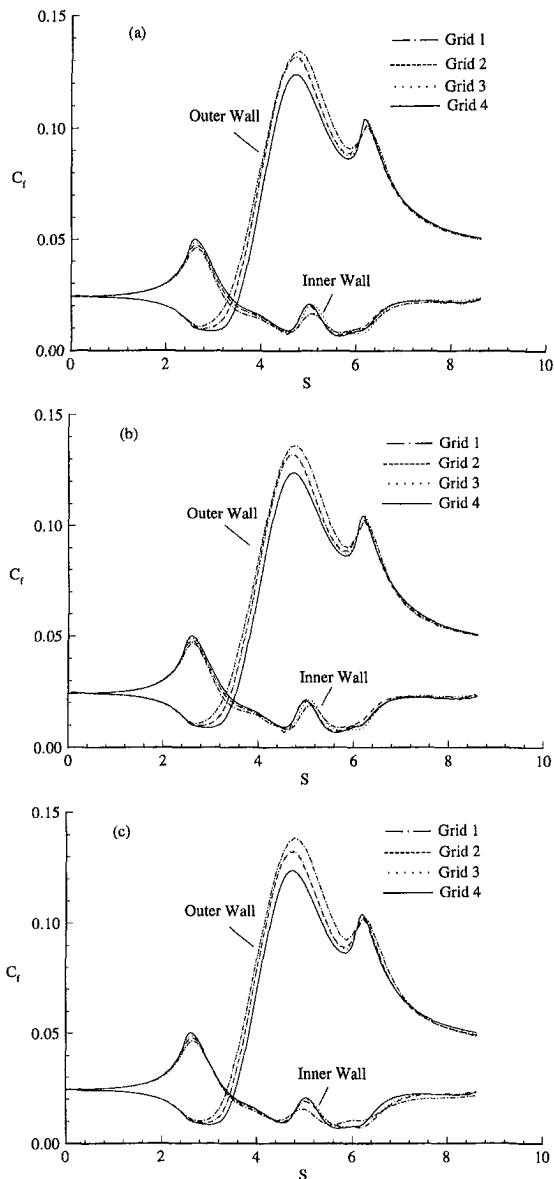


Fig. 2 Effect of grid refinement on C_r distributions along the inner and outer walls of the duct: (a) CDS scheme; (b) CDM scheme; (c) FDS3 scheme

grid independent solutions—achieved in the limit of the grid spacing approaching zero—for consistent discretization schemes should be identical. Indeed on the finest mesh (Grid 4), the FDS3 scheme is seen to produce a local maximum in the streamwise velocity profile at $r^* = 0.2$. Although the level of this maximum is somewhat lower than that obtained by the central-differencing schemes, it is clear that as the grid is refined the FDS3 solution approaches the CDS and CDM results.

The effect of grid refinement on the strength of the secondary motion at the exit of the bend is even more pronounced than that on the corresponding streamwise flow. This is shown in Fig. 4 which depicts the radial velocity profile at the plane of symmetry, at $\theta = 90$ deg, calculated by the three discretization schemes on all four meshes. The CDS and CDM schemes appear to converge toward a grid independent solution in a non-monotonic fashion, similar to that observed for the streamwise velocity profile (Fig. 3). On Grid 2, for instance, both schemes predict a stronger, as compared to their fine mesh (Grid 4) predictions, secondary motion. This notwithstanding, however, the predictions on all three coarse meshes are within 20 percent

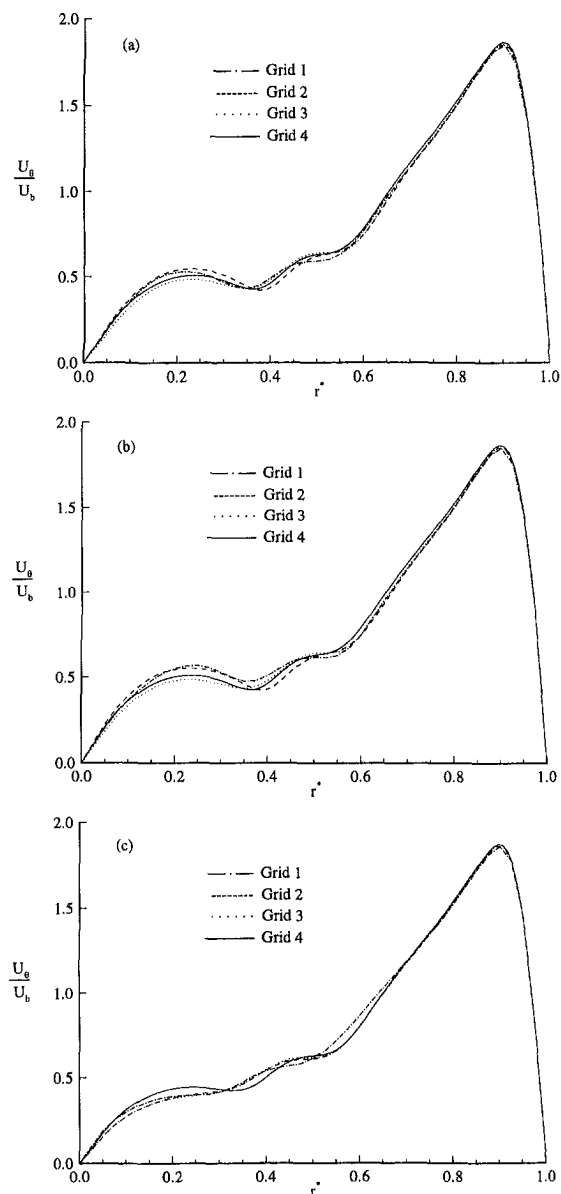


Fig. 3 Effect of grid refinement on streamwise velocity profiles plotted along radial lines on the plane of symmetry at $\theta = 90$ deg: (a) CDS scheme; (b) CDM scheme; (c) FDS3 scheme

of that obtained on the finest mesh. The FDS3 scheme, on the other hand, is seen to converge monotonically since the strength of the secondary motion increases continuously with grid refinement. However, differences as high as 75 percent are observed between the coarsest and finest mesh solutions. As was the case for the streamwise velocity profiles (Fig. 3), Grids 2 and 3 produce identical results. Yet the strength of the secondary motion is seen to change by approximately 45 percent when the finest mesh (Grid 4) is employed.

From the grid sensitivity studies presented above, it is obvious that a mesh which is even finer than Grid 4 is necessary to obtain grid independent solutions. The present results, however, clearly suggest that all three discretization schemes converge, as they should, toward the same solution as the grid spacing approaches zero (see also Figs. 6 and 7). The most surprising, perhaps, trend emerging from these figures is the sensitivity of the FDS3 scheme to grid resolution. To investigate the reasons for this trend, Fig. 5 shows the variation of the average, over all grid nodes, absolute value of the discrete divergence of the velocity field with respect to the reciprocal of an average grid

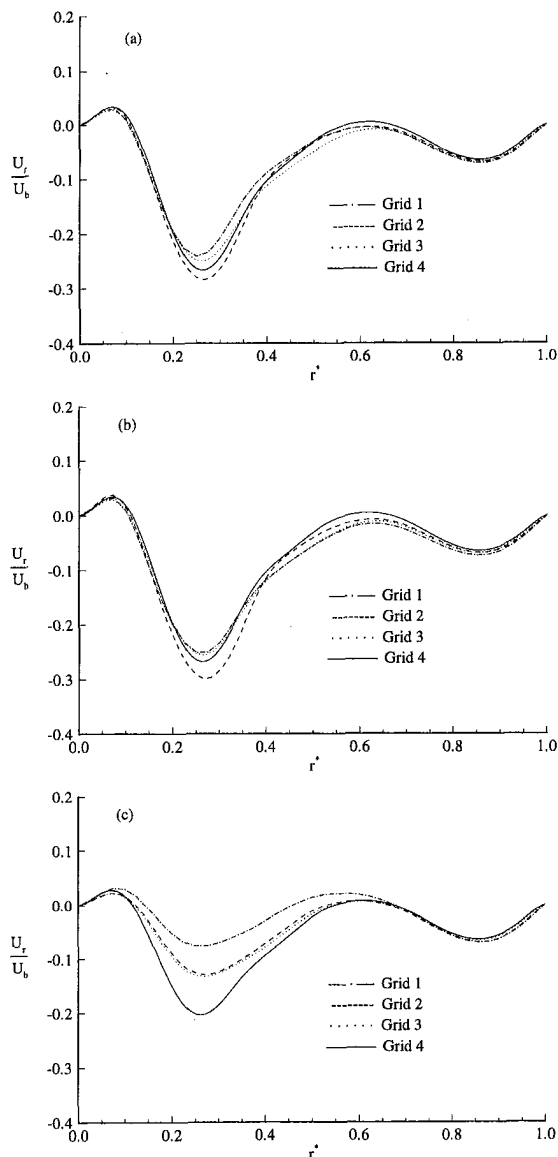


Fig. 4 Effect of grid refinement on radial velocity profiles plotted along radial lines on the plane of symmetry at $\theta = 90$ deg: (a) CDS scheme; (b) CDM scheme; (c) FDS3 scheme

density ($N^{-1/3}$). Three-point central, second-order accurate finite differencing is employed to calculate the divergence of the velocity field for all three cases. As seen in Fig. 5, the FDS3 and CDM schemes introduce the maximum and minimum, respectively, amount of artificial dissipation in the discrete continuity equation on all four meshes. In fact, compared to the CDM scheme, the dissipative terms associated with the FDS3 scheme are consistently one order of magnitude larger.

Comparisons of the Fine Grid (Grid 4) Solutions. The calculated streamwise velocity profiles, plotted along radial lines at three streamwise stations within the bend ($\theta = 30, 60,$ and 90 deg), are compared with each other and the experimental data of Humphrey et al. (1977), in Fig. 6. The most significant differences between the three numerical solutions are observed on the plane of symmetry ($z = 0.$) at the exit of the bend ($\theta = 90$ deg), where the FDS3 scheme predicts a somewhat weaker secondary motion in the vicinity of the inner wall and consequently a lower peak in the streamwise velocity profile. These differences should be attributed to inadequate grid resolution since, as discussed above, Grid 4 is not sufficient for grid inde-

pendent solutions, particularly for the FDS3 scheme. Qualitative and quantitative differences are also observed between the calculations and the measurements at $\theta = 60$ and $\theta = 90$ deg. More specifically, the calculated velocity profiles at $\theta = 60$ deg exhibit very pronounced regions of low velocity in the vicinity of $r^* = 0.4$ and a triple peak structure at $\theta = 90$ deg.

In Fig. 7, measured and computed streamwise velocity profiles are plotted along $z = \text{const.}$ lines at various radial locations within the bend. Similar trends, as those discussed for Fig. 6 above, are observed regarding the agreement between the three calculations and the experimental data. Namely, except for some small differences near the inner wall at $\theta = 60$ and 90 deg, the three discretization schemes produce almost identical solutions, while differences between experiments and calculations are observed at $\theta = 30$ and 60 deg.

The reasons for the discrepancies between measurements and calculations are not entirely clear. However, the present very fine mesh calculations with three different discretization schemes—all converging to the same solution—as well as previous numerical studies, which employed a variety of numerical methods and grid densities, for the same case which reported similar results (Rogers et al., 1991; Yeo et al., 1991; Sotiropoulos et al., 1994) would tend to suggest that the flow conditions in the experiment of Humphrey et al. (1977) do not correspond to those used for the calculations. In a recent experimental study, for instance, Belaidi et al. (1992) investigated the origin of flow instability in 90 deg curved ducts and reported that, under certain conditions, flow unsteadiness was observed near the inner wall of the bend. More specifically, they concluded that: (i) a nonturbulent, low-frequency oscillation develops near the inner wall of the bend where the secondary flows from the side wall boundary layers collide; and (ii) this oscillatory flow pattern appears at lower Reynolds numbers as the bend curvature increases. Given these observations and the present numerical calculations, one may speculate that the differences between the measurements and calculations could be attributed to the presence of unsteady flow in the experiment of Humphrey et al. (1977). Obviously, this point can be clarified only by carrying out fine-mesh time accurate calculations, which are beyond the scope of the present study.

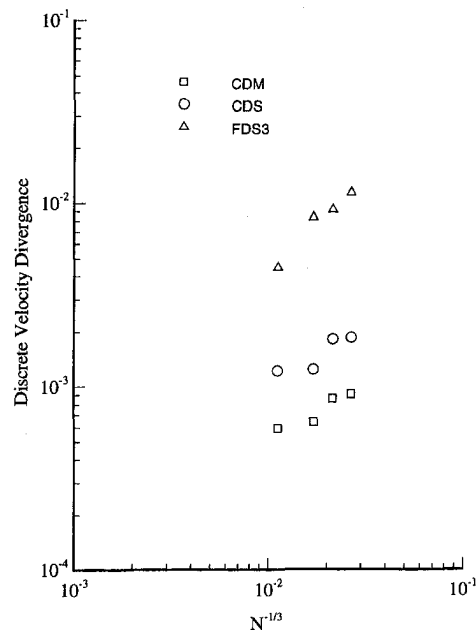


Fig. 5 Effect of grid refinement on the average, over all grid nodes, absolute value of the discrete divergence of the velocity field

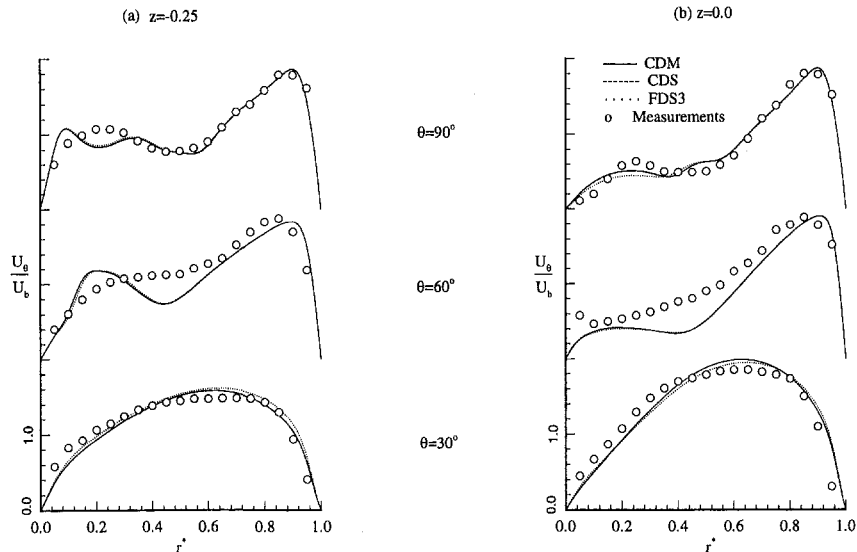


Fig. 6 Measured and calculated, on Grid 4, streamwise velocity profiles along radial lines: (a) $z = -0.25$; (b) $z = 0.0$

Convergence Properties and Computational Efficiency. To investigate the effects of artificial dissipation on the efficiency of the multigrid procedure, Figs. 8 and 9 show the convergence histories for Grids 2 and 5, respectively. To facilitate a fair comparison, all calculations were carried out, starting from the same initial conditions, using a standard V-cycle multigrid algorithm with three grid levels. The CFL number for all three simulations is $CFL = 3.0$ and the pseudocompressibility parameter is set to $\beta = 1$. It should be noted, that the CDS and CDM schemes can operate at higher CFL numbers as compared to the FDS3 scheme—values as high as $CFL = 6$ can be employed. However, $CFL = 3$ was found to yield the fastest overall convergence rate. The residual smoothing coefficients are set equal to 1. in the all three directions. Finally, the artificial dissipation parameter ϵ is set equal to 0.004 for both the CDS and CDM schemes. It is known that larger values of ϵ generally improve the convergence rate at the expense of accuracy. Since computational efficiency is a combination of convergence speed and level of accuracy on a given grid size, the value of ϵ used in this study was selected, after extensive

numerical experiments, so that it produces the most accurate results without significant adverse effects on the stability and robustness of the iterative procedure.

The convergence histories, with Grid 2, are shown in Fig. 8. In this figure, as well as Fig. 9, the vertical axis is the logarithm of the average pressure residual, normalized with the residual at the first iteration, while the horizontal axis is the number of multigrid cycles. It is seen that the FDS3 scheme converges at a constant rate and reaches machine zero after 1000 multigrid cycles. The CDS scheme although initially converges at exactly the same rate, as the FDS3 scheme, slows down dramatically after 600 cycles and reaches machine zero only after 2000 cycles. The use of matrix-valued dissipation further deteriorates the convergence, as the asymptotic convergence rate of the CDM scheme is approximately five times slower than that of both the FDS3 and CDS schemes. It is important to emphasize, however, that for all three schemes converged solutions, up to plotting scale, are typically obtained within 200 multigrid cycles (approximately 320 work units), that is after the residuals have dropped by about four orders of magnitude. The differences in

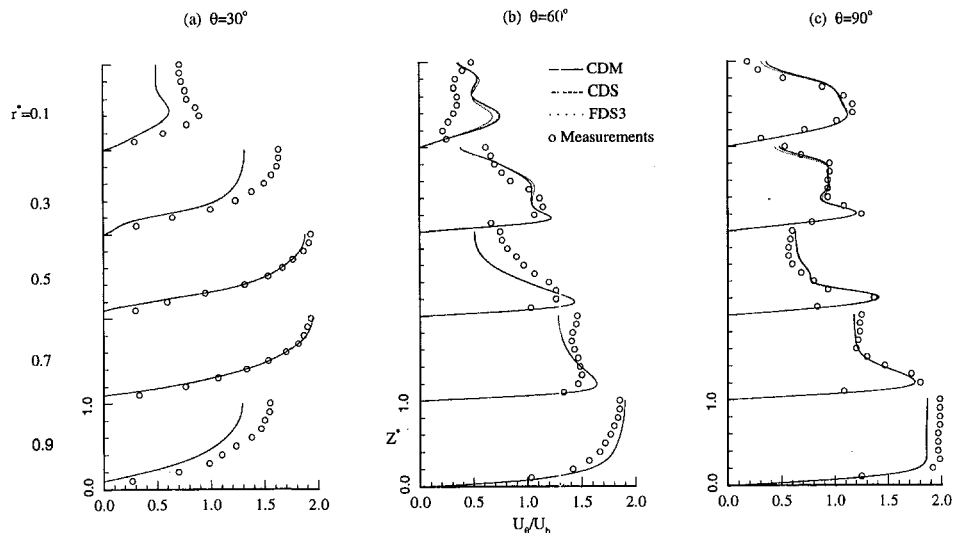


Fig. 7 Measured and calculated streamwise velocity profiles along normal lines: (a) $\theta = 30$ deg; (b) $\theta = 60$ deg; (c) $\theta = 90$ deg

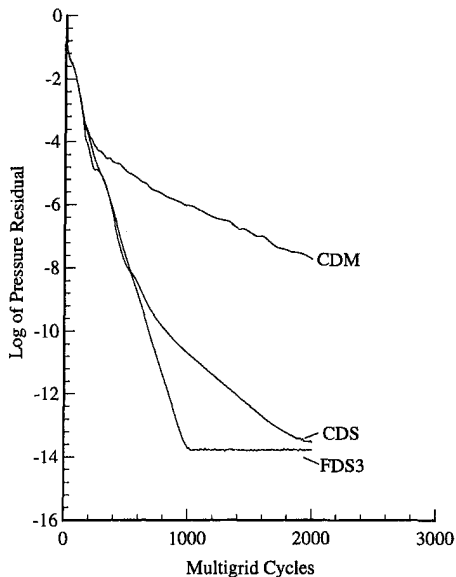


Fig. 8 Effect of artificial dissipation models on convergence history on a uniform mesh (Grid 2)

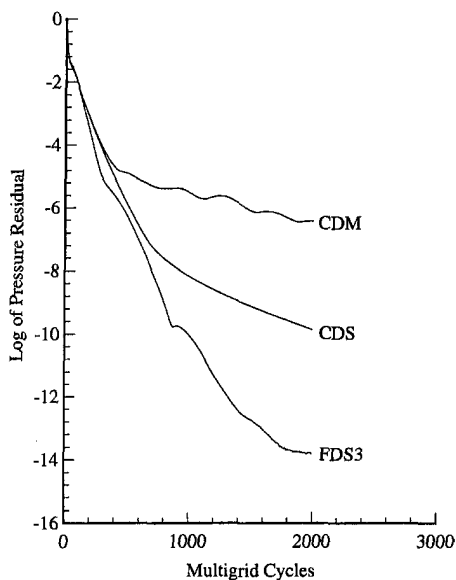


Fig. 9 Effect of artificial dissipation models on convergence history on a stretched grid (Grid 5)

convergence rates observed on Grid 2 are exaggerated on Grid 5 which involves cells with large aspect ratios. As seen in Fig. 9, only FDS3 reaches machine zero although at a rate approximately two times slower than that on Grid 2. For all three schemes, however, converged solutions, up to plotting scale, are obtained within 200–250 multigrid cycles.

Out of the three discretization schemes, the CDS requires the least amount of CPU time per multigrid cycle. Both the CDM and FDS3 schemes can be considerably more expensive due to the additional operations associated with the matrix multiplication necessary to obtain the components of the dissipative terms. As a result, the CDM and FDS3 schemes require 11 and 21 percent more CPU time per cycle, respectively, as compared to the CDS scheme.

Summary and Conclusions

This paper presented and evaluated three different approaches for constructing artificial dissipation terms for three-dimen-

sional artificial compressibility algorithms. Two second-order accurate central-differencing schemes, with explicitly added scalar and matrix dissipation operators, respectively, and a third-order accurate flux-difference splitting upwind scheme were incorporated into a multigrid time-stepping procedure and employed to calculate laminar flow through a strongly curved duct. A systematic grid refinement study was carried out using a series of successively finer meshes with total number of grid nodes ranging from 50,000 to over 700,000. The following conclusions can be drawn from the present study:

1) No grid independent solutions could be established despite the use of very fine computational meshes. Therefore, the present results demonstrate that systematic grid refinement studies, using substantially refined meshes, are required in order to obtain grid converged solutions for complex three-dimensional flows. Marginally refined grids, such as Grids 2 and 3 used in the present study, may produce similar solutions and lead to false conclusions about the grid sensitivity of a discretization scheme.

2) The matrix valued dissipation scheme introduces the least amount of artificial dissipation into the numerical solution. It is, therefore, less sensitive to grid refinement and should be expected to yield more accurate solutions on a fixed grid. The third-order accurate flux-difference splitting upwind scheme, on the other hand, is shown to be very dissipative and very sensitive to grid resolution.

3) The approach employed to construct artificial dissipation terms has a profound effect on the convergence properties of the multigrid algorithm. All three discretization schemes yield converged, to plotting accuracy, solutions within 200–250 multigrid cycles. However, only the upwind scheme is capable of driving the residuals to machine zero on large aspect-ratio grids. The matrix valued dissipation exhibits the worst overall convergence characteristics.

4) The present study points to the conclusion that the observed differences between the measurements of Humphrey et al. (1977) and the numerical solutions could be attributed to the lack of information about the precise experimental conditions rather than to numerical inaccuracies. Such a conclusion is supported by: (i) the fact that three different discretization schemes produced, on a very fine computational mesh, almost identical results which are in overall agreement with several previously reported calculations for the same test case; and (ii) recent experimental findings about the oscillatory nature of curved duct flows. The present fine mesh results could be used as a benchmark solution to validate three-dimensional incompressible NS solvers.

Acknowledgments

This work was partly supported by Grant County Public Utility District No. 2 (Ephrata, Washington) and Chellam County Public Utility District No. 1 (Wenatchee, Washington) while both authors were at the Iowa Institute of Hydraulic Research, The University of Iowa, Iowa City, Iowa. The second author also acknowledges support provided by the School of Civil and Environmental Engineering, Georgia Institute of Technology, Atlanta, Georgia. All computations were carried out on the Cray-C90 supercomputer at the San Diego Supercomputer Center.

References

- Belaidi, A., Jonhson, M. W., and Humphrey, J. A. C., 1992, "Flow Instability in a Curved Duct of Rectangular Cross-Section," *ASME JOURNAL OF FLUIDS ENGINEERING*, Vol. 114, pp. 585–592.
- Celik, I., Chen, C. J., Roache, P. J., and Scheuerer, G., 1993, *Symposium on Quantification of Uncertainty in Computational Fluid Dynamics*, FED Vol. 158, ASME Fluids Engineering Division Summer Meeting, Washington, DC, June 20–24.
- Chorin, A. J., 1967, "A Numerical Method for Solving Incompressible Viscous Flow Problems," *Journal of Computational Physics*, Vol. 2, pp. 12–26.

Ferziger, J. H., 1994, "Comments on the Policy Statement on Numerical Accuracy," *ASME JOURNAL OF FLUIDS ENGINEERING*, Vol. 116, p. 396.

Freitas, C. J., 1993, "Editorial Policy Statement on the Control of Numerical Accuracy," *ASME JOURNAL OF FLUIDS ENGINEERING*, Vol. 115, p. 339.

Harlow, H. F. and Welch, 1965, "Numerical Calculation of Time-Dependent Viscous Incompressible Fluid Flow with Free Surfaces," *Physics of Fluids*, Vol. 8, pp. 2185-2186.

Hartwich, P. M., Hsu, C. H., and Liu, C. H., 1988, "Vectorizable Implicit Algorithms for the Flux-Difference Split, Three-Dimensional Navier-Stokes Equations," *ASME JOURNAL OF FLUIDS ENGINEERING*, Vol. 110, pp. 297-305.

Humphrey, J. A. C., Taylor, A. M. K., and Whitelaw, J. H., 1977, "Laminar Flow in a Square Duct of Strong Curvature," *Journal of Fluid Mechanics* Vol. 83, pp. 509-527.

Jameson, A., 1986, "Multigrid Algorithms for Compressible Flow Calculations," MAE Report 1743, Princeton University, Princeton, N.J.

Jameson, A., Schmidt, W., and Turkel, E., 1981 "Numerical Solutions of the Euler Equations by Finite Volume Methods Using Runge-Kutta Time-Stepping Schemes," *AIAA Paper* 81-1259.

Kwak, D., Chang, J. L. C., Shanks, S. P., and Chakravarthy, S. R., 1986, "A Three-Dimensional Incompressible Navier-Stokes Flow Solver Using Primitive Variables," *AIAA Journal*, Vol. 24, No. 3, pp. 390-396.

Martinelli, L., 1987, "Calculations of Viscous Flows with Multigrid Methods," Ph.D. dissertation, Princeton University, MAE Department.

Merkle, C. L., and Athavale, M., 1987, "Time-Accurate Unsteady Incompressible Flow Algorithms Based on Artificial Compressibility," *AIAA Paper* 87-1137.

Rhie, C. M. and Chow, W. L., 1983, "Numerical Study of the Turbulent Flow Past an Airfoil with Trailing Edge Separation," *AIAA Journal*, Vol. 21, No. 11, pp. 1525-1532.

Rogers, S. E., and Kwak, D., 1990, "Upwind Differencing Schemes for the Time-Accurate Incompressible Navier-Stokes Equations," *AIAA Journal*, Vol. 28, No. 2, pp. 253-262.

Rogers, S. E., Kwak, D., and Kiris, C., 1991, "Steady and Unsteady Solutions of the Incompressible Navier-Stokes Equations," *AIAA Journal*, Vol. 29, No. 4, pp. 603-610.

Rosenfeld, M., Kwak, D., and Vinokur, M., 1991, "A Fractional Step Solution Method for the Unsteady Incompressible Navier-Stokes Equations in Generalized Coordinate Systems," *Journal of Computational Physics*, vol. 94, pp. 102-137.

Tafti, D., 1995, "Alternate Formulations for the Pressure Equation Laplacian on a Collocated Grid for Solving the Unsteady Incompressible Navier-Stokes Equations," *Journal of Computational Physics*, Vol. 116, pp. 143-153.

Shyy, W., Thakur, S., and Wright, J., 1992, "Second-Order Upwind and Central Difference Schemes for Recirculating Flow Computation," *AIAA Journal*, Vol. 30, No. 4, pp. 923-932.

Sotiropoulos, F. and Adballah, S., 1991, "The Discrete Continuity Equation in Primitive Variable Solutions of Incompressible Flow," *Journal of Computational Physics*, Vol. 95, 212.

Sotiropoulos, F., Kim, W. J., and Patel, V. C., 1994, "A Computational Comparison of Two Incompressible Navier-Stokes Solvers in Three-Dimensional Laminar Flows," *Computers Fluids*, Vol. 23, No. 4, pp. 627-646.

Swanson, R. C., and Turkel, E., 1987, "Artificial Dissipation and Central Difference Schemes for the Euler and Navier-Stokes Equations," *AIAA Paper* 87-1107.

Turkel, E., and Vatsa, V. N., 1994, "Effect of Artificial Viscosity on Three-Dimensional Flow Solutions," *AIAA Journal*, Vol. 32, No. 1, pp. 39-45.

Yeo, R. M., Wood, P. E., and Hrymak, A. N., 1991, "A Numerical Study of Laminar 90-Degree Bend Duct Flow with Different Discretization Schemes," *ASME JOURNAL OF FLUIDS ENGINEERING*, Vol. 113, pp. 563-569.

White, F. M., 1991, *Viscous Flow*, McGraw-Hill, New York, p. 120.

APPENDIX

The Jacobian matrices A^j and their eigenvalues are defined as follows ($j = 1, 2, 3$):

$$A^j = \frac{1}{J} \begin{bmatrix} 0 & \beta\xi_{x_1}^j & \beta\xi_{x_2}^j & \beta\xi_{x_3}^j \\ \xi_{x_1}^j & U^j + u_1\xi_{x_1}^j & u_1\xi_{x_2}^j & u_1\xi_{x_3}^j \\ \xi_{x_2}^j & u_2\xi_{x_1}^j & U^j + u_2\xi_{x_2}^j & u_2\xi_{x_3}^j \\ \xi_{x_3}^j & u_3\xi_{x_1}^j & u_3\xi_{x_2}^j & U^j + u_3\xi_{x_3}^j \end{bmatrix} \quad (\text{A.1})$$

$$\lambda_1^j = U^j - C_j, \quad \lambda_2^j = U^j + C_j, \quad \lambda_3^j = \lambda_4^j = U^j \quad (\text{A.2})$$

where,

$$C_j = \sqrt{(U^j)^2 + \beta g^{jj}}$$

The absolute value of A^j (Eq. (12)) can be expressed, after tedious algebraic manipulations, in the following manner (no summation over repeated indices):

$$|A^j| = \frac{1}{2JC_j^2} \{a_{ij}\}, \quad i, j = 1, 2, 3 \quad (\text{A.3})$$

where,

$$a_{11} = C_j(|\lambda_2^j|\lambda_1^j - |\lambda_1^j|\lambda_2^j)$$

$$a_{12} = \beta\xi_{x_1}^j C_j(|\lambda_1^j| - |\lambda_2^j|)$$

$$a_{13} = \beta\xi_{x_2}^j C_j(|\lambda_1^j| - |\lambda_2^j|)$$

$$a_{14} = \beta\xi_{x_3}^j C_j(|\lambda_1^j| - |\lambda_2^j|)$$

$$a_{21} = |\lambda_1^j|(u_1 g^{jj} - \xi_{x_1}^j \lambda_2^j) + |\lambda_2^j|(u_1 g^{jj} - \xi_{x_1}^j \lambda_1^j) - 2|\lambda_3^j|(u_1 g^{jj} - \xi_{x_1}^j U^j)$$

$$a_{22} = |\lambda_1^j|[u_1 \xi_{x_1}^j \lambda_1^j + \beta(\xi_{x_1}^j)^2] + |\lambda_2^j|[u_1 \xi_{x_1}^j \lambda_2^j + \beta(\xi_{x_1}^j)^2] + 2|\lambda_3^j|[(U^j)^2 - \xi_{x_1}^j u_1 U^j + \beta(\xi_{x_2}^j)^2 + \beta(\xi_{x_3}^j)^2]$$

$$a_{23} = \xi_{x_2}^j[|\lambda_1^j|(u_1 \lambda_1^j + \beta\xi_{x_1}^j) + |\lambda_2^j|(u_1 \lambda_2^j + \beta\xi_{x_1}^j) - 2|\lambda_3^j|(u_1 U^j + \beta\xi_{x_1}^j)]$$

$$a_{24} = \xi_{x_3}^j[|\lambda_1^j|(u_1 \lambda_1^j + \beta\xi_{x_1}^j) + |\lambda_2^j|(u_1 \lambda_2^j + \beta\xi_{x_1}^j) - 2|\lambda_3^j|(u_1 U^j + \beta\xi_{x_1}^j)]$$

$$a_{31} = |\lambda_1^j|(u_2 g^{jj} - \xi_{x_2}^j \lambda_2^j) + |\lambda_2^j|(u_2 g^{jj} - \xi_{x_2}^j \lambda_1^j) - 2|\lambda_3^j|(u_2 g^{jj} - \xi_{x_2}^j U^j)$$

$$a_{32} = \xi_{x_1}^j[|\lambda_1^j|(u_2 \lambda_1^j + \beta\xi_{x_2}^j) + |\lambda_2^j|(u_2 \lambda_2^j + \beta\xi_{x_2}^j) - 2|\lambda_3^j|(u_2 U^j + \beta\xi_{x_2}^j)]$$

$$a_{33} = |\lambda_1^j|[u_2 \xi_{x_2}^j \lambda_1^j + \beta(\xi_{x_2}^j)^2] + |\lambda_2^j|[u_2 \xi_{x_2}^j \lambda_2^j + \beta(\xi_{x_2}^j)^2] + 2|\lambda_3^j|[(U^j)^2 - \xi_{x_2}^j u_2 U^j + \beta(\xi_{x_1}^j)^2 + \beta(\xi_{x_3}^j)^2]$$

$$a_{34} = \xi_{x_3}^j[|\lambda_1^j|(u_2 \lambda_1^j + \beta\xi_{x_2}^j) + |\lambda_2^j|(u_2 \lambda_2^j + \beta\xi_{x_2}^j) - 2|\lambda_3^j|(u_2 U^j + \beta\xi_{x_2}^j)]$$

$$a_{41} = |\lambda_1^j|(u_3 g^{jj} - \xi_{x_3}^j \lambda_2^j) + |\lambda_2^j|(u_3 g^{jj} - \xi_{x_3}^j \lambda_1^j) - 2|\lambda_3^j|(u_3 g^{jj} - \xi_{x_3}^j U^j)$$

$$a_{42} = \xi_{x_1}^j[|\lambda_1^j|(u_3 \lambda_1^j + \beta\xi_{x_3}^j) + |\lambda_2^j|(u_3 \lambda_2^j + \beta\xi_{x_3}^j) - 2|\lambda_3^j|(u_3 U^j + \beta\xi_{x_3}^j)]$$

$$a_{43} = \xi_{x_2}^j[|\lambda_1^j|(u_3 \lambda_1^j + \beta\xi_{x_3}^j) + |\lambda_2^j|(u_3 \lambda_2^j + \beta\xi_{x_3}^j) - 2|\lambda_3^j|(u_3 U^j + \beta\xi_{x_3}^j)]$$

$$a_{44} = |\lambda_1^j|[u_3 \xi_{x_3}^j \lambda_1^j + \beta(\xi_{x_3}^j)^2] + |\lambda_2^j|[u_3 \xi_{x_3}^j \lambda_2^j + \beta(\xi_{x_3}^j)^2] + 2|\lambda_3^j|[(U^j)^2 - \xi_{x_3}^j u_3 U^j + \beta(\xi_{x_1}^j)^2 + \beta(\xi_{x_2}^j)^2]$$

The $(A^j)^+$ and $(A^j)^-$ matrices (see Eq. (14)) are given as follows (no summation over repeated indices):

$$(A^j)^\pm = \frac{1}{J} \{a_{ij}^\pm\}, \quad i, j = 1, 2, 3 \quad (\text{A.4})$$

with

$$a_{11}^\pm = \frac{g^{jj}}{2C_j}$$

$$a_{12}^\pm = \frac{\beta\xi_{x_1}^j}{2C_j} (U^j \pm C_j)$$

$$a_{13}^\pm = \frac{\beta\xi_{x_2}^j}{2C_j} (U^j \pm C_j)$$

$$a_{14}^\pm = \frac{\beta\xi_{x_3}^j}{2C_j} (U^j \pm C_j)$$

$$\begin{aligned}
a_{21}^{\pm} &= \frac{g^{jj}}{2C_j^2} [\beta\xi_{x_1}^j + u_1(U^j \pm C_j)] \\
&\quad - \frac{U_j^{\pm}}{C_j^2} [u_1(\xi_{x_3}^j)^2 + u_1(\xi_{x_2}^j)^2 - u_3\xi_{x_1}^j\xi_{x_3}^j - u_2\xi_{x_1}^j\xi_{x_2}^j] \\
a_{22}^{\pm} &= \frac{\xi_{x_1}^j(U^j \pm C_j)[\beta\xi_{x_1}^j + u_1(U^j \pm C_j)]}{2C_j^2} \\
&\quad + \frac{U_j^{\pm}}{C_j^2} [\xi_{x_2}^j(u_2U^j + \beta\xi_{x_2}^j) + \xi_{x_3}^j(u_3U^j + \beta\xi_{x_3}^j)] \\
a_{23}^{\pm} &= \frac{\xi_{x_2}^j(U^j \pm C_j)[\beta\xi_{x_1}^j + u_1(U^j \pm C_j)]}{2C_j^2} \\
&\quad - \frac{U_j^{\pm}\xi_{x_2}^j}{C_j^2} (u_1U^j + \beta\xi_{x_1}^j) \\
a_{24}^{\pm} &= \frac{\xi_{x_3}^j(U^j \pm C_j)[\beta\xi_{x_1}^j + u_1(U^j \pm C_j)]}{2C_j^2} \\
&\quad - \frac{U_j^{\pm}\xi_{x_3}^j}{C_j^2} (u_1U^j + \beta\xi_{x_1}^j) \\
a_{31}^{\pm} &= \frac{g^{jj}}{2C_j^2} [\beta\xi_{x_2}^j + u_2(U^j \pm C_j)] \\
&\quad - \frac{U_j^{\pm}}{C_j^2} [u_2(\xi_{x_3}^j)^2 + u_2(\xi_{x_1}^j)^2 - u_3\xi_{x_2}^j\xi_{x_3}^j - u_1\xi_{x_1}^j\xi_{x_2}^j] \\
a_{32}^{\pm} &= \frac{\xi_{x_1}^j(U^j \pm C_j)[\beta\xi_{x_2}^j + u_2(U^j \pm C_j)]}{2C_j^2} \\
&\quad - \frac{U_j^{\pm}\xi_{x_1}^j}{C_j^2} (u_2U^j + \beta\xi_{x_2}^j) \\
a_{33}^{\pm} &= \frac{\xi_{x_2}^j(U^j \pm C_j)[\beta\xi_{x_2}^j + u_2(U^j \pm C_j)]}{2C_j^2} \\
&\quad + \frac{U_j^{\pm}}{C_j^2} [\xi_{x_1}^j(u_1U^j + \beta\xi_{x_1}^j) + \xi_{x_3}^j(u_3U^j + \beta\xi_{x_3}^j)] \\
a_{34}^{\pm} &= \frac{\xi_{x_3}^j(u^j \pm C_j)[\beta\xi_{x_2}^j + u_2(U^j \pm C_j)]}{2C_j^2} \\
&\quad - \frac{U_j^{\pm}\xi_{x_3}^j}{C_j^2} (u_2U^j + \beta\xi_{x_2}^j) \\
a_{41}^{\pm} &= \frac{g^{jj}}{2C_j^2} [\beta\xi_{x_3}^j + u_3(U^j \pm C_j)] \\
&\quad - \frac{U_j^{\pm}}{C_j^2} [u_3(\xi_{x_1}^j)^2 + u_3(\xi_{x_2}^j)^2 - u_2\xi_{x_2}^j\xi_{x_3}^j - u_1\xi_{x_1}^j\xi_{x_3}^j] \\
a_{42}^{\pm} &= \frac{\xi_{x_1}^j(U^j \pm C_j)[\beta\xi_{x_3}^j + u_3(U^j \pm C_j)]}{2C_j^2} \\
&\quad - \frac{U_j^{\pm}\xi_{x_1}^j}{C_j^2} (u_3U^j + \beta\xi_{x_3}^j) \\
a_{43}^{\pm} &= \frac{\xi_{x_2}^j(U^j \pm C_j)[\beta\xi_{x_3}^j + u_3(U^j \pm C_j)]}{2C_j^2} \\
&\quad - \frac{U_j^{\pm}\xi_{x_2}^j}{C_j^2} (u_3U^j + \beta\xi_{x_3}^j) \\
a_{44}^{\pm} &= \frac{\xi_{x_3}^j(U^j \pm C_j)[\beta\xi_{x_3}^j + u_3(U^j \pm C_j)]}{2C_j^2} \\
&\quad + \frac{U_j^{\pm}}{C_j^2} [\xi_{x_1}^j(u_1U^j + \beta\xi_{x_1}^j) + \xi_{x_2}^j(u_2U^j + \beta\xi_{x_2}^j)]
\end{aligned}$$

where

$$U_j^{\pm} = \frac{1}{2}(U^j \pm |U^j|)$$

A Finite-Element Study of Newtonian and Power-Law Fluids in Conical Channel Flow

S. H. Garrioch

Graduate Student, Department of
Mechanical Engineering,
McGill University, Montreal, QC, H3A 2K6,
Canada

D. F. James

Professor of Mechanical Engineering,
University of Toronto, Toronto, ON,
M5S 1A4, Canada

A numerical study of Newtonian and shear-thinning fluids in high-speed, laminar flow through a conical channel is presented. Using a variety of cone-angles and Reynolds numbers on the order of 100, converging flow is mapped according to several characteristics: the angle at which separation occurs at the cone outlet, the extent to which sink-flow is approximated, and the pressure drop through the cone. While the data provides a fundamental description of conical flow, it may be of particular usefulness to rheologists in establishing an inelastic baseline for a converging-flow rheometer.

1 Introduction

Flow in a conical channel is one of the fundamental internal flows and, indeed, many articles have been devoted to the study of conical converging flows at high Mach numbers and under noninertial conditions. There is, however, a dearth of studies at the moderate flow speeds which commonly occur in industry. At these speeds, both viscous and inertial forces are important, which makes an analytic description of the flow difficult. In this study, we seek to map some of this intermediate flow region.

To broaden the scope of the investigation, power-law fluids are treated in addition to Newtonian fluids. A power-law fluid is an inelastic non-Newtonian fluid with a simplified type of shear-thinning behavior. Shear-thinning is a common trait of non-Newtonian fluids, and the power-law model is simple enough that it can be included in this study without great complexity, thereby extending the applicability of the results. More specifically, the behavior of power-law fluids in a conical channel may prove useful to rheologists employing converging flows to characterize the response of viscoelastic fluids in extensional flow. The conical channel is attractive because, at Reynolds numbers on the order of 10^2 , flow in a converging channel resembles sink flow, producing a simple and mainly-extensional flow field (James and Saringer, 1980). By comparing measurements made with a viscoelastic fluid to the response of an equivalent inelastic fluid, as found in this study, it should be possible to isolate the elastic effects from viscous and inertial ones, and thus determine elastic behavior of the fluid.

The present work, then, is a finite element study of conical channel flow for both Newtonian and power-law fluids. After checking the code against relevant available data, several features of conical flow are investigated. These features include the conical angle for which separation occurs at the junction between the cone and the downstream tube, the extent to which sink-flow is attained, and the pressure drop through the channel.

2 Background

The literature on incompressible conical flow can be traced back to the early 1900's when Harrison (1919) and Bond (1925) developed analytical solutions for creeping Newtonian flow; Harrison described the velocity field while Bond found the pressure field. Their solutions, however, assume purely radial flow throughout and make no allowance for flow adjust-

ments at the cone inlet and outlet. Forsyth (1976) later showed that the radial flow assumption restricts Harrison's and Bond's solutions to small-angle cones. Oka and Takami (1967) made the same assumption of creeping radial flow in analyzing conical flow of power-law fluids. They developed an ordinary differential equation for the velocity field but, unlike Harrison, did not provide either an analytical or a numerical solution to the equation.

There appear to be no relevant experimental studies with Newtonian fluids, but a few studies with non-Newtonian fluids have been reported. Sutterby (1965) measured the pressure drop of dilute polymer solutions through 7.1 and 10.7 deg half-angle cones, varying the downstream Reynolds number (Re) from approximately 1 to 10^4 . His data agree well with an equation he developed for inelastic shear-thinning fluids, an equation derived from the superposition of creeping and potential flow solutions. Based on this agreement, Sutterby concluded that the small angles and the small (2:1) diameter ratio which he used generated only minor elastic normal stresses in the flow. Conversely, James and Saringer (1980) showed that large elastic stresses can be produced in cone flow with a dilute polymer solution provided that the downstream Reynolds number is $O[10^2]$ and the diameter ratio is sufficiently large.

Most of the numerical work on converging flow of non-Newtonian fluids involves a 4:1 step contraction. Among the exceptions, Kwon et al. (1986) and Kajiwara et al. (1993) carried out finite element studies of cone flows, but in both cases inertia was neglected. Jarzebski and Wilkinson (1981) used a finite difference method to model the flow of a power-law fluid in a conical channel, inertia included, and obtained data on the pressure drop, development length, and stress development. Their results, however, are limited to small cone angles and only moderately shear-thinning fluids. Furthermore, no provision is made for the flow to enter or exit the conical channel.

In summary, previous research was based on creeping flows and/or small-angle cones. In the present work, large angles and high Reynolds numbers are treated to broaden our understanding of conical channel flow.

3 Flow System

The chosen flow system consists of a cone attached to upstream and downstream tubes, without interposing fillets. Figure 1 illustrates this geometry and also indicates the origins of the two coordinate systems, cylindrical (r, θ, z) and spherical (R, θ, ϕ), which are used in this work. The finite element program employs cylindrical coordinates, but spherical coordinates are more appropriate for flow in the cone proper, and thus are used when analyzing near-sink flow and presenting results from this

Contributed by the Fluids Engineering Division for publication in the JOURNAL OF FLUIDS ENGINEERING. Manuscript received by the Fluids Engineering Division October 27, 1995; revised manuscript received October 7, 1996. Associate Technical Editor: S. P. Vanka.

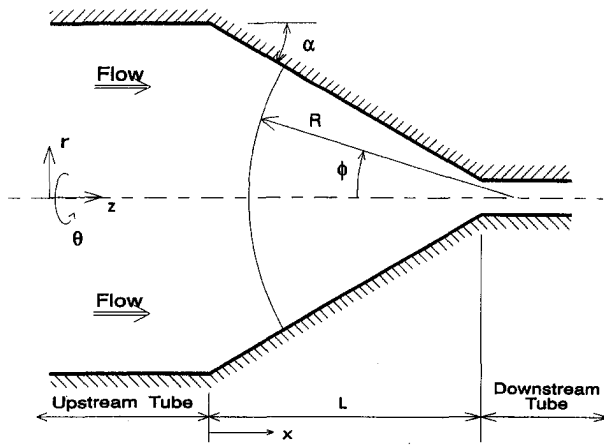


Fig. 1 Channel geometry and coordinate system

region. Sometimes, for convenience, axial locations in the cone are specified by the axial distance x , as shown in Fig. 1, rather than by the axial coordinate z .

The cone is characterized by its half-angle, α , and by the ratio of the inlet diameter to the outlet diameter. Many of the calculations in this study will be carried out for a "standard" half-angle of 30 deg and for a 10:1 diameter ratio. Based on this geometry, the desired flow should experience significant strain. As for appropriate Reynolds numbers, James and Saringer (1980) noted that Re in a converging flow rheometer should be of order 10^2 because lower Re 's will not generate near-sink flow in the core and because higher Re 's will make elastic stresses experimentally undetectable due to dominant inertial effects. Thus, to provide data of interest to rheologists, the Reynolds numbers of primary interest in this investigation are between 100 and 1000.

Flow through the system is taken to be steady, incompressible, axisymmetric, and laminar; body forces are neglected. Thus the governing equations are the equations for the conservation of mass, r -momentum, and z -momentum, which in cylindrical coordinates are:

$$\frac{1}{r} \frac{\partial}{\partial r} (rv_r) + \frac{\partial}{\partial z} (v_z) = 0 \quad (1)$$

$$\rho \left(v_r \frac{\partial v_r}{\partial r} + v_z \frac{\partial v_r}{\partial z} \right) = -\frac{\partial p}{\partial r} + \frac{1}{r} \frac{\partial}{\partial r} (r\tau_{rr}) + \frac{\partial \tau_{rz}}{\partial z} - \frac{\tau_{\theta\theta}}{r} \quad (2)$$

$$\rho \left(v_r \frac{\partial v_z}{\partial r} + v_z \frac{\partial v_z}{\partial z} \right) = -\frac{\partial p}{\partial z} + \frac{1}{r} \frac{\partial}{\partial r} (r\tau_{rz}) + \frac{\partial \tau_{zz}}{\partial z} \quad (3)$$

The no-slip condition is assumed at the wall and the flow is assumed to be fully developed in the upstream tube before it enters the cone, and far downstream in the exit tube.

For a power-law fluid, the shear viscosity (in $\text{Pa} \cdot \text{s}$) is given by

$$\eta = m\dot{\gamma}^{n-1} \quad (4)$$

where m is the consistency index ($\text{Pa} \cdot \text{s}^n$), $\dot{\gamma}$ is the shear rate ($1/\text{s}$), and n is the power-law index. A power-law fluid is shear-thinning for $0 < n < 1$, Newtonian for $n = 1$, and shear-thickening for $n > 1$. One failing of the power-law model is that, for $n < 1$, the viscosity goes to infinity as the shear rate approaches zero, whereas non-Newtonian fluids have a finite viscosity at low shear rates. The error at low shear rates, however, is rarely important because the corresponding shear stress still goes to zero.

Although the power-law model was developed primarily for shearing flows with a single velocity component, it is commonly

extended to more complex flows by substituting the strain rate (d) for the shear rate. In this case, the strain rate is calculated from the second invariant (II) of the rate-of-strain tensor as follows (Bird et al., 1987):

$$II = \sum_i \sum_j \left(\frac{\partial v_i}{\partial x_j} + \frac{\partial v_j}{\partial x_i} \right)^2, \quad (5)$$

$$d = \sqrt{\frac{1}{2} II}. \quad (6)$$

With this broader definition of the deformation rate, the power-law model has the same form as Eq. (4),

$$\eta = md^{n-1}, \quad (7)$$

and this definition is employed for the numerical simulations.

The flow depends on the Reynolds number and a special definition of the number is required here because the viscosity is variable. Consistent with the power-law model, Re is taken to be the generalized Reynolds number,

$$Re = \frac{\rho}{m} \bar{U}^{2-n} D^n, \quad (8)$$

where ρ (kg/m^3) is the density, \bar{U} (m/s) is the average velocity over a cross-section, and D (m) is the diameter of the cross-section. This definition arises naturally when the momentum equations are made dimensionless for power-law fluids (Schwalter, 1978). As defined here, the Reynolds number increases in the flow direction, though the downstream value is the most important because the largest flow gradients are located near the cone outlet. Hence, unless stated otherwise, Re denotes the downstream Reynolds number based on conditions in the outlet tube, i.e., on its diameter and the mean velocity within.

At times in this work, the local Re is more important, and the local Re at z_1 is related to the downstream Re by

$$Re_1 = Re \left(\frac{D_1}{D} \right)^{3n-4}, \quad (9)$$

where D_1 is the diameter at z_1 and D is the downstream tube diameter. Because of the exponent n , different shear-thinning fluids have different local Re 's at the same location in the cone, for the same downstream Re . The importance of this characteristic will become apparent later in the paper.

4 Numerical Method

A finite element program was developed and used to compute the velocity and pressure fields in the channel. We chose to write our own program in order to better understand and fully control the numerical algorithms involved, as well as to create a base code for future calculations with a series of non-Newtonian fluids.

Because the flow is axisymmetric, the computational domain is an r - z plane between the centerline and the wall. The domain is truncated upstream and downstream at distances sufficient to provide approximately fully-developed flow entering and exiting. The inlet tube is two diameters long; simulation results are essentially unchanged for four-diameter-long inlets because the flow chiefly adjusts to the cone within a diameter of the cone inlet. The outlet tube length exceeds the development length, in diameters, given by Shah and London (1978) as $0.5 + 0.05 Re$, which is sufficient to permit gradual decay of the radial velocity. Assuming no-slip conditions at the wall, the boundary conditions are:

$$z = 0: \quad v_z = \bar{U} \left(\frac{3n+1}{n+1} \right) \left[1 - \left(\frac{r}{r_{\text{wall}}} \right)^{1+1/n} \right], \quad v_r = 0 \quad (10a)$$

$$z = z_{\text{outlet}}: \quad \frac{\partial v_z}{\partial z} = 0, \quad v_r = 0 \quad (10b)$$

$$r = 0: \frac{\partial v_z}{\partial r} = 0, \quad v_r = 0 \quad (10c)$$

$$r = r_{\text{wall}}(z): \quad v_z = 0, \quad v_r = 0 \quad (10d)$$

where $z = 0$ is the channel inlet, z_{outlet} is the axial location of the channel outlet, $r = 0$ is the centreline axis, and r_{wall} is the radial location of the wall, which is a function of z . The axial velocity profile at $z = 0$, Eq. (10a), is for fully-developed flow of a power-law fluid (e.g., Bird et al., 1987).

The finite element mesh is composed of Crouzeix-Raviart quadrilateral elements; biquadratic velocity and linear pressure shape functions are used, with continuous velocities and discontinuous pressures at the element boundaries. A sample mesh of the r - z domain is presented in Fig. 2. As shown, elements are concentrated near the cone outlet and channel wall, where large velocity gradients are expected.

The finite element equations are based on a standard Galerkin formulation for Newtonian fluids at low Re and for non-Newtonian fluids at all Re 's. To prevent oscillations in a solution when convection dominates the flow, a streamline upwind/Petrov-Galerkin (SUPG) formulation (Brooks and Hughes, 1982) is employed for Newtonian fluids at $Re > 100$. An SUPG formulation was also attempted for power-law fluids, but it proved unsuccessful (Garrloch, 1994). Solution convergence suffered and, although SUPG did remove some oscillations, it produced others which were not present in the Galerkin solution. These problems may have resulted from the large variations in viscosity within each element (viscosity is a function of the spatial velocity derivatives): an element Peclet number based on the viscosity at the centre of the element may be insufficient for the calculation of a single upwinding factor for the entire element. A literature search was conducted to obtain guidance, but no instances were found in which the SUPG formulation is applied to the momentum equations of power-law fluids. Consequently, a fine mesh is relied on to produce smooth solutions for non-Newtonian fluids at high Re 's. This approach works for viscous flows because, as element size is reduced, the grid Peclet number decreases along with the "one-way" nature of the advection. Thus, oscillations shrink and disappear as the symmetric weighting functions of the Galerkin formulation become more appropriate. Based on exploratory studies of mesh refinement, meshes containing between 550 and 845 elements are used in this research, with a minimum of 10 elements in the r -direction.

Before solving the equation set, a penalty function is implemented to separate the pressure from the velocity and thus to solve for the velocity components alone. For Newtonian fluids, the equations are solved via Newton's method. For non-Newtonian fluids, the viscosities are first calculated based on the velocity gradients of the previous iteration and then the equation set is solved by Newton's method, as suggested by Crochet et al. (1984). Pressure values are subsequently calculated via matrix multiplication.

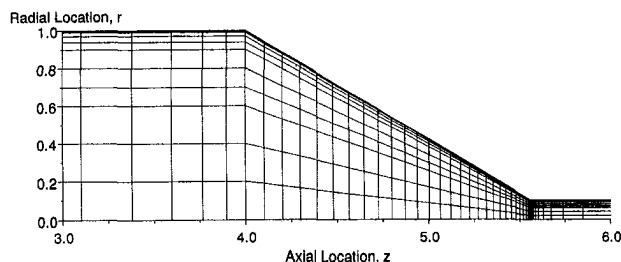


Fig. 2 Typical finite element mesh. Only a portion of the upstream and downstream tubes is shown.

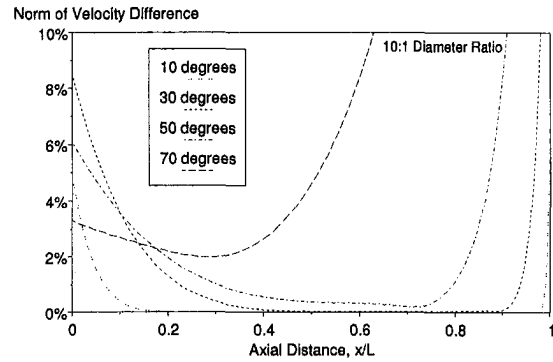


Fig. 3 A measure of the difference between velocities calculated from Harrison's (1919) analytic solution and those found by the present finite element program

5 Code Verification

5.1 Creeping Newtonian Cone Flow. The first test of the finite element program is based on Harrison's (1919) analytical solution for creeping Newtonian flow in a cone. Figure 3 compares the numerical simulation to Harrison's solution by giving a measure of the difference in the velocity fields. The measure is an overall deviation of our finite element velocities from Harrison's solution, defined by

$$\left[\frac{\sum_{i=1}^{nr} (\Delta v_z^2 + \Delta v_r^2)_i}{\sum_{i=1}^{nr} (v_z^2 + v_r^2)_i} \right]^{1/2} \times 100\% \quad (11)$$

where v is the velocity according to Harrison's solution, Δv is the difference between the analytical and the finite-element velocity at each node, i is the node index, and nr is the number of nodes in the r -direction (cylindrical coordinates are used here for convenience). The deviation is calculated for 120 cross-sections along the cone. The curves in Fig. 3 show large discrepancies near the cone inlet and outlet (at 0.0 and 1.0 on the horizontal axis, respectively), which are to be expected because Harrison's solution is for radial cone flow only. Agreement between the Harrison and finite element solutions is excellent for $\alpha = 10$ deg, with differences of less than 0.5 percent from $x/L = 0.1$ to 0.98. As α becomes larger, the agreement is progressively worse because the adjustment lengths increase and because the small-angle assumption implicit in Harrison's solution is less valid. The solution difference is still small for $\alpha = 30$ deg over a portion of the cone length but, at larger half-angles, Harrison's solution has limited accuracy. These results are important for experimentalists because they give the magnitude of upstream and downstream adjustment lengths and they indicate where pressure taps should be located for making measurements where the flow is "radial."

5.2 Pressure Drop for Non-Newtonian Cone Flow. As a test of the accuracy of the power-law formulation, finite element results are checked against pressure drop data from Sutterby's (1965) experiment. He conducted experiments in conical channels with a 0.5 percent Natrosol H solution and his data are especially useful here because his channel included upstream and downstream tubes and because elastic stresses were apparently absent in his flows (Sutterby came to this conclusion because the data did not exhibit the patterns associated with elastic effects). When Sutterby (1966) fit the power-law model to the solution viscosity data, he found that n was 0.521 and that is the value used in the finite element program for this comparison. Pressure drops, between the cone inlet and a downstream location, are compared in Fig. 4 for four wall locations and for a range of flow rates. The solid portions of the lines

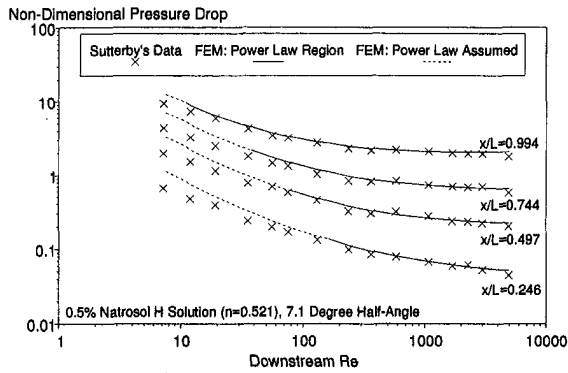


Fig. 4 Comparison of finite element results to Sutterby's (1965) experimental data for pressure drop along the wall in a 2:1 diameter ratio cone. The ordinate indicates the pressure drop from the cone inlet to one of four locations in the cone, nondimensionalized by fluid density and by the square of twice the average upstream velocity.

indicate that local wall shear rates are in the range where the power-law model accurately predicts the viscosity; the dashed portions are for shear rates where the power-law model overpredicts the viscosity. It should be noted that the data points are taken from journal graphs and are therefore accurate only to about ten percent. In general, agreement between the Sutterby and the finite element data is good, especially where the power-law model is valid.

6 Characteristics of Conical Flow

6.1 Critical Half-Angle for Separation. One of the findings from the present work is the half-angle for which separation first appears at the cone exit. Knowledge of this critical half-angle (α_{crit}) is important because the emergence of a recirculation zone will disturb flow in the cone, modifying the flow field under study. Separation is especially disruptive for viscoelastic flow, as it may create a large vortex which completely changes the character of the flow. Because elasticity delays separation, the power-law α_{crit} data are conservative estimates of the critical half-angles for viscoelastic fluids.

The critical half-angle is determined for four fluids, $n = 0.1, 0.3, 0.5, \text{ and } 1.0$, at $Re \geq 30$. The critical value is obtained by performing a series of program runs for integer values of α and checking for separation at each degree. Separation is judged to occur if a negative axial velocity is found in the downstream tube at $r = 0.995 \times \text{downstream radius}$, an arbitrarily-chosen location close to the wall. Because of the difficulty in resolving velocities in the small recirculation zones, the program runs are repeated on a total of three meshes containing 35 by 8, 53 by 11, and 68 by 11 elements (where the number of elements in the z -direction is given first) to ensure mesh independence.

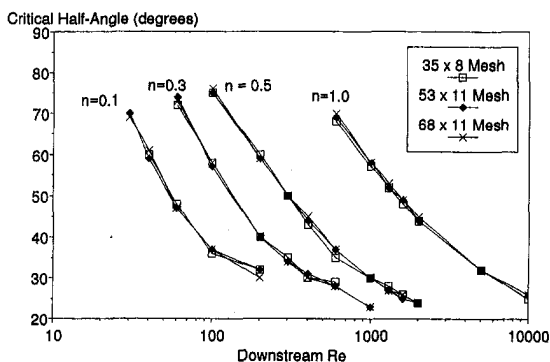


Fig. 5 Critical half-angles for separation

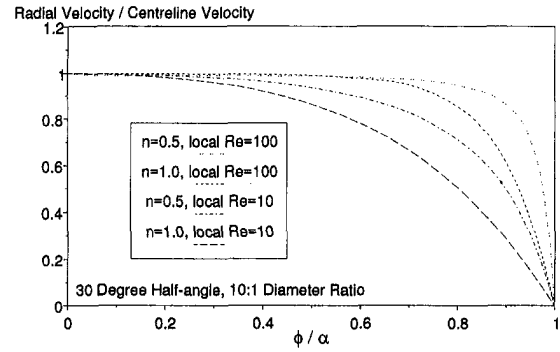


Fig. 6 Radial velocity profiles on the spherical cap located at $x/L = 0.85$

Figure 5 presents the results. The three meshes generate similar values of α_{crit} , although agreement is best for the two finest meshes, as one would expect. Additionally, the agreement is slightly worse at lower n because of difficulties in resolving the very large velocity gradients at the wall. Overall, however, agreement is good, and clearly the more shear-thinning fluids separate more readily. For example, for the 30° half-angle cone, at $n = 0.1$ the flow separates at a downstream Re of 200 while Newtonian flow does not separate at this angle until the Re is 6000. A shear-thinning fluid separates more easily because of its blunt velocity profile which places high momentum flow near the wall. In the remainder of this paper, the Reynolds numbers are chosen such that all flows operate below the onset of separation.

6.2 Near-Sink Flow. As previously stated, one of the interesting features of conical flow is the central zone where sink flow, or near-sink flow, is created at high Reynolds numbers. In this section of the paper, the extent of this core region is identified for a variety of flow conditions, namely for different values of Re , n , and α .

In spherical coordinates, the velocity components for inviscid sink flow are

$$v_R = \frac{k}{R^2}, \quad v_\phi = 0, \quad v_\theta = 0, \quad (12)$$

where k is a (negative) constant and R is the radial distance from the cone apex, as shown in Fig. 1. For viscous flow, the radial velocity (v_R) depends on ϕ as well as R , and this dependence on ϕ is illustrated in Fig. 6. The radial velocity profiles in this figure are on the spherical cap which intersects the axis at $x/L = 0.85$ (a spherical cap is the surface described by a fixed R). The profiles are for a 30° half-angle and for local Reynolds numbers of 10 and 100. The two profiles presented

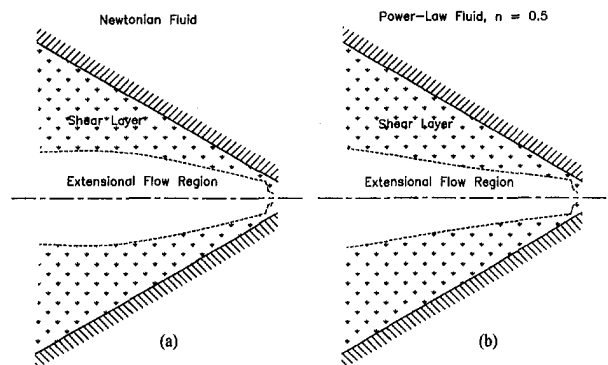


Fig. 7 Plots of the core region, based on a downstream Re of 100 (half-angle of 30° and 10:1 diameter ratio); (a) Newtonian fluid, (b) power-law fluid, $n = 0.5$

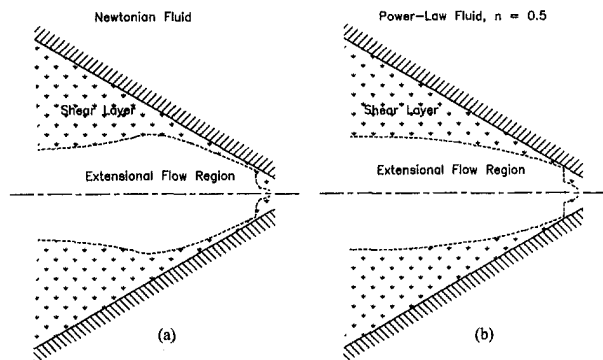


Fig. 8 Plots of the core region for the same conditions as Fig. 7 except that Re is 1000

are for a Newtonian fluid and a power-law fluid with $n = 0.5$. For the higher Re, the profiles of both fluids are substantially flat from the centerline to about $\phi/\alpha = 0.75$. Thus, fluid deformation is predominantly extensional in this core region because shear rates are small. From $\phi/\alpha = 0.75$ to the wall, the shear increases greatly and becomes the dominant mode of deformation. By contrast, at the lower Re, the velocity profiles are closer to parabolic which produces a much smaller core. The central region is of particular interest to rheologists who want to use this region of nearly extensional motion to characterize the extensional flow resistance of a fluid. Hence the following work explores how the size of this region depends on channel geometry and flow conditions.

To identify the extent of the core region, a criterion for its boundary must be established. Analogous to the definition for boundary layer flow, the boundary is taken to be the surface where the local radial velocity is a fixed percentage of the centerline velocity. Actually, two boundary criteria are used in this work:

- (i) $v_R = 0.9 v_{R, \text{centerline}}$;
- (ii) $v_R = 1.01 v_{R, \text{centerline}}$.

The first criterion is the type normally associated with boundary layers and is applied almost everywhere; the second criterion

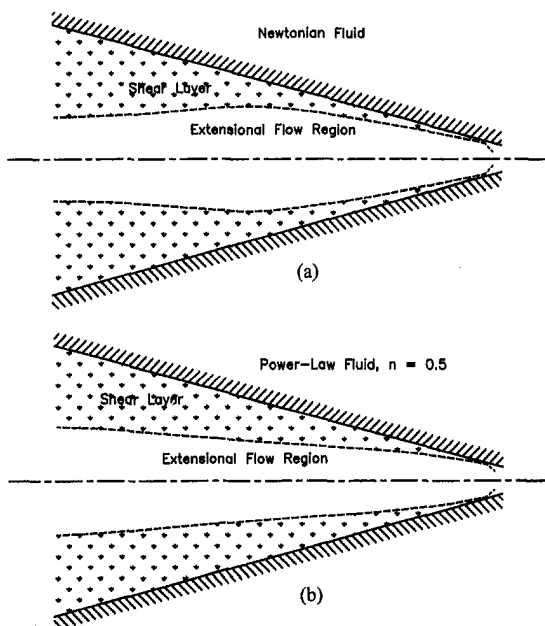


Fig. 9 Plots of the core region, for the same fluids and same Re as Fig. 8, but for a half-angle of 15 deg

Table 1 Local Re's in a 10:1 diameter ratio cone, for a downstream Re of 1000, as calculated from Eq. (9)

x/L	Local Re	
	$n = 1.0$	$n = 0.5$
0.00	100.0	3.162
0.25	129.0	5.981
0.50	181.8	14.10
0.75	307.7	52.52
1.00	1000.	1000.

is necessary near the cone exit where the flow adjusts to the outlet tube and creates a maximum velocity between the wall and the centerline. When the second criterion becomes the governing condition, there is an abrupt decrease in the core region, as will be seen in upcoming figures.

The extent of the core region, as defined above, is shown in Figs. 7 to 9 for several flow conditions. The first figure compares the regions for two fluids, a Newtonian fluid and a power-law fluid with $n = 0.5$, for a downstream Re of 100 and for our standard 10:1 diameter ratio and 30 deg half-angle. The figure shows a modest core region for both fluids and indicates that the relative core size increases in the flow direction, which is expected because the local Re increases in the flow direction. Close to the cone exit, however, the core region shrinks rapidly as the transition from near-sink flow to tube flow begins. The Newtonian fluid's core region is slightly larger than the core of the strongly shear-thinning fluid, a finding which differs from Fig. 6 because of the use of a common downstream Re in Fig. 7, rather than the localized Re in Fig. 6 (the dependence on the power-law index will be discussed in detail later). For the same fluids and same geometry, Fig. 8 illustrates the expected pattern when the Reynolds number is ten times larger: the core regions are noticeably larger, particularly near the exit. Figure 9 shows the influence of cone angle on core size. The 15 deg half-angle produces only a small decrease in the relative size of the core regions compared with the regions in Fig. 8. Thus, Figs. 7 to 9 indicate that near-sink flow is considerably more sensitive to changes in Re than to changes in the power-law index or the cone half-angle.

The effect of the power-law index on the size of the core region deserves further comment. In Fig. 8, both cores expand downstream as the local Re increases, but the Newtonian core is larger from $x/L = 0.32$ to 0.84 because of that fluid's higher local Re's in the cone. These differences in local Re's, for the same downstream Re, as calculated from Eq. (9), are illustrated in Table 1. For $n = 0.5$, the greater sensitivity of the local Re to diameter changes produces lower local Re's in the cone and therefore thicker boundary layers. Past $x/L = 0.84$, however, the two fluids' Re's are comparable and then shear-thinning

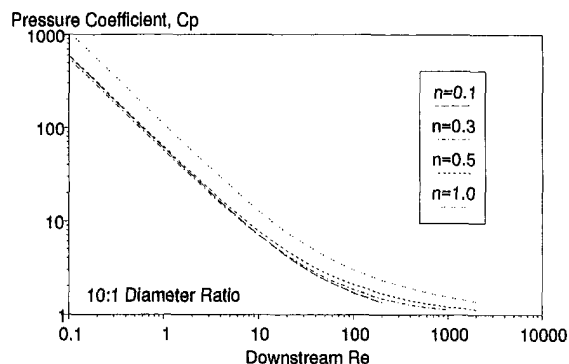


Fig. 10 Pressure drop coefficients for $\alpha = 15$ deg

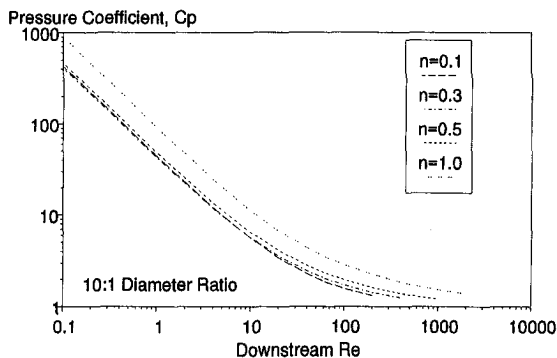


Fig. 11 Pressure drop coefficients for $\alpha = 30$ deg

becomes the dominant factor in producing a wider core boundary for the $n = 0.5$ flow.

6.3 Pressure Drop Through the Conical Channel. Another result of our conical flow computations is the pressure drop through the channel. Pressure drop results for two cone angles, $\alpha = 15$ and 30 deg, are plotted in Figs. 10 and 11 as C_p versus Re . The pressure coefficient (C_p) is defined as

$$C_p = \frac{p_1 - p_0}{\frac{1}{2} \rho \bar{U}_0^2} \quad (13)$$

where p_1 is the pressure one diameter upstream of the cone, p_0 is the pressure one diameter downstream of the cone, ρ is the density, and \bar{U}_0 is the average velocity in the downstream tube. In both figures, the slopes of the C_p curves tend to -1 as Re decreases, as expected, when viscous effects begin to dominate. At high Re , the curves asymptote to $C_p = 1.0$ as inertial effects dominate. However, the asymptotic behavior is less well shown by the low- n curves, which terminate early because separation is observed in the downstream tube, near the cone outlet.

Both graphs show that the non-Newtonian flows may have considerably smaller pressure drop coefficients and therefore smaller pressure drops, than do the Newtonian flows. For example, for $\alpha = 30$ deg and $Re = 100$ in Fig. 11, the Newtonian C_p is 1.46 times as large as the C_p value at $n = 0.5$. The discrepancy in total pressure drop is the result of differences in the viscous and inertial pressure drops. Regarding the viscous component, the shear-thinning of the power-law fluids produces both higher velocity gradients and lower viscosities along the wall, compared to Newtonian fluids, with the net effect of reducing the wall shear stresses. As a result, shear-thinning fluids experience smaller viscous losses. However, the blunter velocity profiles of the power-law fluids cause greater inertial, or dynamic, pressure drops across the cone. For the cases shown in Figs. 10 and 11, the combined viscous and inertial pressure drops are lower for shear-thinning fluids than for Newtonian fluids.

7 Discussion

The primary results of this work are the detailed maps of the flow field and the C_p - Re curves for inelastic conical flow. This information is potentially valuable to the experimentalist who wants to design a converging flow rheometer based on cone flow and who will want to interpret data from it. As expected, there are considerable differences between Newtonian and non-Newtonian behavior. For example, shear-thinning fluids separate more easily and produce smaller pressure drops in cone flow, compared with Newtonian fluids. Additionally, Newtonian fluids have larger near-sink regions. In general, the numerical simulations show that shear-thinning and Newtonian flows are qualitatively similar, but may be quite different quantitatively.

Acknowledgments

The support of the Natural Sciences and Engineering Research Council of Canada is gratefully acknowledged.

References

- Bird, R. B., Armstrong, R. C., and Hassager, O., 1987, *Dynamics of Polymeric Liquids. Volume 1: Fluid Mechanics*, 2nd edition, Wiley, New York.
- Bond, W. N., 1925, "Viscous Flow through Wide-Angled Cones," *Philosophical Magazine*, Vol. 50, pp. 1058–1066.
- Brooks, A. N., and Hughes, T. J. R., 1982, "Streamline Upwind/Petrov-Galerkin Formulations for Convection Dominated Flows with Particular Emphasis on the Incompressible Navier-Stokes Equations," *Computer Methods in Applied Mechanics and Engineering*, Vol. 32, pp. 199–259.
- Crochet, M. J., Davies, A. R., and Walters, K., 1984, *Numerical Simulation of Non-Newtonian Flow*, Elsevier Science Publishers B.V.
- Forsyth, T. H., 1976, "Converging Flow of Polymers," *Polymer-Plastics Technology and Engineering*, Vol. 6, pp. 101–131.
- Garrioch, S. H., 1994, "A Finite Element Study of Power-Law Fluids in Cone Flow," M.A.Sc. dissertation, University of Toronto, Toronto, ON.
- Harrison, W. J., 1919, "The Pressure in a Viscous Liquid Moving through a Channel with Diverging Boundaries," *Proceedings of the Cambridge Philosophical Society*, Vol. 19, pp. 307–312.
- James, D. F., and Saringer, J. H., 1980, "Extensional Flow of Dilute Polymer Solutions," *Journal of Fluid Mechanics*, Vol. 97, pp. 655–671.
- Jarzebski, A. B., and Wilkinson, W. L., 1981, "Non-Isothermal Developing Flow of a Generalized Power-Law Fluid in a Tapered Tube," *Journal of Non-Newtonian Fluid Mechanics*, Vol. 8, pp. 239–248.
- Kajiwar, T., Ninomiya, S., Kuwano, Y., and Funatsu, K., 1993, "Numerical Simulation of Converging Flow of Polymer Melts through a Tapered Slit Die," *Journal of Non-Newtonian Fluid Mechanics*, Vol. 48, pp. 111–124.
- Kwon, T. H., Shen, S. F., and Wang, K. K., 1986, "Pressure Drop of Polymeric Melts in Conical Converging Flow: Experiments and Predictions," *Polymer Engineering and Science*, Vol. 26, pp. 214–224.
- Oka, S., and Takami, A., 1967, "The Steady Slow Motion of a Non-Newtonian Liquid through a Tapered Tube," *Japanese Journal of Applied Physics*, Vol. 6, pp. 423–426.
- Schowalter, W. R., 1978, *Mechanics of Non-Newtonian Fluids*, Pergamon Press.
- Shah, R. K., and London, A. L., 1978, *Laminar Flow Forced Convection in Ducts*, Academic.
- Sutterby, J. L., 1965, "Laminar Converging Flow of Dilute Polymer Solutions in Conical Sections: Part II," *Transactions of the Society of Rheology*, Vol. 9, pp. 227–241.
- Sutterby, J. L., 1966, "Laminar Converging Flow of Dilute Polymer Solutions in Conical Sections: Part I," *AIChE Journal*, Vol. 12, pp. 63–68.

P. S. Addison¹

Lecturer,
Department of Civil and Transportation
Engineering,
Napier University, Merchiston Campus,
Edinburgh, Scotland

D. A. Ervine

Senior Lecturer.

A. H. C. Chan

Reader.

K. J. Williams

Lecturer.

Department of Civil Engineering,
The Rankine Building, Glasgow University,
Glasgow, Scotland

An Experimental Investigation Into the Breakdown of Low Reynolds Number Pulsed Flows at a Pipe Orifice

An experimental investigation into the behavior of pulsed vortex flows in water at a pipe orifice is outlined. An experimental apparatus is described whereby flow pulsations are generated using an electronically controlled motor-piston arrangement. Preliminary investigations are made into the unpulsed system to determine the natural vortex shedding frequency for various Reynolds numbers and orifice diameters. The downstream development of initially axisymmetric, periodically pulsed vortices shed from the orifice plate are then examined. The growth, evolution, and eventual breakdown of the initially axisymmetric vortices are investigated for a range of flow control parameters. Various flow regimes are discerned and an attempt is made to categorize them.

1 Introduction

Pulsatile flows are of interest to many areas of engineering: they are very common within pipeline systems, caused by either mechanical vibration, both internal and external to the fluid system; or flow related phenomena, such as natural vortex shedding from obstructions within the flow field (Marris, 1964) or flow induced vibrations (D'Netto and Weaver, 1987; Weaver et al., 1978). Flow pulsations have a detrimental effect on the accuracy of the orifice plate as a flow metering device in both laminar (Jones and Bajura, 1991) and fully developed turbulent flows, (Downing and Mottram, 1977; Mottram and Robati, 1985), due to an increase in energy dissipated across the device caused by the pulsations.

The behavior of pulsed, laminar flow at a pipe constriction is of specific interest to the biofluid mechanic engineer (Einav S. and Sokolov M., 1993). The breakdown of pulsed flows in the arterial system may occur at natural and mechanical heart valves, or other constrictions (Nerem et al., 1972; Lei et al., 1992; Baldwin et al., 1994; King et al., 1996; Shortland et al., 1996). A breakdown to turbulence can cause a significant change in the flow field which may result in both higher pressure drops and unwanted regions of low velocity recirculation producing areas where deposition and further constriction may occur. Although, over the years, much attention has been given to the problem of vortex flows in engineering fluid dynamics, the prediction of the breakdown processes of vortex flows is still beyond our reach in all but a few cases (Sarpkaya, 1992) and the engineer must resort to experimentation.

The experimental investigation outlined herein attempts to shed light upon the nature of pulsed vortex flows as they evolve subsequent to shedding downstream of circular orifice plates placed in a pipe, (i.e., an idealised constriction). By looking at the relatively simple case of a periodically pulsed, axisymmetric vortex system, in which the frequency and amplitude of the pulsations may be accurately controlled, it is hoped to elucidate the nature of transition to the turbulent state of such flows.

¹ Formerly at the Department of Civil Engineering, Glasgow University, Glasgow, Scotland.

Contributed by the Fluids Engineering Division for publication in the Journal of Fluids Engineering. Manuscript received by the Fluids Engineering Division June 11, 1995; revised manuscript received February 11, 1997. Associate Technical Editor: M. Gharib.

The investigation falls into three distinct sections: (1) the development of an experimental system to produce accurately controllable mass flux pulsations in a pipe system; (2) the determination of the natural vortex shedding frequency for flows through various orifice diameters in a pipe; and (3) the investigation of the behavior of pulsed flows at pipe orifice constrictions. The development of the vortices upon leaving the orifice plate was investigated using both flow visualisation and analysis of velocity-time series taken at various spatial locations within the flow field.

2 Experimental Apparatus and Procedure

2.1 Experimental Arrangement. The experiments were performed on a purpose built test rig, the general layout of which is shown in Fig. 1. The rig accommodates a 4 meter long, 26.00 mm internal diameter, (D_p), high tolerance glass pipe, which consists of 4×1 -meter sections connected together using specially designed couplings. The orifice plates used were located midway along the length of the pipe. This position was sufficient to allow (unpulsed) Hagen-Poiseuille flow to develop fully in the pipe before encountering the orifice plate, (Friedmann et al., 1968). The orifice plates used in the study were 0.50 mm thick, square edged and were designed using B.S. 1042, (1989), sections 1.1 and 1.2 as a guide. Six orifice diameters, D_o , were used, these were from $0.250 D_p$ to $0.875 D_p$ in increments of $0.125 D_p$ —corresponding to 6.50 mm to 22.75 mm in increments of 3.25 mm. At the upstream end of the pipe a header tank is connected to the pipe via a specially designed elliptic entrance piece which ensures a smooth entrance flow development from the tank.

The flow in the pipe was driven by a motor-piston arrangement connected at the downstream end, which allowed highly accurate Reynolds number flows to be generated within the pipe. This is a necessary condition when dealing with transition flows as the intermittent nature of the transition process may cause the Reynolds number to fluctuate for head driven flows and resulting in "periodic" turbulence (Banfi et al., 1981 and Banfi, 1990). The motor driving the piston was controlled using a variable frequency inverter which in turn was controlled by a function generator. This allowed a mean mass flux to be generated within the pipe with the ability to superimpose sinusoidal fluctuations of variable frequency and amplitude on top

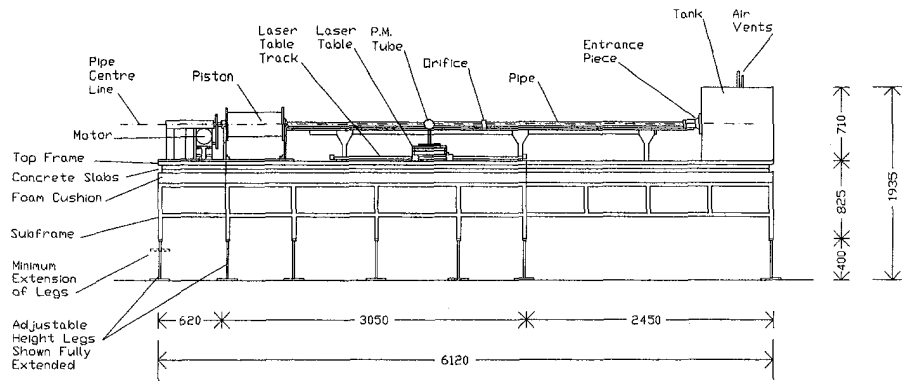


Fig. 1 General layout of the experimental apparatus (all dimensions in mm)

of the mean mass flux. A schematic diagram of the control of the motor-piston arrangement is shown in Fig. 2(a).

The whole experimental apparatus was connected to a steel top-frame located on a concrete base, (see Fig. 1). The concrete base sits on a 150 mm thick, high density foam cushion. Underneath this was the experimental sub-frame which could be tilted to the desired angle, (to allow air to evacuate from the pipe), by utilizing the adjustable legs. The concrete-foam sandwich between the top- and sub-frame was designed to eliminate undesirable vibrations from the surroundings affecting the experimental results. During the experimental tests much effort was made to keep the temperature of, and thus the viscosity of, the water constant, (Kestin et al., 1978). Great care was also taken to ensure that each pipe segment was correctly aligned. Further information, including the alignment procedure, detailed drawings of the apparatus components, tolerances, manufacturer's details etc. is given in Addison (1993).

2.2 Flow Velocity Acquisition. A schematic diagram of the data acquisition arrangement is given in Fig. 2(b). The axial velocity of the flow in the pipe was measured using a one-component Laser Doppler Anemometer (LDA) system, (a DISA LD03). The one-component laser system is limited to measuring one velocity component at a time and hence cannot directly measure Reynolds stresses (Durrani and Greated, 1977; Baldwin et al., 1994). However, for this experimental study one velocity component was sufficient and the LDA system was considered the better tool than its main competitor for point velocity measurement—the hot-wire anemometer—as it has the advantage of being able to carry out velocity measurements within the flowfield without disturbing the flow pattern. This characteristic of the LDA system was particularly useful in this study due to both the relative inaccessibility of the flow field within the glass pipe and the relatively small (radial) spatial scale of the regions of interest. The laser, together with the photomultiplier (PM) unit, was carriage mounted on the experimental rig which allowed for the accurate positioning of the beams within the pipe. The signal from the PM unit was picked up by a DISA 55N20 Doppler Frequency Tracker, the analog

output from which was sent to an IBM P.C. via a Burr-Brown PCI 2000 Interface Card which performed analog to digital conversion with 12 bit resolution. The signal was then converted to a flow velocity time series output from which the turbulence intensity and frequency spectrum could be derived. For each flow configuration investigated, time series comprising 16384 data points sampled at 100 Hz were used.

2.3 Flow Visualization. During the course of the investigation both still photographs and video film were taken of the flow phenomena at the orifice plate for a range of orifice diameters, pipe Reynolds numbers and forcing frequencies, covering an area in the immediate vicinity of the orifice plate. Flow visualization has the advantage of giving an overall picture of events simultaneously over a range of spatial locations in the flow, (Emrich, 1983 and Prenel et al, 1989) although interpretation of the resulting flow patterns must be done with extreme caution (Gursul et al., 1990). In the study presented herein, flow visualization was used to aid the physical interpretation of the LDA data analysis results.

There are many flow visualization agents available, see for example Merzkirch (1987). In this study, natural guanine crystals were used as the flow visualization agent, (Matisse and Gorman, 1984 and Rhee et al., 1984). These crystals were injected into the flow at the header tank and were carried downstream to the orifice plate by the main flow. A suitable light source for the flow visualization was provided by a purpose built light-box, which directed a sheet of light through the main diameter of the pipe. The light-box enabled both flashlight and lamplight to be used.

A 400 ASA professional black and white film with a wide latitude (i.e., it is much less susceptible to over-, and under-exposure) was used to take the photographs of the flow. The film proved suitable for taking high quality pictures in the low lighting conditions, due to its fine grained structure. Video film was also shot of the flow processes at the orifice plate, covering the same parameters as the photographic film. Copies of the video film are held at the Department of Civil and Transporta-

Nomenclature

D_o = orifice diameter	U_{HP} = centerline velocity of unpulsed Hagen-Poiseuille flow	Re_ω = oscillating Reynolds number = $(U_\omega \cdot D_p) / \nu$
D_p = pipe internal diameter	U_ω = cross-sectional mean amplitude of the pulsatile velocity component	S = Strouhal number
f_n = natural shedding frequency of unpulsed vortices	Re_o = orifice Reynolds number	$T.I.$ = turbulence intensity
u'_{rms} = longitudinal velocity fluctuation	Re_p = pipe Reynolds number	Z = downstream distance
\bar{U}_o = mean flow velocity through the orifice plate		ν = kinematic viscosity

Note: All symbols are defined in text.

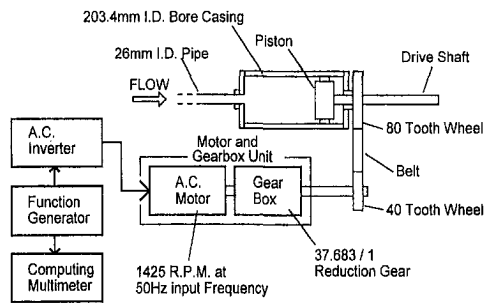


Fig. 2(a) Schematic diagram of the motor-piston arrangement

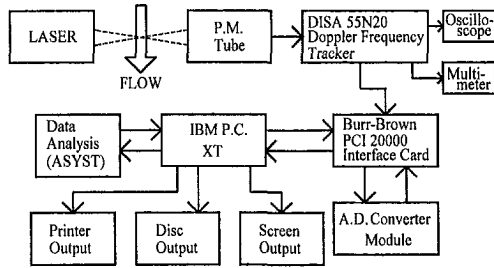


Fig. 2(b) Data acquisition flow chart

tion Engineering at Napier University. Note that all flows are from left to right in the photographs presented herein.

3 Determination of the Natural Vortex Shedding Frequency—The Strouhal Number

Preliminary tests were conducted to find the natural (i.e., unpulsed) frequency of vortex shedding for each of the orifice plates used in the experimental investigation. The frequency of the natural vortex shedding was measured using the LDA system, and confirmed using flow visualization. The Strouhal number, S , was calculated for each observation, and is defined as

$$S = \frac{f_n \cdot D_o}{\bar{U}_o} \quad (1)$$

where f_n is the natural shedding frequency of the vortices, D_o is the orifice diameter, and \bar{U}_o is the mean flow velocity through the orifice plate. The Strouhal number was found over a range of Reynolds numbers for each diameter of orifice plate used in the study. The results for the case of $D_o/D_p = 0.5$ closely match those of the early work by Johansen (1929 and 1933), in which he investigated the vortex shedding at an orifice plate in a 27.00 mm internal diameter glass pipe.

It was found that the Strouhal numbers remain reasonably constant, for each orifice plate, over a range of Pipe Reynolds numbers below 1500. For Re_p approaching the critical Reynolds number (for the breakdown of Hagen-Poiseuille flow of approximately 2300) the Strouhal number tends to increase in value. However, this investigation deals with low Pipe Reynolds numbers and hence constant Strouhal numbers, i.e., the vortex shedding frequency is linearly related to the average flow velocity through the orifice for a given orifice diameter. Figure 3 gives the results of the mean Strouhal number versus the orifice diameter for each orifice plate studied. Reliable results could not be obtained for the 22.75 mm orifice plate ($=0.875 D_p$) as the resulting frequency spectra were very broad band and no distinct peak could be observed. The best fit line is indicated in the figure, together with the 95 percent confidence limits associated with each observed point, (Snedecor and Cochran, 1967). The equation of the best fit line is,

$$S = 0.70643 - 0.13292 \left(\frac{D_o}{D_p} \right) \quad (2)$$

this equation was subsequently used to determine the natural shedding frequency of the flow for each orifice plate at each Reynolds number tested. The forcing frequency, f_f , of the vortex shedding was set equal to the natural frequency for each flow set up. (Note that D_p appears in Eq. (2) although it is a constant in this study ($=26.00$ mm), further experimentation would be required to elucidate the role of D_p in the resulting value of S .)

4 The Evolution of Pulsed Vortices at the Pipe Orifice

4.1 Flow Parameters.

The main tests conducted and reported on herein all involve the generation of pulsed vortex flows at a pipe orifice. By pulsing the main flow, large amplitude, temporally coherent vortices could be generated, and their subsequent evolution was readily amenable to study. The pipe Reynolds number was subcritical for all the tests conducted, increasing from $Re_p = 128$ in increments of 128. To limit the number of parameters studied in this preliminary investigation both the forcing frequency and amplitude of the pulsations were controlled as follows. The forcing frequency was set to the natural vortex shedding frequency, (found from Eq. (2)), for each particular orifice plate diameter and pipe Reynolds number configuration. The forcing amplitude was maintained as a constant fluctuation in the mass flux, corresponding to an oscillating Reynolds number Re_w of 28.8. ($Re_w = (U_w \cdot D_p) / \nu$, where U_w is the cross-sectional mean amplitude of the pulsatile velocity component, D_p is the pipe internal diameter and ν is the kinematic viscosity.) This value of Re_w gave optimum results for vortex growth over the whole range of Reynolds numbers and orifice diameters studied. LDA readings were taken from 90 mm ($3.46 D_p$) upstream to 950 mm ($36.54 D_p$) downstream of the orifice plate for all flow regimes studied, this covered: the upstream flow undisturbed by the orifice plate; the downstream vortex development region; the downstream turbulent region; and the downstream decay region. The LDA positions are indicated in Fig. 4.

4.2 Results and Categorisation of the Flow Regimes.

An attempt was made to put into context the information obtained from the LDA system and both video and photographic film of the events at the orifice plate. It soon became apparent from the flow visualisation and LDA data analysis that two distinct flows were generated at the orifice plate, these were split up into two main categories. The first, whereby the vortex

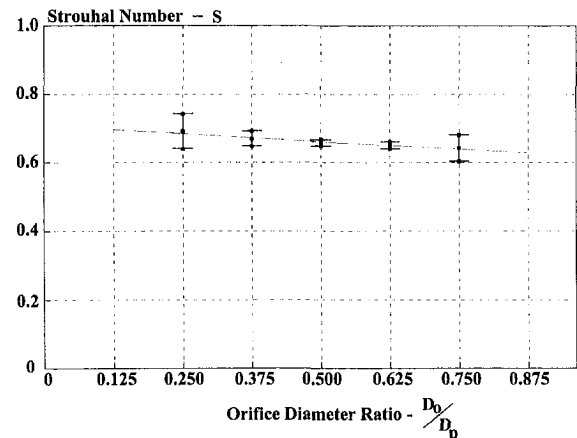


Fig. 3 Strouhal number versus orifice diameter (95 percent confidence limits for S are given on plot. Uncertainty in orifice diameter ratio = ± 0.001).

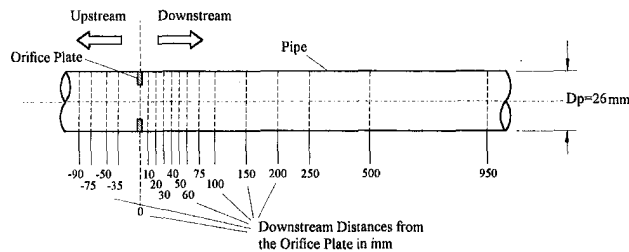


Fig. 4 LDA data acquisition locations

flow produced at the orifice plate dissipates out and the flow streamlines remain axisymmetric. This type of flow, labeled **DIRECTLY DISSIPATING** flow, remains simple, i.e., the most complex structures in the flow are the axisymmetric vortex rings. The second type of flow, which has been labeled **INITIALLY INTERACTING** flow, includes all the flows which upon leaving the orifice plate increase in complexity and degenerate to a turbulent regime. (Note that both flows eventually revert back to the upstream pulsed laminar flow condition.) These two types of flow are outlined in more detail below and summarized in Fig. 8.

(a) *Directly Dissipating Vortex Flows.* This type of flow is typical of low Reynolds number flows. Discrete vortex rings are formed at the edges of the flow issuing from the orifice plate which dissipate out axisymmetrically as they proceed downstream. Figures 5(a) and 5(b) contain examples of such flows. The axisymmetric vortex shedding at the 16.25 mm orifice plate at a pipe Reynolds number of 128 (pulsation frequency = 0.64 Hz) is shown in Fig. 5(a). The flow is from left to right and the light-box is situated at the bottom of the figure, which results in the increased illumination of the lower part of the photograph. The axisymmetric vortex decay is clearly shown in the figure. Figure 5(b) shows the vortex development again for the 16.25 mm orifice plate this time at a pipe Reynolds number of 256 (pulsation frequency = 1.28 Hz). In the photograph of Fig. 5(b) the flow visualization chemical has been introduced only at the upper edge of the orifice plate, this allows for a clear picture of the vortex roll-up process. The discrete axisymmetric vortex rings roll up, reaching a maximum size before dissipating out further downstream. For the case of very low (orifice) Reynolds number flows, vortices are not fully formed and only a series of undulations are noticeable at the jet edge. At all points in such flows, the flow field is axisymmetric.

(b) *Initially Interacting Vortex Flows.* These flows are characterized by the development of nonaxisymmetric disturbances in the flow field downstream of the orifice plate. From flow visualization it was noticed that these flows may be further subdivided as follows:

(i) *Unstable Slow Jet Flow.* As shown in Fig. 5(c) for the 9.75 mm orifice plate at a pipe Reynolds number of 128 (pulsation frequency = 3.07 Hz), vortices appear at the jet edge as it emanates from the orifice aperture. These vortices die out as they proceed downstream. However, the jet itself appears to loose stability causing a weakly fluctuating flow to appear further downstream of the orifice plate. (This flow type is also typical of unpulsed confined flows; see, for example, Koller-Milojevic and Schneider, 1993.)

(ii) *Interacting Vortex Flow.* As with the above flow, discrete vortices are formed at the orifice plate. However, as they proceed downstream they increase in size, until they reach a point at which they interact with the weakly turbulent flow region further downstream. The vortices then breakdown into the weakly turbulent regime, as can be seen in Fig. 5(d). In the photograph, the flow field is illuminated either side of the

orifice plate housing, enabling the upstream laminar flow to be discerned.

The downstream development of the mean centre-line velocities for each of the five flows investigated for the 13.00 mm orifice are presented in Fig. 6(a). The centerline velocities are normalized by dividing them by the downstream centerline velocity of an equivalent unpulsed laminar, Hagen-Poiseuille pipe flow, U_{HP} , (equal to twice the mean flow velocity). The downstream distance, Z , is normalized by the Pipe Diameter, D_p . From the figure, it may be seen that there are two distinct velocity curves corresponding to the directly dissipating and initially interacting flow regimes. For the $Re_p = 128$ flow there is a smooth reduction in the velocity on issuing from the orifice plate to the downstream condition, from the flow visualization it was observed that this flow remains axisymmetric at all points downstream, i.e., it was a directly dissipative flow as defined above. The higher Reynolds number flows, i.e., $Re_p > 128$, are all initially interacting flows consisting of axisymmetric vortices which breakdown to turbulence downstream of the orifice plate. On issuing from the orifice plate, the initially interacting flows have a much sharper reduction in their velocity, with a minimum reached at 3.5 pipe diameters downstream. From this minimum the centerline velocity increases slowly to the downstream con-

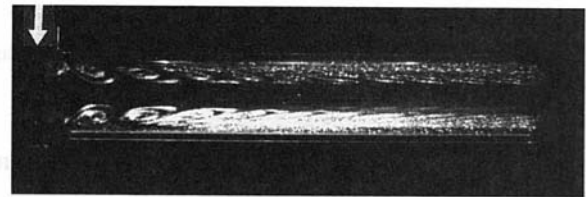


Fig. 5(a)

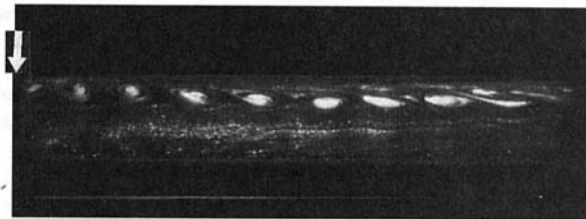


Fig. 5(b)

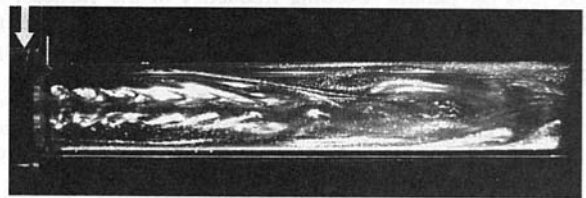


Fig. 5(c)

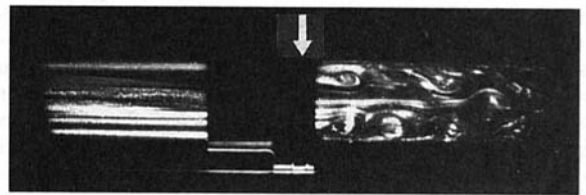


Fig. 5(d)

Fig. 5 Selected flow visualization photographs (the location of the orifice plate is marked in each photograph by an arrow). (a) Directly dissipating flow: $D_o = 16.25$ mm, $Re_p = 128$, $Re_o = 205$, $f_f = 0.64$ Hz; (b) Directly dissipating flow: $D_o = 16.25$ mm, $Re_p = 256$, $Re_o = 410$, $f_f = 1.28$ Hz; (c) Initially interacting flow—unstable slow jet flow: $D_o = 9.75$ mm, $Re_p = 128$, $Re_o = 512$, $f_f = 3.07$ Hz; (d) Initially interacting flow—interacting vortex flow: $D_o = 16.25$ mm, $Re_p = 384$, $Re_o = 614$, $f_f = 1.92$ Hz.

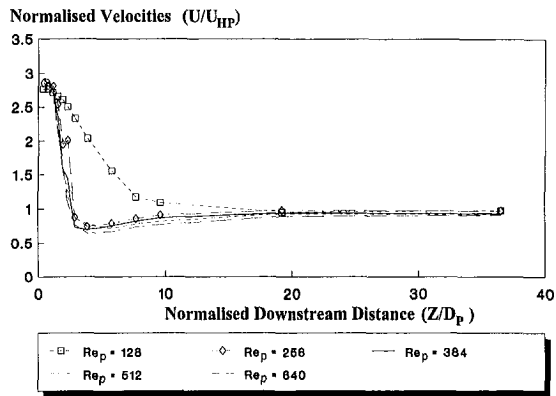


Fig. 6(a) Downstream development of the normalised centre-line velocities (13.00 mm orifice plate, various pipe Reynolds numbers) (uncertainty in normalized velocity = ± 3 percent in normalized downstream distance = ± 0.0096 , with 95 percent confidence).

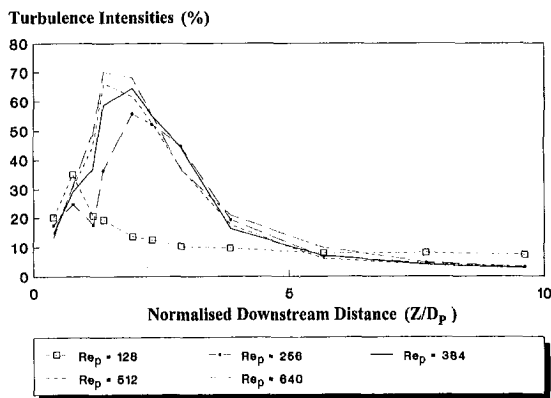


Fig. 6(b) Downstream development of the turbulence intensities (13.00 mm orifice plate, various pipe Reynolds numbers) (uncertainty in turbulence intensities = ± 3 percent in normalized downstream distance = ± 0.0096).

dition as the turbulence dissipates out and the flow reverts back to the pulsed laminar case.

Figure 6(b) contains the results of the relative turbulence intensities corresponding to the flows of Fig. 6(a). This time, however, only the first 10 pipe diameters downstream of the 13.00 mm orifice plate are covered. The turbulence intensity, $T.I.$, being defined as the root mean square of the longitudinal velocity fluctuation, u'_{rms} , divided by U_{HP} , i.e.,

$$T.I. = \frac{u'_{rms}}{U_{HP}} \quad (3)$$

From the figure it is evident that, once again, the directly dissipating and initially interacting flows behave differently. The directly dissipating flow ($Re_p = 128$) reaches a peak value of turbulence intensity soon after leaving the orifice plate, (within one pipe diameter). On the other hand, the initially interacting flows reach a maximum in turbulence intensity at around 2 to 3 pipe (or 4 to 6 orifice) diameters downstream. The maxima for the initially interacting flows, of between 55 and 70 percent, are significantly larger than the maximum $T.I.$ for the directly dissipating flow, of around 35 percent. In fact, the maximum turbulence intensities in the initially interacting flows occur at the maxima of the slopes of the centre-line velocity plots of Fig. 6(a). This is most likely due to the fluctuations (made up from the coherent remnants from the vortices in the now complex flow field together with more complex "turbulent" fluctuations) producing Reynolds stresses which flatten the velocity profile. As the turbulence dissipates out down-

stream, the velocity profile assumes the upstream flow condition.

Frequency spectra were also generated from each time series using a fast Fourier transform, F.F.T. This enabled the frequencies present in the flow to be discerned and served as a further means of categorising the flow regimes. Figure 7 contains selected frequency spectrum plots for an initially interacting flow, namely an $Re_p = 256$ flow through the 13.00 mm orifice plate. The frequency spectra for downstream positions of $0.38 D_p$, $1.53 D_p$, $3.85 D_p$ and $36.54 D_p$ (corresponding to 10 mm, 40 mm, 100 mm and 950 mm) are presented in the figure. In the first plot, the forcing frequency of 2.54 Hz is dominant in the flow, this corresponds to the developing vortex in the flow just downstream of the orifice plate. By $1.53 D_p$ downstream, a distinctive period doubling peak has emerged, due to vortex merging, together with a significant contribution from broad band components as the vortex dominated flow begins to break down. At the $3.85 D_p$ position the spectrum is now composed of low frequency, broad band components, however, the forcing frequency is still discernible in the spectral plot. At the $36.54 D_p$ position the flow has now reverted back to the laminar pulsed flow which exists upstream of the orifice plate. The spectral plot sequence of Fig. 7 is typical of all initially interacting flows. Directly dissipating flows are, however, conspicuous by a single dominant peak in the spectrum at all points in the flow field, i.e., the absence of broad band components.

Figure 8 plots the nondimensional orifice diameter, D_o/D_p , versus the orifice Reynolds number, Re_o . In addition, contours of equal values of Re_p are depicted in the figure. A clearly defined border between directly dissipating and initially interacting flows may be observed. Along this border, unstable slow jet flows occur. The simplest empirical relationship that may be found which adequately defines this border is,

$$\frac{D_o}{D_p} = \tanh \left[\frac{Re_o}{820} \right] \quad (4)$$

this expression is plotted in Fig. 8. Note that Eq. (4), although purely an empirical fit with no theoretically valid reason for the tanh function, approaches a value close to unity for pipe Reynolds numbers approaching the critical value for flow breakdown in Hagen-Poiseuille flow. This is quite reasonable as Hagen-Poiseuille flow is unstable only for finite disturbances input into the flow field, (see for example Keuthe, 1956; Leite, 1957 and 1958, and Corcos and Sellars, 1959). Directly dissipating flows occur at low orifice Reynolds numbers and large orifice diameters, i.e., above the slow jet flow boundary. The initially interacting flows occupy a region below the slow jet boundary in Fig. 8 which correspond to high orifice Reynolds numbers and small orifice diameters. Slow jet flows occur at the boundary which would indicate that this flow regime represents the transition between the Directly Dissipating and Initially Interacting flow types.

5 Concluding Remarks

In general, the breakdown of laminar flows to the turbulent state is an extremely complex process, whereby nonlinearities quickly take control of the transition process. In the study presented herein, the transition process was controlled both temporally and spatially. Pulsations superimposed on the mean mass flux generated periodic, temporally coherent vortices, the subsequent development of which was readily amenable to investigation. All pulsed flows studied were at pipe Reynolds numbers well below the critical value for unpulsed flows in a pipe. In addition, the presence of an orifice plate enabled the transition process to be fixed spatially over a distinct region within the pipe, which allowed various aspects of the transition process to be elucidated using flow visualisation and a one-component LDA system.

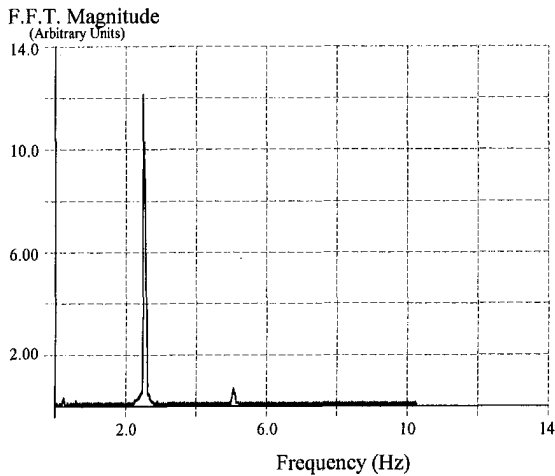


Fig. 7(a) $0.38D_p$ (10 mm) downstream of the orifice plate

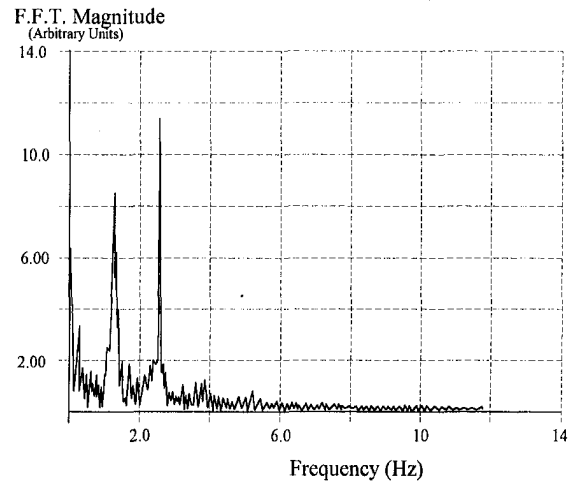


Fig. 7(b) $1.53D_p$ (40 mm) downstream of the orifice plate

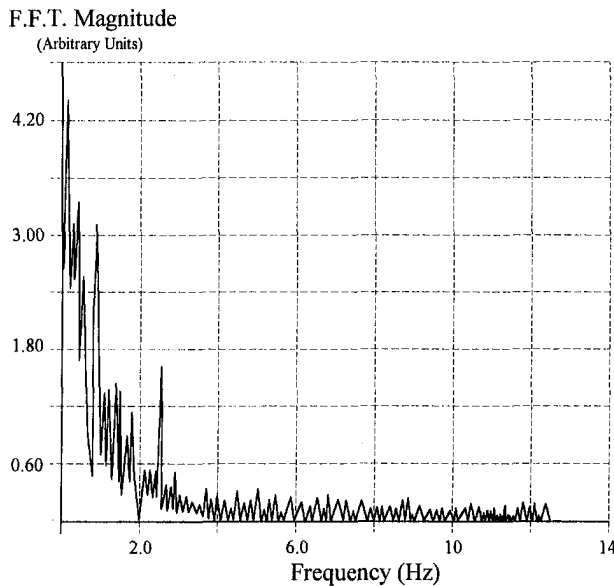


Fig. 7(c) $3.85D_p$ (100 mm) downstream of the orifice plate

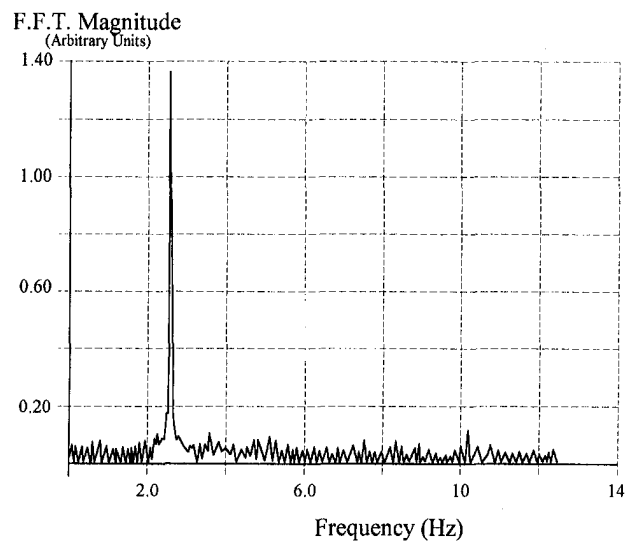


Fig. 7(d) $36.54D_p$ (950 mm) downstream of the orifice plate

Fig. 7 Frequency spectra plots for the 13.00 mm orifice plate, $Re_p = 256$, $f_r = 2.54$ Hz

The main features of the investigation may be summarized as follows:

1 An experimental setup has been described which superimposes accurate and controllable pulsations on the mean mass flux in a pipe system. The system is superior to head driven systems as the mean mass flux may be kept constant throughout the breakdown process, essential for investigating laminar-turbulent transition phenomena in pipe flow.

2 An investigation of unpulsed flows of varying Reynolds numbers and orifice diameters has enabled an empirical relationship to be derived from experimental data for the variation of Strouhal number with orifice diameter for low pipe Reynolds numbers.

3 Pulsed vortex flows have been generated at a pipe orifice. Two distinctive flow regimes were found whereby the shed vortices either dissipate out axisymmetrically, or evolve to more complex, non-axisymmetric state downstream of the orifice: these were labeled Directly Dissipating and Initially Interacting flows, respectively. It was shown that these regimes may be differentiated using flow visualization, downstream centerline velocity data, downstream turbulence intensity data, and downstream frequency spectra. An empirical

relationship was found for the interface between the two flow regimes. On the basis of the flow visualization results alone, initially interacting flows were further subdivided into two sub-groups: unstable slow jet flow and interacting vortex flow.

The investigation outlined herein is a basis for a wider ranging experimental program into an important area of biofluid mechanic research. Future work aims to expand on these preliminary tests by investigating the following: (1) the relationship between the natural vortex shedding frequency and pipe diameter; (2) the effect of pulsation amplitude on the breakdown process (preliminary work by the authors tends to suggest that the breakdown processes follow the same patterns with breakdown occurring at lower Re_p for higher Re_w , as one might expect); (3) the behavior of vortices shed by flow pulsations with frequencies other than the natural vortex shedding frequency—in this case the vortex system will probably behave as forced non-linear oscillator with associated phenomena (Zdravkovich, 1989)—adding more inherent complexity to the system. During the study detailed in this paper no other orifice related frequencies were observed, however, this could be due to the nature of the pulsations, i.e. both large amplitude and at

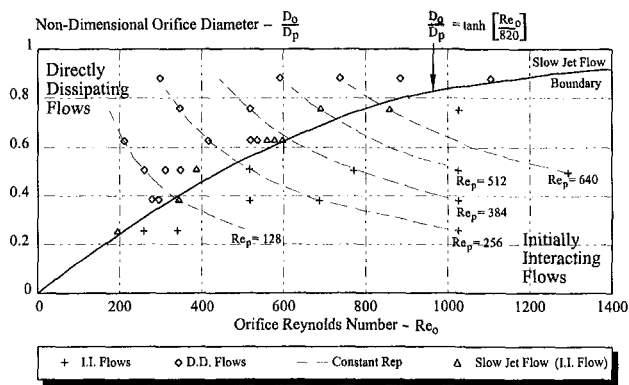


Fig. 8 The relationship between flow type, orifice diameter and Reynolds number (Uncertainty in nondimensional orifice diameters = ± 0.0010 ; in orifice Reynolds number = ± 1 percent)

the natural frequency. It is possible that smaller amplitudes or alternative frequencies may produce a richer variety of flow phenomena.

References

- Addison, P. S., 1993, "The Breakdown to Turbulence of a Forced Vortex Flow at a Pipe Orifice: The Non-Linear Evolution of Initially Axisymmetric Vortices," Ph.D. thesis, No. 9613, University of Glasgow, Scotland.
- Baldwin, J. T., Deutsch, S., Gesolowitz, D. B., and Tarbell, J. M., 1994, "LDA Measurements of Mean Velocity and Reynolds Stress Fields Within an Artificial Heart Ventricle," *ASME Journal of Biomechanical Engineering*, Vol. 116, pp. 190–200.
- Banfi, G. P., 1990, Private Communication.
- Banfi, G. P., De Micheli, R., and Henin, A., 1981, "Velocity Fluctuation Enhancement in the Transition to Turbulence in a Pipe," *Journal of Physics D: Applied Physics*, Vol. 14, pp. 625–632.
- B.S. 1042, 1989, "Pressure Differential Devices," British Standards Institution.
- Corcoss, G. M., and Sellars, J. R., 1959, "On the Stability of Fully Developed Flow in a Pipe," *Journal of Fluid Mechanics*, Vol. 5, pp. 97–112.
- D'Netto, W., and Weaver, D. S., 1987, "Divergence and Limit Cycle Oscillations in Valves Operating at Small Openings," *Journal of Fluids and Structures*, Vol. 1, pp. 3–18.
- Downing, P. M., and Mottram, R. C., 1977, "The Effects of Flow Pulsations on Orifice Plate Flowmeters," *Fluid Measurement in the Mid 1970's*, E. A. Spencer and W. J. Ramsay, eds., H.M.S.O.
- Durrani, T. S., and Greated, C. A., 1977, *Laser Systems in Flow Measurement*, Plenum Press, New York, pp. 159–161.
- Einav, S., and Sokolov, M., 1993, "An Experimental Study of Pulsatile Pipe Flow in the Transition Range," *ASME Journal of Biomechanical Engineering*, Vol. 115, pp. 404–411.
- Emrich, R. J., 1983, "Flow Field Measurement by Tracer Photography," *Experiments in Fluids*, Vol. 1, pp. 179–184.
- Friedmann, M., Gillis, J., and Liron, N., 1963, "Laminar Flow in a Pipe at Low and Moderate Reynolds Numbers," *Applied Scientific Research*, Vol. 19, pp. 426–438.

- Gursul, I., Lusseyran, D., and Rockwell, D., 1990, "On Interpretation of Flow Visualization of Unsteady Shear Flows," *Experiments in Fluids*, Vol. 9, pp. 257–266.
- Johansen, F. C., 1930, "Flow Through Pipe Orifices at Low Reynolds Numbers," *Aeronautical Research Committee, Reports and Memoranda*, No. 1252, H.M.S.O., 1929.
- Johansen, F. C., 1933, "Flow Through Pipe Orifices at Low Reynolds Numbers," *Proceedings of the Royal Society*, Vol. 126a, pp. 231–245.
- Jones, E. H. and Bajura, R. A., 1991, "A Numerical Analysis of Pulsating Laminar Flow Through a Pipe Orifice," *ASME JOURNAL OF FLUIDS ENGINEERING*, Vol. 113, pp. 199–205.
- Kestin, J., Sokolov, M., and Wakeham, W. A., 1978, "Viscosity of Liquid Water in the Range -8 Degree C to 150 Degree C," *Journal of Physic Chemistry Reference Data*, Vol. 7, No. 3, pp. 941–948.
- Keuthe, A. M., 1956, "Some Features of Boundary Layers and Transition to Turbulent Flow," *Journal of Aerospace Sciences*, Vol. 23, pp. 444–452.
- King, M. J., Corden, J., David, T., and Fisher, J., 1996, "A Three-Dimensional, Time Dependent Analysis of Flow Through a Bileaflet Mechanical Heart Valve: Comparison of Experimental and Numerical Results," *Journal of Biomechanics*, Vol. 29, No. 5, pp. 609–618.
- Koller-Milojevic, D., and Schneider, W., 1993, "Free and Confined Jets at Low Reynolds Numbers," *Fluid Dynamics Research*, Vol. 12, pp. 307–322.
- Leite, R. J., 1957, "An Experimental Investigation of the Stability of Initially Symmetric Poiseuille Flow," Report No. OSR-TR-56-2, University of Michigan, Ann Arbor.
- Leite, R. J., 1958, "An Experimental Investigation of the Stability of Poiseuille Flow," *Journal of Fluid Mechanics*, Vol. 5, pp. 81–97.
- Lei, M., Van Steenhoven, A. A., and Van Campen, D. H., 1992, "Experimental and Numerical Analyses of the Steady Flow Field Around an Aortic Bjork-Shiley Standard Valve Prosthesis," *Journal of Biomechanics*, Vol. 25, pp. 213–222.
- Marris, A. W., 1964, "A Review on Vortex Streets, Periodic Wakes and Induced Vibration Phenomena," *ASME Journal of Basic Engineering*, pp. 185–196.
- Matisse, P. and Gorman, M., 1984, "Neutrally Buoyant Anisotropic Particles for Flow Visualization," *Physics of Fluids*, Vol. 27, pp. 759–760.
- Merzkirch, W., 1987, *Flow Visualization*, Second Edition, Academic Press.
- Mottram, R. C. and Robatti, B., 1985, "A Comparison of Effects on Vortex and Orifice Flowmeters," *Fluid Control and Its Measurement*, Vol. 2, Pergamon Press, M. Harada, ed., pp. 957–963.
- Nerem, R. M., Seed, W. A., and Wood, N. B., 1972, "An Experimental Study of the Velocity Distribution and Transition to Turbulence in the Aorta," *Journal of Fluid Mechanics*, Vol. 52, pp. 137–160.
- Prenel, J. P., Porcar, R., and El Rhassouli, A., 1989, "three-dimensional Flow Analysis by Means of Sequential and Volumic Laser Sheet Illumination," *Experiments in Fluids*, Vol. 7, pp. 133–137.
- Rhee, H. S., Koseff, J. R., and Street, R. L., 1984, "Flow Visualization of a Recirculating Flow by Rheoscopic Liquid and Liquid Crystal Techniques," *Experiments in Fluids*, Vol. 2, pp. 57–64.
- Sarpkaya, T., 1992, "Brief Reviews of Some Time-Dependent Flows," *ASME JOURNAL OF FLUIDS ENGINEERING*, Vol. 114, pp. 283–298.
- Shortland, A. P., Black, R. A., Jarvis, J. C., Henry, F. S., Iudicello, F., Collins, M. W., and Salmons, S., 1996, "Formation and Travel of Vortices in Model Ventricles: Applications to the Design of Skeletal Muscle Ventricles," *Journal of Biomechanics*, Vol. 29, No. 4, pp. 503–511.
- Snedecor, G. W. and Cochran, W. G., 1967, *Statistical Methods*, The Iowa State University Press, Ames, Iowa.
- Weaver, D. S., Adubi, F. A., and Kouwen, N., 1978, "Flow Induced Vibrations of a Hydraulic Valve and Their Elimination," *ASME JOURNAL OF FLUIDS ENGINEERING*, Vol. 100, pp. 239–245.
- Zdravkovich, M. M., 1969, "Smoke Observations of the Formation of a Karman Vortex Street," *Journal of Fluid Mechanics*, Vol. 37, pp. 491–496.

Tienfuan Kerh

Professor,
Department of Civil Engineering,
National Pingtung Polytechnic Institute,
Pingtung, Taiwan 91207

J. J. Lee

Professor.

L. C. Wellford

Professor.

Department of Civil Engineering,
University of Southern California,
Los Angeles, CA 90089

Transient Fluid-Structure Interaction in a Control Valve

Numerical investigation on the interaction of a viscous incompressible fluid with a control valve is conducted by using the finite element method and Newmark approach. Variables including displacement, velocity, and acceleration are presented as a function of time to describe movements of the solid system. The velocity vectors, pressure variations, pressure loss coefficients, and energy losses are displayed to reveal the resulting flow fields. It is observed that the motion of the structural element which becomes a moving boundary had a significant influence on the flow fields. In a periodic inlet flow, the motion of the structural system and the resulting flow fields were almost identical for each cycle after the third cycle. The simulated results presented in this paper provide a good description of the induced flow field in a piping system under the effect of a pulsating piston or a wave.

Introduction

The coupled motion of a viscous fluid and a movable structure is an important problem which has many engineering applications. This is exemplified by the numerous articles published dealing with various types of fluid-structure interaction problems. A vast amount of literature in this area concentrated on the investigation of the parametric behaviors of the coupled system; the resulting flow fields were usually not examined in great detail. Olson and Irain (1983) used the finite element method to solve the coupled stream function and the equation of motion of the elastic moving body. They focused on the response of the added mass and damping coefficients as a function of the frequency; details about the corresponding flow fields were not provided. Olson and Pattani (1985) followed the same track by using the primitive variables and applying the nonlinear boundary conditions on the moving body. Their numerical results were obtained for a square body undergoing simple harmonic motion parallel to one of its sides. They have compared their numerical results with experimental observations, and more insights of this type of problem were presented.

Schulkes (1992), studied the motion of an incompressible, viscous fluid in an open flexible container with the container wall modeled by an elastic solid. The linearized Navier-Stokes equations coupled with the elasticity equations were derived to investigate the eigenmodes of the coupled fluid-structure system. The numerical results showed that the viscosity of the fluid is an important factor, which created a boundary layer in the fluid adjacent to the fluid-solid interface, and due to the motion of fluid, a pressure difference was generated to force the solid to undergo a transverse displacement. The flow configurations were simple and the results still lacked details to describe the motion of the fluid with the associated motion of the solid.

Fluid-structure interactions play an important role in many engineering problems. For example, in a water distribution system, in order to safeguard the portable water from contaminations by waste water, cross-connection control using backflow preventers or control valves must be designed to assume its proper operation (see Lee and Schwartz, 1993). Hence, there is no lack of papers on fluid-structure interaction in transient pipe flows (e.g., Fan and Tijsseling, 1992; Lavodij and Tijsseling, 1991; Tijsseling and Lavodij, 1990). However, the study of viscous incompressible fluid interaction with a control valve

in the cross-connection control field is scarce. Kerh et al. (1995a, 1995b) presented works in this area, but the results are only limited to the case of constant inlet flow, and no validations of the numerical scheme were given.

The purpose of this study is to simulate periodic flows through a backflow preventer (control valve) in order to uncover the detailed flow behaviors and provide a critical check for the developed numerical scheme. Instead of focusing on the parametric studies, such as the effects of reducing frequency, damping ratio of the valve, the valve geometry, or a case that flow frequency becomes closer to natural frequency of the structural system, which may produce run-away vibrations. In this paper, we study a specific case whereby the structural system is forced to open by the fluid flow. The displacement, velocity, and acceleration are used to describe the motion of the solid system; in addition, the velocity vectors, pressure variations, pressure loss coefficients, and energy losses are examined to reveal the resulting flow fields.

Derivation of Governing Equations

The governing equations for the fluid are the Navier-Stokes equations and the continuity equation. By converting to tensor notation and employing the Einstein summation convention, the Navier-Stokes equations with variables of velocity $U(u, v, w)$ and pressure p can be represented as

$$\rho[\dot{U}_i + U_j \cdot (U_i)_j] = (\mathcal{J}_{ij})_j, \quad (1)$$

where

$$\mathcal{J}_{ij} = -p\delta_{ij} + \mu[(U_i)_j + (U_j)_i]. \quad (2)$$

Here δ_{ij} represents the Kronecker delta which has unit value for $i = j$ and zero value for $i \neq j$, ρ is the density and μ is the absolute viscosity of the fluid. The dot denotes partial differentiation with respect to time and the parenthesis followed by an index represents partial differentiation with respect to the spatial coordinate indicated by the subscript. The Galerkin weighted residual method with divergence (Gauss) theorem has an equation of the form

$$\int_{\Omega} \rho[\dot{U}_i + U_j(U_i)_j]W_i \cdot d\Omega = \int_{\Gamma} n_j(\mathcal{J}_{ij}W_i) \cdot d\Gamma - \int_{\Omega} \mathcal{J}_{ij}(W_i)_j \cdot d\Omega, \quad (3)$$

Contributed by the Fluids Engineering Division for publication in the JOURNAL OF FLUIDS ENGINEERING. Manuscript received by the Fluids Engineering Division, November 3, 1992; revised manuscript received July 18, 1996. Associate Technical Editor: D. P. Telionis.

where Γ is the boundary of domain Ω , n_j is the j component of the outward unit normal vector on Γ , and W_i are weighting functions. This equation can be written in terms of two-dimensional Cartesian coordinates with normalized variables \mathbf{u} , \mathbf{v} , \mathbf{p} , and for each element, the velocities and pressures are defined as summations of nodal values multiplied by the shape functions. Therefore, the nondimensional presentation of Navier-Stokes equations can be written in matrix form as

$$\begin{pmatrix} M_{ij}^{11} & 0 \\ 0 & M_{ij}^{22} \end{pmatrix} \begin{Bmatrix} \dot{\mathbf{u}}_j \\ \dot{\mathbf{v}}_j \end{Bmatrix} + \frac{1}{\text{Re}} \begin{pmatrix} K_{ij}^{11} & K_{ij}^{12} \\ K_{ij}^{21} & K_{ij}^{22} \end{pmatrix} \begin{Bmatrix} \mathbf{u}_j \\ \mathbf{v}_j \end{Bmatrix} - \begin{pmatrix} C_{ij}^1 \\ C_{ij}^2 \end{pmatrix} \{\mathbf{p}_j\} + \begin{pmatrix} N_{ij}^{11} & 0 \\ 0 & N_{ij}^{22} \end{pmatrix} \begin{Bmatrix} \mathbf{u}_j \\ \mathbf{v}_j \end{Bmatrix} = \begin{Bmatrix} F_i^1 \\ F_i^2 \end{Bmatrix}, \quad (4)$$

where

$$\begin{aligned} M_{ij}^{11} &= \int_{\Omega} W_i N_j \cdot d\Omega = M_{ij}^{22}, \\ K_{ij}^{11} &= \int_{\Omega} [2(W_i)_x(N_j)_x + (W_i)_y(N_j)_y] \cdot d\Omega, \\ K_{ij}^{12} &= \int_{\Omega} (W_i)_y(N_j)_x \cdot d\Omega, \quad K_{ij}^{21} = \int_{\Omega} (W_i)_x(N_j)_y \cdot d\Omega, \\ K_{ij}^{22} &= \int_{\Omega} [(W_i)_x(N_j)_x + 2(W_i)_y(N_j)_y] \cdot d\Omega, \\ C_{ij}^1 &= \int_{\Omega} (W_i)_x M_j \cdot d\Omega, \quad C_{ij}^2 = \int_{\Omega} (W_i)_y M_j \cdot d\Omega, \\ N_{ij}^{11} &= \mathbf{u}_k \int_{\Omega} W_i(N_j)_x N_k \cdot d\Omega + \mathbf{v}_k \int_{\Omega} W_i(N_j)_y N_k \cdot d\Omega = N_{ij}^{22}, \\ F_i^1 &= \int_{\Gamma} W_i \left\{ n_x \left(-\mathbf{p} + \frac{2}{\text{Re}} \mathbf{u}_x \right) + n_y \left[\frac{1}{\text{Re}} (\mathbf{u}_y + \mathbf{v}_x) \right] \right\} \cdot d\Gamma, \\ F_i^2 &= \int_{\Gamma} W_i \left\{ n_x \left[\frac{1}{\text{Re}} (\mathbf{u}_y + \mathbf{v}_x) \right] + n_y \left(-\mathbf{p} + \frac{2}{\text{Re}} \mathbf{v}_y \right) \right\} \cdot d\Gamma. \quad (5) \end{aligned}$$

In the above equations, N_j are the shape functions for the velocity of each element, M_j are defined as the shape functions for the pressure of each element, and Re is the Reynolds number. If Gauss quadrature is applied for the four-node isoparametric element, 1×1 Gauss point is required to evaluate C_{ij} and 2×2 Gauss points are needed for the other matrices. After assembling all element matrices, the global system equation can be written as

$$\mathbf{M}\dot{\mathbf{U}} + \frac{1}{\text{Re}} \mathbf{K}\mathbf{U} - \mathbf{C}\mathbf{P} + \mathbf{N}(\mathbf{U})\mathbf{U} = \mathbf{F}. \quad (6)$$

In the present study, the penalty function finite element method is introduced into the continuity equation to reduce the degrees of freedom for each node and to save computational costs (e.g., Carey and Krishnan, 1987; Hughes et al., 1979; Natarajan, 1992; Ramshaw and Mesina, 1991; Reddy, 1982). Furthermore, the θ family of approximation with Galerkin scheme ($\theta = \frac{2}{3}$) is applied for the integration in the time domain, and the nonlinear term is treated by using the Newton method. Therefore, the normalized consistent penalty type of nonlinear equation of motion can be written as

$$\begin{aligned} & \left\{ \mathbf{M} + \theta \Delta t \left[\frac{1}{\text{Re}} \mathbf{K} + \frac{\lambda}{\mu \text{Re}} \mathbf{K}_p \right. \right. \\ & \quad \left. \left. + \mathbf{N}(\mathbf{U}_{n+1}) + J'(\mathbf{U}_n) \right] \right\} \mathbf{U}_{n+1} \\ &= \Delta t \mathbf{F}_{n+\theta} + \left\{ \mathbf{M} - (1-\theta) \Delta t \left[\frac{1}{\text{Re}} \mathbf{K} + \frac{\lambda}{\mu \text{Re}} \mathbf{K}_p \right. \right. \\ & \quad \left. \left. + \mathbf{N}(\mathbf{U}_n) \right] \right\} \mathbf{U}_n + \theta \Delta t J'(\mathbf{U}_n) \mathbf{U}_n, \quad (7) \end{aligned}$$

where

$$\mathbf{P}_{n+1} = -\frac{\lambda}{\mu \text{Re}} \tilde{\mathbf{M}}^{-1} \mathbf{C}^T \mathbf{U}_{n+1}, \quad (8)$$

and the derivative of the Jacobian matrix is

$$J'(\mathbf{U}_n) = \begin{pmatrix} \mathbf{u}_k \int_{\Omega} W_i N_j (N_k)_x \cdot d\Omega & \mathbf{u}_k \int_{\Omega} W_i N_j (N_k)_y \cdot d\Omega \\ \mathbf{v}_k \int_{\Omega} W_i N_j (N_k)_x \cdot d\Omega & \mathbf{v}_k \int_{\Omega} W_i N_j (N_k)_y \cdot d\Omega \end{pmatrix}. \quad (9)$$

In the above equations, \mathbf{U} is the velocity vector, \mathbf{P} is the pressure vector, \mathbf{M} represents the consistent mass matrix, $\tilde{\mathbf{M}}$ represents the pressure mass matrix, \mathbf{K} refers to the viscous matrix, \mathbf{K}_p is the penalty matrix, $\mathbf{N}(\mathbf{U})$ is the nonlinear advection matrix, \mathbf{C} is the pressure gradient matrix, \mathbf{C}^T is the divergence matrix, and \mathbf{F} is the force vector. Additionally, λ is the penalty parameter and it is governed by the relation $\lambda = 10^6(1 + \mathbf{t})\mu \text{Re}$, where \mathbf{t} denotes the time marching. This makes the penalty parameter grows with each time-step ultimately to attain a value which is large enough to ensure that the continuity constraint is satisfied without affecting the solutions once they converge to a specified tolerance. The global Eq. (7) can now be solved to determine the unknown velocity fields. The distribution of pressure fields can be postcalculated through Eq. (8) on an element basis.

For a dynamic structural system, the equation of motion is

$$\ddot{\mathbf{h}}(\mathbf{t}) + 2\zeta\omega_n\dot{\mathbf{h}}(\mathbf{t}) + \omega_n^2\mathbf{h}(\mathbf{t}) = \mathbf{f}(\mathbf{t}), \quad (10)$$

where $\ddot{\mathbf{h}}(\mathbf{t})$, $\dot{\mathbf{h}}(\mathbf{t})$, and $\mathbf{h}(\mathbf{t})$ represent acceleration, velocity, and displacement, respectively. In addition, ζ is known as the viscous damping factor, ω_n is known as the natural frequency of the system, and $\mathbf{f}(\mathbf{t})$ is an arbitrary excitation force which permits the definition of a nondimensional ratio of response to excitation. The excitation force can be considered as an external force which includes the force acting on the dynamic system caused by the moving fluid. The direction of the force is downward if $\mathbf{f}(\mathbf{t})$ is a positive, and upward if $\mathbf{f}(\mathbf{t})$ is negative. The directions of displacement, velocity, and acceleration are also similarly defined. Among the methods of linear analysis, the Newmark approach (Bathe, 1982) provides an unconditionally stable scheme whose solution converges regardless of the initial conditions and the time step. Therefore, this method is applied to integrate the equilibrium equation of the structural system.

Interpretation of Computational Results

The applicability of the present numerical model and the time integration for the fluid are first verified by simulating Couette flow. Numerical solutions are compared to the analytical solu-

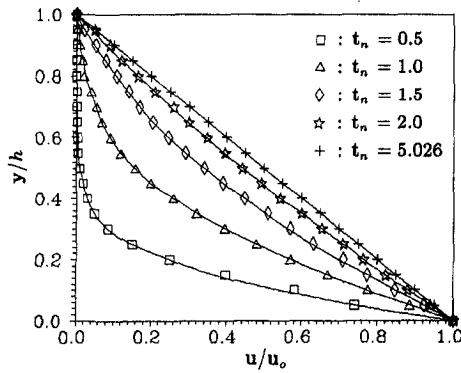


Fig. 1 Comparison of velocity profiles at various t_n for Couette motion (solid line: analytical solution, symbol set: present study; $t_n = \sqrt{16t/h^2 \text{Re}}$, $\text{Re} = 1.0$)

tions at various normalized time steps as shown in Fig. 1, where h is the distance between two plates, and u_0 is the constant velocity for the lower plate at $t = 0$. Very good agreement is found for both the numerical result and the analytical solution. Another comparison of the simulated results with the experimental data for the case of pulsating flow past a bluff body has been studied by Kerh (1994). The numerical scheme proved to be very accurate for these flow motions. Upon successful comparison with the available analytical and experimental results the present model is then applied to more complicated flow problem as formulated below:

Consider now a dynamic structural system placed in the flow domain and supported by two vertical walls which hold the solid body in its static equilibrium position ($\mathbf{h} = 0.0$, $\mathbf{y} = 0.4$). The excitation force and the force generated from the motion of the fluid will drive the moving system to a new equilibrium level. If the forces are insufficient to keep the solid body in the new balanced position, the system will try to return to its original static equilibrium level, i.e., displacement is equal to zero. The movement of the solid body constitutes a moving boundary of the flow domain, and the motion of the solid body will affect the flow field.

A periodic flow is applied at the inlet to investigate the resulting flow fields and the associated motion of the structural system. The velocity profile of the periodic inlet flow is prescribed as $\mathbf{u}(t) = 2(y - y^2) \sin \bar{\omega}t$, $\mathbf{v} = 0.0$. The inlet flow is thus a function of time, and the velocity reverses direction when $\bar{\omega}t > \pi$ (where $\bar{\omega} = 1.0$). With this inlet flow condition, the boundary conditions are: $\mathbf{u} = 0$, $\mathbf{v} = 0$ (no-slip) at the walls, $\mathbf{f}_x = 0$ (traction-free), $\mathbf{v} = 0$ (unidirectional flow) at the outlet region. The compatibility conditions are that the vertical component of velocities are the same at the interfaces and that the horizontal component of velocities are zero.

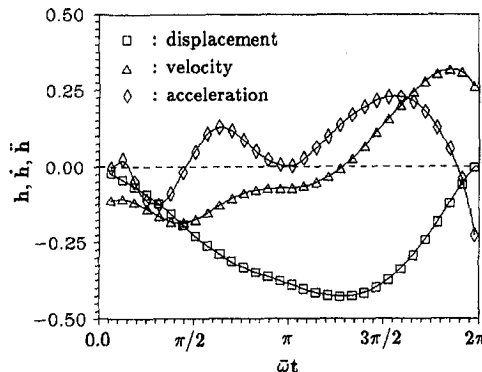


Fig. 2 Variables of the control valve versus $\bar{\omega}t$ (solid line: cycle 1, symbol set: cycle 2; $\text{Re} = 500.0$, $\bar{\omega} = 1.0$, $\zeta = 0.0$, $\omega_n = 0.05$)

The dynamic structural system is placed in the middle of the flow domain with dimensions 27.0×1.0 . The flow domain in the vertical direction is divided into three parts, $\frac{1}{3}$ for the lower vertical wall of length 0.4 , $\frac{1}{3}$ for the displacement (\mathbf{h}) of each time step, $\frac{1}{3}$ for the upper vertical wall of length 0.6 minus the displacement of each time step, and four four-node elements are uniformly placed for each part. Sixty four-node elements with nonuniform sizes are used along the horizontal direction. The sizes of the element in x direction are $(26 - i)/25$ for $i = 1, 2, 3 \dots, 25$; 0.19 for $i = 26, 35$; 0.01 for $i = 27, 34$; 0.1 for $i = 28, 29, 30 \dots, 33$; and $(i - 35)/25$ for $i = 36, 37, 38, \dots, 60$. Thus, a total of 773 nodes (696 elements, Grid 1) resulting in 1546 equations must be solved for each iteration.

For checking the effect of grid system, two other grid systems; namely, Grid 2 and Grid 3 are also used for the simulations. For the Grid 2, the sizes of the element in x direction are $(13/10.5) \times (21 - i)/20$ for $i = 1, 2, 3 \dots, 20$; 0.19 for $i = 21, 28$; 0.01 for $i = 22, 27$; 0.1 for $i = 23, 24, 25, 26$; and $(13/10.5) \times (i - 28)/20$ for $i = 29, 30, 31, \dots, 48$. Whereas, the sizes of the element in y direction are the same as the Grid 1. For the Grid 3, the elements in x direction have the same sizes as the Grid 1, but only three four-node elements are uniformly divided for each part in y direction. Thus, the resulting total numbers of nodes for the Grid 2 and the Grid 3 are 625 nodes (560 elements) and 595 nodes (522 elements), respectively. Each of the two grid systems has less total number of nodes than that of the Grid 1. The computed results for these three grid systems will be compared and discussed later.

The time step, $\Delta t = 0.2$, is chosen for numerical integration of the flow fields in the time domain. Parameters such as Reynolds number $\text{Re} = (\bar{U}h/\nu) = 500$ is based on three times of the maximum averaged inlet velocity (i.e., the characteristic velocity: $\bar{U} = 3 \times \bar{u} = 1.0$, where $\bar{u} = (2/3)u_{\text{max}}$ and the u_{max}

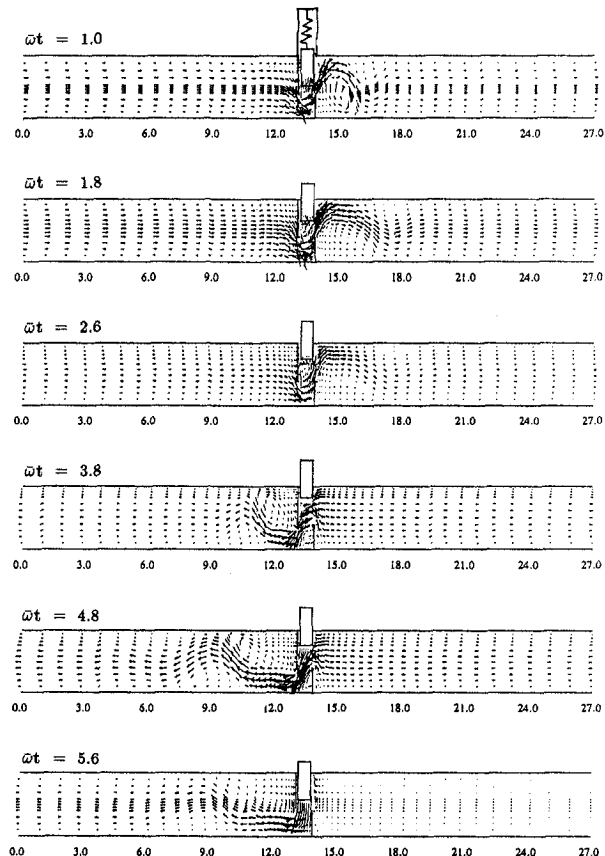


Fig. 3 Velocity vectors at various $\bar{\omega}t$ ($\text{Re} = 500.0$, $\bar{\omega} = 1.0$, $\zeta = 0.0$, $\omega_n = 0.05$)

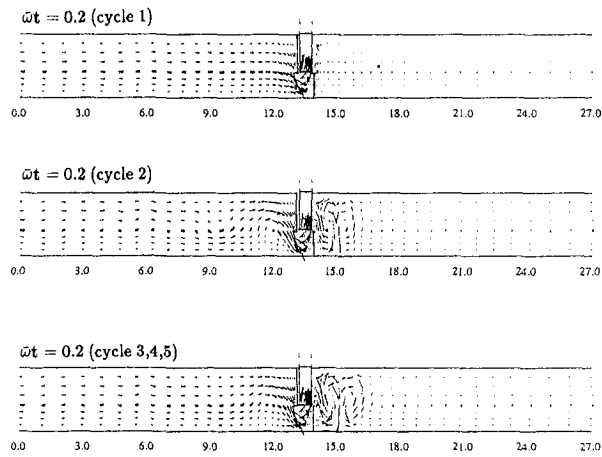


Fig. 4 Velocity vectors at various $\omega t = 0.2$ for five cycles ($Re = 500.0$, $\bar{\omega} = 1.0$, $\zeta = 0.0$, $\omega_n = 0.05$)

is occurred at $y = 0.5$ for $\omega t = \pi/2$), and the height of the channel (i.e., the characteristic length: $h = 1$). In addition, the damping factor ζ is set to zero (no damper), and the natural frequency of the system is taken as 0.05. Due to the influence of the reverse (negative) inlet flow, the structural system is unable to stay at a new position; it will return to its static equilibrium position for one fully cycle ($\omega t = 2\pi$). A total of five cycles are simulated for the present analysis.

The resulting time history of the displacement, velocity, and acceleration of the dynamic system is shown in Fig. 2. It is seen that the structural system with the specified parameters moves upward and reaches the peak displacement of -0.43 (minus sign denotes the upward direction) at $\omega t = 4.0 (1.3\pi)$. At the peak displacement, it can be seen that the velocity approaches zero. The elastic element (the spring) of the structural system forces the structural element to move downward. This downward force combines with the effect of reverse inlet flow causes the structural element to return to its static equilibrium position (zero displacement) very rapidly. The structural system chosen for this study has a stopper thus its downward motion can not exceed the original position. Therefore, finite values of the maximum velocity and acceleration still exist as the structural element returns to its original static position. However, when the structural element hits the stopper, the displacement, velocity, and the acceleration all become zero. The second (or subsequent) cycle exhibits the same behaviors as the first cycle. These behaviors may cause damage to the stopper under repeated fluid-structure interaction over many cycles.

Shown in Fig. 3 are the velocity vector fields at several selected times. It is found that the area of the recirculating regions grows with increasing time. As $\omega t > \pi$, the inlet flow reverses direction, the eddies on the upstream side are gradually formed and the area of recirculation is expanded. By taking the flow fields at the last time step as the initial conditions for the next cycle, the velocity fields at the first time step for five cycles are presented in Fig. 4. No significant difference in the velocity

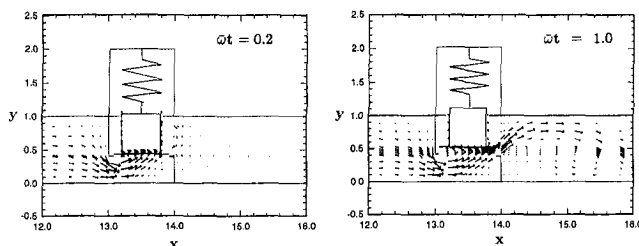


Fig. 5 Blow up of the velocity vectors in the vicinity of the solid system

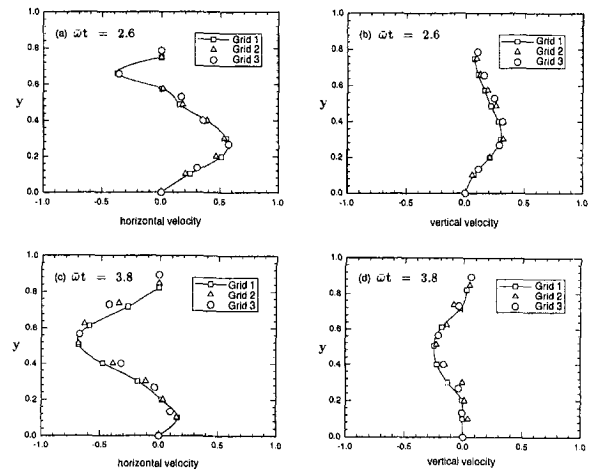


Fig. 6 Comparisons of velocity profiles at the centerline of flow domain ($x = 13.5$) for three grid systems

vectors is seen beyond the third cycle. For the times over the first time step, nearly identical results are exhibited for each cycle. In order to resolve the phenomenon of flow separation, the velocity vectors in the vicinity of the solid system at $t = 0.2$ and $t = 1.0$ are blown up and displayed in Fig. 5. The formed eddies due to the solid-body can be seen more clear from the plots.

Noted that the relative root-mean-square errors for velocity or pressure in the range of $10^{-2} \sim 10^{-3}$ are used as the convergence criteria for iterative procedures in this flow case. To further examine the numerical accuracy for this flow problem, comparisons of velocity profiles for different grid systems as mentioned previously are shown in Fig. 6. For the two time steps ($\omega t = 2.6$ and $\omega t = 3.8$), the results showed that no significant differences in the velocity profiles, either horizontal or vertical component, at the centerline of the flow domain ($x = 13.5$). Thus, the present numerical analysis may consider as a grid-independence, and the results obtained from the Grid 1 are taken for describing the flow fields. Certainly, the numerical accuracy still can be improved by mesh refinement, particularly in the neighborhood of the solid-body, but more computational costs must be taken into account for this transient analysis.

Figure 7 shows the pressure surface plots at two time steps. It can be seen that the pressure decreases from upstream to downstream during the positive inlet flow. On the other hand, the pressure decreases from downstream to upstream region when the reverse inlet flow occurs. To view the trend more clearly, the pressure loss coefficient ($C_p = (p_i - p_o) / (\frac{1}{2}\rho U^2)$, where p_i and p_o are averaged pressures at the inlet and at the outlet, respectively) as a function of ωt is shown in Fig. 8. The pressure loss coefficient gradually increases with increasing time. After reaching the peak at about $\omega t = 1.0 (0.3\pi)$, the

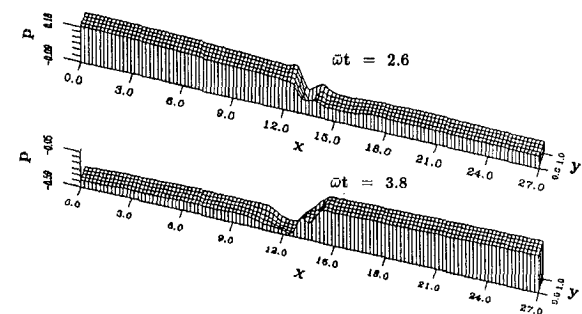


Fig. 7 Pressure surface plots at two time steps ($Re = 500.0$, $\bar{\omega} = 1.0$, $\zeta = 0.0$, $\omega_n = 0.05$)

pressure loss coefficient then gradually decreases and becomes negative value at $\bar{\omega}t > \pi$. However, when $\bar{\omega}t > 5.8(1.8\pi)$, the pressure loss coefficient becomes positive value again.

For practical application, it is informative to estimate the kinetic energy, the pressure loss, and the total energy loss. From the energy loss equation (Henderson, 1966), the nondimensional form of energy loss within two cross-sections (1 and 2) may be represented as

$$H_L = k_e[(\mathbf{p}_{1m} - \mathbf{p}_{2m}) + \frac{1}{2}(\alpha_1 \mathbf{u}_{1m}^2 - \alpha_2 \mathbf{u}_{2m}^2)], \quad (11)$$

where H_L is the total energy loss, k_e is a constant and set to be 1.0 for simplification, and

$$\alpha_1 = \frac{\int_1 \mathbf{u}_1^3 dA}{\mathbf{u}_{1m}^3 A} \quad \text{and} \quad \alpha_2 = \frac{\int_2 \mathbf{u}_2^3 dA}{\mathbf{u}_{2m}^3 A}, \quad (12)$$

are referred to as the energy correction coefficient (known as Coriolis coefficient, they are used for the calculation of kinetic energy), with the subscript m indicating the mean value. The cross sections 1 and 2 are taken as close to the vertical walls as possible. Thus, from the finite element grid system, the x coordinates $13 - \frac{1}{25}$ and $14 + \frac{1}{25}$ are taken for cross-sections 1 and 2, respectively. The variation of energy loss with $\bar{\omega}t$ is shown in Fig. 9. At the first few time steps, the kinetic energy is transferred to move the structural system, the kinetic energy at cross-section 2 is less than that at cross-section 1; thus, the difference of kinetic energy is positive. When the reverse inlet flow occurs the difference of kinetic energy is also positive. Therefore, the difference in kinetic energy is positive most of time. Because the difference in kinetic energy is small when compared with the difference in pressure, the trend for the total energy loss versus time is similar to the plot of pressure loss coefficient as a function of time. As the structural system approaches the stopper (i.e. negative but small inlet flow), the downward movement of the solid element has a contribution to the flow field; therefore, the pressure loss coefficient and the total energy loss still increase as $\bar{\omega}t$ approaches 2π .

Summary and Conclusion

In the present study, a two-dimensional transient analysis has been conducted for the interaction of a viscous, incompressible fluid and a control valve under the effect of a periodic inlet flow. The control valve used for this study simulates the backflow preventer commonly used for cross-connection control in a water distribution system. The consistent penalty function finite element method and a Galerkin θ time integration scheme have been employed to solve the Navier-Stokes equations, and the Newmark approach is used for the integration of the valve-body equation of motion. Coupling is achieved by matching fluid

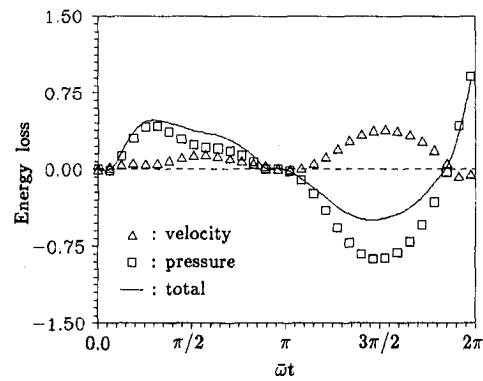


Fig. 9 Energy loss versus $\bar{\omega}t$ (solid line: cycle 1, symbol set: cycle 2; $Re = 500.0$, $\bar{\omega} = 1.0$, $\zeta = 0.0$, $\omega_n = 0.05$)

velocities to the gate velocities of the valve at the interface and by including the forces which the fluid exert on the valve gate in the equation of motion.

Even though flow conditions used for this paper cover a very limited range of the Reynolds number, oscillatory flow frequency, and the natural frequency of the valve-body system, the results demonstrate the significant modification of the flow field due to the moving body. Eddies produced due to flow separation from the boundary are evident in the upstream and downstream locations of the valve-body. Due to the specified periodic flow and the existence of a stopper in the valve body, the solid body will return to its static equilibrium position after each full cycle. Based on the simulated results it is found that the motion of the structural system and the resulting flow fields were almost identical beyond the third cycle. For the positive inlet flow, eddies are formed in the region downstream of the structural body and the pressure decreases from upstream to downstream of the structural body. For the reverse inlet flow, eddies are formed in the region upstream of the structural body and the pressure decreases from downstream to upstream.

Although the difference in the kinetic energy is positive for the majority of the time in a cycle, the difference in kinetic energy is much less than the difference in pressure. Thus, the total energy loss is basically controlled by the difference in pressure. The simulated results presented in this paper provide a good description of the induced flow field in a piping system under the effect of a pulsating piston or a wave.

Acknowledgment

The authors acknowledge the financial support of the USC Foundation for Cross-Connection Control and Hydraulic Research for the present study. The first author also like to express his gratitude to Professor D. P. Telionis of VPISU for many helpful comments.

References

- Bathe, K. J., 1982, *Finite Element Procedures in Engineering Analysis*, Prentice-Hall, New Jersey.
- Carey, G. F., and Krishnan, R., 1987, "Convergence of Iterative Methods in Penalty Finite Element Approximation of the Navier-Stokes Equations," *Computer Methods in Applied Mechanics and Engineering*, Vol. 60, pp. 1-29.
- Fan, D., and Tijsseling, A. S., 1992, "Fluid-Structure Interaction With Cavitation in Transient Pipe Flows," *ASME JOURNAL OF FLUIDS ENGINEERING*, Vol. 114, pp. 268-274.
- Henderson, F. M., 1966, *Open Channel Flow*, Macmillan Series in Civil Engineering, New York.
- Hughes, T. J. R., Liu, W. K., and Brooks, A., 1979, "Finite Element Analysis of Incompressible Viscous Flow by the Penalty Function Formulation," *Journal of Computational Physics*, Vol. 30, pp. 1-60.
- Kerh, T., 1994, "Numerical Calculations for Pulsating Flow Past a Bluff Body," *International Journal of Modelling and Simulation*, Vol. 14, No. 3, pp. 112-116.
- Kerh, T., Lee, J. J., and Wellford, L. C., 1995a, "Responses of Viscous Fluid Interaction with a Moving Structural System," *Developments in Computational*

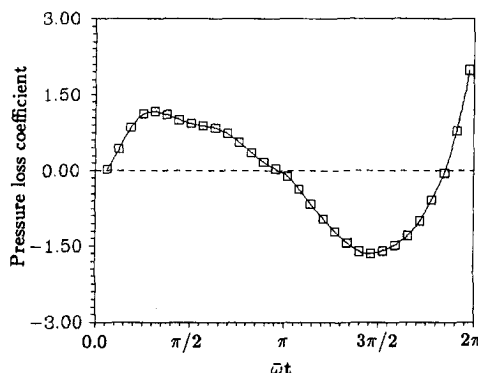


Fig. 8 Pressure loss coefficient versus $\bar{\omega}t$ (solid line: cycle 1, symbol set: cycle 2; $Re = 500.0$, $\bar{\omega} = 1.0$, $\zeta = 0.0$, $\omega_n = 0.05$)

Techniques for Civil Engineering, Topping, B. H. V., ed., Civil-Comp Press, Edinburgh, U.K., pp. 343–347.

Kerh, T., Lee, J. J., and Wellford, L. C., 1995b, "Predictions of Confined Shear Flow Over a Wall Obstacle," *International Journal of Modelling and Simulation*, Vol. 15, No. 1, pp. 22–29.

Lavodij, C. S. W., and Tijsseling, A. S., 1991, "Fluid-Structure Interaction in Liquid-Filled Piping System," *Journal of Fluid-Structure*, Vol. 5, pp. 573–595.

Lee, J. J., and Schwartz, P. H., 1993, "Manual of Cross-Connection Control," Foundation for Cross-Connection Control and Hydraulic Research, University of Southern California, the 8th edition.

Natarajan, R., 1992, "A Numerical Method for Incompressible Viscous Flow Simulation," *Journal of Computational Physics*, Vol. 100, pp. 384–395.

Olson, M. D., and Irani, M. B., 1983, "Finite Element Analysis of Viscous Flow-Solid Body Interaction," *Numerical Methods in Laminar and Turbulent Flow*, pp. 14–24.

Olson, M. D., and Pattani, P. G., 1985, "Nonlinear Analysis of Rigid Body-Viscous Flow Interaction," *Finite Elements in Fluids*, Vol. 6, pp. 307–320.

Ramshaw, J. D., and Mesina, G. L., 1991, "A Hybrid Penalty-Pseudo-compressibility Method for Transient Incompressible Fluid Flow," *Computers and Fluids*, Vol. 20, No. 2, pp. 165–175.

Reddy, J. N., 1982, "On Penalty Function Methods in the Finite-Element Analysis of Flow Problem," *International Journal for Numerical Methods in Fluids*, Vol. 2, pp. 151–171.

Schulkes, R. M. S. M., 1992, "Interactions of an Elastic Solid with a Viscous Fluid: Eigenmode Analysis," *Journal of Computational Physics*, Vol. 100, pp. 270–283.

Tijsseling, A. S., and Lavodij, C. S. W., 1990, "Water Hammer With Fluid-Structure Interaction," *Applied Scientific Research*, Vol. 47, pp. 273–285.

Design of Homologous Ram Pumps

Brian Young

Professor and Head of the Department of
Civil Engineering,
Papua New Guinea University
of Technology,
Lae, Papua New Guinea

The hydraulic ram pump was invented over 200 years ago but became obsolete with the availability of mains water. Ram pumps make use of a renewable energy resource and are environmentally friendly. They are particularly appropriate for use in the developing world as their construction is basic and robust and they are inexpensive and easy to install and maintain. Unfortunately, simple rational design procedures applicable to any size of pump are not available. The paper analyses the behavior of ram pumps under zero recoil conditions from which three nondimensional design relationships, applicable at any delivery head, are derived for beat frequency, quantity delivered, and source capacity in terms of the independent variables. These relationships incorporate constants consistent with existing experimental results. Recommendations are given for the maximum length of drive pipe which supersede traditional rules-of-thumb for the ratios L/D and L/H . The procedure allows selection of all system parameters, including the drive pipe length, for a set of homologous ram pumps.

1 Introduction

The automatic hydraulic ram pump requires no external power source but makes use of the potential energy of the supply to pump a small proportion (from a few l/min to tens of l/min depending on the size of the pump) to heights of up to about 150 m. It has only two moving parts (the delivery and impulse valves) and is relatively cheap. Hydraulic rams were once used in many parts of the world for the supply of water but, with the introduction of mains supplies, they became obsolete. Enthusiasm for environmentally friendly devices using a renewable energy resource (such as wind, water, solar or tide power) has revived interest in their use for regions not served by public utilities. An historical review of ram pump design and analysis has been given by Rennie and Bunt (1981) who describe pumps of different sizes (drive pipe diameters from 12.5 mm to 350 mm) with many different valve designs. Despite this diversity, it is the purpose of this paper to attempt a general, or unified, design approach for ram pumps.

A ram pump system consisting of (a) header tank, (b) drive pipe, (c) pump with impulse and delivery valves, (d) air chamber, and (e) delivery pipe is shown in Fig. 1. The function of the air chamber is to store water at the delivery head between strokes and to absorb the shock of pumping.

The operating cycle (shown in Fig. 2) of a ram pump system consists of the three main phases; acceleration, pumping and recoil. Acceleration of water in the drive pipe (i) occurs when the impulse valve is open and the delivery valve is closed. At a certain critical velocity (u_c), the impulse valve closes abruptly due to hydrodynamic forces overcoming those tending to keep the valve open. Pumping now takes place (ii) as shock waves induced by water hammer pass up and down the drive pipe at the speed of sound, the delivery valve opening in response to each pressure pulse. Reversal of flow (iii) in the drive pipe (recoil) can occur at the end of the pumping stage after closure of the delivery valve. The resulting suction, or the action of gravity alone in the absence of recoil, causes the impulse valve to open and the cycle repeats.

2 Theory

Recoil represents an energy loss. However, at certain delivery heads there is no recoil and it is then that optimum conditions occur (Young, 1996a). The present approach to a general method for the design of ram pump systems is based upon operation at zero recoil using a more precise description of behavior during the acceleration phase than that employed previously.

The action of a ram pump during acceleration and pumping has been described (Young, 1995b). The assumptions therein apply here with the additional requirement that $H/h_m \ll 1$. An expression for the acceleration time T_a derived from the one-dimensional unsteady flow equation, is:

$$T_a = (u_c/2g)(L/H)\kappa_1 \quad (1)$$

and the volume wasted per cycle (V_a) during acceleration (see Fig. 2, (i)) is:

$$V_a = (A_D u_c^2/g)(L/H)\kappa_2 \quad (2)$$

where κ_1 and κ_2 are functions of the velocity ratio ($a = u_c/u_o$) given by:

$$\kappa_1 = \ln\{(1+a)/(1-a)\}/a \quad (2a)$$

and

$$\kappa_2 = \ln\{\cosh(ak_1/2)\}/a^2 \quad (2b)$$

The stepped form of the velocity diagram during pumping (Fig. 2 (ii)) is a consequence of fluid being admitted to the air chamber in quanta corresponding to each pressure pulse N in the drive pipe. The pumping time is:

$$T_p = 2NL/c \quad (3)$$

and the volume pumped per cycle, assuming no delivery side loss, is:

$$V_p = (2V_D u_c/c)N(1 - Nh_o/h_m) \quad (4)$$

For zero recoil, $h_o/h_m = 1/(2N)$, where h_o is the delivery head and $h_m = cu_c/g$, thus:

$$V_p = V_D u_c^2/(2gh_o) \quad (5)$$

Contributed by the Fluids Engineering Division for publication in the JOURNAL OF FLUIDS ENGINEERING. Manuscript received by the Fluids Engineering Division February 12, 1996; revised manuscript received September 4, 1996. Associate Technical Editor: B. Schiavello.

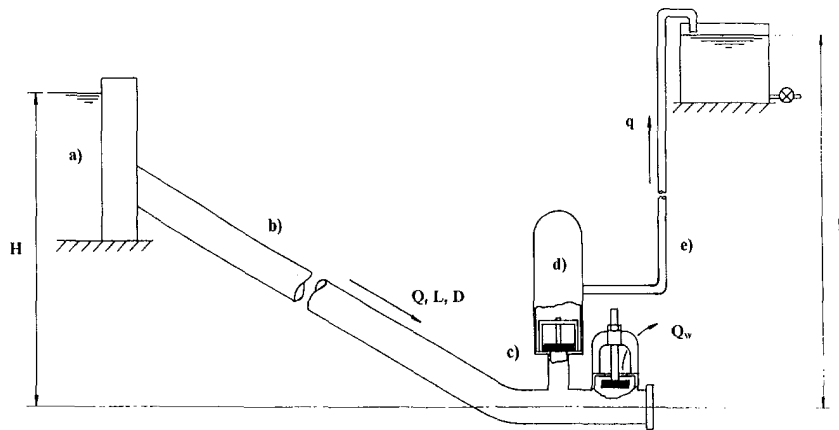


Fig. 1 Layout of a ram pump system

Since behavior of the ram pump is considered under zero recoil conditions ($T_r = 0$), the total cycle time (T_o) is given by:

$$T_o = T_a + T_p$$

or

$$T_o = (u_c / (2g\varphi_1)) (L/H) \quad (6)$$

where

$$\varphi_1 = \{\kappa_1 + 2(H/h_o)\}^{-1} \quad (6a)$$

The quantity wasted (Q_{wo}) is obtained as:

$$Q_{wo} = V_a / T_o = 2A_D u_c \kappa_2 \varphi_1 \quad (7)$$

Similarly, the quantity pumped (q_o) is given by:

$$q_o = V_p / T_o = A_D u_c H \varphi_1 / h_o \quad (8)$$

and the total quantity (Q_o) drawn from the supply is:

$$Q_o = (Q_{wo} + q_o) = A_D u_c \varphi_2 \quad (9)$$

$$\varphi_2 = \{2\kappa_2 + (H/h_o)\} \varphi_1 \quad (9a)$$

Actual values for the dependent variables q (quantity delivered), Q (capacity of source) and n (beat frequency) for any h (delivery head not necessarily corresponding to zero recoil) are determined by modifying Eqs. (6), (8), and (9) as follows:

$$nLu_c / 2gH = C_c \varphi_1 \quad (10)$$

$$qh / Q_c H = C_d \varphi_1 \quad (11)$$

and

$$Q / Q_c = \varphi_2 \quad (12)$$

$$Q_c = A_D u_c,$$

$$C_c = nT_o, \quad (C_c = \text{cycle coefficient})$$

$$C_d = q / q_o, \quad (C_d = \text{discharge coefficient})$$

The parameter Q_c is the maximum flow in the drive pipe which occurs at the instant of impulse valve closure. The two

Nomenclature

a = velocity ratio (u_c / u_o) (-)
 A_D = cross-sectional area of the drive pipe (m^2)
 A_{disc} = valve disk cross-sectional area (m^2)
 c = velocity of sound (m/s)
 C_d = discharge coefficient (-)
 C_c = cycle coefficient (-)
 D = drive pipe diameter (m)
 f = friction factor (-)
 g = acceleration due to gravity (9.81 m s^{-2})
 h = delivery head (m)
 h_m = maximum delivery head (m)
 h_{lim} = limiting delivery head for design (m)
 h_o = delivery head at zero recoil (m)
 H = supply head (m)
 H_s = static head to close impulse valve (m)
 L = length of drive pipe (m)
 L_{max} = maximum drive pipe length (m)

M_v = mass of impulse valve assembly (kg)
 n = beat frequency (Hz)
 N = number of pressure pulses in the drive pipe (-)
 p = friction head loss parameter, (m^{-3})
 q = quantity delivered ($\text{m}^3 \text{ s}^{-1}$)
 q_o = quantity delivered at zero recoil ($\text{m}^3 \text{ s}^{-1}$)
 Q = capacity of source ($\text{m}^3 \text{ s}^{-1}$)
 Q_c = drive pipe flow rate at impulse valve closure ($\text{m}^3 \text{ s}^{-1}$)
 Q_o = capacity of source at zero recoil ($\text{m}^3 \text{ s}^{-1}$)
 Q_w = quantity wasted ($\text{m}^3 \text{ s}^{-1}$)
 Q_{wo} = quantity wasted at zero recoil ($\text{m}^3 \text{ s}^{-1}$)
 R = regression coefficient (-)
 r = geometric parameter for an impulse valve (m^{-1})
 s_v = valve stroke (m)

t = time (s)
 T = period of ram cycle (s)
 T_a = time for acceleration phase (s)
 T_p = time for pumping phase (s)
 T_o = period of ram cycle at zero recoil (s)
 T_r = recoil time, (s)
 u = velocity in drive pipe, (ms^{-1})
 u_c = velocity to close impulse valve (ms^{-1})
 u_o = steady state velocity (ms^{-1})
 V_a = volume wasted per cycle during acceleration (m^3)
 V_D = internal volume of drive pipe (m^3)
 V_p = volume pumped per cycle (m^3)
 $\varphi_{1,2}$ = functions of velocity ratio and head ratio (-)
 $\kappa_{1,2}$ = functions of velocity ratio (-)
 ρ = density of working fluid, (1000 kg m^{-3} for water)
 σ = standard deviation from the mean (various)

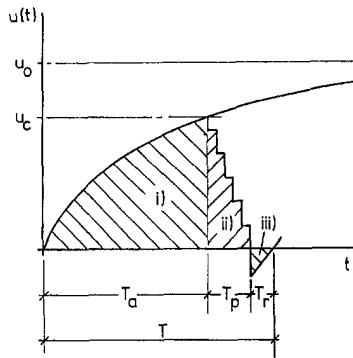


Fig. 2 Drive pipe velocity-time diagram

coefficients C_c and C_d (< 1) are included to allow for the less than ideal performance of a ram pump when not operating at zero recoil and, in the case of the latter, to account additionally for delivery side losses. From Eqs. (9) and (12), we have the generally conservative assumption that $Q = Q_c$.

3 Experimental Verification

The critical velocity (u_c) for a specific ram pump corresponding to a particular impulse valve mass and stroke can only be obtained empirically at present. Experiments on Wilcox ($D = 53$ mm) and Platypus ($D = 76$ mm) ram pumps of Australian manufacture with conventional, vertically mounted, poppet-type impulse valves have been carried out by the author (Young, 1995a, 1996a and b). These tests show that simple linear relationships exist between u_c and impulse valve stroke, s_v , for constant valve mass. Attention is therefore confined here to relationships between critical velocity and impulse valve stroke and mass of the form $u_c = r s_v (g H_s)^{1/2}$ where H_s is the static head required to close the impulse valve (proportional to valve mass) and r is a characteristic parameter, having units of m^{-1} if s_v and H_s are in m. Dynamically similar pumps are assumed to have the same Froude number, $r s_v (= u_c / (g H_s)^{1/2})$.

O'Brien and Gosline (1933) carried out experiments on a 26 mm ram pump of the Gould type having a drive pipe length of 15.1 m, a supply head of 3.54 m and three valve strokes of 5.8, 10.9 and 18.5 mm, H_s was 0.26 m for all tests. All results are shown in Fig. 3.

Krol (1947) performed more than 500 separate tests on a specially constructed 51 mm ram pump. Valve strokes ranged from 1.6 mm to 9.5 mm and H_s was varied between 0.066 m and 0.543 m. The drive pipe length and the supply head were 18.52 m and 3.96 m respectively. The value of r for Krol's ram was $107 m^{-1}$ for the range of tests (Series 10 to 12, 14 to 17, 19 to 21 and 23 to 26) investigated here (see Fig. 4).

N. G. Calvert (1957) derived nondimensional groups for the quantity delivered and wasted similar to those on the left-hand side of Eqs. (11) and (12). The results for a range of pumps ($D = 12.5$ to 63 mm) are presented in the form of graphs in two papers (1957, 1958). The original data has been lost (J. R. Calvert, 1993) so that deductions from this work can only be approximate.

Azoury et al. (1988) have demonstrated that the least drive pipe diameter for practical operation of a ram pump is about 20 to 25 mm, thus results from the smallest of the pumps tested by Calvert have not been included in the present analysis. Young, (1995a) suggested a minimum drive pipe length of 5 m. Deterioration of performance was reported by Calvert when lengths were less than 3 m which supports this recommendation.

The author's tests on a 53 mm Wilcox ram pump (Young, 1995a and 1996a) were for $H = 2.76$ m with $L = 11.8, 15.1$ and 18.3 m and $H = 3.25$ m with $L = 15.1$ m. Impulse valve strokes were from 6 mm to 16 mm in 2 mm steps. H_s was

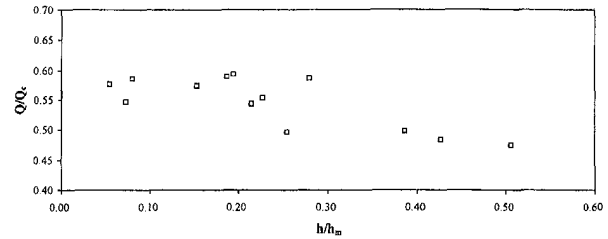


Fig. 3(a) Q/Q_c

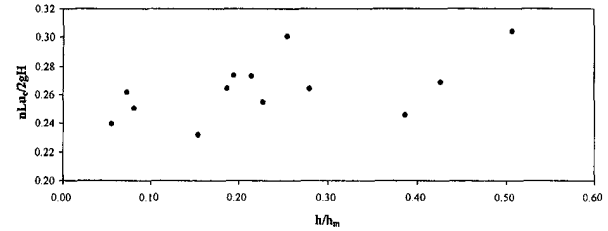


Fig. 3(b) $nLu_c/2gH$

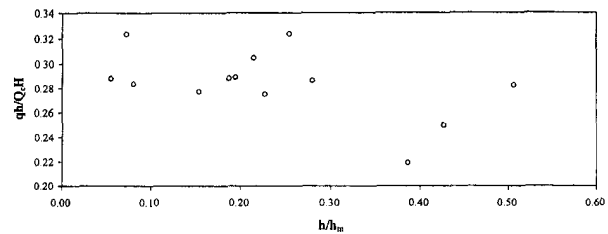


Fig. 3(c) $qh/Q_c H$

Fig. 3 Results for O'Brien and Gosline's Gould ram pump

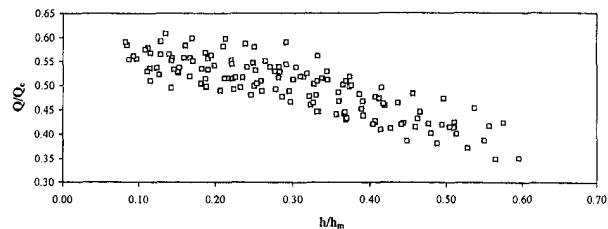


Fig. 4(a) Q/Q_c

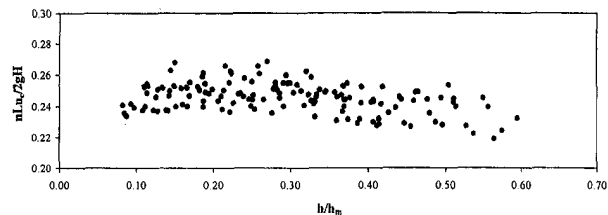


Fig. 4(b) $nLu_c/2gH$

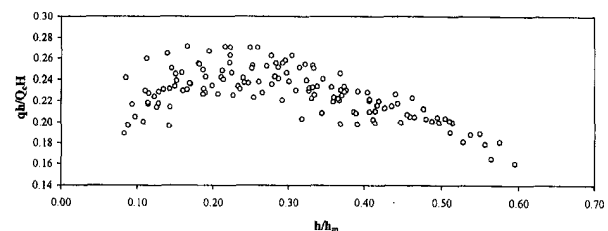


Fig. 4(c) $qh/Q_c H$

Fig. 4 Results for Krol's ram pump

0.33 m for all tests and r was 75 m^{-1} . All results are shown in Fig. 5.

The author's tests on a 76 mm Platypus ram pump (Young, 1996b) were for $H = 3.44 \text{ m}$ with $L = 13.6 \text{ m}$. Impulse valve strokes were 14, 18, 20, 22, and 26 mm. H_s was 0.3 m for all tests and r was 46 m^{-1} . All results are shown in Fig. 6.

Lansford and Dugan (1941) performed three series of tests (with different valve loads and strokes) on each of two Rife ram pumps of diameters 51 mm and 102 mm. The valve loading was not reported, thus it was not possible to determine values of H_s . For the 51 mm ram, $L = 16.7 \text{ m}$ and $H = 2.8 \text{ m}$. For the 102 mm ram, $L = 16.92 \text{ m}$ and $H = 2.74 \text{ m}$. The two pumps were unconventional in that the impulse valve discs were made of an elastic material. The stiffness of the smaller disc was sufficient to allow a performance comparable with a pump fitted with a conventional rigid disc (see Fig. 7). The larger pump, with a more flexible valve disk, showed different characteristics in respect of quantity delivered and source capacity as functions of nondimensional head ratio (see Fig. 8). Specific empirical relationships were determined by linear regression analysis as:

$$qh/Q_c H = 0.45(1 - h/h_m), \quad R^2 = 0.97$$

and

$$Q/Q_c = (0.55 - 0.37 h/h_m), \quad R^2 = 0.96$$

The parameter $nLu_c/2gH$ was found to be largely independent of h/h_m for both pumps and did not appear to be greatly influenced by impulse valve flexibility.

Equations (10) to (12) contain functions of the velocity and head ratios unknown to the designer. Since these equations should represent the behavior of similar ram pumps, the three empirical nondimensional parameters $nLu_c/2gH$, $qh/Q_c H$ and Q/Q_c for the Gould, Krol, Wilcox, Platypus, and Rife tests are shown plotted against h/h_m in Figs. 3 to 8 in order to obtain an indication of typical values for $C_c\phi_1$, $C_d\phi_1$, and ϕ_2 . Only tests

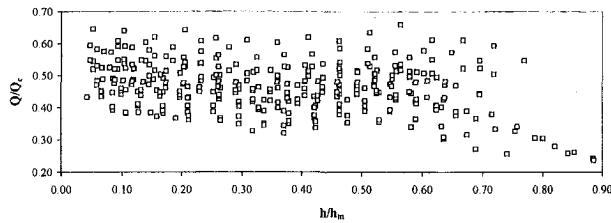


Fig. 5(a) Q/Q_c

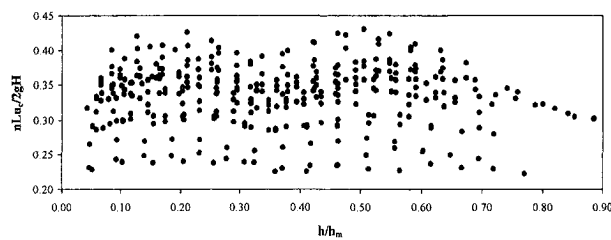


Fig. 5(b) $nLu_c/2gH$

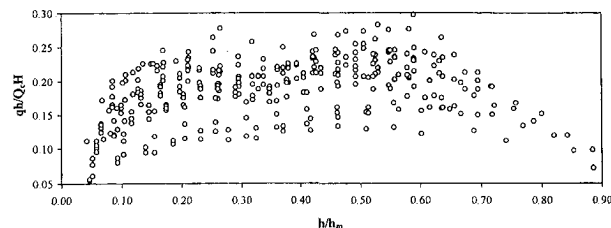


Fig. 5(c) $qh/Q_c H$

Fig. 5 Results for the Wilcox ram pump

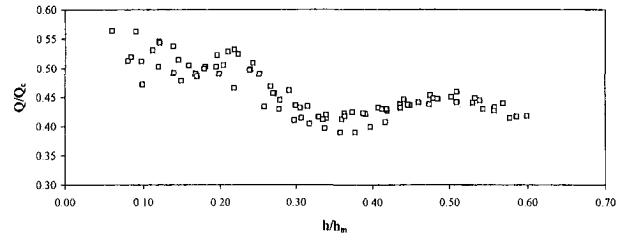


Fig. 6(a) Q/Q_c

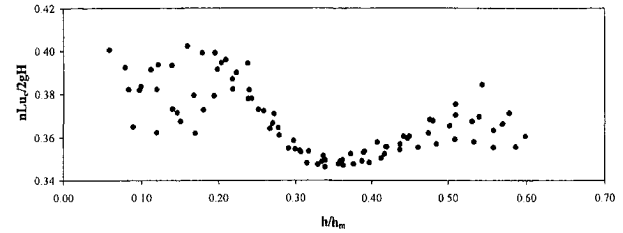


Fig. 6(b) $nLu_c/2gH$

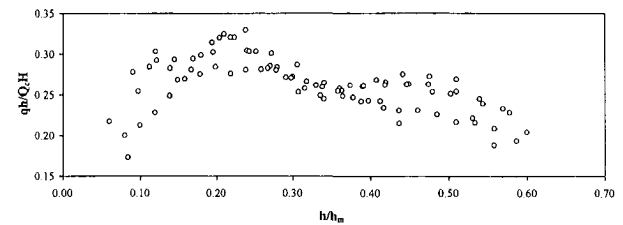


Fig. 6(c) $qh/Q_c H$

Fig. 6 Results for the Platypus ram pump

for which $n < 100$ beats per minute, $h/H > 3$ and $a < 0.8$ are included. The rationale for the latter restriction has been given (Young, 1995a); the limitation on h/H derives from O'Brien and Gosline's paper where it is shown theoretically that h/H cannot be less than 2 and should preferably be greater than 3.

Figures 3 to 8 show that $nLu_c/2gH$ for each of the six pumps had approximately constant values and were not substantially affected by h/h_m for $h/h_m < 0.6$ (Young, 1995a). A similar observation may be made in respect of $qh/Q_c H$ in Figs. 3 to 7. Table 1 gives mean values and corresponding standard deviations σ (where appropriate) for nine ram pumps (including Calvert's). Variations in these parameters between pumps may be explained by geometric and dynamic dissimilarities. The parameter Q/Q_c tended to vary slightly with h/h_m , reducing as h/h_m increased.

The mean of the mean values of $nLu_c/2gH$ from Table 1 for all nine pumps is 0.29 with a standard deviation (σ) of 0.046 and the mean of the mean values of $qh/Q_c H$ for eight of the pumps is 0.272 with $\sigma = 0.047$. Values of Q/Q_c were found from Figs. 3 to 8 to be between 0.4 and 0.6. It is therefore suggested that design values for the parameters in equations (10) to (12) be as follows:

$$nLu_c/2gH = 0.29 \pm 0.05 \quad (13)$$

$$qh/Q_c H = 0.27 \pm 0.05 \quad (14)$$

and

$$Q/Q_c = 0.5 \pm 0.1 \quad (15)$$

It can be shown (Young, 1995a) that the velocity ratio a ($=u_c/u_n$) may be obtained as:

$$a = \{(1 + ps^2L)(H_s/H)\}^{1/2} \quad (16)$$

where

$$p = r^2 f / (2D) \quad \text{and} \quad H_s = M_v / \rho A_{\text{disk}}$$

Ram pump performance deteriorates as the velocity ratio ap-

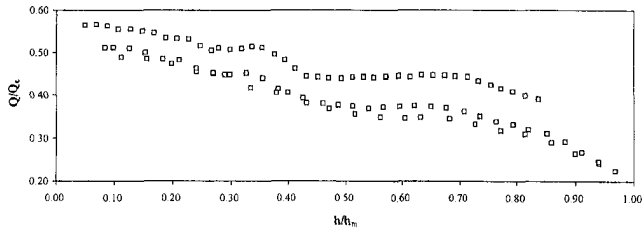


Fig. 7(a) Q/Q_c

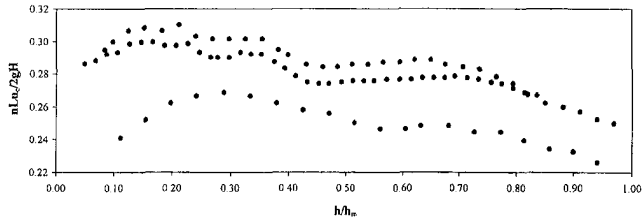


Fig. 7(b) $nLu_c/2gH$

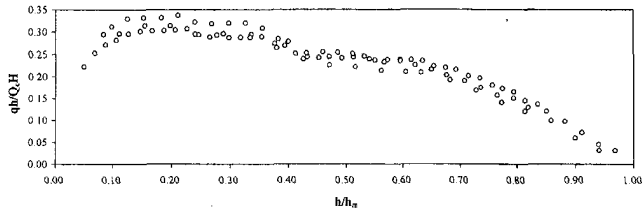


Fig. 7(c) qh/Q_cH

Fig. 7 Results for Lansford and Dugan's 51 mm Rife ram pump

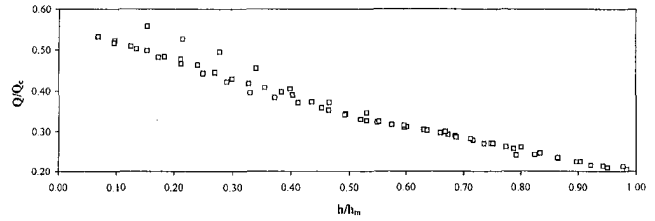


Fig. 8(a) Q/Q_c

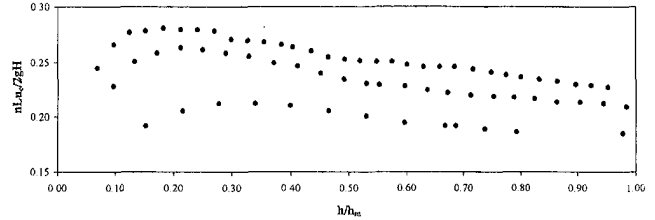


Fig. 8(b) $nLu_c/2gH$

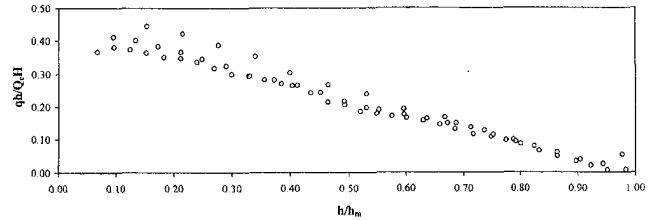


Fig. 8(c) qh/Q_cH

Fig. 8 Results for Lansford and Dugan's 102 mm Rife ram pump

proaches 1.0, thus if a is limited to 0.8, the maximum drive pipe length is obtained as:

$$L_{\max} = \{0.64(H/H_s) - 1\} / (ps_v^2) \quad (17)$$

An additional parameter required is the limiting design delivery head h_{lim} ($=0.6 h_m$) since performance falls off rapidly above this value (Young, 1995a). From experiments on the Wilcox and Platypus ram pumps using a galvanized iron drive pipe with a diameter/wall thickness ratio of 18, a value for the acoustic velocity c was found to be between 1000 and 1200 m/s. This is lower than the theoretical value due to the presence of some 0.01 to 0.02 percent by volume of entrained air sucked in through the impulse valve during recoil. As a conservative assumption, c will be taken here as 1000 m/s. Then, since $h_m = cu_c/g$ and $u_c = rs_v(gH_s)^{1/2}$, we have:

$$h_{\text{lim}} = 191.6 rs_v(H_s)^{1/2} \quad (18)$$

4 Summary and Conclusions

An analysis has been given which describes the performance of an automatic hydraulic ram pump under optimum operating conditions (zero recoil). Equations (10) to (12), together with the findings of Table 1, have been used to derive general design relationships (Eqs. (13) to (15)) applicable to any ram pump for operation at any delivery head less than h_{lim} . The beat frequency, n is expressed in terms of L , H , and u_c ; the delivery quantity, q is dependent upon h , H , and Q_c , while the source capacity, Q is dependent only on Q_c .

For a given pump size and impulse valve setting, quantity delivered is dependent only on h/H and the source capacity is constant. For a given impulse valve setting, beat frequency is dependent only on L/H and is not influenced by pump size as suggested by Calvert.

Using the approach described in this paper, detailed experiments to determine the performance of a particular ram pump are unnecessary. All that is required are a limited number of

tests to find r ; while H_s may be calculated from a knowledge of the cross-sectional area and mass of the valve disc.

The design formulae are independent of acoustic velocity and are therefore not affected by drive pipe material, wall thickness, working fluid or volume fraction of entrained air. However, this factor is of importance in determining the limiting delivery head, h_{lim} .

The ratio L/H , often quoted as a major design criterion, is seen to affect only the cycle time T and has no influence on quantity delivered or wasted. By contrast, the major factor which determines satisfactory pump operation has been shown to be an upper limit on drive pipe length (L_{\max}). This limit is dependent on velocity ratio, pump size, impulse valve stroke and mass and drive pipe friction factor. The maximum permissible velocity ratio has been assumed as 0.8.

Upper limits for the L/D ratio (another traditional design parameter) can be derived from the expression for L_{\max} but are not necessarily in agreement with Calvert (1958). The lower limit of drive pipe length (recommended as 5 m) is not dependent on pump size as suggested by Calvert.

Table 1 Values of $nLu_c/2gH$ and qh/Q_cH for nine ram pumps

Ram	D (mm)	$nLu_c/2gH$		qh/Q_cH	
		Mean	σ	Mean	σ
Calvert "a"	19	0.30	—	0.33	—
Gould	26	0.264	0.0203	0.284	0.0265
Calvert "b"	38	0.29	—	0.34	—
Lansford & Dugan	51	0.284	0.0169	0.276	0.0344
Krol	51	0.245	0.0096	0.228	0.0225
Wilcox	53	0.355	0.0302	0.204	0.0358
Calvert "c"	63	0.27	—	0.25	—
Platypus	76	0.367	0.0155	0.263	0.0311
Lansford and Dugan	102	0.237	0.0262	—	—

Design formulae have been derived from new and existing experimental data for a variety of ram pumps ranging in size from $D = 19$ mm to 102 mm and may be used if two constants (r and H_c) defining the magnitude of the critical velocity are known for a particular impulse valve. The design procedure is considered to err on the conservative side for small to medium size ram pumps, but should be treated as tentative for larger pumps until confirmation is obtained from further experiments. Detailed experimental studies to provide design data for specific pumps are still needed to verify and refine the unified design approach presented in this paper. The author is currently performing tests on the Platypus pump to determine performance at very low supply heads.

References

- Azoury, P. H., Baasri, M., and Najm, H., 1988, "On the Optimum Utilisation of Water Hammer," *Proceedings of the Institution of Mechanical Engineers, Journal of Power Engineering*, Vol. 202, pp. 249–256.
- Calvert, J. R., 1993, Private correspondence.
- Calvert, N. G., 1957, "The Hydraulic Ram," *The Engineer*, Harmsworth Press, London, England, 19 April, 203(5282), pp. 597–600.
- Calvert, N. G., 1958, "Drive Pipe of a Hydraulic Ram," *The Engineer*, Harmsworth Press, London, England, 26 December, 206(5370), p. 1001.
- Krol, J., 1947, "A Theoretical and Experimental Investigation Into the Action of the Automatic Hydraulic Ram," PhD thesis, Pt II, University of London, England.
- Lansford, W. M., and Dugan, W. G., 1941, "An Analytical and Experimental Study of the Hydraulic Ram," *University of Illinois Bulletin*, Vol. Vol. 38(22).
- O'Brien, M. P., and Gosline, J. E., 1993, "The Hydraulic Ram," University of California Publications in Engineering, 3(1).
- Rennie, L. C., and Bunt, E. A., 1981, "The Automatic Hydraulic Ram, Part 1," *South African Mechanical Engineer*, Vol. 31, pp. 258–273.
- Young, B. W., 1995a, "The Design of Hydraulic Ram Pump Systems," *Proceedings of the Institution of Mechanical Engineers, Part A: Journal of Power and Energy*, Vol. 209, No. A4, pp. 313–322.
- Young, B. W., 1995b, "The Analysis of Ram Pumps," Research Monograph CE-01-95, Department of Civil Engineering, Papua New Guinea University of Technology.
- Young, B. W., 1996a, "Simplified Analysis and Design of the Hydraulic Ram Pump," *Proceedings of the Institution of Mechanical Engineers, Part A: Journal of Power and Energy*, Vol. 210, No. A4, pp. 295–303.
- Young, B. W., 1996b, "System Designs for the Platypus Ram Pump," *Agricultural Engineering Australia*, Vol. 25, No. 1, pp. 13–18.

Yoshinobu Tsujimoto

Professor.

Yoshiki Yoshida

Assistant Professor.

Osaka University, Engineering Science,
1-3 Machikaneyama, Toyonaka, 560,
Japan

Hideo Ohashi

President,

Kogakuin University, Mechanical
Engineering, Nishishinjuku 1-24-2,
Shinjuku, Tokyo, 163-91, Japan

Norihiro Teramoto

Engineer, Kubota Corporation

Shin Ishizaki

Engineer, Ishikawajima Harima Heavy
Industries, Inc.

Fluid Force Moment on a Centrifugal Impeller Shroud in Precessing Motion

Experimental results of fluid moment on a centrifugal impeller shroud in precessing motion are discussed based on the bulk flow model to elucidate the fundamental flow mechanism. It is shown that the backshroud/casing clearance flow and the destabilizing fluid force moment can be simulated by the bulk flow model fairly well if the measured behavior of the resistance is correctly incorporated in the model. From the calculations with and without steady and unsteady wall shear stresses, the unsteady component of the clearance flow is shown to be basically a two-dimensional inviscid flow induced by the change in the flow thickness. The effects of the leakage flow rate and the resistance at the leakage flow entry are discussed, paying attention to the steady tangential velocity of the leakage flow.

Introduction

For rotordynamic problems, forces on seals and bearings play important roles. For these problems, see Childs' textbook (1993). For turbomachinery operating at supercritical shaft speed it is also important to understand the characters of unsteady fluid forces on the impeller which occur in response to shaft vibration. They are called "rotordynamic forces (Brennen, 1994)" and considerable knowledge has been obtained for whirling closed type centrifugal impellers. Although the impeller whirling forces are basically stabilizing the rotor vibration (Ohashi and Shoji 1987, Shoji and Ohashi 1987), they become destabilizing under the following conditions: (i) at reduced flow rate (Ohashi and Shoji, 1987, Tsujimoto and Acosta, 1987), (ii) when there is interaction with volute or vaned diffuser (Jery et al., 1985; Adkins and Brennen, 1988; Tsujimoto et al., 1988A, 1988B) or (iii) when the clearance between front shroud and casing of 3-D impeller is small (Jery, 1986; Ohashi et al., 1988; Bolleter et al., 1987; Guinzburg et al., 1994; Childs, 1989). The importance of the shroud/casing clearance flow was shown recently by Smith et al. (1996) from their field experiences.

For precessing motion, Ohashi et al. (1991) have shown that, from direct force measurements, the fluid force moment may become destabilizing for the precessing velocity ratio $0 \leq \Omega/\omega \leq 0.5$. This destabilizing velocity ratio range is quite similar that of whirling cases mentioned in the last paragraph. The present paper focuses on the backshroud/casing clearance flow and attempts have been made to explain the flow mechanism based on the bulk flow model, originally applied by Childs (1989) to estimate the whirling shroud forces. In the present study, the precessing shroud force moments are evaluated from unsteady pressure measurements, which includes the effects of the leakage flow rate and the flow resistance at the entrance of the leakage flow path. In addition, unsteady pressure and velocity field measurements are conducted and the results are com-

pared with those of the bulk flow model. The experimental results are partly reported elsewhere (Yoshida et al., 1996) but the discussions on the flow mechanisms are made in the present paper based on the bulk flow model.

Outline of Experiments

Figure 1(a) shows the experimental apparatus. The impeller is a model of a boiler feed pump with outer radius $R_i = 165$ mm, width $b_2 = 28$ mm, and vane angle from tangent = 24.5 deg and design flow coefficient $\phi_d = 0.106$. Details of the apparatus have been reported by Ohashi et al. (1991). The center of the precessing motion is set at O, the intersection of the centerline of the untilted impeller with the central plane of the impeller discharge. The axis of the impeller executes a precessing motion with a constant precessing angular frequency Ω keeping the apex angle to be $\alpha = 0.9$ deg. The rotational speed of the main shaft is kept to be 677 rpm ($=60\omega/2\pi$) and the precessing velocity ratio Ω/ω is changed between -1.4 and 1.4. Air is used as the working fluid. The flow from the impeller is discharged to a vaneless diffuser of radius ratio 1.45 and then to a circular collector, as shown in Fig. 1(b).

Although the leakage in the backshroud clearance in boiler feed pump is radially outward, inward leakage flow is assumed in this study since it is more common in other types of the pumps. The unsteady pressure is measured using the pressure taps C-F. The unsteady velocity measurements are made at the same radial locations as the pressure taps, by using a hot wire anemometer. The clearance S at the leakage flow entrance is changed to be $S = 1, 2$ and 5 mm. The backshroud/casing clearance at normal position is set to be $H_0 = 7.5$ mm. The circumferential Reynolds number at the leakage flow entry (at impeller outer radius R_i) based on the clearance H_0 was $R_i\omega H_0/\nu = 5850$, and the radial Reynolds number range $U_R H_0/\nu = 0 \sim 193$, where U_R is mean radial velocity at the leakage flow entrance due to leakage flow. The leakage flow exit G is connected to a blower to produce the leakage flow through a flow meter and a flow control valve.

Figure 2 shows the coordinate system. The r -axis is set in the direction of maximum clearance and the t -axis perpendicular

Contributed by the Fluids Engineering Division for publication in the JOURNAL OF FLUIDS ENGINEERING. Manuscript received by the Fluids Engineering Division April 26, 1996; revised manuscript received January 7, 1997. Associate Technical Editor: B. Schiavello.

to it, proceeding by 90 degs from r -axis in the direction of impeller rotation. The precessing angular velocity Ω is positive when it is in the same direction as the impeller rotation ω . The fluid moment M is represented with its radial (M_r) and tangential (M_t) components. For the cases when M_r has the same sign as Ω/ω , it has the effects to promote the precessing motion in the direction of Ω , (with the opposite sign, to damp). On the other hand, $M_t > 0$ shows the moment which has the same effect as the increase of shaft stiffness for bending, for overhung rotor. The moments M_r and M_t are normalized with $M_0 = I\alpha\omega^2$, where $I = \rho\pi R_i^2 b_2^2 i^2$ with $i = \sqrt{R_i^2/4 + b_2^2/12}$ is the moment of inertia of hypothetical fluid disk of thickness b_2 and radius R_i , around the diameter.

Bulk Flow Model

The bulk flow model was first applied by Childs (1989) to estimate the forces on the front shroud of a whirling centrifugal impeller and later by Guinzburg (1994) on a model rotor. The details are not reproduced here. This model assumes a two-dimensional inviscid flow with variable flow thickness H , in which the (empirical) wall shear stress is taken into account as an external body force. The momentum and continuity equations are linearized assuming that the unsteady components of flow thickness, pressure and velocity are sufficiently small. In the present study, the fundamental equations are integrated numerically so as to satisfy the following boundary conditions.

At the leakage flow inlet ($R = R_i = 165$ mm, see Figs. 1 and 5)

(For steady component, represented with suffix 0)

- (a) Radial velocity U_{R0} is given from assumed leakage flow rate
- (b) Tangential velocity $U_{\theta 0} = 0.5 R_i \omega$, caused by equal steady wall friction on both sides of the inlet clearance.
- (c) Pressure P_0 can be given arbitrarily as a reference pressure.

(For unsteady component, represented with suffix 1)

- (d) Unsteady tangential velocity $U_{\theta 1} = 0$, resulting from uniform circumferential distribution of wall friction at the inlet.
- (e) Resistance at the inlet is represented by $P_1/\rho = F(U_{R1})$, the functional form of F is discussed later.

At the leakage flow outlet ($R = R_o = 32.5$ mm, see Fig. 1)

(For unsteady component)

- (f) Constant pressure $P_1 = 0$ is assumed since the leakage flow exits to a relatively large space without flow restriction.

The shear stress representation as proposed by Hirs (1973) is used with Yamada's empirical factors (1962) in the following calculations.

Results and Discussions

The results are shown only for design pump flow coefficient $\phi_d = 0.106$, since it was found that the effects of pump flow rate was quite small. This suggests the validity of the boundary condition (b).

Velocity Distribution Across the Clearance. Figure 3 shows the mean velocity distribution and the amplitude of velocity fluctuation caused by the precessing motion with $\Omega/\omega = 0.2$ and 1, with the leakage flow coefficient $\phi_l = 0$ and the clearance $S = 2$ mm. The measurements are made at location E ($R = 100$ mm, $R/R_i = 0.606$) in Fig. 1. The range of backshroud movement is shown in the figure. The average of the mean tangential velocity is $U_{\theta}/R\omega \approx 0.5$. Small inward velocity (i.e., $U_R < 0$) due to secondary flow is observed near the casing wall but $U_R/R\omega \approx 0$ at the center of the clearance. The amplitude of the velocity fluctuation is relatively uniform over the clearance and it was confirmed that the phase was nearly constant. From this measurement it is expected that the bulk flow model is a good approximation of the clearance flow.

Effects of Loss at the Inlet of Leakage Flow Path. It is generally assumed that the pressure loss ΔP at the inlet is proportional to U_R^2 :

$$\Delta P/\rho = (1 + \xi)(-U_R)^2 \quad (1)$$

The perturbation of this relation gives

$$P_1/\rho = F(U_{R1}) = -(1 + \xi)U_{R0}U_{R1} \quad (2)$$

which gives zero pressure fluctuation ($P_1 = 0$) for the case without leakage ($\phi_l = 0$, $U_{R0} = 0$) irrespective of the value of loss coefficient ξ . Figure 4 shows the comparison of the results of experiment and calculations with the assumption of Eq. (1). The calculation underpredicts the moments significantly.

Under this situation the loss is experimentally examined. Figure 5 shows the dependence of loss on the leakage flow coefficient ϕ_l . (The circumferential Reynolds number $R_i\omega S/\nu$ ($S = 2$ mm) is 1560 and the Reynolds number in the flow direction $V_m S/\nu$ is from 0 to 193 in the experiment.) The pressure loss is estimated from the pressure measurements at pressure taps

Nomenclature

b_2 = impeller outlet width (see Fig. 5)
 H = flow thickness
 H_0 = casing/backshroud clearance
 j = imaginary unit
 K = proportionality constant, Eq. (3)
 M_r = radial component of fluid force moment
 M_t = tangential component of fluid force moment
 P = pressure
 ΔP = pressure loss at the leakage flow entry
 R = radial coordinate
 S = clearance at the leakage flow entry

t = time
 U_R, U_{θ} = radial (positive outward) and circumferential (positive in the direction of impeller rotation) velocity
 V_m = mean velocity at the inlet clearance
 α = apex angle of precessing motion
 ξ = loss coefficient
 θ = circumferential coordinate
 μ = viscosity
 ν = kinematic viscosity
 ρ = density
 ϕ = pump flow coefficient, = pump flow rate/ $(2\pi R_i^2 b_2 \omega)$

ϕ_l = leakage flow coefficient, = leakage flow rate/ $(2\pi R_i^2 b_2 \omega)$
 ω = angular velocity of impeller rotation
 Ω = angular velocity of precessing motion

Suffix

0 = steady component
 1 = unsteady component
 i = inlet to the leakage flow path, at the outer radius of the impeller (see Fig. 1)
 o = exit from the leakage flow path, at the inner radius of the impeller (see Fig. 1)
 r = radial component (see Fig. 2)
 t = tangential component (see Fig. 2)

S=1, 2, 5(mm)

A-F: pressure and velocity measurement locations

G: leakage flow exit

O: center of precession

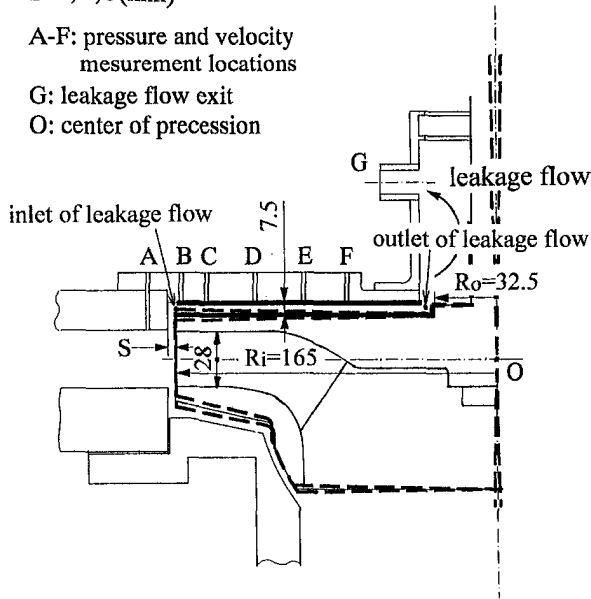


Fig. 1(a) Details around the impeller

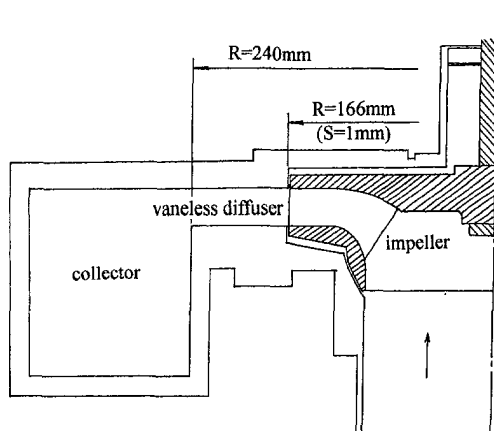


Fig. 1(b) Cross section of the pump (impeller, vaneless diffuser, and collector)

Fig. 1 Experimental apparatus

A ($R/R_i = 1.09$) and B ($R/R_i = 0.989$), taking into account the effect of centrifugal force due to swirl. The loss is rather linear with ϕ_i than parabolic as expected from Eq. (1). For the case with $S = 1$ mm, the loss can be estimated as the sum of pressure loss of Poiseuille flow and the dynamic pressure of the mean leakage flow. However, this gives smaller loss for larger clearance. Even at $\phi_i = 0$, the linear curves have finite slope and thus the inlet pressure P_1 has nonzero value unlike the relation of Eq. (2).

Based on this result the relation

$$P_1/\rho = F(U_{R1}) = KU_{R1} \quad (3)$$

has been used for the boundary condition (e) with K estimated from the slope of the $\Delta P - \phi_i$ curve. The full line in Fig. 6 shows the result under this boundary condition. We observe reasonable agreement. We should note that the destabilizing moment $M_r > 0$ in $0 < \Omega/\omega < 0.5$ is nicely simulated.

The velocity and pressure fluctuation fields as viewed from casing are shown in Fig. 7. The velocity fluctuation is measured at 3 mm from casing in the 7.5 mm casing/backshroud clearance. The direction r is defined as the direction with maximum clearance. These patterns rotate with the angular velocity Ω of

the precessing motion. The pressure distribution on the backshroud was integrated to estimate the fluid force moments M_r and M_t . The experiment and the calculation agree fairly well including their phase relationships.

The above discussions show that the bulk flow model can estimate both the flow field and the resulting force moment once the correct behavior of the inlet loss is used, for the cases with the size of the clearance of the present study.

Effects of Wall Shear Stress. In the perturbation analysis using the bulk flow model, the wall shear stress can be separated into steady (time mean) and unsteady (perturbation) components. Figure 6 compares the results of calculations under the following three conditions, without leakage flow: (1) with steady and unsteady shear stress, (2) with steady but without unsteady stress, and (3) without steady and unsteady shear stress. The steady shear stress controls the steady tangential velocity distribution. Without leakage flow, the tangential velocity becomes $U_{\theta 0} = 0.5 R\omega$ so long as the shear stresses on the casing wall and the backshroud have the same value, irrespective of their magnitude. This tangential velocity distribution is used for the cases of (1) and (2). Without steady shear stress and leakage, $U_{\theta 0}$ can be assumed arbitrarily. However, if we consider an infinitesimal leakage, the steady velocity is deter-

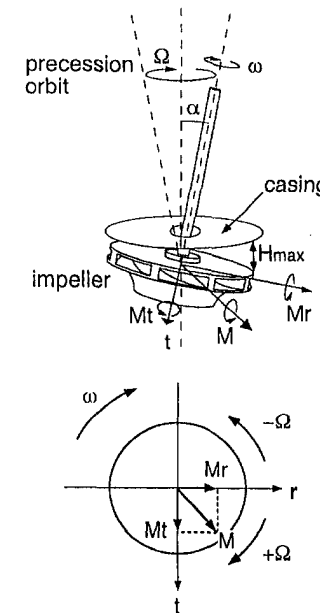


Fig. 2 Coordinate system

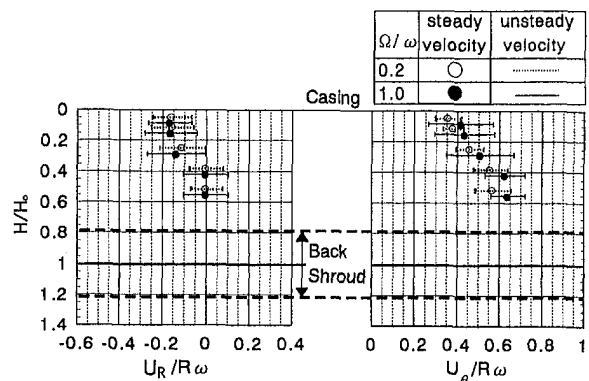


Fig. 3 Velocity distribution over the clearance (normalized by local circumferential velocity $R\omega$ at location E, $R/R_i = 0.606$, $\phi_i = 0$, $S = 2$ mm, uncertainty in velocity measurement is $U_R, U_{\theta}/R_i\omega = \pm 0.01$)

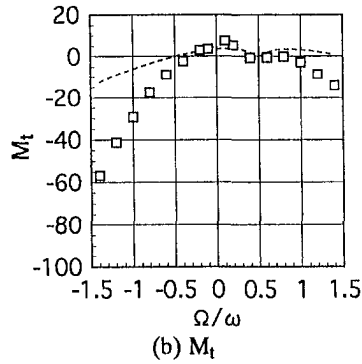
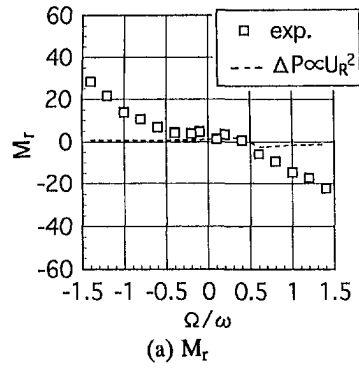


Fig. 4 Normalized moment components (with $\Delta P \propto U_0^2$, $\phi_l = 0$, $S = 2$ mm, uncertainty in M_r , $M_t = \pm 2$ and in $\Omega/\omega = \pm 0.002$)

mined from the conservation of angular momentum and can be written as $U_{\theta 0} = 0.5(R_i^2/R)\omega$ if we assume that $U_{\theta 0} = 0.5 R_i \omega$ at the inlet. This distribution has been used for the calculation of the case (3).

The comparison of the cases (1) and (2) shows that the unsteady shear stress has little effect on the moment components. However, the result of (3) shows that the steady shear stress, i.e., the steady tangential velocity distribution has a large

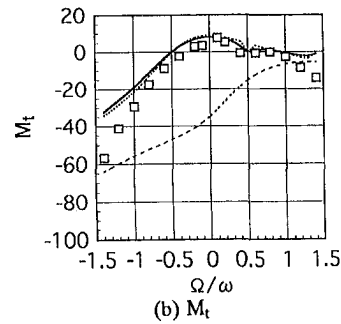
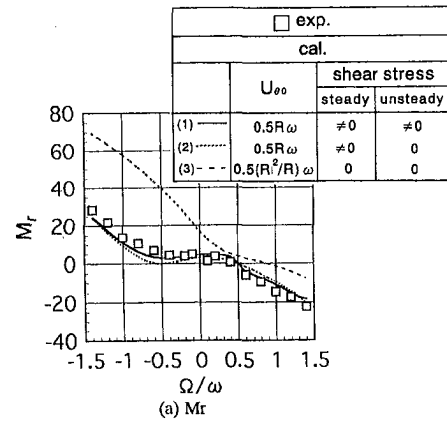


Fig. 6 Normalized moment components (effects of wall shear stress, with $\phi_l = 0$, $S = 2$ mm, uncertainty in M_r , $M_t = \pm 2$ and in $\Omega/\omega = \pm 0.002$)

effect on the moment. These results suggest that the unsteady component is basically a two-dimensional inviscid flow affected by fluid viscosity through the steady tangential velocity distribution and through the pressure loss at the leakage flow entry. The viscosity of the fluid affects the fluid moment through the steady tangential velocity distribution as shown here and through the pressure loss at the leakage flow.

Under the simplifying assumptions of: (a) unsteady wall shear stress can be neglected, (b) flat clearance flow surface with constant flow thickness, (c) no leakage flow—forced vor-

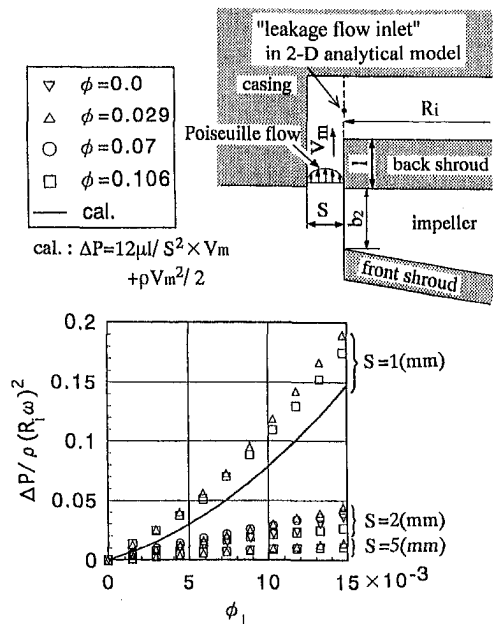


Fig. 5 Pressure loss at the leakage flow inlet (uncertainty in $\Delta P / (\rho(R_i \omega)^2) = \pm 0.005$, in $\phi_l = \pm 0.5 \times 10^{-3}$)

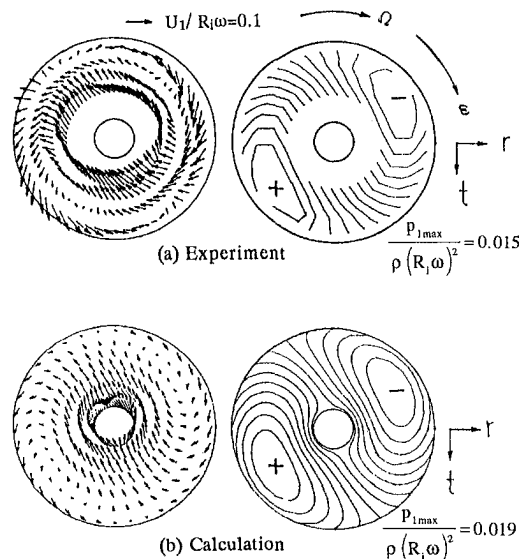


Fig. 7 Velocity and pressure fluctuation fields ($\phi_l = 0$, $S = 2$ mm, $\Omega/\omega = 0.2$, uncertainty in $U_t / (R_i \omega) = \pm 0.01$, in $P_t / (\rho(R_i \omega)^2) = \pm 0.001$)

text distribution of steady tangential velocity $U_{\theta 0} = R\omega^*$. (The number of ω^* would depend on the shear stresses on the shroud and casing. For the case with equal stresses $\omega^* = 0.5\omega$.) The following semi-analytical representation of the flow disturbance can be obtained for the precessing motion with $H = R\alpha e^{j(\Omega t - \theta)}$:

$$U_{R1} = [C_1 R^2 + C_2 R^{-2} + C_3] e^{j(\Omega t - \theta)} \quad (4)$$

$$U_{\theta 1} = (\Omega - \omega^*)(R^2 \alpha / H_0) e^{j(\Omega t - \theta)} - j \left(R \frac{\partial U_{R1}}{\partial R} + U_{R1} \right) \quad (5)$$

$$P_1 = -\rho j \{ j(\Omega - \omega^*) U_{\theta 1} + 2\omega^* U_{R1} \} R \quad (6)$$

where

$$C_1 = -j(3\Omega - 5\omega^*)(\alpha / H_0) / 8$$

and C_2 and C_3 are determined from the boundary conditions ($P_1 / \rho = K_i U_{R1}$ at $R = R_i$ and $P_1 / \rho = K_o U_{R1}$ at $R = R_o$) which can be rewritten as

$$\begin{bmatrix} -j(-\Omega + 3\omega^*)R_o^{-1} - K_o R_o^{-2} - j(\Omega + \omega^*)R_o - K_o \\ -j(-\Omega + 3\omega^*)R_i^{-1} - K_i R_i^{-2} - j(\Omega + \omega^*)R_i - K_i \end{bmatrix} \begin{bmatrix} C_2 \\ C_3 \end{bmatrix} = \begin{bmatrix} j \{ j(\Omega - \omega^*)^2 R_o^3 (\alpha / H_0) + (3\Omega - \omega^*) C_1 R_o^3 \} + K_o C_1 R_o^2 \\ j \{ j(\Omega - \omega^*)^2 R_i^3 (\alpha / H_0) + (3\Omega - \omega^*) C_1 R_i^3 \} + K_i C_1 R_i^2 \end{bmatrix} \quad (7)$$

The fluid force moment can be given by (in dimensional form)

$$\begin{aligned} -M_t + jM_r = & -\rho \pi j \{ j(\Omega + \omega^*)(3\omega^* - \Omega) \\ & \times (R_i^6 - R_o^6) (\alpha / H_0) / 48 + C_3 (\Omega + \omega^*) (R_i^4 - R_o^4) / 4 \\ & + C_2 (3\omega^* - \Omega) (R_i^2 - R_o^2) / 2 \} \quad (8) \end{aligned}$$

We should note that the amplitudes of unsteady flow components and the fluid force moment are inversely proportional to the steady clearance H_0 . With $\omega^* = 0.5\omega$, the above results agree with the case (2) in Fig. 6.

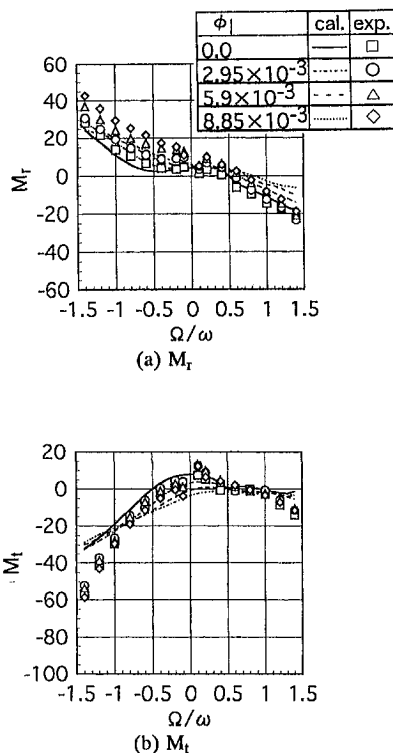


Fig. 8 Normalized moment components (effects of leakage flow rate ϕ_l , with $S = 2$ mm, uncertainty in $M_r, M_t = \pm 2$ and in $\Omega / \omega = \pm 0.002$)

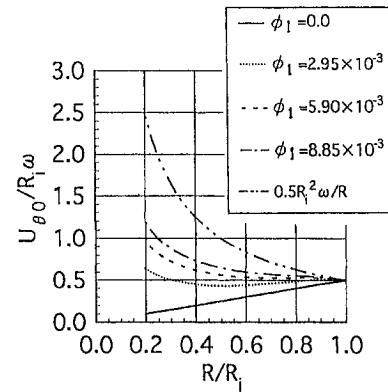


Fig. 9 Effects of leakage flow rate ϕ_l on the steady tangential velocity distribution $U_{\theta 0}(R)$

Effects of Leakage Flow Rate and the Resistance at the Leakage Flow Inlet. Figure 8 shows the effects of leakage flow rate ϕ_l . The value of $\phi_l = 2.95 \times 10^{-3}$ corresponds to 2.8 percent of design flow rate $\phi_d = 0.106$. In both calculations and experiments, M_r increases as the increase in ϕ_l , which results in the increase of the range of destabilization ($M_r > 0$ for $\Omega / \omega > 0$). Figure 9 shows the calculated steady tangential velocity distribution $U_{\theta 0}(R)$ for various leakage flow rate. As the increase in the leakage flow rate, the velocity distribution shifts from forced vortex type ($0.5R\omega$) to free vortex type ($0.5R^2\omega/R$) due to the angular momentum carried by the inward leakage flow. This result, as well as the result in Fig. 6, suggests that the increase in the steady tangential velocity is responsible for the destabilization.

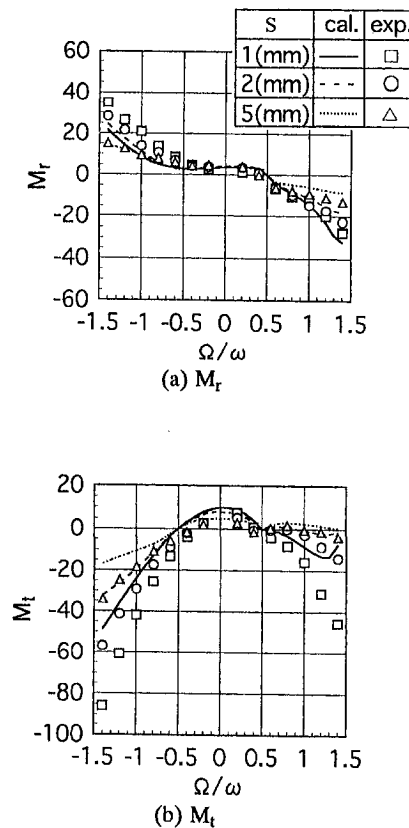


Fig. 10 Normalized moment components (effects of leakage entrance clearance S , with $\phi_l = 0$, uncertainty in $M_r, M_t = \pm 2$ and in $\Omega / \omega = \pm 0.002$)

Figure 10 shows the effects of the resistance at the leakage flow inlet. The measured pressure drop shown in Fig. 5 is used for the calculations. Both M_r and M_i generally increase as the decrease in the clearance S . This is caused by the larger value of K in Eq. (3) or the larger slope of the curves in Fig. 5 for smaller clearance S , which results in larger pressure fluctuation at the inlet of leakage flow and the larger force moment. The destabilizing fluid moment $M_r > 0$ in $0 < \Omega/\omega < 0.5$ is not so largely affected by the size of clearance.

Conclusions

The results of the present study can be summarized as follows.

- (1) The unsteady flow in the backshroud/casing clearance caused by the precessing motion is basically a 2-D inviscid flow with minor effects of unsteady wall shear stress.
- (2) The viscosity of the fluid affects the result through the steady tangential velocity distribution and the pressure loss at the leakage flow inlet.
- (3) The bulk flow model can simulate the clearance flow fairly well if we incorporate the correct behavior of the loss at the leakage flow inlet.
- (4) The inlet pressure drop was linear with the leakage flow rate rather than parabolic as usually expected.
- (5) Destabilizing fluid force moment for precessing motion is observed for small positive precessing velocity ratio.
- (6) The frequency range of destabilizing moment increases as the increase in the leakage flow rate, caused by the increase in the steady tangential velocity in the clearance.

The authors would like to acknowledge the contribution of Mr. Akira Saito in establishing the experimental procedure. This study is partly supported by the Grant-in Aid for Developmental Scientific Research (B) of the Japanese Ministry of Education, Science and Culture.

References

Adkins, D. R., and Brennen, C. E., 1988, "Analyses of Hydraulic Radial Forces on Centrifugal Pump Impellers," *ASME JOURNAL OF FLUIDS ENGINEERING*, Vol. 110, No. 1, pp. 20–28.

Bolleter, U., Wyss, A., Welte, I., and Sturchler, R., 1987, "Measurement of Hydrodynamic Interaction Matrices of Boiler Feed Pump Impellers," *ASME Journal of Vibration, Acoustics, Stress and Reliability in Design*, Vol. 109, No. 2, pp. 144–151.

Brennen, C. E., 1994, *Hydrodynamics of Pumps*, Concepts ETI, and Oxford University Press.

Childs, D. W., 1993, *Turbomachinery Rotordynamics*, Wiley, New York.

Childs, D. W., 1989, "Fluid Structure Interaction Forces at Pump-Impeller-Shroud Surfaces for Rotordynamic Calculations," *ASME Journal of Vibration, Acoustics, Stress and Reliability in Design*, Vol. 111, No. 4, pp. 216–225.

Guinzburg, A., Brennen, C. E., Acosta, A. J., and Caughey, T. K., 1994, "Experimental Results for the Rotordynamic Characteristics of Leakage Flows in Centrifugal Pump," *ASME JOURNAL OF FLUIDS ENGINEERING*, Vol. 116, No. 1, pp. 110–115.

Hirs, G. G., 1973, "A Bulk Flow Theory for Turbulence in Lubricant Film," *ASME Journal of Lubrication Technology*, Apr., pp. 137–146.

Jery, B., Acosta, A. J., Brennen, C. E., and Caughey, T. K., 1985, "Forces on Centrifugal Pump Impellers," *Proceedings of the 2nd International Pump Symposium*, Houston, Texas, pp. 21–32.

Jery, B., 1986, "Experimental Study of Unsteady Hydrodynamic Force Matrices on Whirling Centrifugal Pump Impellers," Ph.D thesis, California Institute of Technology.

Shoji, H., and Ohashi, H., 1987, "Lateral Fluid Forces on Whirling Centrifugal Impeller (1st report: Theory)," *ASME JOURNAL OF FLUIDS ENGINEERING*, Vol. 109, No. 2, pp. 94–99.

Ohashi, H., Imai, H., and Tsuchihashi, T., 1991, "Fluid Force and Moment on Centrifugal Impellers in Precession Motion," *ASME Fluid Machinery Forum, FED-Vol. 119*, pp. 57–60.

Ohashi, H., Sakurai, A., and Nishijima, J., 1988, "Influence of Impeller and Diffuser Geometries on the Lateral Fluid Forces of Whirling Centrifugal Impeller," *NASA CP 3026*, pp. 285–306.

Ohashi, H., and Shoji, H., 1987, "Lateral Fluid Forces on Whirling Centrifugal Impeller (2nd report: Experiment in Vaneless Diffuser)," *ASME JOURNAL OF FLUIDS ENGINEERING*, Vol. 109, No. 2, pp. 100–106.

Smith, D. R., Price, S. M., and Kunz, F. K., 1996, "Centrifugal Pump Vibration Caused by Supersynchronous Shaft Instability Use of Pumpout Vanes to Increase Pump Shaft Stability," *Proceedings of the 13th International Pump Users Symposium*, Houston, Texas, pp. 47–60.

Tsujimoto, Y., and Acosta, A. J., 1987, "Theoretical Study of Impeller and/or Vaneless Diffuser Attributed Rotating Stalls and Their Effects on Whirling Instability of a Centrifugal Impeller," *Work Group on the Behavior of Hydraulic Machinery Under Steady Oscillatory Conditions*, Lille, France.

Tsujimoto, Y., Acosta, A. J., and Brennen, C. E., 1988A, "Theoretical Study of Fluid Forces on Centrifugal Pump Impellers," *ASME Journal of Vibration, Acoustics, Stress and Reliability in Design*, Vol. 110, No. 3, pp. 263–269.

Tsujimoto, Y., Acosta, A. J. and Yoshida, Y., 1988B, "A Theoretical Study of Fluid Forces on a Centrifugal Impeller Rotating and Whirling in a Vaned Diffuser," *NASA CP 3026*, pp. 307–322.

Yamada, Y., 1962, "Resistance of Flow Through Annulus with an Inner Rotating Cylinder," *Bulletin of JSME*, Vol. 5, No. 18, pp. 301–310.

Yoshida, Y., Saito, A., Ishizaki, S., Tsujimoto, Y. and Ohashi, H., 1996, "Measurements of Flow in the Backshroud/Casing Clearance of a Precessing Centrifugal Impeller," *Proceedings of the 6th International Symposium on Transport Phenomena and Dynamics of Rotating Machinery*, Vol. 2, Honolulu, Hawaii, pp. 151–160.

Navier-Stokes Simulations of a Novel Viscous Pump

M. C. Sharatchandra
Postdoctoral Research Associate.

Mihir Sen
Professor. Mem. ASME

Mohamed Gad-el-Hak
Professor. Fellow ASME

Department of Aerospace and
Mechanical Engineering,
University of Notre Dame,
Notre Dame, IN 46556

A numerical study of flow in a novel viscous-based pumping device appropriate for microscale applications is described. The device, essentially consisting of a rotating cylinder eccentrically placed in a channel, is shown to be capable of generating a net flow against an externally imposed pressure gradient. Navier-Stokes simulations at low Reynolds numbers are carried out using a finite-volume approach to study the influence of various geometric parameters. Slip effects for gas flows are also briefly investigated. The numerical results indicate that the generated flow rate is a maximum when the cylinder is in contact with a channel wall and that an optimum plate spacing exists. These observations are in excellent agreement, both qualitatively and quantitatively, with a previous experimental study. Furthermore, it is shown that effective pumping is obtained even for considerably higher Reynolds numbers, thereby extending the performance envelope of the proposed device to non-microscale applications as well. Finally, slip-flow effects appear to be significant only for Knudsen numbers greater than 0.1, which is important from the point of view of microscale applications.

1 Introduction

Interest in the fluid mechanics of micromachines has been boosted by recent impressive advances in the technology of microfabrication (Angell et al., 1983; Gabriel, 1995). There are certain physical effects that become important at these small scales which have to be taken into account in the design of appropriate machinery. Large viscous forces in relation to inertia are one effect, and possible slip at boundary surfaces is another. Due to these differences, macromachines that are simply reduced in size may not work.

From the point of view of applications, pumps are one of the kind of fluid micro-machines that have been conceived. At such small scales, conventional principles of rotating turbomachinery based on centrifugal and inertial forces are not very useful. Reciprocating pumps, though feasible, require rather intricate microfabrication on account of the need for valves and seals, and are more likely than not to produce pulsating rather than steady flows. Since viscous forces tend to be important at small scales, a pump based on viscous action seems to be logical. A viscous-action pump was constructed by Odell and Kovaszny (1971) for the purpose of generating flow without mixing in a stratified fluid. The rather high Reynolds numbers involved are not typical of microscale devices, however, and the device is too complicated for microfabrication. Sen et al. (1996) have suggested a transverse-axis rotary device consisting of a rotating cylinder placed asymmetrically in a channel between two parallel plates. A net flow as high as 10 percent of the surface speed of the rotating cylinder was experimentally observed for Reynolds numbers in the 0.1–10 range. Advantages of the device include its simplicity in construction, the steady flow that is generated, and that it can be powered from outside the duct. The present work numerically addresses the many questions that still remain regarding the performance of the viscous micro-pump in relation to the wide range of geometrical parameters and operating pressure gradients that are possible.

Rotation of an eccentric cylinder between flat plates produces a fairly complicated cellular structure that controls the performance of the device as a pump. Similar flow generated by the

rotation of a cylinder in a closed cavity has been reported by Hellou and Coutanceau (1992). Two pairs of corner vortices were observed for low aspect-ratio containers. These merged to form a pair of larger vortices, one on either side of the cylinder, when the aspect-ratio was increased. Secondary vortices adjacent to the inner ones were also observed at larger container lengths. Similar observations have been made by Kang and Jun (1986) based on Navier-Stokes simulations. It was shown that the vortex size and vorticity increases with an increase in Reynolds number from 1 to 200.

A related problem is that of a cylinder rotating in the vicinity of a plane wall. Kovalenko et al. (1985) have experimentally studied such flows for both rotating and non-rotating cylinders. The distance of the plate from the cylinder was found to have a profound influence on aerodynamic forces. More recently, Liang and Liou (1995) obtained finite-element solutions for low-Reynolds-number flows past a rotating cylinder near an impermeable plane boundary. As expected, the Magnus effect was significantly affected by the presence of the wall.

The viscous pumping mechanism has been shown by Sen et al. (1996) to be feasible for low-Reynolds-number flows. The present work numerically extends the results to parameters that are either difficult, expensive or time-consuming to obtain experimentally. For example, the pressure differences are small and difficult to measure accurately; parameters like the external load and geometry are difficult to vary. In addition the present study will verify the experimental observations and obtain an enhanced understanding of the effects of the vortical structures on the generated flow rates.

It should be mentioned that flow in actual microscale devices may be accompanied by effects such as interfacial forces and slip boundary conditions. For a gas, this comes about when the mean free path of the molecules is no longer a negligibly small fraction of the characteristic length of the flow passage. Beskok and Karniadakis (1994), for example, have studied slip flows in micro-geometries using a CFD approach. More recently, Piekos and Breuer (1995) have performed noncontinuum Monte Carlo analyses of flows in micro-channels and micro-nozzles. There is continuing debate about the nature of such effects for microflows, especially for liquids. With this in mind, the only microscale effect included here is slip at a solid wall using a relation commonly used for gas flows. Most of the results do not consider microscale effects and are hence applicable to the macroscale flows of any viscous fluid.

Contributed by the Fluids Engineering Division for publication in the JOURNAL OF FLUIDS ENGINEERING. Manuscript received by the Fluids Engineering Division May 16, 1996; revised manuscript received January 7, 1997. Associate Technical Editor: S. P. Vanka.

2 Problem Description

Figure 1 shows the geometrical configuration of the problem under investigation. The plate **B** is positioned at a vertical distance $2h$ from the bottom of the tank **A** filled with a viscous fluid. A cylindrical rotor **D** is placed at distances h_U and h_L from the plate **B** and the bottom of the tank, respectively. In the present configuration, fluid flow from left to right in the channel portion is induced by clockwise rotation of the cylinder. We will think of the space within the channel walls, indicated by the dashed line **C**, as the pump portion; the rest will be a load external to the pump.

The following dimensionless parameters

$$s = \frac{h}{a} \quad (1)$$

$$\delta_U = \frac{h_U}{a} \quad (2)$$

$$\delta_L = \frac{h_L}{a} \quad (3)$$

may be defined for the pump section. An eccentricity factor ϵ may be defined as

$$\epsilon = \frac{h_U + a - h}{2a} \quad (4)$$

or

$$\epsilon = \frac{h - a - h_L}{2a} \quad (5)$$

When $\epsilon = 0$, the plates are equally spaced from the rotor. Extreme values of ϵ , i.e., $\pm\epsilon_{\max}$, correspond to the rotor in contact with either of the plates.

There are two kinds of computations that we will consider here, each one for a different purpose:

(a) The first computations will be of the full tank for the purpose of comparing with the experimental results of Sen et al. (1996). For this task the entire fluid region shown in Fig. 1, which will be referred to as the *large-domain*, will be used.

(b) To understand better the performance of the device as a pump, we will run further calculations without the external load. These will be with the region shown in Fig. 1 with the dashed line **C**, subsequently called the *small domain*. The effect of different imposed pressure gradient, cylinder eccentricity and plate spacing, which cannot be easily changed in experiments, will be determined. At the inlet and exit planes, parabolic velocity profiles were specified. This is in accordance both with the large domain calculations performed here and with the experimental observations of Sen et al. (1996): At distances greater than 4 rotor diameters from the rotor the transverse velocity

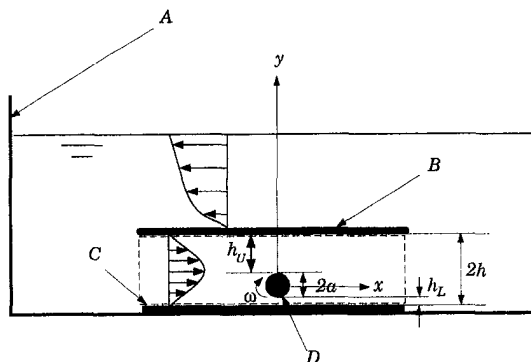


Fig. 1 Schematic of flow configuration

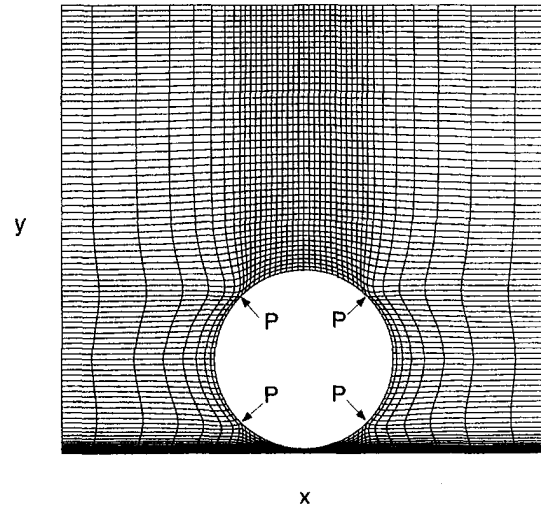


Fig. 2 Grid refinement in vicinity of rotor

profile is parabolic. The value of the bulk velocity across the pump is determined in an iterative fashion, such that the global conservation of both mass and momentum is satisfied.

3 Mathematical Formulation

For micropumping applications, we are interested in low Reynolds numbers for which we do not expect hydrodynamic instabilities and can assume steady flow. The governing equations describing the laminar, incompressible, steady flow of a fluid with constant properties may be expressed in coordinate invariant dimensionless form as

$$\nabla \cdot \mathbf{V} = 0 \quad (6)$$

and

$$\nabla \cdot \left(\mathbf{V}\mathbf{V} - \frac{1}{\text{Re}} \nabla \mathbf{V} \right) + \nabla p = 0 \quad (7)$$

where \mathbf{V} is the dimensionless velocity vector and p is the dimensionless pressure. Here, the velocity and length scales are the rotor surface speed $U = \omega a$ and the cylinder diameter $D = 2a$, respectively. The Reynolds number is defined as $\text{Re} = UD/\nu$, where ν is the kinematic viscosity of the fluid. Pressure is normalized with respect to ρU^2 . We will assume the flow to be two-dimensional since Sen et al. (1996) did not observe significant departures from two-dimensionality in their experiments.

No-slip and no-penetration conditions are assumed to hold for the tangential and normal velocity components at a solid surface, except when slip effects are considered (Section 6.4). For the *large-domain* simulations, a zero-shear condition was applied at the free surface.

The load on the pump section is characterized by a pressure rise. Since this is an externally imposed quantity it is better to nondimensionalize it with respect to a quantity that is not dependent on the pump rotation. So we choose to scale it with $\rho \nu^2 / 4a^2$, instead of ρU^2 , and denote the dimensionless pressure rise by Δp^* . The ratio of these two pressure scales is, of course, Re^{-2} .

Furthermore, the dimensionless bulk velocity in the channel is defined as

$$\bar{u} = \frac{1}{s} \int_0^s u(y) dy \quad (8)$$

where $u(y)$ is the velocity profile at any section. The flow rate is then

$$Q = \bar{u}s \quad (9)$$

3.1 Nonorthogonal Curvilinear Coordinates. Equations (6) and (7) were first transformed to a generalized, nonorthogonal, curvilinear coordinate system. The corresponding equations may be expressed in tensor notation as

$$\frac{\partial}{\partial \xi^i} (C_i V^i) = 0 \quad (10)$$

and

$$\frac{\partial}{\partial \xi^i} (C_i V^i \mathbf{V}) = -J \mathbf{g}^i \frac{\partial p}{\partial \xi^i} + \frac{1}{\text{Re}} \frac{\partial}{\partial \xi^i} \left(D^i \frac{\partial \mathbf{V}}{\partial \xi^i} \right) \quad (11)$$

where we have used the summation convention. The metric terms associated with the convective and diffusive fluxes are given by

$$C_i = \frac{J}{|\mathbf{g}_i|} \quad (12)$$

$$D^i = J(\mathbf{g}^i \cdot \mathbf{g}^j) \quad (13)$$

The nonphysical covariant and contravariant base vectors may be expanded in terms of a Cartesian basis as

$$\mathbf{g}_i = \frac{\partial \mathbf{r}}{\partial \xi^i} = \frac{\partial x_j}{\partial \xi^i} \mathbf{i}_j \quad (14)$$

$$\mathbf{g}^i = \nabla \xi^i = \frac{\partial \xi^i}{\partial x_j} \mathbf{i}_j \quad (15)$$

where the identity

$$\mathbf{g}_i \cdot \mathbf{g}^j = \frac{\partial x_k}{\partial \xi^i} \frac{\partial \xi^j}{\partial x_k} (\mathbf{i}_k \cdot \mathbf{i}_k) = \delta_i^j \quad (16)$$

holds.

The Jacobian J is defined as

$$J = (\mathbf{g}_1 \times \mathbf{g}_2) \cdot \mathbf{n}_p \quad (17)$$

where \mathbf{n}_p is the spatially invariant unit normal vector to the plane in which \mathbf{g}_1 and \mathbf{g}_2 are constrained to lie. The physical contravariant velocity components V^i are obtained by expanding the velocity vector \mathbf{V} in the unit covariant basis \mathbf{e}_i as

$$\mathbf{V} = V^i \mathbf{e}_i \quad (18)$$

where

$$\mathbf{e}_i = \frac{1}{|\mathbf{g}_i|} \mathbf{g}_i \quad (19)$$

There is no summation over i in the last equation.

3.2 Computational Method. Elliptically generated grids were used to discretize the computational domain, following the approaches of Thompson et al. (1982) and Middlecoff and Thomas (1979). The former was used to attract grid lines to specific points and lines in the computational domain, and the latter to achieve near-orthogonality on the domain boundaries and to ensure that the distribution of interior grid points follows the boundary grid-point distribution.

The vector form of the momentum Eq. (11) is first integrated over a control volume, following which it is projected on the

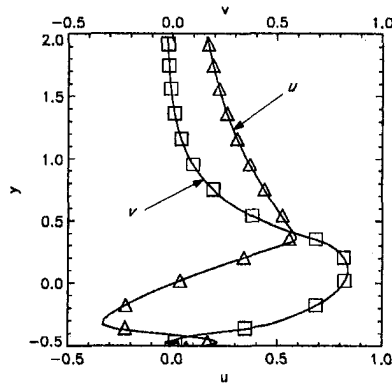


Fig. 3(a)

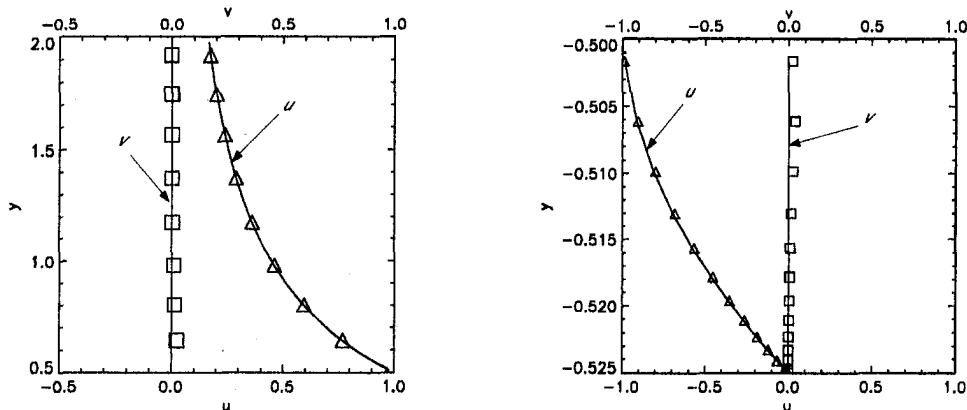


Fig. 3(b)

Fig. 3 Computed and exact velocity profiles for the Wannier problem using a 60×74 Grid. Lines: exact solution; points: computation. (a) $x = -0.6$; (b) $x = 0$.

covariant base vector directions to yield the individual scalar discretized equations in terms of contravariant components. This procedure maintains the strongly conservative form of the governing equations even after the discretization process. While the power-law scheme of Patankar (1979) was formally used to guarantee positive coefficients in the discretized equations, this scheme essentially reverts to central-differencing in the present computations due to the low cell Reynolds numbers involved, thereby minimizing the possibility of false-diffusion. Following the approach of Chen and Patel (1989), pressure-velocity coupling was achieved by means of a modified PISO-SIMPLER type of algorithm on nonstaggered grids. The ensuing system of linearized algebraic equations was solved using a line-by-line tri-diagonal matrix algorithm with under-relaxation of the momentum equations.

The value of the bulk velocity associated with the parabolic velocity profiles specified at the pump inlet and exit, is determined such that it is consistent with the value of the externally imposed pressure gradient. This necessitates an iterative procedure based on an initial guess for the bulk velocity, which is then incremented/decremented accordingly until the computed pressure rise across the pump corresponds to the specified one. Convergence was said to be achieved when the sums of the absolute values of mass and momentum residuals, normalized by the largest terms in the respective equations, dropped below 10^{-4} . Additional details of the computational methodology used may be found in Sharatchandra (1995) and Sharatchandra and Rhode (1994).

3.3 Linear Flow Rate-Pressure Drop Relation. A pump is often characterized by its flow rate Q to pressure drop Δp^* relation. We can show that, for Stokes flow, this relation is linear. Let a flow with zero pressure drop Δp^* be denoted by the superscript 1, and another with zero flow rate Q by 2. Both are for the same pump geometry and rotation rate. We will denote the pump inlet and exit sections by subscripts i and e , respectively.

For the zero pressure drop case we can write $p_1^i(y) = 0$, $p_1^e(y) = 0$, $u_1^i(y) = U_0 f_i(y)$, and $u_1^e(y) = U_0 f_e(y)$, where $(1/s) \int_0^s f_i(y) dy = (1/s) \int_0^s f_e(y) dy = 1$, so that U_0 is the bulk velocity. Also, for the zero flow rate case we have $p_2^i(y) = 0$, $p_2^e(y) = \Delta p_0^*$, $u_2^i(y) = g_i(y)$, and $u_2^e(y) = g_e(y)$, where $(1/s) \int_0^s g_i(y) dy = (1/s) \int_0^s g_e(y) dy = 0$.

Each of these two problems can be solved and the velocity and pressure fields determined. Due to the linearity of the Stokes equations, the velocity and pressure fields corresponding to some intermediate condition between cases 1 and 2 above may be expressed as a linear combination of the two limits. The

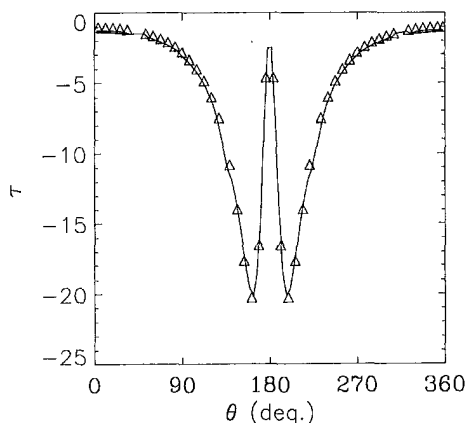


Fig. 4 Shear stress distribution around the rotor for Wannier problem. Line: exact solution; points: computation.

Table 1 Computed values of C_M and L_1 errors. Exact: $C_M = 34.92$.

Grid	C_M	Δ (%)	E_u	E_v
48×58	34.59	0.982	0.0027	0.0015
60×74	34.47	1.301	0.0016	0.0011
72×83	34.73	0.573	0.0013	0.0008
90×93	34.74	0.532	0.0010	0.0007

bulk velocity and pressure rise across the pump may be written generally as

$$\bar{u} = \alpha \bar{u}^1 + (1 - \alpha) \bar{u}^2 \quad (20)$$

$$\Delta p^* = \alpha (\Delta p^*)^1 + (1 - \alpha) (\Delta p^*)^2 \quad (21)$$

Since $\bar{u}^1 = U_0$, $\bar{u}^2 = 0$, $(\Delta p^*)^1 = 0$, and $(\Delta p^*)^2 = \Delta p_0^*$, we can eliminate α to get

$$\frac{\bar{u}}{U_0} = 1 - \frac{\Delta p^*}{\Delta p_0^*} \quad (22)$$

which corresponds to a straight line graph in either $(\bar{u}, \Delta p^*)$ or $(Q, \Delta p^*)$ coordinates.

3.4 Slip Effects. Analysis of rarefied gasdynamics for modest values of the Knudsen number suggests that the continuum hypothesis exemplified by the Navier-Stokes equations is still valid, provided compressibility and slip effects are included (see, for example, the book by Shaaf and Chambré, 1961, and the review article by Muntz, 1989). This model has recently been used by Beskok and Karniadakis (1994) for microscale gas flows. Since slip at the cylinder wall may affect the viscous action which drives the pump, we include a brief look at the effect of slip at fluid-solid interfaces. An expression for the slip velocity tangential to a solid surface was first derived by Maxwell (1879). In the absence of a temperature gradient along the surface, the dimensionless slip velocity is given by (Schaaf and Chambré, 1961)

$$U_{\text{slip}} = U_{\text{surf}} + \frac{2 - \sigma_v}{\sigma_v} \text{Kn} \frac{\partial U}{\partial n} \quad (23)$$

where $\partial U / \partial n$ is the normal derivative of the tangential velocity computed at the wall, and σ_v is a tangential-momentum accommodation coefficient that is unity for diffuse reflection of the gas molecules from a rough solid surface and zero for specular reflection from a perfectly smooth surface. In the context of the present study, U_{surf} is the tangential velocity of the rotor and the Knudsen number Kn is defined as the ratio of the mean free path of the gas molecules to the diameter of the rotor. At the channel walls Eq. (23) is also applicable, with U_{surf} being zero.

Under carefully controlled laboratory conditions, values of σ_v as low as 0.2 have been achieved, as noted by Lord (1976). It is generally accepted that Navier-Stokes analysis using Eq. (23) at the boundaries is valid for values of $\text{Kn} \leq 0.1$. For the present purpose, we regard the term $[(2 - \sigma_v) / \sigma_v] \text{Kn}$ as a composite slip factor whose value ranges from 0 to 1, thereby covering a range of practical interest.

4 Validation of Computational Procedure

The numerical procedure will be validated by comparing with related results published in the literature.

4.1 Wannier Solution. For very low Reynolds numbers corresponding to creeping or Stokes flow, Wannier (1950) has presented an exact solution for the flow between eccentric rotating cylinders. In the limit of the outer cylinder radius tending

¹ At the molecular scale.

Table 2 Computed values of drag, lift and moment coefficients for $Re_\infty = 20$

Grid	$C_D (\alpha = 0.1)$	$C_L (\alpha = 0.1)$	$C_M (\alpha = 0.5)$
90×30	1.992	0.269	1.504
120×40	1.985	0.266	1.517
Badr et al. (1989)	1.991	0.267	1.532

to infinity, the problem is geometrically identical to that of flow past a rotating cylinder in the proximity of a (possibly moving) flat plate. If the plate is stationary, the expressions for the velocity components may be written in terms of d , the distance of the center of the rotating cylinder of radius a from the flat plate.

This problem was solved numerically on the elliptically generated 60×74 grid shown in Fig. 2. In order to simulate conditions compatible with the present problem, we have taken $d = 1.05a$. The proximity of the rotor to the lower plate ensuing from this value of d provides for a stringent test of the numerical method due to the regions of intense shearing stress between the rotor and the plate. The point-attraction scheme of Thompson et al. (1982) was used to refine the grid in the vicinity of the points marked P in Fig. 2. The exact solution was imposed on the domain boundaries, and the solutions were obtained for $Re = 0.5$, so as to stay within the Stokes limit.

Figure 3 compares the exact and computed velocity profiles at various x locations. In Fig. 3(a), the velocity profiles upstream of the cylinder are shown, while in Fig. 3(b) the profiles directly above and below the cylinder are presented. The agreement is good, even in the region between the rotor and the plate where the most intense velocity gradients occur, as indicated in the lower right panel of Fig. 3.

As a more rigorous check of the accuracy and reliability of the numerical method, we compare the computed shear stress distribution at the surface of the cylinder with the corresponding exact solution. The comparison, shown in Fig. 4, is also good. Here, the angle θ is measured clockwise starting from the top of the cylinder. The small discrepancies in the region between the plate and the rotor were seen to diminish with minor grid refinement.

Finally, the effect of grid refinement on the computed moment coefficients defined by

$$C_M = \int_0^{2\pi} \tau d\theta \quad (24)$$

is shown in Table 1. Also shown are the percentage difference Δ , and the L_1 errors in the computed u and v components, E_u and E_v , respectively, all with respect to the exact solution. Based on these results we consider grid independence to be achieved on the 72×83 grid.

4.2 Flow Past a Rotating Cylinder. As a further validation of the method, we also consider uniform flow past a rotating cylinder. This problem has been studied by Badr et al. (1989) and by Ingham (1983), who used vorticity-streamfunction formulations in polar coordinates. The problem is solved here on a grid like the one depicted in Fig. 2. The governing parameters are the Reynolds number, $Re_\infty = U_\infty D/\nu$, and the rotation rate, $\alpha = \omega D/2U_\infty$. Here, U_∞ , D and ω are the freestream velocity,

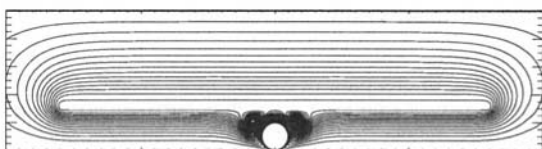


Fig. 5 Streamlines based on large-domain simulations for $s = 1.5$ and $Re = 0.5$

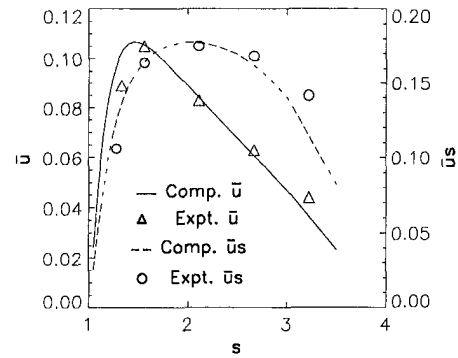


Fig. 6 Variation of bulk velocity and flow rate with s , for $\epsilon \approx \epsilon_{max}$ and $Re = 0.5$

cylinder diameter and angular velocity of the rotating cylinder, respectively.

The effect of grid refinement on the computed values of lift and drag coefficients, C_L and C_D , and the moment coefficient C_M is shown in Table 2. The values of Badr et al. (1989) are also shown, but not those of Ingham (1983) which are questionable on account of sign errors in his expressions for the coefficients. The agreement between the present computations and published results is excellent.

5 Large-Domain Computations and Comparison With Experiments

Results of computations using what we have called the large-domain can be compared to those of the experiments of Sen et al. (1996). Figures 5–8 are for this case. Here the cylinder is placed at a distance of 0.05 rotor radii from the wall which essentially corresponds to the case of maximum eccentricity. Henceforth in this study, the condition $\epsilon \approx \epsilon_{max}$ refers to the aforementioned spacing of the cylinder from the lower wall. The Reynolds number is 0.5. In comparing experimental and numerical results, it should be noted that Sen et al. (1996) defined a Reynolds number with an additional factor of two. Thus their $Re = 1$ corresponds to $Re = 0.5$ in the present study.

The computed streamlines are depicted in Fig. 5, corresponding to a value of $s = 1.5$. For ease of presentation, only a portion of the entire domain is shown. Two symmetric co-rotating vortices exist above the rotor, consistent with experimental observations. The computed pressure rises across the pump for various values of s were found to be of the order of $\Delta p^* = 0.5$, which in terms of physical quantities, corresponds to a pressure rise

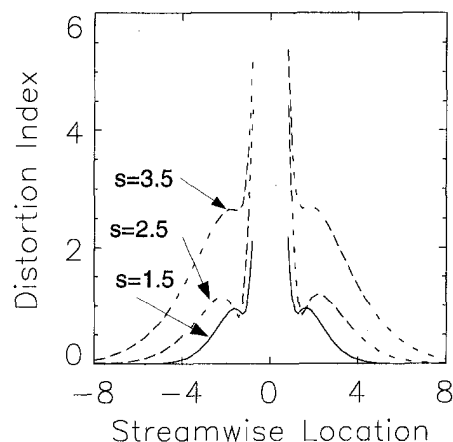


Fig. 7 Deviation from parabolic velocity profile for various s , with $Re = 0.5$

of less than 1 mm of water. Such a small pressure difference was obviously difficult to measure in the experiments of Sen et al. (1996).

The effect of plate spacing on the computed and experimental bulk velocities and flow rates is shown in Fig. 6. The agreement between the computations and the experiments is remarkable. Of course the very low Re, steady, laminar flow under consideration does not involve the complications associated with computations of flows in the transition and turbulent regimes. The experiments, though unsophisticated, also appear to have given good results.

A measure of the deviation from a parabolic velocity profile associated with fully-developed flows is a *distortion index*

$$I_d(x) = \left[\frac{1}{N} \sum_{i=1}^N \{ u_i(x) - \tilde{u}_i \}^2 \right]^{1/2} \quad (25)$$

where \tilde{u}_i is the velocity corresponding to a parabolic profile at the i th node in the y direction; N is the total number of nodes in the y direction. Figure 7 shows the variation of I_d along the length of the channel for three different values of s . It is seen that as s increases, the distortion is spread out; the profiles remain parabolic only very close to the inlet and exit. The distance at which I_d decays to zero is directly proportional to s . In fact, if I_d were plotted against x/s , all three curves would decay to zero at the same x/s location. Clearly, the influence of the larger vortical structures associated with larger plate spacing, as shown in Fig. 8, tends to detract from the parabolic nature of the profiles, even at distances greater than 3 diameters from the rotor. Also noteworthy in Fig. 7 is the symmetry about

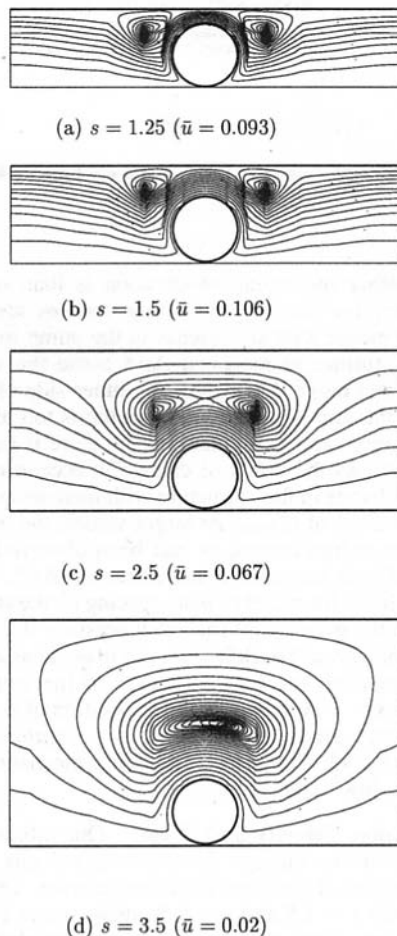


Fig. 8 Streamlines based on large domain simulations for $Re = 0.5$ and $\epsilon \approx \epsilon_{max}$, as a function of plate spacing

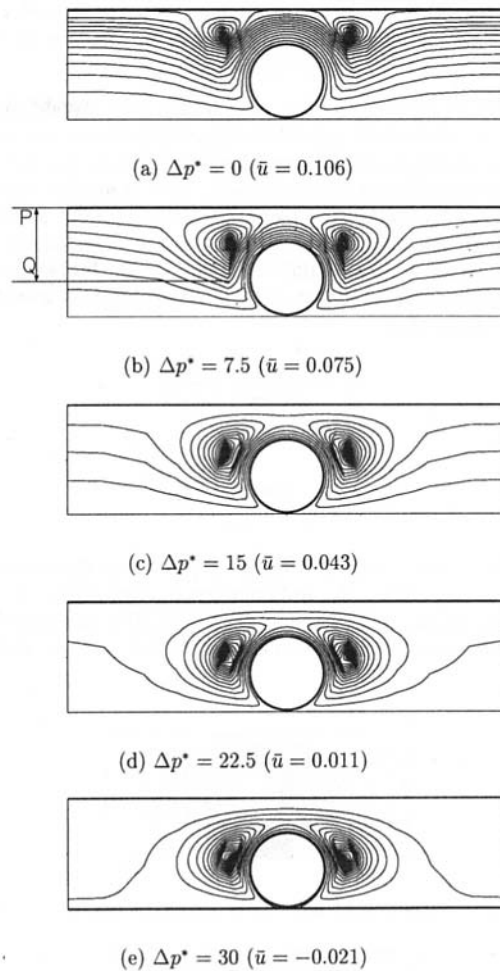


Fig. 9 Streamlines for $Re = 1$, $\epsilon \approx \epsilon_{max}$ and $s = 1.5$, as a function of pump load

$x = 0$, due to the very low Reynolds number for which the flow is essentially in the Stokes regime.

The computed streamlines for various experimental values of s in Fig. 6 are shown in Fig. 8(a)–(d). For a very small spacing, as in Fig. 8(a), the vortices are “squeezed” downward on either side of the rotor and thus have the effect of clogging the flow path across the pump. As s increases, the two vortices on either side gradually tend to merge. The maximum observed flow rate is seen to occur when the tendency to merge is initiated by the appearance of an outer enveloping vortex, surrounding the two inner co-rotating ones.

The computed streamlines are in remarkably good qualitative agreement with the experimental visualizations of Sen et al. (1996). The merging together of the two vortices was observed at more or less the same value of the plate spacing ($s \approx 2$), in both computations and experiments. In addition, the experiments also confirmed the numerical observation that the maximum flowrate was associated with the onset of vortex merging.

6 Small-Domain Computations

We have defined the pump section to be the small domain shown by dashed lines in Fig. 1. This is the section that really drives the flow. It may be connected to any external load or return path, such as the one shown, or any other. We will now study the characteristics of the pump using the small-domain computations and the rest of the figures refer to this case. A parametric study is performed by changing the plate spacing s , eccentricity ϵ , and imposed pressure gradient Δp^* in turn while

keeping the other parameters constant. It must be understood that, because of the nondimensionalization, changes in s or ϵ can entail changes in a combination of a , h , and h_U .

6.1 Flow Patterns. The streamlines give a good qualitative picture of the flow pattern which ultimately determines the operation of the pump. Figure 9(a)–(e) shows the flow patterns corresponding to different loads Δp^* . Note that a positive value of Δp^* implies an adverse pressure gradient across the pump. As in the case of Fig. 8, larger vortex sizes tend to yield smaller flow rates. A quantitative measure of the blockage effect caused by the vortices may be determined in terms of a blockage factor F_b defined as

$$F_b = \frac{\text{vortex size}}{\text{channel height}} \quad (26)$$

or

$$F_b = \frac{\text{distance } PQ}{2h} \quad (27)$$

where PQ is the distance from the top plate to the lowermost point in the trajectory of a fluid particle moving along the separation streamline, as depicted in Fig. 9(b). The blockage factor is seen to consistently rise with increasing adverse pressure

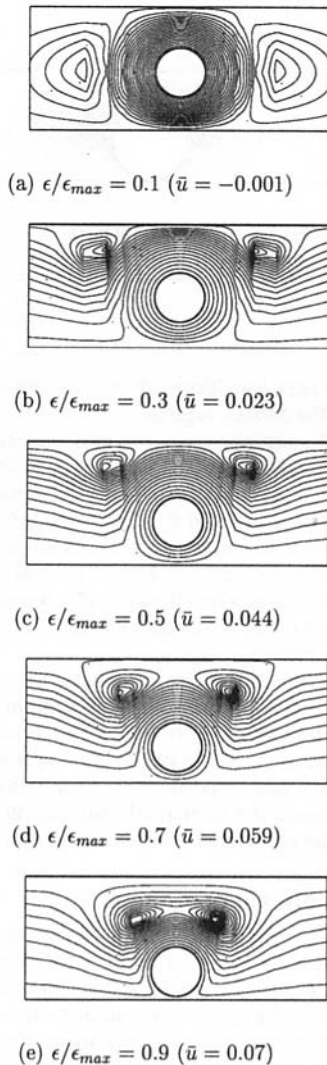


Fig. 10 Streamlines for $Re = 1$, $\Delta p^* = 1$ and $s = 2.5$, as a function of eccentricity. Note: $\epsilon_{max} = 0.75$.

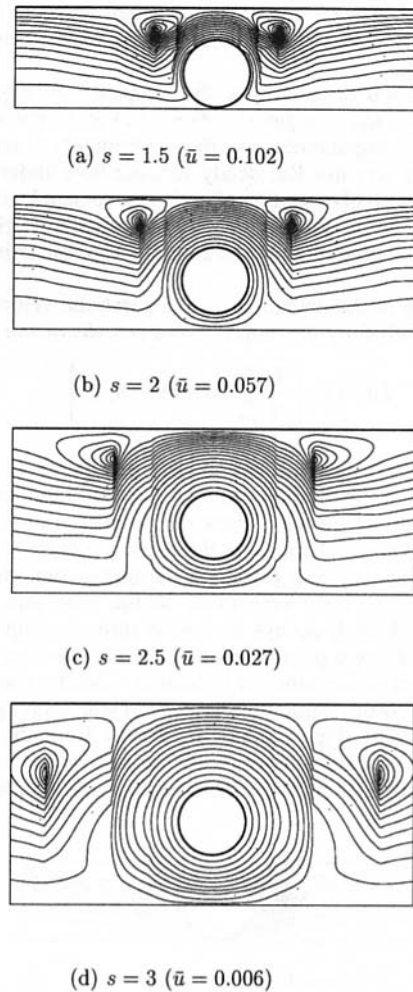


Fig. 11 Streamlines for $Re = 1$, $\Delta p^* = 1$ and $\epsilon = 0.25$, as a function of plate spacing

gradient. Another interesting observation is that, despite the initial tendency for the two co-rotating vortices seen in Figs. 9(a)–(b) to merge with an increase in the pump load as seen in Fig. 9(c), further increases in Δp^* cause the vortices to detach again and move downwards on either side of the rotor. In Fig. 9(e), the imposed load on the pump is too high for the rotor to overcome, and as a consequence, there is backflow.

Figure 10 shows the effect of change in eccentricity. There is a dramatic change in flow structure with increasing eccentricity for small values of ϵ/ϵ_{max} . At larger values, the tendency of the vortices to merge occurs, as had been observed earlier in the context of both increased s and increased Δp^* .

Figure 11 shows the effect of plate spacing on the streamlines. Again, due to the presence of the small pressure rise across the rotor, a tendency toward backflow is seen to occur as s increases. To keep ϵ constant, the rotor is closer to the center of the channel when $s = 3$. Apparently, the imposition of even a small nonzero pressure gradient can result in a negative flow rate for values of $s > 3$. The viscous pumping mechanism is thus ineffective for low values of ϵ/ϵ_{max} .

6.2 Pressure, Velocity and Shear. Quantification of the flow patterns will be through the pressure, velocity and shear fields that are part of the numerical computation. The pressure distributions for $s = 1.5$ and $s = 2.5$ are shown in Fig. 12, for three y locations: at the top plate, at the bottom plate, and at a horizontal plane passing through the rotor centerline. It is seen in both the large and small plate separations that the pressure

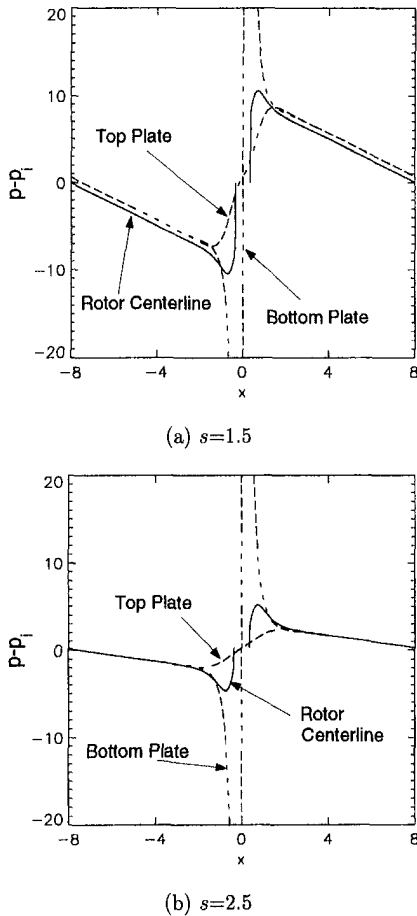


Fig. 12 Streamwise pressure distributions for $Re = 1$. (Note: $\epsilon \approx \epsilon_{max}$ for both cases.)

variation at the bottom wall is the steepest because of the proximity to the rotating cylinder. Due to the scale of the graph, the pressure rise from inlet to exit is imperceptible. Beyond one cylinder diameter from the rotor the pressure gradient is linear. The pressure profiles also display a near invariance with transverse position in these regions which suggests that the velocity profiles therein should be parabolic. Steep gradients are observed at both the "suction" and "pressure" sides of the rotor. The observed front-to-back anti-symmetry is due to the linearity of Stokes flow.

The bulk velocity is one of the most important parameters of the system since it quantifies the pumping effect. Figure 13

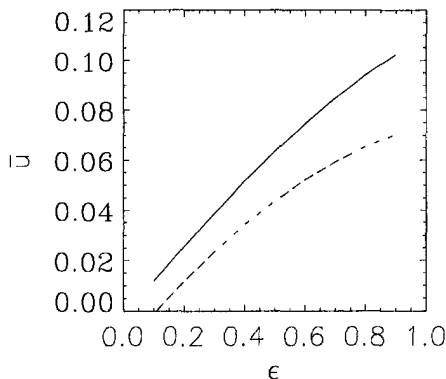


Fig. 13 Effect of eccentricity on \bar{u} for $\Delta p^* = 1$ and $Re = 1$. Solid line: $s = 1.5$; dashed line: $s = 2.5$.

shows the effect of the rotor eccentricity on this velocity. Not surprisingly, the bulk velocity increases with ϵ/ϵ_{max} . In the absence of an imposed Δp^* , both curves would have passed through the origin. A nonzero value of Δp^* was imposed so as to evaluate non-zero values of the performance index η to be defined further on. The effect of plate spacing is more pronounced at higher values of ϵ , because the ratio of the areas above and below the rotor increases as the rotor approaches the lower plate.

The effect on \bar{u} of s by keeping ϵ fixed is shown in Fig. 14. The position of the rotor from both top and bottom plates increases with s , so as to maintain a fixed amount of displacement from the centerline. As a consequence, a monotonic decrease in \bar{u} with s is observed. It should be noted that even though ϵ is held fixed, the ratio ϵ/ϵ_{max} decreases with increased plate spacing, thereby negating the advantage associated with unequal flow areas above and below the rotor.

The entire parameter space of s and ϵ was probed to yield surface plots of $\bar{u}(s, \epsilon)$ as shown in Fig. 15. The peaks in \bar{u} observed for $\epsilon = \epsilon_{max}$ are seen to become less pronounced as the rotor moves closer to the center of the channel. The figure only serves to re-emphasize the point that, though the torques are higher, the maximum flow rate is obtained when the rotor is in contact with the lower plate.

The torque on the rotor is related to the shear stress on the surface of the cylinder. The angular distribution of the latter quantity is shown in Fig. 16. The angle θ is measured clockwise starting from the top of the rotor. Again, the fore-aft symmetry of the distribution is due to the linearity of the Stokes equations. The similarity of the curves in Fig. 16 to that in Fig. 4 is also noteworthy, indicating that the presence of the upper plate does not significantly affect the structure of the flow in the vicinity of the rotor. It is seen, however, that the spacing of the upper plate has a slight influence on the shear stress distribution on the upper surface of the rotor. The presence of the single counterclockwise vortex above the rotor observed for $s = 2.5$ in Fig. 8(c), causes lower velocity gradients directly above the rotor and consequently the lower magnitudes of shear stresses therein, as seen in Fig. 16.

6.3 Pump Performance. We now turn our attention to the overall performance of the device as a pump. A pump may be characterized by its flow rate Q versus Δp^* curve. Figure 17 shows this for $s = 1.5$ and $s = 2.5$. Only for very small values of Δp^* does the pump corresponding to $s = 2.5$ deliver a greater flow rate than the one corresponding to $s = 1.5$. The straight-line behavior of the characteristic curve is to be expected from the analysis in Section 3.3. The values of U_0 and Δp_0^* in Eq. (22) are the intercepts of the pump characteristics with the coordinate axes. The line can be extended both ways to infinity. Thus, pressure differences larger than Δp_0^* will produce a backflow.

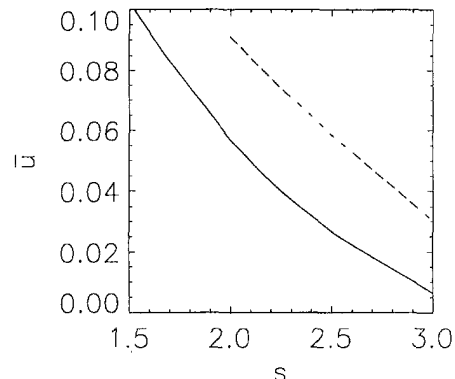


Fig. 14 Effect of plate spacing on \bar{u} for $\epsilon = 0.25$ (solid line) and $\epsilon = 0.5$ (dashed line), for $\Delta p^* = 1$ and $Re = 1$.

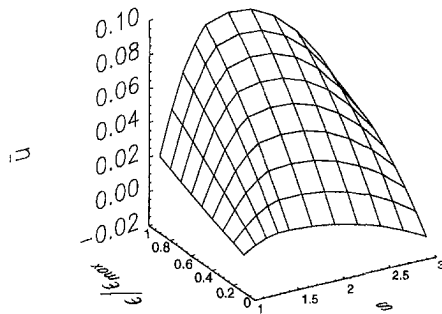


Fig. 15 Surface plot of u versus s and ϵ/ϵ_{\max} , for $\Delta p^* = 1$ and $Re = 1$

The actual operation of a pump is determined by both pump and load characteristics. The latter is the $Q - \Delta p^*$ relation for the load. For the small flow rates under discussion here, we can expect that Q will be proportional to Δp^* . Figure 17 also shows some sample load characteristics as dotted lines, a higher slope indicating a lower resistance to flow. The intersections of the pump and load characteristics yield the operating points. The operating points are stable: if the load resistance were to go up slightly, the pump would supply a larger pressure at a lower flow rate to compensate.

A measure of the pumping efficiency, η , is the ratio of the useful flow power produced to the input energy to the pump. An energy balance shows this performance index to be

$$\eta = \frac{s\bar{u}\Delta p^*}{Re^2 C_M} \quad (28)$$

where C_M is the rotor moment coefficient. Figure 18 shows the variation of η with Δp^* . It is apparent from the figure that the pump corresponding to $s = 1.5$ yields a far superior performance than that corresponding to $s = 2.5$ over a wide range of values of Δp^* . It is relevant to note that C_M is only a weak function of Δp^* for fixed values of s and ϵ . This is because, close to the rotor surface, the flow structure is dictated by the shearing action of the rotating cylinder, rather than the externally imposed pressure gradient; consequently, the shear stress distribution is more or less the same for all values of Δp^* . Since C_M is almost a constant, substitution of Eq. (22) in Eq. (28) shows that the η vs. Δp^* curve should be almost parabolic, which it is. The most efficient pump performance is thus obtained for $\Delta p^* = \Delta p_0^*/2$. The generally low values of η are due to the very high rates of viscous dissipation associated with viscous pumping; a major portion of the shear work imparted to the fluid by the rotor is dissipated as heat.

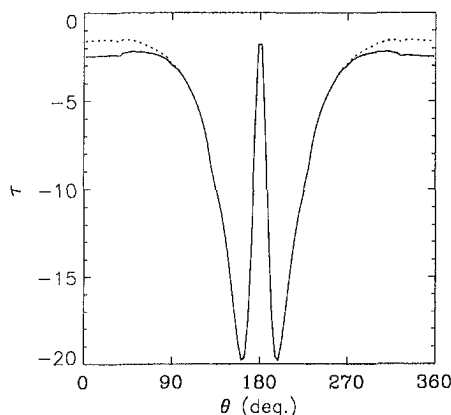


Fig. 16 Shear stress distributions around the rotor surface for $Re = 1$. Solid line: $s = 1.5$; dotted line: $s = 2.5$. [$\epsilon \approx \epsilon_{\max}$ for both cases.]

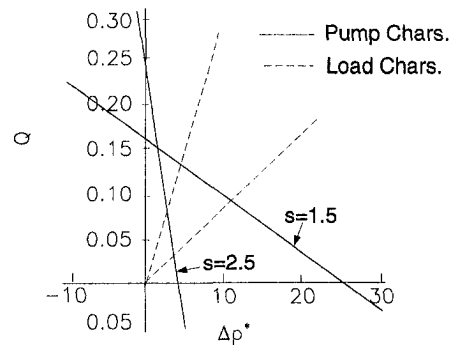


Fig. 17 Pump and load characteristics corresponding to $\epsilon = \epsilon_{\max}$ and $Re = 1$

6.4 Inertial and Slip Effects. Finally, we take up the issue of situations in which the pump may be operating under circumstances different from that described so far. There are two kinds of effects that are important: inertial effects for larger Reynolds numbers, and slip effects for appreciable Knudsen numbers.

The effect of varying the flow Reynolds number Re is shown in Fig. 19. Here, in order to study inertial effects in isolation, the externally imposed pressure gradient is set to zero. It is seen that the ratio of bulk velocity to rotor surface speed starts to decrease significantly only for $Re \geq 100$. What is interesting is that even for $Re \approx 100$, which is well beyond the range of typical micropumps, effective pumping is obtained. This suggests that the current proposed pumping mechanism has potential applications beyond those associated with microscale devices.

Figure 20 shows the streamlines for different values of Re . As Re increases, the symmetry associated with the low inertial forces of Stokes flow gradually disappears and the vortex on the suction side completely disappears at $Re = 50$ as seen in Fig. 20(c). It is quite possible that the flow in the last two panels of Fig. 20 is unstable. As the primary focus of this investigation is the low Re phenomena associated with microscale flows, stability aspects of transitional flows are not considered.

Finally, Fig. 21 shows the effect of introducing slip near the solid boundaries. The flow rate is plotted against the parameter $[(2 - \sigma_v)/\sigma_v] Kn$ so as to cover the spread of values of reflectivity and molecular mean-free-paths associated with various gas-surface combinations. The reduced traction at the rotor surface is apparently a more dominant factor than the reduced drag at the plate. This is because the magnitude of the slip velocity at a surface is directly proportional to the magnitude of the shear

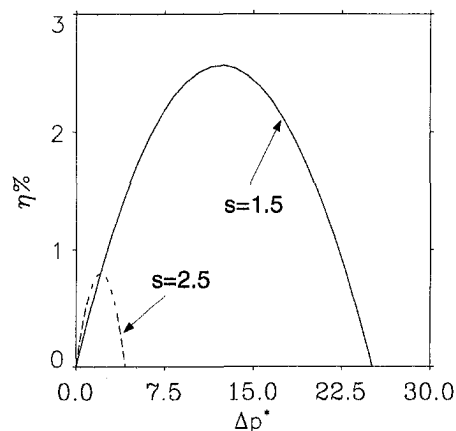


Fig. 18 Variation of performance index with load for $Re = 1$

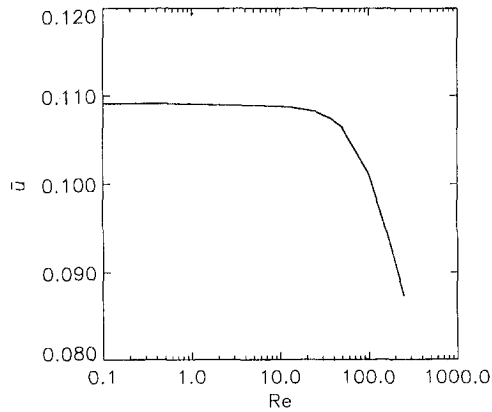


Fig. 19 Variation of \bar{u} with Re for $s = 1.5$, $\Delta p^* = 0$ and $\epsilon \approx \epsilon_{\max}$

stress at that surface. Clearly, far steeper gradients exist in the vicinity of the rotor than in regions adjacent to the upper and lower plates of the channel. Given that most practical applications are more likely than not to involve diffuse ($\sigma_v = 1$) rather than specular ($\sigma_v = 0$) reflection, it may be inferred from the figure, that slip effects are significant only for $Kn > 0.1$. While the results of Fig. 21 are consistent with the physics of the problem under investigation, further study of the mechanism of slip, especially for liquids, is required for a deeper understanding of microscale flows.

7 Conclusions

A full Navier-Stokes simulation of a novel rotary micropump has been carried out. The computations are validated using an exact solution for Stokes flow around a rotating cylinder in the vicinity of a flat plate and other numerical results. Large-domain simulations are made to compare computations with the experiments of Sen et al. (1996), and the agreement is excellent. Pump behavior is studied using small-domain calculations. The effects of varying the plate spacing s and the rotor eccentricity ϵ are probed in detail. The existence of an optimum plate spac-

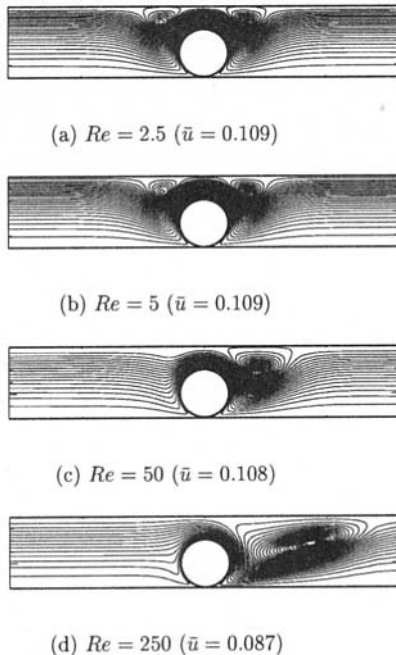


Fig. 20 Streamlines for $s = 1.5$, $\Delta p^* = 0$ and $\epsilon \approx \epsilon_{\max}$, as a function of Reynolds number

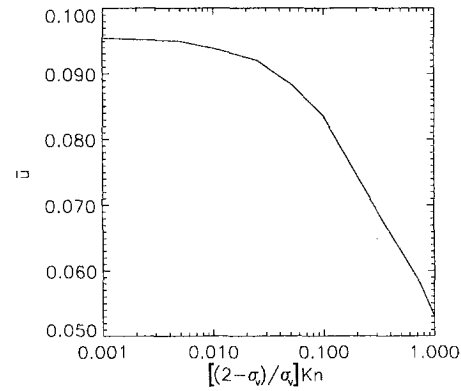


Fig. 21 Slip-flow effects for $s = 2.5$, $\Delta p^* = 0$, $Re = 1$ and $\epsilon \approx \epsilon_{\max}$

ing is demonstrated, and it is shown that the induced flow rate increases monotonically with eccentricity, the maximum being achieved when the rotor is in contact with a channel wall. The changes in vortical structure with plate spacing are shown to affect the induced flow rates; this is explained as a blockage effect in which larger ratios of vortex size to plate spacing are seen to inhibit the flow. The pump characteristics are shown to be a straight line and the superposition of load characteristics yields operating points that are stable. While the induced flow rate does indeed decrease at larger Reynolds numbers, this decrease is not drastic; this is important from the point of view of applications other than micropumps, for example hauling highly viscous liquids in macroducts. Slip effects are studied for gas flows and it is shown that these effects, which tend to reduce the induced flow rate, are significant only for Knudsen numbers greater than 0.1. It should be emphasized that while we have used a specific mathematical model to take into account slip-flow effects, the issue is still an open one especially if liquids are considered.

It is evident that the proposed micropumping device is promising from the point of view of microscopic as well as small-scale macroscopic applications. Its use, particularly in the context of the former application, will be explored in greater detail in the future.

Acknowledgments

This study was performed under a grant from the National Science Foundation, under the Small Grants for Exploratory Research initiative (SGER Grant No. CTS-95-21612). The technical monitors are Dr. Robert Powell and Dr. Roger E. A. Arndt. The authors are grateful to Prof. George Em Karniadakis for bringing the Wannier solution to our attention.

Different versions of this research have been presented at the ASME Symposium on the Application of Microfabrication to Fluid Mechanics, 17–22 November 1996, Atlanta, Georgia, and at the American Physical Society Division of Fluid Dynamics Meeting, 24–26 November 1996, Syracuse, New York.

References

- Angell, J. B., Terry, S. C., and Barth, P. W., 1983, "Silicon Micromechanical Devices," *Scientific American*, Vol. 248, Apr., pp. 44–55.
- Badr, H. M., Dennis, S. C. R., and Young, P. J. S., 1989, "Steady and Unsteady Flow Past a Rotating Cylinder at Low Reynolds Numbers," *Computers and Fluids*, Vol. 17, pp. 579–609.
- Beskok, A., and Karniadakis, G. E., 1994, "Simulation of Heat and Momentum Transfer in Complex Micro-Geometries," *AIAA Journal of Thermophysics and Heat Transfer*, Vol. 8, No. 4, pp. 355–370.
- Chen, H. C., and Patel, V. C., 1989, "The Flow Around Wing-Body Junctions," *Proceedings of the Fourth Symposium on Numerical and Physical Aspects of Aerodynamic Flows*, T. Cebeci, ed., Long Beach, CA, 16–19 Jan.
- Gabriel, K. J., 1995, "Engineering Microscopic Machines," *Scientific American*, Vol. 273, Sept., pp. 150–153.

- Hellou, M., and Coutanceau, M., 1992, "Cellular Stokes Flow Induced by Rotation of a Cylinder in a Closed Channel," *Journal of Fluid Mechanics*, Vol. 236, pp. 557–577.
- Ingham, D. B., 1983, "Steady Flow Past a Rotating Cylinder," *Computers and Fluids*, Vol. 11, pp. 351–386.
- Kang, C. S., and Jun, C. H., 1986, "Steady Flow Induced by a Rotating Cylinder in a Rectangular Tank," *First Triennial International Symposium on Fluid Control and Measurement*, pp. 657–662, Pergamon Press, New York.
- Kovalenko, V. M., Bychkov, N. M., Kisel, G. A., and Dikovskaya, N. D., 1985, "Flow Over Rotating and Nonrotating Circular Cylinders Situated Over a Flat Plate. Part I: Flow Over Rotating Cylinders," *Fluid Mechanics, Soviet Research*, Vol. 14, No. 5, pp. 52–69.
- Liang, W. J., and Liou, J. A., 1995, "Flow Around a Rotating Cylinder Near a Plane Boundary," *Journal of the Chinese Institute of Engineers*, Vol. 18, No. 1, pp. 35–50.
- Lord, R. G., 1976, "Tangential Momentum Coefficients of Rare Gases on Polycrystalline Surfaces," *Proceedings of the Tenth International Symposium on Rarefied Gas Dynamics*, L. Potter, ed., AIAA, New York, pp. 531–538.
- Maxwell, J. C., 1879, "On Stresses in Rarefied Gases Arising from Inequalities of Temperature," *Philosophical Transactions of the Royal Society*, Part I, Vol. 170, pp. 231–256.
- Middlecoff, J. F., and Thomas, P. D., 1979, "Direct Control of the Grid Point Distribution in Meshes Generated by Elliptic Equations," AIAA Paper 79-1462.
- Muntz, E. P., 1989, "Rarefied Gas Dynamics," *Annual Review of Fluid Mechanics*, Vol. 21, pp. 387–417.
- Odell, G. M., and Kovaszny, L. S. G., 1971, "A New Type of Water Channel with Density Stratification," *Journal of Fluid Mechanics*, Vol. 50, pp. 535–557.
- Patankar, S. V., 1979, *Numerical Heat Transfer and Fluid Flow*, Hemisphere, Washington, D.C.
- Piekos, E., and Breuer, K. S., 1995, "DSMC Modeling of Micromechanical Devices," AIAA Paper 95-2089.
- Schaaf, S. A., and Chambré, P. L., 1961, *Flow of Rarefied Gases*, Princeton University Press, Princeton, NJ.
- Sen, M., Wajerski, D., and Gad-el-Hak, M., 1996, "A Novel Pump for MEMS Applications," *ASME JOURNAL OF FLUIDS ENGINEERING*, Vol. 118, No. 3, pp. 624–627.
- Sharatchandra, M. C., 1995, "A Strongly Conservative Finite-Volume Formulation for Fluid Flows in Irregular Geometries Using Contravariant Velocity Components," Ph.D thesis, Texas A&M University, College Station, TX.
- Sharatchandra, M. C., and Rhode, D. L., 1994, "A New Strongly Conservative Finite-Volume Formulation for Fluid Flows in Irregular Geometries using Contravariant Velocity Components, Part 1—Theory," *Numerical Heat Transfer, Part B*, Vol. 26, pp. 39–52.
- Thompson, J. F., Warsi, Z. U. A., and Mastin, C. W., 1982, "Boundary-Fitted Coordinate Systems for Numerical Solution of Partial Differential Equations—a Review," *Journal of Computational Physics*, Vol. 47, pp. 1–108.
- Wannier, G. H., 1950, "A Contribution to the Hydrodynamics of Lubrication," *Quarterly of Applied Mathematics*, Vol. 8, pp. 1–18.

LDV Measurements of Spatially Periodic Flows Over a Detached Solid-Rib Array

Tong-Miin Liou
Professor, Fellow ASME

Chih-Ping Yang
Graduate Student.

Hsin-Li Lee
Graduate Student.

Department of Power Mechanical
Engineering,
National Tsing Hua University, Hsinchu,
Taiwan 30043

Measurements of mean velocities, turbulence intensities, and Reynolds stresses are presented for spatially periodic flows in a duct of width-to-height ratio 2 with a detached solid-rib array. The Reynolds number based on the duct hydraulic diameter and cross-sectional bulk mean velocity (U_b), the pitch to rib-height ratio, and the rib-height to duct-height ratio were 2×10^4 , 10, and 0.133, respectively. The rib-detached-distance to rib-height ratio was varied from 0 to 3.25 (duct axis) to study its effect on wake length and asymmetry, convective velocity and turbulent kinetic energy immediately behind the rib, maximum turbulent shear stress, and turbulence anisotropy. The results showed that the dominant fluid dynamic factors responsible for the reported peak values of local Nusselt number around the detached rib could be identified. Moreover, the turbulence structure parameter distribution and anisotropy were analyzed to examine the basic assumptions embedded in the turbulence models. Furthermore, the secondary-flow mean velocities were found to be one to two order of magnitude smaller than U_b .

Introduction

The arrangement of bluff bodies along the length of a passage to periodically disturb the flow is a widely adopted technique for heat transfer augmentation such as in the cooling panels of a ramjet inlet (Chang and Mills, 1993) or heat exchange systems. Previous heat transfer (Liou and Hwang, 1992) and fluid flow (Liou et al., 1993b) studies indicated that for duct flows with solid-type ribs attached on the walls, the heat transfer is locally reduced immediately downstream of the ribs. To remove the local heat transfer reduction in the rib-wall corners of the attached solid ribs, laser holographic interferometry (LHI) measurements in a rectangular duct with repeated solid ribs detached a small distance from one wall have been performed (Liou et al., 1995) and the results showed the elimination of the aforementioned heat transfer reduction around the rib-wall corners. The present paper focuses on the complementary turbulent fluid flow study.

For fluid flow study, a single circular (Bearman and Zdravkovich, 1978; Marumo et al., 1985; Taniguchi and Miyakoshi, 1990), a triangular (Kamemoto et al., 1984), and a square (Duraio et al., 1988 and 1991; Suzuki et al., 1993) cylinder near a plane wall have been extensively investigated. A common conclusion from these studies is the existence of a critical clearance between the detached cylinder and the wall above which vortex shedding occurs. The critical clearance varies with boundary layer thickness and rib's cross-section shapes. It increases nonlinearly with increasing boundary layer thickness (Taniguchi and Miyakoshi, 1990) and has typical values of 0.25–0.30, 0.35, 0.35–0.5, and 0.55 times characteristic lengths of a circular cylinder, triangular cylinder, square cylinder, and two-dimensional normal plate, respectively. The presence of vortex shedding process greatly augments heat transfer from the channel wall.

For multiple detached solid ribs, some relevant previous works are summarized in Table 1 where the ranges of parameters investigated, techniques used, and physical quantities measured are also listed for reference purpose. Oyakawa and Ma-

buchi (1983) performed flow visualization as well as pressure, temperature, and flow oscillation frequency measurements in a duct flow staggeringly disturbed by detached circular ribs. They reported that heat transfer enhancement by detached ribs is related to the existence of the Karman vortex shedding and the shapes of heat transfer distribution are independent of Reynolds number in the range examined. Kawaguchi et al. (1985) investigated the heat transfer augmentation with circular cylinders positioned in a line and attached to or near one wall at various streamwise pitches by measuring the heat transfer coefficient. They found that among the pitch to cylinder diameter ratios tested, the values 12.5 and 25 are appropriate as far as overall heat transfer augmentation is concerned. Oyakawa et al. (1986) studied how the heat transfer augmentation in the fully developed region is influenced by the shape of band plates and clearance of detached turbulence promoters which are set in staggered arrangement in a rectangular duct. The roles of Karman vortex shedding and reattachment were documented in detail. Yao et al. (1987, 1989) made a study similar to that of Oyakawa and Mabuchi (1983) using thermocouple, hot wire, and flow visualization techniques and found that after the first three cylinders, an almost periodic fully developed state was attained thermally and hydrodynamically. They also stated that heat transfer enhancement downstream of the cylinders could be due to the effect of intermittent reattachment of discrete vortices formed in the separation shear layer starting from the cylinder surface. The work of the MIT group (Karniadakis et al., 1988; Kozlu et al., 1988) revisited Reynolds' analogy for a geometry similar to that used by Kawaguchi et al. (1985) in two-dimensional channel flows at Reynolds numbers ranging from 180 to 945 and 1800 to 270,00. They found that eddy-promoter flows are dramatically less stable than their plane-channel counterparts owing to cylinder-induced shear-layer instability. They also concluded that small-cylinder supercritical eddy-promoter flows roughly reserve the convective-diffusive Reynolds analogy and achieve the same heat transfer rates as plane-cylinder turbulent flows at a much lower Reynolds number and less dissipation. Treidler and Carey (1990) investigated the spatially fully developed channel flow with staggered square ribs detached from two opposite walls using laser-Doppler velocimetry (LDV). They suggested that for low Reynolds numbers of order 500, any bluff bodies placed in the flow should be detached from

Contributed by the Fluids Engineering Division for publication in the JOURNAL OF FLUIDS ENGINEERING. Manuscript received by the Fluids Engineering Division January 3, 1996; revised manuscript received June 6, 1996. Associate Technical Editor: M. S. Triantafyllou.

Table 1 A list of relevant works

Year	Authors	Configuration	A/B	Pi/H	H/De	C/H	Re	Exp. Tech.	Meas. Quantities
1983	Oyakawa Mabuchi		6	4/8 12	0.128	0 0.75	43500 146000	TC FV PT	T P
1985	Kowaguchi et al.			6.25 ∞		0 0.25 1.375	77000	TC	T
1986	Oyakawa et al.		6	4/8 12	0.128	0.09 0.45	7000 90000	TC PT	T P
1987	Yao et al.		9	5	0.056 0.28	0 0.4	6000 80000	TC HW	T U
1988	Kozlu et al.		9	16.65	0.11	1.25	1800 27000	TC PT	T P
1989	Yao et al.		9	5	0.22	0 0.4	8000 60000	TC HW	T
1990	Treidler Carey		4.62	4 10	0.11	1	500 8000	LDV	U
1993	Liou et al.		4	10	0.081	0 1.5	5000 50000	TC LHI	T
1995	Present Study		2	10	0.1	0 3.25	20000	LDV	U

FV: Flow Visualization HW: Hot Wire LDV: Laser Doppler Velocimetry
 LHI: Laser Holographic Interferometry P: Pressure PT: Pitot Tube/Pressure Transducer
 T: Temperature TC: Thermocouple

the channel walls because vortices shed from the rib wakes caused flow oscillation which in turn increased heat transfer. For Reynolds numbers of 2000 or greater the normalized rms did not increase significantly when a gap was introduced. Liou et al. (1995) explored the effect of the detached clearance and Reynolds number on the heat transfer performance of a duct flow with an array of square ribs. They identified various critical clearances based on the heat transfer mechanisms and relative performance among duct flows with detached ribs, attached ribs, and smooth walls.

The above relevant studies have provided valuable information mostly on heat transfer augmentation in a duct with non-square detached ribs arranged in staggered form. The present work therefore focuses on an array of detached square ribs and is a fluid flow study complementary to our previous heat transfer investigation (Liou et al., 1995). Moreover, previous velocity-field measurements in duct flows with repeated ribs were performed for a single value or limited range of rib detached distance-to-height ratio (C/H). In the present study the C/H value is thus varied from 0 (ribs attached onto the wall) to 3.25 (rib's center along the duct centerline). Some turbulence quantities related to turbulence modelling will also be addressed.

Experimental Setup and Conditions

Test Section. The test section was 900 mm in length and 60 mm × 30 mm in cross-sectional area, and made of 5-mm

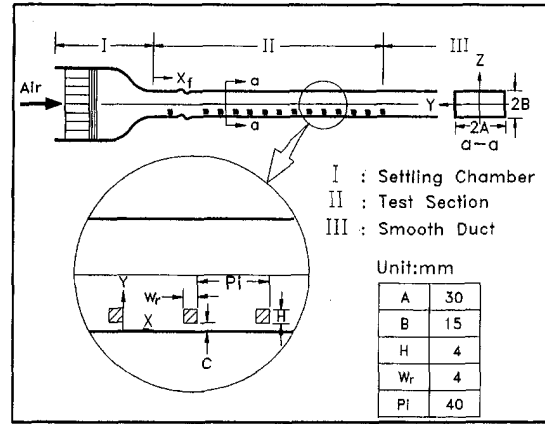


Fig. 1 Sketch of configuration, dimensions, and coordinate system of test section (Uncertainty in H : ± 0.1 mm, in W_r : ± 0.1 mm, in A and B : ± 0.3 mm, in axial position: ± 0.1 mm, in transverse position: ± 0.1 mm, in spanwise position: ± 0.1 mm)

Plexiglas, as shown in Fig. 1. The Plexiglas square ribs of size 4 mm × 4 mm ($W_r/H = 1$ and $H/2B = 0.133$ or $H/D_e = 0.1$) were detached a clearance C from the bottom wall ($Y = 0$). The leading edge of the first rib was placed 100 mm downstream of the bell-shaped 10:1 contraction. There were 19 ribs in the rib array.

Apparatus. The LDV experimental setup and flow system in the present work, Fig. 2, is similar to that described in Liou et al. (1990). Please refer to this earlier paper for more detail. The LDV optics is a two-color four-beam two-component system. A 4-W argon-ion laser with 514.5 nm (green) and 488 nm (blue) lines provided the coherent light sources. Both forward and off-axis scattering configurations were used in the experiment; the former gave a probe volume of 1.69 mm × 0.164 mm and the latter 0.74 mm × 0.164 mm inside the test section. The entire LDV system was mounted on a milling machine

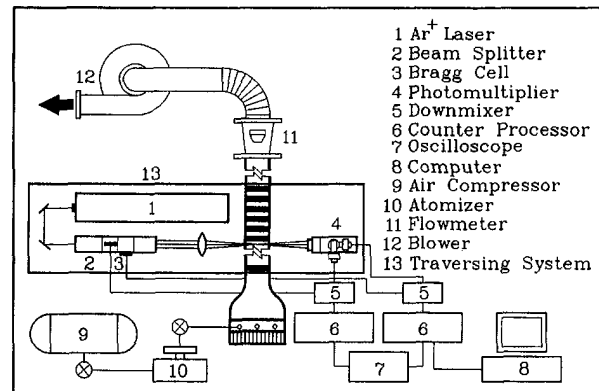


Fig. 2 Schematic drawing of overall experimental system

Nomenclature

A = half width of duct (30 mm)
 B = half height of duct (15 mm)
 C = clearance between rib and wall
 D_e = duct hydraulic diameter (40 mm)
 H = rib height (4 mm)
 k = turbulent kinetic energy, $k \equiv \frac{3}{4}(u'^2 + v'^2)$
 P_i = pitch length (40 mm)

Re_c = Reynolds number ($\equiv \rho U_b D_e / \mu_i$)
 U = streamwise mean velocity
 u = streamwise velocity fluctuation
 u' = streamwise turbulence intensity ($\equiv (u'^2)^{1/2}$)
 U_b = duct bulk mean velocity, $U_b = 7.78$ (m/s)
 $-\overline{uv}$ = turbulent shear stress

V = transverse mean velocity
 v = transverse velocity fluctuation
 v' = transverse turbulence intensity ($\equiv (v'^2)^{1/2}$)
 W = spanwise mean velocity
 w = spanwise velocity fluctuation
 w' = spanwise turbulence intensity ($\equiv (w'^2)^{1/2}$)

with four vibration-isolation mounts, allowing the probe volume to be positioned with 0.01 mm resolution. The light scattered from salt particles with a nominal 0.8 μm was collected into photomultiplier and subsequently downmixed to the appropriate frequency shift of 0.1 to 10 MHz. Then two counter processors with 1 ns resolution were used to process the Doppler signals and feed the digital outputs into a microcomputer for storage and analysis. Depending on the location of the probe volume in the flow, typical coincidence rates were between 500 and 3000 s^{-1} with a 50 μs coincidence window.

Test Conditions. The main parameter investigated was the rib detached distance-to-height ratio C/H with values of 0, 0.38, 0.58, 1, and 3.25. The rib pitch-to-height ratio P_i/H and Reynolds number were fixed at 10 and 2×10^4 , respectively. At a sufficient distance downstream of the first rib, it is expected that the flow pattern will repeat itself from pitch to pitch, i.e., becomes spatially periodic. Along the central plane $Z/A = 0$, LDV measurements of periodically fully developed flow were obtained at 15 to 28 axial stations between the 10th and 11th ribs. Verification of the spatially periodic condition is shown in Fig. 3 by comparing mean and fluctuating component profiles between the 10th and 11th ribs with those between the 11th and 12th ribs for $C/H = 0.38$. The repeatability is found to be within ± 3 percent for both mean and fluctuating components. At each station the measurements were made at 14 to 21 locations. The bulk mean velocity $U_b = 7.78 \text{ m/s}$ was used to non-dimensionalize the experimental results and corresponded to a Reynolds number of 2×10^4 , where the hydraulic diameter of the passage was 40 mm.

There were typically 4096 realizations averaged at each measuring location. The statistical errors in the mean velocity and turbulence intensity were less than 1.6 and 2.2 percent, respectively, for a 95 percent confidence level. Representative values of other uncertainty estimates are noted in figure captions. More detailed uncertainty estimates and velocity bias correlations are included in Liou et al. (1990 and 1993). For the range of

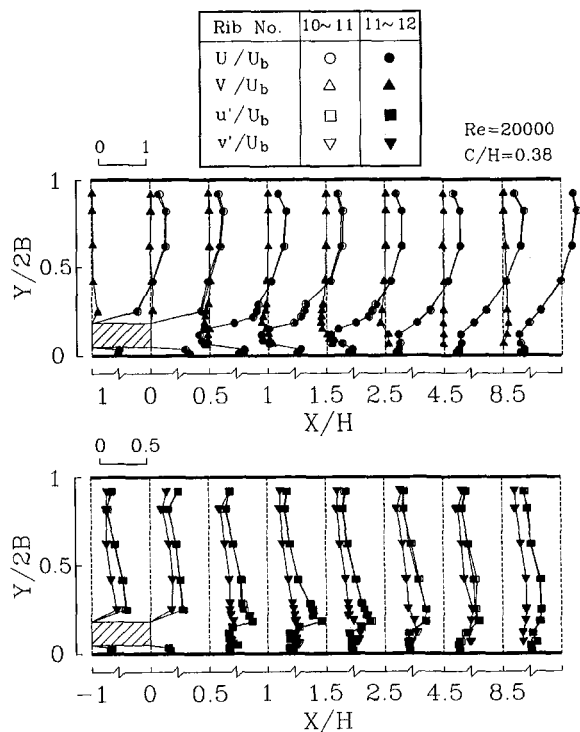


Fig. 3 Verification of spatially periodic flow condition (Uncertainty in U/U_b and V/U_b : less than ± 3.2 percent, in u'/U_b and v'/U_b : less than ± 4.4 percent)

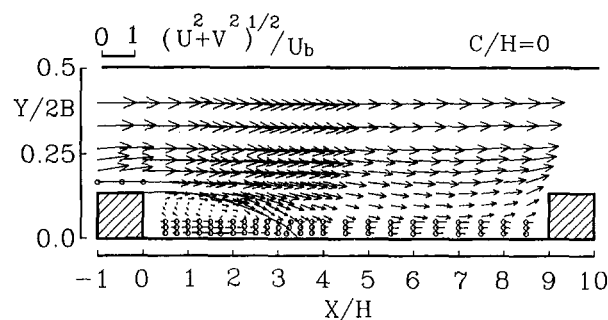


Fig. 4 Mean flow pattern in terms of velocity vectors for $C/H = 0$, $Re = 2 \times 10^4$ and $U_b = 7.78 \text{ m/s}$ (Uncertainty in $(U^2 + V^2)^{1/2}/U_b$: less than ± 3.2 percent; \ominus —: only U -component; solid line: dividing streamline)

atomizer pressure setting used, the saline solution was mixed to produce particles from 0.5 to 1.2 μm . This particle diameter range is able to follow turbulence frequencies exceeding 1 KHz (Durst et al., 1976).

Results and Discussion

Longitudinal Flow Structure

Mean Flow. Figures 4 and 5 depict the periodic fully developed mean flow patterns in one pitch module in terms of vector plots for $C/H = 0$ and $C/H = 0.38$, respectively, as $Re = 2 \times 10^4$. The degree of core flow contraction between the upper wall and rib top as well as flow expansion and separation behind the rib are found to be stronger in the attached-rib case (Fig. 4) than in the detached-rib case (Fig. 5) due to the split of incoming flow into two parts, one flowing above and the other beneath the rib in the latter case. For the case of $C/H = 0$, the separation shear layer with the dividing streamline separating the core flow from the main recirculating flow behind the rib reattaches onto the bottom wall at $X = 3.5 \pm 0.2 H$. This value of reattachment length is close to the $3.7 \pm 0.3 H$ measured by Hijikata et al. (1984) using a hot-wire anemometer for a similar

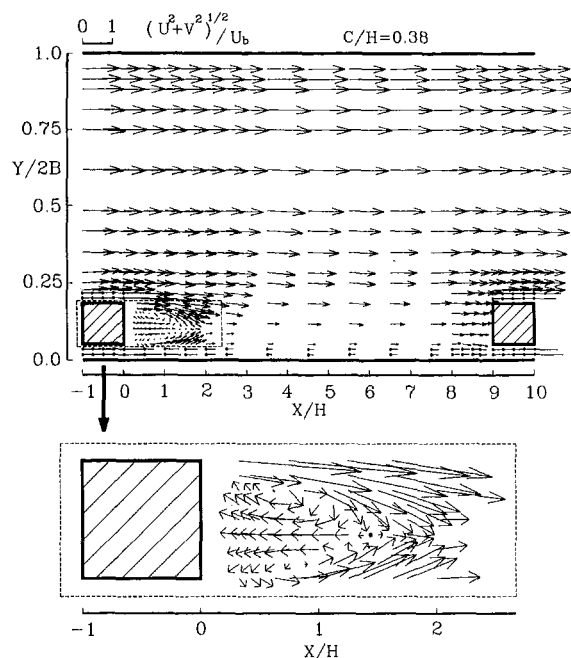


Fig. 5 Mean flow pattern in terms of velocity vectors for the case of $C/H = 0.38$, $Re = 2 \times 10^4$ and $U_b = 7.78 \text{ m/s}$ (see Fig. 4 caption; ●: saddle point)

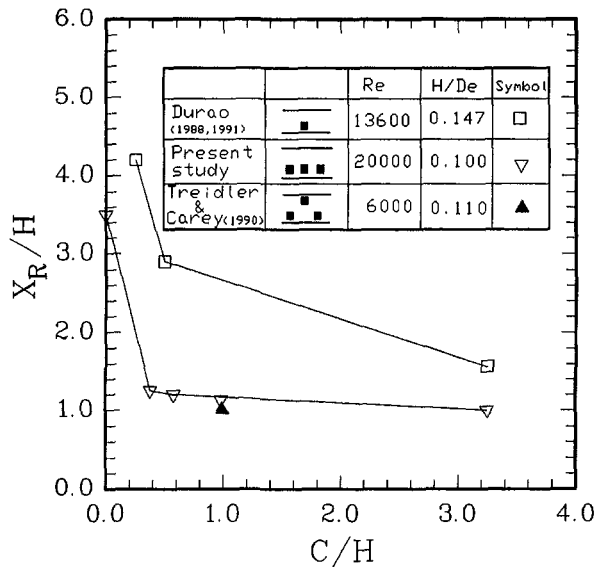


Fig. 6 Dimensionless wake length as a function of rib clearance ratio for both single- and multi-rib cases (Uncertainty in X_R : less than ± 0.2 mm; in C : less than ± 0.1 mm)

flow field with larger pitch ($P_i/H = 15$) and rib height ($H/2B = 0.2$). The measured maximum negative axial mean velocity is $-0.33 U_b$ and occurs at about $X/H = 2.5$. The corner vortex in front of rib can be detected from the nearest-wall LDV data at $X/H = 8.5$ whereas the corner vortex behind the rib, which was not measured by the LDV, can only be revealed from oil-film drop flow-visualization.

For the case of $C/H = 0.38$, the shear layers along the rib top and bottom both separate at rib's rear edge to form a wake of 1.35 rib heights. The wake length X_R/H , defined as the axial position where the saddle point occurs (Fig. 5), decreases with increasing clearance ratio C/H , as shown in Fig. 6 where the results of a single square cylinder and staggered rib arrays obtained by Durao (1988, 1991) and Treidler and Carey (1990), respectively, are also included for comparison. No matter the arrangement is a single or multiple detached ribs, the decrease of the X_R/H with increasing C/H is in a two-stage form, i.e., a rapid decrease associated with the transition from the reattached wake flow to the free wake flow as $C/H < 0.35-0.5 H$ and a weaker decrease associated with gradually decreasing influence of the bottom wall on the free wake as $C/H > 0.35-0.5 H$. Nevertheless, quantitatively the decreasing rate of the wake length in the aforementioned second stage is slower for the present multi-rib case, shortened 0.25 H , than for the single-rib case, shortened 1.3 H , as C/H increases from 0.5 to 3.25 H due to the retardation of the mixing between two separated shear layers by the presence of successive ribs for the present case. For multiple ribs with $C/H = 1$, the wake length in the case of Treidler and Carey (1990) is found to be close to that in the present case although the rib height and Reynolds number are different between the two cases. These wake lengths are important because they quantify the momentum transfer within the recirculating zone and have been widely used as characteristic lengths for computational comparison and modeling reference.

Also note that the wake flow is asymmetric with respect to the half-rib height, as shown in Fig. 5. Figure 7 depicts how the asymmetry varies with C/H . It is seen that the saddle point of the rib wake does not monotonically approach the symmetric axis (the half-rib-height line) $(Y - C)/H = 0.5$ but in a zigzag way, an observation not reported in the past. As the ribs are detached a small distance of $C/H = 0.38$ from the bottom wall, a transverse pressure gradient continues to prevail as in the case

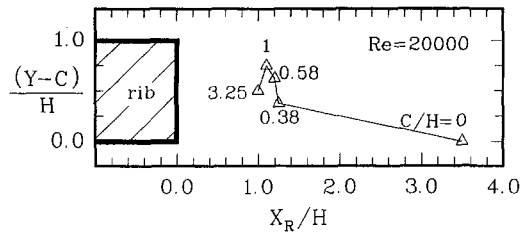


Fig. 7 Location of saddle point relative to rib at various C/H (see Fig. 6 caption)

of $C/H = 0$ (Marumo et al., 1985) resulting in wakes skewed towards the bottom wall with the saddle points located below $(Y - C)/H = 0.5$. When the ribs are detached far enough from the bottom wall, $C/H = 0.58$ or 1 in the present case, the wakes are skewed toward the core-flow side with the saddle points located above $(Y - C)/H = 0.5$ because the higher velocity core-flow over the ribs lowers the pressure in the core region relative to the flow region nearer the bottom wall. For $C/H = 3.2$ the ribs are positioned along the duct centerline and the wake saddle points occurred therefore at $(Y - C)/H = 0.5$. The measured maximum negative axial mean velocities are $(U/U_b)_{\max} = -0.24, -0.25, -0.17,$ and -0.2 occurred at $X/H = 0.75, 0.5, 0.5,$ and 0.5 inside the wake for $C/H = 0.38, 0.58, 1,$ and 3.25 , respectively.

Turbulent Kinetic Energy and Stress. A common source of energy for turbulent velocity fluctuations is shear in the mean flow. The contour maps of the turbulent kinetic energy and Reynolds stress for $C/H = 0$ and 0.38 are thus shown in Figs. 8 and 9, respectively. As expected the shear stress is high in the regions where the mean-velocity gradient is steep (Figs. 4 and 5). The maximum shear stress at each X/H station occurs along a horizontal band of $0.9 \pm 0.1 H$ and $1 \pm 0.1 H$ above the bottom wall for $C/H = 0$ and 0.38, respectively. In the meantime for the case of $C/H = 0$ (Fig. 8) the value of maximum $-\overline{uv}/U_b^2$ increases up to 0.045 as X/H increases from 0 to 2.5, stays at 0.045 for $2.5 \leq X \leq 3.5$, and then decreases with increasing X/H . For the case of $C/H = 0.38$ (Fig. 9) the value of maximum $-\overline{uv}/U_b^2$ increases up to 0.05 as X/H increases from 0 to 1, but subsequently gradually decreases with increasing X/H . Moreover, the shear stress decreases toward the core-flow side and toward the concave corners in front of and behind the rib for $C/H = 0$; however, the shear stress first

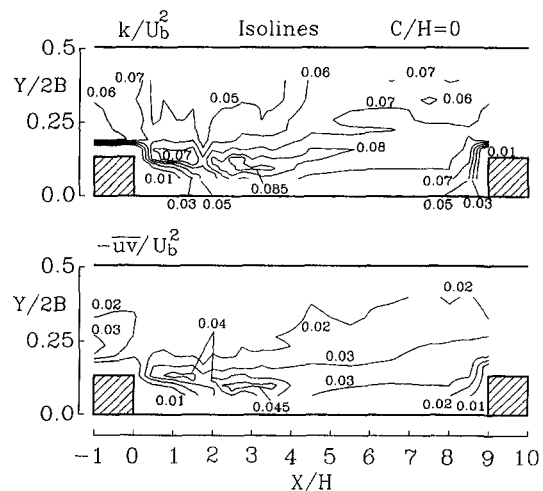


Fig. 8 Contours of turbulent kinetic energy and Reynolds shear stress for $C/H = 0$, $Re = 2 \times 10^4$ and $U_b = 7.78$ m/s (Uncertainty in k/U_b^2 : less than ± 7.4 percent, in $-\overline{uv}/U_b^2$: less than ± 4.8 percent)

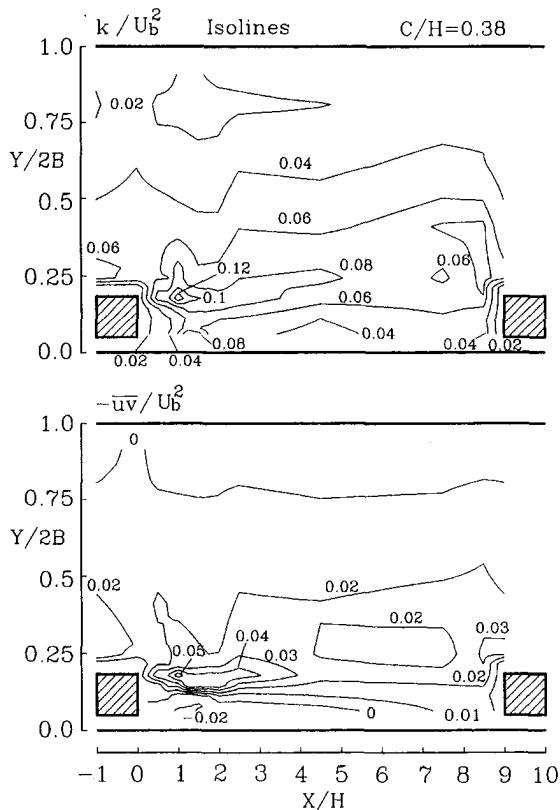


Fig. 9 Contours of turbulent kinetic energy and Reynolds shear stress for $C/H = 0.38$, $Re = 2 \times 10^4$ and $U_b = 7.78$ m/s (see Fig. 8 caption)

decreases and then increases again toward the bottom corner of the detached rib ($C/H = 0.38$) due to the wall jet issuing from the detached clearance.

Similar behavior also occurs for the turbulent kinetic energy k/U_b^2 , as shown in Figs. 8 and 9, because the production of turbulent kinetic energy is related to the product of shear stresses and mean velocity gradients. The peak of maximum turbulent kinetic energy is 8.5 percent and 12 percent of U_b^2 and occurs approximately $1 \pm 0.1 H$ and $0.35 \pm 0.05 H$ upstream of reattachment or wake saddle point for $C/H = 0$ and 0.38, respectively. Notice that for sudden expansion pipe or channel flow the peak of streamwise turbulence intensity was also found to occur at about one step height upstream of reattachment (Eaton and Johnston, 1981). As far as heat transfer improvement is concerned, it is worth pointing out that the values of k/U_b^2 in the region $0 < X/H \leq 1$ behind the rib are higher for $C/H = 0.38$ (Fig. 9) than for $C/H = 0$ (Fig. 8), a rationale for the better heat transfer augmentation immediately behind the rib attained by the detached rib array than by the attached rib array (Liou et al., 1995). There is one more fluid dynamics aspect relevant to the heat transfer worth mentioning here. Figure 10 shows the distributions of nondimensionalized local Nusselt number (Liou et al., 1995), streamwise turbulent kinetic energy, and streamwise mean velocity as functions of streamwise distance X/H for the $C/H = 0.38$ case. Note that u'^2/U_b^2 and U/U_b in Fig. 10 were data obtained along a horizontal line at a distance 0.5 mm from the bottom wall. There exist two local peak values of N_u/N_{us} , one located at about $X/H = 8.5$ (close to the rib's front bottom salient) and the other at the half rib width $X/H = -0.5$ (beneath the rib). The former case appears to be resulted primarily from the high turbulent kinetic energy associated with sudden contraction of the flow around the rib's front bottom salient whereas the latter case is mainly due to

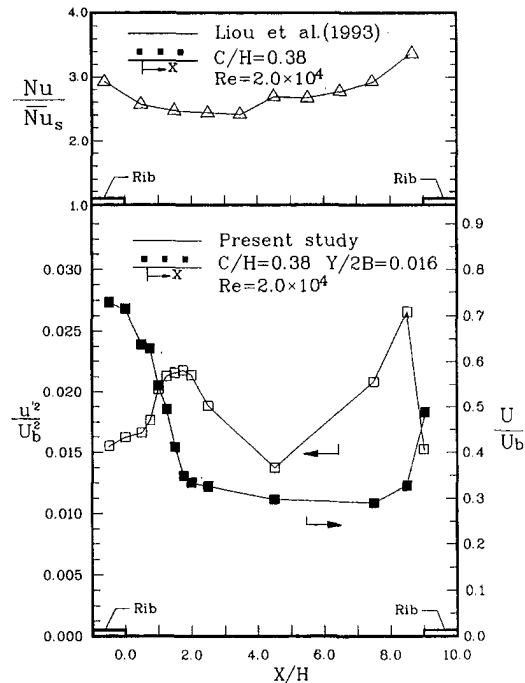


Fig. 10 Distributions of local Nusselt number, axial mean velocity and axial turbulence kinetic energy along the wall for $C/H = 0.38$

the enhanced forced convection through the detached clearance between the rib and bottom duct wall.

Figure 11 depicts how the value and position (relative to the rib) of the nondimensional maximum Reynolds stress change as C/H increases from 0 (wall) to 3.25 (duct center). Two observations can be made. First, for rib positioned not far away from the wall ($C/H \leq 1$) $C/H = 0.38$ achieves the highest value ($=0.05$) of $(-uv/U_b^2)_{max}$. This fluid dynamic result parallels the heat transfer result that $C/H = 0.38$ attains the highest heat transfer augmentation for $C/H \leq 1$ reported previously by Liou et al. (1995). Second, for the range of detached clearance tested, $0.38 \leq C/H \leq 3.25$, the locations where $|-uv/U_b^2|_{max}$ occurs are confined in the range of $1 \pm 0.25 H$ downstream of the detached ribs.

Parameters Relevant to Turbulence Modeling. An assumption embedded in the algebraic Reynolds stress model (Rodi, 1976) is that the transport of \bar{uv} is proportional to the transport of k in the investigated flow field. Figure 12 depicts the contour map of the structure parameter $|\bar{uv}|/k$ for the case of $C/H = 0.38$. It is seen that the measured values of $|\bar{uv}|/k$ are in the region of 0 to 0.5 with 45.5 percent of the $|\bar{uv}|/k$ data falling between 0.2 to 0.4. Higher values of $|\bar{uv}|/k$, 0.3 to 0.5, are found to occur around the shear layer separated from

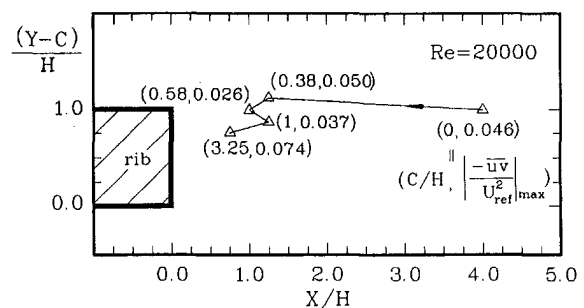


Fig. 11 Magnitude and location relative to rib of maximum Reynolds stress as functions of C/H (see Fig. 8 caption)

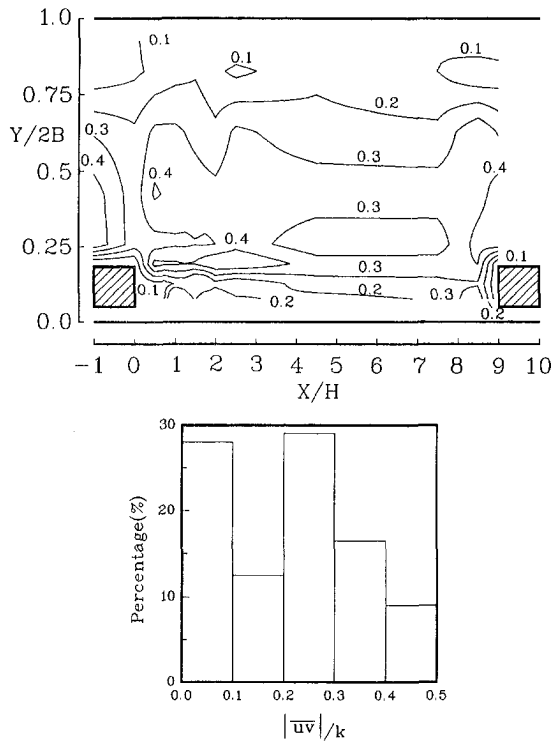


Fig. 12 Structure parameter contours for $C/H = 0.38$ (Uncertainty in $|\overline{uv}|/k$: less than ± 8.8 percent)

rib's top. Because of different degrees of flow complexity, the present measured $|\overline{uv}|/k$ distribution differs from that in jets, wakes, and boundary layer surveyed by Harsha and Lee (1970), in which 70 percent of the data fall in the range of $0.2 < |\overline{uv}|/k < 0.4$. As far as turbulence modelling is concerned, $|\overline{uv}|/k$ is often specified by researchers as 0.3 (Harsha and Lee, 1970) or 0.24 (Launder, 1975). If the present measured $|\overline{uv}|/k$ are averaged over the entire pitch, a value of 0.21 is obtained.

An examination of isotropy for the turbulent flow investigated is useful in guiding turbulence modelling efforts. Figure 13 depicts the distributions of both axial and transverse turbulence intensities in the range of $-1 \leq X/H \leq 8.5$ and $0 \leq Y \leq 0.5$ for $C/H = 0$ and $C/H = 0.38$. In general, u' is larger than v' in most regions. That is the examined turbulent flow is anisotropic with $\overline{u^2} = 1.30$ to $3.42 \overline{v^2}$ and $\overline{u^2} = 0.44$ to $4.0 \overline{v^2}$ for $C/H = 0$ and $C/H = 0.38$, respectively, in the $Z = 0$ plane. The influence of C/H on the ratio between the maxima of the axial and transverse normal stress $\overline{u_{max}^2}/\overline{v_{max}^2}$ for the present duct

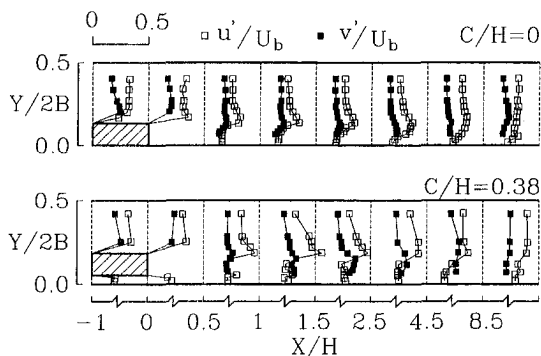


Fig. 13 Selected streamwise and transverse turbulence intensity profiles in one-pitch module for $Re = 2 \times 10^4$ and $U_b = 7.78$ m/s (see Fig. 3 caption)

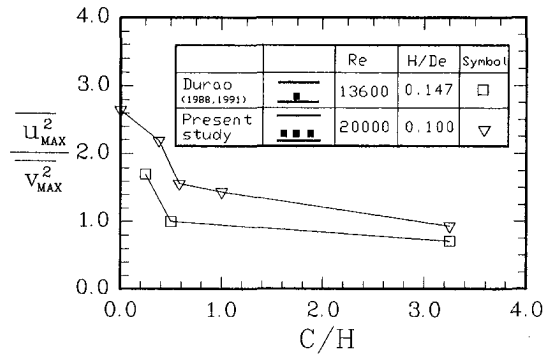


Fig. 14 $\overline{u_{max}^2}/\overline{v_{max}^2}$ versus C/H for duct flows with multiple ribs and single rib detached from the wall (Uncertainty in $\overline{u_{max}^2}/\overline{v_{max}^2}$: less than ± 4.8 percent)

flows with a detached rib array is shown in Fig. 14 where the result for duct flows with a single detached rib (Duroo et al., 1991) is also included for comparison. Both cases indicate an increase of $\overline{u_{max}^2}/\overline{v_{max}^2}$ with decreasing C/H , which is a consequence of increasing wall effect. As C/H is decreased from 3.25 toward 0; the wall effect gradually attenuates the vortex shedding of the rib wake and results in a more intensive reduction in $\overline{v^2}$ than in $\overline{u^2}$.

Spanwise Flow Pattern. Previous hot wire measurements of secondary flow in a rectangular duct of aspect ratio 2:1 with an attached square rib array (Fujita et al., 1989) indicated the presence of only one large longitudinal vortex near a side wall. It is interesting to see how the secondary flow pattern changes as the rib array is detached from one wall. The measured results of V and W mean velocity components in $X/H = 7$ cross-section are depicted in Fig. 15 in terms of a vector plot for the case of $C/H = 0.38$. As one can see, a longitudinal vortex still exists near a side wall; however, the size of vortex near the left side wall $Z^* = -0.5$ is larger than that near the right side wall $Z^* = 0.5$ and bottom wall $Y/2B = 0$. This observed secondary flow pattern for the duct flows with a detached rib array is obviously different from that for the duct flows with an attached rib array. It is also different from the two secondary flow cells and one recirculating cell in each quadrant of a channel cross section in the smooth channel (Speziale, 1986) and in the ribbed channel with attached rib arrays mounted on two opposite walls (Liou et al., 1993a), respectively. Quantitatively, the magnitudes of V and W in Fig. 15 are only 0.01 to $0.1 U_b$ in the present case of $C/H = 0.38$ and approximately four times those in the smooth channel (Speziale, 1986) and 0.4 times those in the duct with an attached rib array (Fujita et al., 1989).

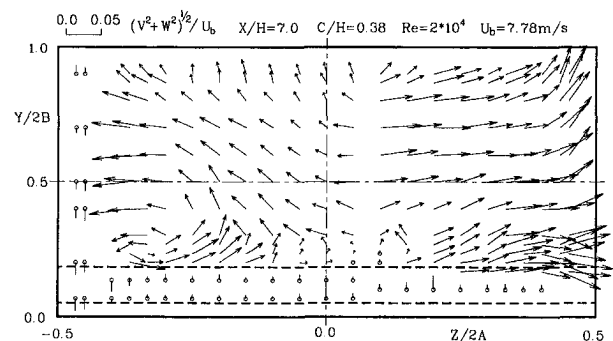


Fig. 15 Secondary flow vectors in $X/H = 7$ plane for $C/H = 0.38$ (Uncertainty in $(V^2 + W^2)^{1/2}/U_b$: less than ± 3.2 percent; \odot : only V -component)

Conclusions

The following main statements are drawn from the data presented:

- (1) As the ribs are detached from the bottom wall toward the duct centerline, the wakes behind the ribs are asymmetric and approach the symmetric shape in a zigzag way.
- (2) The wall jet issued from the clearance between the rib and duct wall for $C/H = 0.38$ generates higher convective velocity and turbulent kinetic energy in the region $0 < X/H \leq 1$ behind the rib, as compared with the case of $C/H = 0$. This fact provides fluid dynamic rationale for the previously reported better heat transfer augmentation immediately behind the rib attained by the detached rib array with appropriate values of C/H than by the attached rib array.
- (3) The present study is able to identify the controlling fluid flow factors responsible for the occurrence of peak values of local heat transfer coefficient around the rib reported in the previous heat transfer study. That is, the peak Nusselt number occurred near the rib's front bottom salient is mainly due to the high turbulent kinetic energy whereas the peak Nusselt number occurred at the half rib width and beneath the rib is mainly due to the enhanced convective velocity.
- (4) The structure parameter $|\overline{uv}|/k$ is found to have a pitch averaged value of 0.21 for the case of $C/H = 0.38$, a value lower than 0.24 or 0.3 adopted in the open literature. The degree of turbulence anisotropy is found to increase with decreasing C/H . The above results provide useful information for examining the basic assumptions embedded in the algebraic Reynolds stress model and the $k-\epsilon$ model.
- (5) For $C/H = 0.38$ measurements in the cross-sectional plane indicate that spanwise and transverse mean velocity components are only 0.01 to 0.1 U_b , which are about 0.4 times those in the duct with an attached rib array.

Acknowledgment

This research was supported by the National Science Council of the Republic of China under Contracts NSC83-0401-E007-014 and NSC84-2212-E007-049.

References

- Bearman, P. W., and Zdravkovich, M. M., 1978, "Flow Around a Circular Cylinder Near a Plane Boundary," *Journal of Fluid Mechanics*, Vol. 89, part 1, pp. 33–47.
- Chang, B. H., and Mills, A. F., 1993, "Turbulent Flow in a Channel with Transverse Rib Heat Transfer Augmentation," *International Journal of Heat and Mass Transfer*, Vol. 30, No. 6, pp. 1459–1469.
- Durao, D. F. G., Heitor, M. V., and Pereira, J. C. F., 1988, "Measurements of Turbulent and Periodic Flows Around a Square Cross-Section Cylinder," *Experiments in Fluids*, Vol. 6, pp. 298–304.
- Durao, D. F. G., Gouveia, P. S. T., and Pereira, J. C. F., 1991, "Velocity Characteristics of the Flow around a Square Cross Section Cylinder Placed Near a Channel Wall," *Experiments in Fluids*, Vol. 11, pp. 341–350.
- Durst, F., Melling, A., and Whitelaw, J. H., 1976, *Principles and Practice of Laser-Doppler Anemometry*, Academic Press, New York, Chapter 9.
- Eaton, J. K., and Johnston, J. P., 1981, "A Review of Research on Subsonic Turbulent Flow Reattachment," *AIAA Journal*, Vol. 19, No. 9, pp. 1093–1100.
- Fujita, H., Yokosawa, H., and Hirota, M., 1989, "Secondary Flow of the Second Kind in Rectangular Ducts with One Rough Wall," *Experimental Thermal and Fluid Science*, Vol. 2, pp. 72–80.
- Harsha, P. T., and Lee, S. C., 1970, "Correlation Between Turbulent Shear Stress and Turbulent Kinetic Energy," *AIAA Journal*, Vol. 8, No. 8, pp. 1508–1510.
- Hijikata, K., Mori, Y., and Ishiguro, T., 1984, "Turbulent Structure and Heat Transfer of Pipe Flow with Cascade Smooth turbulence Surface Promoters," *Transactions of Japan Society of Mechanical Engineers*, Vol. 50, No. 458, pp. 2555–2562.
- Kamemoto, K., Oda, Y., and Masahiro, A., 1984, "Characteristics of the Flow around a Bluff Body Near a Plane Surface," *Bulletin of JSME*, Vol. 27, No. 230, pp. 1637–1643.
- Karniadakis, G. E., Mikic, B. B., and Patera, A. T., 1988, "Minimum Dissipation Transport Enhancement by Flow Destabilization: Reynolds Analogy Revisited," *Journal of Fluid Mechanics*, Vol. 192, pp. 365–391.
- Kawaguchi, Y., Suzuki, K., and Sato, T., 1985, "Heat Transfer Promotion with a Cylinder Array Located Near the Wall," *International Journal of Heat and Fluid Flow*, Vol. 6, No. 4, pp. 249–255.
- Kozlu, H., Mikic, B. B., and Patera, A. T., 1988, "Minimum-dissipation Heat Removal by Scale-matched Flow Destabilization," *International Journal of Heat and Mass Transfer*, Vol. 31, No. 10, pp. 2023–2032.
- Lauder, B. E., Reece, G. J., and Rodi, W., 1975, "Progress in the Development of a Reynolds-Stress Turbulence Closure," *Journal of Fluids Mechanics*, Vol. 68, part 3, pp. 537–566.
- Liou, T. M., Chang, Y., and Hwang, D. W., 1990, "Experimental and Computational Study of Turbulent Flows in a Channel with Two Pairs of Turbulence Promoters in Tandem," *ASME JOURNAL OF FLUIDS ENGINEERING*, Vol. 112, pp. 302–310.
- Liou, T. M., and Hwang, J. J., 1992, "Turbulent Heat Transfer Augmentation and Friction in Periodic Fully Developed Channel Flows," *ASME Journal of Heat Transfer*, Vol. 114, pp. 56–64.
- Liou, T. M., Wu, Y. Y., and Chang, Y., 1993a, "LDV Measurements of Periodic Fully Developed Main and Secondary Flows in a Channel with Rib-Disturbed Walls," *ASME JOURNAL OF FLUIDS ENGINEERING*, Vol. 115, pp. 109–114.
- Liou, T. M., Hwang, J. J., and Chen, S. H., 1993b, "Simulation and Measurement of Enhanced Turbulent Heat Transfer in a Channel with Periodic Ribs on One Principal Wall," *International Journal of Heat and Mass Transfer*, Vol. 36, No. 2, pp. 507–517.
- Liou, T. M., Wang, W. B., and Chang, Y. J., 1995, "Holographic Interferometry Study of Spatially Periodic Heat Transfer in a Channel with Ribs Detached from One Wall," *ASME Journal of Heat Transfer*, Vol. 117, pp. 32–39.
- Marumo, E., Suzuki, K., and Sato, T., 1985, "Turbulent Heat Transfer in a Flat Plate Boundary Layer Disturbed by a Cylinder," *International Journal of Heat and Fluid Flow*, Vol. 6, No. 4, pp. 241–248.
- Oyakawa, K., and Mabuchi, I., 1983, "Fluid Flow and Heat Transfer in a Parallel Plate Duct Containing a Cylinder," *Bulletin of JSME*, Vol. 48, No. 432, pp. 1509–1519.
- Oyakawa, K., Shinzato, T., and Mabuchi, I., 1986, "Effect on Heat Transfer Augmentation of Some Geometric Shapes of a Turbulence Promoter in a Rectangular Duct," *Bulletin of JSME*, Vol. 29, No. 256, pp. 3415–3420.
- Rodi, W., 1976, "A New Algebraic Relation for Calculating the Reynolds Stresses," *ZAMM*, Vol. 56, pp. T219–T221.
- Speziale, C. G., 1986, "The Dissipation Ratio Correlation and turbulent Secondary Flows in Noncircular Ducts," *ASME JOURNAL OF FLUIDS ENGINEERING*, Vol. 108, pp. 118–120.
- Suzuki, H., Fukutani, K., Takishita, T., and Suzuki, K., 1993, "Flow and Heat Transfer Characteristics in a Channel Obstructed by a Square Rod Mounted in Asymmetric Positions," *Proceedings of the 6th International Symposium on Transport Phenomena in Thermal Engineering*, Seoul, Korea, pp. 353–358.
- Taniguchi, S., and Miyakoshi, K., 1990, "Fluctuating Fluid Forces Acting on a Circular Cylinder and Interference with a Plane Wall," *Experiments in Fluids*, Vol. 9, pp. 197–204.
- Treidler, B., and Carey, V. P., 1990, "On the Flows Past an Array of Staggered Ribs in a Channel," *Proceedings of Int'l Symposium on Applications of Laser-Doppler Anemometry to Fluid Mechanics*, Lisbon, Portugal, pp. 4.3.1–4.3.6.
- Yao, M., Nakatani, M., and Suzuki, K., 1987, "An Experimental Study on Pressure Drop and Heat Transfer in a Duct with a Staggered Array of Cylinders," *ASME-JSME Thermal Engineering Joint Conference*, Marto, P. J., and Tanasawa, I., eds., Vol. 5, pp. 189–196.
- Yao, M., Nakatani, M., and Suzuki, K., 1989, "Flow Visualization and Heat Transfer Experiments in a Duct with a Staggered Array of Cylinders," *Experimental Thermal and Fluid Science*, Vol. 2, pp. 193–200.

Axisymmetric Inertial Oscillations in Transient Rotating Flows in a Cylinder

Jae Won Kim

Professor,
Department of Mechanical Engineering,
Sun Moon University,
Kalsan, Tangjung, Asan-si,
Chung Nam 336-840, South Korea

Jae Min Hyun

Professor,
Department of Mechanical Engineering,
Korea Advanced Institute of
Science and Technology,
Kusung-dong, Yusong-ku,
Taejon 305-701, South Korea

A numerical study is made of axisymmetric inertial oscillations in a fluid-filled cylinder. The entire cylinder undergoes a spin-up process from rest with an impulsively-started rotation rate $\Omega(t) = \Omega_0 + \epsilon\omega \cos(\omega t)$. Numerical solutions are obtained to the axisymmetric, time-dependent Navier-Stokes equations. Identification of the inertial oscillations is made by inspecting the evolution of the pressure difference between two pre-set points on the central axis, C_p . In the limit of large time, the inertial frequency thus determined is in close agreement with the results of the classical inviscid theory for solid-body rotation. As in previous experimental studies, the $t^ - (\Omega_0/\omega)$ plots are constructed for inertial oscillations, where t^* indicates the time duration until the maximum C_p is detected. These detailed numerical results are in broad agreement with the prior experimental data. Flow intensifications under the resonance conditions are illustrated based on the numerical results. Depictions are made of the increase in the amplitude of oscillating part of the total angular momentum under the resonance conditions. Also, the patterns of $t^* - (\Omega_0/\omega)$ curves are displayed for different inertial frequency modes.*

1 Introduction

Consider an incompressible, constant-density fluid (density ρ and kinematic viscosity ν) which completely fills a closed straight circular cylinder (radius R and height h). At the initial stage, both the fluid and the cylindrical vessel are at rest. At time $t = 0$, the cylinder is abruptly set into rotation about its central longitudinal axis z with a time-dependent angular frequency $\Omega(t)$. The subsequent motion of the fluid, in response to this impulsively-started rotation of the cylinder, is the subject of this paper.

If the rotation rate of the cylinder is constant, i.e., $\Omega(t) = \Omega_0$, the problem constitutes the celebrated flow model of spin-up from rest. This topic has been extensively studied, and a substantial body of technical literature has been compiled (Wedemeyer, 1964; Weidman, 1976; Watkins and Hussey, 1977; Kitchen, 1981; Hyun et al., 1983; Hyun, 1983; Choi et al., 1989, 1991; Hall et al., 1990; Herbert and Li, 1990; Kim and Hyun, 1995). Of present concern is the case when the cylinder rotation rate includes a small-amplitude, sinusoidally-varying oscillatory component, i.e.,

$$\Omega(t) = \Omega_0 + \epsilon\omega \cos \omega t. \quad (1)$$

This type of time-dependent rotation rate is of relevance from several viewpoints. In actual turn-table experiments, the rotation rate of the practical container is seldom strictly constant. Owing to the unavoidable impurities of the motor output, the resulting rotation speed of the turntable does contain some degrees of time-dependent components. Another point, which is perhaps more significant, is the issue of resonance, which is associated with the inertial oscillations of a rotating fluid. The major focus of the present effort is directed to the detailed behavior of fluid flow when these inertial oscillations are excited by the above-described sinusoidal time variation of the cylinder rotation speed during spin-up.

As is the case in most technological applications as well as in geophysical situations, the system Ekman number, $E \equiv$

$\nu/\Omega_0 h^2$, where ν denotes kinematic viscosity of the fluid, h the characteristic dimension of the container, is very small. Note that the rotational Reynolds number Re is defined to be $Re \equiv E^{-1}$. This gives rise to the distinctive boundary layer-type overall flow character. When the fluid is in steady-state rigid-body rotation with uniform rotation rate Ω_0 , the classical treatise gives a closed-form expression for the eigenfrequencies of inertial oscillations, and experimental verifications of these eigenfrequencies have been reported (e.g., Greenspan, 1968). However, the question of determining the inertial oscillation frequencies in the context of transient spin-up poses a separate problem formulation.

The laboratory turn-table experiment of Fowles and Martin (1975) described the inertial oscillations in the early phases of spin-up when the pre-existing cylinder rotation rate, $\Omega_0 - \Delta\Omega$, was given a step change $\Delta\Omega$ to reach a constant value Ω_0 . A sensitive measurement technique was employed in that study to detect pressure differences. A wide-ranging, systematic turntable experiment was conducted by Aldredge (1977), using a similar method of measuring perturbation pressure differences. The purpose was to assert the existence of axisymmetric inertial oscillations during spin-up from rest when the cylinder rotation rate $\Omega(t)$ includes an oscillatory component, as expressed in Eq. (1). The principal findings of Aldredge's experiment illustrated the change in eigenfrequency with time. The experimental observations were centered on monitoring the rapid increase of perturbation pressure difference Δp over a broad range of the frequency ratio Ω_0/ω . Clearly, as the externally-specified forcing frequency ω approaches the inertial oscillation frequency of the system, a sharp increase in pressure difference Δp is manifested. The experimental results of Aldredge (1977) demonstrated the expected increase in Δp near the resonance frequency. In practical terms, knowledge of the values of resonance frequencies is essential in the design and operation of high-speed rotating fluid machinery. Large increases in perturbation pressure near the resonance conditions could lead to violent system vibrations and severely undermine the performance of fluid-containing high-speed rotating devices. It is stressed here that, within the ranges of the parameters covered in Aldredge's experiments, observations revealed that the flows were highly axisymmetric and laminar. If the Ekman number is extremely

Contributed by the Fluids Engineering Division for publication in the JOURNAL OF FLUIDS ENGINEERING. Manuscript received by the Fluids Engineering Division January 18, 1996; revised manuscript received December 4, 1996. Associate Technical Editor: S. P. Vanka.

small, possible nonaxisymmetry and transition to turbulence may be expected (Rogers and Lance, 1960; Wedemeyer, 1964; Aldredge, 1977; Kitchen, 1980). The purpose of the present work is to acquire an improved understanding of resonance conditions within the realm of the preceding experiments of Aldredge.

An analysis was made by Lynn (1973) on the change in inertial oscillation frequencies with time during spin-up from rest. The well-known spin-up flow model due to Wedemeyer (1964) was adopted as the unperturbed basic-state azimuthal velocity field for Lynn's analysis. For axisymmetric perturbations in an inviscid fluid ($E = 0$), Lynn (1973) obtained an analytical relationship, which allowed numerical calculation of the time-evolving inertial oscillation frequencies. One objective of the laboratory measurements of Aldredge (1977) was to check the experimentally-acquired time-dependency of eigenfrequencies against the theoretical calculations of Lynn (1973). Comparisons revealed qualitative consistency between the two sets of results, but some quantitative discrepancies were also noted. It was found that agreement between measurements and theory was better for low frequency modes. Since the amplitude of the oscillatory part of the cylinder rotation, ϵ , was small, the nonlinear effects on the dependence of inertial oscillation frequency on time were shown to be minor. In summary, the experiments of Aldredge (1977) confirmed the existence of axisymmetric inertial oscillations during spin-up from rest which were excited by the time-varying rotation speed of the container of Eq. (1). It is emphasized here that the experimental observations of Aldredge were based entirely on the pressure measurements at selected locations. This information was used to ascertain the afore-stated inertial frequencies. The report of Aldredge contained no flow visualizations or measurements of velocity field at given frequency ratios. In particular, no descriptions were provided of the changes in flow patterns as the frequency ratio Ω_0/ω encompassed a range which covers the neighborhood of the expected eigenfrequencies.

In the present paper, numerical solutions to the governing axisymmetric, unsteady Navier-Stokes equations will be sought. The comprehensive numerical solutions will serve to verify the time-evolving inertial oscillation frequencies, which had been measured in the experiments (Aldredge, 1977) and predicted by the inviscid theoretical model (Lynn, 1973). A more poignant advantage of the present numerical results lies in the breadth and depth of the available flow data. Exploiting the numerical solutions, the global flow structure, in particular, the meridional circulation, in conjunction with the time-evolving resonance frequencies, will now be illuminated. In view of the fact that no depictions had been presented of the overall flow patterns by the prior experiments or by the analytical predictions, the present numerical endeavors will complement the previous undertakings on inertial oscillations in spin-up from rest.

2 Review of the Preceding Theory

Wedemeyer (1964) proposed an elegant model to portray the transient flow process during spin-up from rest when the cylinder rotation speed is constant, i.e., $\Omega(t) = \Omega_0$. Under the assumption that direct effects of viscosity are confined to the boundary layers, the azimuthal velocity field is shown to be divided into the nonrotating zone in the central region and the rotating region at large radii. These two regions are separated by a moving velocity shear front. The velocity components in the azimuthal and radial directions are independent of the axial coordinate z in the interior core, which rephrases the Taylor-Proudman theorem. In the course of model construction, considerable amounts of judicious approximations and heuristic arguments were incorporated. The qualitative capabilities of the model have since been vali-

dated by numerous experimental and numerical investigations (Weidman, 1976; Watkins and Hussey, 1977; Kitchen, 1981; Hyun et al., 1983; Hyun, 1983; Choi et al., 1989, 1991; Kim and Hyun, 1995). Using the Wedemeyer (1964) solution as the basic state, Lynn (1973) proceeded to set up perturbation equations for an inviscid fluid to look for inertial oscillations when the cylindrical rotation rate is prescribed by a time-dependent form, Eq. (1). Solutions were obtained for perturbation velocity and pressure in each of the two regions. Based on the equality of pressure and velocity at the shear front, a relationship emerges in which the dependency of the inertial oscillation frequency on time is described. Obviously, in the large-time limit since the container was switched on, the inertial oscillation frequencies tend to those classical solutions for a cylinder of fluid in solid-body rotation at Ω_0 (Greenspan, 1968), i.e.,

$$\left(\frac{\Omega_0}{\omega}\right)_{k,i} = \frac{1}{2} \left\{ \left(\frac{\gamma_i}{K}\right)^2 + 1 \right\}^{1/2}, \quad K \equiv \frac{\pi R k}{h}, \quad (2)$$

where γ_i is the i th root of the Bessel function $J_1(x) = 0$. The (k, i) pair denotes the mode of the inertial oscillation indicating the number of waves in the axial (z) and radial (r) direction, respectively. Values obtainable from Lynn's theoretical model for $t \rightarrow \infty$ are consistent with Eq. (2).

It is important, however, to recall the fundamental assumptions and limitations that are inherent in the above theoretical development of Lynn (1973). As remarked earlier, the experiment of Aldredge (1977) was intended to provide observations of the time-evolution of the inertial oscillation frequencies. The plot of time (t) versus the value of (Ω_0/ω) at which a peak disturbance pressure appears is a major output of the experiment. Comparisons were conducted between the theoretical predictions and experimental measurements as to the time dependency of resonance frequencies. These studies are now subject to verification and enhancement by the present numerical computations.

3 Problem Formulation and Numerical Model

A schema of flow configuration, together with the cylindrical coordinate system (r, θ, z), is shown in Fig. 1. For $t < 0$, both the cylinder and the fluid are at rest. At the initial instant $t = 0$, the cylinder begins impulsively rotating about the longitudinal axis z with rotation speed, $\Omega(t)$ given in Eq. (1). The task is to describe the ensuing time-dependent fluid motion.

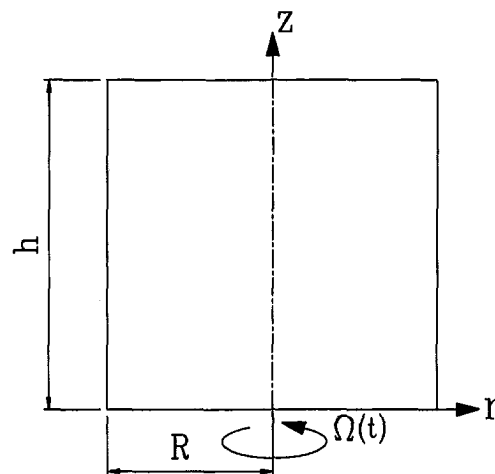


Fig. 1 Schematic diagram of the flow configuration

The governing equations are the unsteady axisymmetric Navier-Stokes equations and continuity equation:

$$\frac{\partial u}{\partial t} = -\frac{1}{r} \frac{\partial(ru^2)}{\partial r} - \frac{\partial(uw)}{\partial z} - \frac{1}{\rho} \frac{\partial p}{\partial r} + \frac{v^2}{r} + \nu \left(\nabla^2 u - \frac{u}{r^2} \right), \quad (3a)$$

$$\frac{\partial v}{\partial t} = -\frac{1}{r} \frac{\partial(ruv)}{\partial r} - \frac{\partial(vw)}{\partial z} - \frac{uv}{r} + \nu \left(\nabla^2 v - \frac{v}{r^2} \right), \quad (3b)$$

$$\frac{\partial w}{\partial t} = -\frac{1}{r} \frac{\partial(ruw)}{\partial r} - \frac{\partial w^2}{\partial z} - \frac{1}{\rho} \frac{\partial p}{\partial z} + \nu \nabla^2 w. \quad (3c)$$

$$\frac{1}{r} \frac{\partial(ru)}{\partial r} + \frac{\partial w}{\partial z} = 0. \quad (4)$$

In the above, the velocity components are (u, v, w) , corresponding to the (r, θ, z) direction, respectively; p the pressure; and ∇^2 the Laplacian operator.

The initial and boundary conditions for the fluid can be written as

$$u = v = w = 0, \quad \text{for } t < 0, \quad (5a)$$

$$u = w = 0, v = r[\Omega_0 + \epsilon \omega \cos(\omega t)], \text{ on the cylinder sidewall as well as the top and bottom endwall disks for } t \geq 0. \quad (5b)$$

As stated earlier, Ω_0 denotes the mean angular velocity of the system; and ϵ the amplitude and ω the frequency of the sinusoidally-varying disturbance component.

The standard problem of spin-up from rest may be recovered by setting $\epsilon \equiv 0$ in the above formulation. For $\epsilon \neq 0$, the present problem may be interpreted to be a continuous spin-up and spin-down from the state of rotation with an average rotation rate Ω_0 . For the case $\epsilon \equiv 0$, the previous studies (e.g., Wedemeyer, 1964) elaborated that the principal phase of transient fluid motions is accomplished over the spin-up timescale $T \equiv h/(\nu \Omega_0)^{1/2}$. This gives a guidance on the length of time-marching integration of numerical computations.

A finite-difference numerical model, due originally to Warn-Varnas et al. (1978), was applied to integrate the above set of governing equations. This numerical procedure has been validated and utilized for a variety of rotating fluid flows (Warn-Varnas et al., 1978; Hyun et al., 1982; Hyun et al., 1983; Hyun and Kim, 1987). In the present runs, a staggered grid of typically (42×84) mesh points in the $(r \times z)$ plane was adopted. Grid stretching was implemented to cluster grid points near the solid boundaries. The time step Δt was chosen to be sufficiently small so that high-resolution data were secured to assess the principal features of time-evolution. Typically, one period of the perturbation rotation $(2\pi/\omega)$ was resolved by 8 time steps. Extensive convergence tests of grid-interval and time step were carried out, and the outcome indicated that the present schemes produced stable, consistent and accurate numerical results.

In order to verify the numerical results of the present model, quasi-steady periodic solutions for the flow induced by a torsionally-oscillating lid were obtained. These results, in a broad range of relevant parameters, have been compared with the analytical predictions of Rosenblat (1960). These two sets of the results were mutually consistent, which provided credence to the capability of the present model of accurately portraying unsteady rotating flows.

4 Results and Discussion

First, it is necessary to establish that the oscillations in the numerical solutions are indeed the inertial oscillations. For this

purpose, as was done by Aldredge (1977), the classical solution for the inertial oscillation frequencies, Eq. (2), of an inviscid fluid in a state of rigid-body rotation at Ω_0 provides a reference. Guided by the experimental measurements of Aldredge (1977), several sets of time-marching integrations were performed using different values of (Ω_0/ω) in the immediate neighborhood of a value specified by Eq. (2). Since the present system is viscous and is influenced by nonlinearities, the resonance frequencies will not be precisely equal to the values of Eq. (2). The dimensionless pressure difference, as the fluid is fully spun-up, between the cylinder center $(r = 0, z = h/2)$ and the center of the top disk $(r = 0, z = h)$, i.e., $C_p = |\Delta p|/\rho \epsilon \omega^2 R^2$, is plotted against (Ω_0/ω) , encompassing the expected resonance frequency. For all computations in the present study, $E = 5 \times 10^{-6}$, the cylinder aspect ratio $(h/R) = 2.0$, and $\epsilon = 0.06$. Figure 2 displays an exemplary plot of the maximum values of C_p for varying (Ω_0/ω) for the primary mode of oscillation, i.e., the (2, 1) mode. For the (2, 1) mode, which indicates two cells in the axial direction and one cell in the radial direction, Eq. (2) gives $(\Omega_0/\omega) = 0.7873$. Clearly, it is discernible that resonance is manifest, as demonstrated by a sharp increase in C_p , very close to this anticipated value $(\Omega_0/\omega) = 0.7873$. Fig. 2 serves to exemplify the fact that the system triggers inertial oscillations at selected values of (Ω_0/ω) . Also, the accuracy and robustness of the present numerical computations are ascertained by the comparisons shown in Fig. 2. It is found that the bandwidth of frequency ratios (Ω_0/ω) in which C_p shows substantial increases is very narrow so that a rapid decay of the pressure response away from the resonance frequency is seen. As stated earlier, Fig. 2 demonstrates only the enlarged view of the behavior of C_p in the immediate neighborhood of the occurrence of the anticipated primary mode, which is close to $(\Omega_0/\omega) \cong 0.787$. Smaller peaks of C_p will be seen for other discrete value of (Ω_0/ω) , corresponding to higher modes of oscillation.

The detailed time history of the pressure response, as represented by the above-defined C_p , for varying values of (Ω_0/ω) is illustrated in Fig. 3. Similar plots were obtained in Aldredge's experiment, and the present results are closely corroborative of the experimental observations. Each of the pressure traces of Fig. 3 starts from the initial onset of the cylinder rotation ($t = 0$) up to roughly five spin-up timescales $(O[h/(\nu \Omega_0)^{1/2}])$. It is evident that the maximum amplitude of pressure disturbances increases rapidly as the oscillation frequency approaches the resonance frequency for the (2, 1) mode, $(\Omega_0/\omega) \cong 0.78$. It is emphasized that the inertial oscillation frequency given in Eq.

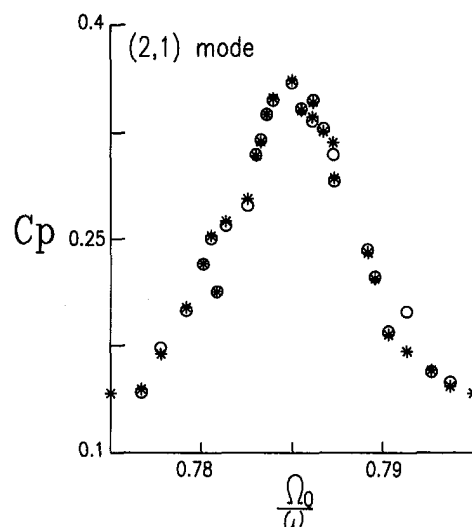


Fig. 2 Plots of maximum values of C_p vs. (Ω_0/ω) for the (2, 1) mode. O, the measurements by Aldredge; *, the present results.

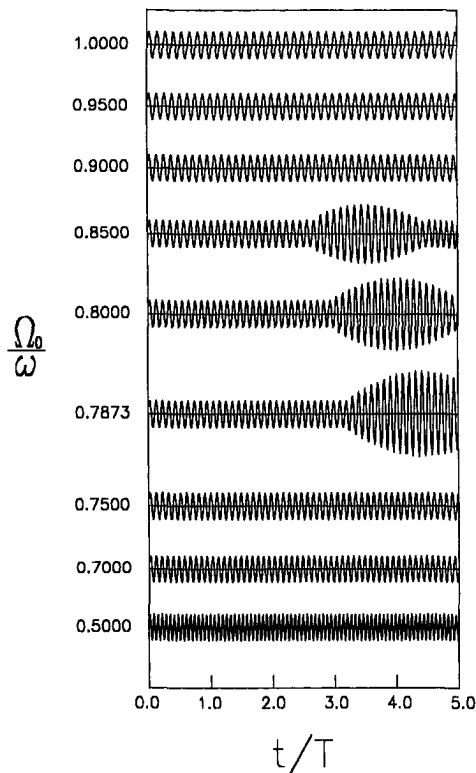


Fig. 3 Time histories of the pressure response near the (2, 1) mode. The ordinate denotes the scaled time t/T .

(2) is strictly based on an inviscid linearized analysis about the state of solid-body rotation at Ω_0 . Notice that the plots of Fig. 3 reveal the transient results in the course of spin-up of the present system, which is viscously-controlled and nonlinear. As is clear in Fig. 3, when (Ω_0/ω) is farther away from the resonance frequency ratio, the pressure response remains virtually unaffected. The amplification of the pressure disturbance in the neighborhood of resonance is visible in Fig. 3, (Ω_0/ω) being centered approximately on 0.80 for maximum response. The onset of the amplification of pressure perturbation is found to be triggered at about 3 spin-up timescales after the switch-on of the system.

For the (2, 2) mode, plots similar to Fig. 3 were constructed and carefully inspected. Of interest is the variation in the time interval t_b between the system switch-on and the beginning of the amplification of the pressure disturbances, as (Ω_0/ω) encompasses a range surrounding the anticipated resonance frequency, $(\Omega_0/\omega) \cong 1.22$. Figure 4 demonstrates such a plot against the normalized time, $\tau_b = t_b/T$. It is obvious that the time shortens as (Ω_0/ω) increases. This finding is consistent with the trend observed in Aldredge's experiment.

As pointed out in previous discussions, for a given set of numerical computation or an experimental run, the value of (Ω_0/ω) is fixed. For each run, namely, for a prescribed value of (Ω_0/ω) , the time t^* , which measures the time duration from the system switch-on until the occurrence of maximal pressure disturbance, is computed by examining the numerical flow data. Figure 5 exemplifies such a plot, i.e., the time interval (t^*) versus the frequency ratio (Ω_0/ω) for the case of the (2, 2) mode. In line with the original presentation of Aldredge's report, the time (t^*) is normalized by the spin-up timescale $T[\equiv h/(\nu\Omega_0)^{1/2}]$, and the negative of this nondimensional time is shown in the argument of the exponential function. Therefore, as time increases, the vertical coordinate of Fig. 5 is scanned from top to bottom. The large-time limit corresponds to the condition on the horizontal axis of Fig. 5. Clearly, at large times

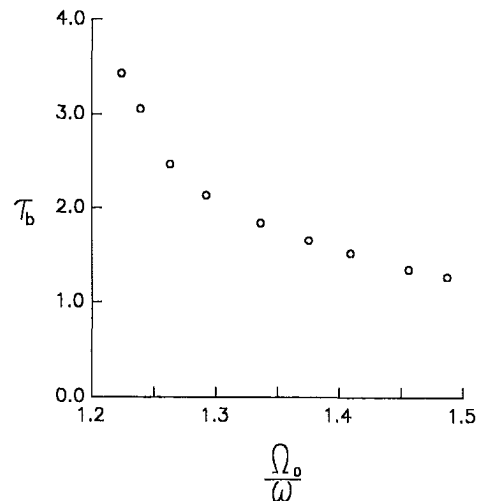


Fig. 4 Scaled time duration τ_b since the system switch-on to the occurrence of the peak pressure for the (2, 2) mode

when the mean-state of the system has been fully spun-up at Ω_0 , the (2, 2) mode of inertial frequency is at $(\Omega_0/\omega) = 1.22$. This value is close to the linearized inviscid prediction based on Eq. (2). As demonstrated in Fig. 5, the present numerical results are in close agreement with the experimental measurements of Aldredge (1977). The analytical solutions of Lynn (1973), based on a strictly linearized inviscid formulation, is also in qualitative consistency with the present results. These exercises establish that the time interval t^* to reach the maximal response of pressure disturbances decreases as (Ω_0/ω) increases.

Figure 6 illustrates the plot of the nondimensional pressure disturbances versus the above-stated time duration t^* . It should be pointed out that Fig. 6 reflects a compilation of a large number of computational sets (or experimental runs), each of which employs different values of (Ω_0/ω) . In other words, the time t^* shown in the horizontal coordinate of Fig. 6, may also be interpreted to signify the corresponding value of (Ω_0/ω) in accordance with the relation $\exp(-t^*/T)$ versus (Ω_0/ω) displayed in Fig. 5. The present numerical data are seen to be in close agreement with the experimental measurements. As indicated in Fig. 6, the pressure perturbation C_p is large for small (Ω_0/ω) , and C_p decreases as (Ω_0/ω) increases.

Several points may be summarized from Figs. 5 and 6. First, it is confirmed that, during the course of system spin-up to $\Omega(t)$, inertial oscillations are indeed triggered at certain selected frequencies. However, since the fluid motions are in a transient developmental stage, for an externally-specified set (Ω_0/ω) , the

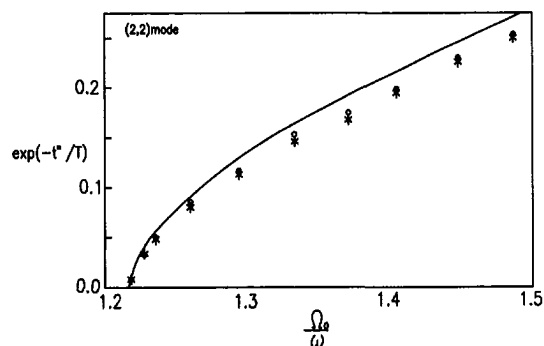


Fig. 5 Variation of the time duration (t^*/T) to reach the occurrence of the peak pressure for the (2, 2) mode. —, the analytic predictions of Lynn; \circ , the measurements of Aldredge; *, the present results.

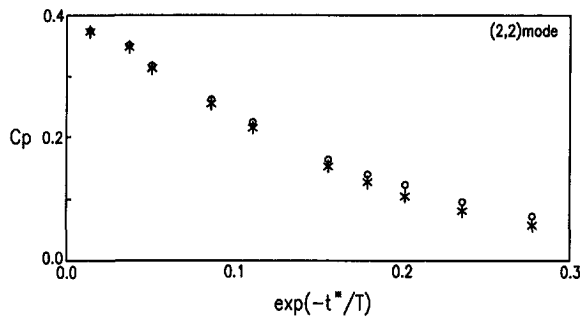


Fig. 6 Dependence of the peak pressure coefficients on the time duration (t^*/T) for the (2, 2) mode. \circ , the measurements of Aldredge; *, the present results.

occurrence of maximal pressure disturbances takes place some time after the system is switched on. This time duration t^* varies with (Ω_0/ω) , and the present numerical results are in close consistency with the prior experimental measurements.

The foregoing discussions to identify resonance have been based on inspecting the pressure responses at discrete selected locations in the fluid. This provides a handy tool to verify the existence of inertial oscillations during the spin-up process to $\Omega(t)$, and this approach was taken in the previous experiments of Aldredge. The advantage of numerical computations lies in the fact that full details of flow data are procured.

Numerically-constructed flow visualizations have been implemented in the present study, which will depict the dynamic features. The meridional flow patterns in the axial plane are illustrated in Fig. 7 for $E = 5 \times 10^{-6}$ and $(h/R) = 2.0$. Plots of the meridional stream function Ψ are displayed. Here, Ψ is defined such that $u = (1/r)\partial\Psi/\partial z$ and $w = (-1/r)\partial\Psi/\partial r$. Figs. 7(a) and (c) exemplify the flow structure under a near-

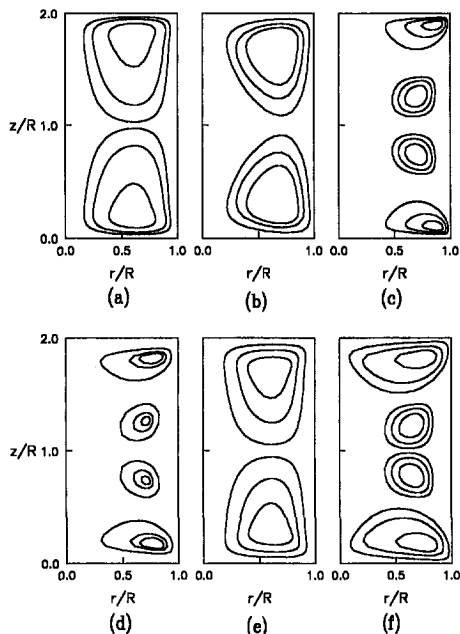


Fig. 7 Typical plots of the meridional stream function Ψ , normalized by $E^{-1/2}\Omega_0 h^2 R$. $\Delta\Psi$ denotes the contour increment. Frames (a), (b) and (e) show the (2, 1) mode, and frames (c), (d) and (f) the (4, 1) mode. Frames (a) and (c) correspond to near-resonance conditions. (a) $\Psi_{\max} = 0.3$, $\Psi_{\min} = -0.3$, $\Delta\Psi = 0.1$, $\Omega_0/\omega = 0.7873$, $t/T = 4.47$; (b) $\Psi_{\max} = 0.015$, $\Psi_{\min} = -0.015$, $\Delta\Psi = 0.005$, $\Omega_0/\omega = 0.5000$, $t/T = 1.0$; (c) $\Psi_{\max} = 0.3$, $\Psi_{\min} = -0.3$, $\Delta\Psi = 0.1$, $\Omega_0/\omega = 0.5847$, $t/T = 2.5$; (d) $\Psi_{\max} = 0.015$, $\Psi_{\min} = -0.015$, $\Delta\Psi = 0.005$, $\Omega_0/\omega = 0.8000$, $t/T = 1.5$; (e) $\Psi_{\max} = 0.015$, $\Psi_{\min} = -0.015$, $\Delta\Psi = 0.005$, $\Omega_0/\omega = 0.7873$, $t/T = 1.0$; (f) $\Psi_{\max} = 0.015$, $\Psi_{\min} = -0.015$, $\Delta\Psi = 0.005$, $\Omega_0/\omega = 0.5847$, $t/T = 3.5$.

resonance condition [$t/T = 4.47$, $(\Omega_0/\omega) = 0.7873$] for the (2, 1) mode, and [$t/T = 2.5$, $(\Omega_0/\omega) = 0.5847$] for the (4, 1) mode, respectively. As remarked earlier, the flow for the (2, 1) mode is characterized by two cells in the cylinder, while four cells are seen for the (4, 1) mode. Similar pictures are exhibited in Figs. 7(b) and 7(d) under off-resonance conditions [$t/T = 1.0$, $(\Omega_0/\omega) = 0.50$] for the (2, 1) mode and [$t/T = 1.5$, $(\Omega_0/\omega) = 0.80$] for the (4, 1) mode, respectively. The times at which the contours are displayed are chosen which would reveal maximum values of the stream function. The flow structures in Fig. 7 demonstrate that, as the resonance condition is approached, the global flows are intensified to occupy bigger regions of the cylinder and the maximum value of the stream function increases substantially. Under off-resonance conditions, the extent of meridional flow is reduced. Note that in Fig. 7, the magnitudes of Ψ are of different orders, which indicates enormous amplifications of flows under resonance conditions. As remarked earlier, these quantitative results serve to underscore the immense magnification of fluid motions when the system is properly tuned, i.e., when the externally-specifiable frequency ratio (Ω_0/ω) is close to the resonance condition. The symmetry of flow with respect to the cylinder mid-depth is maintained, as exhibited in the flow depictions of Fig. 7. It is worth mentioning that, since the present system is transient in nature, a proper tuning requires a correct frequency ratio (Ω_0/ω) as well as a compatible timing. Figures 7(e) and 7(f) demonstrate the weakening of the meridional flows when the appropriate resonance timings are not realized.

The numerical results are rearranged to depict the temporal evolution of C_p for varying values of (Ω_0/ω) . Figure 8 is qualitatively consistent with the conceptualization of Aldredge (1977).

It is of interest to assess the changes in the physical flow variables that are manifested due to the time-dependent fluid motions. For this purpose, the amplitude of the oscillating component of the total angular momentum of the fluid in the cylinder is considered. In technological applications, this information is useful in specifying the proper size and the operating range of the drive motor. The amplitude of the oscillating part of the angular momentum may be evaluated as $M = 2\pi\rho \int_0^h \int_0^R v_{oc} r^2 dr dz$, where v_{oc} denotes the amplitude of the oscillating component of the azimuthal velocity. Figure 9 displays the behavior of M for the (2, 1) mode, normalized by $M_0 \equiv 2\pi\rho R^4 \Omega_0 h$. As clearly demonstrated in Fig. 9, for a given set of (Ω_0/ω) , the substantial augmentation of the oscillating component of the total angular momentum of the fluid is discernible

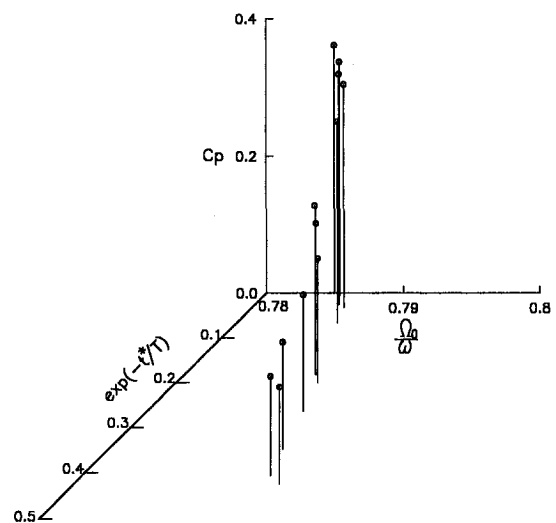


Fig. 8 Temporal evolution of C_p for varying values of Ω_0/ω

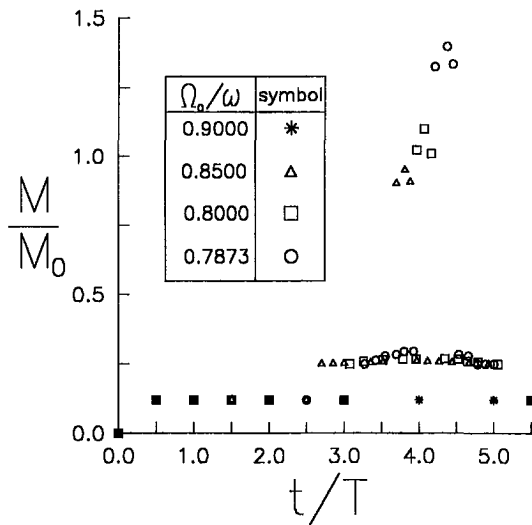


Fig. 9 Time-dependent behavior of the amplitude of the oscillating component of the total angular momentum, M , for the mode (2, 1)

at the instant specified by t^* in the previous plots. In other words, the oscillating part of the angular momentum of the fluid system is greatly intensified when resonance is triggered around the time t^* for the corresponding value of the inertial frequency ω for a given value of Ω_0 . The intensification of fluid motions, as exemplified by the increase of the fluid angular momentum, becomes more conspicuous as the resonance condition is more closely satisfied.

Finally, the changes in the time-dependency of the eigenfrequencies, as shown in the $t^* - (\Omega_0/\omega)$ plots, are displayed in Figs. 10 and 11 for different modes. Obviously, the individual cell size is smaller for the (4, 2) mode than (2, 1) mode. The present numerical results are seen to be in close agreement with the measurements of Aldredge, although appreciable departures are noticed between these results and the analytical predictions of Lynn. As time elapses, inertial oscillations of higher frequencies, i.e., (Ω_0/ω) being smaller for a fixed Ω_0 , are excited when a mode of higher-order cells is considered.

5 Conclusions

Numerical solutions of the governing axisymmetric, time-dependent Navier-stokes equations point to the existence of inertial oscillations at selected frequencies (Ω_0/ω) . The pres-

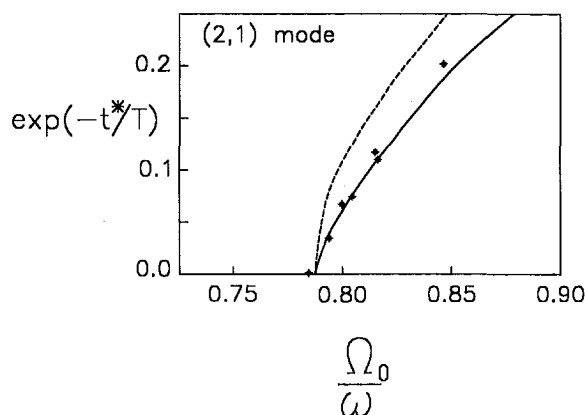


Fig. 10 Time dependence of the inertial frequencies for the (2, 1) mode. ---, the analytic prediction by Lynn; \oplus , the measurements by Aldredge; —, the present results.

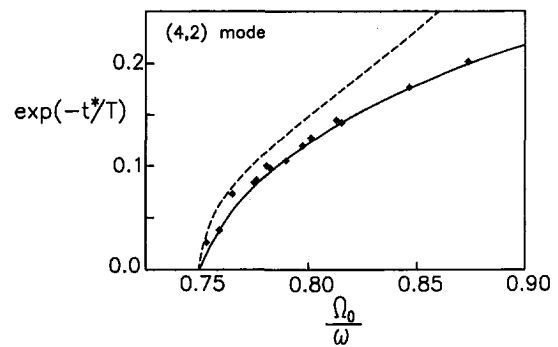


Fig. 11 Same as in Fig. 10 except for the (4, 2) mode

ence of a peak value of C_p leads to the identification of the resonance frequency (Ω_0/ω) .

In the course of spin-up to the system rotation rate $\Omega(t)$, the numerical solutions yield the time history of C_p for a given value of (Ω_0/ω) . The time duration up to the onset of pressure disturbance amplification is seen to decrease as (Ω_0/ω) increases for a given mode. Also, the time interval t^* until the maximal pressure disturbance occurs decreases as (Ω_0/ω) increases. These results on time-dependent inertial frequencies are consistent with the preceding experimental observations. The pressure perturbation, as expressed by C_p , increases as (Ω_0/ω) decreases for a given mode.

Flow visualizations have been obtained based on the numerical data. The meridional flow patterns indicate that, as the resonance conditions are approached, immense intensifications of the fluid motions occur.

Acknowledgment

Appreciation is extended to the referees who provided constructive and helpful comments. This work was supported in part by a research grant from the Samsung Electronics, Korea.

References

- Aldredge, K. D., 1977, "Axisymmetric Inertial Oscillations of a Fluid in a Cylindrical Cavity during Spin-up from Rest," *Geophys. Astrophys. Fluid Dynamics*, Vol. 8, pp. 279–301.
- Choi, S., Kim, J. W., and Hyun, J. M., 1989, "Transient Free Surface Shape in an Abruptly-Rotating, Partially-Filled Cylinder," *ASME JOURNAL OF FLUIDS ENGINEERING*, Vol. 111, pp. 431–439.
- Choi, S., Kim, J. W., and Hyun, J. M., 1991, "Experimental Investigation of the Flow with a Free Surface in an Impulsively Rotating Cylinder," *ASME JOURNAL OF FLUIDS ENGINEERING*, Vol. 113, pp. 245–249.
- Fowles, W. W., and Martin, P. J., 1975, "A Rotating Laser Doppler Velocimeter and Some New Results on the Spin-up Experiment," *Geophys. Fluid Dynam.*, Vol. 7, pp. 67–72.
- Greenspan, H. P., 1968, *The Theory of Rotating Fluids*, Cambridge University Press, Cambridge.
- Hall, P., Sedney, R., and Gerber, N., 1990, "Dynamics of the Fluid in a Spinning Coning Cylinder," *AIAA Journal*, Vol. 28, No. 5, pp. 828–835.
- Herbert, Th., and Li, R., 1990, "Computational Study of the Flow in a Spinning and Nutating Cylinder," *AIAA Journal*, Vol. 28, No. 9, pp. 1596–1604.
- Hyun, J. M., Fowles, W. W., and Warn-Varnas, A., 1982, "Numerical Solutions for the Spin-up of a Stratified Fluid," *Journal of Fluid Mechanics*, Vol. 117, pp. 71–90.
- Hyun, J. M., 1983, "Spin-up from Rest in a Differentially Rotating Cylinder," *AIAA Journal*, Vol. 21, No. 9, pp. 1278–1282.
- Hyun, J. M., Leslie, F., Fowles, W. W., and Warn-Varnas, A., 1983, "Numerical Solutions for Spin-up from Rest in a Cylinder," *Journal of Fluid Mechanics*, Vol. 127, pp. 263–281.
- Hyun, J. M., and Kim, J. W., 1987, "Flow Driven by a Shrouded Spinning Disk with Axial Suction and Radial Inflow," *Fluid Dynamic Research*, Vol. 2, pp. 175–182.
- Kim, J. W., and Hyun, J. M., 1995, "Propagation of the Velocity Shear Front in Spin-up from Rest in a Cut-cone," *ASME JOURNAL OF FLUIDS ENGINEERING*, Vol. 117, No. 1, pp. 58–61.

Kitchen, C. W. Jr., 1980, "Navier-Stokes Equations for Spin-up in a Filled Cylinder," *AIAA Journal*, Vol. 18, pp. 929-934.

Lynn, Y. M., 1973, "Free Oscillations of a Liquid during Spin-up," USA Ballistic Research Laboratories, Report No. 1663.

Rogers, M. H., and Lance, G. N., 1960, "The Rotationally Symmetric Flow of a Viscous Fluid in the Presence of an Infinite Rotating Disk," *Journal of Fluid Mechanics*, Vol. 7, pp. 617-637.

Rosenblat, S., 1960, "Flow between Torsionally Oscillating Disks," *Journal of Fluid Mechanics*, Vol. 6, pp. 388-399.

Warn-Varnas, A., Fowles, W. W., Piacsek, S., and Lee, S. M., 1978, "Numerical Solutions and Laser-Doppler Measurements of Spin-up," *Journal of Fluid Mechanics*, Vol. 85, pp. 609-639.

Watkins, W. B., and Hussey, R. G., 1977, "Spin-up from Rest in a Cylinder," *Physics of Fluids*, Vol. 20, pp. 1596-1604.

Wedemeyer, E. H., 1964, "The Unsteady Flow within a Spinning Cylinder," *Journal of Fluid Mechanics*, Vol. 20, pp. 383-399.

Weidman, P. D., 1976, "On the Spin-up and Spin-down of a Rotating Fluid. Part I: Extending the Wedemeyer Model. Part II: Measurements and Stability," *Journal of Fluid Mechanics*, Vol. 77, pp. 685-735.

A Numerical Study on Motion of a Sphere Coated With a Thin Liquid Film at Intermediate Reynolds Numbers

S. Kawano
Associate Professor.

H. Hashimoto¹
Professor Emeritus.

Institute of Fluid Science,
Tohoku University,
2-1-1 Katahira, Aoba-ku,
Sendai 980-77, Japan

The steady viscous flow past a sphere coated with a thin liquid film at low and intermediate Reynolds numbers ($Re \leq 200$) was investigated numerically. The influences of fluid physical properties, film thickness, and Reynolds number on the flow pattern were clarified. Temperature field around the compound drop was also analyzed. The strong dependence of flow pattern on the characteristics of heat transfer was recognized. The empirical equation of the drag coefficient for the compound drop was proposed. Furthermore, the explicit adaptability of the drag coefficient equation for a gas bubble, a liquid drop, and a rigid sphere in the range of Reynolds number $Re \leq 1000$ was confirmed.

Introduction

The compound multiphase drops have received considerable attention because they could be applied to direct-contact heat exchanger or liquid membrane technology (Johnson and Sadhal, 1985). The ultimate goal of this study is to produce sequentially millimeter-sized multilayer rigid shells or balls by solidifying the compound drops, which could be applied to high functional medicines, foods, solid fuels, artificial organs, compound structural materials, energy storage systems and so on (Lee et al., 1986). The sequential production of millimeter-sized gas-liquid compound drops, which were named as liquid shells or as encapsulated drops, was investigated using the liquid-liquid-gas system shown in Fig. 1(a) (Hashimoto and Kawano, 1990). Spherical rigid shells with millimeter-sized diameter were produced sequentially by solidifying the liquid shells based on the control of the injection gas flow rate, the liquid physical properties and the temperature of liquid field in the liquid-liquid-gas system (Kawano et al., 1996). Furthermore, the liquid-solid compound drops with millimeter-sized diameter could be produced by the system shown in Fig. 1(b). When a rigid ball passed through the liquid-liquid interface, the upper liquid material (liquid 1) surrounded the ball as a spherical layer under the specific conditions of the ball inertia force and the physical properties of two liquids. On the other hand, the multilayer rigid shells or balls with micrometer-sized diameter, which were called as microcapsules, could be produced in mass production by controlling the interfacial polymerization or the coacervation in the physicochemical method (Kondo and Koishi, 1981; Yadav et al., 1990). The liquid films covering the solid spheres in this microencapsulation process played a role to protect the core material from mechanical and chemical damage. Some kinds of microcapsules had been commercialized already.

The drag coefficient of a multiphase compound drop is one of the most basic design data for predicting the terminal velocity in these practical applications. There are several theoretical reports on the drag for the case of completely engulfed drops (Rushon and Davies, 1983; Sadhal and Oguz, 1985; Oguz and Sadhal, 1987) or for the case of partially engulfed drops

(Johnson, 1981; Sadhal and Johnson, 1983; Johnson and Sadhal, 1983; Vuong and Sadhal, 1989). However, they were applied only in a creeping flow and were not useful for a flow with higher velocity in such industrial applications as described above because they were done based on the Stokes' approximate theory. For the production of compound drops in the system shown in Fig. 1 or in some microencapsulation processes, it is obviously necessary to investigate the effect of finite-Reynolds-number flow on the drag.

As the first step to investigate the motion of multiphase compound drops, the present paper dealt with a liquid-solid compound drop, that is, a rigid sphere completely coated with a thin liquid film. The steady, viscous and incompressible flow past the compound drop at low and intermediate Reynolds numbers ($Re \leq 200$) was analyzed numerically by the computational code developed here. The heat transfer characteristics were also analyzed under the conditions of the constant rigid sphere temperature and constant fluid physical properties. The flow and thermal patterns were also made clear for the various flow conditions. The drag coefficient and the mean Nusselt number of the compound drop were quantitatively investigated. The present research would provide the fundamental knowledge and important design data for the sequential production of multilayer rigid balls.

Mathematical Model

The schematic of a liquid-solid compound drop (inner radius R and outer radius ζ') and coordinates system are shown in Fig. 2. The compound drop in a uniform stream (velocity U , temperature T_∞) of an immiscible fluid (phase 2) is assumed to be a rigid sphere completely coated with a thin liquid film (phase 1). In the limit of the thin coating liquid film and the large interface tension, the outer interface of liquid film is assumed to be concentric with the inner rigid sphere. The inner rigid sphere is assumed to have constant temperature T_w and the heat generation by friction is assumed to be negligibly small. The physical properties of fluids are also assumed to be constant. These assumptions are rather crude, but the data of drag coefficient or mean Nusselt number obtained here seem to be practical enough for some industrial applications for the cases of relatively small radius ratio $\zeta (= \zeta'/R)$, large outer interface tension, and small difference between T_∞ and T_w .

¹ Presently, Ebara Research Co., Ltd., 2-1 Honfujisawa 4-chome, Fujisawa-shi 251, Japan.

Contributed by the Fluids Engineering Division for publication in the JOURNAL OF FLUIDS ENGINEERING. Manuscript received by the Fluids Engineering Division November 28, 1995; revised manuscript received November 23, 1996. Associate Technical Editor: S. P. Vanka.

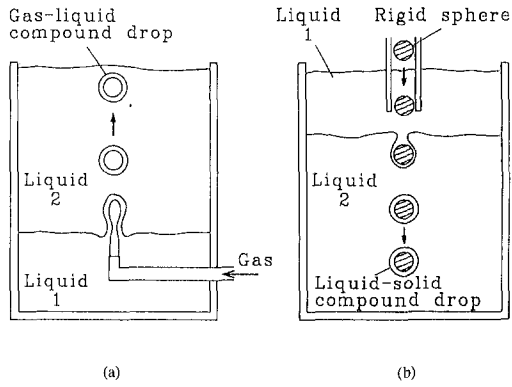


Fig. 1 Sequential compound drop production device. (a) Gas-liquid compound drop; (b) liquid-solid compound drop

The Navier-Stokes equations for steady, viscous, incompressible and axisymmetric flow in terms of the stream function ψ_i and vorticity ω_i are written in spherical coordinates as follows:

$$E^2 \psi_i = \omega_i r \cdot \sin \theta, \quad (1)$$

$$\frac{\hat{R}e_i}{2} \left\{ \frac{\partial \psi_i}{\partial r} \cdot \frac{\partial}{\partial \theta} \left(\frac{\omega_i}{r \cdot \sin \theta} \right) - \frac{\partial \psi_i}{\partial \theta} \cdot \frac{\partial}{\partial r} \left(\frac{\omega_i}{r \cdot \sin \theta} \right) \right\} \sin \theta = E^2 (\omega_i r \cdot \sin \theta), \quad (2)$$

where

$$E^2 = \frac{\partial^2}{\partial r^2} + \frac{\sin \theta}{r^2} \cdot \frac{\partial}{\partial \theta} \left(\frac{1}{\sin \theta} \cdot \frac{\partial}{\partial \theta} \right), \quad (3)$$

$\hat{R}e_i$ is rigid sphere Reynolds number defined in Eq. (6), and subscript i is equal to 1 or 2 and indicates phase 1 or phase 2, respectively. The continuity equations are automatically satisfied by introducing ψ_i . The velocity components V_i are related to ψ_i in the following equations:

$$V_{r,i} = \frac{-1}{r^2 \cdot \sin \theta} \cdot \frac{\partial \psi_i}{\partial \theta}, \quad V_{\theta,i} = \frac{1}{r \cdot \sin \theta} \cdot \frac{\partial \psi_i}{\partial r}, \quad (4)$$

where subscripts r and θ indicate the radial direction and the tangential direction, respectively. The time-dependent energy equations are expressed as follows:

$$\frac{\partial T_i}{\partial t} + V_{r,i} \frac{\partial T_i}{\partial r} + \frac{V_{\theta,i}}{r} \cdot \frac{\partial T_i}{\partial \theta} = \frac{2}{\hat{R}e_i \cdot Pr_i} \cdot \frac{1}{r^2} \left\{ \frac{\partial}{\partial r} \left(r^2 \frac{\partial T_i}{\partial r} \right) + \frac{1}{\sin \theta} \cdot \frac{\partial}{\partial \theta} \left(\sin \theta \frac{\partial T_i}{\partial \theta} \right) \right\}, \quad (5)$$

where T_i is temperature, t is time and Pr_i is Prandtl number defined in Eq. (6). All quantities have been made dimensionless using the following forms:

$$r = \frac{r'}{R}, \quad \zeta = \frac{\zeta'}{R}, \quad \psi_i = \frac{\psi'_i}{UR^2}, \quad \omega_i = \frac{\omega'_i R}{U}, \quad V_i = \frac{V'_i}{U},$$

$$\hat{R}e_i = \frac{2R\rho_i U}{\mu_i}, \quad Pr_i = \frac{c_{pi} \mu_i}{k_i},$$

$$T = \frac{T' - T_\infty}{T_w - T_\infty}, \quad t = \frac{t' U}{R}, \quad (6)$$

where c_{pi} is specific heat, k_i is thermal conductivity, μ_i is viscosity and ρ_i is density, and an apostrophe means a given value with dimension.

The boundary conditions are expressed as follows.

(1) Freestream condition at $r \rightarrow \infty$:

$$\frac{\psi_2}{r^2} \rightarrow \frac{1}{2} \sin^2 \theta \quad (7)$$

$$T_2 \rightarrow 0 \quad (T' = T_\infty) \quad (8)$$

(2) Conditions at the outer interface of the compound drop ($r = \zeta$):

Zero radial velocity

$$\frac{\partial \psi_1}{\partial r} = \frac{\partial \psi_2}{\partial r} = 0 \quad (9)$$

Continuity of tangential velocity

$$\frac{\partial \psi_1}{\partial r} = \frac{\partial \psi_2}{\partial r} \quad (10)$$

Continuity of tangential stress

$$\frac{\partial}{\partial r} \left(\frac{1}{r^2} \cdot \frac{\partial \psi_2}{\partial r} \right) = \kappa \frac{\partial}{\partial r} \left(\frac{1}{r^2} \cdot \frac{\partial \psi_1}{\partial r} \right) \quad (11)$$

Continuity of temperature

$$T_1 = T_2 \quad (12)$$

Continuity of heat flow

$$\frac{\partial T_2}{\partial r} = \lambda \frac{\partial T_1}{\partial r} \quad (13)$$

(3) Conditions at the inner interface between the liquid shell and the rigid sphere ($r = 1$):

Non-slip condition

$$\frac{\partial \psi_1}{\partial r} = \frac{\partial \psi_1}{\partial \theta} = 0 \quad (14)$$

Uniform wall temperature

$$T_1 = 1 \quad (T' = T_w) \quad (15)$$

(4) Condition at the axis of symmetry at $\theta = 0, \pi$:

$$\psi_i = \omega_i = \frac{\partial T_i}{\partial \theta} = 0 \quad (16)$$

Dimensionless parameters $\kappa (= \mu_1/\mu_2)$ and $\lambda (= k_1/k_2)$ represent the viscosity ratio and thermal conductivity ratio, respectively. In this paper, compound drop Reynolds number $Re (= 2\zeta' \rho_2 U/\mu_2)$, ζ , κ , density ratio $\gamma (= \rho_1/\rho_2)$, Pr_1 , Pr_2 , and λ are the fundamental dimensionless parameters.

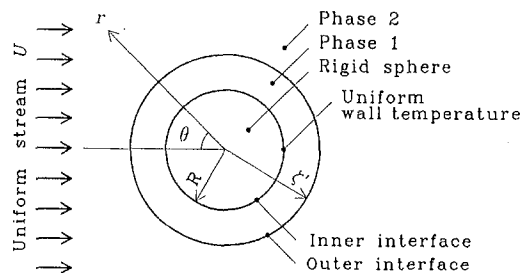


Fig. 2 Schematic of liquid-solid compound drop

Numerical Method

An exponential grid size in the radial direction was used by employing the substitution $r = \exp(Z)$ and taking equal intervals in Z . After this transformation, Eqs. (1) and (2) were rewritten as finite difference equations using the centered spatial differences of second-order accuracy and were solved by the successive overrelaxation method. Equation (5) was also rewritten using the centered spatial differences of second-order and the backward time differences of second-order. Equation (5) was also solved by the alternate direction iterative method. This numerical code for T_i was developed based on the multipoint implicit method.

In the mesh system, the radial step size for Z was 0.0125, the angular step size was 1.5 degrees and the dimensionless position of the outer boundary was 54.6 which corresponded to $r = \infty$. The iteration procedure was repeated until variations of ψ_i , ω_i and T_i per iteration became less than a specified tolerance. The tolerance was chosen to be 0.0001 for ψ_i , ω_i , and 0.00001 for T_i . The time step for T_i was 0.01. The initial condition ($t = 0$) for T_i is subjected as follows:

$$\begin{cases} T_i = 0 & \text{at } r > 1 \\ T_i = 1 & \text{at } r = 1 \end{cases} \quad (17)$$

As the preliminary calculations, the flow and thermal patterns around a gas bubble, a liquid drop and a rigid sphere in $Re \leq 200$ were obtained applying the present numerical code. The data of streamlines, drag coefficient, thermal patterns and heat transfer coefficient agreed well with the previous well-used data

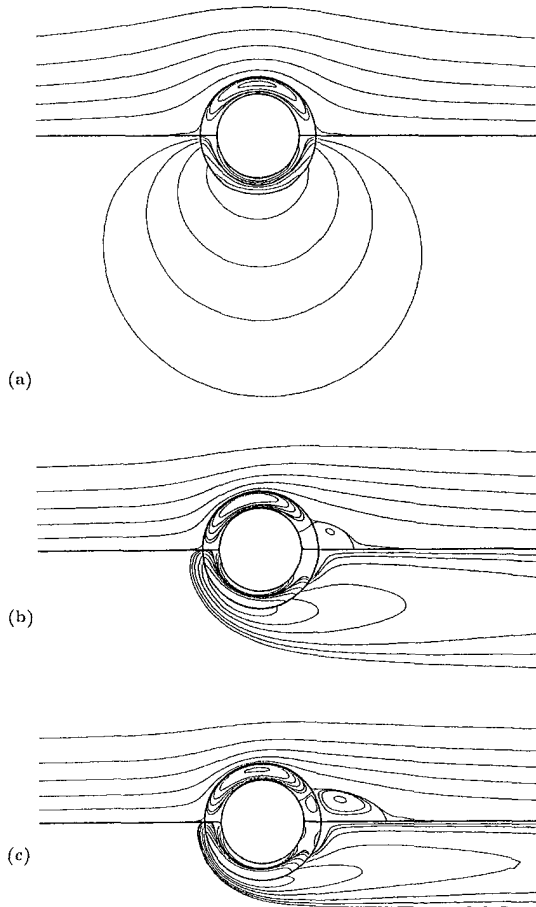


Fig. 3 Streamlines (upper half) and iso-vorticity lines (lower half) for various Re at $\zeta = 1.4$, $\kappa = 0.592$ and $\gamma = 1.21$. (Flow direction is left to right.) (a) $Re = 0.14$; (b) $Re = 70$; (c) $Re = 200$

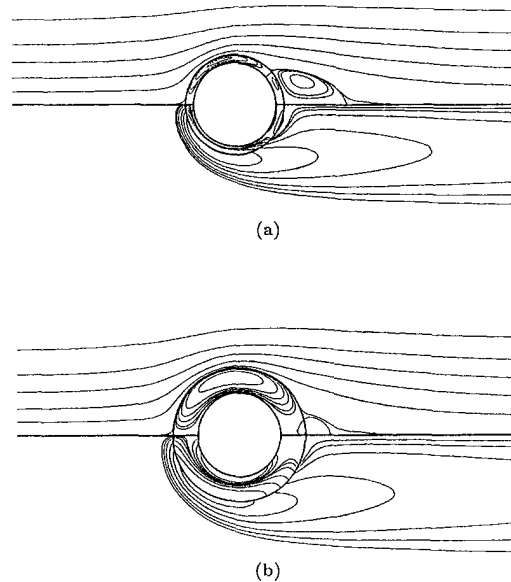


Fig. 4 Streamlines (upper half) and iso-vorticity lines (lower half) for various ζ at $Re = 100$, $\kappa = 0.592$ and $\gamma = 1.21$. (Flow direction is left to right.) (a) $\zeta = 1.2$; (b) $\zeta = 1.6$

(Clift et al., 1978). The validity of the present numerical code for the case of compound drop was also examined, where it is described below as a part of the discussions.

Numerical Results and Discussion

Flow Past a Compound Drop. Figure 3 shows the sample of streamlines (upper half) and iso-vorticity lines (lower half) for various Re . The values of ψ_i are equal to -5×10^p , -2×10^p , -1×10^p , 0, 0.0002, 0.05, 0.2, 0.5, 1 and 2, where the coefficient of the exponent p is equal to -3 or -2 . The values of ω_i are equal to -0.2 , 0, 0.01, 0.05, 0.1, 0.2, 0.5, 1, and 2. The flow direction is left to right. The values of κ and γ are decided by considering that the phase 1 is distilled water and the phase 2 is kerosene. Increase of Re corresponds to the practical situation that the compound drop velocity, the radius or the phase 2 density increases or that the phase 2 viscosity decreases. Generally, the sequential production of millimeter-sized or larger sized compound drop with relatively high moving velocity is difficult although such compound drop is desirable for the functional applications as described above. At small Re ($Re = 0.14$), symmetry versus upstream and downstream is apparent in the streamlines and the iso-vorticity lines. As Re increases (for example, $Re = 70$), the vorticity is convected downstream and the separation appears. The center of strong eddy in spherical phase 1 layer, which is in the clockwise direction and is named as eddy 1, is moved upstream. At $Re = 200$, another internal weak eddy, which is in the counterclockwise direction and is named as eddy 2, appears in phase 1 beside the external wake. The center of eddy 1 moves downstream compared with the case of $Re = 70$. As Re increases, the wake length L' becomes larger and the separation angle θ_s of the external flow decreases. The effects of Re on L' and θ_s have the same qualitative tendency as the flow past a rigid sphere (Pruppacher et al., 1970). Figure 4 shows the flow patterns for various ζ . Small ζ corresponds to the practical situation of thin shell thickness in comparison with the inner radius of compound drop. The effects of ζ on the flow patterns, the drag coefficient and the heat transfer coefficient are the fundamental knowledge because the control of ζ in the production process of compound drop is very important for the practical applications. As ζ increases, the center of eddy 1 moves downstream, L' becomes small, and θ_s becomes large. The reason for these phenomena

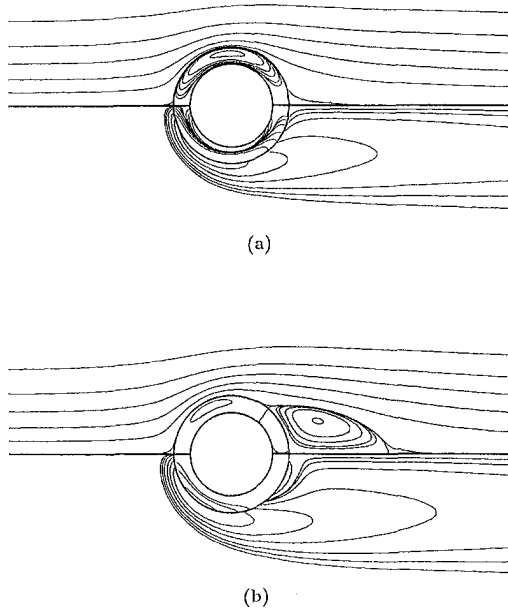


Fig. 5 Streamlines (upper half) and iso-vorticity lines (lower half) for various κ at $Re = 100$, $\zeta = 1.4$ and $\gamma = 1.21$. (Flow direction is left to right.) (a) $\kappa = 0.3$; (b) $\kappa = 30$

is that a mobility (that is, the velocity of outer interface due to the external main flow) of phase 1 may become large as ζ increases and that the mobility of the outer interface may prevent the development of a boundary layer in the external flow. The much larger ζ case is not so practical because it is difficult to maintain the concentricity of compound drop interfaces owing to the effects of gravity and the phase 1 flow. Figure 5 shows the flow patterns for various κ . Large κ corresponds to the practical situation of large phase 1 viscosity or small phase 2 viscosity. In our developed production device of gas-liquid compound drop shown in Fig. 1(a), the relatively large liquid 1 (phase 1) viscosity is required (Hashimoto and Kawano, 1990; Kawano et al., 1996) for stable production. This tendency must be the same in the device shown in Fig. 1(b). At very small κ ($\kappa = 0.3$), there is no separation because the phase 1 layer moves easily (large mobility). At very large κ ($\kappa = 30$), the internal eddy becomes weak, $L (=L'/2\zeta')$ is 0.861 and θ_S is 126 degrees. These values are almost the same as those in the experimental and numerical results of the flow past a rigid sphere (Pruppacher et al., 1970). Figure 6 shows the flow patterns for various γ . Large γ corresponds to the practical situation of large phase 1 density or small phase 2 density. The value of γ depends on the production technique of compound drop and the density of the core material. At small γ ($\gamma = 0.3$), an external attached wake and two internal eddies appear. As γ increases, the wake becomes small and the center of eddy 1 moves downstream because the phase 1 inertia force increases with γ .

Heat Transfer. Figure 7 shows the sample of time-dependent isothermal patterns, $T_i = 0.1n$ ($n = 1 \sim 10$). The values of Pr_1 , Pr_2 , and λ are decided by considering that the phase 1 is distilled water and the phase 2 is kerosene (at 360 K). From Fig. 7, high temperature region is convected downstream from the point close to the flow separation. In Fig. 7(c), the pseudo-steady state seems to be achieved. This state means that the temperature gradient at both inner and outer interfaces reaches the constant value (tolerance is 0.0001 per time step). We will discuss the pseudo-steady state below. Figure 8 shows the variation of local Nusselt number Nu with θ for various Re . Nu is defined as

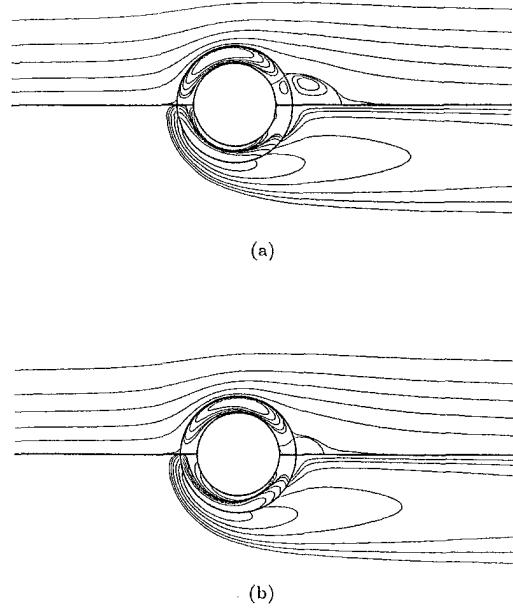


Fig. 6 Streamlines (upper half) and iso-vorticity lines (lower half) for various γ at $Re = 100$, $\zeta = 1.4$ and $\kappa = 0.592$. (Flow direction is left to right.) (a) $\gamma = 0.3$; (b) $\gamma = 10$

$$Nu = \frac{2Rq}{k_1(T_w - T_\infty)} = -2 \left(\frac{\partial T_1}{\partial Z} \right)_{Z=0} \quad (18)$$

Here, q is denoted as the local heat flux at $r = 1$. In $Re \leq 14$, Nu decreases with θ . On the other hand, in $Re \geq 70$, Nu has a maximum value around the separation angle. This remarkable change of Nu for change of Re corresponds obviously to the change of flow structure shown in Fig. 3, that is, eddies 1 and 2 become strong. The maximum of Nu increases with Re . Nu may be also effected strongly by the separation angle. Nu in

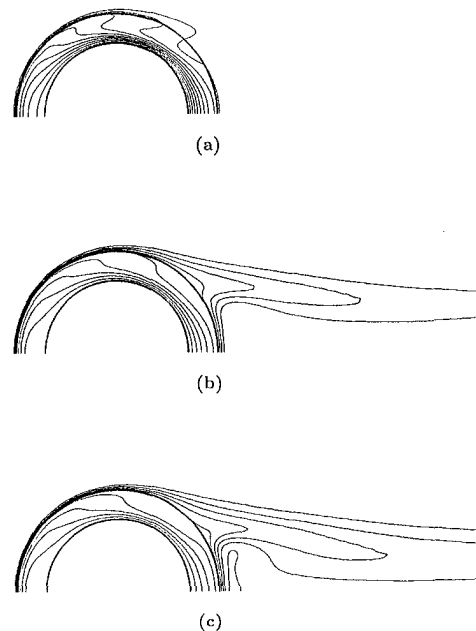


Fig. 7 Time-dependent isothermal pattern at $Re = 200$, $\zeta = 1.4$, $\kappa = 0.592$, $\gamma = 1.21$, $Pr_1 = 2.06$, $Pr_2 = 13.6$ and $\lambda = 6.33$. (Flow direction is left to right. Inner rigid sphere has uniform high temperature, and freestream has uniform low temperature.) (a) $t = 10$; (b) $t = 30$; (c) $t = 54.9$

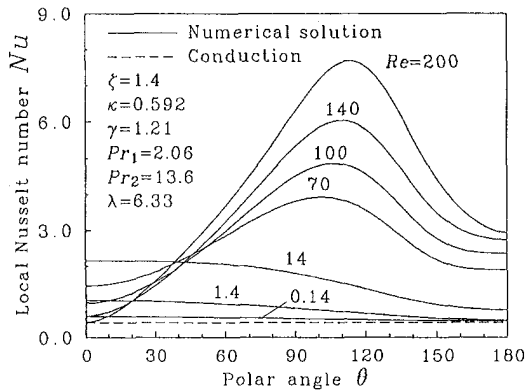


Fig. 8 Variation of Nu with θ for various Re

the heat conduction is derived analytically as $Nu = 2\zeta/(\lambda + \zeta - 1)$. When $Re \rightarrow 0$, the numerical solution approaches the analytical solution ($Nu = 0.416$). Figure 9 shows the variation of mean Nusselt number Nu_m with Re. Nu_m is defined as

$$Nu_m = - \int_0^\pi \left(\frac{\partial T_1}{\partial Z} \right)_{z=0} \sin \theta \cdot d\theta. \quad (19)$$

When $Re \rightarrow 0$, the numerical solution approaches the analytical solution ($Nu_m = 2\zeta/(\lambda + \zeta - 1) = 0.416$). In Fig. 9, the dash-dotted line shows the mean Nusselt number for a rigid sphere ($Nu_m = 2 + 0.6 Re^{1/2} Pr_2^{1/3}$) obtained by Ranz and Marshall (1952). In the case of compound drop, Nu_m is smaller than that for the rigid sphere. The reason is that the spherical phase 1 layer prevents heat transfer. On the other hand, the statistical curve obtained from the numerical data at the conditions in Fig. 9 is expressed as

$$Nu_m = 0.416 + 0.334 \cdot Re^{1/2}. \quad (20)$$

The deviation between Eq. (20) and the numerical data is from -1.42 to 6.86 percent. Figure 9 suggests that the Nu_m is approximately expressed in a function of $Re^{1/2}$ and that the tendency is very similar to a rigid sphere. Figure 10 shows the variations of Nu_m with ζ , κ and γ . The plots in the figure indicate the numerical solutions. Because the convection effect becomes large as the mobility and inertia force of phase 1 become large, Nu_m increases as ζ and γ increase or as κ decreases. Figure 11 shows the variations of Nu_m with Pr_1 , Pr_2 and λ . Large Pr corresponds to the practical situation of large specific heat, large viscosity or small thermal conductivity. Generally, the molten metals have small Pr, where the metallic compound drop have

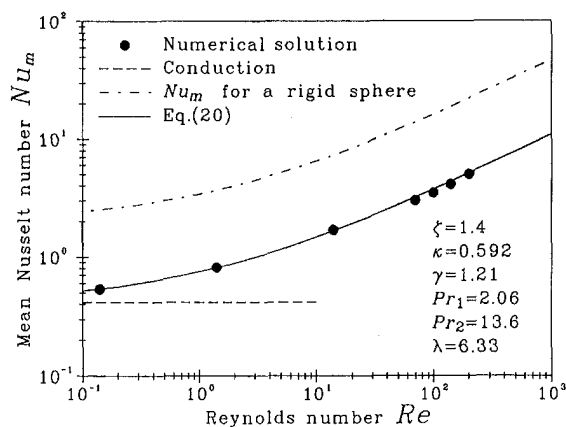


Fig. 9 Variation of Nu_m with Re

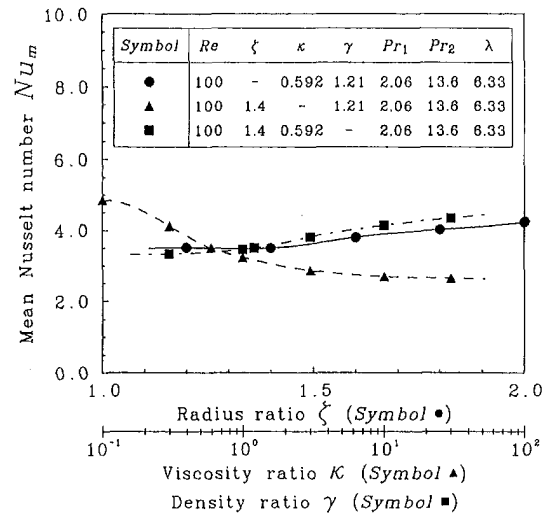


Fig. 10 Variations of Nu_m with ζ , κ and γ

a lot of industrial applications, and most of oils have large Pr, which are often used as liquid 2 in the device shown in Fig. 1(a) (Kawano et al., 1996). Large λ corresponds to the practical situation of large phase 1 thermal conductivity or small phase 2 one. In the production of compound drop made of molten metals using the device shown in Fig. 1, the λ becomes large. In Fig. 11, because the thermal boundary layer thickness in both phase 1 and 2 becomes thin as Pr increases, the temperature gradient at the inner interface, which corresponds to Nu_m , increases as Pr increases. Furthermore, because the temperature gradient of phase 1 at outer interface becomes larger rather than that of phase 2 as λ decreases, Nu_m increases as λ decreases for the case of relatively small ζ . These discussions are introduced for a special physical property model, but it is very important to estimate what dimensionless parameter is the most effective in heat transfer. From Figs. 10 and 11, it is found that the effect on Nu_m is the strongest in λ and declines in the order Pr_2 , κ , γ , and Pr_1 at $Re = 100$ and $\zeta = 1.4$.

Drag Coefficient. An analytical solution of drag coefficient C_d based on the Stokes' theory ($Re \rightarrow 0$) for a liquid-solid compound drop has been obtained by Rushton and Davies (1983) as follows:

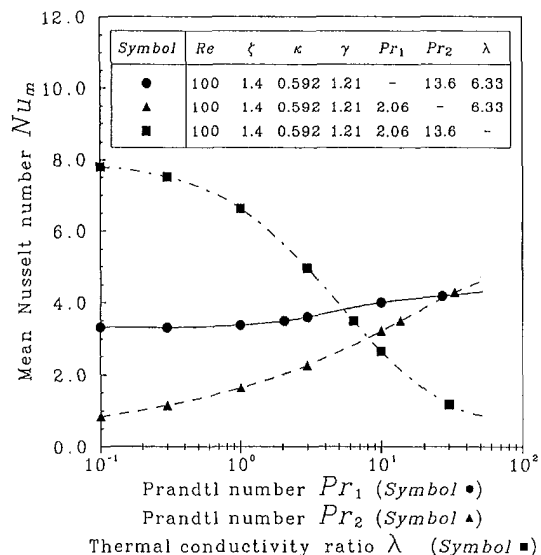


Fig. 11 Variations of Nu_m with Pr_1 , Pr_2 and λ

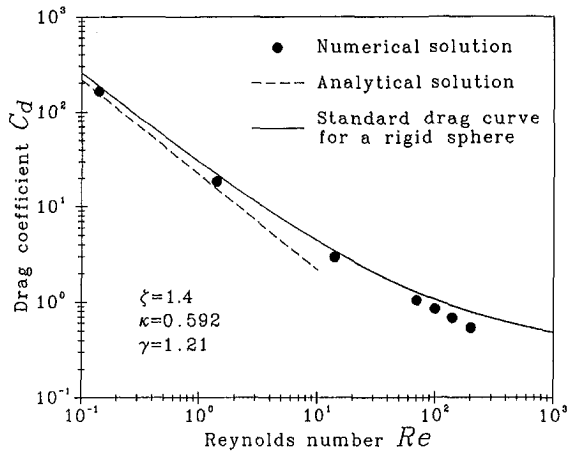


Fig. 12 Variation of C_d with Re

$$C_d = \frac{\text{Drag force}}{\frac{1}{2} \rho_2 U^2 (\zeta')^2} = \frac{16B}{Re}, \quad (21)$$

where

$$B = \frac{1 + 3\kappa b}{1 + 2\kappa b}, \quad b = \frac{(\zeta + 1) \cdot (2\zeta^2 + \zeta + 2)}{(\zeta - 1) \cdot (4\zeta^2 + 7\zeta + 4)}. \quad (22)$$

The value of C_d for the compound drop obtained from the velocity field, shown in Figs. 3–6 at intermediate Reynolds numbers ($Re \leq 200$), is shown in Fig. 12. The closed circle shows the present numerical solutions of the compound drop and the broken line shows the analytical solution in Eq. (21). The numerical solution approaches the analytical solution in the range of very small Re . In this numerical code, the calculation error becomes large as ζ increases. However, for example, even at $\zeta = 2.0$, $Re = 0.1$, $\kappa = 0.592$, and $\gamma = 1.21$, the numerical solution of C_d is 219 and the analytical solution is 206 (the error is limited within 6.3 percent). The solid line in Fig. 12 shows the standard drag curve for a rigid sphere (Abraham, 1970). It is found that C_d for a compound drop is smaller than that for a rigid sphere because of the phase 1 motion. The variations of C_d with ζ , κ and γ are shown in Fig. 13. It is found that C_d decreases as ζ increases. C_d approaches the value for a rigid sphere (Abraham, 1970) at $\zeta \rightarrow 1$ and the value for a spherical liquid drop (Dandy and Leal, 1989) at $\zeta \rightarrow \infty$. On

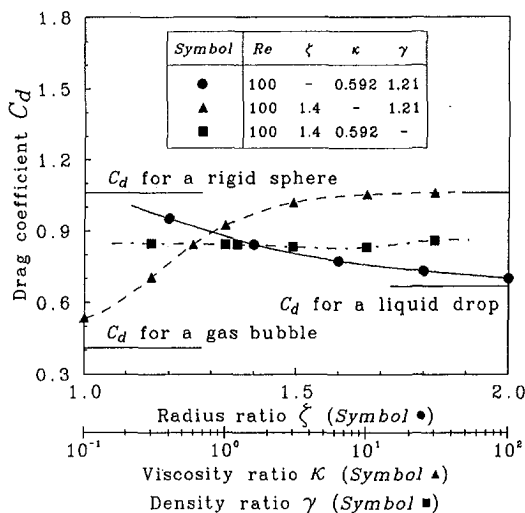


Fig. 13 Variations of C_d with ζ , κ and γ

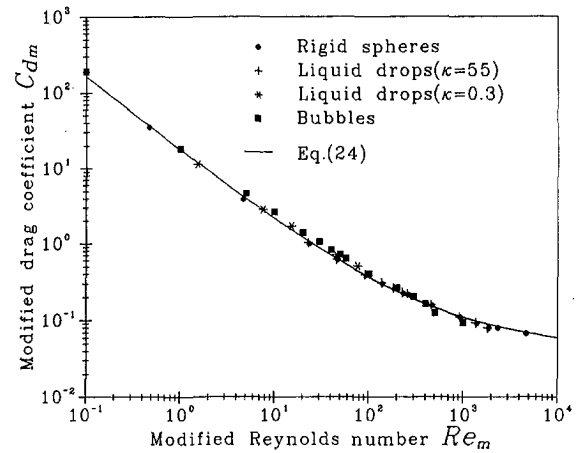


Fig. 14 Comparison of C_{dm} between prediction and previous data of gas bubbles, liquid drops and rigid spheres (Clift et al., 1978)

the other hand, C_d increases as κ increases. C_d approaches the value for a rigid sphere at $\kappa \rightarrow \infty$ and the value for a spherical gas bubble (Dandy and Leal, 1989) at $\kappa \rightarrow 0$. C_d varies very little with γ , but the flow pattern depends on γ as shown in Fig. 6.

As described above, the present numerical calculations are confirmed to approach the reliable well-known or analytical results at $Re \rightarrow 0$, $\zeta \rightarrow 1$ or ∞ and $\kappa \rightarrow 0$ or ∞ .

The empirical equation of C_d for the compound drop is derived here as follows based on the theory by Abraham (1970) of C_d for a rigid sphere. So long as the boundary layer is laminar, drag force D is derived from dimensional analysis as $D = \text{constant} \cdot \rho_2 u^2 d^2$. Here, d is the size of body and u is the representative velocity. Considering the mobility of phase 1 and the boundary layer thickness, we assume that the specified momentum $M (=u \cdot d)$ would be expressed as follows:

$$M = U \cdot \zeta' \left\{ 1 + \frac{9.06}{\sqrt{Re}} \left(\frac{1.5}{B} \right)^n \right\}. \quad (23)$$

B is 1 ~ 1.5 in a compound drop or in a liquid drop, B is 1.5 in a rigid sphere, and B is 1 in a gas bubble. B seems to be closely connected to the shear stress at the outer interface. From Eqs. (21)–(23) and the result of dimensional analysis, the following equation is obtained:

$$C_d = \frac{0.195}{2.25^n} \cdot B^{2n+1} \left\{ 1 + \frac{9.06}{\sqrt{Re}} \left(\frac{1.5}{B} \right)^n \right\}^2. \quad (24)$$

Equation (24) and the C_d equation for a rigid sphere (Abraham, 1970) agree precisely with each other at $\zeta \rightarrow 1$ or $\kappa \rightarrow \infty$, that is, M becomes $U \cdot \zeta' (1 + \delta'/\zeta')$. Here, δ' is the boundary layer thickness of the rigid sphere for the point of about 80 degrees ($\delta'/\zeta' = 9.06/\sqrt{Re}$) (Abraham, 1970). And Eq. (24) and Eq. (21) also agree precisely at $Re \rightarrow 0$. The coefficient n is decided statistically so that the deviation against all numerical data (they are 30 in all) becomes the smallest. n is determined to be 1.9. The deviation between the numerical data and the values predicted from Eq. (24) with $n = 1.9$ is from -10.8 to 6.52 percent.

Furthermore, the adaptability of Eq. (24) with $n = 1.9$ to the drag coefficient for a gas bubble, a liquid drop and a rigid sphere is discussed here. Figure 14 shows the comparison of previous data with the predicted values. The actual data of drag coefficient ($0.1 \leq Re \leq 1000$) are plotted by referring to the review by Clift et al. (1978) as the most reliable data. The solid line in Fig. 14 shows the predicted values obtained from Eq.

(24) with $n = 1.9$. The modified Reynolds number Re_m and the modified drag coefficient C_{dm} are defined as follows:

$$Re_m = Re \cdot B^{2n}, \quad C_{dm} = \frac{C_d}{B^{2n+1}}. \quad (25)$$

It is seen from Fig. 14 that the previous data ($0.1 \leq Re_m \leq 4668$) and the predicted values for Re_m have good agreement and that the deviation between them is from -18.4 to 17.7 percent. Consequently, Eq. (24) with $n = 1.9$ is practical enough to estimate their drag coefficient and can also be useful for estimating the compound drop in $Re > 200$ with high accuracy.

Conclusions

The steady viscous flow past the spherically concentric liquid-solid compound drop at low and intermediate Reynolds numbers ($Re \leq 200$) was obtained numerically. The principal results obtained here are as follows.

(1) Flow patterns and thermal patterns around the compound drop were investigated numerically in $Re \leq 200$. The variations of their patterns with ζ , κ , γ , Pr_1 , Pr_2 , and λ were also made clear quantitatively.

(2) The drag coefficient C_d for the compound drop was obtained numerically. The empirical equation of C_d was also proposed. The deviation between the values predicted from the proposed equation and the numerical data in $Re \leq 200$ was from -10.8 to 6.52 percent.

(3) The empirical equation of C_d proposed here could also be applied to the drag coefficient for a gas bubble, a liquid drop and a rigid sphere. The deviation between the predicted values and the previous reliable data in $Re_m \leq 4668$ ($Re \leq 1000$) was from -18.4 to 17.7 percent.

References

Abraham, F. F., 1970, "Functional Dependence of Drag Coefficient of a Sphere on Reynolds Number," *Physics of Fluids*, Vol. 13, pp. 2194-2195.

Clift, R., Grace, J. R., and Weber, M. E., 1978, *Bubbles, Drops, and Particles*, Academic Press, p. 131.

Dandy, D. S., and Leal, L. G., 1989, "Buoyancy-Driven Motion of a Deformable Drop Through a Quiescent Liquid at Intermediate Reynolds Numbers," *Journal of Fluid Mechanics*, Vol. 208, pp. 161-192.

Hashimoto, H., and Kawano, S., 1990, "A Study on Encapsulated Liquid Drop Formation in Liquid-Liquid-Gas Systems: Fundamental Mechanism of Encapsulated Drop Formation," *JSME, International Journal*, Ser. II, Vol. 33, pp. 729-735.

Johnson, R. E., 1981, "Stokes Flow Past a Sphere Coated With a Thin Fluid Film," *Journal of Fluid Mechanics*, Vol. 110, pp. 217-238.

Johnson, R. E., and Sadhal, S. S., 1983, "Stokes Flow Past Bubbles and Drops Partially Coated With Thin Films: Part 2. Thin Films With Internal Circulation—a Perturbation Solution," *Journal of Fluid Mechanics*, Vol. 132, pp. 295-318.

Johnson, R. E., and Sadhal, S. S., 1985, "Fluid Mechanics of Compound Multiphase Drops and Bubbles," *Annual Review of Fluid Mechanics*, Vol. 17, pp. 289-320.

Kawano, S., Hashimoto, H., Ihara, A., and Shin, K., 1996, "Sequential Production of mm-Sized Spherical Shells in Liquid-Liquid-Gas Systems," *ASME JOURNAL OF FLUIDS ENGINEERING*, Vol. 118, pp. 614-618.

Kondo, T., and Koishi, M., 1981, *Microcapsules*, Sankyo, pp. 1-82, In Japanese.

Lee, M. C., Kendall, J. M. Jr., Bahrami, P. A., and Wang, T. G., 1986, "Sensational Spherical Shells," *Aerospace America*, Vol. 24, pp. 72-76.

Oguz, H. N., and Sadhal, S. S., 1987, "Growth and Collapse of Translating Compound Multiphase Drops: Analysis of Fluid Mechanics and Heat Transfer," *Journal of Fluid Mechanics*, Vol. 179, pp. 105-136.

Pruppacher, H. R., LeClair, B. P., and Hamielec, A. E., 1970, "Some Relations Between Drag and Flow Pattern of Viscous Flow Past a Sphere and a Cylinder at Low and Intermediate Reynolds Numbers," *Journal of Fluid Mechanics*, Vol. 44, pp. 781-790.

Ranz, W. E., and Marshall, W. R. Jr., 1952, "Evaporation From Drops," *Chemical Engineering Progress*, Vol. 48, pp. 141-146, 173-180.

Rushton, E., and Davies, G. A., 1983, "Settling of Encapsulated Droplets at Low Reynolds Numbers," *International Journal of Multiphase Flow*, Vol. 9, pp. 337-342.

Sadhal, S. S., and Johnson, R. E., 1983, "Stokes Flow Past Bubbles and Drops Partially Coated With Thin Films: Part 1. Stagnant Cap of Surfactant Film—Exact Solution," *Journal of Fluid Mechanics*, Vol. 126, pp. 237-250.

Sadhal, S. S., and Oguz, H. N., 1985, "Stokes Flow Past Compound Multiphase Drops: The Case of Completely Engulfed Drops/Bubbles," *Journal of Fluid Mechanics*, Vol. 160, pp. 511-529.

Vuong, S. T., and Sadhal, S. S., 1989, "Growth and Translation of a Liquid-Vapour Compound Drop in a Second Liquid: Part 1. Fluid Mechanics," *Journal of Fluid Mechanics*, Vol. 209, pp. 617-637.

Yadav, S. K., Suresh, A. K., and Khilar, K. C., 1990, "Microencapsulation in Polyurea Shell by Interfacial Polycondensation," *AIChE Journal*, Vol. 36, pp. 431-438.

B. V. Antohe
Doctorate Student.

J. L. Lage
J. L. Embrey Associate Professor.
Mem. ASME

Mechanical Engineering Department,
Southern Methodist University,
Dallas, TX 75275-0337

D. C. Price
Senior Member, Technical Staff,
Aero-Thermal Technology Branch.
Mem. ASME

R. M. Weber
Senior Member, Technical Staff,
Advanced Programs Division.
Mem. ASME

Defense Systems & Electronics Group,
Texas Instruments,
Plano, TX 75086-9305

Experimental Determination of Permeability and Inertia Coefficients of Mechanically Compressed Aluminum Porous Matrices

A heat exchanger, using mechanically compressed microporous matrices, is being developed for cooling high power electronics. The thermal efficiency of this new device depends on the hydraulic characteristics (porosity ϕ , permeability K , and Forchheimer coefficient c_F) of the matrix inserted in it. These quantities have to be obtained experimentally as predictive models do not exist. Twenty-eight compressed matrices are initially chosen for experimental testing. Based on structural requirements, nine matrices are selected for full hydraulic characterization. The determination of permeability and inertia coefficient of each matrix is performed following a proposed direct methodology based on the curve fitting of the experimental results. This methodology is found to yield more consistent and accurate results than existing methods. The uncertainty of the experimental results is evaluated with a new and general procedure that can be applied to any curve fitting technique. Results indicate that the tested matrices have a unique characteristic, that of a relatively wide porosity range, from 0.3 to 0.7, within a relatively narrow permeability range, from $1.0 \times 10^{-10} \text{ m}^2$ to $12 \times 10^{-10} \text{ m}^2$. The inertia coefficient varies from 0.3 to 0.9. These hydraulic characteristics lead to a microporous heat exchanger performing within requirements.

Background

The continuous need to improve heat transfer in heat exchangers is brought about by advanced engineering applications, as for instance the design of high frequency microwave systems, laser diodes, plasma processing, high energy beam dumps and stoppers, and high-power optical structures in general.

Mesh and brush inserts (Bergles, 1985) can be considered precursors of modern microchannel (Walpole and Missaggia, 1993) and microsintered (Lindemuth et al., 1994) heat transfer enhancing techniques. The fundamental challenge is to improve the frequently weak heat transfer at the fluid side of the heat exchanger by increasing the solid-fluid interface area (fin effect) and/or by inducing fluid mixing (turbulence and dispersion effects).

Kuzay et al. (1991), for instance, presented a study in which a conductive metal wool filled copper tube is used on the design of a cooling device for an advanced photon source. Experimental results indicate an increase of over six times on the heat transfer coefficient. A recent experimental work by Peng et al. (1995) indicated that flat-plate rectangular microchannels are capable of dissipating in excess of 10 kW/m^2 with single phase convective cooling. Results presented by Lindemuth et al. (1994) showed that sintered heat sinks can dissipate over 3 MW/m^2 . All these previous studies support our expectations that a microporous cold plate can exhibit exceptional thermal performance.

A new microporous heat exchanger design (Lage et al., 1996) is being considered for cooling high frequency micro-

wave systems. The design consists of brazing a mechanically compressed microporous metallic layer inside the coolant passage of the heat sink device. The main advantages of this design, as compared with metal wool filling, microchannels, and microsintering techniques, are: (1) much broader physical characterization (e.g., porosity range from 30 to 90 percent), (2) precise specification (good repeatability), (3) good structural rigidity, and (4) superior manufacturing characteristics (brazing).

The material considered for the microporous insert, aluminum alloy 6101-O porous matrix, has been carefully chosen. It possesses unique properties, namely low density (for small to negligible impact on the total weight of the system), intrinsic mechanical strength (for structural rigidity), and good material compatibility (for brazing the porous layer with the heat sink surfaces). In addition, the thermal conductivity of this porous material is much higher than that of the coolants used in electronics. Therefore, the effective thermal conductivity of the saturated porous region is higher than the thermal conductivity of the clear (of porous matrix) region.

The original uncompressed porous matrix can be manufactured in densities (ratio of solid material volume to total volume) varying from two percent to 15 percent. The void size can be independently selected from 400 to 1600 pores per meter. The matrix density can be artificially increased by mechanically compressing it. This is very advantageous as it provides means to broaden the range of hydraulic parameters of the final microporous layer. Moreover, it enlarges the contact (interface) area between the porous layer and the solid surfaces of the heat sink. This in turn facilitates the brazing process and, in consequence, improves the heat transfer across the interface and the structural rigidity of the heat sink. Compressed matrices are considered the best candidates for the purpose at hand. This study focuses on their hydraulic characterization.

Contributed by the Fluids Engineering Division for publication in the JOURNAL OF FLUIDS ENGINEERING. Manuscript received by the Fluids Engineering Division January 19, 1996; revised manuscript received December 4, 1996. Associate Technical Editor: F. Giralt.

The rate of fluid flow through the heat sink is determined by the composition of the fluid (coolant) flow passage. The pressure drop across the porous layer, for a given flow rate and fluid dynamic viscosity, depends on the structure of the medium characterized by its permeability and inertia (or Forchheimer) coefficient. These two properties of the metallic microporous insert have to be obtained experimentally as predictive models for this type of porous layers do not exist.

In what follows, we report results of testing mechanically compressed microporous layers regarding their hydraulic characteristics. We propose a consistent methodology for calculating the hydraulic parameters and for estimating their uncertainties. We also briefly demonstrate that our proposed methodology leads to more accurate results, for the same experimental data set, than the results obtained by using existing methodologies. For comparison we will make reference to two experimental works. The first is the excellent reference of Givler and Altobelli (1994). In it, the authors followed an existing methodology to obtain the permeability K and the inertia coefficient c_F of a high porosity (0.972) polyurethane foam. The high uncertainties of the K and c_F values obtained by them, respectively, 27.3 percent and 36.4 percent, prompted us to devise a more precise methodology. We will also use for comparison the procedure followed by Ward (1964), a classic reference, in obtaining permeability and inertia coefficient of several media.

Theoretical Considerations

The steady-state unidirectional pressure drop between two locations in a homogeneous, uniform, and isotropic porous medium, fully saturated with a newtonian incompressible fluid, can be obtained from the Forchheimer-extended Darcy equation (Joseph et al., 1982)

$$\frac{\Delta p}{L} = \frac{\mu}{K} v_D + \frac{c_F}{\sqrt{K}} \rho v_D^2 \quad (1)$$

As Eq. (1) indicates, the functional relationship between pressure drop and Darcy speed is quadratic, $y(x) = \alpha x + \beta x^2$, where y represents $\Delta p/L$, x represents v_D , α represents μ/K , and β represents $c_F \rho / \sqrt{K}$. Coefficients α and β are referred to as the first-order and the second-order permeability coefficients, respectively. These coefficients are determined experimentally, leading to porous medium permeability, K , and inertia coefficient, c_F , once fluid density, ρ , and dynamic viscosity, μ , are known.

A usual approach for determining α and β consists of two steps as indicated in the recent work of Givler and Altobelli (1994). The first step is to restructure Eq. (1) writing it in the form (Ergun, 1952)

$$\frac{\Delta p}{Lv_D} = \frac{\mu}{K} + \frac{c_F}{\sqrt{K}} \rho v_D \quad (2)$$

In this case, the functional is linear, $z(x) = \alpha + \beta x$, where x represents v_D and z represents $\Delta p/(Lv_D)$. In this particular case, the coefficient α is obtained from the intersection of the analytical least square best fit of the experimental data, $\alpha + \beta x$, and the z axis. This is equivalent to taking the limit of Eq. (2) as speed v_D tends to zero. The determination of the permeability of the medium follows directly from the definition of the first order permeability coefficient.

The second-order permeability coefficient, and consequently the inertia coefficient c_F , follows from a second step, rewriting Eq. (2) in the form (Ahmed and Sunada, 1969)

$$\frac{\Delta p}{Lv_D^2} = \frac{\mu}{Kv_D} + \frac{c_F}{\sqrt{K}} \rho \quad (3)$$

The functional is represented by $w(x) = \alpha/x + \beta$, where w is $\Delta p/(Lv_D^2)$. The second-order permeability coefficient β is determined graphically by an asymptotic extrapolation as x tends to infinity. Knowing β , a relation between the inertia coefficient and the permeability of the matrix is found.

An interesting and common feature of both steps is the extrapolation of experimental results to zero velocity limit (the first step, for determining α) and to infinite velocity limit (the second step, for determining β). The uncertainties of α and β are easily estimated from a combination of systematic error (e.g., error associated with measuring Δp and v_D) and the error associated with the curve fitting of the experimental data.

It is well known that extrapolation of experimental data can be misleading, therefore it should be avoided. The determination of α and β , as previously described, relies on extrapolation of curves obtained by curve fitting the experimental data. A natural question would be: why not have coefficients α and β determined directly from the curve fitting equations that are necessary for the extrapolations? Why extrapolate?

As a matter of fact, either Eq. (2) or (3) could provide both, α and β , values directly from the least square curve fittings of the experimental data, with no need to extrapolate the curves (see, for instance, Firoozabadi, 1995, who used only Eq. (2) to estimate both values, K from extrapolation and c_F from the slope of the fitting curve, of sandstone). The accuracy of using the curve fitting Eqs. (2) or (3) is poor though when compared with obtaining K and c_F from the least square curve fitting of the data using the quadratic Eq. (1). This is so because the uncertainty of the velocity measurements propagates to the ordinate of the curve fitting if Eqs. (2) or (3) are used, deteriorating the final accuracy of the coefficients (see the scatter of data in Givler and Altobelli, 1994, when their experimental data is plotted in the $\Delta p/Lv_D$ or $\Delta p/Lv_D^2$ format).

Nomenclature

B = bias limit
 C = average pore size, Eq. (21)
 c_F = Forchheimer coefficient
 d = initial aluminum matrix density
 H = channel height, m
 K = permeability, m^2
 k_B = constant, Eq. (20)
 Kn = Knudsen number, Eq. (19)
 L = porous matrix length, m
 n = number of data points
 p = pressure, Pa
 P = precision limit
 Q = volumetric flow rate, m^3/s
 r = compression ratio
 R_m = radius of collision cross section, m

Re = Reynolds number
 S = cross section area, m^2
 T = temperature, $^{\circ}C$
 U = uncertainty
 v_D = Darcy velocity, m/s
 W = channel width, m
 x = curve fitting variable
 y, z, w = curve fitting functions
 α = first-order permeability coefficient
 β = second-order permeability coefficient
 Δ = difference
 ϕ = porosity

λ = mean path of gas molecules, Eq. (23), m
 μ = dynamic viscosity, m^2/s
 ρ = density, kg/m^3
 σ = standard deviation

Subscripts

c = compressed microporous layer
 D = Darcy
 f = clear (of porous matrix) fluid block
 \max = maximum value
 p = block with microporous layer
 s = solid
 0 = uncompressed porous matrix

It seems clear that extrapolation can be avoided. The question that remains to be answered is how to estimate the uncertainties of α and β if they are obtained directly from the best curve fitting equation of the experimental data. This question might indicate why this approach has not been pursued before. Notice that the extrapolation method described previously allows α and β to be obtained from a single value of each graph. A unique relationship exists between the coefficients α and β and one single value of $\Delta p/Lv_D$ (at v_D equal to zero) and of $\Delta p/Lv_D^2$ (at $v_D \rightarrow \infty$), respectively. Therefore, the uncertainties of α and β can be easily estimated (e.g., average standard deviation of $\Delta p/Lv_D$ and of $\Delta p/Lv_D^2$ values, respectively). When obtaining α and β from the curve fitting equation, all values of Δp and v_D are involved (that is why the results are more accurate) as they all affect the coefficients of the curve fitting equation. It is imperative then to account for the uncertainty of each and every Δp and v_D data points independently. The mathematical procedure of estimating the uncertainty of each curve fitting coefficient is detailed later on.

Experimental Equipment and Procedure

The experimental setup is designed to obtain accurate determination of the flow (Darcy velocity) and pressure drop across a test block. The dimensions of the porous matrix are chosen to conform with the heat sink design for phased-array radars being considered by Texas Instruments.

All aluminum blocks have inlet and outlet plena connected by a 76.2 mm long (L), 50.8 mm wide (W), and 1.0 mm thick (H) test channel (Fig. 1). A porous layer is bonded with a very thin coating of Sheldahl T1401 adhesive to the internal surface of the test channel and to the lateral surfaces with 1177/cab-sil filling. The bonding is carefully done to minimize possible adhesive intrusion through the pores of the layers. The top surface is secured flush with the porous layer, as top and bottom covers are bolted together.

Each porous layer is obtained by compressing a 1570 pores per meter aluminum 6101-O alloy matrix in the direction perpendicular to the flow direction (along H , Fig. 1). The compression is done slowly to avoid *shearing* the matrix. Visual and X-ray inspections do not reveal any nonuniformity in the structure of the matrix. Hydraulic tests rotating the porous matrix position relative to the flow direction indicates that the matrix is isotropic. The compression ratio, $r = H_0/H$ (where H_0 is the

initial matrix thickness and H is the final matrix thickness), varies from four to fourteen. Recall that all samples are compressed to a final thickness of one millimeter ($H = 1.0$ mm). The initial (uncompressed) density of the porous inserts, $d = 1 - \phi$ (where ϕ is the initial volumetric porosity of the matrix), varies from two percent to ten percent. The compressed porous layer is characterized, from a manufacturing perspective, by four parameters: initial density, number of pores per meter, final thickness, and compression ratio.

The volumetric porosity of a porous matrix is, by definition,

$$\phi = 1 - \frac{V_s}{V} \quad (4)$$

where V_s is the solid phase volume, and V is the total volume of the porous matrix. The solid (aluminum) volume of each porous layer is calculated by weighing each porous sample after compression, and dividing it by the aluminum alloy density (2681.4 kg/m^3). The total volume is measured directly. The porosity of each compressed layer is then obtained from Eq. (4).

An initial attempt was made to measure the permeability and inertia coefficient with poly-alpha-olefin fluid, or PAO, a synthetic oil commonly used in cooling military avionic devices. The experimental setup for oil is presented in Fig. 2(a).

The main component of the PAO flow loop is a Neslab chiller (1.7 kW of cooling capacity at 20°C , and temperature stability of $\pm 0.1^\circ\text{C}$) to maintain constant inlet PAO temperature. The system can provide 550 kPa of pressure drop across the test section. A $5 \mu\text{m}$ filter is positioned upstream of the test section to eliminate the contamination problem (clogging of the porous passages by solid particles). Inlet and outlet flow static pressures are obtained with independent pressure gauges for 690 kPa of pressure, accurate to ± 345 Pa.

The volumetric flow rate of coolant circulating through the system is checked by a $6.3 \times 10^{-5} \text{ m}^3/\text{s}$ turbine flow meter, accurate to ± 0.1 percent of full scale. For small flow rate a stop watch and fluid reservoir (for measuring fluid volume) are used instead. A large amount of PAO is taken for reducing the reading uncertainty of the collected volume. At extremely low flow rate, the collecting time becomes increasingly long and the process extremely tedious. In this case a smaller volume is collected and the reservoir is weighed with a calibrated scale before and after collecting the fluid. The difference in weights and the PAO

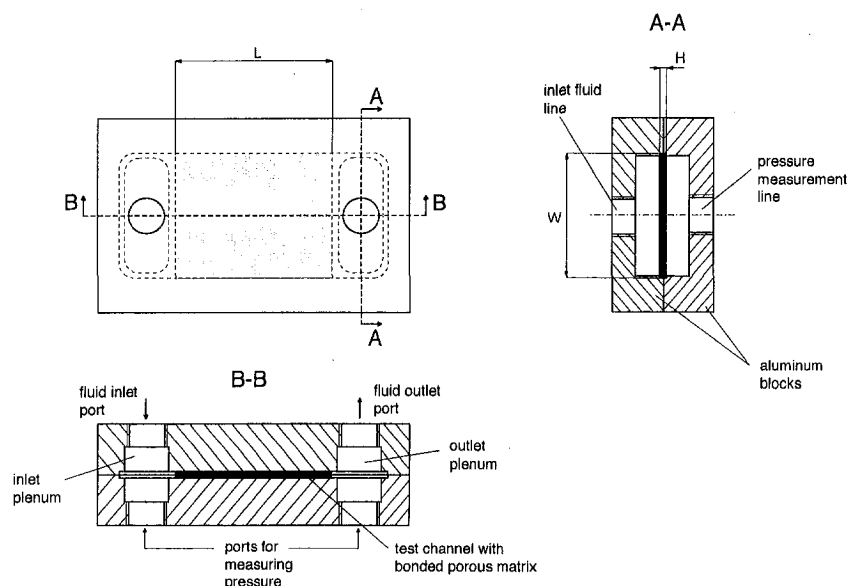


Fig. 1 Test block design with aluminum porous matrix

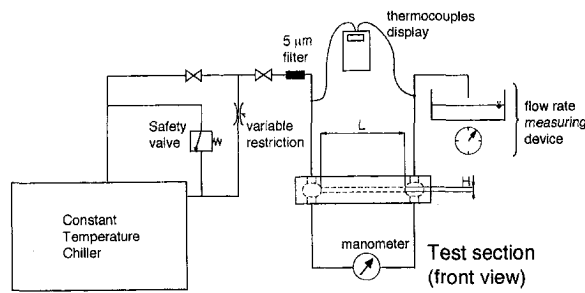


Fig. 2(a) PAO

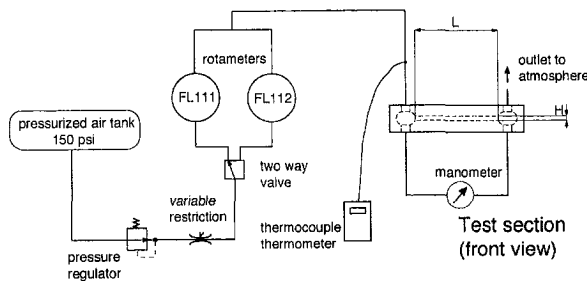


Fig. 2(b) Air

Fig. 2 Experimental setup

density are used to compute the fluid volume. The uncertainty of fluid velocity obtained from the stopwatch/reservoir method is conservatively estimated as four percent.

It is worth mentioning that PAO dynamic viscosity is very sensitive to temperature changes. Two type *K* thermocouples (0.2 mm diameter, $\pm 0.5^\circ\text{C}$ accurate) are placed near the inlet and outlet of the test section for monitoring the fluid temperature that varied from 17°C to 19°C throughout the experiments. The kinematic viscosity of PAO is computed with the following correlation, obtained by curve fitting experimental data (Chevron, 1981)

$$\nu(T) = 2.035 \times 10^{-8} T^{-1.087} \quad (5)$$

with T being the inlet PAO temperature (same as outlet for all tests) measured in degrees Celsius.

Within our temperature range the kinematic viscosity of PAO varies by 11.3 percent. Other thermophysical properties are comparatively insensitive to temperature variation, e.g., density varies by 0.18 percent within the same temperature range.

Notice that for the PAO case, the limiting parameter is the total pressure drop across the block. A safe limit of about 400 kPa is exercised throughout the experiment limiting the maximum flow speed obtainable with each block. Note that before every experiment we let the PAO flow for at least five minutes through the porous block at a high flow rate (pressure drop of over 500 kPa) to wash out air bubbles possibly trapped within the pores.

Another setup is built for performing measurements using air as fluid, instead of PAO. The primary reasons for this second flow apparatus are: (1) to verify the consistency of the porous media flow model as applied to flow through the compressed aluminum microporous matrix; (2) to check the experimental methodology when using a different fluid; (3) to bring to negligible levels the temperature influence on fluid viscosity; (4) to extend experimental results to higher Reynolds number values and so broadening the validity range of K and c_F .

The air flow apparatus (Fig. 2(b)) includes a pressure regulator to adjust the maximum inlet air pressure (the inlet air line is linked to an external tank holding compressed air at 1.0 MPa). The air flow rate ranges from 1.7×10^{-6} to 7.2×10^{-5} m^3/s corresponding to an air velocity range of 0.033 to 1.436

m/s . The rotameters (OMEGA FL111 and FL112) are calibrated to two percent of the reading value. Their repeatability is of half percent of the reading value.

The differential pressure is measured between the inlet and outlet ports of the block. A 300 Pa gauge micromanometer manufactured by Combustion Instruments Ltd. (0.1 Pa accurate) is utilized to measure the very small pressure drop. For the moderate pressure drop regime a 0.5 kPa gauge inclined portable manometer, manufactured by Dwyer Inc., is used. The uncertainty of the instrument is 2.5 Pa. Two U-shaped manometers, one 78.5 kPa, accurate to 10 Pa, and one 46.5 kPa, accurate to 30 Pa, are used to measure the pressure drop at higher range.

Pressure and flow readings at small flow rates are performed with different (smaller scale) instruments. This procedure allows much lower uncertainty values in the low pressure and velocity range than using the high range measurement devices.

It is important to point out that the pressure range used in the air test is small enough to neglect any compressibility effect. Therefore, the density dependence on pressure, that can be approximately modeled by using the ideal gas law, is not accounted for here.

The inlet air temperature is recorded for correcting the air density and viscosity. A type J thermocouple wire is inserted in the air stream with the temperature displayed by a 450 AJT OMEGA thermocouple thermometer. The air properties are obtained by linear interpolation as a function of temperature (Air Properties Table, Bejan, 1993). The outlet air temperature is also measured with a portable thermocouple thermometer. Air temperature difference between inlet and outlet is negligible (within thermocouple uncertainty of 0.5°C) for all experiments.

Air test results represent the arithmetic average of at least five experimental runs for each block. For each test block the data acquisition starts at low flow rate, increasing in finite steps. No hysteresis is observed when acquiring data reducing the flow rate. The repeatability of the experimental data is within the uncertainty of the results.

Porosity of Compressed Matrices

The final (compressed) porosity is an important parameter as it allows the prediction of fluid speed within the pores (v) of the matrix from the Dupuit-Forchheimer relation, $v_D = \phi v$.

A theoretical correlation for predicting the compressed porosity is proposed. Assuming isovolumetric compression of solid phase (aluminum) and constant surface area perpendicular to the compression direction, the final (compressed) porosity, ϕ_c , relates to the initial sample porosity and compression ratio as

$$\phi_c = 1 - rd \quad (6)$$

Figure 3 presents a comparison between measured values and theoretically estimated porosity (continuous lines), versus compression ratio (r), of twenty eight compressed porous layers with different initial densities. In general, the agreement is quite good—there is a maximum deviation of twenty percent. Note that the compression of the original porous matrix is not isovolumetric: the lateral sides of the matrix (parallel to the compression direction) are unconstrained to avoid consolidation of material within this region and the consequent nonuniform characteristics. We strongly suspect this to be the cause for the discrepancy.

By inspecting all compressed porous layers, nine were chosen as best candidates for building a microporous cold plate based upon their available brazing surface and structural integrity. These samples were further tested for permeability and inertia coefficient as detailed next.

Permeability and Inertia Coefficient of Compressed Matrices

From the experimental measurements, a Darcy velocity is computed for each pressure drop by dividing the volumetric

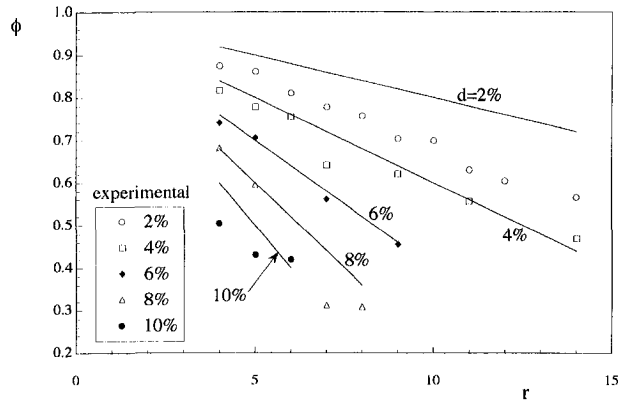


Fig. 3 Compression ratio and initial density effects on the porosity of the aluminum matrices; comparison with theoretical estimate. Maximum uncertainty estimate for porosity measurements is 5.7 percent and for compression ratio is 2.5 percent.

flow rate, Q , by the cross-sectional area of the test channel ($=WH$):

$$v_D = \frac{Q}{S} \quad (7)$$

The pressure differential, produced by the porous layer only, is computed by subtracting the pressure drop of the clear (no porous insert) block, Δp_f , from the pressure drop of the specific porous sample, Δp_p , at each velocity

$$\Delta p(v_D) = \Delta p_p(v_D) - \Delta p_f(v_D) \quad (8)$$

For the pairs $(v_D, \Delta p/L)$ a quadratic interpolation following Eq. (1) is performed, using the least-square method. Coefficients α and β are then obtained directly from the quadratic interpolation leading to the permeability and Forchheimer coefficients for each specific porous layer.

Figures 4 and 5 present a sample of the experimental results of air in graphical form. In Fig. 4, the compression ratio effect is presented considering a porous layer of initial density equal to 4 percent and compression ratio equal to 7, 9, 11, and 14. The initial density effect is presented in Fig. 5, for a constant compression ratio equal to seven and initial layer density equal to four, six, and eight percent. The corresponding least square curve fitting equation and the coefficients are included in the graphs.

The first important observation is that, indeed, the blocks with compressed microporous layers behave as a porous medium, that is, the pressure drop varies quadratically with speed.

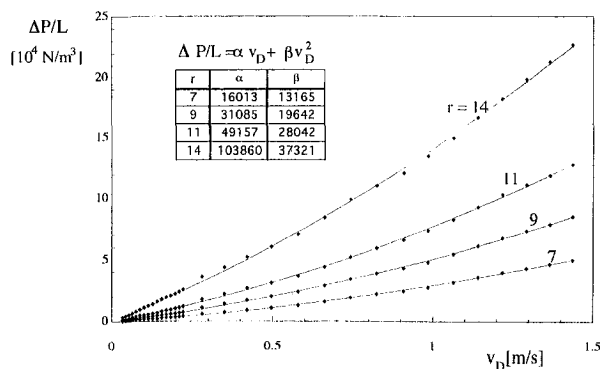


Fig. 4 Compression ratio influence on the pressure gradient of matrices with same initial density, $d = 4$ percent. Maximum uncertainty estimates: 2.5 percent for pressure gradient data and 2.5 percent for velocity measurements.

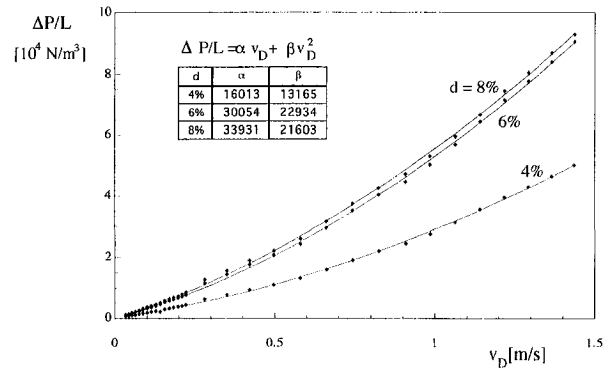


Fig. 5 Initial density influence on the pressure gradient of matrices with same compression ratio, $r = 7$. Maximum uncertainty estimates: 2.5 percent for pressure gradient data and 2.5 percent for velocity measurements.

Notice that the pressure drop is more sensitive to changes in compression ratio at high flow speed (Fig. 4). The hydraulic behavior of a compressed matrix seems to become insensitive to changes in the initial matrix density for d beyond a certain threshold value. For compression ratio equal to 7, for instance, the threshold initial density value is close to six percent (Fig. 5).

Table 1 summarizes the hydraulic results obtained for each of the nine blocks tested. The uncertainty values for the permeability and Forchheimer coefficients and the maximum Knudsen number of each experiment, calculated following the methodologies presented later on, are also included. The last row presents equivalent permeability and Forchheimer coefficient values of a clear block (with no porous material). Notice in this case that the inertia coefficient is very small because no form drag affects flow through a clear channel (its uncertainty is then irrelevant).

The permeability of the matrix decreases with the increase in initial aluminum matrix density and with the increase of its compression ratio. The Forchheimer coefficient does not have a monotonic variation. It presents, however, a general tendency to increase with increased compression ratio and matrix density. Figure 6 presents the variation of permeability and inertia coefficient as function of initial density and compression ratio. Also included in this figure are the results obtained by testing the matrices with PAO.

The maximum discrepancy between the permeability results obtained with air and PAO is 18 percent. The difference in inertia coefficient is as large as 51 percent, increasing with the decrease in permeability. What happens is that the velocity range achieved with the PAO apparatus, for maximum allowable pressure drop, is insufficient to provide enough points in the form drag dominated regime. The permeability based Reynolds number equal to one can indicate the transition from linear ($Re_K < 1$) to quadratic ($Re_K > 1$) regime. All air experiments are performed at $Re_{K,max} > 1$ as compared to some PAO experiments in which $Re_{K,max} < 1$. For instance, the maximum Re_K for testing a 4 percent initial density matrix compressed 14 times with PAO is equal to 0.14, while the corresponding value for air is 1.24. One can then expect the inertia coefficient obtained with air to be more representative than the one obtained with PAO.

Uncertainty Analysis

Givler and Altobelli (1994) determined graphically the first-order permeability coefficient (α) from the best linear fit of $\Delta p/(Lv_D)$ and v_D and the second-order permeability coefficient (β) from the asymptote (infinite Darcy velocity) of the hyperbolic fit of $\Delta p/(Lv_D^2)$ versus v_D . From α and β the permeability and the Forchheimer coefficient were obtained. Figure 7 pre-

Table 1 Permeability and Forchheimer coefficient values for aluminum matrices, tested with air, their corresponding experimental uncertainties, and maximum Knudsen number

d [%]	r	Coefficient values		Uncertainties		Kn_{max}
		K [10^{-10} m^2]	c_F	U_K [%]	U_{c_F} [%]	
4	7	11.36	0.371	5.4	8.0	0.800
4	9	5.85	0.397	4.7	8.8	0.479
4	11	3.70	0.451	4.5	9.2	0.238
4	14	1.75	0.413	3.6	11.5	0.117
6	7	6.06	0.471	5.2	8.2	0.456
6	9	3.17	0.534	4.7	8.8	0.220
8	5	9.24	0.383	5.2	8.2	0.472
8	7	5.36	0.418	4.7	8.8	0.243
10	5	2.72	0.838	5.8	7.9	0.256
N/A	N/A	912.70	0.012	3.1	15.2	N/A

sents, as an example, the pressure versus velocity results with air flow for a block with a ten percent dense and five compression ratio microporous layer in it.

The coefficients α and β of this block are estimated by extrapolation as 64.4×10^3 and as 7.5×10^4 , respectively. The corresponding permeability is $2.83 \times 10^{-10} \text{ m}^2$ and the inertia coefficient is 1.05. When compared against the values obtained from the curve fitting method, respectively, $2.72 \times 10^{-10} \text{ m}^2$ and 0.838, these values are four percent and 25 percent different.

The uncertainty in determining α and β is considered by Givler and Altobelli (1994) to be given by the standard deviation of the experimental points to the best curve fit, being $\sigma_\alpha = 3177$ and $\sigma_\beta = 18240$ (the measurement errors were neglected by them). For the data of Fig. 7 the uncertainties of α and β are:

$$U_\alpha = \frac{\sigma_\alpha}{\alpha} = 4.9\% \quad \text{and} \quad U_\beta = \frac{\sigma_\beta}{\beta} = 24.3\% \quad (9)$$

Using the propagation error on the K equation (Kline and

McClintock, 1953), and assuming negligible uncertainties in the viscosity value, then:

$$U_K = U_\alpha = 4.9\% \quad (10)$$

For the Forchheimer coefficient the error propagation gives:

$$U_{c_F} = \sqrt{\left(\frac{U_K}{2}\right)^2 + U_\beta^2} = 24.5\% \quad (11)$$

We do not recommend the extrapolation method followed by Givler and Altobelli (1994) for computing K and c_F for two reasons. First, the visual determination of the asymptotic value of $\Delta p / (Lv_D^2)$ can vary tremendously as the ordinate unit scale is usually very high (see bottom graph of Fig. 7 in which ordinate scale reads in units of 10^5). Therefore, a very small displacement of the asymptote leads to a very large numeric variation of $\Delta p / (Lv_D^2)$. Second, by dividing the pressure gradient by v_D the error in the velocity measurement propagates to

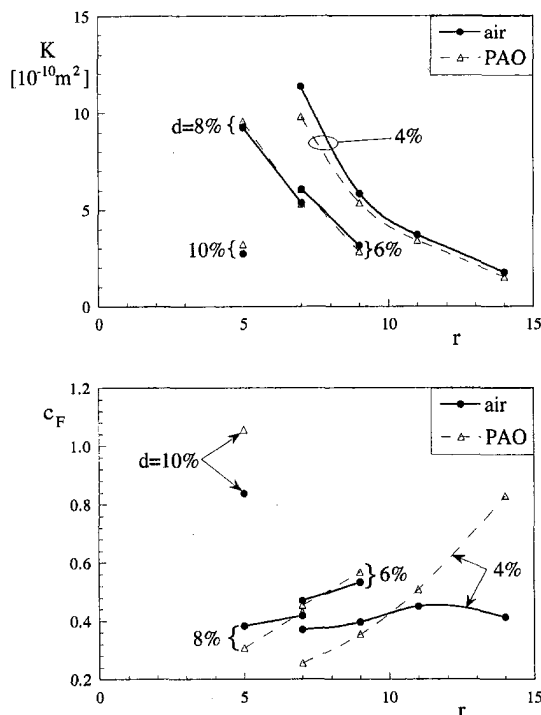


Fig. 6 Permeability and Forchheimer coefficient as function of initial foam density (d) and compression ratio (r). Maximum uncertainty estimates: 5.8 percent for permeability data, 11.5 percent for inertia coefficient, and 2.5 percent for compression ratio. (See Table 1 for individual estimates.)

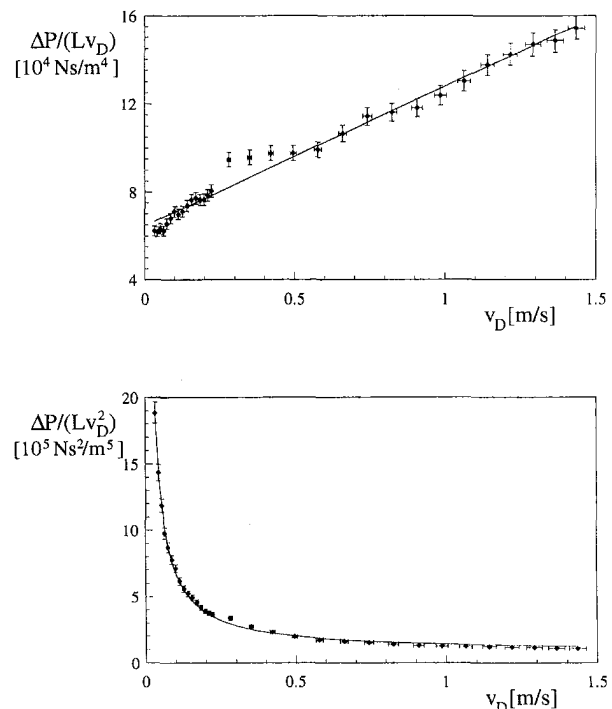


Fig. 7 Pressure versus velocity graph for determining first and second order permeability coefficients according to Givler and Altobelli (1994). Horizontal and vertical error bars indicate local uncertainties: 3.5 percent for ordinate values of top graph, 4.3 percent for ordinate values of bottom graph, 2.5 percent for abscissa values of both graphs.

the new terms, $\Delta p/(Lv_D)$ and $\Delta p/(Lv_D^2)$, increasing the uncertainty of the "raw" fitting data.

The alternative, as explained previously, relies on the curve fitting to estimate coefficients α and β . In what follows a methodology for estimating the uncertainties of parameters obtained directly from the curve fitting equation is proposed. The results obtained with the same block as used in Fig. 7 (ten percent dense matrix compressed five times) are used to highlight the differences between our new methodology and the one followed by Givler and Altobelli (1994).

The uncertainty analysis of curve fitting, as opposed to the extrapolation method, considers the errors in measuring the data. To obtain the measuring errors, we follow the experimental procedure step by step, starting with the fluid velocity obtained from measuring the volumetric flow rate, Q , and the flow cross-sectional area, S (Eq. (7)). In this case, the sources of error are the volumetric flow rate measurements and the length measurements. The accuracy (P_Q) of the rotameters is two percent of the reading value, and they have repeatability (U_Q) of 0.5 percent of the reading value. The errors in the length measurements can be neglected by comparison with the errors associated with the flow rate. Using the Kline and McClintock (1953) method on Eq. (7), the Darcy velocity uncertainty is

$$U_{v_D} = U_Q = \sqrt{B_Q^2 + P_Q^2} = 2.1\% \quad (12)$$

The pressure gradient (LHS of Eq. (1)) has errors from the pressure drop determination and the length measurement (negligible compared with the first one). In measuring the pressure drop we consider the repeatability to be zero so the uncertainty is given by the bias limit

$$U_{\Delta p} = B_{\Delta p} \quad (13)$$

The maximum bias limit is given by the least count using the smallest pressure measured with that instrument. On this basis, a bias limit is estimated for each manometer: inclined manometer, $U_{\Delta p} = 2$ percent; U -water manometer, $U_{\Delta p} = 2.5$ percent; U -mercury manometer, $U_{\Delta p} = 2$ percent. The pressure drop bias error is conservatively taken to be the maximum of the three uncertainties, that is $U_{\Delta p} = 2.5$ percent.

We now consider the error propagation from the experimental data to coefficients α and β due to the curve fitting process. The parabolic curve fitting from the least square method using n pairs (x_i, y_i) (x represents the Darcy velocity and y the pressure gradient) gives the "best" parabola $\alpha x + \beta x^2$. The equations for determining α and β , from least squares, are:

$$\alpha = \frac{\frac{\sum_{i=1}^n x_i y_i}{n} \left(\frac{\sum_{i=1}^n x_i^4}{n} \right) - \left(\frac{\sum_{i=1}^n x_i^2 y_i}{n} \right) \left(\frac{\sum_{i=1}^n x_i^3}{n} \right)}{\left(\frac{\sum_{i=1}^n x_i^2}{n} \right) \left(\frac{\sum_{i=1}^n x_i^4}{n} \right) - \left(\frac{\sum_{i=1}^n x_i^3}{n} \right) \left(\frac{\sum_{i=1}^n x_i^2}{n} \right)} \quad (14)$$

$$\beta = \frac{\frac{\sum_{i=1}^n x_i^2 y_i}{n} \left(\frac{\sum_{i=1}^n x_i^2}{n} \right) - \left(\frac{\sum_{i=1}^n x_i y_i}{n} \right) \left(\frac{\sum_{i=1}^n x_i^3}{n} \right)}{\left(\frac{\sum_{i=1}^n x_i^2}{n} \right) \left(\frac{\sum_{i=1}^n x_i^4}{n} \right) - \left(\frac{\sum_{i=1}^n x_i^3}{n} \right) \left(\frac{\sum_{i=1}^n x_i^2}{n} \right)} \quad (15)$$

"Perfect data" (no measurement error) will lie perfectly along the parabola, so there will be no error in determining α and β . A deviation from the parabola, deviation produced by the measurement errors, will induce an error in the value of the coefficients α and β . Therefore, from the point of view of uncertainty analysis, the variables (values at each point) can be considered as independent. The propagation of errors (Kline and McClintock method) is:

$$(\Delta\alpha)^2 = \sum_{i=1}^n \left(\frac{\partial\alpha}{\partial x_i} \Delta x_i \right)^2 + \sum_{i=1}^n \left(\frac{\partial\alpha}{\partial y_i} \Delta y_i \right)^2 \quad (16)$$

where Δx_i and Δy_i are the corresponding velocity and pressure

gradient errors at point i . These errors are computed as the actual value of x (or y) times the uncertainty of measuring x (or y). The partial derivatives of α with respect to each experimental point x_i and y_i are obtained from the least square formula, Eq. (14) (or Eq. (15)). Once $\Delta\alpha$ is obtained from (16), the α -uncertainty can be calculated using $U_\alpha = \Delta\alpha/\alpha$. A similar formula is derived for β . The K and c_F uncertainties are derived from the definitions of α and β , and their corresponding uncertainties.

We note in passing that the methodology for estimating the uncertainties of parameters obtained directly from an equation curve fitting the experimental data is general. The fundamental step is to utilize, in the Kline-McClintock model, the least square equations to compute the local derivatives of the parameter being considered. Notice that every single data point counts, as each one influences the curve fitting equation, therefore influencing the final parameter value.

For the block of Fig. 7, a six percent uncertainty is obtained for both coefficients α and β . The corresponding uncertainties of K and c_F are

$$U_K = U_\alpha = 5.8\% \quad (17)$$

and

$$U_{c_F} = \sqrt{\left(\frac{U_K}{2} \right)^2 + U_\beta^2} = 7.9\% \quad (18)$$

Notice that the permeability uncertainty is comparable to the value obtained via extrapolation (Eqs. (10) and (17)). However, the inertia coefficient uncertainty is much lower (Eqs. (11) and (18)) indicating a more accurate value. Notice that among all nine blocks (Table 1) the highest permeability uncertainty is 5.8 and the highest inertia coefficient uncertainty is 11.5 percent.

Limitations

Values of permeability and inertia coefficient obtained experimentally are likely to be dependent on the velocity range used, as indicated by Macdonald et al. (1979). This aspect has been tested in three different respects, as described next.

One aspect is the ability of having the permeability value determined from applying the Darcy equation to a single data point (pressure drop and velocity pair) as done by Ward (1964). To illustrate this aspect better, we present in Fig. 8 (top) permeability values versus flow speed for a block with a four percent initial density matrix compressed seven times. Each permeability value is computed directly from the Darcy equation using one pressure gradient value and the corresponding velocity value.

Included in the graph is the corresponding permeability-based Reynolds number for each flow velocity. Keep in mind that these Reynolds values vary not only because the flow velocity is varying but also because the computed permeability, used to calculate Re_K , varies from point to point. As the square root of permeability drops slower than the increase in flow speed this local Reynolds number increases with velocity, therefore, it can be used to delineate the flow regime.

It is worth noting the permeability plateau at very low speeds ($v_D < 0.2$ m/s, $Re_K < 0.4$). This represents the Darcy linear regime, where any data pair (flow speed, pressure gradient) produces a reasonable value for the permeability of the medium. Notice that outside the linear range, the permeability varies substantially with flow speed, from 9.9×10^{-10} to 5.2×10^{-10} (or 90 percent). Even for a Re_K range up to one, considered the transition Re_K value from linear to quadratic regime, the permeability of the medium varies from 9.9×10^{-10} to 6.8×10^{-10} m², that is a 46 percent variation. The conclusion is that unless one is absolutely sure the flow regime is only linear,

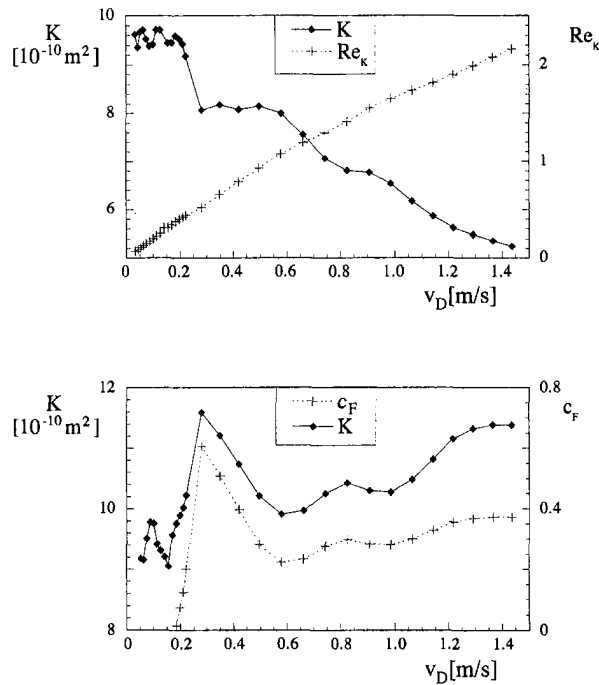


Fig. 8 *Top*: Permeability derived from Darcy law applied to a single data point and the corresponding permeability based Reynolds number; *Bottom*: Permeability and Forchheimer coefficient derived from the quadratic curve fitting for increasing velocity range.

calculating the permeability of the medium from one data point is improper and, in general, underestimates the correct value by a large fraction.

The second aspect to be characterized is the sensitivity of the coefficients K and c_F on the experimental velocity range utilized. Figure 8 (bottom) presents the evolution of each coefficient, calculated following the quadratic curve fitting method described previously. At each velocity, all experimental data points up to this velocity are used in the curve fitting. For instance, the permeability and inertia coefficient values at $v_D = 0.5$ m/s are calculated using all the experimental data for $0 \leq v_D \leq 0.5$ m/s. Notice that the permeability value computed in this way varies by 29.8 percent throughout the velocity range considered in the graph. The inertia coefficient is even more sensitive to the velocity range utilized. We notice the difficulty in measuring the inertia coefficient at low velocities. For $v_D < 0.2$ m/s, c_F oscillates between a negative and a positive value, typical of interpolating an essentially straight (linear) group of experimental data with a quadratic equation. It seems imperative then to provide the velocity range (Re_k) from which K and c_F are computed.

The third and last aspect has to do with using air as the testing fluid. As indicated previously, air provides a larger velocity range than PAO specially at the high end of the velocity spectrum. However, one concern of using air flow is the possibility of achieving Knudsen regime at the low end of the spectrum. As Kaviany (1991) mentioned, at low pressure and small pore size (which is related with permeability) a velocity slip can occur as the mean path of the gas molecules approaches the pore dimension. This “slippage” effect reveals itself as an increase in the flow rate as the pressure gradient is decreased, a fact that leads to an apparently higher permeability.

The Knudsen number is defined as:

$$Kn = \frac{\lambda}{C} \quad (19)$$

with the mean path of gas molecules, λ , computed from

$$\lambda = \frac{k_B T}{2^{2.5} \pi R_m^2 p} \quad (20)$$

where the constant $k_B = 1.381 \times 10^{-23}$ J/K and the radius of collision cross section for air is $R_m = 1.805 \times 10^{-10}$ m. The pore dimension, C , is estimated from the Karman-Kozeny equation:

$$C \sim (1 - \phi) \sqrt{\frac{150K}{\phi^3}} \quad (21)$$

In Table 1 the maximum Knudsen number Kn_{max} , is computed from Eq. (19) using K from the same table and the minimum pressure of each matrix experiment. Recall that the Knudsen regime is established when $Kn > 1$, with a transition region from linear flow regime to Knudsen flow regime starting at $Kn \sim 0.14$. The Kn_{max} values of Table 1 suggest that all tests are performed out of the Knudsen regime. Some blocks might have a few initial data points in the transition region what do not influence the determination of the fitting coefficients because there are enough data points in the viscous regime to counterbalance their weak effect.

Conclusions

Mechanically compressed aluminum matrices, considered in the design of heat exchangers for cooling high power microelectronics systems, are tested for hydraulic characterization using air and PAO. These matrices are manufactured in aluminum alloy at various densities and void sizes.

Fundamental theory, based on the Forchheimer-extended Darcy flow model, is invoked for computing the permeability and inertia coefficient of the matrices. These hydraulic parameters are fundamental for the design and optimization of the micro heat exchangers. The assumed porous medium behavior of these matrices is confirmed experimentally.

Existing methodologies for determining permeability and inertia coefficient of porous media present a high degree of inaccuracy (extrapolation and visual graphical estimation). A more consistent and precise methodology, avoiding graphical extrapolation, is proposed. This methodology is based on direct curve fitting of the experimental results considering the values of each and every data point. The obtained permeability and inertia coefficient values are more consistent with the experimental range utilized. Moreover, the inertia coefficient value is more precise because the method does not rely on visual estimation of an asymptotic value. A general procedure for calculating uncertainties of parameters obtained by curve fitting experimental results is also presented.

Twenty-eight compressed matrices, having distinct characteristics, are manufactured for testing. The porosity variation of these matrices, from 30 to 90 percent, suggests a broad hydraulic performance. A simple theory for estimating the final (compressed) porosity of the matrices is presented and successfully tested against experimental results.

Nine of these matrices, chosen as primary candidates for the micro heat exchangers, are hydraulically tested and their parameters evaluated and presented. The parameter values vary as: $0.3 < \phi < 0.7$, $1.0 \times 10^{-10} \text{ m}^2 < K < 12 \times 10^{-10} \text{ m}^2$, $0.3 < c_F < 0.9$. With these hydraulic characteristics a series of microporous heat exchangers for cooling high frequency microwave systems can be manufactured within the design requirements set forth by Lage et al. (1996).

A final section is included in which some of the limitations of calculating the hydraulic parameters of porous materials from experimental data is discussed. The inaccuracies of measuring and calculating their values following existing methodologies are demonstrated. Our results indicate that the determination of K by curve fitting is always more meaningful than obtaining K from only one data point; if one is confident that the velocity range used for determining K is within the Darcy (linear) re-

gime, the K obtained from linear interpolation should fall very close to any K obtained from each data point. The difficulty is on predicting a priori where the Darcy regime is. Even if one tries to determine the velocity range of linear regime using the $Re_K \sim 1$ criterion one will not succeed because K is not known. So, one cannot determine at what velocity Re_K becomes 1 to decide the limit of linear regime until the value of K is obtained experimentally.

The importance of reporting the range of validity of the results is highlighted. Although the permeability and the inertia coefficients are not flow rate dependent (because constant coefficients correlate very well the experimental data), both coefficients are shown to be velocity-range dependent. Our explanation for this is simple: the linear and the quadratic effects are always present. Depending on the velocity range one effect will be stronger (or weaker) than the other, and this will be reflected in the value of the coefficients for the linear and quadratic terms! Therefore, it is important that K and c_F values be associated with the velocity range from which they are determined. Moreover, these values of K and c_F cannot be used with confidence for predicting hydraulic behavior at velocities outside this range.

Finally, the Knudsen flow regime effect, important at low air speed, is demonstrated not to affect the experimental results.

Acknowledgments

The financial and technical support provided by Texas Instruments is greatly appreciated. We are grateful to the referees for their careful review of this manuscript.

References

- Ahmed, N., and Sunada, D. K., 1969, "Nonlinear Flow in Porous Media," *Proceedings ASCE Journal of the Hydraulic Division*, Vol. 95, pp. 1847–1857.
- Bejan, A., 1993, *Heat Transfer*, Wiley, p. 646.

- Bergles, A. E., 1985, "Techniques to Augment Heat Transfer," *Handbook of Heat Transfer Applications*, W. M. Rohsenow et al., eds., McGraw-Hill, New York.
- Chevron, 1981, Synfluid Synthetic Fluids, Physical Property Data.
- Ergun, S., 1952, "Fluid Flow through Packed Columns," *Chemical Engineering Progress*, Vol. 48, pp. 89–94.
- Firoozabadi, A., 1995, "High-Velocity Flow in Porous Media," *Society of Petroleum Engineers Reservoir Engineering*, May, pp. 149–152.
- Givler, R. C., and Altobelli, S. A., 1994, "A Determination of the Effective Viscosity for the Brinkman-Forchheimer Flow Model," *Journal of Fluid Mechanics*, Vol. 258, pp. 355–370.
- Joseph, D. D., Nield, D. A., and Papanicolaou, G., 1982, "Nonlinear Equation Governing Flow in a Saturated Porous Medium," *Water Resources Research*, Vol. 18, pp. 1049–1052.
- Kaviany, M., 1991, *Principles of Heat Transfer in Porous Media*, Springer-Verlag, New York, p. 17 and pp. 333–337.
- Kline, S. J., and McClintock, S. A., 1953, "Describing Uncertainties in Single-Sample Experiment," *Mechanical Engineering*, Vol. 75, pp. 3–8.
- Kuzay, T. M., Collins, J. T., Khounsary, A. M., Morales, G., 1991, "Enhanced Heat Transfer with Metal-Wool-Filled Tubes," *Proceedings ASME/JSME Thermal Engineering Joint Conference*, Vol. 5, pp. 451–459.
- Lage, J. L., Weinert, A. K., Price, D. C., and Weber, R. M., 1996, "Numerical Study of a Low Permeability Microporous Heat Sink for Cooling Phased-Array Radar Systems," *International Journal of Heat and Mass Transfer*, Vol. 39, pp. 3633–3647.
- Lindemuth, J. E., Johnson, D. M., and Rosenfeld, J. H., 1994, "Evaluation of Porous Metal Heat Exchangers for High Heat Flux Applications," *Heat Transfer in High Heat Flux Systems*, A. M. Khounsary, T. W. Simon, R. D. Boyd, and A. J. Ghajar, eds., ASME HTD 301, pp. 93–98.
- Macdonald, I. F., El-Sayed, M. S., Mow, K., and Dullien, F. A. L., 1979, "Flow through porous media: The Ergun equation revisited," *Industrial Engineering Chemistry Fundamentals*, Vol. 18, pp. 199–208.
- Peng, X. F., Wang, B. X., Peterson, G. P., and Ma, H. B., 1995, "Experimental Investigation of Heat Transfer in Flat Plates with Rectangular Microchannels," *International Journal of Heat and Mass Transfer*, Vol. 38, pp. 127–137.
- Walpole, J. N., and Missaggia, L. J., 1993, "Microchannel Heat Sinks for Two-dimensional Diode Laser Array," *Surface Emitting Semiconductor Lasers And Arrays*, Vol. 1, G. A. Evans and J. M. Hammer, eds., Academic Press, New York.
- Ward, J. C., 1964, "Turbulent Flow in Porous Media," *Proceedings ASCE Journal of the Hydraulic Division*, Vol. 90 (HY5), pp. 1–12.

Tip Vortex Formation and Cavitation

B. H. Maines

Engineering Specialist,
Lockheed Martin Tactical Aircraft Systems,
Fort Worth, TX 76018

R. E. A. Arndt¹

Professor,
Saint Anthony Falls Laboratory,
University of Minnesota,
Minneapolis, MN

This paper summarizes recent research on the relation between boundary layer flow, tip vortex structure for a finite span wing, and cavitation. Three hydrofoils of elliptic planform of aspect ratio 3 were constructed with different NACA cross sections. Using a sprayed oil droplet technique to visualize the boundary layer flow, each foil was found to have dramatically different flow separation characteristics on both the suction and pressure sides. Careful examination of the tip region suggests that while the initial stages of vortex roll-up from the pressure side are similar for each hydrofoil section, the vortex boundary layer interaction on the suction side differs for each section. The degree of interaction was observed to increase as the lifting efficiency decreased. Over the Reynolds number range tested, tip vortex cavitation inception has been observed to follow an almost universal scaling. Differences in this scaling law are correlated with the degree of vortex/boundary layer interaction.

I Introduction

The formation of a wing tip vortex has been studied extensively with recent investigations concentrating on the region where initial roll-up of the vortex occurs. This region is of special interest in the study of tip vortex cavitation. McCormick (1962), was the first to study tip vortex cavitation in detail. He attempted to relate inception to the angle of attack, α , and Reynolds number, Re . He suggested that inception in a wing tip vortex should follow the relation

$$\sigma \approx \alpha^m Re^n \quad (1)$$

where $m \approx 1.4$ and $n \approx 0.35$. Following McCormick's lead, others, such as Billet and Holl (1979) and Arndt (1981), have shown that cavitation inception should scale as

$$\sigma_i = -C_{p0} \left[\frac{C_L}{4\pi} \right]^2 \left[\frac{c_0}{a} \right]^2 \quad (2)$$

where C_{p0} depends on the circulation distribution, C_L is the lift coefficient, c_0 the root chord and a is the vortex core radius. Thus, cavitation inception scales with the inverse of the core radius squared. McCormick developed a Reynolds number scaling law by assuming continuity of the viscous boundary layer flow into the core radius. This approach shows that the core radius, a , scales with the square root of the pressure side boundary layer thickness which infers that

$$\frac{c_0}{a} \sim Re^{(n/2)} \quad (3)$$

The reader is referred to Maines and Arndt (1993) for a recent summary of McCormick's work. Substitution of this Reynolds scaling relation into Eq. (2) yields the now familiar result

$$\sigma_i = KC_L^2 Re^n \quad (4)$$

Equation (4) has been confirmed experimentally by Platzer and Souders (1980), Fruman et al. (1992), and Arndt and Dugue (1992). These studies have shown n to be approximately 0.4. The discrepancy between $\alpha^{1.4}$ and C_L^2 in Eq. (4) is discussed

by Arndt and Keller (1992). It should be noted at this point that several authors, such as Billet and Holl (1979), Fruman et al. (1992), and Fruman (1994), assume that the vortex core, a , is directly proportional to the boundary layer thickness. This assumption leads to the conclusion that $\delta \sim c_0 Re^{-0.2}$ which is typical for a fully turbulent boundary layer. On the other hand, the original McCormick hypothesis leads to the conclusion that the boundary layer thickness scales with $c_0 Re^{-0.4}$, which appears reasonable for a transitional boundary layer. Both schools of thought lead to the same conclusion that the power n in Eq. (4) should vary for flows with transitional Reynolds numbers. It is important to note that the exponent, n , in Eq. (4) remains constant over a range of Reynolds numbers.

Several studies have shown that the core radius does indeed scale with Reynolds number or boundary layer characteristics (Quadrelli 1985; Steinbring et al., 1991; Katz and Galdo, 1989; Fruman et al., 1992; and McAlister and Takahashi, 1991); but none have sufficient data to determine the proper relationship between the boundary layer thickness and core radius. Despite the core radius scaling, it is important to note that σ_i has been found to scale with $Re^{0.4}$ for many foil planforms and cross sections across the Reynolds number range 420,000 to 2,800,000 (Platzer and Souders, 1980; Fruman et al., 1992; and Arndt and Dugue, 1992; Maines and Arndt, 1993; Fruman et al., 1994; Ma, 1994).² Thus, neither assumption for core radius versus boundary layer thickness fully explains the observed scaling with a fixed power of Reynolds number over a wide range of Reynolds numbers in which the Reynolds power law for boundary layer thickness should vary. More detailed boundary layer studies are required to resolve this issue.

Until detailed quantitative boundary layer measurements are made in the tip region, oil film techniques are one method to observe the boundary layer characteristics on wings or hydrofoils. These studies provide general insight into the relation between the boundary layer and the tip vortex. Patel and Hancock (1972) observed the boundary layer interaction of a streamwise vortex passing over a 2D airfoil. As the vortex approached the wing's surface, strong vortex/boundary layer interaction was observed. The classic s-shaped oil streaks associated with the vortex helical flow were clearly visible as was the streamwise separation. Flow patterns along the streamwise separation line also indicated the presence of a secondary vortex

¹ Present address: National Science Foundation, Room 525, 4201 Wilson Blvd. Arlington, VA 22230.

Contributed by the Fluids Engineering Division for publication in the JOURNAL OF FLUIDS ENGINEERING. Manuscript received by the Fluids Engineering Division January 30, 1996; revised manuscript received February 11, 1997. Associate Technical Editor: J. Katz.

² It is important to note that this conclusion is reached only after defining σ_i in terms of critical pressure rather than vapor pressure (Fruman, 1994, Arndt and Keller, 1992). This is especially important at low Re where the velocity is also low.

structure. A qualitative relationship between the oil streamline deflections and vortex strength was observed by Green and Duan (1994) by varying the tip shape on a rectangular planform wing. It has also been shown that deflection of oil flow streamlines on the pressure side near the tip appears to be invariant with Reynolds number (Quadrelli, 1985). In addition, Grow (1969) observed flow angles to also be independent of aspect and taper ratio for wings with similar boundary layer development.

Additional information on vortex roll-up has been obtained using smoke and dye visualization as well as with more quantitative techniques such as LDV measurements and numerical studies. Francis and Katz (1988) visualized the vortex roll-up around a rectangular planform wing using a fluorescing dye and laser sheet. Detailed measurements were obtained describing the position and structure of the vortex throughout the roll-up process. Fruman et al. (1992) and Fruman et al. (1994) have performed LDV studies with elliptic wings at different Reynolds numbers, angles of attack and planforms. It was observed that the maximum tangential velocities in the core occur very close to the tip. In addition, planform effects on vortex strength diminished rapidly downstream of the tip. The recent numerical studies of Song et al. (1994) support this view. Taking all these studies into account, a picture of the vortex roll-up process begins to emerge.

This study concentrates on the Reynolds number region in which the powers of C_L and Reynolds number have been observed to be invariant. Over this range of Reynolds numbers, experimental results (Fruman, 1994 and Maines and Arndt, 1993) show that the constant K in Eq. (4) is different for elliptic foils having different cross sections. In addition, it was found that the correlation between σ_i and $C_L^2 Re^{0.4}$ may not be linear for all hydrofoil sections. When the relationship is linear, as in Eq. (4), Maines and Arndt (1993) suggest that variations of the constant K could be related to differences in the circulation distribution within the core or in the constant of proportionality between boundary layer growth and Reynolds number.

In the current study, elliptical hydrofoils with different cross sections but the same planform were chosen so that only the boundary layer development varied. It is not the intent of this study to develop a design procedure. The objective is to examine the details of the interaction between the tip vortex and viscous boundary layer development with a view toward a better understanding of the observed variations in the constant K in the cavitation inception scaling law.

II Experimental Methods

Complementary research in air and water permits comparisons to be made between cavitation inception, lift and drag, and boundary layer characteristics of several different hydrofoils. This experimental research was conducted in a water tunnel and two wind tunnels (Maines and Arndt, 1993). In this study, three hydrofoils of elliptic planform with an aspect ratio of 3 were examined. The airfoil sections chosen were a NACA 66₂-415 $a = 0.8$, a modified NACA 4215, and a NACA 16-020. Two sets of hydrofoils were manufactured. Each of the foils in the smaller set had a root chord c_0 , of 81 mm and half span b , of 95 mm while for the larger set, $c_0 = 129.4$ mm and $b = 152.4$ mm. Testing included lift and drag measurements and cavitation inception experiments at various Reynolds numbers.

Wind tunnel tests utilizing the larger foils were conducted to determine the boundary layer characteristics at 56 m/s, $Re \approx 485,000$.

Oil flow data were obtained using a spray of fine droplets of an oil and titanium-oxide mixture. The wind tunnel was run at the test velocity for approximately 20 to 30 seconds until the oil pattern was no longer changing. No change of oil streamline deflections were observed during start-up or shut-down. This technique highlighted the details of the average boundary layer characteristics including flow separation, reattachment and tip vortex formation. Earlier data obtained by Arndt et al. (1991) and Quadrelli (1985), used a more traditional grid of larger oil drops. This older visualization technique did not reveal the details of the boundary layer flow near the tip.

A summary of the uncertainty analysis is discussed below. Details of this analysis are published in Maines (1995). Information related to the boundary layer separation and reattachment were obtained through direct measurement of the photographs using transparent overlays with chordwise and spanwise designations. The estimated uncertainty in chordwise position is $\pm 1-2$ percent. Characteristics of the vortex footprint obtained from oil flow pictures were measured by digitizing each photograph. Measurements could thus be made in a precise manner and the uncertainty in x, y coordinates was estimated to be less than ± 0.5 percent of the root chord. It was determined that the reported flow angles should only be used as a qualitative indicator of the true oil flow streamline directions. Uncertainty in flow angles was computed to range from ± 3 to ± 12 percent for 90 to 45 deg. Cavitation tests and force measurements were obtained over a velocity range of 7.5 m/s to 20 m/s. Velocity was determined from the nozzle differential pressure as calibrated with a pitot probe. The resulting uncertainty was found to be less than ± 0.6 percent. Over this velocity range, uncertainty in measured C_L was less than ± 1.2 percent. The uncertainty in absolute pressure as measured with a manometer was determined to be less than ± 1.0 percent. The uncertainty in velocity and absolute pressure measurements however do not constitute the major uncertainty in cavitation inception measurements. Uncertainty in cavitation number is due to the nuclei size and number and is thus a measurement of the variability of conditions rather than a true measure of uncertainty.

III Lift Measurements

Lift measurements of the three foils are shown in Fig. 1. Comparison is made with respect to zero lift which is approximately -2.7° for the 66₂-415, -4.3° for the 4215, and 0 deg for the symmetric 16-020. Notice that above $(\alpha - \alpha_0) \approx 6^\circ$, where α is the geometric angle of attack and α_0 is the angle of zero lift, that the lift curve for the 16-020 deviates dramatically from the 66₂-415 and the 4215. Thus equal lift coefficients above $C_L \approx 0.3$, require a much higher angle of attack for the 16-020 than for the other two foil cross sections. The decrease in the lift curve slope for the 16-020 above $(\alpha - \alpha_0) = 6.0$ degrees can be related to the boundary layer separation characteristics. The 4215 has excellent lifting characteristics and does not reach stall until $(\alpha - \alpha_0) \approx 32^\circ$.

As mentioned in Arndt and Dugue (1992), significant discrepancies in the measured lift and drag occurred between the Saint Anthony Falls Laboratory (SAF) data and the results reported by Arndt and Keller (1992) that were obtained in the

Nomenclature

a = viscous core radius

c_0 = root chord radius

C_L = lift coefficient

C_{po} = vortex pressure drop factor (dimensionless)

K = correlation factor (dimensionless)

m = exponent

n = exponent

Re = Reynolds number, Uc_0/ν

U = free stream velocity

α = angle of attack

ν = kinematic viscosity

σ_i = cavitation index at inception

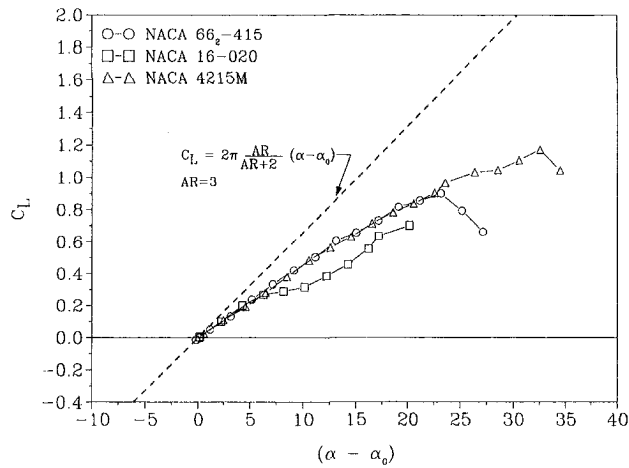


Fig. 1 Measured lift for three foils at $Re \approx 4.8 \times 10^5$ (SAFHL Facility) Uncertainty: $C_L, \pm 1.2\%$, $\alpha, \pm 0.1$ deg.

cavitation research facility at the Versuchsanstalt für Wasserbau in Oberrach, Germany.³ The SAF tunnel cross section was 190 mm \times 190 mm while the Oberrach tunnel had a cross section of 300 mm \times 300 mm. The larger set of hydrofoils was used in the Oberrach tunnel to insure that the measurements were made with the same relative blockage in each facility. The major difference in the two facilities is that the SAF facility has a low turbulence level due in part to its large contraction ratio, whereas the turbulence level in the Oberrach facility is significantly higher (A. P. Keller, private communication). This can greatly affect the lift characteristics as discussed in Stack (1931). For thick airfoils, Stack measured an increase in maximum lift of up to 15 percent between low and high turbulence. In addition, data published by Loftin and Smith (1949) have shown the lift curve slope to increase with Reynolds number for several airfoil cross sections. Presumably the higher turbulence level in the Oberrach facility simulates testing at a higher Reynolds number. This is consistent with the fact that the Oberrach lift data have a steeper slope. Fruman et al. (1992) have also found significant Reynolds number effects on the lift curve slope for the NACA 16-020 in this transitional Reynolds number range.

In this paper, comparisons to the oil film data are made with the lift measurements in the SAF facility since both sets of data were obtained in low turbulence facilities.

IV Boundary Layer Characteristics

The boundary layer characteristics for the three foils studied are dramatically different and will be presented as graphs of the separation/reattachment lines and bubble lengths versus angle of attack. To give the reader an idea of the detail obtained with the oil technique used, Fig. 2 shows a typical photograph of the suction side at low lift coefficients. In general, the boundary layer flow forward of the separation line remained two dimensional out to the tip while reattachment was two dimensional out to approximately 80 or 90 percent of the span, at low angles of attack. At higher angles of attack, the boundary layer both forward and aft of separation is more three dimensional in nature due to interaction with the tip vortex. The oil flow visualizations provided a strong indication that the separation bubbles were laminar. When excess or undissolved oil/titanium

³ When the discrepancy in the measured lift between the two facilities was first noted, the lift balances in both facilities were re-calibrated. No significant errors were found and it must be assumed the measured discrepancies are real. Although the blockage was the same in both facilities, the SAF test section had corner fillets in the test section. The effect of these fillets was analyzed with a numerical model. No significant effect of the fillets on lift could be found.

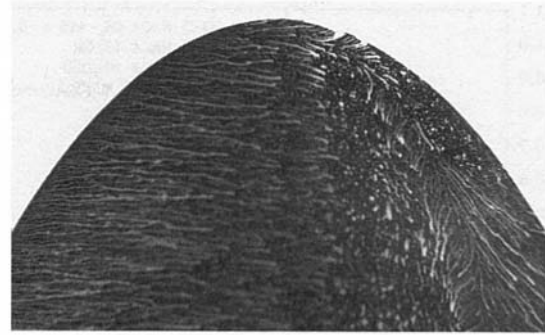


Fig. 2 Tip flow details on the suction side of the 66₂-415 at $C_L = 0.4$ ($Re = 4.85 \times 10^5$, Flow is from left to right)

oxide mixture produced a localized surface discontinuity, the flow was tripped and failed to separate in a narrow region downstream.

Both the 16-020 and the 66₂-415 develop a favorable pressure gradient to approximately 60–70 percent of the chord from the leading edge at low angles of attack. As the angle of attack increases, the suction peak for both the 16-020 and the 66₂-415 shifts forward to the leading edge. The suction peak of the 16-020 shifts forward at a lower lift coefficient than the 66₂-415. This is in contrast to the suction peak of the 4215 which occurs near the leading edge for all lift coefficients, thereby inducing a separation line at an almost constant relative chord position until stall occurs.

Figure 3 shows the separation lines for the three foils on the suction side at a relative spanwise position of $y/b \approx 0.8$. The boundary layer characteristics for the three foils are significantly different over much of the angle of attack range. The 16-020 and the 66₂-415 exhibit similar characteristics at low angles of attack with the separation line maintaining a constant relative chordwise position. The sudden shift of the separation line forward corresponds to a forward translation of the suction peak with a sharp increase in drag. The drag bucket for the 66₂-415 extends to $C_L = 0.6$ which corresponds to approximately $(\alpha - \alpha_0) = 13$ deg for the SAF data. Note that the position for separation on the 66₂-415 changes markedly in the angle of attack range 12–14 deg. This is consistent with the calculated results for pressure distribution in this angle of attack range (Abbott and von Doenhoff, 1949). Similarly, the shift of the separation line for the 16-020 occurs at approximately 8 deg. However, at slightly smaller angles the flow appears to remain fully attached with no separation on the surface. This is repre-

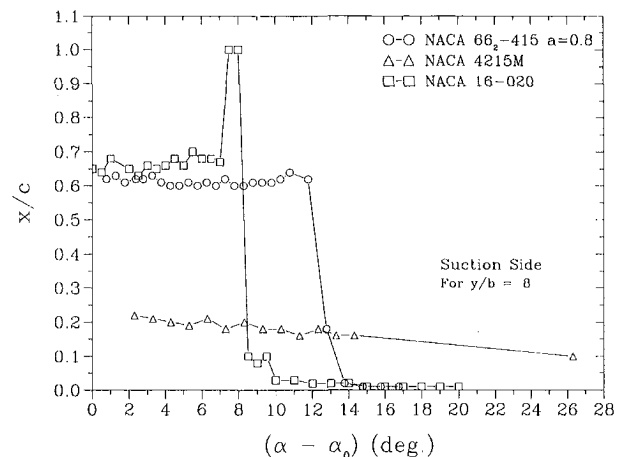


Fig. 3 Suction side separation lines on the three foils ($Re \approx 4.85 \times 10^5$) Uncertainty: $x/c, \pm 1\%$, $\alpha, \pm 0.5$ deg.

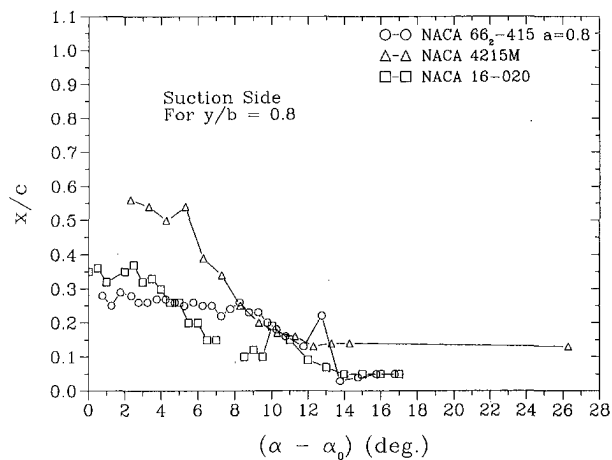


Fig. 4 Suction side bubble lengths ($Re \approx 4.85 \times 10^5$) Uncertainty: x/c , $\pm 1\%$, α , ± 0.5 deg.

sented by the value of the separation line being at $x/c = 1.0$. The 4215 shows very little change in the position of the separation line which shifts forward only approximately 10 percent of the chord over an angle of attack range of 26 deg.

Also of interest is flow reattachment which is clearly visible in Fig. 2. The recirculation zone within the separation bubble is distinguishable by the herring bone pattern near the trailing edge. Notice the three-dimensional nature of the surface flow near the tip. Very near the tip outboard of $y/b \approx 0.9$, two separation zones appear with indications of the presence of the tip vortex very close to the surface. Figure 4 shows the bubble lengths for the foils at approximately 80 percent of the span referenced to the local chord. As expected, the length of the bubble decreases as the angle of attack increases. It is interesting to note that for the range $5 \text{ deg} < (\alpha - \alpha_0) < 10 \text{ deg}$, the bubble length for the 16-020 is shorter than the other two foils. This is precisely the region in which the lift curve slope decreases for the 16-020 in Fig. 1. At high angles of attack, the separation bubbles for the 16-020 and the 66₂-415 are very short and confined to the leading edge of the wing. There is a significant bubble on the 4215 for the entire range of angle of attack.

Similarly on the pressure side, noticeable differences exist in the boundary layer characteristics. Separation on the pressure side is denoted by open symbols in Fig. 5. As expected, as the

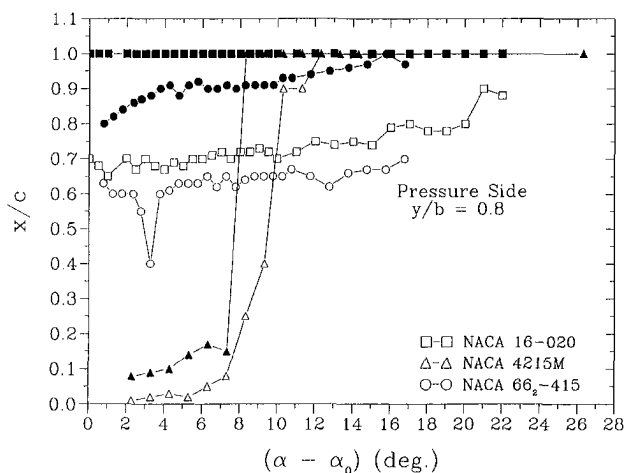


Fig. 5 Pressure side separation (open symbols) and reattachment (closed symbols) for the three foils. ($Re = 4.85 \times 10^5$) Uncertainty: x/c , $\pm 1\%$, α , ± 0.5 deg.

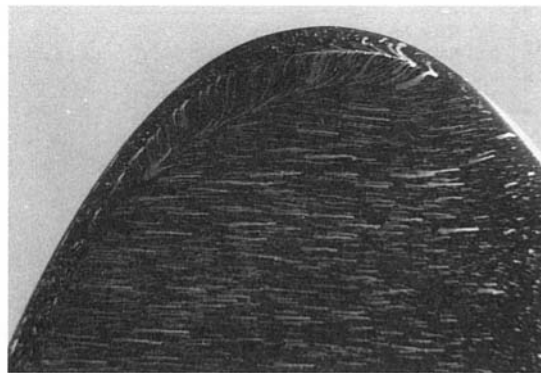


Fig. 6(a) Suction side boundary layer on the 16-020 at $C_L \approx 0.60$ ($Re = 4.85 \times 10^5$, Flow is from left to right)

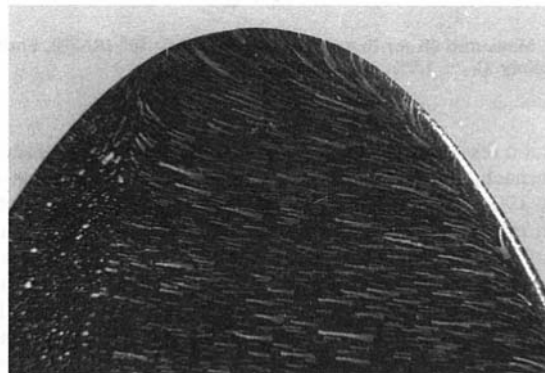


Fig. 6(b) Pressure side boundary layer on the 16-020 at $C_L \approx 0.60$ ($Re = 4.85 \times 10^5$, Flow is from right to left)

angle of attack is increased, separation shifts rearward toward the trailing edge. At low angles, the 4215 exhibits a leading edge separation due to its unique cross section characteristics. As incidence is increased, separation is seen to shift rearward. Included in Fig. 5 as solid symbols are the reattachment lines. Note that at all angles the flow fails to reattach on the 16-020 due to its extreme thickness near the trailing edge. At high incidence angles, flow on the 4215 also does not reattach. It is interesting to note that for the 66₂-415, the separation bubble remains nearly constant with angle of attack.

V Vortex Roll-Up

A detailed study of the near tip region was performed to determine the relation between boundary layer characteristics and vortex roll-up. Previously, Maines and Arndt (1993) noted that while the suction side boundary layer characteristics varied greatly, the pressure side characteristics were similar. It was inferred from surface flow streamlines that the maximum tangential velocities in the vortex were very close to the tip based on the location of the maximum spanwise deflections. In this study a closer examination was made by digitizing the photographs and performing measurements of the vortex footprint and deflections.

Figures 6(a) and (b) show streamline patterns of developed vortex/boundary layer interaction near the tip region of the NACA 16-020 suction and pressure side, respectively, at $C_L = 0.60$. In Fig. 6(a), the vortex footprint characterized by the s-shaped oil streaks clearly defines the separation and reattachment of the vortex flow. At this angle the vortex footprint is very large and extends forward, parallel to the leading edge of the foil, similar in behavior to a swept wing at incidence. Note that the vortex structure develops downstream of the leading edge separation bubble. Additional features on the suction side include the secondary vortex between the primary and the tip

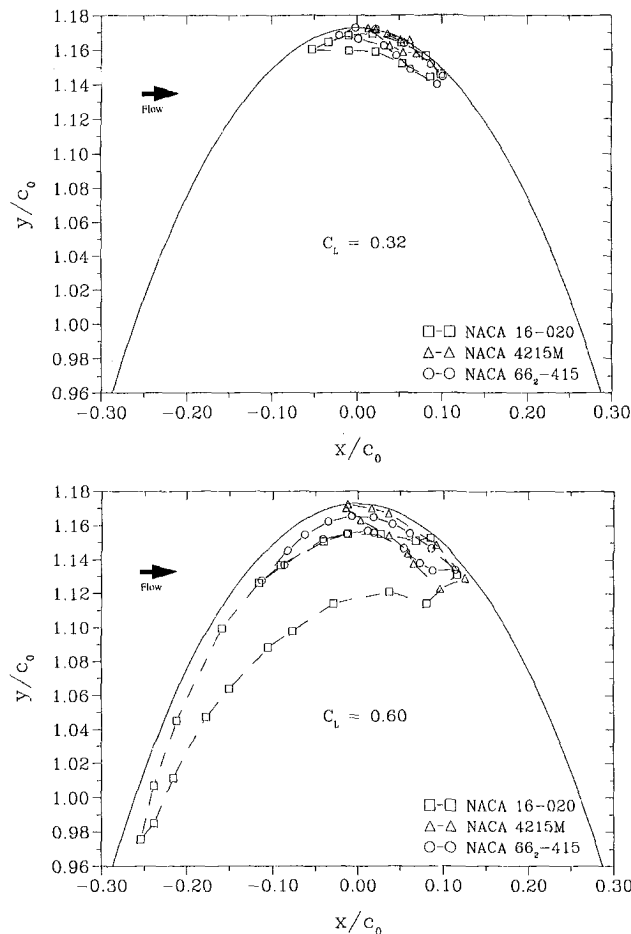


Fig. 7 Vortex footprint for each foil at different lift coefficients ($Re = 4.85 \times 10^5$, Flow is from left to right) Uncertainty: $\pm 0.5\%$

as indicated by the oil streaks moving inboard from tip to the main vortex separation line. Secondary vortices have also been observed by Francis and Katz (1988), who utilized laser sheet flow visualization to observe the vortex roll-up from a rectangular planform wing, and also by Patel and Hancock (1972), as mentioned previously. In Fig. 6(b), the spanwise flow is clearly evident on the pressure side. Note that fluid from the separation bubble is also being entrained into the vortex.

Figures 7(a) and (b) contain a summary of the vortex footprint on the suction side for all three foil sections at $C_L = 0.32$ and $C_L = 0.60$. The vortex footprint is defined as the area contained between the vortex separation and reattachment lines. The vortex origin is shown to progress forward as the angle of attack increases. Note, however, that at equal lift coefficient, the vortex footprint size and origin are different for each foil indicating different levels of vortex/boundary layer interaction for each foil section. As a general rule, at low angles of attack and lift coefficients, the footprint of each foil section begins near the tip and is wedged shaped similar to that shown for the 4215 in Fig. 7(a). However, as the angle increases, the vortex footprint size increases. In addition, both the size and shape of the footprint appear to be related to the boundary layer separation characteristics presented in Fig. 3. For the 66₂-415 and 16-020, after the separation bubble shifts forward, a leading edge vortex forms which slowly merges with the tip vortex as the angle of attack increases further. This is in contrast to the 4215. Since the separation bubble for the 4215 is virtually fixed, so is the shape and origin of the vortex footprint. However, the size of the footprint does increase with increasing C_L . The variation of the vortex footprint area with lift coefficient is shown

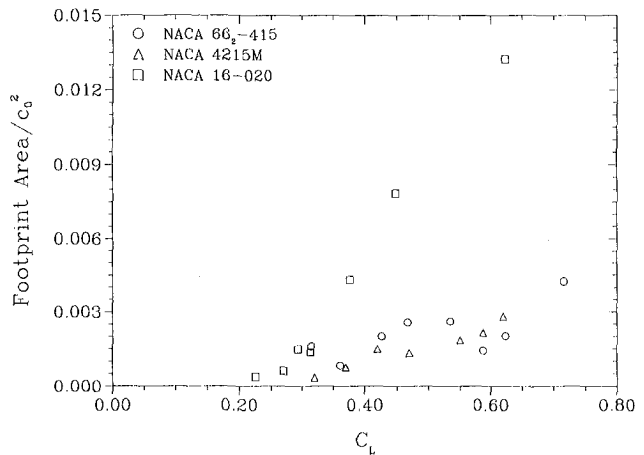


Fig. 8 Vortex footprint area versus lift coefficient ($Re = 4.85 \times 10^5$) Uncertainty: Area/ c_0^2 , $\pm 5\%$, C_L , $\pm 1.2\%$

in Fig. 8. Note that both the 66₂-415 and the 4215 show approximately equal levels of boundary layer interaction even though the characteristic footprint shape is different. At low C_L , the 16-020 footprint size is similar to the other two foil sections. However, for $0.30 < C_L < 0.35$, a sharp rise in the level of interaction occurs. The lift curve slope is also observed to decrease markedly in the same range of lift coefficient as depicted in Fig. 1.

Platzter and Souders (1980) did not observe a vortex footprint on the suction side of their 66₂-415. Probably because their oil film data were obtained at very low values of lift coefficient. In the present study, the vortex footprint was observed to decrease in size and move outboard until it was no longer detectable as C_L is decreased. These boundary layer observations are consistent with those made by Francis and Katz (1988). Their results show that the vortex attachment line and vortex center on the suction surface moves inboard with downstream distance and increasing angle. It is interesting to note that numerical studies by Shamroth and Briley (1979), and Mansour (1984) as well as the experimental studies by Francis and Katz (1988) indicate that during initial roll-up the vortex is very close to the surface and has an elliptical shape with the major axis parallel to the foil. This would explain the wide vortex foot prints observed in the oil film data.

Although large differences in the boundary layer separation characteristics were observed on the pressure side, oil film data

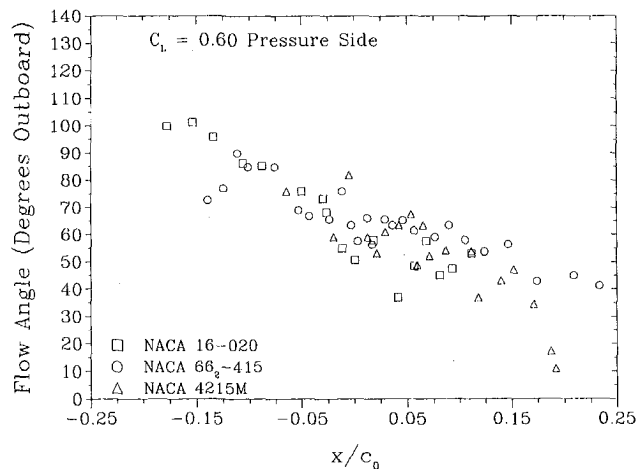


Fig. 9 Pressure side boundary layer spanwise flow angles ($Re = 4.85 \times 10^5$) Uncertainty: Flow angle, $\pm 12\%$, x/c_0 , $\pm 0.5\%$

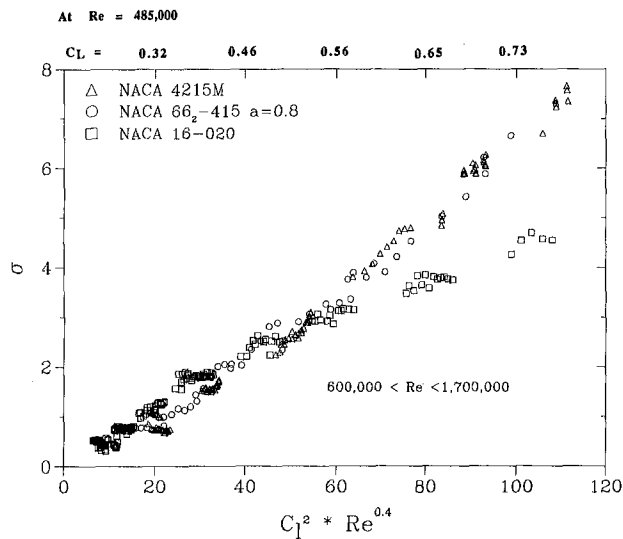


Fig. 10 Correlation of cavitation data with measured lift (top scale provides convenient reference to oil film data)

show similarities between each foil section near the tip. As shown in Fig. 6(b), streamlines, in general, are outward in the span-wise direction toward the tip to form the vortex. At low lift coefficients, slight differences in the spanwise flow angles with chordwise position are observed. However, it is interesting to note that the maximum deflection angles downstream of the tip are of the same magnitude and occur at similar locations. As the lift increases, flow patterns at the tip become more similar as shown in Fig. 9. Note that for all chordwise positions, the magnitude of the flow turning angle is approximately equal. These data suggest that the initiation of vortex roll-up is similar for all hydrofoil sections tested.

VI Cavitation Scaling

It is believed that the constant of proportionality in Eq. (4) depends on the boundary layer development. Data from the current study indicates that the constant, K , depends on the degree of vortex/boundary layer interaction on the suction side. Figure 10 shows cavitation number for all three foils over a range of lift coefficients and Reynolds numbers. The lift coefficients printed along the top of the figure correspond to a constant Reynolds number of 485,000 and thus are representative of the oil flow test conditions. These data were calculated using the critical pressure p_c , (Keller and Eichmann, 1989) rather than the vapor pressure, p_v . The critical pressure was determined by plotting p_0 at inception vs $U^{2.4}$ for various angles. The exponent, $m = 2.4$, was chosen based on achieving the best linear correlation between p_0 and U . Extrapolation to $U = 0$ defines p_c .

The data appear well correlated with $C_L^2 Re^{0.4}$ although each foil has a slightly different slope. The slopes, K , are 0.073, 0.068, and 0.059 for the 4215, 66₂-415, and 16-020, respectively. Thus, for equal values of C_L and Reynolds number, a higher constant K indicates a lower core pressure. Recall that oil film data indicate that although the pressure side separation characteristics differ, the near tip boundary layer flow angles are equal, suggesting a similar initial vortex roll-up for each foil. As the vortex interacts with the suction side more boundary layer fluid is entrained which increases the core radius and reduces the pressure drop across the vortex. Recall from Fig. 8, that the greatest vortex/boundary layer interaction was for the 16-020 with decreasing interaction for the 66₂-415 and 4215, respectively. This is consistent with the trends observed in the constant K . Notice also in Fig. 10, the decrease in slope for the 16-020 occurs between $0.35 < C_L < 0.40$ corresponding to an

increase in core pressure. Similar trends for K have been observed by Fruman (1994). This change in slope is also consistent with the sudden increase in vortex/boundary layer interaction between $0.30 \leq C_L \leq 0.35$ as shown in Fig. 8.

It should also be mentioned that Pichon et al. (1995) found that tripping the boundary layer of a 16-020 hydrofoil resulted in a relatively linear $C_L - \alpha$ curve and much better agreement with the $C_L^2 Re^{0.4}$ relationship. After tripping, their value for K was 0.048 which is still lower than the value obtained in this study. Clearly detailed measurements of the roll-up process are necessary before this discrepancy can be clarified.

VII Conclusions

A test program has been conducted to determine the effect of boundary layer development on vortex roll-up from a finite span wing. Comparisons were made at equal lift coefficients for three elliptic wings of different cross sections. The general boundary layer characteristics were found to be quite dissimilar with respect to both the separation and reattachment lines on the pressure and suction side. The 16-020 and the 66₂-415 exhibited aft suction side separation bubbles which shifted forward to the leading edge as the angle of attack increased. The 4215 suction side separation bubble near the leading edge shifted forward only slightly over the whole angle of attack range tested. Vortex/boundary layer interaction was found to be strongly coupled to the separation characteristics of each foil cross section, and lift coefficient. At moderate lift coefficients, measured flow angles on the pressure side show only small differences between each foil near the tip, however as C_L increases, flow angles are approximately equal in magnitude. Equivalent flow angles suggest that the initiation of vortex roll-up from the pressure side is similar for all foils tested. Examination of tip vortex cavitation characteristics indicates that while trends with C_L and Reynolds number may approach a universal relation, the constant of proportionality is related to the vortex/boundary layer interaction on the suction side. Analysis indicates that a hydrofoil cross section that requires a relatively higher angle of attack to develop a given lift coefficient, produces a higher degree of suction side vortex/boundary interaction. This results in a corresponding increase in core pressure and hence a decrease in cavitation number. It should be emphasized that the scaling of σ_i with C_L^2 has only been confirmed for hydrofoils with an elliptical loading.

Acknowledgments

The authors would especially like to thank Dr. Andreas Keller of the Versuchsanstalt für Wasserbau, Oberrach, Germany and Christian Dugue formerly of Ecole Nationale Supérieure de Technique Avancées, Paris, France for their extensive contributions to this project. This study was supported by the Office of Naval Research. Dr. Edwin Rood was the contract monitor.

References

- Abbott, I. H., and von Doenhoff, A. E., *Theory of Wing Sections*, McGraw-Hill, New York, 1949.
- Arndt, R. E. A., 1981, "Cavitation in Fluid Machinery and Hydraulic Structures," *Annual Review Fluid Mechanics*, Vol. 13, pp. 273-328.
- Arndt, R. E. A., Arakeri, V. H., and Higuchi, H., 1991, "Some observations of tip-vortex cavitation," *Journal of Fluid Mechanics*, Vol. 229, pp. 269-289.
- Arndt, R. E. A., Dugue, C., 1992, "Recent Advances in Tip Vortex Cavitation Research," *Proc. Intl. Symp. on Propulsors and Cavitation*, Hamburg, Germany, June.
- Arndt, R. E. A., and Keller, A. P., 1992, "Water Quality Effects on Cavitation Inception in a Trailing Vortex," *ASME JOURNAL OF FLUIDS ENGINEERING*, Vol. 114, Sept., pp. 430-438.
- Billet, M. L., and Holl, W. J., 1979, "Scale effects on various types of limited cavitation," *International Symposium on Cavitation Inception*, ASME Winter Annual Meeting, New York, pp. 11-23.
- Francis, T. B., and Katz, J., 1988, "Observations on the Development of a Tip Vortex on a Rectangular Hydrofoil," *ASME JOURNAL OF FLUIDS ENGINEERING*, Vol. 110, June, pp. 208-215.

- Fruman, D. H., 1994, "Recent Progress in the Understanding and Prediction of Tip Vortex Cavitation," *2nd Intl. Symp. on Cavitation*, Tokyo, Apr.
- Fruman, D. H., Dugue, C., Pauchet, A., Cerrutti, P. and Briancon-Marjolet, L., 1992, "Tip Vortex Roll-Up and Cavitation," *Nineteenth Symposium on Naval Hydrodynamics*, Seoul, Korea, Aug.
- Fruman, D. H., Cerrutti, P., Pichon, T., and Dupont, P., 1994, "Effect of Hydrofoil Planform on Tip Vortex Roll-up and Cavitation," *2nd Intl. Symp. on Cavitation*, Tokyo, April.
- Green, S. I., and Duan, S. Z., 1994, "The Ducted Tip—A Hydrofoil Geometry with Superior Cavitation Performance," to be published in ASME JOURNAL OF FLUIDS ENGINEERING.
- Grow, T. L., 1969, "Effect of a Wing on its Tip Vortex," *Journal of Aircraft*, Vol. 6, No. 1, Jan–Feb, pp. 37–41.
- Katz, J., and Galdo, J., 1989, "Effect of Roughness on Rollup of Tip Vortices on a Rectangular Hydrofoil," *Journal of Aircraft*, Vol. 26, No. 3, pp. 247–253.
- Keller, A. P., and Eichmann, G., 1989, "Velocity and Size Scale Effects for Incipient Cavitation of Axisymmetric Bodies in Water of Different Quality," *Proceedings, International Symposium on Cavitation Inception*, ASME, New York, pp. 79–86, Dec.
- Loftin, L. K., and Smith, H. A., 1949, "Aerodynamic Characteristics of 15 NACA Airfoil Section at Seven Reynolds Numbers from 0.7×10^6 to 9.0×10^6 ," NACA TN 1945.
- Ma, Dong, 1994, "Experimental Studies of Water Quality Effects on Tip Vortex Cavitation," MS thesis, University of Minnesota.
- Maines, B. H., and Arndt, R. E. A., 1993, "Viscous Effects on Tip Vortex Cavitation," *Intl. Symp. Cavitation Inception*, ASME, N.Y., Winter.
- Maines, B. H., 1995, "Tip Vortex Formation and Cavitation," Ph.D. thesis, University of Minnesota.
- Mansour, N. N., 1984, "Numerical Simulation of the Tip Vortex off a Low Aspect Ratio Wing at Transonic Speed," AIAA-84-0522, Jan.
- McAlister, K. W., and Takahashi, R. K., 1991, "NACA 0015 Wing Pressure and Trailing Vortex Measurements," NASA TP-3151, Nov.
- McCormick, B. W., 1962, "On Cavitation Produced by a Vortex Trailing From a Lifting Surface," *ASME Journal of Basic Engineering*, Sept., pp. 369–379.
- Patel, M. H., and Hancock, G. J., 1972, "Some Experimental Results of the Effect of a Streamwise Vortex on a Two-dimensional wing," *Aeronautical Journal*, Apr., pp. 151–155.
- Pichon, T., Fruman, D. H. and Billard, J.-V. (1995) "Effect of Tripping laminar to Turbulent Boundary Layer Transition on Tip Vortex Cavitation" *International Symposium on Cavitation, CAV '95*, May, Deauville, France
- Platzer, G. P., and Souders, W. G., 1980, "Tip Vortex Cavitation Characteristics and Delay on a Three-dimensional Hydrofoil," 19th American Towing Tank Conference, University of Michigan, Ann Arbor.
- Quadtelli, J. C., 1985, "An Experimental Investigation of Vortex Roll-up for and Elliptically Loaded Wing," M.S. thesis University of Minnesota, Apr.
- Shamroth, S. J., and Briley, W. R., 1979, "A Viscous Flow Analysis for the Tip Vortex Generation Process," NASA CR-3184, October.
- Song, C. C. S., Chen, C., Wang, Q., 1994, "Simulation of Tip Vortex Flow and Cavitation," *XVII IAHR Symposium*, Beijing.
- Stack, John, 1931, "Tests in the Variable Density Wind Tunnel to Investigate the Effects of Scale and Turbulence on Airfoil Characteristics," NACA TN 364, Feb.
- Steinbring, D. R., Farrell, K. J., and Billet, M. L., 1991, "The Structure of a Three-Dimensional Tip Vortex at High Reynolds Numbers," ASME JOURNAL OF FLUIDS ENGINEERING, Vol. 113, Sept., pp. 496–503.

Numerical Modeling of the Thermodynamic Effects of Cavitation

Manish Deshpande
Post-Doctoral Scholar.

Jinzhong Feng
Senior Research Associate.

Charles L. Merkle
Professor.

Propulsion Engineering Research Center,
Department of Mechanical Engineering,
The Pennsylvania State University,
University Park, PA 16802

A Navier-Stokes solver based on artificial compressibility and pseudo-time stepping, coupled with the energy equation, is used to model the thermodynamic effects of cavitation in cryogenic fluids. The analysis is restricted to partial sheet cavitation in two-dimensional cascades. Thermodynamic effects of cavitation assume significance in cryogenic fluids because these fluids are generally operated close to the critical point and also because of the strong dependence of the vapor pressure on the temperature. The numerical approach used is direct and fully nonlinear, that is, the cavity profile evolves as part of the solution for a specified cavitation pressure. This precludes the necessity of specifying the cavity length or the location of the inception point. Numerical solutions are presented for two-dimensional flow problems and validated with experimental measurements. Predicted temperature depressions are also compared with measurements for liquid hydrogen and nitrogen. The cavitation procedure presented is easy to implement in engineering codes to provide satisfactory predictions of cavitation. The flexibility of the formulation also allows extension to more complex flows and/or geometries.

Introduction

Cavitation has presented a persistent challenge to the design of inducers and turbopumps. Here we concentrate on the thermodynamic effects associated with "sheet" cavitation in cryogenic fluids. Sheet cavitation refers to the large cavitation bubble that appears adjacent to the body surface when the local pressure drops below the fluid vapor pressure. Such a bubble has a distinct interface between the vapor and the fluid over most of the cavity. The cavity is sustained by a continuous vaporization process whose rate is determined by local geometry and flow conditions. The shape and size of the cavity are, therefore, dependent on the physical properties of the working fluid and the local fluid pressure, velocity and temperature.

Unlike the cavitation pressures observed in traditional fluids, the pressures observed inside cavities in cryogenic fluids is substantially lower than the vapor pressure corresponding to the free-stream temperature. The reason for this is that the temperature of the liquid in the immediate vicinity of the liquid-vapor interface is depressed below the free-stream temperature because the latent heat of vaporization must be extracted from the bulk liquid. Because of the very strong variation of thermodynamic properties in cryogenic fluids the temperature depression (usually negligible) is quite substantial. The volume of fluid that is affected by the cooling action of the evaporation and the magnitude of the temperature depression is determined by the thermal boundary layer that is induced at the liquid-vapor interface. The temperature depression in this local thermal boundary layer reduces the local vapor pressure of the fluid, which leads to a lower observed cavity pressure. As a result, the cavity size is smaller than it would be if there were no temperature depression effects present.

Thermodynamic effects of cavitation are generally more significant in cryogenic fluids than in room temperature fluids such as water, because they are typically operated closer to their critical point. In addition, the slope of the vapor pressure-temperature curve of cryogenic fluids is much steeper than that for

water (Fig. 1). As a result, the temperature depression observed for cryogenic fluids is generally larger than that observed for room temperature fluids, and the change in vapor pressure is more significant because of the slope of the vapor pressure curve. Although typical temperature depressions in cryogenic fluids are only one to two Kelvin, this corresponds to changes in vapor pressure of typically a factor of two. Hence the effect of cavitation is quite noticeable on a macroscopic level.

Previous analyses of cavitation can be split into two groups. The goal of the first group has been to predict the size and shape of the cavitation bubble. For these analyses, the cavity pressure is taken as known (generally corresponding to the free-stream temperature) and thermodynamic effects are not addressed. The goal of the second group has been to predict the temperature depression for a known cavity geometry. For the predictions of the geometrical effects of the cavitation bubble, potential flow theory has been used extensively (Tulin, 1953; Wu, 1972; Geurst, 1959; Uhlman, 1987), and analyses based on both conformal mapping and surface singularity distributions have been used. Although potential flow theory gives reasonable predictions for cavity geometries, it provides no rational means for predicting the temperature depression effect, because as noted above, the temperature depression arises because of the thermal boundary layer in the liquid. Boundary layer effects are of course omitted in potential flow theory.

The analyses of thermodynamic effects have generally been focussed on obtaining correlations for temperature depression as a function of flow conditions and liquid properties. Particular methods of importance include the B-factor method (Stahl and Stepanoff, 1956; Hord, 1972; Moore and Ruggeri, 1968) and the entrainment theory method (Holl and Wislicenus, 1961; Billet and Weir, 1975; Billet et al., 1981). Both of these result in correlations for temperature depression that take the form, $\Delta T = B(\rho_v/\rho_l)(H_{fg}/C_p)$ where B is a constant. In the B-factor method, B, is based on the ratio of "vapor volume" to "liquid volume" affected by the vaporization process. The value of B is found by dimensional analysis and correlation of existing data. One obvious short-coming of this approach is that it is the flow rates of liquid and gas, not their volumes that determine the thermodynamic effects. Conversion from volume ratio to flux ratio can of course be easily effected by multiplying by a

Contributed by the Fluids Engineering Division for publication in the JOURNAL OF FLUIDS ENGINEERING. Manuscript received by the Fluids Engineering Division November 15, 1994; revised manuscript received October 7, 1996. Associate Technical Editor: S. P. Vanka.

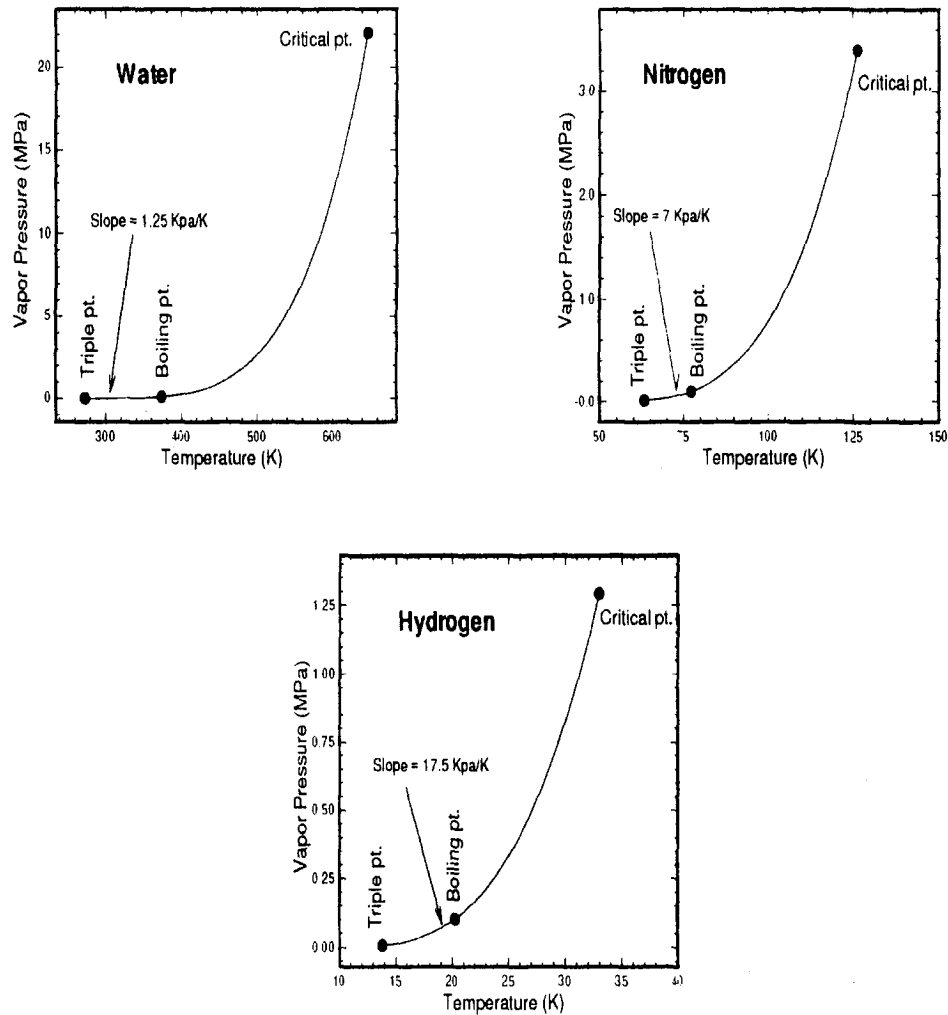


Fig. 1 Vapor pressure dependence on temperature for various fluids

velocity ratio, but either flux ratios or volume ratios should provide the same results in the dimensional analyses.

The entrainment theory avoids reliance upon the volume of the fluid involved by correlating the proportionality constant, B , on the basis of the volume flow rate through the cavity and associated Nusselt, Reynolds and Prandtl numbers. This volume flow rate is, however, very difficult to ascertain, and is again found by dimensional analyses and correlation of data. Although comparisons of these two methods for the same data are not

available, it would appear that they should give identical results, or nearly so.

A more recent analysis of thermodynamic effects in cavitation (Fruman et al., 1991) identifies the vapor production rate in the cavity and the heat exchange at the liquid-vapor interface as being the two primary issues in predicting temperature depression. They apply the concepts of the above-mentioned entrainment theory and set the vapor flow rate through the cavity equal to the experimentally determined

Nomenclature

C = airfoil chord length	p_c = cavitation pressure	α = angle of attack
C_p = specific heat of fluid, negative cavitation number	Pr = Prandtl number	α_t = thermal diffusivity
e = total energy	q_l = heat transfer from liquid to cavity	β = artificial compressibility factor
$E = \xi$ flux vector	Q = volume flux through cavity; primary dependent variable vector	Γ = modified identity matrix
$E_v = \xi$ viscous flux vector	Re = Reynolds number	ξ, η = transformed coordinates
$F = \eta$ flux vector	T = local fluid temperature	ρ_l = fluid density
$F_v = \eta$ viscous flux vector	u = x -direction velocity component	ρ_v = vapor density
J = Jacobian of coordinate transformation	u_c = vapor velocity within cavity	μ_t = effective fluid viscosity
H_{fg} = heat of vaporization	u_∞ = velocity at inlet	τ = pseudo time variable
k = thermal conductivity of fluid	$U = \xi$ -direction contravariant velocity	Ω = boundary condition vector
n = normal direction vector	$v = y$ -direction velocity component	
p = local static pressure	$V = \eta$ -direction contravariant velocity	
	x, y = Cartesian coordinates	

Subscripts

ξ, η = differentiation with respect to transformed coordinates

flow rate of non-condensable gas that is necessary to maintain a cavity of the same length. They then estimate the thermal boundary layer effects on the basis of a rough flat plate, turbulent boundary layer theory. Their results do not require empirical correlation, but are in reasonable agreement with the data from Hord (1972).

In the present paper, we attempt to determine both the geometrical characteristics of the cavity along with the temperature depression effect by utilizing numerical solutions of the combined Navier-Stokes equations and the energy equation. The solution of the Navier-Stokes equations in combination with an algebraic turbulence model provides the details of the cavity geometry, while the solution of the energy equation provides the thermal boundary layer in the fluid from which the detailed thermodynamic effects and, in particular, the temperature depression in the vicinity of the cavity interface can be obtained. The complete numerical solution determines the thermal boundary layer on the interface directly, and avoids the necessity of having to estimate its characteristics. This resulting theory provides temperature depression predictions that are in reasonable agreement with Hord's data while also predicting cavity shapes that agree well with his measurements. For completeness, comparisons of predicted cavity shapes are made with the measurements of Shen and Dimotakis (1989). The results that are presented are restricted to steady two-dimensional flows, although the analysis can easily be extended to unsteady or three-dimensional flows.

Theory and Numerical Model

The complete flow and temperature fields, including the cavity shape, are described by the incompressible, two-dimensional Navier-Stokes equations, and the energy equation.

$$\begin{aligned}\nabla \cdot \hat{V} &= 0 & \text{Continuity} \\ (\hat{V} \cdot \nabla) \hat{V} &= -\nabla p + \mu_t \nabla^2 \hat{V} & \text{Momentum} \\ (\hat{V} \cdot \nabla) e &= -k_t \nabla^2 T + \mu_t \Phi & \text{Energy}\end{aligned}$$

where the density has been absorbed in the pressure. When written in a strongly conservative form in generalized coordinates using the unsteady artificial compressibility formulation (Merkle and Tsai, 1986), the above equations become

$$\Gamma \frac{\partial Q}{\partial \tau} + \frac{\partial}{\partial \xi} (E - E_v) + \frac{\partial}{\partial \eta} (F - F_v) = 0 \quad (1)$$

where Q , E , and F are

$$Q = \begin{pmatrix} p \\ u \\ v \\ T \end{pmatrix}, \quad E = \begin{pmatrix} U \\ uU + y_\eta p \\ vU - x_\eta p \\ UT \end{pmatrix}, \quad F = \begin{pmatrix} V \\ uV - y_\xi p \\ vV + x_\xi p \\ VT \end{pmatrix}$$

and

$$\begin{aligned}\Gamma &= \text{diag} (1/\beta, 1, 1, 1) \\ E_v &= \frac{k}{J} \Gamma \left[(\nabla \xi \cdot \nabla \xi) \frac{\partial (JQ)}{\partial \xi} + (\nabla \xi \cdot \nabla \eta) \frac{\partial (JQ)}{\partial \eta} \right] \\ F_v &= \frac{k}{J} \Gamma \left[(\nabla \xi \cdot \nabla \eta) \frac{\partial (JQ)}{\partial \xi} + (\nabla \eta \cdot \nabla \eta) \frac{\partial (JQ)}{\partial \eta} \right]\end{aligned}$$

where

$$k = \text{diag} (0, \mu_t/\rho, \mu_t/\rho, k_t/\rho C_p)$$

Here J is the Jacobian of the metric terms, U and V are the contravariant velocities in the ξ and η directions, respectively, as above,

$$\begin{aligned}U &= uy_\eta - vx_\eta \\ V &= vx_\xi - uy_\xi\end{aligned}$$

The quantity μ_t represents the effective viscosity including contributions from both the molecular and the turbulent parts. The turbulent contribution appears as the Reynolds stress in the averaged equations. In the present calculation, this Reynolds stress is calculated by applying the algebraic Baldwin-Lomax turbulence model (Baldwin and Lomax, 1978). In the energy equation k_t represents the effective thermal conductivity including a turbulent contribution. This contribution is calculated from the turbulent viscosity, calculated as above, and a turbulent Prandtl number which is fixed at 0.9.

The time derivatives in Eq. (1) are added for computational purposes to enable a time marching scheme to advance the flow variables in the system. When the solution converges, the time derivatives in the equations approach zero and the steady-state Navier-Stokes solution is recovered. The time derivative in the continuity equation has no physical meaning but its coefficient β is chosen to scale the eigenvalues of the system to the same order of magnitude so that efficient convergence rate can be achieved. In general, curvilinear coordinates, β is defined by:

$$\beta = \frac{(U + V)^2}{(x_\xi^2 + x_\eta^2 + y_\xi^2 + y_\eta^2)} \quad (2)$$

A four-stage Runge-Kutta explicit time-marching algorithm is used to advance the Navier-Stokes/coupled energy system of equations in pseudo-time. The solution converges when the time-derivatives become zero so that the solution approaches the steady-state solution corresponding to the governing equations and the specified boundary conditions.

Central-differencing is used for all spatial derivatives. Local time-stepping is used to improve convergence. A fourth-order artificial viscosity (Kwak et al., 1986) is used to prevent odd-even splitting in the numerical solution.

The inviscid portion of the coupled equations becomes hyperbolic with the addition of the artificial time derivative. This enables the use of the Method of Characteristics (MOC) procedure to formulate the inflow and outflow boundary conditions, analogous to compressible flow. In the present solution, the total pressure and the inflow angle are specified at the upstream, while the static pressure is specified at the downstream boundary. These boundary conditions are complemented by information obtained from out-running characteristics computed from the hyperbolic nature provided by the artificial compressibility formulation. Boundary conditions at the body surface in the absence of cavitation are the no-slip condition, and a specified wall temperature. These are augmented by applying the normal momentum equation on the surface. Boundary conditions on the cavity interface are discussed in the next section.

Cavitation Model

The fundamental characteristics of the cavitation analysis are determined by the cavity model and the boundary conditions applied at the cavity surface. The cavity is modeled as a constant pressure region. Since neither the cavity surface profile nor its location is known prior to the solution, an iterative procedure is needed to enforce both the pressure and the velocity conditions. In brief, any particular point on the cavity surface is switched from a "solid wall" point to a "cavity" point if the pressure drops below the local cavity pressure. The boundary conditions on these points is then switched to the cavitation boundary conditions. This allows the normal velocity on the cavitating surface to deviate from zero enabling the cavity location to be determined by tracing

the streamline that bounds the cavity. The cavity profile is established by ensuring that the thickness is non-negative at each point. Negative cavity thicknesses correspond to the cavity interface moving inside the airfoil surface. Points with negative cavity thickness are treated as noncavitating points in the next time step. This check on cavity thickness is the primary technique that allows the cavity length to contract if necessary as the iteration proceeds. The cavity is also checked for continuity under the constraint that only a single-cavity be allowed to exist on the foil surface. If multiple cavities exist, the longer of the two cavities is retained.

The cavitation model described above completely defines both the cavity pressure and the location of the cavity interface. The cavity is sustained by a continuous vaporization process whose rate is dependent on geometry and flow conditions. The shape and size of the cavity are therefore dependent on the physical properties of the working fluid and the local fluid pressure, velocity and temperature. The pressure within the cavity is determined by the liquid vapor pressure at the temperature of the interface. In cryogenic fluids, the pressure inside these cavities is substantially lower than the vapor pressure associated with the free-stream temperature as noted above. The volume of fluid that is affected by the cooling action of the evaporation and the magnitude of the temperature depression are determined by the thermal boundary layer that is induced at the liquid-vapor interface. The temperature depression in this local thermal boundary layer reduces the local vapor pressure of the fluid, which leads to a lower observed cavity pressure. As a result, the cavity size is smaller than it would be if there were no temperature depression effects present.

The constant pressure assumption has, however, been used extensively in previous analyses of cavity geometrical characteristics, on the basis that support of longitudinal pressure gradients inside the cavity is very difficult to justify because of the density ratio between the liquid and vapor. This ratio is approximately 1000:1 for water, and is generally 50:1 for cryogenic fluids.

The analysis of the thermodynamic effects of cavitation requires the solution of the energy equation for the energy transfer at the cavity interface coupled with the Navier-Stokes equations. Although potential flow theories and Euler analyses give reasonable predictions for the cavity geometries and pressures, they provide no rational means for predicting the temperature depression effects. As noted above, the temperature depression arises because of the thermal boundary layer in the liquid over the interface. The computation of this boundary layer necessitates the solution of both the energy and the Navier-Stokes equations.

The boundary conditions for modeling the thermal effects of cavitation are a combination of the cavity surface boundary conditions, discussed in the previous section, augmented by the boundary conditions for the energy equation, which are obtained from an energy balance at the cavity interface as outlined below.

At the liquid-vapor interface, the heat required for production of the vapor is supplied from the liquid adjacent to the interface. The heat flux required to vaporize the fluid evaporated from an elemental portion of the liquid-vapor interface is given as

$$q_l ds = \rho_v H_{fg} dQ \quad (3)$$

where q_l is the heat flux, ds is an elemental surface area on the interface, ρ_v is the density of the vapor, H_{fg} is the latent heat of the liquid, and dQ is the volume flow rate of the vapor added to the cavity in the area, ds . The heat conducted to the liquid-vapor interface is given by,

$$q_l = -k \frac{dT}{dn} \quad (4)$$

An energy balance at the cavity surface is accomplished by equating the heat fluxes in Eqs. (3) and (4). This yields the

following relation for the normal temperature gradient at the liquid surface,

$$\frac{dT}{dn} = - \frac{\rho_v}{k} H_{fg} \frac{dQ}{ds} = - \frac{\rho_v}{\rho_l \alpha_l C_p} \frac{H_{fg}}{C_p} \frac{dQ}{ds} \quad (5)$$

where $\alpha_l = \rho_l C_p / k$ is the thermal diffusivity of the liquid.

This normal temperature gradient is used as the boundary condition for the energy equation on the cavity interface. It is the presence of this heat sink that depresses the temperature at the interface and gives rise to the thermal boundary layer in the liquid.

The computation of the energy balance in Eq. (5) requires a knowledge of the rate of vaporization of the liquid along the entire length of the cavity interface. Unfortunately, this is not available in analyses such as the present one that treat the cavity as a constant pressure region. Thus, whereas the energy equation allows us to compute the thermal diffusion in the liquid, the omission of a mass balance in the vapor phase prevents us from determining the rate of vaporization and the corresponding magnitude of the heat release needed. The task of modeling the flowfield inside the cavity is, however, not a trivial one. While the evaporation process and the fluid dynamics throughout most of the cavity is straightforward, the condensation process in the aft portion of the cavity is not. This process is characterized by strong unsteady effects, condensation, and growth of droplets distributed throughout the rear portion of the cavity, and eventual coagulation of the distributed liquid into a continuous phase. In addition, it is likely that much of the condensation process occurs when large segments of gas break off from the bubble and, after being engulfed by the surrounding liquid, are condensed somewhere downstream of the attached cavity. While these effects may be modeled by a complete two-phase analysis, the model is certain to have much arbitrariness and to require much empirical information that is not now available. There have, to date, been no attempts to measure the mass flow through a cavity, or to provide information on the global rate of vaporization. Such measurements are extremely difficult and are not expected in the near term. In view of this complexity and the lack of experimental evidence, we have here taken a simple bounding analysis for the evaporation rate in the cavity.

The postulate here is that the net mass flow through the cavity will be bounded on the upper side by a uniform flux of vapor at the free-stream velocity, that occupies the entire cavity height, h , and by zero (no evaporation) on the lower side. That is to say the average velocity, u_{avg} through the cavity will be between $0 \leq u_{avg} \leq u_\infty$. This gives us a bounded order of magnitude for the vaporization rate. Accordingly we relate the volume flux entering the cavity to the increase in the cavity height, dh , and the bulk vapor velocity within the cavity, u_c , as $dQ = u_c dh$. Inserting this relation into Eq. (5) gives

$$\frac{dT}{dn} = - \frac{\rho_v}{\rho_l} \frac{Re}{C} \frac{Pr}{C_p} \frac{H_{fg}}{C_p} \frac{dh}{ds} \frac{u_c}{u_\infty} \quad (6)$$

where the Reynolds number is based on the airfoil chord, C . For the present calculations this relation, that specifies the normal temperature gradient at the cavity interface, is used as the additional boundary condition on the cavity surface for the energy equation. The bulk velocity within the cavity is taken equal to the free-stream velocity, $u_c = u_\infty$, thereby giving an upper bound on the mass flux within the cavity. Other assumptions for this mass flux would provide a shift in the predicted magnitude of the temperature depressions but no qualitative difference in the results. The results suggest that this assumption is qualitatively realistic.

The thermal boundary condition on the remaining noncavitating portion of the body surface, has been set to a constant temperature corresponding to the temperature of the free-stream. Other thermal boundary conditions can easily be incorporated on the noncavitating surface. The present constant tem-

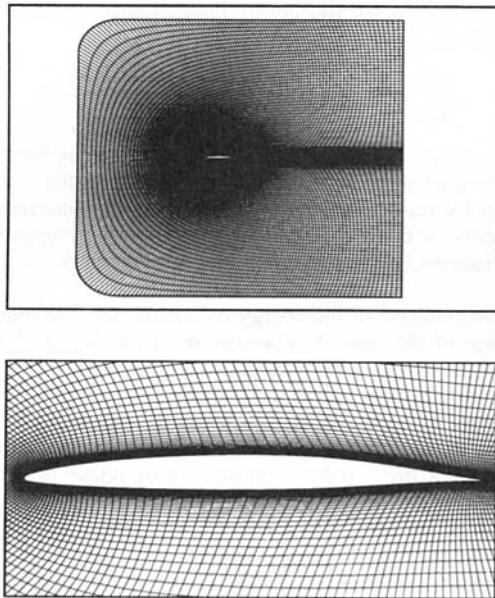


Fig. 2 Details of airfoil geometry and C-grid used in Navier-Stokes computations for cavitating flow over NACA66(MOD) airfoil. Grid size is 262×91 .

perature condition should closely resemble an adiabatic condition.

Results

Based on the theory described above, a computer program has been developed to compute the complete flowfield around a cavitating body, the cavity size and shape, and the thermodynamic effects that are present in two-dimensional sheet cavity flows. To demonstrate the capabilities of the model in the absence of thermodynamic effects, we begin by presenting predictions of the cavity shapes for flow over a NACA66(MOD) + $a = 0.8$ hydrofoil in water. These predictions are then compared with the corresponding experimental measurements of Shen and Dimotakis (1989) of the pressure distribution around the cavitating airfoil, including the pressure distribution in the cavity region and the cavity length.

The geometry of the airfoil and the near-field details of the C-grid used for the computations are shown in Fig. 2.¹ Shen's experiments with this airfoil were conducted with the airfoil centered in a water tunnel whose walls were five chord lengths apart. The presence of these walls was simulated in the computations by placing an inviscid boundary at that location. This outer boundary condition implies that tunnel wall boundary layer effects have been omitted. This omission should have little effect on the pressure distribution around the airfoil for the present level of tunnel blockage.

The calculated pressure distribution on the non-cavitating hydrofoil is compared with experimental measurements in Fig. 3 for a chord Reynolds number of 1.2×10^6 . The airfoil is at an angle of attack of one degree. The pressure distribution on the suction surface is in good agreement with the measurements. Similar calculations based on an isolated airfoil, and based on potential flow theory show the importance of including both the tunnel wall effects and the viscous effects. Further, laminar flow calculations showed considerable pressure distribution

¹During review, it was brought to our attention that the foil used in these experiments was not the standard NACA66(MOD) section but, because of manufacturing considerations, was actually slightly thicker near the trailing edge (termed as NACA66 (DTMB modified)). The airfoil section used here corresponds to this modified geometry.

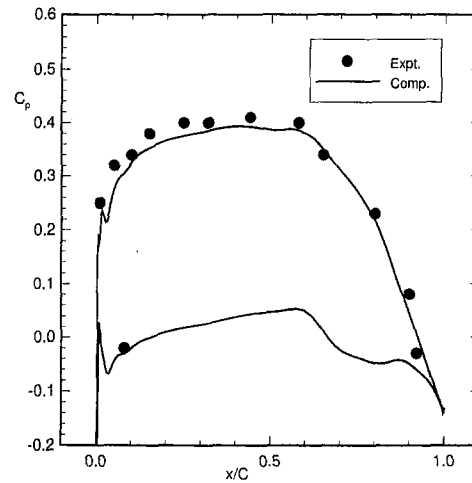


Fig. 3 Pressure distribution on a NACA66(MOD) hydrofoil for noncavitating flow—comparison between Navier-Stokes computations and experimental measurements from Shen and Dimotakis at one degree angle of attack

shifts due to separation. Overall, this comparison (as well as numerous others not shown here (Deshpande, 1994)) shows that our Navier-Stokes calculation gives satisfactory agreement with experimental measurements, and so we next turn to predictions of cavitation regions on this same airfoil.

Measurements for the same Reynolds number (1.2×10^6) but an angle of attack of four degrees, show a significant cavitation region on the suction side. Predictions of this cavitating condition are compared with pressure measurements in Fig. 4. The profile of the cavity shape on the airfoil at this condition is also shown in Fig. 4. Because these experiments were conducted in water where thermodynamic effects are negligible, the pressure level in the cavity was taken directly from the experiment (a cavitation number of 1.0) and input to the computer code. (The measured cavity pressures in Shen's experiments were in excellent agreement with the vapor pressure corresponding to the free-stream temperature.) The predicted cavity length is in good agreement with the measured cavity length as the figure shows, and in addition, the predicted steep pressure rise in the cavity termination region is confirmed by the experi-

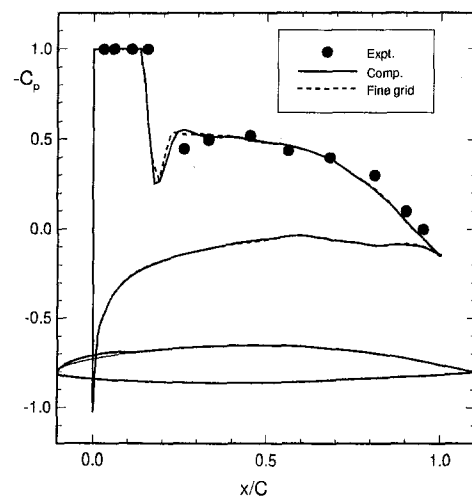


Fig. 4 Pressure distribution and cavity profiles on a NACA66(MOD) hydrofoil for cavitating flow—comparison between nonlinear Navier-Stokes computations and experimental measurements from Shen and Dimotakis at four degrees angle of attack. Computations shown on two grids (262×91 and 523×181) showing numerical convergence.

ment. To verify the numerical accuracy of the results, computations are presented for both a 262×91 grid and a 523×181 grid. As can be seen the cavity size and the pressure distribution are converged. The differences between the two grids is due to increased resolution of the singularity near the cavity termination point and is therefore an effect of the choice of afterbody condition and not of numerical accuracy.

Details of the computed flow field are shown in Fig. 5. The final computed grid is shown in the figure and the deformed grid around the cavity profile can be clearly identified. Also shown are the near-field pressure contours and the velocity vectors for this case. Details of the vector field show the boundary layer on the airfoil surface. The transition from the cavity surface to the viscous airfoil wall can also be clearly identified in the figure.

The favorable comparison of the pressure distribution over the remainder of the airfoil indicates that the shape of the cavity is also well predicted. We therefore conclude that the model provides a reasonable prediction of the cavitation region. This model has also been demonstrated to satisfactorily predict midchord cavitation (Deshpande et al., 1993), which is difficult to predict using indirect methods such as potential flow formulations. Consequently, we now turn to predictions of the thermodynamic effect on cavitation.

For the evaluation of the thermodynamic effects of the model, we use the two-dimensional airfoil, temperature depression data of Hord (1972). Hord has presented temperature data for both liquid hydrogen and liquid nitrogen. The airfoil geometry in the experiment was constructed from a tapered plate with a cylindrical head for the leading edge. The airfoil was sting mounted from the rear. The cryogenic tunnel used was quite narrow (the height of the tunnel was about five times the airfoil thickness), so that the airfoil formed a significant blockage in the tunnel. Inclusion of the wall effect is paramount to obtain the correct pressure distribution and the proper cavity size. For the present comparisons, we again omitted the boundary layers on the tunnel walls. Hord's experiments were conducted with a symmetric airfoil at zero degrees angle of attack, so symmetric cavitation regions were produced on both sides of the airfoil. Our computations took advantage of the symmetry and computed the flow over one side of the airfoil.

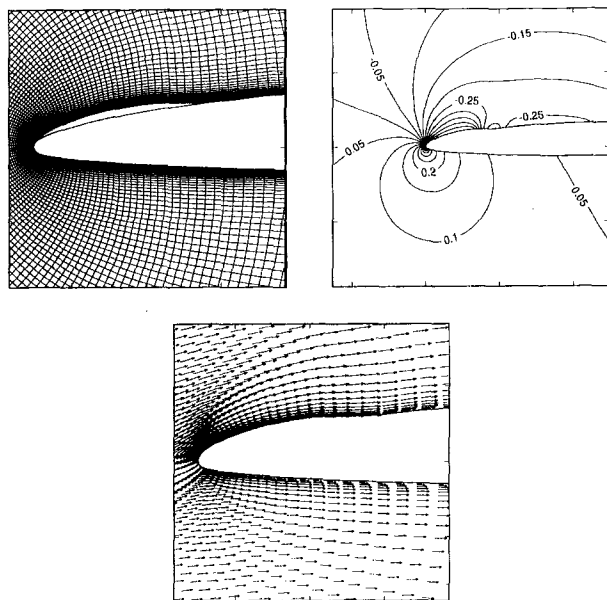


Fig. 5 Details of final computed grid, pressure contours and velocity vectors over NACA66(MOD) hydrofoil. Vectors are shown in increments of two grid points.

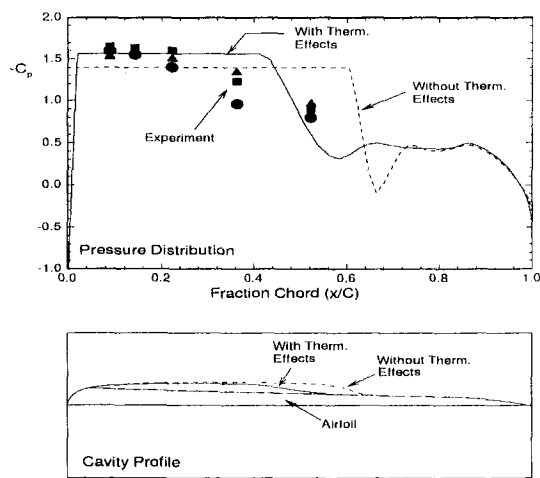


Fig. 6 Comparison of pressure distribution between nonlinear Navier-Stokes computations and experimental measurements of Hord for three cases with and without thermodynamic effects

The experiments covered a range of free-stream temperatures, free-stream pressures and upstream inflow velocities. Because it was impossible to control any of these precisely, the data points are scattered throughout this three-dimensional space. We have selected a number of representative cases for comparison with our calculations. Some of the numerical results together with comparisons with experimental measurements are shown in Figs. 6–10.

Figure 6 shows the measured and calculated pressure distributions over the airfoil for a case where the cavity length is approximately half the chord. Cavity predictions are presented both with and without the effect of fluid temperature depressions. As can be seen the agreement between the calculation and the experiment is quite satisfactory both in terms of cavitation pressure and cavity length (as indicated by the pressure distribution) for the case where thermodynamic effects are included, but the cavity is much over-predicted when the thermodynamic effects are neglected. The predicted cavity shape from the numerical calculation is also shown on the figure.

Temperature depressions for liquid hydrogen are presented in Fig. 7 as a function of the cavity length. The calculated temperature depressions correspond to three different upstream velocities. The experimental data, which are for a velocity range of about 25 to 55 m/s show nondimensional temperature depres-

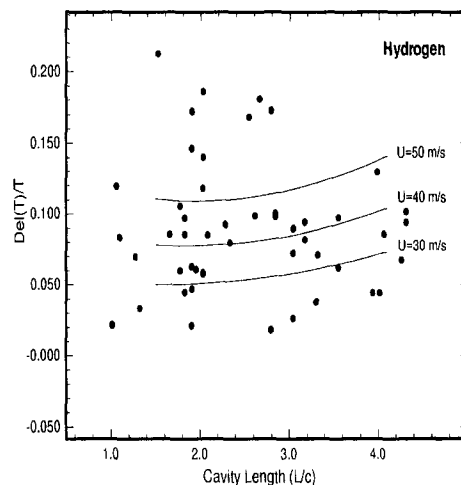


Fig. 7 Temperature depression versus cavity length for hydrogen-comparisons with Hord

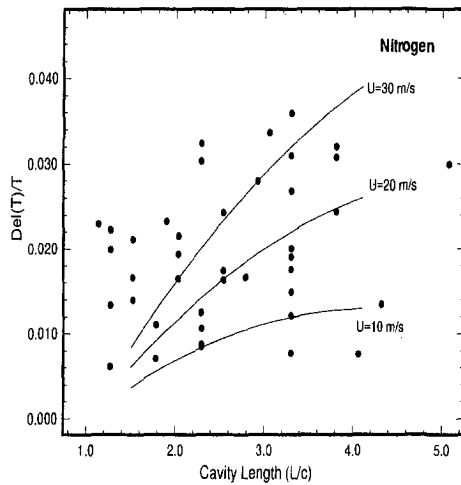


Fig. 8 Temperature depression versus cavity length for nitrogen. Comparisons with Hord

sions up to 0.18. The analysis predicts similar magnitudes (up to 0.16). In addition, the analysis predicts that $\Delta T/T$ increases with free-stream velocity, a prediction that appears intuitively correct, but one that cannot be discerned clearly from the experimental data.

The corresponding results for liquid nitrogen are presented in Fig. 8 along with the appropriate experimental data. Both the analysis and the experiment indicate the temperature depression for nitrogen is considerably less than that for hydrogen. The maximum ($\Delta T/T$) in both measurements and predictions is about 0.04. This reduction arises because of the lower vapor/fluid density ratio and the lower heat of vaporization for nitrogen. Again the effects of velocity cannot be discerned in the experimental data.

To illustrate the thermodynamic effect on the cavitation performance of different working fluids, a demonstrative comparison of the temperature depressions among hydrogen, nitrogen and water is presented in Fig. 9. The cryogenic fluids introduce much stronger evaporative cooling effects as compared to the room-temperature fluid. The temperature depression in hydrogen is almost an order of magnitude greater than that of water. More importantly the vapor pressure of cryogenic liquids is a very strong function of temperature (Ref. Fig. 1). As a result,

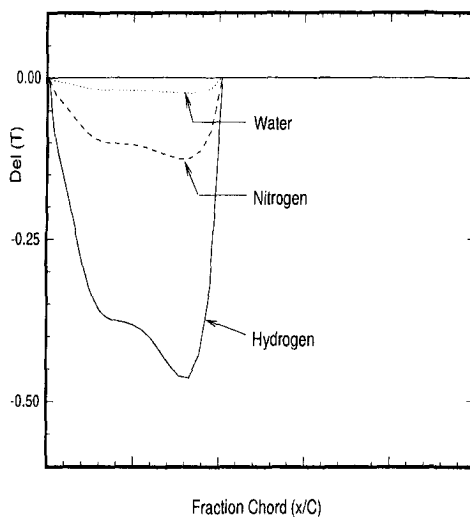


Fig. 9 Comparison of temperature depression for water, nitrogen and hydrogen over a NACA0012 airfoil at five degrees angle of attack

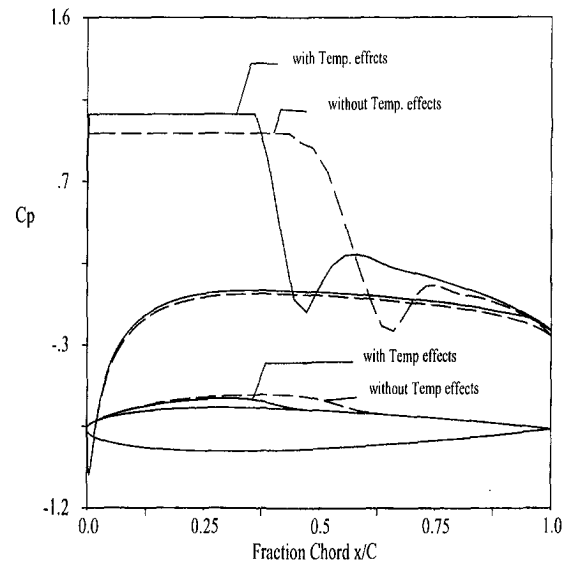


Fig. 10 Cavitation calculations with and without temperature depression effects for a NACA0012 airfoil at five degrees angle of attack

the temperature depression may appear to be small relative to the free-stream temperature, but the local vapor pressure change due to subcooling is significant. For such fluids this strong dependence of vapor pressure on local temperature can lead to substantially different predictions of cavitation performance based on cavitation pressure with or without considering the temperature depressions. To put this in numerical perspective, cavitation analyses both before and after altering the vapor pressure for both liquid hydrogen and water are presented in Fig. 10. The correction of vapor pressure is based on the maximum temperature depression which is calculated using a vapor pressure corresponding to the free-stream bulk temperature. As one may expect, the cavity for water does not change because of the relative independence of its vapor pressure on temperature as well as its minimal temperature depression. For liquid hydrogen, however, the cavity shape is considerably different and the cavity length is reduced about 30 percent after modifying the vapor pressure.

Conclusion

Cavitation in cryogenic fluids involves not only mass transfer due to evaporation, but also heat transfer corresponding to the latent heat of the vaporizing fluid. The thermodynamics coupled with the fluid flow adjacent to the cavity require that the details of the thermal boundary layer in the liquid be known before the temperature depression, and hence the cavity pressure, can be determined. In the present analysis, we include for the first time such a detailed model through the numerical solution of the combined Navier-Stokes and energy equations. The results of the model are first justified for non-cryogenic fluids (water) where thermodynamic effects are not significant. Comparisons show the Navier-Stokes analysis is in reasonable agreement with experiment for the case where thermodynamic effects are absent. The application of the model to cryogenic flows where thermodynamic effects are important provides a direct prediction of the thermodynamic effects in the liquid. Results here show a reduction of 20–40 percent in the cavity length because of the temperature depression effect. Comparisons with experiment show that the magnitude of the temperature depression predicted by the model is in reasonable qualitative agreement with available measurements and that the model correctly predicts the thermodynamic differences between hydrogen and nitrogen. Predicted cavitation bubble sizes in liquid hydrogen are also in good agreement with experiment. Finally although the

model predicts that the temperature depression increases monotonically with the free-stream velocity, this effect cannot be discerned from the measurements, even though it does appear plausible. In summary, the model appears to provide an acceptable approach for inquiries of engineering concern in cryogenic cavitation. Additional work is needed to assess the detailed physics of the vaporization process, as well as effects of non-steadiness and three-dimensionality.

Acknowledgments

This work was supported by the Propulsion Engineering Research Center, Pennsylvania State University under NASA US-ERC Grant NAGW-1356.

References

- Baldwin, B. S., and Lomax, H., 1978, "Approximate and Algebraic Model for Separated Turbulent Flows," AIAA Paper 78-257, *AIAA 16th Aerospace Sciences Meeting*, Huntsville, AL.
- Billet, M. L., and Weir, D. S., 1975, "The Effect of Gas Diffusion of the Flow Coefficient of a Ventilated Cavity," *ASME JOURNAL OF FLUIDS ENGINEERING*, Vol. 97.
- Billet, M. L., Holl, J. W., and Weir, D. S., 1981, "Correlations of Thermodynamic Effects for Developed Cavitation," *ASME JOURNAL OF FLUIDS ENGINEERING*, Vol. 103.
- Deshpande, M., Feng, J., and Merkle, C. L., 1994, "Cavity Flow Predictions Based on the Euler Equations," *ASME JOURNAL OF FLUIDS ENGINEERING*, Vol. 116, pp. 36-44.
- Deshpande, M., Feng, J., and Merkle, C. L., 1993, "Navier-Stokes Analysis of 2-D Cavity Flow," *Cavitation and Multiphase Flow Forum*, Washington, D.C.
- Deshpande, M., 1994, "Computational Fluid Dynamic Modeling of Cavitating Flows," Ph.D. dissertation, Department of Mechanical Engineering, The Pennsylvania State University.
- Fruman, D. H., Benmansour, I., and Sery, R., 1991, "Estimation of the Thermal Effects on Cavitation of Cryogenic Liquids," *Cavitation and Multiphase Flow Forum*, ASME, FED, Vol. 109.
- Geurst, J. A., 1959, "Linearized Theory for Partially Cavitating Hydrofoils," *International Shipbuilding Progress*, Vol. 6, No. 60.
- Holl, J. W., and Wislicenus, G. F., 1961, "Scale Effects on Cavitation," *ASME Journal of Basic Engineering*, Vol. 83.
- Hord, J., 1972, "Cavitation in Liquid Cryogenics: 2 Hydrofoils," NASA CR-2156.
- Kwak, D., Chang, J. L. C., Shanks, S. P., and Chakravarthy, S. R., 1986, "A Three-Dimensional Navier-Stokes Flow Solver Using Primitive Variables," *AIAA Journal*, Vol. 24.
- Merkle, C. L., Tsai, Y.-L. Peter, 1986, "Application of Runge-Kutta Schemes to Incompressible Flows," AIAA Paper 86-0553, *24th Aerospace Sciences Meeting*, Reno, NV.
- Moore, R. D., and Ruggeri, R. S., 1968, "Prediction of Thermodynamic Effects on Developed Cavitation Based on Liquid-Hydrogen and Freon-114 Data in Scaled Venturis," NASA TN D-4899.
- Shen, Y. T., and Dimotakis, P. E., 1989, "The Influence of Surface Cavitation on Hydrodynamic Forces," *Proceedings 22nd ATTC*, St. Johns.
- Stahl, H. A., and Stepanoff, A. J., 1956, "Thermodynamic Aspects of Cavitation in Centrifugal Pumps," *ASME Journal of Basic Engineering*, Vol. 78, No. 8.
- Tulin, M. P., 1953, "Steady Two-Dimensional Cavity Flows About Slender Bodies," David Taylor Model Basin Report 834.
- Uhlman, J. S., 1987, "The Surface Singularity Method Applied to Partially Cavitating Hydrofoils," *Journal of Ship Research*, Vol. 31, No. 2.
- Wu, T. Y., 1972, "Cavity and Wake Flows," *Annual Review of Fluid Mechanics*, Vol. 4.

Ensemble-Average Equations of a Particulate Mixture

L. M. Liljegren

Senior Research Engineer,
Analytic Sciences Department,
Pacific Northwest Laboratory,
Richland, WA 99352

A method of evaluating the transfer terms appearing in the ensemble-average fluid transport equation is developed and applied to obtain the transport equations describing flow of a dilute particulate mixture containing solid spherical particles. The equations apply in the limit where interactions between phases are both quasi-steady and viscous, which is defined as flows that meet the three criterion $Re_f(a/L)^2 \ll 1$, $\nu_f \tau / a^2 \gg 1$, and $Re_p \ll 1$. In this limit, the terms describing transfer of momentum between the two phases of the mixture are evaluated to $O(1)$ in the particle radius and $O(\gamma_p)$ in the particle phase density. The continuity equations and consistency principle are exact. When the first two conditions are not met, the transport equations require the terms that describe virtual mass forces; when the third is not met, the transport equations require terms that describe Oseen corrections to the drag term.

1 Introduction

Many two-phase models have been proposed and are widely used to model the flow of particulate mixtures. The advantage of these models over simpler mixture models is the ability to predict separate velocities for each phase. It can be demonstrated that in many steady-state flows the difference between the average velocity of each phase is $O(a^2)$; the proof requires some knowledge of the averaged equations. When an average two-phase flow model is used, this velocity difference can be predicted to leading order only if the closure describing momentum transfer is complete to $O(1)$. It can also be shown that to obtain distinct individual velocities of each phase, as required to apply separate boundary conditions for each phase in an internal flow, the continuity equation and consistency principle must be $O(a^2)$ in the particle radius. The goal of this analysis is to develop a two-phase model that can be used to predict flow of a particulate mixture in the limit where particle-fluid interactions are quasi-steady and dominated by viscous mechanisms. The closures provided are sufficiently detailed to allow independent boundary conditions to be specified for each phase. A two-phase model with truncations to the appropriate level is developed here.

The form of a two-phase model is not unique. Several definitions of average concentration and average velocity of the particle phase appear in the literature. To leading order, all terms in a two-phase model are identical, regardless of the preferred choice of averaged velocity and concentration. However, the higher-order terms appear different, depending on the definitions selected. To ensure that a two-phase model will achieve a higher order than a mixture model, i.e., a model in which the velocities of the two phases are assumed equal, it is necessary to provide a full derivation of all terms in all five equations comprising the two-phase model. All equations should be developed using the same method and the same definitions of variables. The primary difference between this derivation and other higher order models (Nigamatulin 1979; Passman 1986; and Hwang and Shen, 1989 and 1991) is that this one uses consistent definitions for average particle velocity and density and a consistent truncation of the higher order terms based on Taylor series expansions.

¹ Presented, in part, at the ASME Fluid Engineering Conference, Washington D.C. 1993.

² Pacific Northwest Laboratory is operated for the U.S. Department of Energy by Battelle Memorial Institute under Contract DE-AC06-76RLO 1830.

Contributed by the Fluids Engineering Division for publication in the JOURNAL OF FLUIDS ENGINEERING. Manuscript received by the Fluids Engineering Division October 3, 1994; revised manuscript received June 7, 1996. Associate Technical Editor: R. L. Panton.

2 Ensemble Averaging Rules

Some preliminaries are required prior to deriving any two-phase model. These preliminaries include definitions of the ensemble-average, a conditional average and particle centered averages, definitions of phase densities, and rules for taking averages of derivatives. The rules and notation are described here.

The idea of an ensemble average is widely used when describing flows of viscous mixtures (Batchelor, 1972 and Hinch, 1977) and the idea has been extended to two-phase flows to develop two-phase formulations (Joseph et al., 1990 and Drew and Lahey, 1993). Some of the advantages of ensemble averaging over volume averaging of particulate flows are described in Hinch (1977).

To apply the idea to obtain a two-phase model, it is convenient to define the indicator function for the fluid phase I_f which takes on the value 1 when fluid is present and 0 when particles are present. The fluid phase density γ_f is defined as the ensemble-average of the presence of the fluid phase $\gamma_f = \langle I_f \rangle$; and describes the probability that a point is occupied by fluid. The particle indicator function in a two-phase mixture obeys $I_p = 1 - I_f$, and the particle phase density as defined $\gamma_p = \langle I_p \rangle$. So, the following consistency rule applies: $\gamma_p + \gamma_f = 1$. Because of the properties of the indicator function, $\langle \Psi | I_f = 1 \rangle = \langle I_f \Psi \rangle / \langle I_f \rangle$. Following the notation of Hinch (1977), the slash is used to imply a conditional average; because it is cumbersome, the conditional average will henceforth be indicated using an overbar and a superscript to denote the type of conditioning. So, the conditional average based on the presence of the fluid will be written as $\langle \Psi | I_f = 1 \rangle \equiv \bar{\Psi}^f$. Using the relations outlined previously the following holds $\gamma_f \bar{\Psi}^f = \langle I_f \Psi \rangle$.

The two-phase model developed here will rely on the phase densities and conditional averages defined previously. However, evaluation of the closure terms in a two-phase model requires use of two other ensemble-average quantities, which are based on particle centers. The particle number density $N_p(x)$ is the probability density function for particles centers, referred to as the number density. The conditional average of an arbitrary quantity Ψ when a particle center is at x , which will be denoted $\bar{\Psi}^c(x)$.

The algebraic relationship between the two types of averages may be specified when the size, shape, and orientation of particles are known. When the particle phase consists of monodispersed spheres, the average when any portion of a particle occupies x occurs whenever a particle center is located at $x + y$ with $y < a$. So, $\gamma_p \bar{\Psi}^c(x) = \iiint_{V_a} N_p(x + y) \bar{\Psi}^c(x + y) d\tau$, where the integral is performed over a sphere of radius a surrounding

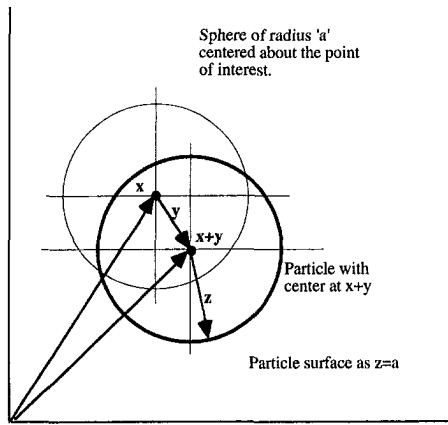


Fig. 1 Definition of coordinate system for integration over a particle surface

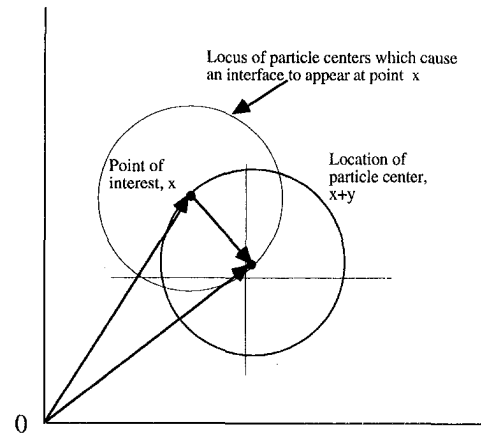


Fig. 2 Particle centered on $x + y$. Location of interest is point "x."

the point of interest. A typical situation is shown in Fig. 1. When the length scale ℓ describing variations in ensemble-average quantities is small compared to the size of a particle, the integral may be approximated by expanding the integrand in a Taylor series.

$$\gamma_p \bar{\Psi}^p(x) = \iiint_{v_a} \left\{ [N_p \bar{\Psi}^c]_x + y_i \left[\frac{\partial (N_p \bar{\Psi}^c)}{\partial x_i} \right]_x + \frac{y_i y_j}{2!} \left[\frac{\partial^2 (N_p \bar{\Psi}^c)}{\partial x_i \partial x_j} \right]_x + \dots \right\} dV \quad (1)$$

where once again the integration is performed over all space contained in a small sphere of radius a surrounding the point of interest; the subscript x is used to indicate that spatial derivatives are evaluated at x . Note that the Taylor series expansion is useful only when average quantities vary a small amount over the diameter of a particle.

Because averaging is a linear operator, the following two general results hold for all particulate flows

$$\frac{\partial}{\partial x_i} \langle I_f \Psi \rangle = \frac{\partial}{\partial x_i} (\gamma_f \bar{\Psi}^f) = \left\langle \frac{\partial I_f}{\partial x_i} \Psi \right\rangle + \left\langle I_f \frac{\partial \Psi}{\partial x_i} \right\rangle \quad (2)$$

$$\frac{\partial \langle I_f \Psi \rangle}{\partial t} = \frac{\partial \langle \gamma_f \bar{\Psi}^f \rangle}{\partial t} = \left\langle \frac{\partial I_f}{\partial t} \Psi \right\rangle + \left\langle I_f \frac{\partial \Psi}{\partial t} \right\rangle \quad (3)$$

When averaging rules are applied to transport equations, terms of the form $\langle \partial I_f / \partial x_i \Psi \rangle$ appear with great frequency. They must be evaluated to achieve closure. Occasionally, these quantities may be evaluated exactly. However, useful results generally require approximate evaluations that apply to special cases. For that case where the particle is spherical, an interface can be located at a position x only when a particle center lies somewhere on a sphere of radius a centered on x . A typical situation is shown in Fig. 2; the particle center is located at $x + y$. If the indicator function for the particle phase were represented by a Heavyside function centered at $x + y$, then the gradient of the indicator function may be represented using a delta function. So, $\partial I_f / \partial x_i = -\delta(r - a) n_{fi}$, where r is the radial coordinate centered on the particle and n_{fi} is the outward facing normal vector for the fluid. The average is determined by integrating over all possible cases where an interface occurs at x ; that is

$$\left\langle \frac{\partial I_f}{\partial x_i} \Psi \right\rangle(x) = - \iiint_{v_a} N_p(x + y) \bar{\Psi}'(x|x + y) \delta(|y| - a) n_{fi} dV \quad (4)$$

where the integral is performed over all space and $\bar{\Psi}'(x|x + y)$ is the conditional average when a particle center is at $x + y$.

Nomenclature

a = particle radius
 A_a = surface area of a volume with radius a
 F_{isc} = the force exerted on a particle by solid collisions
 F_{ip} = the force exerted on a particle by fluid
 g_i = acceleration due to gravity
 G = velocity gradient
 I_κ = indicator function for phase κ
 ℓ = characteristic length scale describing changes in averaged quantities
 $n_{\kappa i}$ = outward facing normal for phase κ
 N_p = number density or probability density function for particle centers
 p = pressure
 U_o = characteristic velocity
 u_i = fluid velocity
 v_i = particle velocity

x_i = coordinate
 y_i = coordinate
 z_i = coordinate
 $Re_f = \rho_f \bar{u}_i^f \ell / \mu_f$ is the Reynolds number of the flow based on a characteristic length scale and the fluid properties
 $Re_p = \rho_f (\bar{u}_i^f - \bar{v}_i^p) a / \mu_f$ is the Reynolds number of the flow based on the particle radius and the relative velocity between the two phases
 v_p = volume of a spherical particle with radius a
 \bar{v} = volume
 $\bar{\Psi}^k$ = arbitrary quantity averaged over phase k
 $\delta(x)$ = kronecker delta
 ν_f = kinematic viscosity of the fluid phase

τ = characteristic time scale
 ρ_k = material density of k th phase
 γ_k = phase density of k th phase
 μ_f = dynamic viscosity of the fluid
 ω_{ij}^p = averaged rate of rotation of individual particles

Subscripts and Superscripts

c = particle centers
 I = interface
 f = fluid phase
 m = mixture
 p = particle phase
 Ψ' = fluctuating value of an arbitrary quantity
 $\hat{\Psi}$ = disturbed quantity
 Ψ'' = undisturbed quantity

Integrating reduces the volume integral to an integral over the surface of a sphere of radius a centered on x . This results in

$$\left\langle \frac{\partial I_f}{\partial x_i} \Psi \right\rangle(x) = - \int \int_a N_p(x+y) \bar{\Psi}'(x|x+y) n_{fi} dA \quad (5)$$

Once again, when a/L is small, the integrand may be expanded in a Taylor series resulting in a relation that can be applied to develop approximate closures

$$\left\langle \frac{\partial I_f}{\partial x_i} \Psi \right\rangle(x) = - \int \int_a \left\{ [N_p \bar{\Psi}']_{y=0} + y_i \left[\frac{\partial (N_p \bar{\Psi}')}{\partial x_i} \right]_{y=0} + \frac{y_i y_j}{2!} \left[\frac{\partial^2 (N_p \bar{\Psi}')}{\partial x_i \partial x_j} \right]_{y=0} + \dots \right\} n_{fi} dA \quad (6)$$

Developing rules that apply to other specific shapes or arbitrary size distributions is straightforward, but results in integrals that will be more tedious to evaluate. For polydispersed mixtures of spheres, the rule becomes

$$\left\langle \frac{\partial I_f}{\partial x_i} \Psi \right\rangle = - \int_{-\infty}^{\infty} da \int \int_a N_{pa}(a, x+y) \bar{\Psi}' n_{fi} dA(a) \quad (7)$$

where $N_{pa}(a, x)da$ is the probability density the radius of a particle with its center at x will have a radius between $(a, a + da)$.

3 Ensemble-Average Transport Equations

The ensemble averaging theorems will be applied to obtain transport equations. The approach will be to specify the equations of motion that apply inside each phase, multiply by the indicator function, and then apply the averaging theorems. This approach is similar to that described by Joseph et al. (1990) and Drew and Lahey (1993). This process will result in a set of ensemble-average transport equations for each phase that apply to a very wide range of flows, but which must be closed to obtain actual predictions. Because the most restricted assumptions arise during closure, only general steps are illustrated in this section. Closure is described in Section 4.

The restrictions that apply to results in this section are: 1) the particle and fluid phases are continua with constant physical properties, 2) no mass transfer occurs between phases, 3) the particle phase is rigid, but of arbitrary shape, 4) the fluid phase is Newtonian, 5) the particles are large compared to the mean free path of the fluid molecules, and 6) collisions between particles will be neglected.

3.1 Equations of Motion Inside the Two Phases. Conservation of mass and momentum inside individual particles obey the relation that applies in all continua. They are expressed as

$$\partial \rho_p / \partial t + \partial (\rho_p v_i) / \partial x_i = 0 \quad (8)$$

$$\partial \rho_p v_i / \partial t + \partial (\rho_p v_j v_i) / \partial x_j = \partial \tau_{pij} / \partial x_j + \rho_p g_i \quad (9)$$

where ρ_p is the particle density, v_i is the velocity inside the particle, and τ_{pij} is the stress tensor inside the particle.

Decomposing the velocity at any point inside the particle into the translational velocity of the particle center v_i^o and the rate of rotation about the center ω_{ij}^o results in

$$\partial \tau_{pij} / \partial x_j = F_{fpi}(x|x+y)/v_p + F_{sci}(x|x+y)/v_p - [\partial \rho_p \omega_{ij}^o / \partial t + \rho_p \omega_{ij}^o \omega_{ij}^o] y_j \quad (10)$$

where F_{fpi} is the force exerted on the particle by fluid and F_{sci} is the force exerted on a particle due to collisions with other solids.

The sum of the two externally applied forces is equal to the integral of the stress tensor over the particle surface; $(F_{fpi} + F_{sci})(x|x+y) = \int \int \tau_{pij}(x+y+z) n_{pj} dA$ where the integral is performed over all z on the surface of a particle with its center at $x+y$.

Because the scope of this analysis is restricted to obtaining equations that describe dilute particulate flows, the effect of collisions between solids will be neglected and the net force on the particle due to collisions will be set to zero; $F_{sci} = 0$. Models that account for the effect of collisions are described by Batchelor (1974) and Jenkins and Savage (1983). When the entire particle is surrounded by fluid, the force exerted by the fluid on a particle can be evaluated by integrating the total stress tensor acting over the surface of a particle: $F_{fpi} = \int \int \{ -p \delta_{ij} + \mu_f [\partial u_i / \partial x_j + \partial u_j / \partial x_i] \} n_{pj} dA$.

Continuity and momentum inside the fluid phase are similar to those inside the particle, and for a Newtonian fluid with constant viscosity μ_f and density ρ_f

$$\partial \rho_f / \partial t + \partial (\rho_f u_i) / \partial x_i = 0 \quad (11)$$

$$\begin{aligned} \partial (\rho_f u_i) / \partial t + \partial (\rho_f u_j u_i) / \partial x_j \\ = \partial / \partial x_j (-p \delta_{ij} + \mu_f [\partial u_i / \partial x_j + \partial u_j / \partial x_i]) + \rho_f g_i \end{aligned} \quad (12)$$

where p is the pressure, μ_f is the fluid viscosity, and ρ_f is the fluid density.

3.2 Ensemble Averaging Applied to Transport Equations. The ensemble-average continuity equations are obtained by taking the scalar product of the particle indicator function and (8) and then applying the averaging rules. When the fluid and particle phases are incompressible, the indicator function obeys both $\langle \partial I_f / \partial t + u_i \partial I_f / \partial x_i \rangle = 0$ and $\langle \partial I_p / \partial t + v_i \partial I_p / \partial x_i \rangle = 0$ (Joseph et al., 1990). So, for an incompressible discrete phase in any two-phase flow with no mass transfer, the continuity and momentum equations for the particle phase become

$$\partial \gamma_p / \partial t + \partial (\gamma_p \bar{v}_i^p) / \partial x_i = 0 \quad (13)$$

$$\begin{aligned} \rho_p \{ \partial (\gamma_p \bar{v}_i^p) / \partial t + \partial (\gamma_p \bar{v}_i^p \bar{v}_j^p + \gamma_p \bar{v}_i^p \bar{v}_j^p) / \partial x_j \} \\ = \langle I_p \partial \tau_{pij} / \partial x_j \rangle(x) + \rho_p \gamma_p g_i \end{aligned} \quad (14)$$

When there are no collisions between particles or between particles and solid surfaces, the closure may be written as

$$\begin{aligned} \langle I_p \partial \tau_{pij} / \partial x_j \rangle(x) \\ = \gamma_p \overline{F_{fpi}^p} / v_p - \overline{\gamma_p \{ \partial \rho_p \omega_{ij}^o / \partial t + \rho_p \omega_{ij}^o \omega_{ij}^o \} y_j^p} \end{aligned} \quad (15)$$

The ensemble-average continuity equation and momentum equations for the fluid phase become

$$\partial \rho_f \gamma_f / \partial t + \partial (\rho_f \gamma_f \bar{u}_i^f) / \partial x_i = 0 \quad (16)$$

$$\begin{aligned} \{ \partial (\rho_f \gamma_f \bar{u}_i^f) / \partial t + \partial (\rho_f \gamma_f \bar{u}_i^f \bar{u}_j^f + \rho_f \gamma_f \overline{u_i^f u_j^f}) / \partial x_j \} \\ = \frac{\partial}{\partial x_j} \{ -\gamma_f \bar{p}^f \delta_{ij} + \mu_f [\partial \bar{u}_i^m / \partial x_j + \partial \bar{u}_j^m / \partial x_i] \} \\ + I_i + \rho_f \gamma_f g_i \end{aligned} \quad (17)$$

where $\bar{u}_i^m = \gamma_f \bar{u}_i^f + \gamma_p \bar{v}_i^p$ and $I_i = -\langle \partial I_f / \partial x_i \tau_{fij} \rangle$ represents momentum transport due to stress at the particle surfaces. The subsidiary result $\gamma_f (\partial u_i / \partial x_j + \partial u_j / \partial x_i)^f = \partial \bar{u}_i^m / \partial x_j + \partial \bar{u}_j^m / \partial x_i$ obtained by Joseph et al. (1990) was used to evaluate the average strain rate in the fluid phase and applies for any shape of the particle phase.

4 Closure of Two-Phase Models

To obtain a predictive model, I_i and \bar{F}^p and $\gamma_p(\partial\rho_p\omega_{ij}^o/\partial t + \rho_p\omega_{ij}^o\omega_{ij}^o)y_j^p$ must be expressed in terms of average velocities, pressures, and phase densities. Many closures and closure methods have been proposed. The terms do not appear to have been evaluated to obtain a complete two-phase model that is simultaneously correct to $O(1)$ in drag and $O(a^2)$ in continuity and momentum. Closures that are correct to this order are obtained here.

The closure developed here applies to the special case which has been described. Five additional assumptions are added to those described in Section 3. These assumptions and their consequences are: 1) The solid phase consists of monodispersed spherical particles. 2) Spatial variations are small in average field variables such as velocity, pressure, and phase density over a distance equal to one particle radius. This assumption limits application to flows with $a/\ell \ll 1$. 3) The flow near each particle is quasi-steady. The assumption that the flow is quasi-steady near the particle limits final application to flows where the products $Re_p(a/\ell)^2 \ll 1$ and $v_f\tau/a^2 \gg 1$ where τ is a time scale describing changes in averaged quantities. Although individual particles must accelerate as they travel through a spatially varying flow, the first criterion ensures that the effects of virtual mass due to spatial gradients are small compared to linear drag. The second ensures that the effects of virtual mass due to local transients are small compared to linear drag. It can be shown that when these two criteria are met, the effect of virtual mass is $O(a^2/\ell^2)$. When the flow does not meet these requirements, the closure describing transfer of momentum between phases must contain terms that capture the effect of virtual mass terms which will be the leading order effect. Although the restriction that $Re_p(a/\ell)^2 \ll 1$ appears more severe than the initial restriction $a/\ell \ll 1$, this is often not the case. When the transport equations are applied to high Reynolds number flows near boundaries, the characteristic length scale describing changes in the average velocity is the boundary layer thickness, δ ; the Reynolds number based on this length scale is 1. So, the two restrictions are equivalent near boundaries. 4) The flow near each particle may be described using Stokes equations which hold when $Re_p \ll 1$, where Re_p is the Reynolds number based on the relative velocity between the two phases and the particle radius. This restriction can be severe for high Reynolds number gas-solid flows. The magnitude of Re_p may be evaluated prior to applying the transport equations by recognizing that in high Reynolds number gas-solid flows $Re_p = O((\rho_f - \rho_p)/\rho_f Re^2(a/\ell)^3)$ (Maxey and Riley, 1983). The final restriction is 5) the flow field in the vicinity of an individual particle is not affected by the presence of neighboring particles. This limits evaluation of the effect of the particles on the stress tensor to obtaining terms that are $O(\gamma_p)$ and lower in the particle phase density.

Example flows that meet all criteria simultaneously include: a very dilute mixture of 10 micron glass particles conveyed by air flowing at $Re = 10^4$ through a 10 cm pipe line, a very dilute mixture of 100 micron plastic particles conveyed in water flowing at $Re = 10^4$ in a 10 cm pipe. In general, the transport equations apply to flows of some dilute solid-liquid mixtures and gas-solid flows which are currently being handled at Hanford. Many wastes contain very small particles and flows generally occur in large scale equipment; concentrations vary. Flows of interest include pneumatic conveyance of wastes, motion of aerosols in tank domes, transport of slurries in pipelines, motion of undissolved metals in glass melts, and motion of particulate in water stored in basins. In many cases, higher-order transport equations of this type are required to predict features of interest, such as segregation of large and small particles during waste retrieval; the potential for segregation must be understood to assess safety hazards arising from the potential for criticality in tanks. Evaluations of this nature require transport equations that

can correctly describe the particle concentration and relative velocity between phases to leading order.

4.1 Closure of Particle Phase: Ensemble-Average Force.

The average force appearing in (15) represents the force that is exerted on the particle phase when any portion of a particle occupies x ; the relationship between the average force exerted on a particle phase whenever the particle phase occupies x , and the average force exerted on an individual particle with a center at $x + y$ is

$$\gamma_p \bar{F}_{ifp}^p / v_p(x) = \iiint_{V_a} [\bar{F}_{ifp}^c(x|x+y) N_p(x+y) / \tau_p] dy, \quad (18)$$

where $\bar{F}_{ifp}^c(x|x+y)$ is the conditional average force on a particle with its center located at $x + y$.

When γ_p is small, the average force acting on an individual particle, $\bar{F}_{ifp}^c(x|x+y)$, can be estimated by evaluating the force exerted as a result of flow around a single isolated particle, neglecting the presence of all other particles and averaging. On average, the effect of other particles on this force will be $O(\gamma_p)$ compared to the leading order effect. For Stokes equations, the effect of neighboring particles is known to affect the final solution for the effective stress tensor of a mixture to $O(\gamma_p^2)$ (Batchelor and Green, 1972).

Consider a single particle suspended in an infinite fluid. Far from the particle, the fluid velocity and pressure will vary in some manner that is unaffected by the presence of the particle. The velocity and pressure in this region will be referred to as the undisturbed velocity and pressure field. This undisturbed velocity may be inherently random, as in a turbulent flow, or may be deterministic as might occur in a laminar flow. Near the particle, the velocity will be affected by the particle, and will be considered disturbed. Using this idea, the pressure and the velocity at a point $x + y + z$ on the surface of the sphere with its center at $x + y$ are decomposed as $p(x + y + z) = p^o(x + y + z) + \bar{p}(z|x + y)$ and $u_i(x + y + z) = u_i^o(x + y + z) + \bar{u}_i(z|x + y)$. It is now possible to define forces acting on the particle due to the undisturbed field, $F_{ifp}^o(x|x + y)$, and the disturbed field \bar{F}_{ifp} . The total force acting on such a particle is then $F_{ifp} = F_{ifp}^o + \bar{F}_{ifp}$.

The leading order contribution of the undisturbed field to the average force exerted on particles with centers at $x + y$ is $\bar{F}_{ifp}^o(x|x + y) = v_p \partial/\partial x_i [-\bar{p}^f \delta_{ij} + \mu_f (\partial u_i/\partial x_j + \partial u_j/\partial x_i)^f](x + y)$. Expanding again in a Taylor series about x , the leading order contribution to the particle momentum equation is $\gamma_p \bar{F}_{ifp}^o(x) = v_p \gamma_p \partial/\partial x_i [-\bar{p}^f \delta_{ij} + \mu_f (\partial u_i/\partial x_j + \partial u_j/\partial x_i)^f](x)$.

Expanding the ensemble-average strain rate reveals the closure for this force contains terms that are $O(\gamma_p^2)$. The contribution due to the disturbed portion of the force has not yet been presented, but the proposed method of estimating that contribution cannot capture terms of $O(\gamma_p^2)$. So, for the purposes of the model being developed, the contribution of the undisturbed velocity to average force terms may be represented as

$$\gamma_p \bar{F}_{ifp}^o / \tau_a(x) = \gamma_p \partial/\partial x_i [-\bar{p}^f \delta_{ij} + \mu_f (\partial \bar{u}_i^f/\partial x_j + \partial \bar{u}_j^f/\partial x_i)](x). \quad (19)$$

The force \bar{F}_{ifp} acting on an individual particle with its center at $x + y$ is $\bar{F}_{ifp}(x|x + y) = -6\pi\mu_f a(v_i^o - u_i^o - (a^2/6)\partial^2 u_i^o/\partial x_j \partial x_j)(x + y)$ where v_i^o is the translational velocity of the particle center. The contribution of the disturbance velocity in this instance is then

$$\gamma_p \frac{\overline{F}_{fp}^p}{v_p}(x) = -\frac{1}{v_p} \iiint_{v_p} 6\pi\mu_f a \left(v_i^o - u_i^o - \frac{a^2}{6} \frac{\partial^2 u_i^o}{\partial x_j \partial x_j} \right) \times (x+y) N_p(x+y) d\mathcal{V} \quad (20)$$

where $v_p = 4/3\pi a^3$ is the volume of an individual particle. Expanding all average terms in the integral in Taylor series, integrating, recognizing that the volume of a particle is proportional to a^3 and then neglecting terms that are proportional to a^2 and γ_p^2 on the right-hand side results in

$$\gamma_p \frac{\overline{F}_{fp}^p}{v_p}(x) = -\frac{6\pi\mu_f a}{v_p} \left\{ \gamma_p (\overline{v_i^o} - \overline{u_i^f}) - \frac{a^2}{10} \left(\frac{\partial^2 \gamma_p \overline{u_i^f}}{\partial x_j \partial x_j} - \overline{u_i^f} \frac{\partial^2 \gamma_p}{\partial x_j \partial x_j} \right) - \frac{a^2}{6} \gamma_p \left(\frac{\partial^2 u_i^f}{\partial x_j \partial x_j} \right) \right\} \quad (21)$$

Before proceeding, it is worthwhile to discuss some higher order terms that do not act on single particles. The terms appear in this type of formulation because the average force exerted on the particle phase at x has contributions from particles with centers anywhere on the surface of a sphere of radius a around x . For example, if the ensemble-averaged fluid velocity near the point $(0, 0, 0)$ varies as Gx_2^2 , then the average force on a particle with translational velocity $v^o = 0$ and centered at either of the two positions $(0, \pm a, 0)$ will be $F_1 = 6\pi\mu_f a(Ga^2) + \pi\mu_f a^3 G$. The average force exerted on the particle, when its center is at $(\pm a, 0, 0)$, will be due to the Faxen drag contribution only, $F_1 = \pi\mu_f a^3 G$. As a result, the higher-order contributions to the average force acting on the particle phase has contributions due to the Faxen term and a contribution that represents smearing of the average of the linear drag term. The argument justifying the appearance of the extra linear drag terms may be extended to explain all other higher order terms. In essence, these higher-order terms represent a smearing out of stresses acting on the surface of individual particles over a region equal to the size of an individual particle. These terms do not appear in the two-phase model based on $\overline{v_i^o}$ and N_p provided in the Appendix. However, the smearing of the force results in additional terms in the fluid momentum equations regardless of the choice of primitive variable for the particle phase.

Because the force terms contains the average translational velocity $\overline{v_i^o}$ it must be developed further to obtain a final form that uses $\overline{v_i^f}$. The first two terms in the conversion between these two velocities are $\gamma_p \overline{v_i^o} = \gamma_p \overline{v_i^f} - (a^2/15) \partial \gamma_p \omega_{ij}^o / \partial x_j$. It is shown in the companion paper that for $a/\ell \ll 1$, the difference between the average fluid and particle velocities $\overline{v_i^o} - \overline{u_i^f}$ is $O(a/\ell)^2$. This also holds for differences in the rate of rotation; that is $2\overline{\omega_{ij}^o} - (\partial \overline{u_i^f} / \partial x_j - \partial \overline{u_j^f} / \partial x_i)$ is $O(a/\ell)^2$. So, terms that are proportional to these differences may be neglected everywhere except in the linear drag term where the particle volume, which is proportional to a^3 , appears in the denominator. Neglecting these differences, the two average forces become

$$\gamma_p \frac{\overline{F}_{fp}^p + \overline{F}_{fp}^o}{v_p} = -\frac{6\pi\mu_f a}{v_p} \left\{ \gamma_p (\overline{v_i^o} - \overline{u_i^f}) - \frac{a^2}{10} \frac{\partial}{\partial x_j} \left(\gamma_p \left(\frac{\partial \overline{u_i^f}}{\partial x_j} + \frac{\partial \overline{u_j^f}}{\partial x_i} \right) \right) - \frac{a^2}{15} \gamma_p \frac{\partial^2 \overline{u_i^f}}{\partial x_j \partial x_j} \right\} + \gamma_p \frac{\partial}{\partial x_i} \left[-\overline{p^f} \delta_{ij} + \mu_f \left(\frac{\partial \overline{u_i^f}}{\partial x_j} + \frac{\partial \overline{u_j^f}}{\partial x_i} \right) \right] \quad (22)$$

To complete the closure, it can be shown that rotational terms $\gamma_p (\partial \rho_p \omega_{ij}^o / \partial t + \rho_p \omega_{ij}^o \omega_{ij}^o) \gamma_j^p$ are proportional to a^2 and so may be neglected in this model. The terms must be retained to obtain an $O(a^2)$ model. Evaluating this term to higher order is rela-

tively simple as it may be shown that $2\overline{\omega_{ij}^o} - (\partial \overline{u_i^f} / \partial x_j - \partial \overline{u_j^f} / \partial x_i) = 0$ to leading order.

4.2 Closure of Fluid Phase: Evaluation of I_i . The stress tensor at the surface of the particle is required to evaluate I_i . Once again, the closure may be decomposed to determine the contributions due to the undisturbed I_i^o and the disturbed quantities \tilde{I}_i . Decomposing in the manner previously described, the total pressure and velocity at the point x are $u_i(x|x+y) = u_i^o(x) + \tilde{u}_i(x|x+y)$ and $p(x|x+y) = p^o(x) + \tilde{p}(x|x+y)$. The mean contribution of the undisturbed field may be obtained directly using the assumptions described in Section 3.

$$I_i^o = - \left\{ \frac{\mu_f}{\gamma_f} \left(\frac{\partial \overline{u_i^m}}{\partial x_j} + \frac{\partial \overline{u_j^m}}{\partial x_i} \right) - \overline{p^f} \delta_{ij} \right\} \frac{\partial \gamma_f}{\partial x_j} \quad (23)$$

The contribution from the velocity disturbance is obtained by solving Stokes equations to obtain the stress at a point x at the surface of a particle with its center as $x+y$, incorporating the results into the closure rule (6) and integrating.

$$\tilde{I}_i = \frac{6\pi\mu_f a}{v_a} \left[\gamma_p (\overline{v_i^o} - \overline{u_i^f}) - \frac{a^2}{10} \left(\frac{\partial^2 \gamma_p \overline{u_i^f}}{\partial x_j \partial x_j} - \overline{u_i^f} \frac{\partial^2 \gamma_p}{\partial x_j \partial x_j} \right) + \frac{a^2}{15} \frac{\partial^2}{\partial x_j \partial x_j} (\gamma_p (\overline{v_i^o} - \overline{u_i^f})) - \frac{a^2}{6} \gamma_p \frac{\partial^2 \overline{u_i^f}}{\partial x_j \partial x_j} \right] + 3 \frac{\partial}{\partial x_j} \left[\gamma_p \mu_f \left(\frac{\partial \overline{u_{mi}}}{\partial x_j} - \overline{\omega_{ij}^o} \right) \right] \quad (24)$$

As discussed during evaluation of the particle transport equation, higher-order terms proportional to either the differences in the velocities $(\overline{v_i^o} - \overline{u_i^f})$ and differences in rates of rotation of the two phases $2\overline{\omega_{ij}^o} - (\partial \overline{u_i^f} / \partial x_j - \partial \overline{u_j^f} / \partial x_i)$ and terms proportional to γ_p^2 will be neglected. There are several possible forms for the closure that agree to $O(1)$; one of the simpler possible $O(1)$ momentum closures is

$$I_i = \tilde{I}_i + I_i^o = \frac{6\pi\mu_f a}{v_a} \left[\gamma_p (\overline{v_i^o} - \overline{u_i^f}) - \frac{a^2}{10} \frac{\partial}{\partial x_j} \left(\gamma_p \left(\frac{\partial \overline{u_i^f}}{\partial x_j} + \frac{\partial \overline{u_j^f}}{\partial x_i} \right) \right) - \frac{a^2}{15} \gamma_p \frac{\partial^2 \overline{u_i^f}}{\partial x_j \partial x_j} \right] + \frac{3}{2} \frac{\partial}{\partial x_j} \left[\gamma_p \mu_f \left(\frac{\partial \overline{u_i^f}}{\partial x_j} + \frac{\partial \overline{u_j^f}}{\partial x_i} \right) \right] - \left\{ \mu_f \left(\frac{\partial \overline{u_i^f}}{\partial x_j} + \frac{\partial \overline{u_j^f}}{\partial x_i} \right) - \overline{p^f} \delta_{ij} \right\} \frac{\partial \gamma_f}{\partial x_j} \quad (25)$$

4.3 Momentum Equations. Substituting in the relation for the closure terms results in an ensemble-averaged transport equation for fluid and particle momentum that is valid to first order in the particle radius and the particle phase density. The forms based on γ_p and $\overline{v_i^f}$ are

$$\left\{ \partial (\rho_f \gamma_f \overline{u_i^f}) / \partial t + \partial (\rho_f \gamma_f \overline{u_i^f} \overline{u_j^f} + \rho_f \gamma_f \overline{u_i^f} \overline{u_j^f}) / \partial x_j \right\} = \frac{\partial}{\partial x_j} \left\{ -\gamma_f \overline{p^f} \delta_{ij} + \mu_f \left(1 + \frac{3\gamma_p}{2} \right) \left(\frac{\partial \overline{u_i^f}}{\partial x_j} + \frac{\partial \overline{u_j^f}}{\partial x_i} \right) \right\} + \frac{\partial \gamma_p}{\partial x_j} \left\{ -\overline{p^f} \delta_{ij} + \mu_f \left(\frac{\partial \overline{u_i^f}}{\partial x_j} + \frac{\partial \overline{u_j^f}}{\partial x_i} \right) \right\} + \rho_f \gamma_f g_i$$

$$+ \frac{6\pi\mu_f a}{\tau_a} \left[\gamma_p (\bar{v}_i^p - \bar{u}_i^f) - \frac{a^2}{10} \frac{\partial}{\partial x_j} \left(\gamma_p \left(\frac{\partial \bar{u}_i^f}{\partial x_j} + \frac{\partial \bar{u}_j^f}{\partial x_i} \right) \right) - \frac{a^2}{15} \gamma_p \frac{\partial^2 \bar{u}_i^f}{\partial x_j \partial x_j} \right] \quad (26)$$

$$\begin{aligned} & \rho_p \left\{ \frac{\partial(\gamma_p \bar{v}_i^p)}{\partial t} + \frac{\partial(\gamma_p \bar{v}_i^p \bar{v}_j^p + \gamma_p \bar{v}_i^p \bar{v}_j^p)}{\partial x_j} \right\} \\ &= \gamma_p \frac{\partial}{\partial x_i} \left[-\bar{p}^f \delta_{ij} + \mu_f \left(\frac{\partial \bar{u}_i^f}{\partial x_j} + \frac{\partial \bar{u}_j^f}{\partial x_i} \right) \right] \\ &+ \rho_p \gamma_p g_i - \frac{6\pi\mu_f a}{\tau_a} \left\{ \gamma_p (\bar{v}_i^p - \bar{u}_i^f) \right. \\ &\left. - \frac{a^2}{10} \frac{\partial}{\partial x_i} \left(\gamma_p \left(\frac{\partial \bar{u}_i^f}{\partial x_j} + \frac{\partial \bar{u}_j^f}{\partial x_i} \right) \right) - \frac{a^2}{15} \gamma_p \frac{\partial^2 \bar{u}_i^f}{\partial x_j \partial x_j} \right\} \quad (27) \end{aligned}$$

The complete system requires use of the consistency relation $\gamma_p + \gamma_f = 1$ and continuity Eqs. (12) and (15). Models based on other definitions of the particle concentration and average particle velocity are provided in the Appendix.

5 Conclusions

Ensemble-average theorems were applied to obtain transport equations describing conservation of momentum and mass for the particulate phase of a fluid-solid mixture containing small spherical particles. A system of equations is provided; it consists of two exact continuity equations that apply to all incompressible two-phase flows, two momentum transport equations that apply to discrete flows containing rigid spherical particles, and a consistency principle requiring the sum of the phase densities to be zero. All truncation error is relegated to the momentum transport equations. Truncation error in the momentum equations is $O(1)$ in the particle radius and $O(\gamma_p)$ in the phase density. The continuity and consistency principles are exact.

References

- Batchelor, G. K., 1974, "Transport Properties of Two-Phase Materials with Random Structure," *Annual Review of Fluid Mechanics*, 6, 227–255.
- Batchelor, G. K., and Green, J. T., 1972, "The Determination of the Bulk Stress in a Suspension of Spherical Particles to Order C^2 ," *Journal of Fluid Mechanics*, Vol. 56, pp. 401–427.
- Drew, D. A., and Lahey, R. T., 1993, "Analytical Modeling of Multiphase Flow" Chapter 16 of *Particulate Two-Phase Flow*, Roco, M., ed.
- Givler, R. C., 1987, "An Interpretation for the Solid-Phase Pressure in Slow, Fluid-Particle Flows," *International Journal of Multiphase Flow*, Vol. 13, pp. 717–722.
- Hinch, E. J., 1977, "An Averaged-Equation Approach to Particle Interactions in a Fluid Suspension," *Journal of Fluid Mechanics*, Vol. 83, pp. 695–720.
- Hwang, G. J., and Shen, H. H., 1989, "Modeling the Solid Phase Stress in a Fluid-Solid Mixture," *International Journal of Multiphase Flow*, Vol. 15(2), pp. 257–268.
- Hwang, G. J., and Shen, H. H., 1991, "Modeling the Phase Interaction in the Momentum Equations of a Fluid-Solid Mixture," *International Journal of Multiphase Flow*, Vol. 17(1), pp. 45–47.
- Jenkins, J. T., and Savage, S. B., 1983, "A Theory for the Rapid Flow of Identical Smooth, Nearly Elastic, Spherical Particles," *Journal of Fluid Mechanics*, Vol. 130, pp. 187–202.
- Joseph, D. D., Lundgren, T. S., Jackson, R., and Saville, D. A., 1990, "Ensemble-Averaged and Mixture Theory Equation for Incompressible Fluid-Particle Suspensions," *International Journal of Multiphase Flow*, Vol. 16, pp. 35–42.
- Maxey, M. R., and Riley, J. J., 1983, "Equation of Motion for a Small Rigid Sphere in a Non-Uniform Flow," *Physics of Fluids*, Vol. 26, pp. 883–889.
- Nigamatulin, R. I., 1979, "Spatial Averaging of Heterogeneous and Dispersed Systems," *International Journal of Multiphase Flow*, Vol. 5(5), pp. 353–386.
- Passman, S. L., 1986, "Forces on the Solid Constituent in a Multiphase Flow," *Journal of Rheology*, Vol. 30, pp. 1076–1083.

APPENDIX

Other Forms of Transport Equations

Alternate forms for the transport equations exist. Because alternate forms appear in the literature, and other forms can be more convenient when applied to specific problems, two other forms are provided here. Regardless of the choice of primitive variables, additional effort is required to achieve higher order. All forms of the two-phase model will require: an $O(a^2)$ model for the velocity covariances, $\bar{u}_i^p \bar{u}_j^p$ and $\bar{v}_i^p \bar{v}_j^p$, a transport equation to determine the first nonzero contribution to the difference in the rotations rates $2\bar{\omega}_i^p - (\partial \bar{u}_i^f / \partial x_j - \partial \bar{u}_j^f / \partial x_i)$ and further evaluation of the momentum closure to retain all $O(a^2)$ terms, which include terms proportional to the relative velocity between phases. To achieve a higher than $O(\gamma_p)$ closure in the phase density will require more effort in evaluating the flow near surfaces.

There are two convenient alternate forms. Equations based on N_p and \bar{v}_i^c have several advantages, including the fact that, to the order presented here, all terms in the momentum transfer equation relate directly to forces acting on individual particles.

$$\left(N_p v_p + \frac{a^2}{10} \frac{\partial^2 N_p}{\partial x_i \partial x_i} v_p \right) + \gamma_f = 1 \quad (A1)$$

$$\partial N_p / \partial t + \partial(N_p \bar{v}_i^c) / \partial x_i = 0 \quad (A2)$$

$$\partial \rho_f \gamma_f / \partial t + \partial(\rho_f \gamma_f \bar{u}_i^f) / \partial x_i = 0 \quad (A3)$$

$$\begin{aligned} & \{ \partial(\rho_f \gamma_f \bar{u}_i^f) / \partial t + \partial(\rho_f \gamma_f \bar{u}_i^f \bar{u}_j^f + \rho_f \gamma_f \bar{u}_i^f \bar{u}_j^f) / \partial x_j \} \\ &= \frac{\partial}{\partial x_i} \left\{ -\gamma_f \bar{p}^f \delta_{ij} + \mu_f \left(1 + \frac{3N_p v_p}{2} \right) \left(\frac{\partial \bar{u}_i^f}{\partial x_j} + \frac{\partial \bar{u}_j^f}{\partial x_i} \right) \right\} \\ &+ \frac{\partial N_p v_p}{\partial x_j} \left\{ -\bar{p}^f \delta_{ij} + \mu_f \left(\frac{\partial \bar{u}_i^f}{\partial x_j} + \frac{\partial \bar{u}_j^f}{\partial x_i} \right) \right\} + \rho_f \gamma_f g_i \\ &+ \frac{6\pi\mu_f a}{v_p} \left[N_p v_p (\bar{v}_i^c - \bar{u}_i^f) - \frac{a^2}{6} N_p v_p \frac{\partial^2 \bar{u}_i^f}{\partial x_j \partial x_j} \right] \quad (A4) \end{aligned}$$

$$\begin{aligned} & \rho_p \left\{ \frac{\partial(N_p v_p \bar{v}_i^c)}{\partial t} + \frac{\partial(N_p v_p \bar{v}_i^c \bar{v}_j^c + N_p v_p \bar{v}_i^c \bar{v}_j^c)}{\partial x_j} \right\} \\ &= N_p v_p \frac{\partial}{\partial x_i} \left[-\bar{p}^f \delta_{ij} + \mu_f \left(\frac{\partial \bar{u}_i^f}{\partial x_j} + \frac{\partial \bar{u}_j^f}{\partial x_i} \right) \right] \\ &+ \rho_p N_p v_p g_i - \frac{6\pi\mu_f a}{v_p} \left\{ N_p v_p (\bar{v}_i^c - \bar{u}_i^f) - \frac{a^2}{6} N_p v_p \frac{\partial^2 \bar{u}_i^f}{\partial x_j \partial x_j} \right\} \quad (A5) \end{aligned}$$

The truncation errors in this form arise in three locations. These are: the Einstein viscosity correction, the momentum transfer term in the fluid equation, and the consistency principle. To achieve the order equivalent to the model in the body of the paper, the consistency principle cannot be truncated to $(N_p v_p) + \gamma_f = 1$, as is commonly done. When the consistency principle is truncated, the relative velocity between phases between may be obtained, but gradients in the particle number density along streamlines and the first order correction to the individual velocities cannot be obtained.

A model based on \bar{v}_i^p and γ_p is also possible.

$$\gamma_p + \gamma_f = 1 \quad (A6)$$

$$\partial \gamma_p / \partial t + \partial(\gamma_p \bar{v}_i^p) / \partial x_i = 0 \quad (A7)$$

$$\partial \rho_f \gamma_f / \partial t + \partial(\rho_f \gamma_f \bar{u}_i^f) / \partial x_i = 0 \quad (A8)$$

$$\begin{aligned}
& \{ \partial(\rho_f \gamma_f \bar{u}_i^f) / \partial t + \partial(\rho_f \gamma_f \bar{u}_i^f \bar{u}_j^f + \rho_f \gamma_f \bar{u}_i^f \bar{u}_j^{f'}) / \partial x_j \} \\
& = \frac{\partial}{\partial x_j} \left\{ -\gamma_f \bar{p}^f \delta_{ij} + \mu_f \left(1 + \frac{3\gamma_p}{2} \right) \left(\frac{\partial \bar{u}_i^f}{\partial x_j} + \frac{\partial \bar{u}_j^f}{\partial x_i} \right) \right\} \\
& + \frac{\partial \gamma_p}{\partial x_j} \left\{ -\bar{p}^f \delta_{ij} + \mu_f \left(\frac{\partial \bar{u}_i^f}{\partial x_j} + \frac{\partial \bar{u}_j^f}{\partial x_i} \right) \right\} + \rho_f \gamma_f g_i \\
& + \frac{6\pi \mu_f a}{\tau_a} \left[\gamma_p (\bar{v}_i^{op} - \bar{u}_i^f) - \frac{a^2}{10} \left(\frac{\partial^2 \gamma_p \bar{u}_i^f}{\partial x_j \partial x_j} - \bar{u}_i^f \frac{\partial^2 \gamma_p}{\partial x_j \partial x_j} \right) \right. \\
& \quad \left. - \frac{a^2}{6} \gamma_p \frac{\partial^2 \bar{u}_i^f}{\partial x_j \partial x_j} \right] \quad (A9)
\end{aligned}$$

$$\begin{aligned}
& \rho_p \left\{ \frac{\partial(\gamma_p \bar{v}_i^{op})}{\partial t} + \frac{\partial(\gamma_p \bar{v}_i^{op} \bar{v}_j^{op} + \gamma_p \bar{v}_i^{op} \bar{v}_j^{op'})}{\partial x_j} \right\} \\
& = \gamma_p \frac{\partial}{\partial x_i} \left[-\bar{p}^f \delta_{ij} + \mu_f \left(\frac{\partial \bar{u}_i^f}{\partial x_j} + \frac{\partial \bar{u}_j^f}{\partial x_i} \right) \right] + \rho_p \gamma_p g_i \\
& - \frac{6\pi \mu_f a}{\tau_a} \left[\gamma_p (\bar{v}_i^{op} - \bar{u}_i^f) - \frac{a^2}{10} \left(\frac{\partial^2 \gamma_p \bar{u}_i^f}{\partial x_j \partial x_j} - \bar{u}_i^f \frac{\partial^2 \gamma_p}{\partial x_j \partial x_j} \right) \right. \\
& \quad \left. - \frac{a^2}{6} \gamma_p \frac{\partial^2 \bar{u}_i^f}{\partial x_j \partial x_j} \right] \quad (A10)
\end{aligned}$$

The truncation errors in this form appear in the momentum transfer terms only.

Simulation of Chaotic Particle Motion in Particle-Laden Jetflow and Application to Abrasive Waterjet Machining

Z. Yong

Senior Researcher, Mem. ASME

R. Kovacevic

Professor, Mem. ASME

Center for Robotics and
Manufacturing Systems,
University of Kentucky,
Lexington, KY 40506-0108

A novel method is presented for modeling the abrasive waterjet machining process. Particle motion on the cross section of particle-laden jetflow is simulated in order to quantify the erosion contributions of millions of particles having different kinematic behaviors. The simulation is performed using fractal point sets with chaotic behavior for the cases of circular and noncircular (elliptical, triangular) jets. The jetflow constructed can be endowed with any desired velocity profile and/or particle flowrate. In association with a classical constitutive equation for estimating the penetration ability of a particle, the drilling and cutting operations are simulated and verified by experiment for titanium, glass, and other materials. Roughness and waviness of the cutting surfaces are also simulated and there is good consistency between theory and experiment. Triangular and elliptical jetflows are utilized to explore potential applications of noncircular abrasive waterjets.

1 Introduction

In general, there are two fundamental issues in modeling and simulation of three-dimensional (3D) abrasive waterjet (AWJ) machining. One is to find the constitutive equation—the relation between the depth of penetration by a high speed abrasive particle and other machining parameters, including the jet speed, material property, impact angle, surface geometry, etc. The other is to quantify the dynamic nature of particle-laden jetflow, reflecting disordered particle motion, the influence of nozzle geometry and movement, and characteristics of three-phase flow such as laminar and turbulent velocity profiles. The first issue focuses on the local erosion rate by individual particles while the second one emphasizes the global description of surface formation. For instance, waviness on lateral surfaces of cut is not affected by the erosion rate of a single particle, but does depend on the nozzle speed and total depth of cut. Evidence for this claim is that similar waviness also occurs in laser and other beam cutting processes.

To date, much attention has been paid to the first issue and remarkable progress has been achieved by scholars and engineers regarding different impact conditions (Finnie, 1958; Bitter, 1962; Neilson and Gilchrist, 1967; Tilly and Sage, 1970; Hutchings, 1979; Gulden, 1979; Hashish, 1984; Zeng and Kim, 1992; Yong and Kovacevic, 1997a). However, the results of single particle analysis alone are not enough to precisely describe an on-line AWJ machining process. In addition, the trajectories of millions of particles with chaotic dynamic behavior must be quantitatively described.

Particles in AWJ differ greatly from each other in terms of their velocities and positions at different moments, and most importantly, their disordered behavior directly affects the depth of cut as well as the surface quality. In fact, because of the lack of a theoretical basis for the particle motion in jetflow, namely the second issue, empirical models to date are incapable of reflecting many important characteristics of a kerf, such as 3D surface configuration, roughness and waviness as well as the

machining parameters that influence them like the traverse speed of a nozzle. In addition, conventional models break down when engineers and researchers change nozzle shapes (Hongawa et al., 1992; Hashish, 1994; Rankin and Wu, 1995) from a circular one to noncircular ones, or when they use alternative techniques during a machining operation, such as rotating a nozzle along with the straight movement, or accelerating and decelerating it for controlling the depth of cut.

It is essential for a robust model to balance the weight of two research orientations. At present, it is impractical to establish a series of nonlinear partial differential equations for describing locations and velocities of particles simply because researchers are still struggling with the accurate analysis of turbulence in one-phase flow. However, in order to model and simulate an AWJ machining process, it is virtually impossible to avoid such an analysis since the cutting action in AWJ machining is actually the result of the accumulation of an enormous number of tiny craters and/or ditches generated by particles, as shown in Figs. 1–2. This suggests that a new approach must be developed to meet practical needs.

The strategy adopted in the present research is to simulate particle motion on the cross section of a particle-laden jetflow by using fractal point sets with chaotic features. Here a point represents a particle and its coordinates define the position of the particle. It is important to point out that a general point set is not directly applicable unless it satisfies strict physical and mathematical constraints. For example, it should be able to have any desired velocity profile and flowrate, be suitable to any nozzle shape, and possess global axisymmetry and uniformity. After desired particle-laden flow is constructed, several AWJ machining operations are simulated and compared with experimental data. The results show that the approach developed is very effective and industrially applicable as an optional tool to reduce expensive and time-consuming tests.

2 Simulation of Particle Motion

In light of the physical and geometric conditions forming three-phase flow (abrasives, water and air) in the mixing tube, three assumptions are introduced to describe the characteristics of particle motion in a circular cross section of the multiphase flow. First, the appearance of particles on the cross section is

Contributed by the Fluids Engineering Division for publication in the JOURNAL OF FLUIDS ENGINEERING. Manuscript received by the Fluids Engineering Division August 3, 1995; revised manuscript received January 12, 1997. Associate Technical Editor: M. W. Reeks.

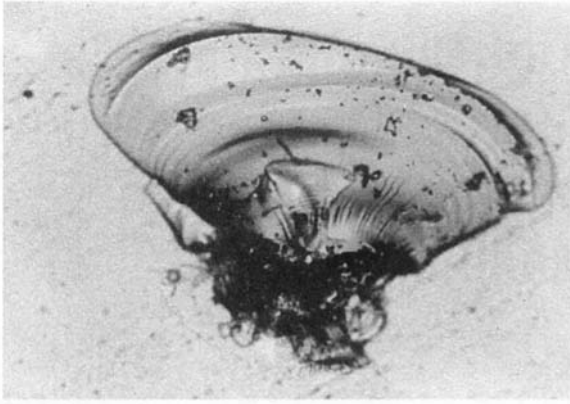


Fig. 1 A crater (X200) generated by an abrasive particle with average diameter 460 μm impinging on a glass plate

unpredictable or disordered for both laminar and turbulent flows. Second, globally speaking, the particle distribution on the cross section is approximately axisymmetrical after the particle number passing through the section exceeds a certain value. Third, the particle number through a subdomain of the cross section should be approximately equal to the particle number through another symmetric subdomain. The third feature is termed the global uniformity of particles. In the subsequent analysis, laminar and turbulent particle-laden flows are distinguished by their particle distribution and velocity profiles.

2.1 An Original Point Set. In order to describe instant particle motion on the cross section of particle-laden jetflow, a particle is assumed to be a mathematical point in space and its size and shape are not considered at this step. In this case, the key point for simulation is to find such a point set that possesses the above three features of particle motion on the cross section. After extensive examinations on the above three features of numerous fractal point sets under the Cartesian and polar systems, it is confirmed (Yong and Kovacevic, 1997b, c) that the following point set can be used to simulate the particle motion on the cross section of jetflow, given by

$$f_p = \{(x_1, y_1), (x_2, y_2), \dots, (x_n, y_n)\} \quad (1)$$

$$= \{(r_1, \theta_1), (r_2, \theta_2), \dots, (r_n, \theta_n)\} \subset J$$

$$0 \leq r_n = (x_n^2 + y_n^2)^{1/2} \leq 1 \quad (2)$$

$$0 \leq \theta_n = \arctan\left(\frac{y_n}{x_n}\right) < 2\pi \quad (n = 0, 1, 2, \dots) \quad (3)$$

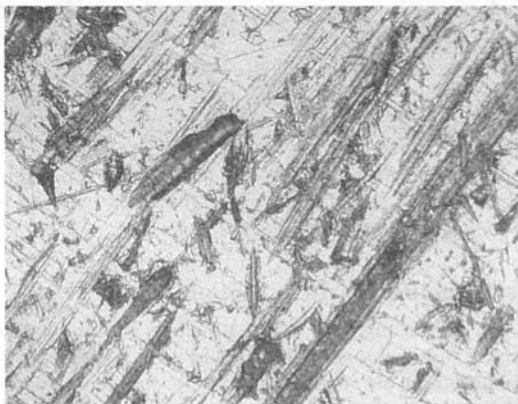


Fig. 2 Ditches (X200) on the titanium surface generated by particles

where $J = \{(\xi_1, \eta_1), (\xi_2, \eta_2), \dots, (\xi_N, \eta_N)\}$ is a Julia set (fractal point set) produced by the nonlinear iterative equations

$$\xi_{N+1} = \{[R(\xi_N, \eta_N)]^2 + [I(\xi_N, \eta_N)]^2\}^{1/4} \cos [\theta(\xi_N, \eta_N)/2] - 0.368 \quad (4)$$

$$\eta_{N+1} = \{[R(\xi_N, \eta_N)]^2 + [I(\xi_N, \eta_N)]^2\}^{1/4} \sin [\theta(\xi_N, \eta_N)/2] + 0.4436 \quad (5)$$

with

$$R(\xi_N, \eta_N) = \xi_N^3 - 3\xi_N\eta_N^2 + 1.24(\eta_N^2 - \xi_N^2) \quad (6)$$

$$I(\xi_N, \eta_N) = -\eta_N^3 + 3\eta_N\xi_N^2 - 2.48\eta_N\xi_N \quad (7)$$

$$-\pi < \theta(\xi_N, \eta_N) = \arctan\left[\frac{I(\xi_N, \eta_N)}{R(\xi_N, \eta_N)}\right] \leq \pi \quad (8)$$

$$x_n = 5\xi_N + 0.70, \quad y_n = 5\eta_N - 1.5 \quad (9)$$

Hereinafter, a particle on the cross section is positioned by the coordinates of a point, namely, a point in f_p will represent a particle. The particle distribution of f_p on a circular region and their unpredictable appearance are shown in Fig. 3 where the straight line connecting two points stands for the relative order of appearance of two particles. The axisymmetry and uniformity of f_p can be verified (Yong and Kovacevic, 1997b, c) by employing the rotating mapping function $T(\alpha) = e^{i\alpha}$ where α ($0 \leq \alpha < 2\pi$) is the rotating angle on the complex plane. Demonstration of the two properties are not displayed for compactness.

2.2 Velocity Profile of Point Set. After meeting three general properties of particle motion, the point set f_p is still not ready to represent particles on the cross section of particle flow because the velocity profile of f_p , along the normal direction of the cross section, may not be equivalent to that of particles. In the following, a governing equation for determining the velocity profile of f_p is introduced so that f_p can be endowed with any desired velocity profile. For the simplification of mathematical treatments, the mixture of particle, water, and air in jetflow is assumed to be uniform.

Based on the mass conservation principle, particles of f_p can be linked to their velocities through the equation

$$R_f = \frac{N_{xy}}{N_0} = \left(\int_{t_1}^{t_2} dt \iint_{S_{xy}} V_z ds \right) / \left(\int_{t_1}^{t_2} dt \iint_{S_0} V_z ds \right) \quad (10)$$

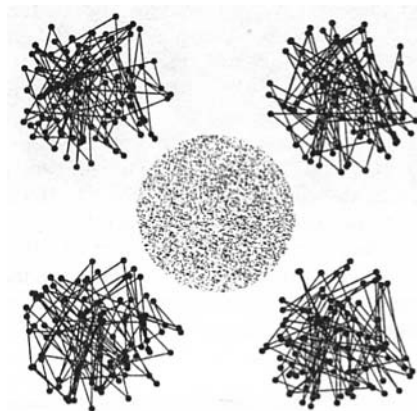


Fig. 3 Particle distribution on the circular region and their disordered appearance at different moments

giving

$$V_z = \left(\int_{t_1}^{t_2} dt \iint_{S_0} V_z ds \right) \frac{\partial^3 R_f}{\partial x \partial y \partial t} \quad (11)$$

In Eq. (10), R_f physically stands for the abrasive flowrate ratio; $V_z(t, x, y) = v_z/v_{zmax}$ is the dimensionless normal velocity of a particle at the point (x, y) and the instant t , v_z is the average normal velocity profile of the particle and v_{zmax} is the maximum velocity of jetflow; S_{xy} is an arbitrarily-shaped subarea of the cross section S_0 of particle-laden jetflow; N_{xy} is the number of particles passing through S_{xy} in the time interval $t - t_1$ and N_0 is the number of particles passing through S_0 during $t_2 - t_1$. Note that when the jetflow is assumed to be steady and axisymmetrical Eq. (11) can be simplified to

$$V_z = \left(2\pi \int_0^1 V_z(r) r dr \right) \frac{\partial R_f}{r \partial r} \quad (12)$$

In terms of (10) and (12), the velocity profile V_z and flowrate ratio R_f of f_p are drawn in Fig. 4 and two analytical equations

$$V_z^* = (1 - r)^{1/10} \quad (13)$$

$$R_f^* = 1 - (1 - r)^{11/10} (1 + \frac{11}{10}r) \quad (14)$$

are also plotted as approximate representations of V_z and R_f . The irregularity of V_z and R_f results from the disordered nature of particles in f_p .

In most cases, abrasive waterjet can be treated as a steady flow and hence for simplicity in the subsequent discussion the velocity profile of particle-laden flow is considered as to be time-independent.

2.3 New Point Sets. When the off-line simulation needs a new particle source or point set \bar{f}_p defined on an arbitrarily-shaped domain \bar{S}_0 with desired velocity profile \bar{V}_z , and/or flowrate ratio \bar{R}_f , the mapping technique is applied to convert f_p into \bar{f}_p through the integral equation

$$R_f = \bar{R}_f \Leftrightarrow \left(\iint_{S_{xy}} V_z^* ds \right) / \left(\iint_{S_0} V_z^* ds \right) = \left(\iint_{\bar{S}_{xy}} \bar{V}_z ds \right) / \left(\iint_{\bar{S}_0} \bar{V}_z ds \right) \quad (15)$$

where the subdomain \bar{S}_{xy} or \bar{S}_0 contains unknown coordinates (x, y) or (r, θ) of particles in \bar{f}_p . The physical meaning of (15) is that corresponding to a group of points in S_{xy} , another group of particles in \bar{S}_{xy} is determined through (15) which possesses the velocity profile $\bar{V}_z(x, y)$.

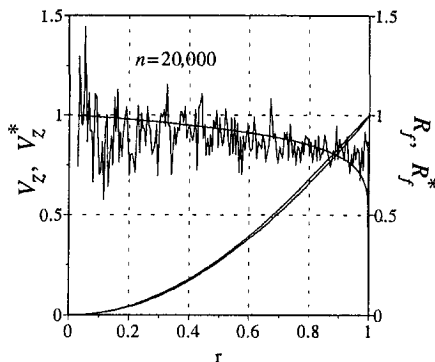


Fig. 4 Velocity profile and flowrate ratio of the original point set and their analytical approximation

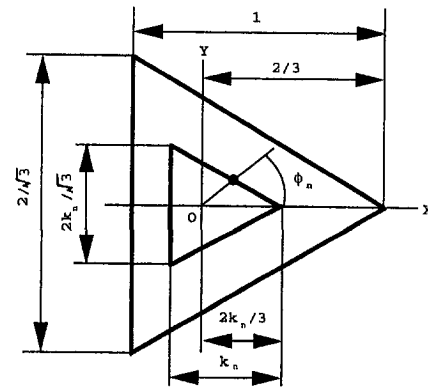


Fig. 5 Geometry of the triangular cross section of jet flow

For laminar jetflow, the average velocity profile of particles is assumed to be similar to that of one-phase waterjet. This assumption is based on the experimental discovery that the similarity exists between the average velocity profiles of particles and their transporting medium (e.g., Alajbegovic et al., 1994). In addition, two important points should be emphasized here for this assumption. (i) The average velocity profile is chosen for obtaining a group of one-to-one mapping equations through Eq. (15), the unpredictable or chaotic properties of particles in the new source will not be changed because they are relevant to appearing positions and orders with respect to each other. As a matter of fact, the oscillating characteristic of the factual velocity profile for a new source, like the old one shown in Fig. 4, will always retain due to the disordered property. (ii) The average velocity profile can be any desired form, numerical or analytical, which depends on the practical needs.

From known results in fluid mechanics (Shames, 1962 and Currie, 1992), one can find

$$\bar{V}_z = 1 - \beta(x, y) \quad (16)$$

where

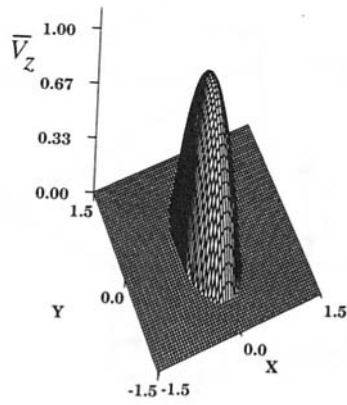
$$\beta(x, y) = \frac{x^2}{a^2} + \frac{y^2}{b^2} \quad (\text{elliptical flow}) \quad (17)$$

$$\beta(x, y) = \frac{27}{4a^2} \left[x^2 + y^2 - \frac{x}{a} (x^2 - 3y^2) \right] \quad (\text{equilateral triangular flow}) \quad (18)$$

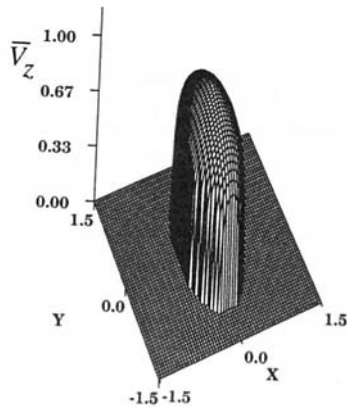
$$\beta(x, y) = \frac{4}{b^2} \left[x^2 + \frac{8b^2}{\pi^3} \sum_{m=1,3,5}^{\infty} (-1)^{(m-1)/2} \text{ch} \left(\frac{m\pi}{b} y \right) \cos \left(\frac{m\pi}{a} x \right) \right] \times \frac{1}{m^3 \text{ch} \left(\frac{m\pi a}{2b} \right)} \quad (\text{rectangular flow}) \quad (19)$$

where a and b are constants. As shown in Fig. 5, an analytical result is given here for equilateral triangular flow as an illustrative example. From (13) and (14) one can get

$$\left(\iint_{S_{xy}} V_z^* ds \right) / \left(\iint_{S_0} V_z^* ds \right) = \frac{(\theta_n + \pi)}{2\pi} \left[1 - (1 - r_n)^{11/10} (1 + \frac{11}{10}r_n) \right] \quad (-\pi \leq \phi_n < \pi) \quad (20)$$



(a)



(b)

Fig. 6 Average velocity profiles of elliptical flow. (a) Laminar flow. (b) Turbulent flow.

where (r_n, θ_n) are the polar coordinates of the n th particle in f_p . After substitution of (18) into the right side of (15), tedious calculations lead to

$$\left(\iint_{S_{xy}} \bar{V}_z ds \right) / \left(\iint_{S_0} \bar{V}_z ds \right) = k_n^2 \Phi(\phi_n) \quad (0 \leq k_n \leq 1) \quad (21)$$

where

$$\Phi = \frac{1}{2} + \frac{4 \tan \phi_n (3\sqrt{3} + 27 \tan \phi_n + 14\sqrt{3} \tan^2 \phi_n)}{81 (1 + \sqrt{3} \tan \phi_n)^3} \quad (0 \leq \phi_n \leq 2\pi/3) \quad (22)$$

$$\Phi = \frac{5}{6} + \frac{\sqrt{3} \tan \phi_n (21 - \tan^2 \phi_n) + 54}{324} \quad (2\pi/3 \leq \phi_n \leq \pi) \quad (23)$$

$$\Phi = \frac{1}{6} + \frac{27 - 69\sqrt{3} \tan \phi_n + 135 \tan^2 \phi_n - 25\sqrt{3} \tan^3 \phi_n}{81 (1 - \sqrt{3} \tan \phi_n)^3} \quad (-2\pi/3 \leq \phi_n \leq 0) \quad (24)$$

$$\Phi = \frac{\tan \phi_n (21 - \tan^2 \phi_n)}{108\sqrt{3}} \quad (-\pi \leq \phi_n \leq -2\pi/3) \quad (25)$$

In terms of (15, 20, 21), two mapping equations for determining two variables k_n and ϕ_n of Eq. (21) are of forms

$$k_n = [1 - (1 - r_n)^{11/10} (1 + \frac{11}{10} r_n)]^{1/2} \quad (26)$$

$$\Phi(\phi_n) = \frac{\theta_n + \pi}{2\pi} \quad (27)$$

The coordinates (x_n, y_n) of the n th particle in triangular point set f_p are ascertained by

(a) $0 \leq \phi_n \leq 2\pi/3$:

$$y_n = x_n \tan \phi_n = \frac{2k_n}{3(1 - \sqrt{3} \tan \phi_n)} \tan \phi_n \quad (28)$$

(b) $-2\pi/3 \leq \phi_n \leq 0$:

$$y_n = x_n \tan \phi_n = \frac{2k_n}{3(1 + \sqrt{3} \tan \phi_n)} \tan \phi_n \quad (29)$$

(c) $-\pi \leq \phi_n \leq -2\pi/3$ and $2\pi/3 \leq \phi_n \leq \pi$:

$$x_n = -\frac{k_n}{3}, y_n = -\frac{k_n}{3} \tan \phi_n \quad (30)$$

Mapping functions for other types of flow are not given here for brevity, but the following simulation processes will use results for elliptical jetflow. It can be seen from (22–30) that the unpredictable behavior inherited from the original one still remains in the new one.

The seventh-root law (Shames, 1962) for the average velocity profile of an axisymmetrical turbulent pipe flow is extended to describe noncircular flow. That is, the general average velocity profile for noncircular turbulent jetflow is given by

$$\bar{V}_z = (1 - \sqrt{|\beta(x, y)|})^{1/7} \quad (31)$$

where $\beta(x, y)$ is ascertained by (17–19) for different nozzle shapes. Two patterns are displayed in Figs. 6(a, b), to show the difference between two types of elliptical jetflow.

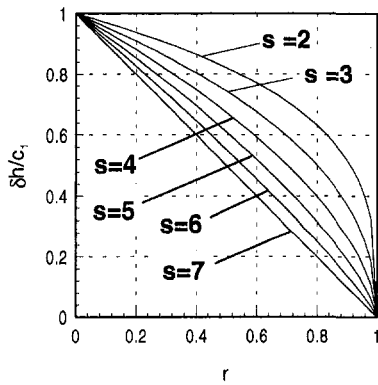
Equation (31) is considered to be valid if it can generate the sharp change of velocity gradients near the nozzle wall, similar to many experimental results for both one-phase or multiphase flow (Shame, 1962; Lee and Durst, 1982; Alajbegovic, 1994). The concern over the shape of the velocity profile arises because it is relevant to the cutting quality of AWJ. As stated above, one can choose any velocity profile as the average one for a new particle source based on practical needs. Two approaches are designed to ensure the completeness of creating new particle sources. Theoretically, a feedback control algorithm is developed for checking the consistency between the defined velocity profile and the factual velocity profile of particles. Experimentally, the shapes of holes drilled by AWJ are compared with simulation results (Yong and Kovacevic, 1997d). Very good agreement is confirmed between theory and experiment.

3 Simulation of AWJ Machining

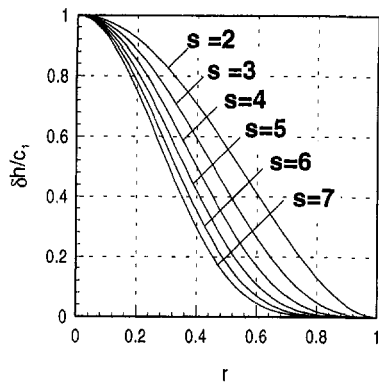
During simulation of an AWJ machining process, according to previous results, the relation between the average penetration depth δh_n generated by the n th particle and other parameters is defined by

$$\delta h_n = c_1 [V_z(x_n, y_n)]^s \quad (32)$$

where the exponent s is taken as 2 in the following simulation, c_1 is a constant determined by the test of one on-line cut, and $V_z(x_n, y_n)$ is the dimensionless normal velocity of the particle at an instant t . The time is measured by abrasive flowrate \dot{m} .



(a)



(b)

Fig. 7 The possible shapes of the kerf's bottom derived from the constitutive equation for erosion rate. (a) Turbulent velocity profile. (b) Laminar velocity profile.

For example, 10^4 th particle strikes the surface at the 0.5 second if $\dot{m} = 2 \times 10^4$ (particles)/s. Equation (32) does not specify the influences of individual parameters, such as the impact angles, the possible rotation and the geometry of a particle, due to the following reasons:

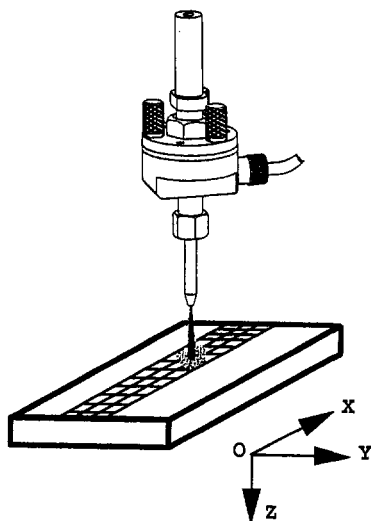


Fig. 8 Illustration of the memory cell approach

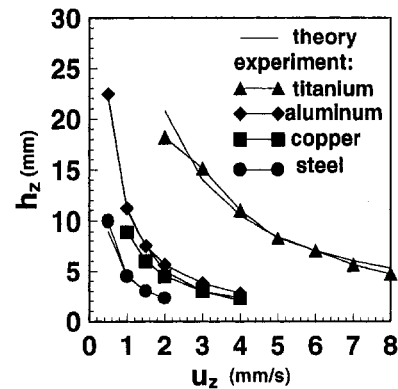


Fig. 9 Comparison between theory and experiment for cutting different materials (circular jet)

- The macro erosion rate of particles depends mainly on velocities and the number of particles striking the surface. Usually, a very small area can experience thousands of impacts from particles.
- It is impractical to instantly measure angles and rotations of millions of particles in a few seconds under the harsh machining environment.
- A brief equation is more efficient for either off-line simulation or on-line control (Kovacevic, 1992) after its accuracy is confirmed by experiments.

More importantly, the constant c_1 of Eq. (32) acts as a synthetic parameter that can reflect the influences of different parameters in a sense of average measurement.

How to determine the value of the exponent s has long been an interesting subject when only the erosion rate of one single particle is analyzed. Nevertheless, this issue becomes less influential when millions of different particles and their velocities are all taken into account. Some findings are introduced as follows.

In the present model, the maximum depth of drilling is independent of the exponent s according to

$$(\delta h_i)_{\max} = c_1 [V_{z,\max}(x_i, y_i)]^s = c_1 (V_{z,\max}(x_i, y_i) = 1). \quad (33)$$

As a result, the maximum depth h_z at the center of a hole has the form

$$h_z = \sum_{j=1}^J \delta h_j = \sum_{j=1}^J c_1 = Jc_1 \quad (34)$$

where J is the number of particles hitting the given point. In this circumstance, the variation of s is irrelevant to the calculation of

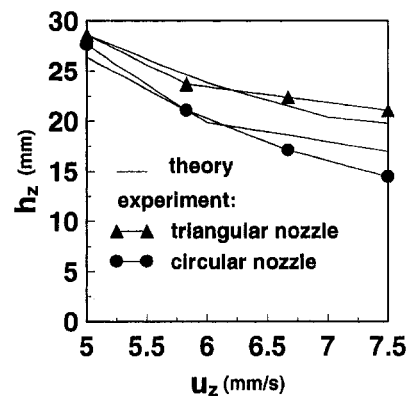


Fig. 10 Comparison between theory and experiment for cutting different materials (triangular jet)

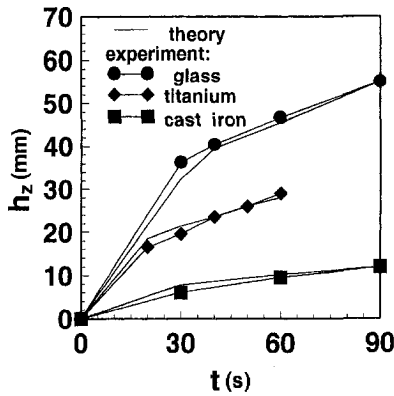


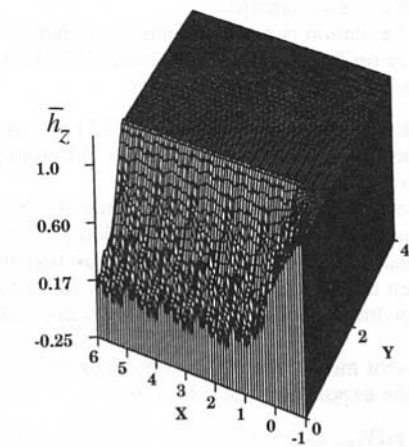
Fig. 11 Comparison between theory and experiment for drilling titanium, glass, and cast iron

h_z . So long as the value of c_1 is determined by a drilling test, the maximum depth for a material depends solely on the total number of particles striking the given area. The exponent s does lead to changes on the shape of a kerf through changing the

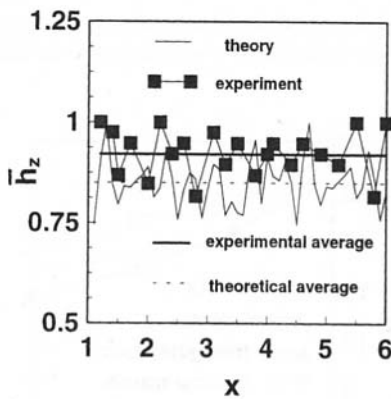
erosion rate. However, the value range of $n = 2 \sim 3$ here proves to be more reasonable. Because the shape of a kerf on the cross section of a workpiece is similar to the curve given by Eq. (32), the possible shapes of a kerf are plotted in Figs. 7 (a, b). Experiments show that the shape of a kerf matches well with the curves obtained with $n = 2 \sim 3$. Other shapes of kerfs are rarely seen in practical situation, particularly, $n = 5 \sim 7$ for turbulent flow.

A memory technique is introduced to record quantities and kinematic histories of particles passing through a given area of the workpiece to be cut, as explained in Fig. 8. When the particle jetflow with a moving nozzle travels over the erosion region, the erosion rates in different parts of the region greatly differ. The region is divided into a network, and each element of the network serves as a memory cell to record the histories of particles passing through it. Their penetration abilities are evaluated by use of Eq. (32). The final shape of a kerf is the accumulation of results of all the cells over the erosion region. Major simulation parameters are listed as follows

- traverse rate of a nozzle $u_z = 0.5 \sim 4.0/s$ (length unit/second)
- particle flowrate $\dot{m} = 2 \sim 8 \times 10^4/s$ (particle number/second)
- dimensionless radius of the nozzle $r_z = 1$ (length unit) for the circular nozzle

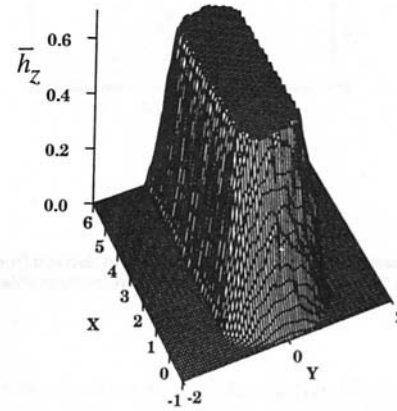


(a)

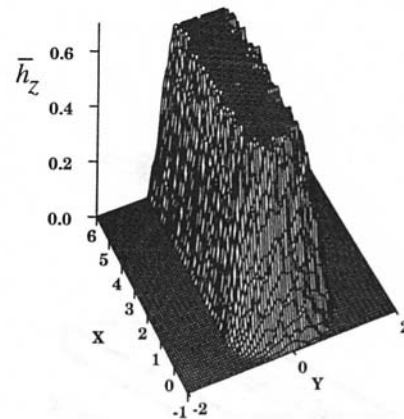


(b)

Fig. 12 Evaluation of roughness. (a) 3D configuration of bottom surface roughness. (b) A comparison between theory and experiment.



(a)



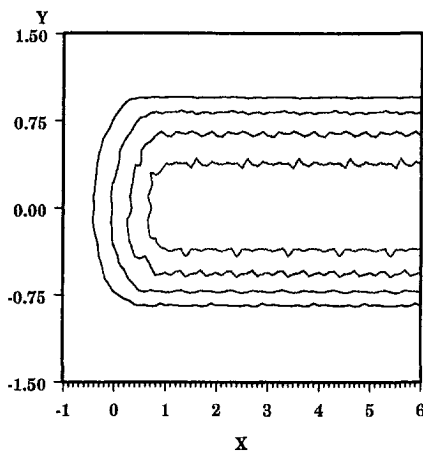
(b)

Fig. 13 3D configuration of kerfs. (a) $u_z = 0.5$ mm/s. (b) $u_z = 4.0$ mm/s.

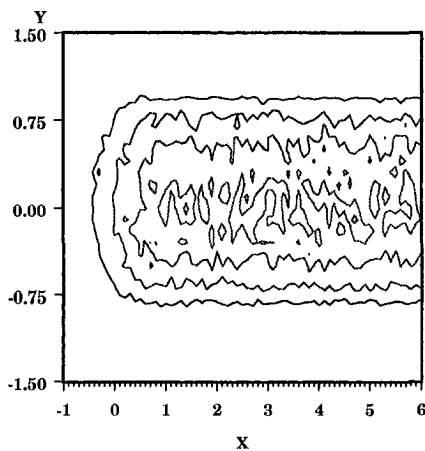
- area of a memory cell $a_{xy} = 0.1 \times 0.1$ (length \times length)
- dimensionless depth of cut $\bar{h}_z = h_z/h_{z\max}$ (h_z -depth of cut in a cell)
- total cutting length $L = 7$ (length unit) with no mask protection
- rotation angles of an elliptical nozzle $\gamma_z = 0 \sim 2\pi$
- ratio of the minor axis to the major axis of an elliptical nozzle $b/a = 0.5/1.0$.

In tests carried out by the authors, experimental conditions vary with workpiece materials, including waterjet pressure, abrasive flowrate and size and material, nozzle diameter and standoff distance. They are not all listed for brevity but are available on request.

3.1 Simulation of Cutting. The cutting simulation is conducted for titanium, annealed aluminum, carbon steel, and copper. As shown in Fig. 9, the consistency between theory and experiment justifies the validity of the model along with constitutive Eq. (32). The depth of cut is obviously a nonlinear function of nozzle speed u_z . At this point, the model proves to be very competitive with other models because only one cut is needed to determine a physical constant in Eq. (32). Moreover, other models break down when the nozzle shape is no longer



(a)



(b)

Fig. 14 Contour maps for measurement of waviness. (a) $u_z = 0.5$ mm/s. (b) $u_z = 4.0$ mm/s.

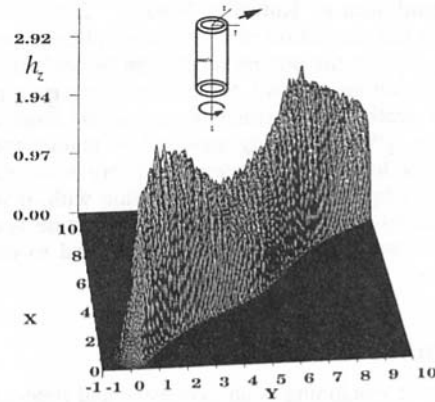


Fig. 15 3D configuration of a cut generated by a rotating and moving elliptical nozzle

a circular one. A comparison between equilateral triangular and circular jetflow is given in Fig. 10 where experimental data were given by Rankin and Wu (1995) from cutting aluminum. One advantageous feature of the present model is that any shape of jetflow can be simulated without principle difficulty.

3.2 Simulation of Drilling. The constitutive equation for drilling differs from Eq. (32) because of potential damping effects with the increase in depth of drilling (Yong and Kovacevic, 1997d). Still, only one physical constant involves the estimation of erosion rates. A comparison between theoretical and experimental results is plotted in Fig. 11 for drilling titanium, glass and cast iron, for ductile, brittle and quasi-brittle materials. It follows that the drilling model has very good accuracy.

3.3 Simulation of Roughness and Waviness. As indicated earlier, previous models failed to reflect parameters of surface quality, such as roughness and waviness, because they are caused mostly by distinct kinematic features of millions of particles, nozzle shape, travel speed, etc.. A theoretical 3D configuration that shows the roughness on the bottom of a kerf is displayed in Fig. 12(a). The roughness results from the irregularity of the depth. A comparison between theory and experiment is given in Fig. 12(b) where the experimental counterpart of Fig. 12(a) is obtained by measuring the depth of cut on an aluminum specimen. In simulation, the traverse speed u_z of the nozzle is $u_z = 2.0$ mm/s and the abrasive flowrate is $\dot{m} = 8 \times 10^4$ (particles/s). Calculations show that the error between the theoretical average and experimental depths is 7.6 percent.

Many experiments have demonstrated that very severe waviness occurs on the lateral surfaces of a workpiece when the travel speed of the nozzle increases from 0.5 mm/s to 4.0 mm/s (e.g., Hashish, 1992). However, previous models are incapable of including the intrinsic surface feature in association with other 3D parameters. Figures 13(a, b) are 3D configurations of two cuts corresponding to $u_z = 0.5$ mm/s and $u_z = 4.0$ mm/s, respectively. The waviness on the lateral surfaces is clearly visible in Fig. 13(b). Relative quantitative waviness of a cut can be determined by employing the contour map of a 3D configuration as displayed in Figs. 14(a, b) where the dimensionless heights of contours are 0.2, 0.4, 0.6, and 0.8. Note that at the different depth of cut the waviness is different. For example, results show that at the height $\bar{h}_z = 0.6$, the surface waviness w_z changes from $w_z = 0.18$ to $w_z = 0.65$ when the traverse speed of a nozzle increases from 0.5 mm/s to 4.0 mm/s. Experimental verification of theoretical waviness involves many sophisticated techniques and it will be discussed in a separate paper.

3.4 Simulation of Rotating Nozzle. The above discussions aim at the simulation of well-known phenomena in AWJ machining. In fact, the present model can be applied to explore many new functions of AWJ. Here is an example for producing the curved depth of cut which is one of the most important topics in the AWJ machining area and no mature method has been found yet to date. The strategy used here is to use a moving and rotating elliptical nozzle in association with, if necessary, the mask technique. The 3D cutting configuration is displayed in Fig. 15. Clearly, this is a potential method to control the depth of cut.

4 Conclusion and Discussion

3D abrasive machining is an expensive and time-consuming process, especially when an innovation needs to be justified. The cost may not pay off in many cases mainly because many parameters influence the machining outcome. For example, when a noncircular nozzle is applied to the shop floor, engineers and researchers have to get through lengthy experiments to verify its validity by changing machining conditions, such as the orientation and traverse speed of the nozzle, the water pressure, the flowrate of abrasives and so on. This makes it very difficult to find optimal parameters for a specific purpose.

Simulation is possibly the best way to solve the problem. In the present work, fractal point sets with chaotic behavior are employed to represent particles on the cross section of jetflow. These point sets can be endowed with any velocity profile and shape to meet practical needs. One of the most important functions carried by the model is that it is capable of simulating general motion of a nozzle on which many operations on the shop floor rely. The cutting, drilling, evaluation of surface quality, innovation of nozzle shape and the depth control are reported in this paper and selective experiments are conducted to verify its effectiveness and accuracy. Results confirm that it is a robust model and has potential to be an industrially applicable one.

In this research, less attention is paid to the investigation of constitutive equations for different working environments. This does not mean, however, that this topic is not worth further consideration. As a matter of fact, many subjects relevant to this topic have probably not been addressed so far, such as the dynamic property of workpiece material subjected to very localized impact loading or the influence of strain rates, multi-impacts of chaotic particles, instability of particles due to the loss of penetration ability, etc.. According to the results reported in this work, a classical formulas developed previously performs accurately for the most common AWJ machining process, such as cutting and drilling.

Acknowledgment

The authors would like to thank the National Science Foundation for the support of this project under Grant DMI-9523010. The appreciation is extended to the Allison Engine Company, United Technologies Pratt & Whitney, and the Flow International Corporation for their support as the cosponsors.

References

- Alajbegovic, A., et al., 1994, "Phase Distribution and Turbulence Structure for Solid/Fluid Upflow in a Pipe," *Int. J. Multiphase Flow*, Vol. 20, pp. 453–479.
- Bitter, J. G. A., 1963, "A Study of Erosion Phenomena—Part I," *Wear*, Vol. 16, pp. 5–21.
- Bitter, J. G. A., 1963, "A Study of Erosion Phenomena—Part II," *Wear*, Vol. 16, pp. 169–190.
- Currie, I. G., 1992, *Fundamental Mechanics of Fluid*, McGraw-Hill, New York.
- Finnie, I., 1958, "The Mechanisms of Erosion of Ductile Metals," *Proceedings of the Third National Congress of Applied Mechanics*, ASME, pp. 527–532.
- Finnie, I., 1960, "Erosion of Surfaces by Solid Particles," *Wear*, Vol. 3, pp. 87–103.
- Gulden, M. E., 1979, "Solid Particle Erosion of High Technology Ceramics," *ASTM STP664*, W. F. After, ed., pp. 101–122.
- Hashish, M., 1984, "A Modeling Study of Metal Cutting with Abrasive-Waterjets," *ASME Journal of Engineering Materials and Technology*, Vol. 106, pp. 88–100.
- Hashish, M., 1992, "Three Dimensional Machining with Abrasive Waterjet," *Jet Cutting Technology*, Vol. 13, pp. 605–620.
- Hashish, M., 1994, "Controlled-Depth Milling Techniques Using Abrasive Waterjet," *Jet Cutting Technology*, Vol. 13, 449–461.
- Hongawa, H., et al., 1992, "Annular Jet and Its Applications," *Journal of Jet Technology Society of Japan*, Vol. 9, pp. 1–11 (in Japanese).
- Hutchings, I. M., 1979, "Mechanisms of the Erosion of Metals by Solid Particles," *ASTM STP 664, Erosion: Prevention and Useful Applications*, pp. 59–76.
- Kovacevic, R., 1992, "Monitoring of Depth of Abrasive Waterjet Penetration," *Int. J. Mach. Tools Manufact.*, Vol. 1, pp. 55–72.
- Lee, S. L. and Durst, F., 1982, "On the Motion of Particle in Turbulent Duct Flow," *Int. J. Multiphase Flow*, Vol. 8, pp. 125–146.
- Neilson, J. H., and Gilchrist, 1968, "Erosion by a Stream of Solid Particles," *Wear*, Vol. 11, pp. 111–122.
- Rankin, G. J. and Wu, S. S., 1995, "Abrasive Waterjet Cutting with a Shapejet," *Proceeding of 7th American Water Jet Conference*, Houston, Texas, pp. 219–228.
- Shames, I. H., 1962, *Mechanics of Fluids*, McGraw-Hill, New York.
- Tilly, G. P., and Sage, W., 1970, "The Interaction of Particle and Material Behavior in Erosion Processes," *Wear*, Vol. 16, pp. 447–465.
- Yong, Z., and Kovacevic, R., 1997a, "Effects of Water-Mixture Film on Impact Contact in Abrasive Waterjet Machining," *International Journal of Mechanical Science*, Vol. 39, pp. 729–739.
- Yong, Z., and Kovacevic, R., 1997b, "Fundamentals of Constructing Particle-Laden Flow by Fractal Point Sets and Predicting 3D Solid Erosion Rates," *International Journal of Chaos, Solitons and Fractals*, Vol. 8, pp. 207–220.
- Yong, Z., and Kovacevic, R., 1997c, "Feedback Control of Chaotic Point Sets with Arbitrary Velocity Profile," in press.
- Yong, Z., and Kovacevic, R., 1997d, "Modeling of Jetflow Drilling with Consideration of Chaotic Erosion Histories of Particles," *Wear*, in press.
- Zeng, J., and Kim, T. J., 1992, "Development of an Abrasive Waterjet Kerf Cutting Model for Brittle Materials," *Jet Cutting Technology*, Vol. 13, pp. 483–501.

E. A. Ervin
Assistant Professor,
Department of Mechanical and
Aerospace Engineering,
The University of Dayton,
Dayton, OH 45469

G. Tryggvason
Associate Professor,
Department of Mechanical Engineering and
Applied Mechanics,
The University of Michigan,
Ann Arbor, MI 48109

The Rise of Bubbles in a Vertical Shear Flow

Full numerical simulations of two- and three-dimensional bubbles in a shear flow, by a finite difference front tracking method, are presented. The effects of inertial, viscous, gravitational, and surface forces on the lift of a deformable bubble rising due to buoyancy in a vertical shear flow, are examined. Bubbles with a large surface tension coefficient migrate toward the downward moving fluid, as predicted analytically for a cylinder or a sphere in a shear flow. Bubbles with smaller surface tension deform, and generally migrate in the opposite direction. The combined effects of the shear flow and the buoyancy deform the bubble in such a way that the circulation around the deformed bubbles is opposite to that of undeformed bubbles.

Introduction

Bubbles in shear flows are of underlying importance in many processes. While it is often the collective behavior of many bubbles that is of most engineering relevance, rather than the motion of individual bubbles, the global properties of a multi-phase flow are usually determined by the smallest scales in the flow. The coupling of the bubble motion to that of the outer liquid flow is central to understanding the dynamics of bubbles. While a number of studies have focused on the drag on bubbles, the lift is poorly understood. Although a body of literature is available for rigid particles, the effect of deformation has received little attention.

A spinning body in translational motion will experience a force in a direction perpendicular to both the direction of motion and the rotation axis. As shown in Fig. 1, the nonuniform fluid flow causes the particle to rotate, resulting in a force in the y -direction:

$$\mathbf{F} = \beta \rho_2 V (\boldsymbol{\omega} \times \mathbf{U}_{P/F}). \quad (1)$$

Here, $|\boldsymbol{\omega}|$ is equal to the velocity gradient, G , which is taken to be constant far from the particle (Fig. 1), and $\mathbf{U}_{P/F}$ is the relative velocity of the particle with respect to the fluid. For inviscid flow around a rigid two-dimensional cylinder, β is 2.0 and V is the cross-sectional area, πa^2 (Batchelor, 1967). For inviscid flow around a rigid sphere, β is 0.5 and V is the sphere volume (Auton, 1988). The resulting lift force on the particle, also known as the Magnus effect, causes lateral migration across the streamlines of the outer flow in the direction of \mathbf{F} .

Bretherton (1962) examined the migration of nonspherical rigid particles in a shear flow where the shear Reynolds number, G_R , is very small. Saffman (1965) examined the lift of a sphere in a shear flow where G_R , and the slip Reynolds number, Re , are both small, showing that the lift force is:

$$\mathbf{F} = -6.46a^2 |\mathbf{U}_{P/F}| \sqrt{\rho_1 \mu_1} |G| \text{sign}(G). \quad (2)$$

McLaughlin (1991, 1993) extended the range of G_R relative to Re , and included the effect of a nearby wall. Dandy and Dwyer (1990) numerically examined a fixed sphere in a shear flow at finite Re . They used a body fitted grid and a finite volume method and found that the lift force is proportional to the shear rate and the square of the fluid velocity. Recent experimental studies by Sridhar and Katz (1995), of very small spherical bubbles interacting with a vortex, showed a similar trend as predicted by the various theoretical models. Their experiments

were carried out under different conditions than those for which the theories were valid, and therefore yielded considerable quantitative differences in the results. However, the differences show the sensitivity of the lift force on a rigid body to the competing influences of inertial, viscous, and gravitational forces, and illustrate the incomplete state of the knowledge about lift on bubbles in shear flows.

In addition to inertia, other factors such as wall proximity, non-sphericity and non-Newtonian fluid properties, shear gradients and deformability can influence the motion of particles, as described by Leal (1980). Asymmetric deformation, in particular, causes the particle to migrate laterally to an equilibrium position. Quantifiable observations of the lateral migration of neutrally buoyant drops in shear flow were first made by Goldsmith and Mason (1962) and by Karnis and Mason (1967). Duplication of the experiments with a solid particle showed no lateral migration, indicating that the migration is deformation induced. Models of this phenomenon have assumed Stokes flow (for example, Uijttewaala et al., 1993). Simulations of a deformable particle in shear flow have generally been limited to droplets with minute G_R in an infinite flow regime with no relative motion (Rallison, 1984). More recent studies have included walls or finite G_R (for example, Zhou and Pozrikidis, 1993 and Kang and Leal, 1987, 1989). No attempt appears to have been made to model a deformable particle in inertia-induced motion.

Kariyasaki (1987) performed an experiment releasing both deformable and solid bodies in a simple vertical shear flow generated by a belt driven mechanism in a fluid filled tank. Both solid particles and liquid droplets were introduced at the top of the tank and both were observed to migrate laterally toward one of the belts. However, measured displacement traces of the particles showed that the direction of migration of the droplets was opposite to that of the solid particles. Kariyasaki also released gas bubbles at the bottom of the tank. The bubbles rose due to buoyancy and again, drifted in a direction opposite to that expected from the theoretical predictions for a solid particle. Although the deformation was not quantified, the bubbles and drops were highly deformed.

The objective of this study is to gain insight into the fundamental behavior of bubbles rising in a simple shear flow by full numerical simulation of the Navier-Stokes equations. The physical problem is defined and the numerical technique is outlined briefly in the next section. The following sections show a number of two-dimensional results to explain the basic mechanisms and their dependency on the governing parameters of the flow. Finally, it is shown that three-dimensional simulations confirm the two-dimensional predictions.

Numerical Procedure

The front-tracking method consists of a finite difference approximation of the full Navier-Stokes equations with explicit

Contributed by the Fluids Engineering Division for publication in the JOURNAL OF FLUIDS ENGINEERING. Manuscript received by the Fluids Engineering Division December 25, 1994; revised manuscript received September 4, 1996. Associate Technical Editor: R. W. Metcalfe.

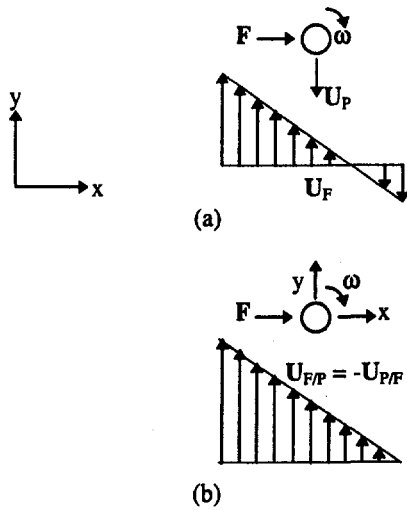


Fig. 1 Schematic of particle force due to relative motion in a nonuniform flow (a) viewed from an external frame of reference (b) viewed from the particle

tracking of a distinct free boundary at the interface between the bubble and the ambient fluid. Unverdi and Tryggvason (1992a) introduced the method to track one or more bubbles rising through a quiescent flow, and they numerically simulated both two- and three-dimensional rising bubbles (Unverdi and Tryggvason, 1992a, 1992b). The method is described below.

The Navier-Stokes equations govern the fluid motion both inside and outside the bubbles and a single vector equation can be written for the whole flow field. In conservative form:

$$\begin{aligned} \frac{\partial \rho \mathbf{U}}{\partial t} + \nabla \cdot \rho (\mathbf{U} \otimes \mathbf{U}) = & -\nabla p + (\rho_o - \rho) \mathbf{g} \\ & + \nabla \cdot \mu [(\nabla \otimes \mathbf{U}) + (\nabla \otimes \mathbf{U})^T] \\ & - \int_{\text{Front}} \kappa_f' \mathbf{n}_f' \delta^i(\mathbf{x} - \mathbf{x}_f') dA_f' \quad (3) \end{aligned}$$

where \otimes denotes the tensor product of two vectors. Surface forces are added at the interface between the bubbles and the ambient fluid. δ^i is a two or three-dimensional delta function obtained by multiplying together one-dimensional delta functions. The dimension is denoted by $i = 2$ or 3 . κ_f' is the curvature for two-dimensional flow and twice the mean curvature for three-dimensional flows. Formally, the integral is over the entire front, thereby adding the delta functions together to create a force that is concentrated at the interface, but smooth along the surface of the bubbles. The primed variables are evaluated at \mathbf{x}_f' , the front position. In the actual numerical code, the integral is evaluated only for points close to the front.

The mass conservation equation can be written:

$$\frac{D\rho}{Dt} + \rho \nabla \cdot \mathbf{U} = 0 \quad (4)$$

where $D()/Dt$ is the material derivative. The equations of state for the density and viscosity:

$$\frac{D\rho}{Dt} = 0 \quad (5)$$

$$\frac{D\mu}{Dt} = 0 \quad (6)$$

simply state that density and viscosity within each fluid remain constant. Equations (4) and (5) can therefore be combined:

$$\nabla \cdot \mathbf{U} = 0 \quad (7)$$

for the entire domain, which, when combined with the momentum equations leads to a nonseparable elliptic equation for the pressure.

These equations implicitly enforce the proper stress conditions at the fluid interface. If we integrate Eq. (3) over a small volume containing the interface, most of the terms go to zero in the limit of infinitesimal volume, resulting in:

$$\{-p\mathbf{n} + \mu\mathbf{n} \cdot [(\nabla \otimes \mathbf{U}) + (\nabla \otimes \mathbf{U})^T]\} = \sigma \kappa_f' \mathbf{n} \quad (8)$$

where the outer braces denote the jump across the interface. This is, of course, the usual statement of continuity of stresses

Nomenclature

A = surface area
 a = radius of undeformed bubble
 A_p = projected area ($A_p = 2a$ for 2D bubble)
 d = diameter of undeformed bubble
 C = lift force coefficient, $C = 2|\mathbf{F}| \text{sign}(\mathbf{F}) / (\rho_1 v_{p/f}^2 A_p)$
 Ca = capillary number, $Ca = Ga\mu_1/\sigma$
 D = deformation, $(1 - E)/(1 + E)$
 E = ellipse ratio: minor axis to major axis
 \mathbf{F} = lift force, $\mathbf{F} = \beta \rho_2 V (\boldsymbol{\omega} \times \mathbf{U}_{p/f})$
 Fr = Froude number, $Fr^2 = G^2 a/g$
 fx = lift force in x direction
 G = velocity gradient, $G = \partial v/\partial x = 2U_o/l$
 G_R = Reynolds number calculated using G , $G_R = \rho_1 G a^2 / \mu_1$
 \mathbf{g} = gravitational acceleration vector
 l = distance between sheared walls
 \mathbf{n}_f = unit vector normal to bubble surface, pointing out
 p = fluctuating pressure

Re = Reynolds number calculated with $v_{p/f}$, $Re = \rho_1 v_{p/f} d / \mu_1$
 t = time
 \mathbf{U} = velocity vector
 U_o = nominal velocity of sheared wall
 v = velocity component in vertical direction
 V = volume (3-D)
 We = Weber number, $We = \rho_1 G^2 a^3 / \sigma$
 \mathbf{x} = position vector
 x, y, z = cartesian coordinates (bubble centroid)

Superscripts

i = flow dimension index

Subscripts

1 = fluid material property
 2 = bubble or drop material property
 D = drag force

F = fluid (vector)
 f = bubble front
 P = particle vector
 P/F = particle vector relative to fluid vector

Greek

α = finite shear rate, $\alpha = 0.5 * G / v_{p/f} = 0.5 * G_R / Re$
 β = coefficient for lift force, \mathbf{F}
 Γ = circulation, cm^2/s
 δ = delta function, $\delta(0) = 1$
 θ = angle between the path and the vertical axis
 η = density ratio, $\eta = \rho_2 / \rho_1$
 κ = twice the average front curvature (3-D)
 λ = viscosity ratio, $\lambda = \mu_2 / \mu_1$
 μ = dynamic viscosity
 ρ = density
 ρ_o = density of an equivalent homogeneous system
 σ = surface tension
 $\boldsymbol{\omega}$ = vorticity vector

at a fluid boundary, showing that the tangential stresses are continuous and that the normal stresses are balanced by surface tension. Integrating the mass conservation Eq. (4) across the interface shows that the continuity of the normal velocities is also satisfied.

A finite difference discretization of the above equations advances the flow field over a staggered mesh while additional computational elements explicitly track the interface between the two fluids. Since the fluids are incompressible, the front motion is determined solely from the velocity field that is interpolated from the grid. The tracked interface carries the jump in fluid properties that are distributed onto the grid to reconstruct the density or viscosity fields. The separation between the two fluids is not completely abrupt but has a finite thickness on the order of a grid spacing. This thickness remains constant, as there is no numerical diffusion, and provides stability and smoothness to the solution. The thickness does, however, depend on the size of the grid used; in the limit of infinitely high resolution, the thickness goes to zero. As shown later in the paper, the resolution tests demonstrate that the solution converges relatively fast under grid refinement. The tracked interface locates the surface tension forces and the interface position provides the basis to update the density and viscosity fields. To keep the elements at an optimum size and shape, it is imperative to reconfigure the interface at each time step, particularly in the case of the three-dimensional surfaces. The present study used a version of the numerical method that is second order both in time and space. The time step is automatically updated at each time step to ensure stability. The calculations were performed in double precision on a work station, or on a Cray Y-MP that uses a 64-bit word making single precision equivalent to double precision on a 32-bit machine. Further details of the code and its verification are given in Ervin (1993).

The problem is described in Fig. 2. Assume that an initially spherical bubble with radius a , density ρ_2 , viscosity μ_2 , and surface tension coefficient σ is suspended in a fluid of density ρ_1 , and viscosity μ_1 . The region is bounded in the x -direction by rigid walls moving in opposite directions with a constant velocity U_0 . The boundaries are periodic in the other two directions. In the case of the two-dimensional models, the bubble is initially a cylinder. Gravity acts in the negative y -direction,

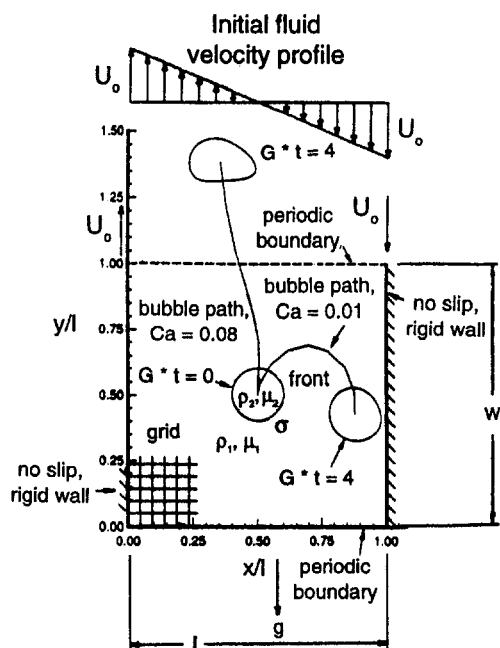


Fig. 2 Effect of Ca on bubble motion. $G_R = 16.0$, $Fr^2 = 0.20$, $\eta = 0.025$, $\lambda = 0.10$, and $a/l = 0.10$.

resulting in motion of the bubble, relative to the suspending fluid. Along with the viscosity and density ratios, λ and η , respectively, and the ratio a/l , the three-independent dimensionless groups that define the problem are the shear Reynolds number, $G_R = \rho_1 G d^2 / \mu_1$, the Froude number squared, $Fr^2 = G^2 a / g$, and the capillary number, $Ca = G a \mu_1 / \sigma$ (alternatively, the Weber number, $We = \rho_1 G^2 a^3 / \sigma$). Position and size are scaled by l , deformation by a , velocity by U_0 , time by G , and stress by μG . Here, the width of the periodic domain is equal to l .

For the results presented in the following sections, the density ratio is $\eta = 0.025$. While the intent was to simulate a gas bubble in water, previous studies by Unverdi and Tryggvason (1992a) have shown that decreasing η further did not have such a significant effect on the results that it warranted the ensuing computational cost. Also, the ratio of dynamic viscosity is of the order of 10, thus $\lambda = 0.10$. The bubble is released at time zero into an initially linear velocity field (Couette flow) from a position centered in the periodic directions (y/l or z/l is 0.5) while the initial x/l varies.

Results and Discussion

This section presents numerical simulations of buoyant deformable bubbles in a linear vertical shear flow. Beginning with a two-dimensional model, the effects of deformation of sheared bubbles on circulation, migration and lift are investigated. More realistic three-dimensional bubbles are then considered.

Effect of Deformation on Migration. In this section, the effect of Ca on bubble deformation and migration is analyzed with constant G_R and Fr^2 . Figure 2 shows the effect of deformation on two bubbles with $G_R = 16.0$, $Fr^2 = 0.20$, and $a/l = 0.1$, initially at $x/l = 0.500$, computed on a 128 by 128 grid. The bubble contours are plotted at time $G^*t = 4$, along with their path. The bubble with the greatest surface tension ($Ca = 0.01$) remained fairly cylindrical. It initially rose in the positive y -direction, but then migrated toward the wall that moved in the negative y -direction, and eventually turned in the negative y -direction. The bubble migration was in the direction of the lift force, F (Eq. (1)), due to the clockwise rotation induced by the sheared walls and the upward relative motion of the bubble. In contrast, the bubble with a lower surface tension coefficient ($Ca = 0.08$) developed an inverted tear drop shape. It rose and then migrated toward the upward moving wall in a manner similar to the deformed bubbles and drops described by Kariyasaki (1987).

Figure 3 shows the path of the two-dimensional bubbles resolved on 32^2 , 64^2 , and 128^2 grids. The bubble fronts for $Ca = 0.01$ are plotted at time $G^*t = 1.5$ (Fig. 3(a)) and for $Ca = 0.08$ at $G^*t = 3.0$ (Fig. 3(b)). While all runs show similar behavior, the exact path of the coarsely resolved bubble differs somewhat from the better resolved ones, and its shape has large irregularities on the bottom ($Ca = 0.08$). The bubble with 64^2 grid resolution has slight irregularities on the bottom, but the shape is nearly identical to the best resolved bubble. The latter moves slightly faster than the former, so that if we wait long enough, the actual positions will be different although the paths are nearly identical. The size of the bubble, a/l , was based on a preliminary study to reduce wall effects while allowing the bubble to develop a sufficient Re . The cross-sectional area of the bubble was calculated using Stokes' theorem at each time step as a check on the solution, with satisfying results.

The following set of figures examine the bubbles described in Fig. 2. The initially cylindrical bubbles were released from a noncentered x -value. This was to examine each bubble after any changes to its shape and migration by the time the bubble reached the center of the flow domain, with reduced wall effects. The bubble with $Ca = 0.01$ started from $x/l = 0.175$ and continuously migrated in the positive x -direction as before, until it

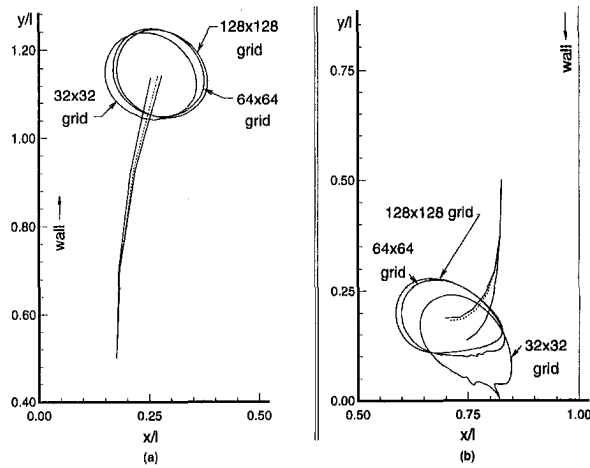


Fig. 3 Effect of grid resolution on a two-dimensional bubble. $G_R = 16.0$, $Fr^2 = 0.20$, $\eta = 0.025$, $\lambda = 0.10$ and $a/l = 0.10$. (a) $Ca = 0.01$ and $G^*t = 1.5$, (b) $Ca = 0.08$ and $G^*t = 3.0$.

encountered the wall. The deformed bubble, $Ca = 0.08$, started from $x/l = 0.825$ and migrated in the negative x -direction, as when it was released midway between the walls. Since this bubble started out near the wall moving in the negative y -direction, it moved in the negative y -direction before buoyancy had a significant effect.

Figure 4 shows the flow field as seen from a coordinate frame moving with the individual bubble centroids, at a time when each bubble solution has reached a steady shape (no further deformation) in the center of the flow region. This occurred at $G^*t = 3.0$ for the cylindrical bubble ($Ca = 0.01$, Fig. 4(a)), and at $G^*t = 7.0$ for the low surface tension bubble ($Ca = 0.08$, Fig. 4(b)). Velocity vectors and streamlines are shown with respect to the bubble frame of reference, and the velocity unit shown in the figures represents the velocity of the wall. The bubble front is overlaid on the velocity field. The steady shape of each bubble was a distorted ellipse, with the minor axis aligned with the direction of the bubble motion. The side of the bubble approaching the respective wall had a higher radius of curvature. This was especially pronounced for the bubble with $Ca = 0.08$. The internal flow within a bubble rising in a quiescent flow generally consists of two vortices of equal strength but opposite circulation, driven by flow past the bubble. Since the bubbles of Fig. 4 are rising with respect to the flow, such vortices are expected. Furthermore, the vortex on the side that has larger relative motion should be stronger, and this is exactly what is observed. The predominant vortex in the round bubble ($Ca = 0.01$, Fig. 4(a)) rotated in the clockwise direction required by the outer shear flow, and was located in the side of the bubble facing the downward moving wall. In the case of the high Ca bubble, the vortex in the side facing the upward moving wall was the larger of the two and rotated in the counter-clockwise direction. The clockwise vortex filled the smaller end of the bubble.

Figure 5 shows the bubble circulation ($\Gamma/U_o/l$) as a function of time for each of the two bubbles of Fig. 4. From the sheared walls, the bubble circulation was expected to be negative (clockwise). This was the case, initially, when both bubbles were fairly cylindrical. However, the deformed bubble quickly began to shift to a positive circulation. Thus it appears that the counter-clockwise vortex seen in Fig. 4(b) dominated the overall circulation of the deformed bubble. This result confirms the lift acceleration effect: the unexpected migration direction of the deformed bubble is due to a counter-clockwise circulation. Interestingly, the circulation of the cylindrical bubble also increased under the influence of the wall, suggesting that both

wall and deformation influence the lift acceleration and the bubble migration.

Parametric Study of Lift. A parametric study evaluated the effect of varying G_R , Fr^2 , and Ca on bubble lift force and deformation, at $a/l = 0.1$. These parameters, especially Ca , were selected to be in the critical range where the lift force changes direction. G_R and Fr^2 , particularly the latter, were limited by computational requirements. The lift force was calculated by applying a force on the bubble to hold it centered between the two walls. Figure 6 presents the lift force coefficient, C_{fx} , as a function of Ca , for four combinations of G_R and Fr^2 . One of the curves corresponds to $G_R = 16.0$ and $Fr^2 = 0.20$, as in the previous section. The bubble with a high surface tension ($Ca = 0.01$) had a positive C_{fx} , toward the downward moving wall. This was comparable to a solid cylindrical parti-

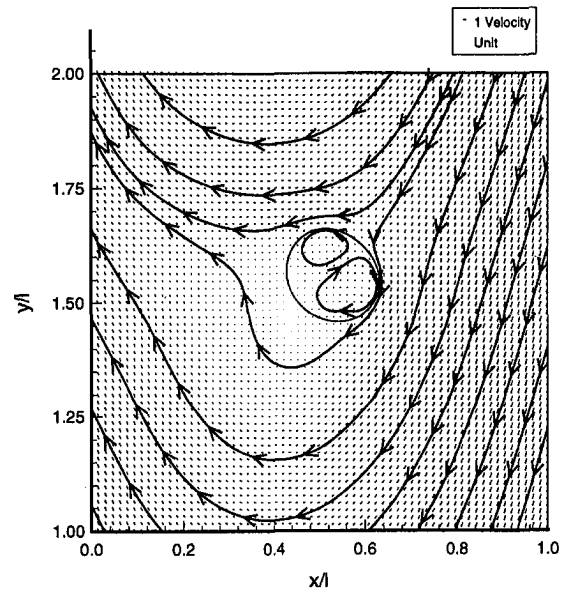


Fig. 4(a)

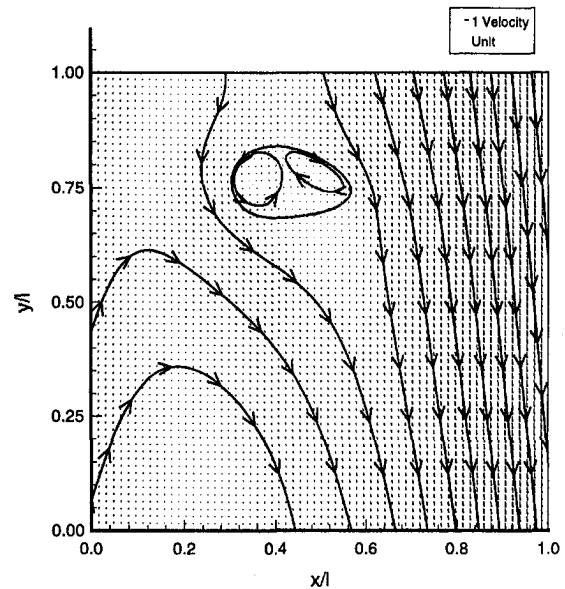


Fig. 4(b)

Fig. 4 Velocity field with respect to the centroid of a steady bubble. $G_R = 16.0$, $Fr^2 = 0.20$, $\eta = 0.025$, $\lambda = 0.10$ and $a/l = 0.10$. (a) $Ca = 0.01$, $G^*t = 3$ and initial $x/l = 0.175$, (b) $Ca = 0.08$, $G^*t = 7$ and initial $x/l = 0.825$.

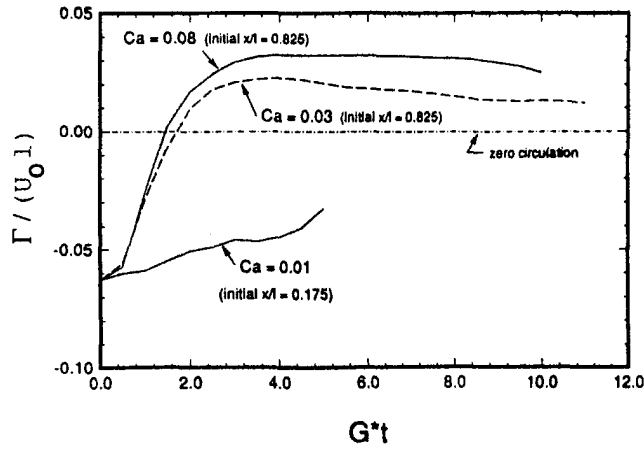


Fig. 5 Bubble circulation (Γ/U_0l) as a function of time. $G_R = 16.0$, $Fr^2 = 0.20$, $\eta = 0.025$, $\lambda = 0.10$ and $a/l = 0.10$.

cle, as expected due to the tendency of a low Ca bubble not to deform. Increasing Ca resulted in a negative lift force, toward the upward moving wall. This agrees with the results of Fig. 2. The consequence of reducing the shear Reynolds number ($G_R = 8.0$) was to increase C_{fx} in the positive x -direction. These bubbles behaved more as solid cylindrical particles even at higher Ca. Reducing Fr^2 to a value of 0.18, however, increased C_{fx} in the negative x -direction.

The lift coefficient of the low Ca cylindrical bubble at $G_R = 8$, $Fr^2 = 0.2$ is 2.0. This is similar to the theoretical lift coefficient of 1.3 for a buoyant rigid sphere in low Re flow, from Eq. (2) (Saffman, 1965). The Re for this bubble is 9.0, and the corresponding calculated drag coefficient is 3.0, which corresponds very well to experimental results for solid cylinders (Schlichting, 1979). However, this result must be somewhat fortuitous: the expected lower friction drag on the bubble is apparently offset by increased drag due to wall effects.

The lift force results can be considered further by looking at the bubble deformation (Fig. 7), where D is defined as:

$$D = (1 - E)/(1 + E). \quad (9)$$

Here, E is the ratio of the minor to major axes of an ellipse. E was calculated by equating the area moments of inertia of the bubble, as tracked by the front, to those of an ellipse. Again, one of the curves corresponds to $G_R = 16.0$ and $Fr^2 = 0.20$. The bubble with $Ca = 0.01$ had a low deformation ($D = 0.0844$) which explains why a positive lift force accelerated it like a

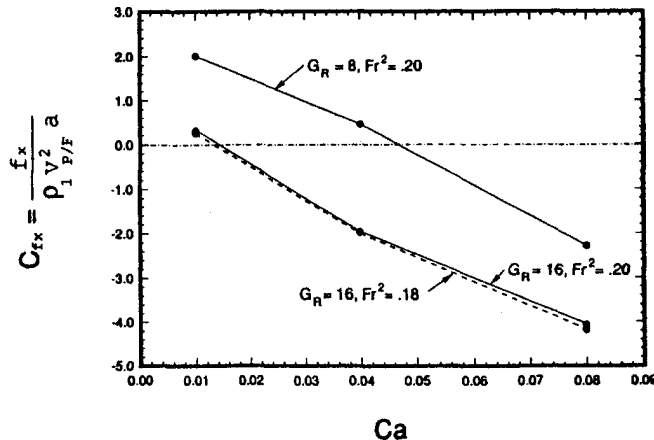


Fig. 6 Variation of lift force coefficient (C_{fx}) with Ca. $\eta = 0.025$, $\lambda = 0.10$ and $a/l = 0.10$.

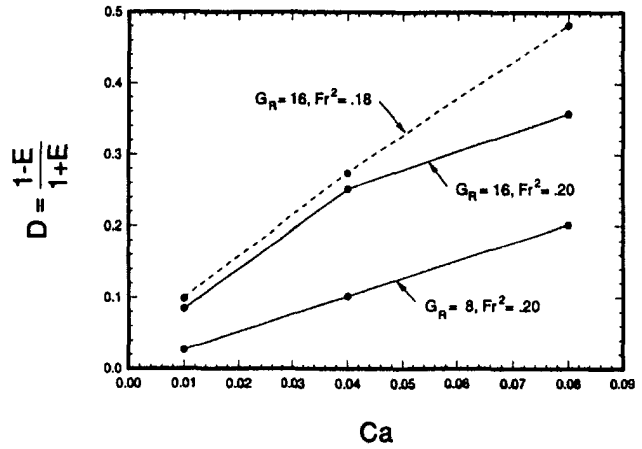


Fig. 7 Variation of deformation (D) with Ca. $\eta = 0.025$, $\lambda = 0.10$ and $a/l = 0.10$.

solid cylindrical particle. Lower surface tension increased D and thus increased the deformation induced lift force in the negative x -direction. Decreasing the relative influence of inertia ($G_R = 8.0$), decreased both D and the negative lift that is caused by deformation. A decreased Froude number ($Fr^2 = 0.18$) increased the deformation. The larger terminal velocity associated with a lower Fr may have contributed to the negative lift force as well as any deformation induced circulation.

Three-Dimensional Calculations. Simulations of two three-dimensional bubbles at $G_R = 16.0$, $Fr^2 = 0.15$ and $a/l = 0.15$ are now considered. Preliminary studies revealed that the three-dimensional bubbles migrated more slowly than their two-dimensional counterparts. Slower migration of the three-dimensional bubbles might be expected from examination of Eq. (1) where β is 0.5 for a sphere and 2 for a two-dimensional cylinder. Thus, a lower Fr was selected than that of the two-dimensional bubbles described earlier.

Due to the memory limits of the Cray Y-MP, a 64^3 grid was used. The bubble size, a/l , was increased for greater resolution within the bubble than would be obtained with a smaller bubble at this grid density. We repeated the 64^3 simulations on a 32^3 grid and found that the behavior is similar, though the results are not identical. Figure 8 shows the bubble path for both resolutions with the bubble shapes at $G^*t = 3.6$ for $Ca = 0.01$ (Fig. 8(a)) and at $G^*t = 2.4$ for $Ca = 0.07$ (Fig. 8(b)). While the computation was not repeated on a grid finer than 64^3 , a more extensive resolution study in two-dimensions was performed

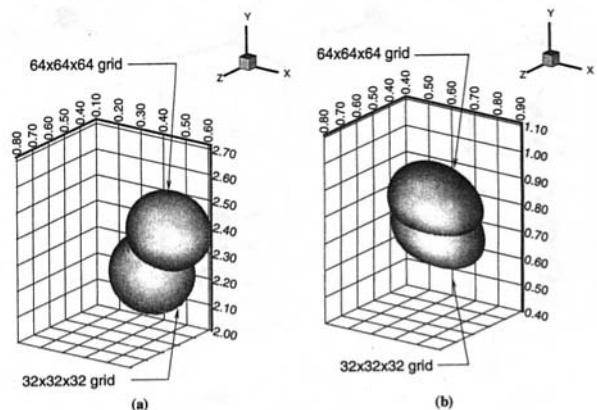


Fig. 8 Effect of grid resolution on a three-dimensional bubble. $G_R = 16.0$, $Fr^2 = 0.15$, $\eta = 0.025$, $\lambda = 0.10$ and $a/l = 0.15$. (a) $Ca = 0.01$ and $G^*t = 3.6$, (b) $Ca = 0.07$ and $G^*t = 2.4$.

(Fig. 3). By comparing the three-dimensional and the two-dimensional results on the 32^2 and the 64^2 grids, the convergence rates are seen to be very comparable. Since the 128^2 grid results in two-dimensions suggest that the 64^2 grid results are nearly fully converged, we believe that the same is true for the three-dimensional results, especially with the increased bubble size.

A bubble with $Ca = 0.01$ was started at $x/l = 0.175$ (Fig. 9(a)), near the upward moving wall, and another bubble with $Ca = 0.07$ was put at $x/l = 0.825$ (Fig. 9(b)). As in the case of the two-dimensional bubbles, the two three-dimensional bubbles were released near one of the walls so that the flow field and the bubble would have sufficient time to adjust to one another by the time the bubble moved to the center of the channel.

Figure 9(a) shows the low Ca bubble ($Ca = 0.01$) at five moments in time. The bubble deformed little and migrated toward the downward moving wall, as anticipated. After an initial start-up period, the bubble moved at a constant rate upwards and in the positive x -direction. Due to the relatively high terminal velocity of the bubble, it is anticipated that it would continue to move upward and eventually reach a steady x -value due to the influence of the downward moving wall. The bubble shape and motion were steady by $G^*t = 1.8$.

The bubble with $Ca = 0.07$ is shown in Fig. 9(b). This bubble deformed into an egg-like shape and migrated in the negative x -direction as it rose, like the two-dimensional bubble with $Ca = 0.08$. Though not apparent from Fig. 9(b), the bubble moved in the negative y -direction a very small distance before buoyancy had a significant effect, due to its initial location in the negative shear regime. The bubble moved at a constant rate and maintained a constant shape after $G^*t = 2.7$.

Figure 10 examines the flow field at a time when the individual bubbles were steady in terms of the deformation and flow field, and when the bubbles had moved away from the walls, at $G^*t = 3.6$. These figures depict the flow field with velocity vectors, as seen from a frame of reference moving with bubble centroid, in the x - y plane perpendicular to the walls through the bubble centroid ($z/l = 0.50$). The bubble front is overlaid on the velocity field. The flow field of the nearly spherical bubble ($Ca = 0.01$) is illustrated in Fig. 10(a). A counter-clockwise vortex is present in the left-hand side of the bubble, and a stronger clockwise vortex is seen to the right of the counter-clockwise vortex. The velocity field of the deformed bubble ($Ca = 0.07$) is shown in Fig. 10(b). A counter-clockwise vortex is located in the left-hand side of the bubble, and a weaker clockwise vortex is seen in the right-hand side of the bubble. The

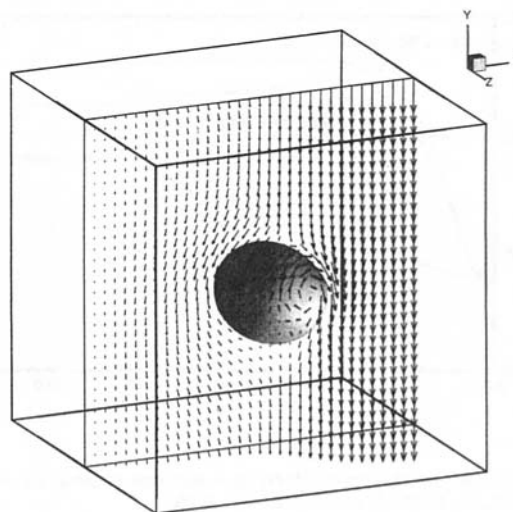


Fig. 10(a)

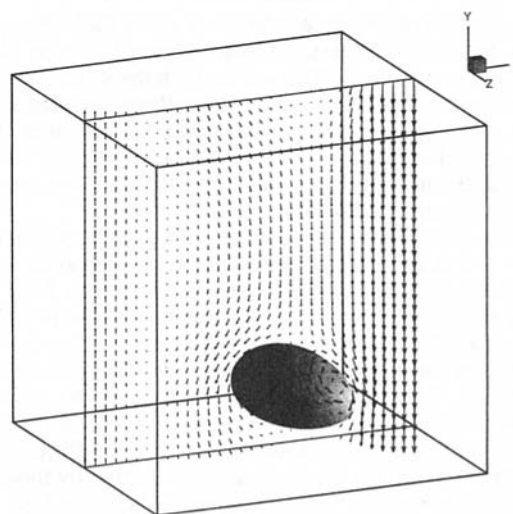


Fig. 10(b)

Fig. 10 Three-dimensional velocity field with respect to the centroid of a steady bubble. $G_R = 16.0$, $Fr^2 = 0.15$, $\eta = 0.025$, $\lambda = 0.10$ and $a/l = 0.15$, $G^*t = 3.6$ and $z/l = 0.5$. (a) $Ca = 0.01$ and initial $x/l = 0.255$. (b) $Ca = 0.07$ and initial $x/l = 0.725$.

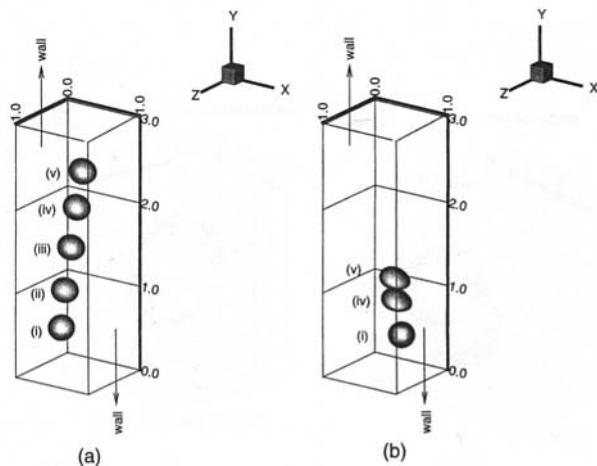


Fig. 9 Motion of a three-dimensional bubble. $G_R = 16.0$, $Fr^2 = 0.15$, $\eta = 0.025$, $\lambda = 0.10$ and $a/l = 0.15$. $G^*t =$ (i) 0.0, (ii) 0.09, (iii) 1.8, (iv) 2.7 and (v) 3.6. (a) $Ca = 0.01$, (b) $Ca = 0.07$.

similarity between the three-dimensional flow in the center plane and the two-dimensional flow field presented in the previous section suggests that the two-dimensional simulations capture the essential features of the fully three-dimensional results. Figure 10 shows that deformation associated with a higher Ca strengthens the vortex rotating counter to the sheared walls. The strength of the counter rotating vortex is due to the net counter-clockwise circulation around the bubble which determines the net lift, resulting in a bubble that moves in a direction opposite to that of an undeformed bubble (Fig. 9).

Figure 11 depicts the relative bubble velocity in the y -direction ($v_{p/F}/U_o$), along with Re/G_R . The relative velocity for both bubbles increased rapidly from zero at early times and then slowly began to level. The steady state lift of the fully three-dimensional bubbles has not been examined, as was done for the two-dimensional ones. However, assuming that lift and drag are balanced by the buoyancy force, we can estimate both from the path of the bubbles. Similar analysis on experimentally obtained paths of unsteady bubbles in a vortex has been done by Shridar and Katz (1995), who also estimated the effect of various unsteady terms. Here, the motion of the bubbles is essentially steady state through most of the channel. For the spherical

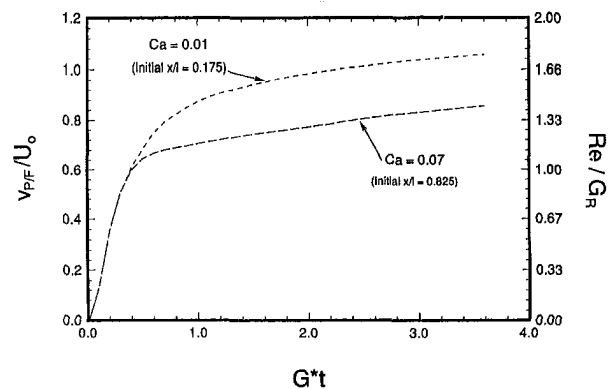


Fig. 11 Bubble rise velocity (v_{PF}/U_0) and Re/G_R as a function of time. $G_R = 16.0$, $Fr^2 = 0.15$, $\eta = 0.025$, $\lambda = 0.10$ and $a/l = 0.15$.

bubble, using the velocities near $G^*t = 3$, when the bubble is in the middle of the channel, the force balance results in:

$$C_{fx} = \frac{2}{3} \left(\frac{G_R}{Fr^*Re} \right)^2 \sin(\theta) = 0.265, \quad (10)$$

where $\theta = 9.93$ deg is the angle between the path and the vertical axis. This can be compared with Shridar and Katz (1995) where the drag coefficient is plotted against the nondimensional shear rate. In their notation, our shear rate is $\alpha = 0.5^*(G_R/Re) = 0.294$, and $C_{fx} = 0.265$ matches their data. While the Reynolds number ($Re = 9.4$) is somewhat lower than those used by Shridar and Katz, their results showed little dependency on the Reynolds number. It is possible that contamination effects were not completely absent in the experiment. The drag coefficient for the spherical bubble, computed in the same way as the lift coefficient, was found to be:

$$C_D = \frac{2}{3} \left(\frac{G_R}{Fr^*Re} \right)^2 \cos(\theta) = 4.54, \quad (11)$$

which is actually slightly higher than what one would expect for a rigid sphere (see Clift, Grace and Weber, 1978). We have, however, neglected all unsteady effects that should be subtracted from the drag force before we find C_D , as well the effects of deformation, finite channel width, and bubble viscosity. All of these can be expected to increase the drag.

Conclusions

Full numerical simulations of deformable buoyant bubbles in a simple vertical shear flow proved satisfactory in that the bubble motions followed previous experimental results. A close examination of the flow characteristics provided a complete explanation of the underlying mechanisms. While spherical bubbles migrated laterally in the same direction as solid spheres, deformable bubbles behaved differently. Buoyancy and shear result in asymmetric deformations that force a circulation around the bubble which opposes the mean shear of the flow. This results in a lift force, F , in a direction opposite to that of solid spherical particles. This mechanism might explain other influences on bubble migration besides gravity, such as non-Newtonian fluids and walls, that also produce asymmetric deformation. A three-dimensional model was used to verify the insights obtained with a two-dimensional model.

The influence of the governing parameters on the resulting lateral lift of a bubble was assessed. Bubbles with a large Ca were more easily distorted, due to the reduction in surface tension, resulting in a lift force controlled by deformation. Increasing G_R and hence the amount of inertia in the flow also increased the deformation and, as a consequence, the negative lift force. Expanding the influence of the gravitational force, by decreasing Fr^2 , also increased the deformation and the deformation induced lift force.

Acknowledgments

This work was supported by the Fluid Dynamics Division of the Office of Naval Research, contract number N00014-91-J-1084, with Dr. E. P. Rood as technical monitor. Some of the calculations were performed at the San Diego Supercomputer center, which is sponsored by the National Science Foundation and some of the calculations were performed at the Ohio Supercomputer center, award number PNS370-2. G. T. would like to thank Professor J. Katz for useful discussions.

References

- Auton, T. R., 1987, "The Lift Force on a Spherical Body in a Rotational Flow," *Journal of Fluid Mechanics*, Vol. 183, pp. 199–218.
- Batchelor, G. K., 1967, *An Introduction to Fluid Dynamics*, Cambridge University Press, Cambridge, Great Britain.
- Bretherton, F. P., 1962, "The Motion of Rigid Particles in a Shear Flow at Low Reynolds Number," *Journal of Fluid Mechanics*, Vol. 14, pp. 284–304.
- Clift, R., Grace, J. R., and Weber, M. E., 1978, *Bubbles, Drops, and Particles*, Academic Press, San Diego, CA.
- Dandy, D. S., and Dwyer, H. A., 1990, "A Sphere in Shear Flow at Finite Reynolds Number: Effect of Shear on Particle Lift, Drag, and Heat Transfer," *Journal of Fluid Mechanics*, Vol. 216, pp. 381–410.
- Ervin, E. A., 1993, "Computations of Bubbles and Drops in Shear Flow," Ph.D. thesis, The University of Michigan, Ann Arbor, MI.
- Goldsmith, H. L., and Mason, S. G., 1962, "The Flow of Suspensions Through Tubes. I. Single Spheres, Rods, and Discs," *Journal of Colloid Science*, Vol. 17, pp. 448–476.
- Kang, I. S., and Leal, L. G., 1989, "Numerical Solution of Axisymmetric, Unsteady Free-Boundary Problems at Finite Reynolds Number. II. Deformation of a Bubble in a Biaxial Straining Flow," *Physics of Fluids A*, Vol. 1, pp. 644–690.
- Kang, I. S., and Leal, L. G., 1987, "Numerical Solution of Axisymmetric, Unsteady Free-boundary Problems at Finite Reynolds Number. I. Finite-Difference Scheme and its Application to the Deformation of a Bubble in a Uniaxial Straining Flow," *Physics of Fluids*, Vol. 30, pp. 1929–1940.
- Karnis, A., and Mason, S. G., 1967, "Particle Motions in Sheared Suspensions. XXIII. Wall Migration of Fluid Drops," *Journal of Colloid Science*, Vol. 24, pp. 164–169.
- Kariyasaki, A., 1987, "Behavior of a Single Gas Bubble in a Liquid Flow with a Linear Velocity Profile," *Proc. of the 1987 ASME-JSME Thermal Engineering Joint Conference*, ASME, New York, NY, pp. 261–267.
- Leal, L. G., 1980, "Particle Motions in a Viscous Fluid," *Annual Review of Fluid Mechanics*, Vol. 12, pp. 435–476.
- McLaughlin, J. B., 1993, "The Lift on a Small Sphere in Wall-Bounded Linear Shear Flows," *Journal of Fluid Mechanics*, Vol. 246, pp. 249–265.
- McLaughlin, J. B., 1991, "Inertial Migration of a Small Sphere in Linear Shear Flows," *Journal of Fluid Mechanics*, Vol. 224, pp. 261–274.
- Rallison, J. M., 1984, "The Deformation of Small Viscous Drops and Bubbles," *Annual Review of Fluid Mechanics*, Vol. 16, pp. 45–66.
- Saffman, P. G., 1965, "The Lift on a Small Sphere in Slow Shear Flow," *Journal of Fluid Mechanics*, Vol. 22, pp. 385–400, and Corrigendum, *Journal of Fluid Mechanics*, Vol. 31 (1968), pp. 624.
- Schlichting, H., 1979, *Boundary-Layer Theory*, 7th edition, McGraw-Hill, New York, NY.
- Sridhar, G., and Katz, J., 1995, "Drag and Forces on Microscopic Bubbles Entrained by a Vortex," *Physics of Fluids*, Vol. 7, pp. 389–399.
- Uijtewaal, W. S. J., Nijhof, E.-J., and Heethaar, R. M., 1993, "Droplet Migration, Deformation, and Orientation in the Presence of a Plane Wall: A Numerical Study Compared with Analytical Theories," *Physics of Fluids A*, Vol. 5, pp. 819–825.
- Unverdi, S. O., and Tryggvason, G., 1992a, "A Front-tracking Method for Viscous, Incompressible, Multi-Fluid Flows," *Journal of Computational Physics*, Vol. 100, pp. 25–37.
- Unverdi, S. O., and Tryggvason, G., 1992b, "Computations of Multi-Fluid Flows," *Physica D*, Vol. 60, pp. 70–83.
- Zhou, H., and Pozrikidis, C., 1993, "The Flow of Suspensions in Channels: Single Files of Drops," *Physics of Fluids A*, Vol. 5, pp. 311–324.

Time-Dependent Vortex Breakdown in a Cylinder With a Rotating Lid

Kazuyuki Fujimura,¹ Hide S. Koyama,¹
and Jae Min Hyun²

1 Introduction

Characteristics of flows and associated transport phenomena of a viscous fluid in a rotating vessel have been extensively studied (Greenspan, 1968). One canonical configuration is the flow of an incompressible fluid which fills a closed cylindrical container. Flow is driven by one endwall disk lid of the container, which rotates steadily about the longitudinal axis of the cylinder. The other endwall disk and the cylindrical sidewall are stationary. The resulting axisymmetric flow is characterized by two principal nondimensional parameters, i.e., the Reynolds number $Re \equiv \Omega R^2/\nu$, and the cylinder aspect ratio $Ar \equiv H/R$, which is assumed $O(1)$, here Ω denotes the angular frequency of the rotating disk; R and H the cylinder radius and height, respectively; and ν the kinematic viscosity of the fluid. As is the case in most technological applications and in geophysical situations, attention is focused to the cases of $Re \gg 1$. For the containers of $Ar \sim O(1)$, the dominant flow is expectedly in the circumferential (azimuthal) direction. However, due to the complex dynamic interplay between the pressure gradient, viscous effects, curvature effects and Coriolis effects, a distinctive meridional flow is induced. In general, in the bulk of the interior region, the rotating lid gives rise to axial motions toward the disk in the central radial portions. Since the container is closed, near the cylindrical sidewall, the axial flow is in the direction pointed away from the rotating lid, thereby maintaining the overall mass continuity.

Escudier (1984), in systematically-organized flow visualization studies, demonstrated the changes in the flow character as Re and Ar encompass wide ranges. One significant finding was a definitive experimental reconfirmation of the vortex breakdown phenomenon in the context of rotating flows. The flow visualization pictures, in which the lower lid was rotating, clearly indicate that, for a given Ar , as Re exceeds a certain critical value Re_{cr} , one stagnation point appears in the central axis. Below this point, a recirculation region is seen, and the overall flow structure under-

goes substantial changes from the patterns of $Re < Re_{cr}$. The flow visualization of Escudier illustrated the existence of two or three stagnation bubbles in the central axis, depending on Ar and Re . Companion numerical computations of this vortex breakdown have been performed by several workers (see, e.g., Lugt and Haussling, 1982; Lugt and Abboud, 1987; Daube and Sorensen, 1989; Lopez, 1990; Tsitverblit, 1993).

Lopez (1990) examined the evolution of the time-dependent stream function in response to an impulsively-started rotation of the endwall. It was shown by the calculations of Lopez that, when Re is low, the transient stream function approaches the steady-state value in an oscillatory manner. However, for high Re , the stream function displays a periodic behavior, and the location of vortex breakdown also oscillates along the central axis.

The objective of this paper is to address experimentally the vortex breakdown phenomena when the rotation rate of the endwall is given a step change from rest. The opposite case of spin-down to rest is also of concern. The impetus is to portray the transient adjustment process of fluid in response to the impulsive change of the rotation rate of the endwall from or to the state of rest.

A brief description of the laboratory turntable facility, together with some novel features of visualization and observation methodologies, will be given with a view toward establishing the credibility of the present experimental setup. The previous visualization studies of Escudier (1984) are repeated and slightly extended. After the verification of the experimental devices is completed, illustrative flow visualizations are conducted to capture the transient vortex breakdown phenomenon. The present paper intends to provide an experimental validation of the existence of vortex breakdown in the case of a spin-up (or a spin-down) of one shrouded endwall disk.

2 Experimental Facilities and Methods

A high-quality precision-controlled turntable apparatus has been fabricated. The power drive was connected to the motor by means of a timing belt. The maximum rotation rate of the turntable was 1000 rpm, which far exceeded the limit used in Escudier's experiment. The rotation rate was controlled to an accuracy of 0.7 percent. The angular-roll bearing unit is employed for the turntable axis. This has the advantage of suppressing the eccentric motions and vertical vibrations. In addition to the selection of a precision bearing set (JIS P4-Class), a forced-circulation lubrication method is adopted to withstand high-speed rotations.

An AC-servo motor (Nikki Denso Co., 7.5 kW, NA 20-370F) was used for the power drive. This is suitable for a high-speed, large-torque device with easy speed control. A motor with a large rating was chosen to reduce the lag time of the turntable when an abrupt change of rotation rate was implemented. A rotary encoder was built into the servo motor; this permitted a precision digital-control of the rotation rate.

A cylindrical container was mounted attached to the flange of the turntable. The material of the container was pyrexglass,

¹ Graduate Student and Professor, respectively, Department of Mechanical Engineering, Tokyo Denki University, Chiyodaku, Tokyo 101, Japan.

² Professor, Department of Mechanical Engineering, Korea Advanced Institute of Science and Technology, Yusong-ku, Taejon 305-701, South Korea. Mem. ASME.

Contributed by the Fluids Engineering Division of THE AMERICAN SOCIETY OF MECHANICAL ENGINEERS. Manuscript received by the Fluids Engineering Division July 6, 1995; revised manuscript received December 12, 1996. Associate Technical Editor: A. F. Ghoniem.

and the inner radius $R = 71.35 \pm 0.05$ mm, and the thickness of the container wall was 3.5 mm. The top endwall of the cylinder was movable; this allowed the height-to-radius aspect ratio $Ar = 0 \sim 8.0$. Notice that this range of Ar enables experiments of substantially larger aspect ratio than the previous ones. The top endwall can be rotated by a separate drive attached to the top of the turntable. To reduce the lens effect, a square-shaped outer tank was installed surrounding the cylindrical container. Furthermore, a precision-temperature control was achieved by circulating a constant-temperature water (accurate to $\pm 0.1^\circ\text{C}$) between the cylinder outer surface and the inner surface of the square outer tank. In this series of experiments, high-precision temperature measurements of the working fluid inside the cylinder were of primal importance. The working fluid used was a water-glycerin mixture (80 percent glycerin by weight). It is notable that the dependence of the kinematic viscosity ν on temperature is appreciable (approximately 5 percent per degree centigrade).

In actual experimental runs, the working fluid was poured into the cylinder. A constant-temperature water (at $25.0 \pm 0.1^\circ\text{C}$) was forced to circulate inside of the outer tank so as to attain thermal equilibrium between the interior working fluid and the outer circulating water. While the temperature of the working fluid was maintained constant within an accuracy of 0.05°C , the kinematic viscosity of the fluid was measured in accordance with the established procedure (JIS Z8803).

In order to implement flow visualizations, fluorescein sodium was selected as dye. In the preparation stage, a small amount of this dye was poured into and well mixed with the working fluid. A tiny quantity of this working fluid, which contains the resolved dye, was injected into the main body of fluid in the cylinder through a hole of 1 mm diameter at the center of the bottom endwall. The injection was effectuated by using a constant-volume pump (Tokyo Rikakikai Co., MP-3).

For steady cases, the meridional plane of the cylinder was illuminated by a sheet beam of about 1 mm width, which was produced from the light of slide projectors. For unsteady cases, the illumination was provided by a pulsed sheet beam, which was formed from an array of four stroboscopes. The visualized flow patterns were photographed by an auto-driven camera, and, at the same time, the images were monitored by two CCD cameras (Sony Co., XC-77RR) which were aligned perpendicular to and parallel to the rotation axis.

3 Experimental Results

Experiments With a Steadily-Rotating Endwall. The well-documented vortex-breakdown experiment of Escudier (1984) was repeated to give credence to the capability of the present experiment. Figure 1 displays the Re versus H/R diagram in which the boundary curves are drawn to show the various regimes of breakdown. In the present experiment, the top endwall disk is rotated. The overall uncertainty in the value of Re is less than 1 percent. The estimate is based upon the precisions achieved in the measurement of ν and of the fluid temperature, and of ω .

It was observed in Escudier's experiment that, as Re increases, the location of vortex breakdown moves to the upstream region, i.e., the region closer to the bottom endwall disk. A quantitative measurement was undertaken in the present experiment to delineate the variance of the axial locations of breakdown with Re . Figure 2 illustrates the axial heights (h_0/H) of the stagnation points from the bottom endwall. The white and black symbols in Fig. 2 denote, respectively, the locations of the first and second stagnation points. Clearly, as Re increases, the positions of the stagnation points move toward the upstream region (closer to the bottom endwall). This trend remains unchanged as the cylinder aspect ratio varies. It is also observed that, as Re increases, the rate of change of (h_0/H) for the first stagnation point is reduced, suggesting that h_0/H of the first

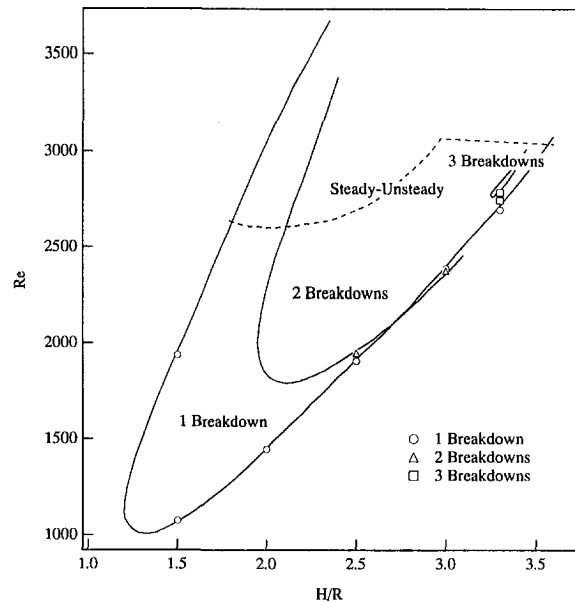


Fig. 1 Regime diagram for the case of a steadily-rotating endwall. Curves are based on the data of Escudier (1984), and symbols denote the present results.

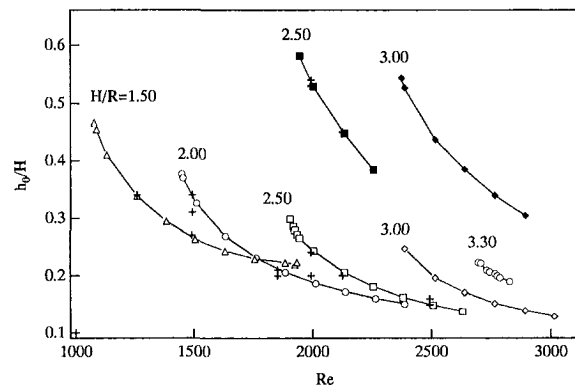


Fig. 2 Locations of the stagnation points for the case of a steadily-rotating endwall. The white and black symbols refer, respectively, to the first and second breakdowns. The previously-published data are shown by +.

stagnation point approaches a certain asymptotic level as Re becomes very large. The present data are shown to be highly compatible with the existing results, both numerical and experimental (Escudier, 1984; Lugt and Abboud, 1987; Lopez, 1990; Tsitverblit, 1993).

Spin-Up of the Endwall. Figure 3 exemplifies the sequence of visualized flow patterns at $Re = 2.20 \times 10^3$ and $H/R = 2.50$, when the settling time for the top endwall to reach the set value of the rotation rate was less than 100 ms. The elapsed time from the switched-on instant is shown in seconds. At very small times, the flow near the axis is nearly axial toward the top endwall; the dye line forms an almost straight path. Soon afterwards, at mid-heights, the dye line thickens, and the velocities become weaker, and the stagnation point begins to be seen. After this, the appearance of a recirculating zone below this stagnation point is conspicuous. The dye lines downstream of the stagnation point (toward the rotating endwall) do not stay on the axis; they periodically move around the axis. At intermediate times, vortex shedding takes place in a periodic manner in the downstream region of the recirculating zone. The recirculating zone is seen to oscillate in the axial direction while

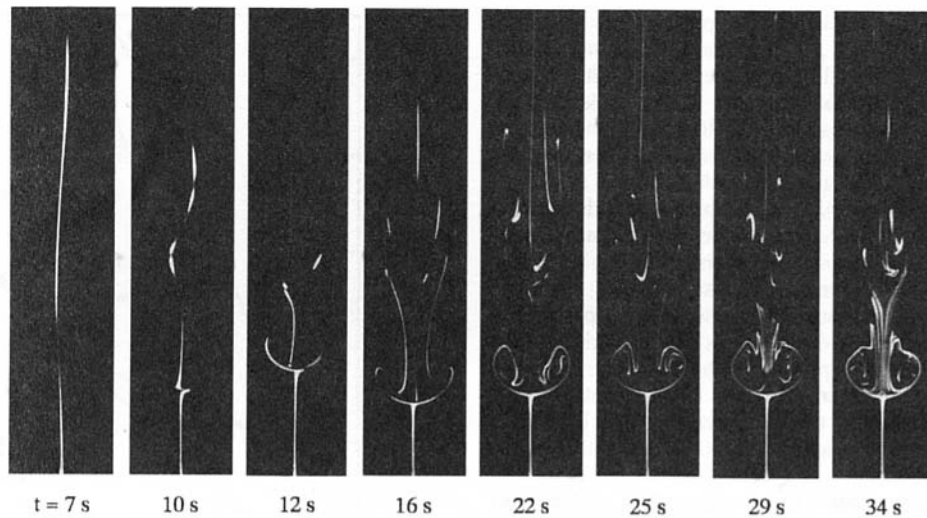


Fig. 3 Flow visualizations for the case of a spin-up from rest of the top endwall. $Re = 2.20 \times 10^3$ and $H/R = 2.50$.

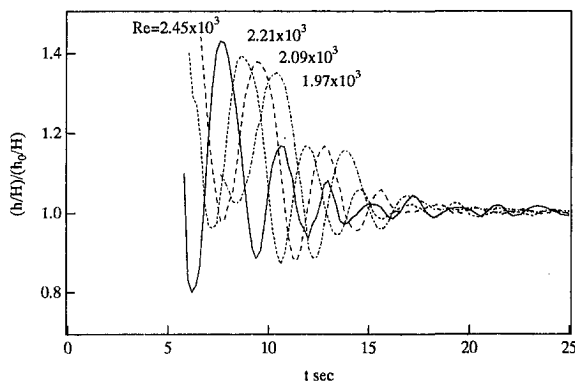


Fig. 4 Time-dependent variation of the location of the upstream stagnation in the spin-up process. $Re = 1.97 \times 10^3$, 2.09×10^3 , 2.21×10^3 and 2.45×10^3 , and $H/R = 2.0$.

periodic vortex shedding is carried out. The amplitude of this oscillation becomes small as time elapses further, and the stagnation point tends to approach a certain steady-state location.

However, even after the stagnation point settles to a steady-state level, it is seen that, in the downstream region of the recirculating zone, slight periodic motions remain. The first-hand impression of the global flow pattern was that the vortex breakdown phenomena could not be characterized to be strictly axisymmetric, although a conclusive statement may be made only after further detailed observations have been accomplished.

Another significant issue is the time-dependent variation of the location of the upstream stagnation point in the spin-up process. Figure 4 illustrates for $H/R = 2.0$ the relative change of this location h , normalized by the corresponding steady-state value h_0 . For this problem, several sets of the experiments were repeated. The outcome of these exercises confirms a high degree of reproducibility of the present experiments. The principal findings clearly point to the fluid damping. It is also noted that when H/R is held constant, as Re increases, the time duration to reach the onset of the stagnation point shortens. Furthermore, as Re increases, after the formation of the recirculating zone, the frequency of oscillation of the recirculating zone increases. In addition, the time needed to settle into the steady state increases with increasing Re . It is also evident that flow processes possess considerable nonlinearities. These issues will be dealt with in further detail in subsequent papers.

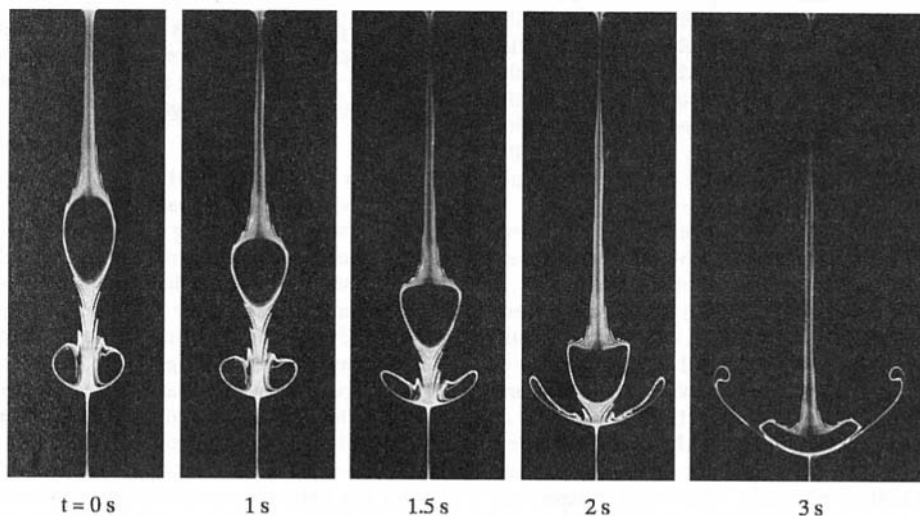


Fig. 5 Flow visualizations for the case of a spin-down to rest of the top endwall. $Re = 2.20 \times 10^3$ and $H/R = 2.50$.

Spin-Down of the Endwall. After a sufficient time in the steady state has passed, the rotating endwall was stopped, and the time-evolution of spin-down flows is photographed in Fig. 5. Immediately after the arrest of the endwall, vigorous Ekman pumping is manifested in the vicinity of the top endwall, which produces intense downward fluid motions. This causes the stagnation point of vortex breakdown to move toward the bottom endwall in very early phases. However, as the Ekman pumping brings about the meridional motion, the angular momentum in the bulk of the interior fluid is reduced. This, in turn, leads to a further reduction of the effectiveness of the Ekman pumping. Consequently, the stagnation point moves upward, and at larger times, the stagnation point ceases its motion. It has been amply observed in the present experiment that the time for the fluid to come to rest in the case of spin-down is substantially shorter than the time for the fluid to reach the steady state in the case of spin-up.

Summary

The experiment for a steadily-rotating endwall has been reproduced. The regime diagram of Re versus H/R of the present experiment was in excellent agreement with the preceding reports. As Re increases, the recirculation region is seen to move toward the rotating endwall and finally settle to an appropriate location.

Quantitative measurements have been carried out of the time-dependent vortex breakdown and the movement of the stagnation point in the context of spin-up and spin-down of an endwall disk. In the case of spin-up, the vortex oscillates along the axis until it reaches a steady-state position. The time to settle to the state of rest in spin-down is found to be measurably shorter than the time to achieve the steady state in spin-up.

Acknowledgment

This work was supported in part by the Center for Research, Tokyo Denki University and also in part by the Japan Society for the Promotion of Science on a Cooperative Research under Japan-Korea Cooperative Research Projects.

References

- Daube, O., and Sorensen, J. N., 1989, "Simulation numerique de l'ecoulement periodique axisymetrique dans une cavite cylindrique," *Comptes Rendus Academy de Science*, Vol. II, pp 463-469.
- Escudier, M. P., 1984, "Observations of the Flow Produced in a Cylindrical Container by a Rotating Endwall," *Experiments in Fluids*, Vol. 2, pp 189-196.
- Greenspan, H. P., 1968, *The Theory of Rotating Fluids*, Cambridge University Press.
- Lopez, J. M., 1990, "Axisymmetric Vortex Breakdown. Part I. Confined Swirling Flow," *Journal of Fluid Mechanics*, Vol. 221, pp. 533-552.
- Lugt, H. J., and Abboud, M., 1987, "Axisymmetric Vortex Breakdown with an Without Temperature Effects in a Container with a Rotating Lid," *Journal of Fluid Mechanics*, Vol. 179, pp 179-200.
- Lugt, H. J., and Haussling, H. J., 1982, "Axisymmetric Vortex Breakdown in Rotating Fluid Within a Container," *ASME Journal of Applied Mechanics*, Vol. 49, pp. 921-923.
- Tsitverblit, N., 1993, "Vortex Breakdown in a Cylindrical Container in the Light Continuation of a Steady Solution," *Fluid Dynamics Research*, Vol. 11, pp. 19-35.

Flow Characteristics of a Bluff Body Cut From a Circular Cylinder

S. Aiba¹ and H. Watanabe¹

This is a report on an investigation of the flow characteristics of a bluff body cut from a circular cylinder. The volume removed

¹ Professor and Research Associate, respectively, Department of Mechanical Engineering, Akita Technical College, Akita 011, Japan.

Contributed by the Fluids Engineering Division of THE AMERICAN SOCIETY OF MECHANICAL ENGINEERS. Manuscript received by the Fluids Engineering Division September 5, 1995; revised manuscript received April 2, 1996. Associate Technical Editor: M. Ghareb.

from the cylinder is equal to $d/2(1 - \cos \theta_s)$, where d and θ_s are the diameter and the angular position (in the case of a circular cylinder, $\theta_s = 0$ deg), respectively. θ_s ranged from 0 deg to 72.5 deg and Re (based on d and the upstream uniform flow velocity U_∞) from 2.0×10^4 to 3.5×10^4 . It is found that a singular flow around the cylinder occurs at around $\theta_s = 53$ deg when $Re > 2.5 \times 10^4$, and the base pressure coefficient ($-C_{pb}$) and the drag coefficient C_D take small values compared with those for other θ_s .

Introduction

A bluff body used in practice has large dynamic drag resulting from separation of the flow over the cylinder. A large number of studies on the dynamic drag have concerned a bluff body placed transversely in a stream (e.g., Goldstein, 1965; Sovran et al., 1978; and Bearman, 1980). In the case of a circular cylinder in crossflow, the drag coefficient C_D is almost 1.2 in the range of Reynolds number $Re = 10^4 \sim 10^5$ (based on the cylinder diameter d and the mean flow velocity U_∞). A reduction in the C_D of a circular cylinder is realized when the cylinder has a roughened surface in that Reynolds number range. However, it is not easy to obtain a roughened surface and the contaminations in the flow accumulate on the cylinder surface (e.g., Achenbach, 1971). Because a tube bank composed of circular cylinders is often used in heat exchangers for example, it is very important to solve these problems without extreme reduction of the area used for heat transfer. In this work, we study the flow characteristics around a two-dimensional bluff body with the cross section shown in Fig. 1, which is relatively easy to manufacture.

Experimental Apparatus and Procedure

The blow-down wind tunnel used in the present experiments has a rectangular test section 325 mm high and 225 mm wide (Aiba et al., 1979). The free-stream turbulence intensity is about 0.003 throughout the experiments. Two types of test model were employed in this study, as shown in Fig. 1. Type I was produced by cutting both sides of the circular cylinder in parallel with the y axis. The width e of the test cylinder of this type is given by $d \cdot \cos \theta_s$. Only the front side of the cylinder was cut in type D. Two values of the cylinder diameter d , 20 mm and 30 mm, were used. The test model with $d = 20$ mm was used for the measurements of the base pressure coefficient ($-C_{pb}$) and that with $d = 30$ mm for C_D . We used the angles of $\theta_s = 0, 36.9, 45.6, 49.5, 53, 56.6, 60, 66.4, \text{ and } 72.5$ deg for each type.

The surface of the test cylinders was carefully polished and a 1.0 mm static hole was drilled in the rear surface at the center section of each cylinder. The static base pressure coefficient is defined as $(-C_{pb}) = -(p_b - p_\infty)/1/2(\rho U_\infty^2)$, where p_b , ρ , and

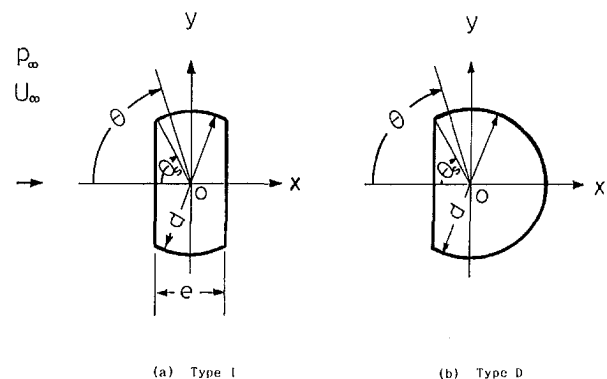


Fig. 1 Test sections and coordinate systems. (a) Type I (b) Type D

Spin-Down of the Endwall. After a sufficient time in the steady state has passed, the rotating endwall was stopped, and the time-evolution of spin-down flows is photographed in Fig. 5. Immediately after the arrest of the endwall, vigorous Ekman pumping is manifested in the vicinity of the top endwall, which produces intense downward fluid motions. This causes the stagnation point of vortex breakdown to move toward the bottom endwall in very early phases. However, as the Ekman pumping brings about the meridional motion, the angular momentum in the bulk of the interior fluid is reduced. This, in turn, leads to a further reduction of the effectiveness of the Ekman pumping. Consequently, the stagnation point moves upward, and at larger times, the stagnation point ceases its motion. It has been amply observed in the present experiment that the time for the fluid to come to rest in the case of spin-down is substantially shorter than the time for the fluid to reach the steady state in the case of spin-up.

Summary

The experiment for a steadily-rotating endwall has been reproduced. The regime diagram of Re versus H/R of the present experiment was in excellent agreement with the preceding reports. As Re increases, the recirculation region is seen to move toward the rotating endwall and finally settle to an appropriate location.

Quantitative measurements have been carried out of the time-dependent vortex breakdown and the movement of the stagnation point in the context of spin-up and spin-down of an endwall disk. In the case of spin-up, the vortex oscillates along the axis until it reaches a steady-state position. The time to settle to the state of rest in spin-down is found to be measurably shorter than the time to achieve the steady state in spin-up.

Acknowledgment

This work was supported in part by the Center for Research, Tokyo Denki University and also in part by the Japan Society for the Promotion of Science on a Cooperative Research under Japan-Korea Cooperative Research Projects.

References

- Daube, O., and Sorensen, J. N., 1989, "Simulation numerique de l'ecoulement periodique axisymetrique dans une cavite cylindrique," *Comptes Rendus Academy de Science*, Vol. II, pp 463-469.
- Escudier, M. P., 1984, "Observations of the Flow Produced in a Cylindrical Container by a Rotating Endwall," *Experiments in Fluids*, Vol. 2, pp 189-196.
- Greenspan, H. P., 1968, *The Theory of Rotating Fluids*, Cambridge University Press.
- Lopez, J. M., 1990, "Axisymmetric Vortex Breakdown. Part I. Confined Swirling Flow," *Journal of Fluid Mechanics*, Vol. 221, pp. 533-552.
- Lugt, H. J., and Abboud, M., 1987, "Axisymmetric Vortex Breakdown with an Without Temperature Effects in a Container with a Rotating Lid," *Journal of Fluid Mechanics*, Vol. 179, pp 179-200.
- Lugt, H. J., and Haussling, H. J., 1982, "Axisymmetric Vortex Breakdown in Rotating Fluid Within a Container," *ASME Journal of Applied Mechanics*, Vol. 49, pp. 921-923.
- Tsitverblit, N., 1993, "Vortex Breakdown in a Cylindrical Container in the Light Continuation of a Steady Solution," *Fluid Dynamics Research*, Vol. 11, pp. 19-35.

Flow Characteristics of a Bluff Body Cut From a Circular Cylinder

S. Aiba¹ and H. Watanabe¹

This is a report on an investigation of the flow characteristics of a bluff body cut from a circular cylinder. The volume removed

¹ Professor and Research Associate, respectively, Department of Mechanical Engineering, Akita Technical College, Akita 011, Japan.

Contributed by the Fluids Engineering Division of THE AMERICAN SOCIETY OF MECHANICAL ENGINEERS. Manuscript received by the Fluids Engineering Division September 5, 1995; revised manuscript received April 2, 1996. Associate Technical Editor: M. Ghareb.

from the cylinder is equal to $d/2(1 - \cos \theta_s)$, where d and θ_s are the diameter and the angular position (in the case of a circular cylinder, $\theta_s = 0$ deg), respectively. θ_s ranged from 0 deg to 72.5 deg and R_e (based on d and the upstream uniform flow velocity U_∞) from 2.0×10^4 to 3.5×10^4 . It is found that a singular flow around the cylinder occurs at around $\theta_s = 53$ deg when $R_e > 2.5 \times 10^4$, and the base pressure coefficient ($-C_{pb}$) and the drag coefficient C_D take small values compared with those for other θ_s .

Introduction

A bluff body used in practice has large dynamic drag resulting from separation of the flow over the cylinder. A large number of studies on the dynamic drag have concerned a bluff body placed transversely in a stream (e.g., Goldstein, 1965; Sovran et al., 1978; and Bearman, 1980). In the case of a circular cylinder in crossflow, the drag coefficient C_D is almost 1.2 in the range of Reynolds number $R_e = 10^4 \sim 10^5$ (based on the cylinder diameter d and the mean flow velocity U_∞). A reduction in the C_D of a circular cylinder is realized when the cylinder has a roughened surface in that Reynolds number range. However, it is not easy to obtain a roughened surface and the contaminations in the flow accumulate on the cylinder surface (e.g., Achenbach, 1971). Because a tube bank composed of circular cylinders is often used in heat exchangers for example, it is very important to solve these problems without extreme reduction of the area used for heat transfer. In this work, we study the flow characteristics around a two-dimensional bluff body with the cross section shown in Fig. 1, which is relatively easy to manufacture.

Experimental Apparatus and Procedure

The blow-down wind tunnel used in the present experiments has a rectangular test section 325 mm high and 225 mm wide (Aiba et al., 1979). The free-stream turbulence intensity is about 0.003 throughout the experiments. Two types of test model were employed in this study, as shown in Fig. 1. Type I was produced by cutting both sides of the circular cylinder in parallel with the y axis. The width e of the test cylinder of this type is given by $d \cdot \cos \theta_s$. Only the front side of the cylinder was cut in type D. Two values of the cylinder diameter d , 20 mm and 30 mm, were used. The test model with $d = 20$ mm was used for the measurements of the base pressure coefficient ($-C_{pb}$) and that with $d = 30$ mm for C_D . We used the angles of $\theta_s = 0, 36.9, 45.6, 49.5, 53, 56.6, 60, 66.4, \text{ and } 72.5$ deg for each type.

The surface of the test cylinders was carefully polished and a 1.0 mm static hole was drilled in the rear surface at the center section of each cylinder. The static base pressure coefficient is defined as $(-C_{pb}) = -(p_b - p_\infty)/1/2(\rho U_\infty^2)$, where p_b , ρ , and

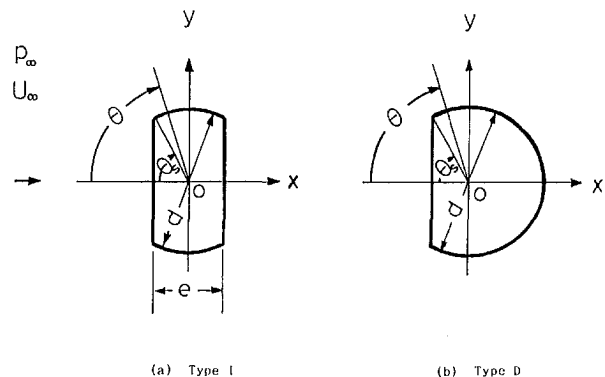


Fig. 1 Test sections and coordinate systems. (a) Type I (b) Type D

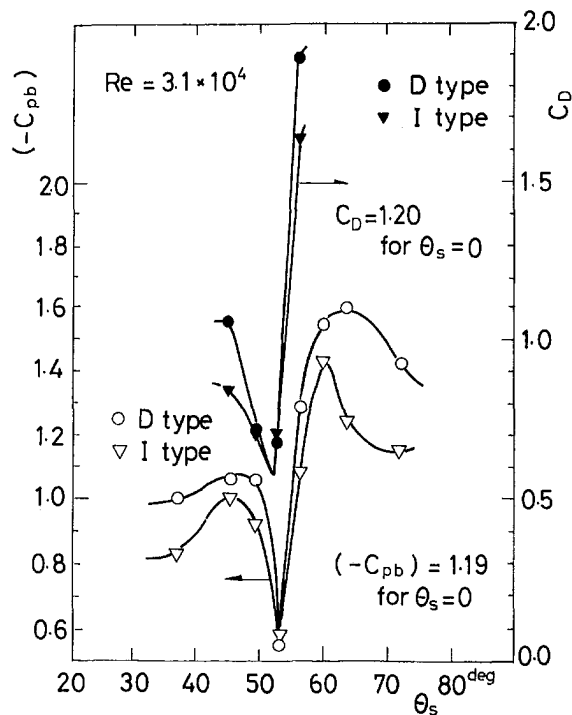


Fig. 2 The variations of $(-C_{pb})$ and C_D with θ_s at $Re = 3.1 \times 10^4$ (statistical uncertainties: ± 8 and ± 6 percent for the base pressure and the drag fluctuations, respectively).

U are the pressure at the rear face of the cylinder, density, and velocity, respectively, and the subscript ∞ denotes upstream. The pressure difference $(p_b - p_\infty)$ was determined from the static pressure of the pitot tube situated upstream of the test cylinder and the pressure of the rear face of the cylinder. The aspect ratios are 11.25 and 7.5 for $d = 20$ mm and 30 mm, respectively. These aspect ratios are not large enough to neglect the end effects. Therefore, measurements are carried out at a location where the boundary layer along the wall of the tunnel has not developed significantly. The oil flow pattern method was used for flow visualization. By this means, the influence of the end effects was observed in the range of 10 mm to 20 mm. For the drag tests, each model was attached to the wind tunnel balance with 0.2-mm-diameter piano wire. The drag coefficient C_D is defined by $\text{drag}/(0.5\rho U_\infty S)$, where S is the cross-sectional area of the model.

The mean velocities in the cross section along the y axis were measured with a constant-temperature hot-wire anemometer with a linearizing circuit. The hot wire was a 0.005 mm tungsten wire of effective length 1 mm and was set parallel to the cylinder axis and normal to the mean flow direction. In this study, it was not necessary to consider the effect of the wall, because the smallest distance between the hot wire and the wall was of the order of 10^{-3} mm in the vicinity of the cylinder wall surface.

Results and Discussions

The results for the base pressure coefficient $(-C_{pb})$ and the drag coefficient C_D are shown as a function of θ_s for $Re = 3.1 \times 10^4$ in Fig. 2. No correction for the tunnel wall effects was made. The minimum of $(-C_{pb})$ appears at around $\theta_s = 53$ deg for both types (in type I, $e/d = 0.6$ when $\theta_s = 53$ deg), and takes a value of $0.5 \sim 0.55$. These characteristics are obtained in a very narrow range of θ_s ($50 \text{ deg} < \theta_s < 57 \text{ deg}$). In such a Reynolds number regime, $(-C_{pb})$ takes the value 1.19 for a circular cylinder ($\theta_s = 0$), as shown in the figure. For the normal plate, $(-C_{pb})$ is 1.28 (e.g., Roshko, 1955). It is found that $(-C_{pb})$ for $\theta_s = 53$ deg takes smaller values than that for

$\theta_s = 0$. Therefore, the flow characteristics around the cylinder for $\theta_s = 53$ deg are mainly discussed hereafter. $(-C_{pb})$ for $\theta_s = 53$ deg depends on the Reynolds number. When $Re < 2.5 \times 10^4$, $(-C_{pb})$ decreases with increasing Re and is almost constant in the region $Re > 2.5 \times 10^4$. That is, there exists a critical Reynolds number Re_{cc} of around $Re = 2.5 \times 10^4$. Our discussions concern the range $Re > Re_{cc}$.

When the curvature of the shear flow from the normal surface to the uniform air flow, as shown in Fig. 1, equals that of the circular cylinder, the shear layer separated from the normal surface attaches to the circular surface and transitions to a turbulent boundary layer along the circular surface. It was observed, by means of the oil flow patterns, that when $Re = 3.1 \times 10^4$ and $\theta_s = 53$ deg, the laminar boundary layer separated at around $\theta = 57$ deg and reattached at around $\theta = 69$ deg, then the turbulent boundary layer was shed from the cylinder at about $\theta = 110$ deg. This was also confirmed from the profiles of the velocity (measured using the hot-wire anemometer) in the vicinity of the cylinder surface at $x/d = 0$, when $\theta_s = 53$ deg.

The results for C_D in the range $45 \text{ deg} < \theta_s < 57 \text{ deg}$ and for $\theta_s = 0$ deg are also shown in Fig. 2. It is obvious that the variations of C_D at around $\theta_s = 53$ deg are nearly identical to those for $(-C_{pb})$ and that C_D in the range $50 \text{ deg} < \theta_s < 53 \text{ deg}$ take minimum values. These values are almost 50 percent of C_D for the circular cylinder.

Conclusions

- (1) The flow characteristics are singular in the vicinity of $\theta_s = 53$ deg, and $(-C_{pb})$ takes a minimum value of $0.5 \sim 0.55$ in both types of cylinder, when $\theta_s = 53$ deg and $Re > 2.5 \times 10^4$. In the vicinity of $\theta_s = 53$ deg, the value of C_D for each model is minimum and about 50 percent of that for the circular cylinder.
- (2) The critical Reynolds number Re_{cc} is around $Re = 2.5 \times 10^4$ in the case of $\theta_s = 53$ deg.

Acknowledgments

The authors thank their former students, Messrs. K. Sasaki, K. Tezuka, M. Nara, and H. Hosino, for their assistance in the experiments.

References

- Achenbach, E., 1971, "Influence of Surface Roughness on the Cross-Flow around a Circular Cylinder," *Journal of Fluid Mechanics*, Vol. 46, pp. 321–335.
- Aiba, S., Ota, T., and Tsuchida, H., 1979, "Heat Transfer and Flow Around a Circular Cylinder with Tripping-Wires," *Wärme-und Stoffübertragung*, Vol. 12, pp. 221–231.
- Bearman, P. W., 1980, "Bluff Body Flows, Applicable to Vehicle Aerodynamics-Review," *ASME JOURNAL OF FLUIDS ENGINEERING*, Vol. 102, pp. 265–274.
- Goldstein, S., ed., 1965, *Modern Developments in Fluid Dynamics*, Dover Publications, New York.
- Sovran, G., Morel, T., and Marson, Jr., W. T., ed., 1978, *Aerodynamic Drag Mechanism of Bluff Bodies and Road Vehicles*, Plenum Press, New York.
- Roshko, A., 1955, "On the Wake and Drag of Bluff Bodies," *Journal of Aeronautical Sciences* Vol. 22, pp. 124–132.

A Design Method for Contractions With Square End Sections

Fuh-Min Fang¹

Introduction

A contraction is a major component of a wind or water tunnel. As the flow passes this transitional segment, it is accelerated so

¹ Associate Professor, Department of Civil Engineering, National Chung-Hsing University, 250 Kuo-Kuang Road, Taichung, Taiwan.

Contributed by the Fluids Engineering Division of THE AMERICAN SOCIETY OF MECHANICAL ENGINEERS. Manuscript received by the Fluids Engineering Division October 30, 1995; revised manuscript received January 8, 1997. Associate Technical Editor: H. Hashimoto.

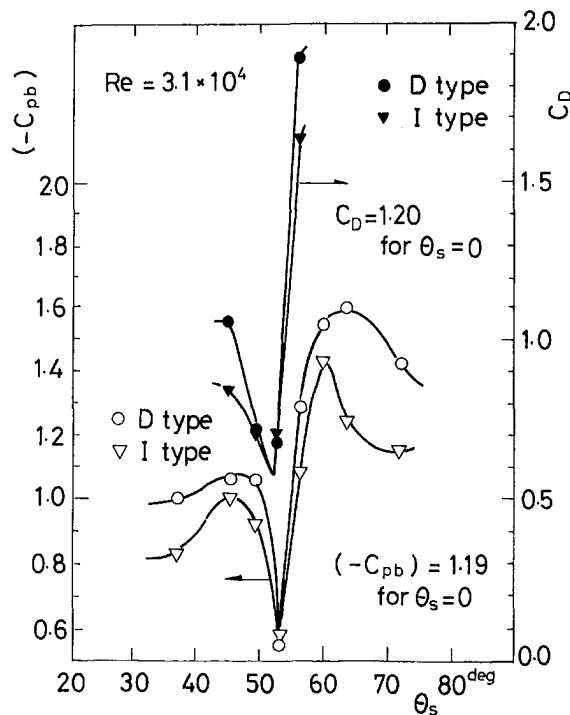


Fig. 2 The variations of $(-C_{pb})$ and C_D with θ_s at $Re = 3.1 \times 10^4$ (statistical uncertainties: ± 8 and ± 6 percent for the base pressure and the drag fluctuations, respectively).

U are the pressure at the rear face of the cylinder, density, and velocity, respectively, and the subscript ∞ denotes upstream. The pressure difference $(p_b - p_\infty)$ was determined from the static pressure of the pitot tube situated upstream of the test cylinder and the pressure of the rear face of the cylinder. The aspect ratios are 11.25 and 7.5 for $d = 20$ mm and 30 mm, respectively. These aspect ratios are not large enough to neglect the end effects. Therefore, measurements are carried out at a location where the boundary layer along the wall of the tunnel has not developed significantly. The oil flow pattern method was used for flow visualization. By this means, the influence of the end effects was observed in the range of 10 mm to 20 mm. For the drag tests, each model was attached to the wind tunnel balance with 0.2-mm-diameter piano wire. The drag coefficient C_D is defined by $\text{drag}/(0.5\rho U_\infty S)$, where S is the cross-sectional area of the model.

The mean velocities in the cross section along the y axis were measured with a constant-temperature hot-wire anemometer with a linearizing circuit. The hot wire was a 0.005 mm tungsten wire of effective length 1 mm and was set parallel to the cylinder axis and normal to the mean flow direction. In this study, it was not necessary to consider the effect of the wall, because the smallest distance between the hot wire and the wall was of the order of 10^{-3} mm in the vicinity of the cylinder wall surface.

Results and Discussions

The results for the base pressure coefficient $(-C_{pb})$ and the drag coefficient C_D are shown as a function of θ_s for $Re = 3.1 \times 10^4$ in Fig. 2. No correction for the tunnel wall effects was made. The minimum of $(-C_{pb})$ appears at around $\theta_s = 53$ deg for both types (in type I, $e/d = 0.6$ when $\theta_s = 53$ deg), and takes a value of $0.5 \sim 0.55$. These characteristics are obtained in a very narrow range of θ_s ($50 \text{ deg} < \theta_s < 57 \text{ deg}$). In such a Reynolds number regime, $(-C_{pb})$ takes the value 1.19 for a circular cylinder ($\theta_s = 0$), as shown in the figure. For the normal plate, $(-C_{pb})$ is 1.28 (e.g., Roshko, 1955). It is found that $(-C_{pb})$ for $\theta_s = 53$ deg takes smaller values than that for

$\theta_s = 0$. Therefore, the flow characteristics around the cylinder for $\theta_s = 53$ deg are mainly discussed hereafter. $(-C_{pb})$ for $\theta_s = 53$ deg depends on the Reynolds number. When $Re < 2.5 \times 10^4$, $(-C_{pb})$ decreases with increasing Re and is almost constant in the region $Re > 2.5 \times 10^4$. That is, there exists a critical Reynolds number Re_{cc} of around $Re = 2.5 \times 10^4$. Our discussions concern the range $Re > Re_{cc}$.

When the curvature of the shear flow from the normal surface to the uniform air flow, as shown in Fig. 1, equals that of the circular cylinder, the shear layer separated from the normal surface attaches to the circular surface and transitions to a turbulent boundary layer along the circular surface. It was observed, by means of the oil flow patterns, that when $Re = 3.1 \times 10^4$ and $\theta_s = 53$ deg, the laminar boundary layer separated at around $\theta = 57$ deg and reattached at around $\theta = 69$ deg, then the turbulent boundary layer was shed from the cylinder at about $\theta = 110$ deg. This was also confirmed from the profiles of the velocity (measured using the hot-wire anemometer) in the vicinity of the cylinder surface at $x/d = 0$, when $\theta_s = 53$ deg.

The results for C_D in the range $45 \text{ deg} < \theta_s < 57 \text{ deg}$ and for $\theta_s = 0$ deg are also shown in Fig. 2. It is obvious that the variations of C_D at around $\theta_s = 53$ deg are nearly identical to those for $(-C_{pb})$ and that C_D in the range $50 \text{ deg} < \theta_s < 53 \text{ deg}$ take minimum values. These values are almost 50 percent of C_D for the circular cylinder.

Conclusions

- (1) The flow characteristics are singular in the vicinity of $\theta_s = 53$ deg, and $(-C_{pb})$ takes a minimum value of $0.5 \sim 0.55$ in both types of cylinder, when $\theta_s = 53$ deg and $Re > 2.5 \times 10^4$. In the vicinity of $\theta_s = 53$ deg, the value of C_D for each model is minimum and about 50 percent of that for the circular cylinder.
- (2) The critical Reynolds number Re_{cc} is around $Re = 2.5 \times 10^4$ in the case of $\theta_s = 53$ deg.

Acknowledgments

The authors thank their former students, Messrs. K. Sasaki, K. Tezuka, M. Nara, and H. Hosino, for their assistance in the experiments.

References

- Achenbach, E., 1971, "Influence of Surface Roughness on the Cross-Flow around a Circular Cylinder," *Journal of Fluid Mechanics*, Vol. 46, pp. 321–335.
- Aiba, S., Ota, T., and Tsuchida, H., 1979, "Heat Transfer and Flow Around a Circular Cylinder with Tripping-Wires," *Wärme-und Stoffübertragung*, Vol. 12, pp. 221–231.
- Bearman, P. W., 1980, "Bluff Body Flows, Applicable to Vehicle Aerodynamics-Review," *ASME JOURNAL OF FLUIDS ENGINEERING*, Vol. 102, pp. 265–274.
- Goldstein, S., ed., 1965, *Modern Developments in Fluid Dynamics*, Dover Publications, New York.
- Sovran, G., Morel, T., and Marson, Jr., W. T., ed., 1978, *Aerodynamic Drag Mechanism of Bluff Bodies and Road Vehicles*, Plenum Press, New York.
- Roshko, A., 1955, "On the Wake and Drag of Bluff Bodies," *Journal of Aeronautical Sciences* Vol. 22, pp. 124–132.

A Design Method for Contractions With Square End Sections

Fuh-Min Fang¹

Introduction

A contraction is a major component of a wind or water tunnel. As the flow passes this transitional segment, it is accelerated so

¹ Associate Professor, Department of Civil Engineering, National Chung-Haing University, 250 Kuo-Kuang Road, Taichung, Taiwan.

Contributed by the Fluids Engineering Division of THE AMERICAN SOCIETY OF MECHANICAL ENGINEERS. Manuscript received by the Fluids Engineering Division October 30, 1995; revised manuscript received January 8, 1997. Associate Technical Editor: H. Hashimoto.

that a low-turbulence, uniform flow condition can be achieved in the test section. Generally, the contraction ratio (CR) is the most dominant factor which affects the extent of flow uniformity, the possibility of flow separation, and downstream turbulence level. Once it is determined, the nozzle contour and length, which also control the flow uniformity and the boundary layer growth, become the second design choices.

In principle, the problem of contraction design is to search for the optimum shape with minimum nozzle length for a desirable flow quality requirement at the nozzle end. When the length is reduced, the contraction costs less and fits into a smaller space. In addition, the boundary layer will generally be thinner due to the combined effects of decreased length of boundary layer development and increased favorable pressure gradients in the contraction. On the other hand, it leads to an increase of the possibility of flow separation, which results in undesirable flow patterns and flow unsteadiness.

Due to wall curvature, the local velocity profile in a contraction is essentially not uniform. The potential flow velocity along the wall can increase monotonically only for a contraction with infinite length. When a contraction is finite, however, there exist two adverse pressure gradient regions along the wall (Fig. 1), where the flow might separate.

By far, the most direct way for engineering contraction design is that suggested by Morel (1975 and 1977), who proposed the use of a combination of two matched cubics as the basic shape of 2-D and axisymmetric contractions. Morel's design procedure starts by prescribing a level of velocity nonuniformity at the contraction exit, which leads to a corresponding minimum wall pressure near the exit. Based on design charts resulting from potential flow calculations, the contraction length is determined to avoid the occurrence of separation.

Present Design Approach

The present work attempts to extend the goal of Morel's to three-dimensional cases. Particularly, a set of design plots are presented for square-to-square contractions. The contraction shape under consideration is a combination of two matched cubics, described as (Fig. 2):

$$y, z = \begin{cases} (h_1 - h_2) \cdot \left[1 - \frac{1}{X^2} \cdot \left(\frac{x}{L} \right)^3 \right] + h_2, & x < x_m \\ \frac{(h_1 - h_2)}{(1 - X)^2} \cdot \left(1 - \frac{x}{L} \right)^3 + h_2, & x > x_m \end{cases} \quad (1)$$

where x_m denotes the location of the matched point and $X = x_m/L$. To attain a more extensive design than any other available method, the flow characteristics along corners are ana-

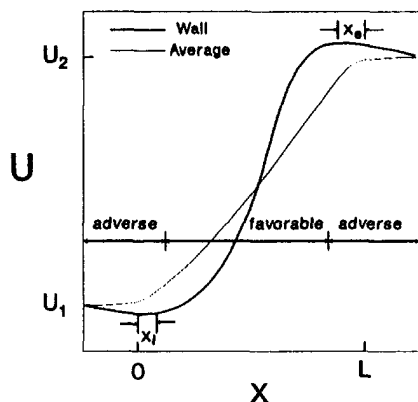


Fig. 1 Schematic of wall and average velocity distribution within a contraction

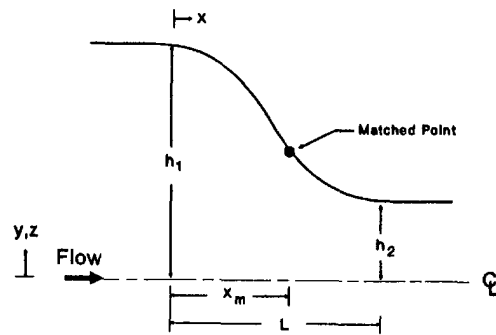


Fig. 2 Schematic of the contraction (half plane)

lyzed based on numerical results to check for the possibilities of separation. Similar to what was done by Morel, the present study does not suggest a close-form solution to the nozzle design but a trial-and-error procedure to search for an optimum one by using numerical simulations on a one-parameter family.

Design Criteria

The proposed design method considers a level to avoid flow separation, an acceptable flow uniformity at the exit and the minimum nozzle length as the most important factors. Although the turbulence intensity at the contraction exit is also important, it is not considered in the proposed design, since it depends on the turbulence level at the nozzle entrance and the contraction ratio (Prandtl, 1933; Ramjee and Hussain, 1976), which are usually prescribed at the beginning of the design stage.

As the avoidance of separation is considered, two pressure coefficients are used here, defined as

$$Cp_e = 1 - \left(\frac{U_e}{U_c} \right)^2$$

and

$$Cp_i = 1 - \left(\frac{U_i}{U_c} \right)^2, \quad (2)$$

where U_e and U_i are the velocities corresponding to the locations of the minimum and the maximum corner pressures; U_1 and U_2 are the velocities at far upstream and downstream. These two coefficients are so defined that can be directly applied into the Stratford criterion (Stratford, 1959) to check for the possibility of flow separation.

Another important parameter is the exit nonuniformity, u_2 , as

$$u_2 = \frac{\Delta U_{\max}}{U_2}, \quad (3)$$

where ΔU_{\max} is the largest velocity variation in the exit section.

To examine the possibility of boundary layer relaminarization, a third parameter, κ' , is used and defined as

$$\kappa' = \max \left[\frac{1}{(U_f/U_2)^2} \cdot \frac{d(U_f/U_2)}{d(x/H_1)} \right], \quad (4)$$

where U_f is the local free-stream velocity at the corner; $H_1 (=2h_1)$ is the width of the upstream section. When the kinematic viscosity of the flow is known, κ' can be used to predict the occurrence of relaminarization according to the criterion suggested by Back et al. (1970), as

$$K = \frac{\nu}{U_f^2} \frac{dU_f}{dx} = \frac{\kappa'}{Re_h} = 2 \times 10^{-6}, \quad Re_h = \frac{U_2 \cdot H_1}{\nu} \quad (5)$$

Numerical Results

The numerical computations adopt a finite-volume Euler solver to obtain potential-flow results within a contraction. The

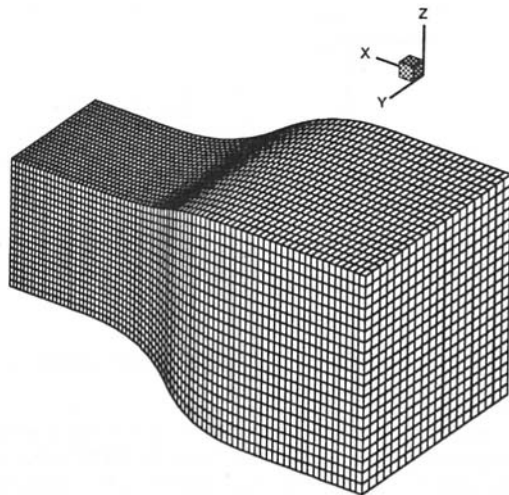


Fig. 3 Typical computational mesh ($80 \times 20 \times 20$)

assumption is that in the absence of separation, a low-turbulence flow in a majority portion of the domain stays as a potential one. Since the boundary layer in a contraction is generally very thin in comparison with the size of the local cross-section, the error of the result is considered to be acceptable in most engineering applications. In all calculations, the contraction is preceded and followed by a straight duct with a length of one-half the width of the contraction end section. Figure 3 illustrates a typical computation mesh system. Further investigations reveal that the relative error produced by this mesh is no more than 3 percent.

The calculations are performed at discrete values of three geometrical parameters, contraction ratio (CR), L/H_1 , and x_m/L , selected within ranges of general engineering applications. Figure 4 shows the variations of the pressure coefficients (Cp_i and Cp_e) with respect to x_m/L and L/H_1 for two typical contraction ratios. As x_m/L increases, Cp_i tends to decrease with a trade of an increase of Cp_e value. Physically, as the matched point moves toward downstream, the extent of the velocity overshoot near the inlet becomes less significant. On the other hand, it will magnify the overshoot near the downstream section because of an increase of the wall curvature near the exit.

To apply the Stratford criterion for turbulent separation, the locations of the pressure extremes and the longitudinal pressure gradients are needed. Numerical results reveal that the normalized forms of x_i and x_e (the distances between the extremes and the neighboring end) depend mildly on L/H_1 . For different contraction ratios, the relationships are plotted in Fig. 5 and 6 with respect to the location of the matched point. When the

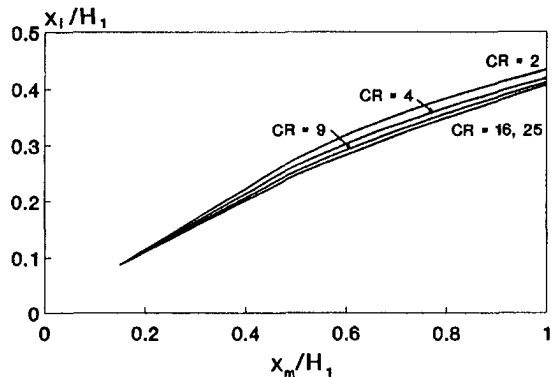


Fig. 5 Normalized distance from nozzle beginning to corner pressure maximum

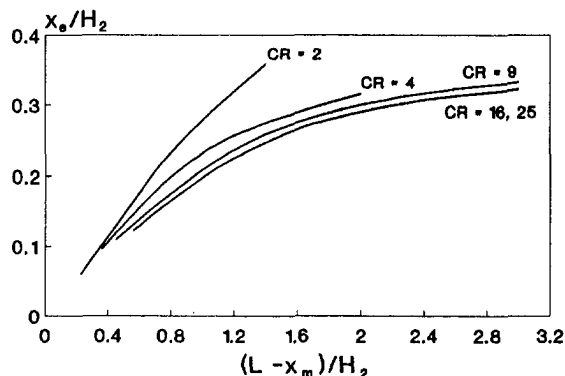


Fig. 6 Normalized distance from nozzle exit to corner pressure minimum

matched point is away from one of the ends, the location of the extremes tends to move toward the same direction.

As the adverse pressure gradients in the streamwise direction are approximated over a range from $0.5 Cp$ to $0.9 Cp$ (Morel, 1975), the resulting adverse pressure gradients near the location of possible separation appear to be strong functions of the magnitudes of the pressure extremes, L/H_1 and CR , and depends mildly on x_m/L . Figures 7 and 8 show that the longitudinal pressure gradients increase as the magnitudes of the corresponding pressure coefficients increase.

The resulting κ' values, which relates to the occurrence of relaminarization, are plotted in Fig. 9. They show that as CR increases, the maximum of κ' increases. This implies that relaminarization is prone to occur when the contraction ratio is large.

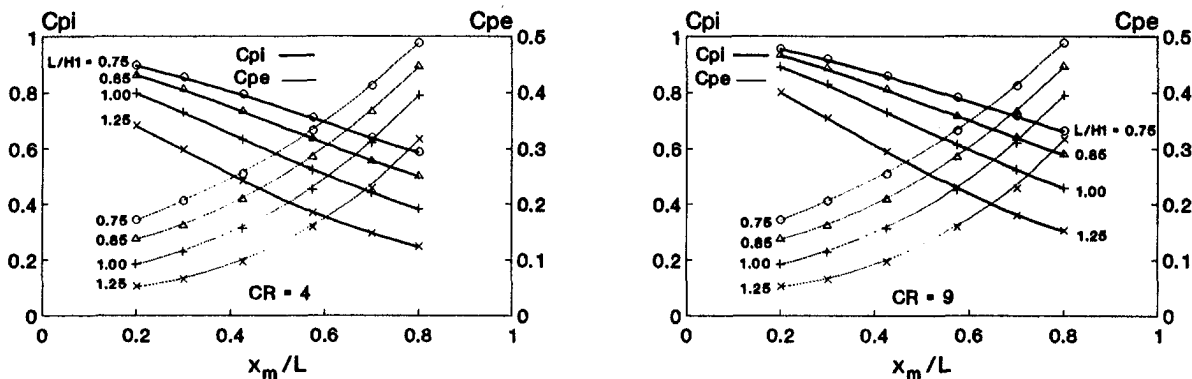


Fig. 4 Corner pressure coefficients

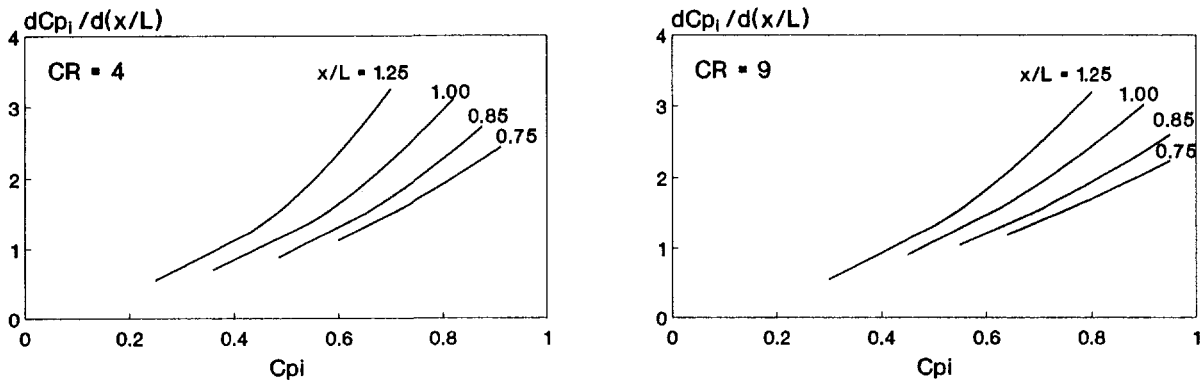


Fig. 7 Normalized adverse pressure gradient versus Cp_i near the location of possible separation

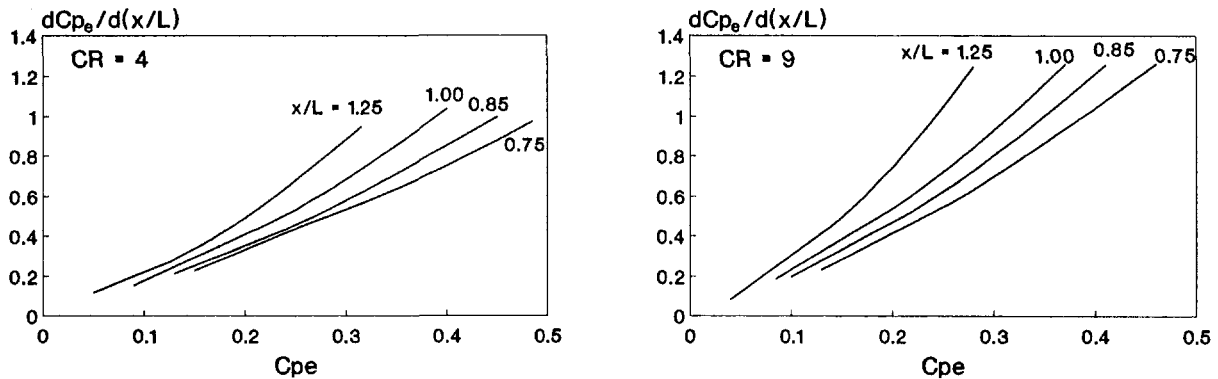


Fig. 8 Normalized adverse pressure gradient versus Cp_e near the location of possible separation

Moreover, when CR is fixed, the more the matched point approaches the upstream end, the more possibly the boundary layer becomes relaminarized.

Finally, the downstream nonuniformity (u_2), are plotted in relation to x_m and CR in Fig. 10. Generally, u_2 decreases as CR increases. In addition, when the matched point moves downstream or the nozzle length is reduced, the exit flow becomes less uniform.

Approach of the Suggested Design Method

Stratford (1959) estimated that the pressure rise at separation of turbulent boundary layers is at order of 6 to 10 times of that of separating laminar boundary. Therefore, although the consideration of flow separation in the first adverse-pressure gradient region (the one near the contraction entrance section) is generally more critical (Morel, 1975), it may not be true should relaminarization occurs. On the other hand, since the velocity non-uniformity decays rapidly as the flow goes further downstream to the test section, it is considered that u_2 should

not be treated as a very important factor of the design unless the following section is extremely short or the contraction is such that it leads to an abnormally large nonuniformity at the exit. Accordingly, different from what Morel suggested, the exit-velocity non-uniformity is not chosen to be the first parameter to determine for the design. Instead, the design procedure starts with the avoidance of relaminarization, which also eliminates the possibility of separation near the contraction exit.

As the separation is of concern, certain approximations are needed so as to apply the Stratford criterion (Stratford, 1959), as

$$Cp_i \cdot \left(x_b \cdot \frac{dCp_i}{dx} \right)^{1/2} = 0.35 \cdot (10^{-6} \cdot R_x)^{0.1}, \quad (6)$$

where x_b is the travelling distance of the boundary layer. The maximum allowable value of Cp_i without the occurrence of separation near the contraction inlet can then be obtained by

$$(Cp_i)_{\max} = 0.35 \cdot \frac{(10^{-6} \cdot R_x)^{0.1}}{(x_b \cdot dCp_i/dx)^{1/2}}, \quad R_x = \frac{U_i \cdot x_b}{\nu} \quad (7)$$

The boundary layer travelling distance, x_b , consists of two parts:

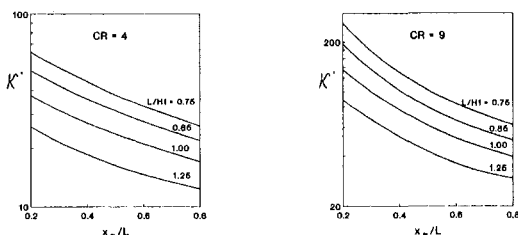


Fig. 9 Dimensionless acceleration parameter

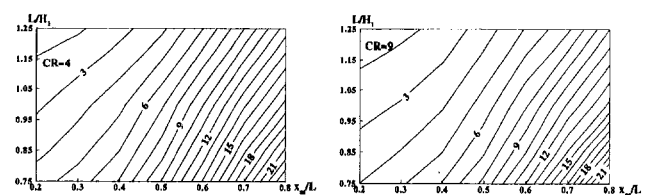


Fig. 10 Nonuniformity at contraction exit (in percentage)

the one from the nozzle beginning to the virtual origin of the boundary layer (x_o) and the other one from the beginning of the contraction to the separation point; the former can be generally estimated by the distance from the nearest screen or honeycomb upstream to the nozzle entrance and the latter can be approximated by a length of $0.9 x_i$ (Morel, 1975).

Suggested Design Method

When the contraction area ratio (CR), the dimensions of the end sections (H_1 and H_2), the distance from the closest upstream screen or honeycomb to the beginning of the contraction (x_o), the maximum design speed after the nozzle exit (U_2), and the level of exit velocity nonuniformity are prescribed, the suggested procedure of contraction designs starts with the consideration of the avoidance of relaminarization. With given values of CR, H_1 and U_o , Re_h is calculated to find out the allowable ranges of L/H_1 and x_m/L without causing relaminarization based on Eq. (5) and Fig. 8. The next step is to pick up the smallest L/H_1 and x_m/L , which lead to the lowest construction cost and the best exit velocity uniformity. However, since a small x_m/L value leads to a large Cp_i and a tendency to separate near the inlet, one may need to increase the x_m/L value (but still keep the same L/H_1) so that the possible separation is avoided. To apply the separation criterion, the procedure is as follows:

- (1) Find Cp_i from Fig. 4.
- (2) Evaluate $x_b = x_o + 0.9 (x_i)$, where x_i can be found from Fig. 5.
- (3) Find dCp_i/dx from Fig. 7.
- (4) Calculate the Reynolds number (Re_x) and $(Cp_i)_{max}$ based on Eq. (7).
- (5) Compare the values of Cp_i from step (1) and $(Cp_i)_{max}$ from step (4).

If either separation cannot be avoided (Cp_i is greater than $(Cp_i)_{max}$) or the exit flow nonuniformity (from Fig. 10) is not acceptable for all x_m/L values, the next step is to increase the nozzle length by selecting a larger L/H_1 value. By repeating the same process, the final design would be the one which satisfies all design considerations.

Conclusions

A comprehensive design method for contractions with square end sections is proposed. To achieve a nonseparated flow with prescribed flow quality at the exit of the contraction, a step-by-step procedure in selecting an appropriate set of geometric parameters is established to determine the geometry of the contracting wall.

Acknowledgment

The study was funded by the National Science Council in Taiwan under grant number NSC 80-0410-E-005-25.

References

- Back, L. H., Cuffel, R. F., and Massier, P. F., 1970, "Laminarization of a Turbulent Boundary Layer in Nozzle-Flow-Boundary Layer and Heat Transfer Measurements with Wall Cooling," *ASME Journal of Heat Transfer*, Vol. 92, No. 1, pp. 333–344.
- Batchelor, G. K., and Proudman, I., 1972, "A Generalized Theory for the Design of Contraction Cones and Other Low-Speed Ducts," NASA TN D-6962.
- Morel, T., 1975, "Comprehensive Design of Axisymmetric Wind Tunnel Contractions," *ASME JOURNAL OF FLUIDS ENGINEERING*, pp. 225–233.
- Morel, T., 1977, "Design of Two-Dimensional Wind Tunnel Contractions," *ASME JOURNAL OF FLUIDS ENGINEERING*, pp. 371–378.
- Prandtl, L., 1933, "Attaining Steady Air Stream in Wind Tunnels," NACA TM No. 726.
- Ramjee, V. and Hussain, A., 1976, "Influence of the Axisymmetric Contraction Ratio on Free-Stream Turbulence," *ASME JOURNAL OF FLUIDS ENGINEERING*, pp. 506–515.
- Stratford, B. S., 1959, "The Prediction of Separation of the Turbulent Boundary Layer," *Journal of Fluid Mechanics*, Vol. 5, pp. 1–16.

Turbulence Modification in the Limiting Cases of Heavy- and Tracer-Particles

D. I. Graham¹

Introduction

The presence of nonfluid particles in a turbulent fluid flow leads to momentum transfer between the fluid and particle phases. For low particle concentrations this process is not sufficient to modify the primary flow and the momentum transfer can be assumed to be a one-way process from fluid to particles. However, if the concentration of the particle phase is sufficiently high, the presence of particles can lead to significant modification of the primary flow turbulence. The review of this "turbulence modulation effect" by Gore and Crowe (1992) shows that turbulence levels are enhanced for large particles, while small particles attenuate turbulence levels. It is the latter case, in this note, in which we are interested.

Analysis of turbulence modulation effects shows that correlations between fluid velocities and concentrations are important. This is particularly true for particles with Stokes numbers (defined as the ratio of the characteristic times of particle and the turbulence) of the order of unity. In this note, we are mainly interested in the two limiting cases $St \rightarrow 0$ and $St \rightarrow \infty$, and in both of these cases the concentration is independent of the fluid and particle velocities in forced isotropic turbulence (Squires and Eaton, 1990). In the following analysis, then, uniform particle concentration is assumed.

In the following section, an expression for the fluid turbulence kinetic energy source term $\langle S_k \rangle$ due to the momentum transfer from a particulate phase is derived. The underlying turbulent flow is assumed to be homogeneous, isotropic, and stationary. It should be noted that shortcomings in the modeling of the corresponding source term $\langle S_e \rangle$ in the energy dissipation equation have recently been pointed out (Squires and Eaton, 1994). In this paper, we shall show that some numerical models can lead to spurious nonzero contributions to $\langle S_k \rangle$ for tracer-particles.

Analysis

Assuming that the only forces acting on a particle moving through a turbulent fluid flow are Stokesian drag and gravitational forces, the i -component of the particle equation of motion is

$$\frac{du_{pi}}{dt} = \beta(u_{fi} - u_{pi}) + g_i \left(1 - \frac{\rho_f}{\rho_p} \right), \quad (1)$$

where u_{fi} and u_{pi} are the instantaneous fluid and particle velocities, g_i is the acceleration due to gravity, ρ_f and ρ_p are the densities of the fluid and particle, and β is the reciprocal relaxation time scale of the particle.

The equation for the fluid-phase turbulence kinetic energy k can be written in the form (Launder, 1990)

¹Lecturer School of Mathematics and Statistics, University of Plymouth, Drake Circus, Plymouth, Devon PL4 8AA, U.K.

Contributed by the Fluids Engineering Division of THE AMERICAN SOCIETY OF MECHANICAL ENGINEERS. Manuscript received by the Fluids Engineering Division November 5, 1995; revised manuscript received December 3, 1996. Associate Technical Editor: M. W. Reeks.

the one from the nozzle beginning to the virtual origin of the boundary layer (x_o) and the other one from the beginning of the contraction to the separation point; the former can be generally estimated by the distance from the nearest screen or honeycomb upstream to the nozzle entrance and the latter can be approximated by a length of $0.9 x_i$ (Morel, 1975).

Suggested Design Method

When the contraction area ratio (CR), the dimensions of the end sections (H_1 and H_2), the distance from the closest upstream screen or honeycomb to the beginning of the contraction (x_o), the maximum design speed after the nozzle exit (U_2), and the level of exit velocity nonuniformity are prescribed, the suggested procedure of contraction designs starts with the consideration of the avoidance of relaminarization. With given values of CR, H_1 and U_o , Re_h is calculated to find out the allowable ranges of L/H_1 and x_m/L without causing relaminarization based on Eq. (5) and Fig. 8. The next step is to pick up the smallest L/H_1 and x_m/L , which lead to the lowest construction cost and the best exit velocity uniformity. However, since a small x_m/L value leads to a large Cp_i and a tendency to separate near the inlet, one may need to increase the x_m/L value (but still keep the same L/H_1) so that the possible separation is avoided. To apply the separation criterion, the procedure is as follows:

- (1) Find Cp_i from Fig. 4.
- (2) Evaluate $x_b = x_o + 0.9(x_i)$, where x_i can be found from Fig. 5.
- (3) Find dCp_i/dx from Fig. 7.
- (4) Calculate the Reynolds number (Re_x) and $(Cp_i)_{max}$ based on Eq. (7).
- (5) Compare the values of Cp_i from step (1) and $(Cp_i)_{max}$ from step (4).

If either separation cannot be avoided (Cp_i is greater than $(Cp_i)_{max}$) or the exit flow nonuniformity (from Fig. 10) is not acceptable for all x_m/L values, the next step is to increase the nozzle length by selecting a larger L/H_1 value. By repeating the same process, the final design would be the one which satisfies all design considerations.

Conclusions

A comprehensive design method for contractions with square end sections is proposed. To achieve a nonseparated flow with prescribed flow quality at the exit of the contraction, a step-by-step procedure in selecting an appropriate set of geometric parameters is established to determine the geometry of the contracting wall.

Acknowledgment

The study was funded by the National Science Council in Taiwan under grant number NSC 80-0410-E-005-25.

References

- Back, L. H., Cuffel, R. F., and Massier, P. F., 1970, "Laminarization of a Turbulent Boundary Layer in Nozzle-Flow-Boundary Layer and Heat Transfer Measurements with Wall Cooling," *ASME Journal of Heat Transfer*, Vol. 92, No. 1, pp. 333–344.
- Batchelor, G. K., and Proudman, I., 1972, "A Generalized Theory for the Design of Contraction Cones and Other Low-Speed Ducts," NASA TN D-6962.
- Morel, T., 1975, "Comprehensive Design of Axisymmetric Wind Tunnel Contractions," *ASME JOURNAL OF FLUIDS ENGINEERING*, pp. 225–233.
- Morel, T., 1977, "Design of Two-Dimensional Wind Tunnel Contractions," *ASME JOURNAL OF FLUIDS ENGINEERING*, pp. 371–378.
- Prandtl, L., 1933, "Attaining Steady Air Stream in Wind Tunnels," NACA TM No. 726.
- Ramjee, V. and Hussain, A., 1976, "Influence of the Axisymmetric Contraction Ratio on Free-Stream Turbulence," *ASME JOURNAL OF FLUIDS ENGINEERING*, pp. 506–515.
- Stratford, B. S., 1959, "The Prediction of Separation of the Turbulent Boundary Layer," *Journal of Fluid Mechanics*, Vol. 5, pp. 1–16.

Turbulence Modification in the Limiting Cases of Heavy- and Tracer-Particles

D. I. Graham¹

Introduction

The presence of nonfluid particles in a turbulent fluid flow leads to momentum transfer between the fluid and particle phases. For low particle concentrations this process is not sufficient to modify the primary flow and the momentum transfer can be assumed to be a one-way process from fluid to particles. However, if the concentration of the particle phase is sufficiently high, the presence of particles can lead to significant modification of the primary flow turbulence. The review of this "turbulence modulation effect" by Gore and Crowe (1992) shows that turbulence levels are enhanced for large particles, while small particles attenuate turbulence levels. It is the latter case, in this note, in which we are interested.

Analysis of turbulence modulation effects shows that correlations between fluid velocities and concentrations are important. This is particularly true for particles with Stokes numbers (defined as the ratio of the characteristic times of particle and the turbulence) of the order of unity. In this note, we are mainly interested in the two limiting cases $St \rightarrow 0$ and $St \rightarrow \infty$, and in both of these cases the concentration is independent of the fluid and particle velocities in forced isotropic turbulence (Squires and Eaton, 1990). In the following analysis, then, uniform particle concentration is assumed.

In the following section, an expression for the fluid turbulence kinetic energy source term $\langle S_k \rangle$ due to the momentum transfer from a particulate phase is derived. The underlying turbulent flow is assumed to be homogeneous, isotropic, and stationary. It should be noted that shortcomings in the modeling of the corresponding source term $\langle S_e \rangle$ in the energy dissipation equation have recently been pointed out (Squires and Eaton, 1994). In this paper, we shall show that some numerical models can lead to spurious nonzero contributions to $\langle S_k \rangle$ for tracer-particles.

Analysis

Assuming that the only forces acting on a particle moving through a turbulent fluid flow are Stokesian drag and gravitational forces, the i -component of the particle equation of motion is

$$\frac{du_{pi}}{dt} = \beta(u_{fi} - u_{pi}) + g_i \left(1 - \frac{\rho_f}{\rho_p}\right), \quad (1)$$

where u_{fi} and u_{pi} are the instantaneous fluid and particle velocities, g_i is the acceleration due to gravity, ρ_f and ρ_p are the densities of the fluid and particle, and β is the reciprocal relaxation time scale of the particle.

The equation for the fluid-phase turbulence kinetic energy k can be written in the form (Launder, 1990)

¹Lecturer School of Mathematics and Statistics, University of Plymouth, Drake Circus, Plymouth, Devon PL4 8AA, U.K.

Contributed by the Fluids Engineering Division of THE AMERICAN SOCIETY OF MECHANICAL ENGINEERS. Manuscript received by the Fluids Engineering Division November 5, 1995; revised manuscript received December 3, 1996. Associate Technical Editor: M. W. Reeks.

$$\rho_f \frac{\partial k}{\partial t} + \rho_f \bar{u}_i \frac{\partial k}{\partial x_i} = P + F + G - \phi - \epsilon + d + \langle S_k \rangle \quad (2)$$

where P , F , and G represent turbulence generation from mean-strain, rotation, and body forces, respectively, ϕ is the pressure-strain correlation, d is the diffusion term, ϵ is the turbulent dissipation, and $\langle S_k \rangle$ is the contribution due to the presence of particles. In this note, we are interested only in the particle contribution $\langle S_k \rangle$.

If the particle concentration is uniform, the mean momentum source due to particles is given by

$$\langle S_{u_i} \rangle = -C\rho_p \langle \beta(u_{f_i} - u_{p_i}) \rangle, \quad (3)$$

where C is the particle volume fraction and the angled brackets denote ensemble-averaging.

Berlemont et al. (1990) show that the corresponding source per unit volume for the turbulence kinetic energy is given by

$$\langle S_k \rangle = \langle u'_{f_i} S'_{u_i} \rangle \quad (4)$$

where the summation convention is assumed for repeated i -indices and dashes refer to fluctuating values: $u'_{f_i} = u_{f_i} - \langle u_{f_i} \rangle$ and $S'_{u_i} = S_{u_i} - \langle S_{u_i} \rangle$. Assuming that β is constant, Eq. (4) can be written as

$$\langle S_k \rangle = -C\beta\rho_p \langle (u'_{f_i} u'_{f_i}) - \langle u'_{f_i} u'_{p_i} \rangle \rangle \quad (5)$$

For the purpose of the following analysis, we assume homogeneous isotropic turbulence, in which case $\langle u'_{f_i} u'_{f_i} \rangle = 3u'^2$, where u' is the turbulence intensity. In Appendix A, it is shown that the fluid/particle velocity correlation $\langle u'_{f_i} u'_{p_i} \rangle$ is given by

$$\langle u'_{f_i} u'_{p_i} \rangle = \beta u'^2 \int_0^\infty e^{-\beta\tau} R_{f_{ii}}^p(\tau) d\tau \quad (6)$$

where $R_{f_{ij}}^p(\tau)$ is the steady-state auto-correlation of the fluid velocities seen by particles.

The source term S_k then becomes

$$\langle S_k \rangle = -C\beta\rho_p u'^2 \left(3 - \beta \int_0^\infty e^{-\beta\tau} R_{f_{ii}}^p(\tau) d\tau \right). \quad (7)$$

For heavy particles, $\beta \rightarrow 0$ and Eq. (7) approaches the well-known form

$$\langle S_k \rangle \rightarrow -2C\beta\rho_p k, \quad (8)$$

since the turbulence kinetic energy is given by $k = 3u'^2/2$ in homogeneous isotropic turbulence.

For tracer particles, on the other hand, $\beta \rightarrow \infty$, so that $1/\beta \rightarrow 0$. In order to investigate the magnitude of the source term $\langle S_k \rangle$ for this limiting case, Eq. (6) is first rewritten as

$$\langle u'_{f_i} u'_{p_i} \rangle = \int_0^\infty e^{-t'} u'^2 R_{f_{ii}}^p(t'/\beta) dt'. \quad (9)$$

Next, $R_{f_{ij}}^p(t'/\beta)$ is expanded as a Taylor series around $t'/\beta = 0$:

$$R_{f_{ij}}^p(t'/\beta) = \sum_{n=0}^{\infty} \frac{1}{n!} R_{f_{ij}}^{p(n)}(0) \left(\frac{t'}{\beta} \right)^n. \quad (10)$$

The correlation $\langle u'_{f_i} u'_{p_i} \rangle$ is given by substituting (10) into (9) and integrating term by term, leading to

$$\langle u'_{f_i} u'_{p_i} \rangle = u'^2 \left(3 + \frac{R_{f_{ii}}^{p(0)}}{\beta} \right) + O\left(\frac{1}{\beta^2} \right). \quad (11)$$

Thus, using the above expression in Eq. (5),

$$\begin{aligned} \langle S_k \rangle &= C\beta\rho_p u'^2 \left(\frac{R_{f_{ii}}^{p(0)}}{\beta} \right) + O\left(\frac{1}{\beta} \right) \\ &\rightarrow 3C\rho_p u'^2 R_L^p(0) = 2C\rho_p k R_L^p(0) \text{ as } \beta \rightarrow \infty \quad (12) \end{aligned}$$

where $R_L(\tau)$ is the Lagrangian fluid velocity auto-correlation.

For physically realistic turbulence, $R_L^p(0) = 0$ (Hinze, 1975). However, in many of the numerical models of particle dispersion reported in the literature, this is not necessarily the case. For example, if the commonly-used ‘‘Eddy Interaction Model’’ developed by Gosman and Ioannides (1981) is used, the resulting linear auto-correlation leads to $R_L^p(0) = -1/(2\tau_L)$, where the Lagrangian integral time scale is equal to τ_L (Wang and Stock, 1992). The Poisson process used by Ormancey and Martinon (1984) leads to an exponential auto-correlation function, for which $R_L^p(0) = -1/\tau_L$. The Frenkel functions used by Berlemont et al. (1990) lead to $R_L^p(0) = -1/\{(m^2 + 1)\tau_L\}$, where m is the number of ‘‘negative loops’’ in the Frenkel function. When used to model tracer-particles, numerical models, such as those above, give rise to spurious (negative) contributions to the turbulence kinetic energy equations in $k - \epsilon$ solvers. Similar behavior can be expected if the models are used for ‘‘light’’ particles with low inertia.

Conclusion

Source terms due to viscous drag on dispersed-phase particles in a simple turbulent flow have been analyzed. Momentum and turbulence kinetic energy sources have been investigated. It is shown that certain numerical models for particle dispersion lead to nonzero turbulence kinetic energy sources in the limiting case of tracer-particles, whereas in physical turbulence the source terms vanish.

References

- Berlemont, A., Desjonqueres, P., and Gouesbet, G., 1990, ‘‘Particle Lagrangian Simulation in Turbulent Flows,’’ *Int. J. Multiphase Flows*, Vol. 16(1), pp. 19–34.
- Friedlander, S. K., 1957, ‘‘Behavior of Suspended Particles in a Turbulent Fluid,’’ *A.I.Ch.E. Journal*, Vol. 3, pp. 381–385.
- Gore, R. A. and Crowe, C. T., 1989, ‘‘Effect of Particle Size on Modulating Turbulent Intensity,’’ *International Journal of Multiphase Flow*, Vol. 15, pp. 279–285.
- Gosman, A. D., and Ioannides, E., 1981, ‘‘Aspects of Computer Simulation of Liquid-Fueled Combustors,’’ Paper 81-0232, AIAA 19th Aerospace Meeting, St. Louis, Mo.
- Hinze, J. O., 1975, *Turbulence (2nd edition)*, McGraw-Hill, New York.
- Lauder, B. E., 1990, ‘‘Turbulence Modelling for the Nineties: Second Moment Closure . . . and Beyond?’’ *Proc. Twelfth Int. Conf. on Numerical Methods in Fluid Dynamics*, K. W. Morton, ed., Lecture Notes in Physics 371, Springer-Verlag, Berlin.
- Ormancey A., and Martinon A., 1984, ‘‘Prediction of Particle Dispersion in Turbulent Flows,’’ *Physico-Chemical Hydrodynamics*, Vol. 5, pp. 229–240.
- Squires, K. D., and Eaton, J. K., 1990, ‘‘Particle Response and Turbulence Modification in Isotropic Turbulence,’’ *Physics of Fluids A*, Vol. 2, pp. 1191–1203.
- Squires, K. D., and Eaton, J. K., 1994, ‘‘Effect of Selective Modification of Turbulent on Two-Equation Models for Particle-Laden Turbulent Flows,’’ *ASME JOURNAL OF FLUIDS ENGINEERING*, Vol. 116, pp. 778–784.
- Wang, L.-P., and Stock, D. E., 1992, ‘‘Stochastic Trajectory Models for Turbulent Diffusion: Monte Carlo Process versus Markov Chains,’’ *Atmos. Env.* 26A, pp. 1599–1607.

APPENDIX A

Evaluation of $\langle u'_{f_i} u'_{p_i} \rangle$

The fluid/particle velocity correlation $\langle u'_{f_i} u'_{p_i} \rangle$ is evaluated using a method similar to that used by Friedlander (1957). Equation (1) is first simplified by referring to the particle velocity relative to the ‘‘drift velocity’’ $V_{s_i} = g_i/\beta(1 - (\rho_f/\rho_p))$,

$$v_{p_i} = u_{p_i} - V_{s_i}, \quad (13)$$

leading to a modified equation of motion

$$\frac{dv_{p_i}}{dt} = \beta(u_{f_i} - v_{p_i}). \quad (14)$$

Since $\langle u_{f_i} \rangle$ and $\langle v_{p_i} \rangle$ are constant in homogeneous turbulence, this can be written as

$$\frac{d}{dt}(v_{p_i} - \langle v_{p_i} \rangle) = \beta(u_{f_i} - v_{p_i}). \quad (15)$$

Assuming that $\langle v_{p_i} \rangle = \langle u_{f_i} \rangle$ and that the initial particle velocity is equal to the drift velocity, the solution to this equation is given by

$$v_{p_i}(t) - \langle v_{p_i} \rangle = \beta e^{-\beta t} \int_0^t e^{+\beta t'} (u_{f_i}(t') - \langle u_{f_i} \rangle) dt' \quad (16)$$

or

$$u'_{p_i}(t) = \beta e^{-\beta t} \int_0^t e^{+\beta t'} u'_{f_i}(t') dt' \quad (17)$$

Note here that we are eventually interested in the long-time steady-state behavior of the turbulent flow so that initial particle velocities are unimportant.

Multiplying both sides of this equation by $u'_{f_i}(t)$, and taking an ensemble average gives

$$\langle u'_{f_i}(t) u'_{p_i}(t) \rangle = \beta e^{-\beta t} \int_0^t e^{+\beta t'} \langle u'_{f_i}(t) u'_{f_i}(t') \rangle dt', \quad (18)$$

which can be written in the form

$$\langle u'_{f_i}(t) u'_{p_i}(t) \rangle = \beta u'^2 \int_0^t e^{-\beta \tau} R_{f_i}^p(t, \tau) d\tau \quad (19)$$

where

$$R_{f_i}^p(t, \tau) = \frac{\langle u'_{f_i}(t) u'_{f_i}(t + \tau) \rangle}{u'^2} \quad (20)$$

is the auto-correlation of the fluid velocities seen by the particle.

In the long-time limit,

$$\langle u'_{f_i}(t) u'_{p_i}(t) \rangle = \beta u'^2 \int_0^\infty e^{-\beta \tau} R_{f_i}^p(\tau) d\tau \quad (21)$$

where

$$R_{f_i}^p(\tau) = \lim_{t \rightarrow \infty} R_{f_i}^p(t, \tau) \quad (22)$$

is the steady-state auto-correlation.

A Short Comparison of Damping Functions of Standard Low-Reynolds-Number k - ϵ Models

A. N. Rousseau,¹ L. D. Albright,² and K. E. Torrance³

Introduction

In the near-wall region of a turbulent flow, the energy-containing scales of the turbulence are not sufficiently larger than

¹ Postdoctoral Fellow, Institut National de la Recherche Scientifique (INRS)-Eau 2800 rue Einstein, Suite 105, C. P. 7500, Ste-Foy, P. Q. Canada G1V 4C7.

² Professor, Department of Agricultural and Biological Engineering, Cornell University, Ithaca, NY 14853-5701.

³ Sibley School of Mechanical and Aerospace Engineering, Cornell University, Ithaca, NY 14853-5701.

Contributed by the Fluids Engineering Division of THE AMERICAN SOCIETY OF MECHANICAL ENGINEERS. Manuscript received by the Fluids Engineering Division January 24, 1996; revised manuscript received January 8, 1997. Associate Technical Editor: S. P. Vanka.

the Kolmogorov scales for the energy equilibrium hypothesis to be valid. This means the Prandtl-Kolmogorov formula and some of the standard closure models of the modeled transport equations of turbulence cannot be directly applied in this region of the flow.

In terms of low-Reynolds-number k - ϵ modeling, an indirect application of the Prandtl-Kolmogorov formula in the near-wall region of a turbulent flow has generally been accomplished by either: (i) introducing damping functions f_μ , f_1 and f_2 in the troublesome formula and/or expressions, or (ii) modifying both the eddy-viscosity model and the modeled transport equations (Patel et al., 1985). In the second approach, additional terms are usually included in the k -equation, and either an $\tilde{\epsilon}$ -equation (Mansour and Shih, 1989; Yang and Shih, 1991, 1993a, b), or an asymptotically-correct ϵ -equation is substituted for the ϵ -equation (So et al., 1992). Although both of the above modeling approaches are of equal importance, the scope of this technical note only extends to the first of the two and, since the function f_μ is directly involved in the production term of the modeled ϵ -equation, the use of a function f_1 throughout the near wall region is not considered.

In most wall-bounded flows, including wall-jet flows, the thickness of the near-wall region is very weakly dependent on the Reynolds number of the flow (Launder and Rodi, 1981, 1983; Spalart, 1988). Therefore, it is imperative the damping functions f_μ and f_2 of any standard low-Reynolds-number k - ϵ models asymptotically satisfy the limiting behavior of near-wall turbulence in the viscous sublayer ($x_j^+ \leq 5$) and beyond the buffer layer ($x_j^+ \geq 45$).

Damping functions have usually been evaluated by comparing computed profiles of flow properties and/or flow parameters with those estimated from experiments involving high-Reynolds-number pipe flows, boundary-layer flows, or channel flows (Patel et al., 1985). With the increasing availability of high-resolution, direct numerical simulation (DNS) data for channel flows (Kim et al., 1987; Handler et al., 1989) and boundary layers (Spalart, 1988), it is possible to compute these functions at low-to-moderate Reynolds numbers and to compare them in terms of their expected accuracy to predict the limiting behavior of near-wall turbulence and the k - ϵ budgets (Mansour et al., 1989; Miner et al., 1991).

The objective of this technical note is to compare and determine which of the damping functions of standard low-Reynolds-number k - ϵ models can be used with confidence to compute wall-bounded flows without separation, reattachment, or stagnation points.

Limiting Behavior of Damping Functions f_μ and f_2

The limiting behavior of the damping functions f_μ and f_2 in the viscous sublayer was deduced by Chapman and Kuhn (1986). Their simulation data of three Navier-Stokes computational models of the incompressible viscous sublayer showed that as $x_j^+ \rightarrow 0$ (for $x_j^+ \leq 0.3$), $k \sim x_j^{+2}$, $\epsilon \rightarrow \epsilon_w$, and $\nu_i \sim x_j^{+3}$. From $f_\mu = \nu_i \epsilon / C_\mu k^2$, this suggests $f_\mu \sim x_j^{+1}$. Meanwhile, using the results of Chapman and Kuhn (1986), Myong and Kasagi (1990) inferred $f_2 \sim x_j^{+2}$ (since $\epsilon^2/k \sim x_j^{+2}$), forcing the dissipation term, ϵ^2/k , to a constant as $x_j^+ \rightarrow 0$, namely to the viscous dissipation of ϵ at the wall. On the other end, Patel et al. (1985) pointed out that as $x_j^+ \rightarrow 45$ both f_μ and f_2 should tend to unity (clear separation between energy-containing scales and Kolmogorov scales).

Comparison of Standard Damping Functions

Patel et al. (1985) examined seven low-Reynolds-number k - ϵ models of which those of Launder and Sharma (1974), Lam and Bremhorst (1981), and Chien (1982) performed reasonably well but whose influence extended beyond the near-wall region. Unfortunately, due to a lack of high-resolution data, Patel et al.

$$\frac{dv_{p_i}}{dt} = \beta(u_{f_i} - v_{p_i}). \quad (14)$$

Since $\langle u_{f_i} \rangle$ and $\langle v_{p_i} \rangle$ are constant in homogeneous turbulence, this can be written as

$$\frac{d}{dt}(v_{p_i} - \langle v_{p_i} \rangle) = \beta(u_{f_i} - v_{p_i}). \quad (15)$$

Assuming that $\langle v_{p_i} \rangle = \langle u_{f_i} \rangle$ and that the initial particle velocity is equal to the drift velocity, the solution to this equation is given by

$$v_{p_i}(t) - \langle v_{p_i} \rangle = \beta e^{-\beta t} \int_0^t e^{+\beta t'} (u_{f_i}(t') - \langle u_{f_i} \rangle) dt' \quad (16)$$

or

$$u'_{p_i}(t) = \beta e^{-\beta t} \int_0^t e^{+\beta t'} u'_{f_i}(t') dt' \quad (17)$$

Note here that we are eventually interested in the long-time steady-state behavior of the turbulent flow so that initial particle velocities are unimportant.

Multiplying both sides of this equation by $u'_{f_i}(t)$, and taking an ensemble average gives

$$\langle u'_{f_i}(t) u'_{p_i}(t) \rangle = \beta e^{-\beta t} \int_0^t e^{+\beta t'} \langle u'_{f_i}(t) u'_{f_i}(t') \rangle dt', \quad (18)$$

which can be written in the form

$$\langle u'_{f_i}(t) u'_{p_i}(t) \rangle = \beta u'^2 \int_0^t e^{-\beta \tau} R_{f_{ij}}^p(t, \tau) d\tau \quad (19)$$

where

$$R_{f_{ij}}^p(t, \tau) = \frac{\langle u'_{f_i}(t) u'_{f_j}(t + \tau) \rangle}{u'^2} \quad (20)$$

is the auto-correlation of the fluid velocities seen by the particle.

In the long-time limit,

$$\langle u'_{f_i}(t) u'_{p_i}(t) \rangle = \beta u'^2 \int_0^\infty e^{-\beta \tau} R_{f_{ij}}^p(\tau) d\tau \quad (21)$$

where

$$R_{f_{ij}}^p(\tau) = \lim_{t \rightarrow \infty} R_{f_{ij}}^p(t, \tau) \quad (22)$$

is the steady-state auto-correlation.

A Short Comparison of Damping Functions of Standard Low-Reynolds-Number k - ϵ Models

A. N. Rousseau,¹ L. D. Albright,² and K. E. Torrance³

Introduction

In the near-wall region of a turbulent flow, the energy-containing scales of the turbulence are not sufficiently larger than

¹ Postdoctoral Fellow, Institut National de la Recherche Scientifique (INRS)-Eau 2800 rue Einstein, Suite 105, C. P. 7500, Ste-Foy, P. Q. Canada G1V 4C7.

² Professor, Department of Agricultural and Biological Engineering, Cornell University, Ithaca, NY 14853-5701.

³ Sibley School of Mechanical and Aerospace Engineering, Cornell University, Ithaca, NY 14853-5701.

Contributed by the Fluids Engineering Division of THE AMERICAN SOCIETY OF MECHANICAL ENGINEERS. Manuscript received by the Fluids Engineering Division January 24, 1996; revised manuscript received January 8, 1997. Associate Technical Editor: S. P. Vanka.

the Kolmogorov scales for the energy equilibrium hypothesis to be valid. This means the Prandtl-Kolmogorov formula and some of the standard closure models of the modeled transport equations cannot be directly applied in this region of the flow.

In terms of low-Reynolds-number k - ϵ modeling, an indirect application of the Prandtl-Kolmogorov formula in the near-wall region of a turbulent flow has generally been accomplished by either: (i) introducing damping functions f_μ , f_1 and f_2 in the troublesome formula and/or expressions, or (ii) modifying both the eddy-viscosity model and the modeled transport equations (Patel et al., 1985). In the second approach, additional terms are usually included in the k -equation, and either an $\tilde{\epsilon}$ -equation (Mansour and Shih, 1989; Yang and Shih, 1991, 1993a, b), or an asymptotically-correct ϵ -equation is substituted for the ϵ -equation (So et al., 1992). Although both of the above modeling approaches are of equal importance, the scope of this technical note only extends to the first of the two and, since the function f_μ is directly involved in the production term of the modeled ϵ -equation, the use of a function f_1 throughout the near wall region is not considered.

In most wall-bounded flows, including wall-jet flows, the thickness of the near-wall region is very weakly dependent on the Reynolds number of the flow (Launder and Rodi, 1981, 1983; Spalart, 1988). Therefore, it is imperative the damping functions f_μ and f_2 of any standard low-Reynolds-number k - ϵ models asymptotically satisfy the limiting behavior of near-wall turbulence in the viscous sublayer ($x_j^+ \leq 5$) and beyond the buffer layer ($x_j^+ \geq 45$).

Damping functions have usually been evaluated by comparing computed profiles of flow properties and/or flow parameters with those estimated from experiments involving high-Reynolds-number pipe flows, boundary-layer flows, or channel flows (Patel et al., 1985). With the increasing availability of high-resolution, direct numerical simulation (DNS) data for channel flows (Kim et al., 1987; Handler et al., 1989) and boundary layers (Spalart, 1988), it is possible to compute these functions at low-to-moderate Reynolds numbers and to compare them in terms of their expected accuracy to predict the limiting behavior of near-wall turbulence and the k - ϵ budgets (Mansour et al., 1989; Miner et al., 1991).

The objective of this technical note is to compare and determine which of the damping functions of standard low-Reynolds-number k - ϵ models can be used with confidence to compute wall-bounded flows without separation, reattachment, or stagnation points.

Limiting Behavior of Damping Functions f_μ and f_2

The limiting behavior of the damping functions f_μ and f_2 in the viscous sublayer was deduced by Chapman and Kuhn (1986). Their simulation data of three Navier-Stokes computational models of the incompressible viscous sublayer showed that as $x_j^+ \rightarrow 0$ (for $x_j^+ \leq 0.3$), $k \sim x_j^{+2}$, $\epsilon \rightarrow \epsilon_w$, and $\nu_t \sim x_j^{+3}$. From $f_\mu = \nu_t \epsilon / C_\mu k^2$, this suggests $f_\mu \sim x_j^{+1}$. Meanwhile, using the results of Chapman and Kuhn (1986), Myong and Kasagi (1990) inferred $f_2 \sim x_j^{+2}$ (since $\epsilon^2/k \sim x_j^{+2}$), forcing the dissipation term, ϵ^2/k , to a constant as $x_j^+ \rightarrow 0$, namely to the viscous dissipation of ϵ at the wall. On the other end, Patel et al. (1985) pointed out that as $x_j^+ \rightarrow 45$ both f_μ and f_2 should tend to unity (clear separation between energy-containing scales and Kolmogorov scales).

Comparison of Standard Damping Functions

Patel et al. (1985) examined seven low-Reynolds-number k - ϵ models of which those of Launder and Sharma (1974), Lam and Bremhorst (1981), and Chien (1982) performed reasonably well but whose influence extended beyond the near-wall region. Unfortunately, due to a lack of high-resolution data, Patel et al.

Table 1 Near-wall behavior of standard f_μ -functions (for $x_j^+ \leq 0.3$)

Low Reynolds k - ϵ models	f_μ	$f_\mu \sim x_j^{+n}$
Lam and Bremhorst (1981)	$[(1 - \exp(-0.0165k^{+0.5}x_j^+))^2] \left[1 + \frac{20.5}{\text{Re}_t}\right]$	x_j^{+2}
Nagano and Tagawa (1990)	$\left[1 - \exp\left(\frac{-x_j^+}{26}\right)\right]^2 \left(1 + \frac{4.1}{\text{Re}_t^{0.75}}\right)$	x_j^{+1}
Myong and Kasagi (1990)	$\left[1 - \exp\left(\frac{-x_j^+}{70}\right)\right] \left(1 + \frac{3.45}{\text{Re}_t^{0.5}}\right)$	x_j^{+1}
Miner et al. (1991)	$0.04 + 0.96 \left\{1 - \exp\left[\frac{-(x_j^+ - 8)}{26}\right]\right\}^2$	x_j^{+1}
Speziale et al. (1992)	$\left[\tanh\left(\frac{-x_j^+}{70}\right)\right] \left(1 + \frac{3.45}{\text{Re}_t^{0.5}}\right)$	$10^{-1} - 10^{-2}x_j^+$

Table 2 Near-wall behavior of standard f_2 -functions (for $x_j^+ \leq 0.3$)

Low Reynolds k - ϵ models	f_2	$f_2 \sim x_j^{+n}$
Lam and Bremhorst (1981)	$1 - \exp(-\text{Re}_t^2)$	x_j^{+8}
Nagano and Tagawa (1990)	$\left[1 - \exp\left(\frac{-x_j^+}{6}\right)\right]^2 \left\{1 - 0.3 \exp\left[-\left(\frac{\text{Re}_t}{6.5}\right)^2\right]\right\}$	x_j^{+2}
Myong and Kasagi (1990)	$\left[1 - \exp\left(\frac{-x_j^+}{5}\right)\right]^2 \left\{1 - 0.22 \exp\left[-\left(\frac{\text{Re}_t}{6}\right)^2\right]\right\}$	x_j^{+2}
Speziale et al. (1992)	$\left[1 - \exp\left(\frac{-x_j^+}{4.9}\right)\right]^2 \left\{1 - 0.22 \exp\left[-\left(\frac{\text{Re}_t}{6}\right)^2\right]\right\}$	x_j^{+2}

(1985) were unable to verify the limiting behavior of f_μ and f_2 in the viscous sublayer. Nagano and Tagawa (1990) and Myong and Kasagi (1990) proposed two similar low-Reynolds-number k - ϵ models that correctly satisfied the limiting behavior of f_μ and f_2 in the viscous sublayer. However, they did not attempt to demonstrate that their models were solely restricted to the near-wall region. Using DNS data for a channel flow, Miner et al. (1991) developed a wall damping function f_μ that obeyed the aforementioned, near-wall, modeling requirements. Speziale et al. (1992) proposed a new low Reynolds-number k - τ model with asymptotically correct f_μ and f_2 . Their damping functions are similar to those of Myong and Kasagi (1990). The above functions f_μ and f_2 are listed in Tables 1 and 2, respectively. Since the damping functions f_μ and f_2 of Launder and Sharma (1974) and Chien (1982) required the use of an $\tilde{\epsilon}$ -equation they are not included in Tables 1 and 2.

Methodology

The damping functions of Tables 1 and 2 were compared in terms of their expected behavior in the near-wall region. Their limiting behavior near the wall (for $x_j^+ \leq 0.3$) was approximated using Taylor series expansions about $x_j^+ = 0$ (note for $x_j^+ \leq 0.3$, $1 - \exp(-\beta x^n) = \beta x^n$, and $\text{Re}_t \sim x_j^{+3}$, as $x_j^+ \rightarrow 0$). The DNS data base of Kim et al. (1987) for a channel flow at $\text{Re} = 3300$ (based on half channel width and centerline velocity), was used to compute the expected profiles of f_μ and f_2 of the studied models. Figure 1 presents the distributions of k^+ and ϵ^+ for this DNS data base. Note ϵ^+ peaks at the wall and k^+ at $x_j^+ \approx 15$, well within the buffer layer. In the near-wall region, these distributions are nearly independent of Re , whereas beyond the buffer layer, the length and shape of the distributions are a function of Re . The f_μ -profiles were also compared with the experimental profiles of Patel et al. (1985), high-Reynolds-number pipe flows, boundary-layer flows, and

channel flows, and the DNS profiles of Handler et al. (1989) for channel flow at $\text{Re} = 2215$ (Miner et al., 1991).

Results

The expected behavior of f_μ and f_2 near the wall (for $x_j^+ \leq 0.3$) is summarized in Tables 1 and 2. Of all the studied functions, the f_μ - and f_2 -functions of Lam and Bremhorst (1981), $f_\mu \sim x_j^{+2}$ and $f_2 \sim x_j^{+8}$, and the f_μ function of (Miner et al., 1991), $f_\mu \sim 10^{-1} - 10^{-2}x_j^+$, are the only ones not satisfying the near-wall requirements of $f_\mu \sim x_j^{+1}$ and $f_2 \sim x_j^{+2}$.

Figures 2(a) and 2(b) show, in addition to the experimental f_μ -profiles of Patel et al. (1985) and the DNS profiles of Handler et al. (1989), those computed f_μ -functions of Lam and Bremhorst (1981), Nagano and Tagawa (1990), Myong and Kasagi (1990), Speziale et al. (1992), and Miner et al. (1991). The f_μ -profiles of Patel et al. (1985) and Handler et al. (1989) are essentially identical and independent of Re . Both profiles reach

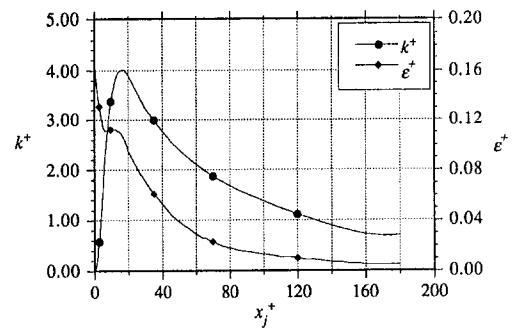


Fig. 1 DNS data of Kim et al. (1987) for a channel flow at $\text{Re} = 3300$: k^+ and ϵ^+

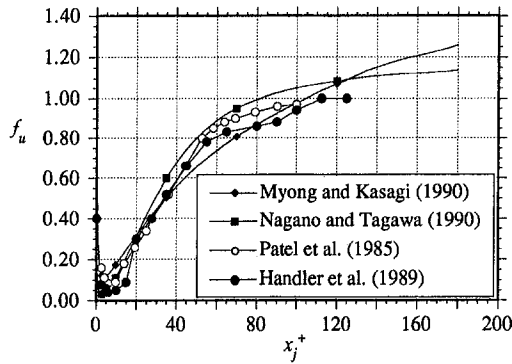


Fig. 2(a)

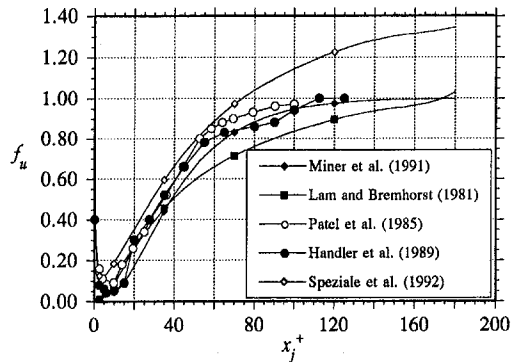


Fig. 2(b)

Fig. 2 Comparison of the damping function f_μ estimated from the experimental data of Patel et al. (1985) and the DNS data of Handler et al. (1989) with those of: (a) Nagano and Tagawa (1990), Myong and Kasagi (1990); and (b) Lam and Bremhorst (1981), Miner et al. (1991), and Speziale et al. (1992).

their upper limit value of unity at $x_j^+ > 100$. Also, as expected, their influential roles are mostly restricted to the near-wall region, that is, for $x_j^+ > 50$, $f_\mu > 0.75$.

For the buffer layer, the calculated f_μ -functions of Lam and Bremhorst (1981), Nagano and Tagawa (1990), and Miner et al. (1991) agree very well with those of Patel et al. (1985) and Handler et al. (1989). However, beyond the buffer layer, the calculated f_μ -functions of Speziale et al. (1992), Nagano and Tagawa (1990), and Myong and Kasagi (1990) exceed the required limit of unity for values of x_j^+ greater than 75, 80, and 105, respectively. Furthermore, beyond the buffer layer the computed f_μ -function of Lam and Bremhorst (1981) does not model very well the f_μ -profiles of Patel et al. (1985) and Handler et al. (1989). Finally, for $x_j^+ > 5$, the calculated f_μ -function of Miner et al. (1991) is the most consistent with the f_μ -profiles of Patel et al. (1985) and Handler et al. (1989).

Figure 3 presents the computed f_2 -profiles of Lam and Bremhorst (1981), Nagano and Tagawa (1990), Myong and Kasagi (1990). The f_2 profile of Speziale et al. (1992) is not presented since it is identical to that of Myong and Kasagi (1990). All functions reach the asymptotic value of unity within the buffer layer. However, those of Nagano and Tagawa (1990) and Myong and Kasagi (1990) show a smoother transition between their wall values and their asymptotic value of unity. Indeed, while the influence of the f_2 -function of Lam and Bremhorst (1981) is mostly confined to the viscous sublayer, those of Nagano and Tagawa (1990) and Myong and Kasagi (1990) extend over the entire near-wall region.

Discussion

The above comparison has shown that, although the calculated f_μ -functions of Speziale et al. (1992), Nagano and Tagawa

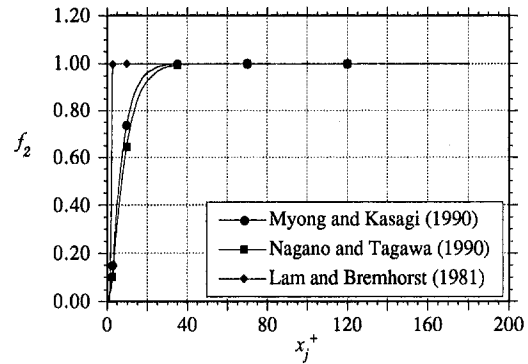


Fig. 3 Computed profiles of the damping function f_2 of Lam and Bremhorst (1981), Nagano and Tagawa (1989), and Myong and Kasagi (1989)

(1990), and Myong and Kasagi (1990) satisfied the near-wall requirements of $f_\mu \sim x_j^{+ -1}$, they exceeded the required limit of unity for values of x_j^+ greater than 75, 80, and 105, respectively. Perhaps this can be explained by examining the expressions defining these functions.

These f_μ -functions are the product of two expressions that solely depend on Re_τ and x_j^+ (see Table 1). According to Nagano and Tagawa (1990) and Myong and Kasagi (1990), the expression which depends on Re_τ represents the change of length scales for the dissipation rate at low and high turbulence Reynolds number. Meanwhile, the expression which depends on x_j^+ represents the ratio of length scales for turbulent momentum transport and for the dissipation rate, that is the wall proximity effect (Speziale et al., 1992; Myong and Kasagi, 1990). As shown in Fig. 4, for all functions, the Re_τ expression predom-

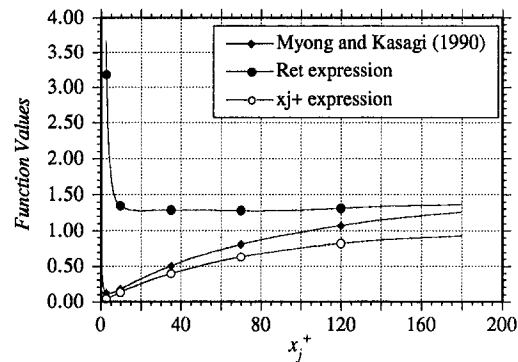


Fig. 4(a)

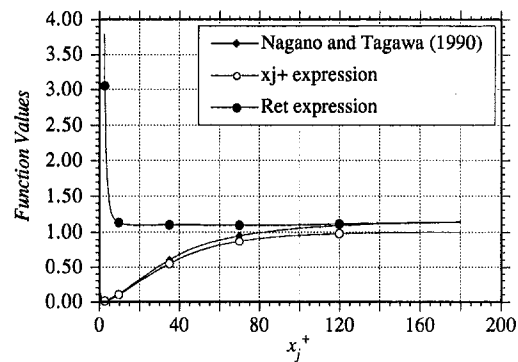


Fig. 4(b)

Fig. 4 Computed profiles of the x_j^+ expression, the Re_τ expression and the resulting f_μ damping function of: (a) Myong and Kasagi (1989) and (b) Nagano and Tagawa (1989)

inated in the viscous sublayer while the x_j^+ expression predominated beyond the viscous sublayer, $x_j^+ > 8$.

A closer examination of Fig. 4 also reveals the f_μ -functions of Nagano and Tagawa (1990), and Myong and Kasagi (1990) exceeded their required limit of unity because their Re_t expressions did not reach their asymptotic value of unity beyond the viscous sublayer region. The same remarks are applicable to the f_μ -function of Speziale et al. (1992), however, for simplicity it was not included in Fig. 4. The former observation was due to the low turbulence levels of the studied channel flow, $Re \sim O(10^2)$, and also because the constants of the Re_t expressions were derived using high turbulence flow arguments. These facts suggest that perhaps the f_μ -functions of Speziale et al. (1992), Nagano and Tagawa (1990), and Myong and Kasagi (1990) are better suited for high turbulence flows, that is, for flows where the turbulence Reynolds number is $O(10^3)$.

Conclusions

The results and analyses of this technical note have shown: (i) the calculated f_μ -function of Lam and Bremhorst (1981) did not meet the required near-wall behavior and did not model very well the experimental results of Patel et al. (1985) or the DNS f_μ -profiles of Handler et al. (1989); (ii) the computed f_μ -functions of Speziale et al. (1992), Nagano and Tagawa (1990), and Myong and Kasagi (1990) satisfied the near-wall requirements of $f_\mu \sim x_j^{+1}$, but exceeded the required limit of unity for values of x_j^+ greater than 75, 80, and 105, respectively; (iii) the f_μ -function of Miner et al. (1991) did not satisfy the near-wall requirements of f_μ but for $x_j^+ > 5$ agreed with the experimental data of Patel et al. (1985) and the DNS data of Handler et al. (1989); (iv) the f_2 -function of Lam and Bremhorst (1981) did not satisfy the near-wall requirement but reached a maximum value of unity within the viscous sublayer; finally, (v) the f_2 -functions of Nagano and Tagawa (1990), Myong and Kasagi (1990), and Speziale et al. (1992) met the required near-wall behavior and reached their required values of unity beyond the buffer layer.

Although the f_μ -function of Miner et al. (1991) did not exhibit the proper behavior for $x_j^+ \leq 0.3$, this exercise has indicated that, of all the studied functions, it is the best suited function for $x_j^+ > 5$. Therefore, the f_μ -function of Miner et al. (1991) with either the f_2 -function of Nagano and Tagawa (1990), Myong and Kasagi (1990), or Speziale et al. (1992) constitute an appropriate set of damping functions for computing turbulent wall-bounded flows without separation, reattachment, or stagnation points.

References

- Chapman, D. R., and Kuhn, G. D., 1986, "The Limiting Behavior of Turbulence Near a Wall," *Journal of Fluid Mechanics*, Vol. 170, pp. 265–292.
- Chien, K.-Y., 1982, "Predictions of Channel and Boundary-Layers Flows with a Low-Reynolds-Number Turbulence Model," *AIAA Journal*, Vol. 20, No. 1, pp. 33–38.
- Handler, R. A., Hendricks, E. W., and Leighton, R. I., 1989, "Low Reynolds Number Calculations of Turbulent Channel Flow: A General Discussion," NRL Memorandum Report 6410, Naval Research Laboratory, Washington, DC.
- Kim, J. P., Moin, P., and Moser, R., 1987, "Turbulent Statistics in Fully Developed Channel Flow at Low Reynolds Number," *Journal of Fluid Mechanics*, Vol. 117, pp. 133–166.
- Lai, Y. G., and So, R. M. C., 1990, "On Near-Wall Turbulent Flow Modeling," *Journal of Fluid Mechanics*, Vol. 221, pp. 641–673.
- Lam, C. K. G., and Bremhorst, K. A., 1981, "Modified Form of the k - ϵ Model for Predicting Wall Turbulence," *ASME JOURNAL OF FLUIDS ENGINEERING*, Vol. 103, pp. 456–460.
- Launder, B. E., and Rodi, W., 1981, "The Turbulent Wall Jet," *Progress in Aeronautical Sciences*, Vol. 19, pp. 81–128.
- Launder, B. E., and Rodi, W., 1983, "The Turbulent Wall Jet—Measurements and Modeling," *Annual Review in Fluid Mechanics*, Vol. 15, pp. 429–459.
- Launder, B. E., and Sharma, B. I., 1974, "Application of the Energy-Dissipation Model of Turbulence to the Calculation of Flow Near a Spinning Disc," *Letters in Heat and Mass Transfer*, Vol. 1, No. 2, pp. 131–138.
- Mansour, N. N., and Shih, T. H., 1989, "Advancements in Turbulence Modeling," *Forum on Turbulent Flows—1989*, San Diego, FED-Vol. 76, W. M. Bower, M. J. Morris, eds., ASME, New York, pp. 129–141.

Mansour, N. N., Kim, J., and Moin, P., 1989, "Near-Wall k - ϵ Turbulence Modeling," *AIAA Journal*, Vol. 27, No. 8, pp. 1068–1073.

Miner, E. W., Swean Jr, T. F., Handler, R. A., and Leighton, R. I., 1991, "Examination of Wall Damping for the k - ϵ Turbulence Model Using Direct Simulations of Turbulent Channel Flow," *International Journal Numerical Methods in Fluids*, Vol. 12, pp. 609–624.

Myong, H. K., and Kasagi, N., 1990, "A New Approach to the Improvement of k - ϵ Turbulence Model for Wall-Bounded Shear Flow," *JSME International Journal*, Series II, Vol. 33, No. 1, pp. 63–72.

Nagano, Y., and Tagawa, M., 1990, "An Improved Model for Boundary Layer Flows," *ASME JOURNAL OF FLUIDS ENGINEERING*, Vol. 112, March pp. 33–39.

Patel, V. C., Rodi, W., and Scheuerer, G., 1985, "Turbulence Models for Near-Wall and Low Reynolds Number Flows: A Review," *AIAA Journal*, Vol. 23, No. 9, pp. 1308–1319.

So, R. M. C., Zhang, H. S., and Speziale, C. G., 1992, "Near-Wall Modeling of the Dissipation Rate Equation," *AIAA Paper 92-0441*, Jan.

Spalart, P. R., 1988, "Direct Simulation of a Turbulent Boundary Layer up to $Re_\theta = 1410$," *Journal of Fluid Mechanics*, Vol. 187, pp. 61–98.

Speziale, C. G., Abid, R., and Anderson, E. C., 1992, "A Critical Evaluation of Two-Equation Models for Near-Wall Turbulence," *AIAA Journal*, Vol. 30, No. 2, pp. 324–331.

Yang, Z., and Shih, T. H., 1991, "A k - ϵ Modeling of Near-Wall Turbulence," *4th International Symposium in Computational Fluid Dynamics, A Collection of Technical Papers*, Vol. 11, Sept. 9–12, University of California, Davis, pp. 1305–1310.

Yang, Z., and Shih, T. H., 1993, "A New Time Scale Based k - ϵ Model for Near-Wall Turbulence," *AIAA Journal*, Vol. 31, No. 7, pp. 1191–1198.

Yang, Z., and Shih, T. H., 1993, "A Galilean and Tensorial Invariant k - ϵ Model for Near-Wall Turbulence," *AIAA Paper 93-3105*, July.

Simultaneous Velocity and Temperature Patterns in the Far Region of a Turbulent Cylinder Wake

A. Vernet,¹ G. A. Kopp,² J. A. Ferré,³ and F. Giralt⁴

1 Introduction

The importance of the instantaneous three-dimensionality in statistically two-dimensional flows is well known going back to the pioneering work of Theodorsen (1952), Townsend (1956), and Grant (1958). Theodorsen predicted that the predominant structure in turbulence should be a horseshoe-like vortex. Townsend and Grant, from an analysis of experimental data in a turbulent wake, found two dominant structures, namely, "mixing jets" and double rollers, which could be different manifestations of the large-scale motions related to Theodorsen's horseshoe-like vortices. Mumford (1983) and Ferré and Giralt (1989a) inferred the presence of such rollers from ensemble-averages of multi-probe measurements of the streamwise velocity component in the far wake of a circular cylinder.

Giralt and Ferré (1993) determined the two-component velocity patterns associated with the average double roller and spanwise vortices in the homogeneous and nonhomogeneous planes of the far wake. These authors inferred from their results

¹ Researcher.

² Researcher.

³ Professor.

⁴ Professor.

Escola Tècnica Superior d'Enginyeria Química, Universitat Rovira i Virgili, Carretera de Salou, s/n 43006 Tarragona, Spain.

Contributed by the Fluids Engineering Division of THE AMERICAN SOCIETY OF MECHANICAL ENGINEERS. Manuscript received by the Fluids Engineering Division June 17, 1996; revised manuscript received November 12, 1996. Associate Technical Editor: D. R. Williams.

inated in the viscous sublayer while the x_j^+ expression predominated beyond the viscous sublayer, $x_j^+ > 8$.

A closer examination of Fig. 4 also reveals the f_μ -functions of Nagano and Tagawa (1990), and Myong and Kasagi (1990) exceeded their required limit of unity because their Re, expressions did not reach their asymptotic value of unity beyond the viscous sublayer region. The same remarks are applicable to the f_μ -function of Speziale et al. (1992), however, for simplicity it was not included in Fig. 4. The former observation was due to the low turbulence levels of the studied channel flow, $Re_\tau \sim O(10^2)$, and also because the constants of the Re, expressions were derived using high turbulence flow arguments. These facts suggest that perhaps the f_μ -functions of Speziale et al. (1992), Nagano and Tagawa (1990), and Myong and Kasagi (1990) are better suited for high turbulence flows, that is, for flows where the turbulence Reynolds number is $O(10^3)$.

Conclusions

The results and analyses of this technical note have shown: (i) the calculated f_μ -function of Lam and Bremhorst (1981) did not meet the required near-wall behavior and did not model very well the experimental results of Patel et al. (1985) or the DNS f_μ -profiles of Handler et al. (1989); (ii) the computed f_μ -functions of Speziale et al. (1992), Nagano and Tagawa (1990), and Myong and Kasagi (1990) satisfied the near-wall requirements of $f_\mu \sim x_j^{+1}$, but exceeded the required limit of unity for values of x_j^+ greater than 75, 80, and 105, respectively; (iii) the f_μ -function of Miner et al. (1991) did not satisfy the near-wall requirements of f_μ but for $x_j^+ > 5$ agreed with the experimental data of Patel et al. (1985) and the DNS data of Handler et al. (1989); (iv) the f_2 -function of Lam and Bremhorst (1981) did not satisfy the near-wall requirement but reached a maximum value of unity within the viscous sublayer; finally, (v) the f_2 -functions of Nagano and Tagawa (1990), Myong and Kasagi (1990), and Speziale et al. (1992) met the required near-wall behavior and reached their required values of unity beyond the buffer layer.

Although the f_μ -function of Miner et al. (1991) did not exhibit the proper behavior for $x_j^+ \leq 0.3$, this exercise has indicated that, of all the studied functions, it is the best suited function for $x_j^+ > 5$. Therefore, the f_μ -function of Miner et al. (1991) with either the f_2 -function of Nagano and Tagawa (1990), Myong and Kasagi (1990), or Speziale et al. (1992) constitute an appropriate set of damping functions for computing turbulent wall-bounded flows without separation, reattachment, or stagnation points.

References

- Chapman, D. R., and Kuhn, G. D., 1986, "The Limiting Behavior of Turbulence Near a Wall," *Journal of Fluid Mechanics*, Vol. 170, pp. 265–292.
- Chien, K.-Y., 1982, "Predictions of Channel and Boundary-Layers Flows with a Low-Reynolds-Number Turbulence Model," *AIAA Journal*, Vol. 20, No. 1, pp. 33–38.
- Handler, R. A., Hendricks, E. W., and Leighton, R. I., 1989, "Low Reynolds Number Calculations of Turbulent Channel Flow: A General Discussion," NRL Memorandum Report 6410, Naval Research Laboratory, Washington, DC.
- Kim, J. P., Moin, P., and Moser, R., 1987, "Turbulent Statistics in Fully Developed Channel Flow at Low Reynolds Number," *Journal of Fluid Mechanics*, Vol. 117, pp. 133–166.
- Lai, Y. G., and So, R. M. C., 1990, "On Near-Wall Turbulent Flow Modeling," *Journal of Fluid Mechanics*, Vol. 221, pp. 641–673.
- Lam, C. K. G., and Bremhorst, K. A., 1981, "Modified Form of the $k-\epsilon$ Model for Predicting Wall Turbulence," *ASME JOURNAL OF FLUIDS ENGINEERING*, Vol. 103, pp. 456–460.
- Launder, B. E., and Rodi, W., 1981, "The Turbulent Wall Jet," *Progress in Aeronautical Sciences*, Vol. 19, pp. 81–128.
- Launder, B. E., and Rodi, W., 1983, "The Turbulent Wall Jet—Measurements and Modeling," *Annual Review in Fluid Mechanics*, Vol. 15, pp. 429–459.
- Launder, B. E., and Sharma, B. I., 1974, "Application of the Energy-Dissipation Model of Turbulence to the Calculation of Flow Near a Spinning Disc," *Letters in Heat and Mass Transfer*, Vol. 1, No. 2, pp. 131–138.
- Mansour, N. N., and Shih, T. H., 1989, "Advancements in Turbulence Modeling," *Forum on Turbulent Flows—1989*, San Diego, FED-Vol. 76, W. M. Bower, M. J. Morris, eds., ASME, New York, pp. 129–141.

Mansour, N. N., Kim, J., and Moin, P., 1989, "Near-Wall $k-\epsilon$ Turbulence Modeling," *AIAA Journal*, Vol. 27, No. 8, pp. 1068–1073.

Miner, E. W., Swean Jr, T. F., Handler, R. A., and Leighton, R. I., 1991, "Examination of Wall Damping for the $k-\epsilon$ Turbulence Model Using Direct Simulations of Turbulent Channel Flow," *International Journal Numerical Methods in Fluids*, Vol. 12, pp. 609–624.

Myong, H. K., and Kasagi, N., 1990, "A New Approach to the Improvement of $k-\epsilon$ Turbulence Model for Wall-Bounded Shear Flow," *JSME International Journal*, Series II, Vol. 33, No. 1, pp. 63–72.

Nagano, Y., and Tagawa, M., 1990, "An Improved Model for Boundary Layer Flows," *ASME JOURNAL OF FLUIDS ENGINEERING*, Vol. 112, March pp. 33–39.

Patel, V. C., Rodi, W., and Scheuerer, G., 1985, "Turbulence Models for Near-Wall and Low Reynolds Number Flows: A Review," *AIAA Journal*, Vol. 23, No. 9, pp. 1308–1319.

So, R. M. C., Zhang, H. S., and Speziale, C. G., 1992, "Near-Wall Modeling of the Dissipation Rate Equation," *AIAA Paper 92-0441*, Jan.

Spalart, P. R., 1988, "Direct Simulation of a Turbulent Boundary Layer up to $Re_\tau = 1410$," *Journal of Fluid Mechanics*, Vol. 187, pp. 61–98.

Speziale, C. G., Abid, R., and Anderson, E. C., 1992, "A Critical Evaluation of Two-Equation Models for Near-Wall Turbulence," *AIAA Journal*, Vol. 30, No. 2, pp. 324–331.

Yang, Z., and Shih, T. H., 1991, "A $k-\epsilon$ Modeling of Near-Wall Turbulence," *4th International Symposium in Computational Fluid Dynamics, A Collection of Technical Papers*, Vol. 11, Sept. 9–12, University of California, Davis, pp. 1305–1310.

Yang, Z., and Shih, T. H., 1993, "A New Time Scale Based $k-\epsilon$ Model for Near-Wall Turbulence," *AIAA Journal*, Vol. 31, No. 7, pp. 1191–1198.

Yang, Z., and Shih, T. H., 1993, "A Galilean and Tensorial Invariant $k-\epsilon$ Model for Near-Wall Turbulence," *AIAA Paper 93-3105*, July.

Simultaneous Velocity and Temperature Patterns in the Far Region of a Turbulent Cylinder Wake

A. Vernet,¹ G. A. Kopp,² J. A. Ferré,³ and F. Giralt⁴

1 Introduction

The importance of the instantaneous three-dimensionality in statistically two-dimensional flows is well known going back to the pioneering work of Theodorsen (1952), Townsend (1956), and Grant (1958). Theodorsen predicted that the predominant structure in turbulence should be a horseshoe-like vortex. Townsend and Grant, from an analysis of experimental data in a turbulent wake, found two dominant structures, namely, "mixing jets" and double rollers, which could be different manifestations of the large-scale motions related to Theodorsen's horseshoe-like vortices. Mumford (1983) and Ferré and Giralt (1989a) inferred the presence of such rollers from ensemble-averages of multi-probe measurements of the streamwise velocity component in the far wake of a circular cylinder.

Giralt and Ferré (1993) determined the two-component velocity patterns associated with the average double roller and spanwise vortices in the homogeneous and nonhomogeneous planes of the far wake. These authors inferred from their results

¹ Researcher.

² Researcher.

³ Professor.

⁴ Professor.

Escola Tècnica Superior d'Enginyeria Química, Universitat Rovira i Virgili, Carrer de Salou, s/n 43006 Tarragona, Spain.

Contributed by the Fluids Engineering Division of THE AMERICAN SOCIETY OF MECHANICAL ENGINEERS. Manuscript received by the Fluids Engineering Division June 17, 1996; revised manuscript received November 12, 1996. Associate Technical Editor: D. R. Williams.

that the temperature patterns previously reported by Ferré and Giralt (1989*b*), which were consistent with the multi-point temperature correlations determined by LaRue and Libby (1974) in a passively-heated wake, were the average thermal footprints of the double-roller eddies. However, there is no conclusive experimental evidence in the literature as to how the velocity and temperature patterns reported previously are related.

In the present analysis, temperature and two-components of the instantaneous velocity vector are measured simultaneously at several locations spanning the homogeneous direction of the wake to determine the relationship between the coherent motions and the thermal field in the far wake. Evidence is given that Grant's "mixing jets" and double rollers are really different aspects of the same average structure postulated by Theodorsen.

2 Details of the Experiments and Analysis of Data

A cylinder of diameter $D = 15$ mm, fitted with an electrical resistance, was placed in the open return wind tunnel situated in the turbulence laboratory of the Universitat Rovira i Virgili. This tunnel has a test section 60×60 cm square by 3 m long and a freestream turbulence level of about 0.1 percent. The cylinder was mounted through holes in the tunnel walls and had an aspect ratio of 40. The electrical resistance provided a maximum temperature excess of 2.0 K at the measurement location of $150D$. The freestream velocity was $U_o = 10$ m/s, so that the Reynolds number based on the cylinder diameter was 9700.

A rake of 5 X -wires and 6 resistance thermometers (i.e., cold-wires) were positioned in the horizontal ($x - z$) plane. All signals were low-pass filtered at 2 kHz and sampled at 5 kHz per channel for 40 s using a 12 bit A/D converter. The X -wires and the cold-wires were alternated so that simultaneous (in time) temperature (θ) and velocity patterns could be identified. The rake was located in the upper half of the wake at $y/l_o = 1$ at $x/D = 150$, where x is the streamwise direction (u -velocity component), y the lateral direction (v -velocity component), and $l_o = 60$ mm is the location where the mean velocity defect is half the maximum value at this streamwise location. The spanwise coordinate z (w -velocity component) is parallel to the cylinder axis. The locations of the cold-wires and X -wires were $z/l_o = \pm 0.25; \pm 0.75; \pm 1.25$ and $0.00; \pm 0.50; \pm 1.00$, respectively. The X -wires were positioned so that either θ , u and v or θ , u and w could be simultaneously measured.

Two points should be emphasized. First, the temperature and velocity measurements are simultaneous in time, not in space, with adjacent cold and X -wires separated by $0.25l_o$ (15 mm). Second, in the plane of measurement ($y/l_o = 1$) the intermittency factor is about 0.95 and, thus, most of the velocity and temperature fluctuations are turbulent fluctuations.

The pattern-recognition (PR) technique used to obtain ensemble-averages from the instantaneous fluctuating velocity or temperature signals is described by Ferré and Giralt (1989*a*, *b*). Fluctuations are calculated by subtracting from each signal its mean value. In the present study a hot-to-cold temperature transition (see Fig. 3 of Ferré and Giralt, 1989*b*) has been used as the initial template for temperature pattern recognition.

Briefly, the pattern-recognition procedure is as follows. An initial template is cross-correlated with the recorded data and the points where the cross-correlation coefficient attains a maximum, and is above some threshold level, identify the appearance of individual events that are similar to the template. These events are then ensemble-averaged. In order to eliminate the bias introduced by the selection of the template, this ensemble-average is used as the new template and the procedure is repeated. The procedure is continued until the resulting ensemble-average is equal to the penultimate template (i.e., the penultimate ensemble-average). In this way, by the process of iteration, the bias of the initial template is removed from the analysis. Then, at the same locations within the recorded data files where

temperatures are ensemble-averaged, velocities and correlations are also averaged. In this way, velocities are "conditionally sampled" based upon temperature information only, and the educed average velocity and correlation patterns correspond unambiguously to those for temperature.

The modified PR technique of Kopp et al. (1997), which uses the eigenvectors from proper orthogonal decomposition (POD) as initial templates, is not the best choice to analyze the horizontal (homogeneous) plane data because in this case we want to obtain conditionally sampled velocities based on prescribed temperature patterns.

3 Results and Discussion

The ensemble-average of the temperature fluctuations, $\langle \theta \rangle / \theta'$, corresponding to rapid hot-to-cold temperature transitions is shown in Fig. 1, where $\theta' = 0.35$ K is the rms value of the temperature fluctuations at $y/l_o = 1.0$. In this and following figures $Z^* = z/l_o$ and $X^* = -U_o t/l_o$, with flow moving from left to right. More than 900 temperature events were selected for the average of Fig. 1, which accounts for 45 percent of the data recorded. At $Z^* = 0$ the average temperature pattern is characterized by a progressive rise in temperature followed by a steep hot-to-cold transition. Results also show that the hotter spot (hotter than the average) is surrounded by colder (colder than the average) fluid motions, both upstream and also in the spanwise direction.

Figure 2 shows the resulting ensemble-averaged $u + w$ velocity fluctuations associated with the temperature data contributing to Fig. 1. It is observed that a double roller configuration in the velocity field is associated with the hot-to-cold transition in the temperature field. This velocity pattern is similar to that determined by Giralt and Ferré (1993) at $x/D = 420$ in an unheated wake using PR on velocity data only. It is observed from Figs. 1 and 2 that the hotter temperatures are located in the centerplane of the double roller and are associated with negative streamwise velocity fluctuations, i.e., fluid motions with a deficit of momentum. Colder fluid is associated with positive streamwise velocity fluctuations, i.e., fluid motions with an excess of momentum. These results are consistent with the single point correlations of Fabris (1979) who found that the correlation between u and θ is negative in the upper half of the wake. It is important to note again that these structures are nearly fully turbulent since the intermittency factor at $y/l_o = 1$ is about 0.95 and, therefore, the temperature of the colder spot in Fig. 1 is higher than the ambient temperature of the potential flow.

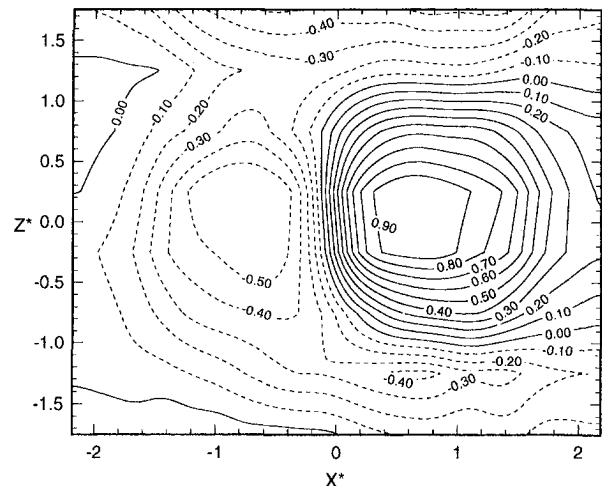


Fig. 1 Ensemble-average of the temperature fluctuations, $\langle \theta \rangle / \theta'$, associated with hot-to-cold transitions in the wake

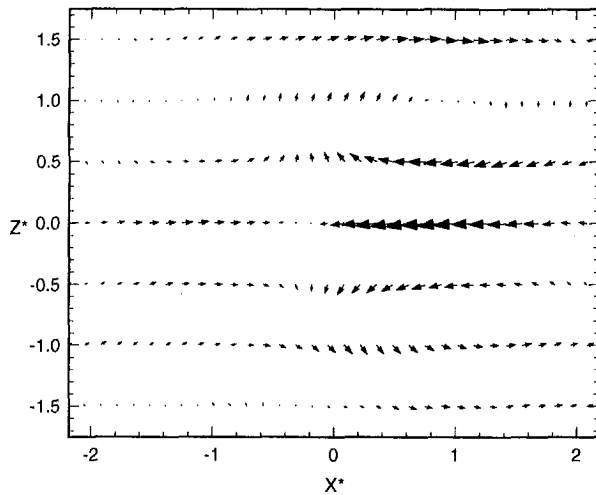


Fig. 2 Ensemble-average of the $u + w$ velocity fluctuations corresponding to events contributing to Fig. 1. The peak values of $\langle u \rangle / U_0$ and $\langle w \rangle / U_0$ are 0.0246 and 0.0107, respectively.

A second important observation from Fig. 2 is the existence of a critical point at $X^* = -0.2$ and $Z^* = 0$. This critical point, which is a saddle point according to the classification of Perry and Chong (1987), coincides with the region of maximum rate of change of temperature from hotter to colder regions of the average thermal structure. It is likely that the saddle point of Fig. 2 is the horizontal representation of the saddle point identified by Antonia et al. (1987) in their vertical plane measurements. These authors also used the temperature field in the horizontal plane to identify the large-scale structure of the far wake.

This saddle point can also be observed in the ensemble average of the velocity field reported by Giralt and Ferré (1993, see Fig. 3 of their paper for the horizontal plane), but is significantly smeared. The present "conditional averaging" technique identifies the sharp hotter-to-colder temperature transition at $y/l_0 = 1$, and because the saddle points occur at this sharp temperature transition, they are well aligned. In the work of Giralt and Ferré (1993) alignment is based on events in the velocity field. Since the double rollers they identified vary in size, the saddle point (which occurs upstream of this structure) is smeared by the process of ensemble-averaging.

The analysis of the θ , u , and v data obtained with the X -wires positioned at the same Z^* locations, but rotated 90 deg from the horizontal plane, is summarized in Fig. 3. This figure only includes the "conditionally averaged" v -velocity fluctuations

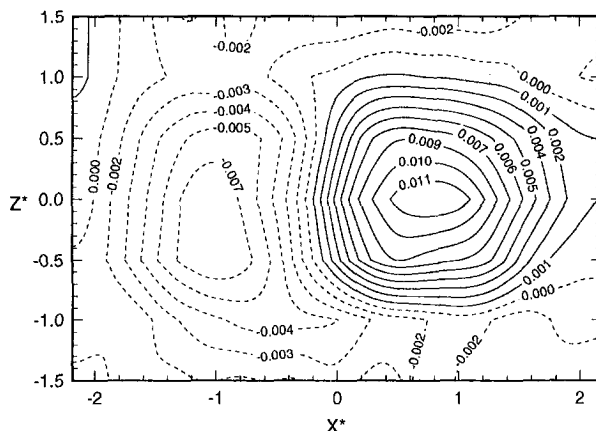


Fig. 3 Ensemble-average of the lateral velocity fluctuations, $\langle v \rangle / U_0$, corresponding to events contributing to Fig. 1

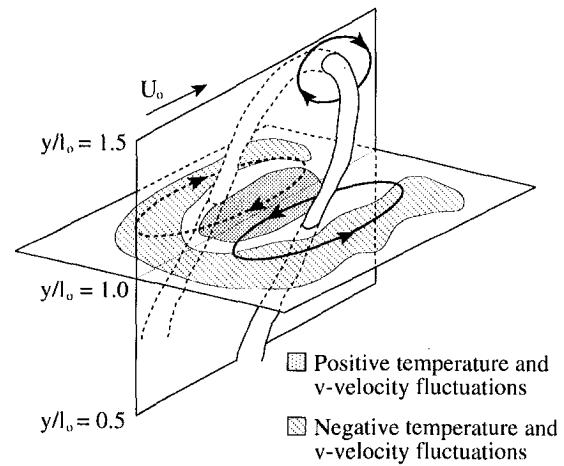


Fig. 4 A sketch of the horseshoe-like eddy, with the current results from the horizontal plane superimposed

associated with the hot-to-cold transition of Fig. 1 because the θ and u results are identical to those depicted in Figs. 1 and 2. A comparison of Figs. 1 and 3 clearly shows that the patterns of the ensemble-averaged temperature and lateral velocity fluctuations have essentially the same topology. The hotter spot in the central portion of the double roller structure is associated with positive (outward) lateral velocity fluctuations, while the surrounding regions of colder fluid motions have negative (inward) lateral velocity fluctuations. These signs correspond to the upper half of the wake, where present data were measured, and are consistent with the single point correlations of v and θ found by Fabris (1979). These v -velocity fluctuations are also consistent with the saddle points observed by Antonia et al. (1987) in the vertical plane.

Theodorsen (1952) postulated that the predominant structure in turbulence is a horseshoe vortex. Ferré and Giralt (1989a, b) found evidence, based on separate temperature and velocity measurements in both the horizontal and vertical planes, that the average structure related to the entrainment process was indeed a horseshoe shaped eddy with its "legs" (i.e., the "double roller eddies") shear aligned and connected at the top with spanwise vorticity (called "spanwise vortices"). Figure 4 includes a sketch of the horseshoe vortex tube described by Theodorsen, as well as the associated recirculating motions and temperature patterns reported in Figs. 1–3, respectively. Figure 4 illustrates how the present results and those of Antonia et al. (1987) and Giralt and Ferré (1993), represented by a slice through the vertical centerplane, are consistent with the existence of such a vortex. It appears that Grant's (1958) "mixing jets" and double rollers are different aspects of the same structure because of the strong outward v -velocities in the center of the horseshoe, represented by the dotted patch between the two "legs." In other words, the outward lateral velocity fluctuations in the centerplane of the double roller structure are these "mixing jets."

Figure 5 shows the ensemble-averaged shear stress, $\langle uv \rangle / \bar{u} \bar{v}_{\max}$, in the horizontal plane that corresponds to the temperature events contributing to the pattern of Fig. 1, where $\bar{u} \bar{v}_{\max} = -0.0303 \text{ m}^2/\text{s}^2$ is the maximum value of the (time-averaged) Reynolds shear stress at $x/D = 150$. The highest shear stress levels occur in the centerplane of the double roller eddies where both the coherent streamwise and lateral velocity fluctuations have, respectively, the largest negative and positive magnitudes (Figs. 2 and 3) and the temperature fluctuations have the largest magnitude (Fig. 1). Fabris (1983) showed that the triple correlation $uv\theta$ is negative in the upper half of the wake, consistent with the present results. The maximum negative value of this triple-correlation occurs in the centerplane of the double roller structure. (Note that $uv\theta$ has not been measured simultane-

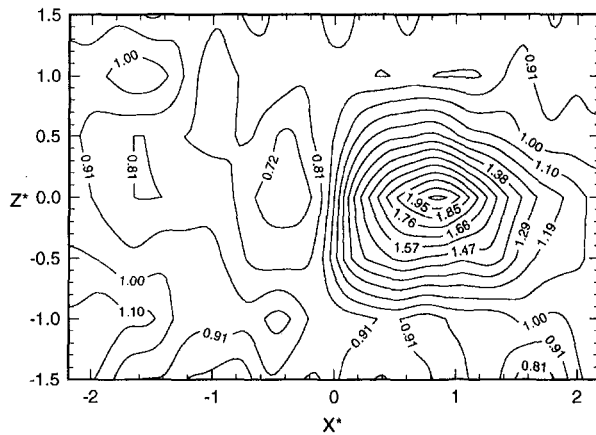


Fig. 5 Ensemble-average of the shear stress, $\langle uv \rangle / \overline{uv}_{max}$, corresponding to events contributing to Fig. 1

ously in space. However, because the temperature and velocity probes are alternated in the rake, and the measurements are simultaneous in time, this result can be inferred.)

In addition, the $\langle uv \rangle$ isocontours occupy a narrower span than the hotter (positive) temperature fluctuations and are found to be highly three-dimensional. Clearly, the double roller (horseshoe) structures are responsible for maintaining the correlation between the streamwise and lateral velocity fluctuations, the correlation being largest in the centerplane of the structure.

4 Conclusions

The pattern recognition analysis of simultaneous temperature and velocity measurements made in the horizontal (homogeneous) plane in the far region of plane turbulent wake generated by a passively-heated circular cylinder confirm that the average large-scale dominant structure in this flow is a double roller eddy, with backflow in the center. The structure is also characterized by a strong outward lateral motion that is associated with hotter fluid and contributing significantly to the lateral spreading of the heated wake. These rolling and outwardly moving motions of hotter fluid are followed by weaker inward motions of colder fluid. The two regions are separated by a rapid hot-to-cold transition in the temperature field and by a saddle point in the velocity field. The correlation between the streamwise and lateral velocity fluctuations is largest in the centerplane of the horseshoe-like structures. Thus, Grant's mixing jets and double roller structures are different aspects of the same structure, a horseshoe shaped vortex.

Acknowledgments

This work was financially supported by DGICYT project PB91-0551 and NATO Collaborative Research Grant 960142. The hardware and a portion of the software were supported by PB93-0656-C02-01. Computer support was granted by the Servei de Tecnologia Química of the Universitat Rovira i Virgili. G. A. Kopp was financially supported by NSERC Canada and the Universitat Rovira i Virgili.

References

- Antonia, R. A., Browne, L. W. B., Bisset, D. K., and Fulachier, L., 1987, "A Description of the Organized Motion in the Turbulent far Wake of a Cylinder at low Reynolds Number," *Journal of Fluid Mechanics*, Vol. 184, pp. 423-444.
- Fabris, G., 1979, "Conditional Sampling Study of the Turbulent Wake of a Cylinder. Part 1," *Journal of Fluid Mechanics*, Vol. 94, pp. 673-709.
- Fabris, G., 1983, "Third-Order Conditional Transport Correlations in the Two-Dimensional Turbulent Wake," *Physics of Fluids*, Vol. 26, pp. 422-428.
- Ferré, J. A., and Giralt, F., 1989a, "Pattern-Recognition Analysis of the Velocity Field in Plane Turbulent Wakes," *Journal of Fluid Mechanics*, Vol. 198, pp. 27-64.

Ferré, J. A., and Giralt, F., 1989b, "Some Topological Features of the Entrainment Process in a Heated Turbulent Wake," *Journal of Fluid Mechanics*, Vol. 198, pp. 65-77.

Giralt, F., and Ferré, J. A., 1993, "Structure and Flow Patterns in Turbulent Wakes," *Physics of Fluids A*, Vol. 5, pp. 1783-1789.

Grant, H. L., 1958, "The Large Eddies of Turbulent Motion," *Journal of Fluid Mechanics*, Vol. 4, pp. 149-190.

Kopp, G. A., Ferré, J. A., and Giralt, F., 1997, "The Use of Pattern Recognition and Proper Orthogonal Decomposition in Identifying the Structure of Fully-Developed Free Turbulence," *ASME JOURNAL OF FLUIDS ENGINEERING*, Vol. 119, published in this issue pp. 289-296.

LaRue, J. C., and Libby, P. A., 1974, "Temperature Fluctuations in the Plane Turbulent Wake," *Physics of Fluids*, Vol. 17, pp. 1956-1967.

Mumford, J. C., 1983, "The Structure of the Large Eddies in Fully Developed Turbulent Shear Flow. Part 2. The Plane Wake," *Journal of Fluid Mechanics*, Vol. 137, pp. 447-456.

Perry, A. E., and Chong, M. S., 1987, "A Description of Eddy Motions and Flow Patterns Using Critical Points," *Annual Review of Fluid Mechanics*, Vol. 19, pp. 125-155.

Theodorsen, T., 1952, "Mechanism of Turbulence," *Proceedings of the 2nd Midwestern Conference of Fluid Mechanics*, Ohio State Univ., Columbus.

Townsend, A. A., 1956, *The Structure of Turbulent Shear Flow*, Cambridge University Press, Cambridge.

The Response of a Turbulent Boundary Layer to a Square Groove

B. R. Pearson,¹ R. Elavarasan,¹ and R. A. Antonia¹

1 Introduction

The d-type rough surface, which is characterized by equally spaced transverse square grooves, has attracted a fair amount of attention recently because of the possibility that a zero pressure gradient boundary layer can be exactly self-preserving on this surface (Rotta, 1962). In such a boundary layer, the magnitude of the skin friction coefficient is independent of x , the streamwise distance. It has been suggested that the use of sparsely spaced square grooves could result in an overall reduction in the total turbulent skin friction drag compared to the smooth wall equivalent (Tani et al., 1988). The current investigation focuses on the effect of just one square groove, on a turbulent boundary layer, with a view to study the interaction between the groove flow and the boundary layer, as well as the way the boundary layer relaxes downstream of the groove. The laser doppler velocimetry (LDV) technique is used for velocity measurements. Accurate measurements of the near-wall mean velocity profile are used to determine the skin friction, c_f . The laser induced fluorescence (LIF) technique is used for visualizing the flow over, and within, the groove.

2 Experimental Setup

The experiments are conducted in a closed circuit constant-head vertical water tunnel. A description of the facility is available in Zhou and Antonia (1992). The test section of the tunnel is made of clear acrylic and is 2 m long and 250 mm square. The single groove (width w = height k = 5 mm) geometry is

¹ Postgraduate Student, Postdoctoral Research Fellow, and Professor, respectively, Department of Mechanical Engineering, University of Newcastle, N. S. W. 2308, Australia.

Contributed by the Fluids Engineering Division of THE AMERICAN SOCIETY OF MECHANICAL ENGINEERS. Manuscript received by the Fluids Engineering Division April 10, 1996; revised manuscript received February 11, 1997. Associate Technical Editor: F. Hussain.

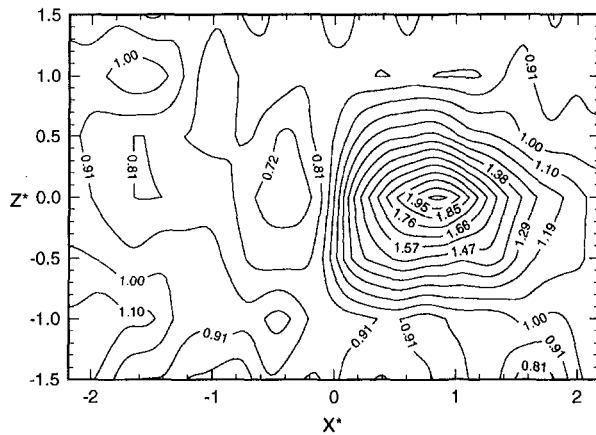


Fig. 5 Ensemble-average of the shear stress, $\langle uv \rangle / \overline{uv}_{max}$, corresponding to events contributing to Fig. 1

ously in space. However, because the temperature and velocity probes are alternated in the rake, and the measurements are simultaneous in time, this result can be inferred.)

In addition, the $\langle uv \rangle$ isocontours occupy a narrower span than the hotter (positive) temperature fluctuations and are found to be highly three-dimensional. Clearly, the double roller (horseshoe) structures are responsible for maintaining the correlation between the streamwise and lateral velocity fluctuations, the correlation being largest in the centerplane of the structure.

4 Conclusions

The pattern recognition analysis of simultaneous temperature and velocity measurements made in the horizontal (homogeneous) plane in the far region of plane turbulent wake generated by a passively-heated circular cylinder confirm that the average large-scale dominant structure in this flow is a double roller eddy, with backflow in the center. The structure is also characterized by a strong outward lateral motion that is associated with hotter fluid and contributing significantly to the lateral spreading of the heated wake. These rolling and outwardly moving motions of hotter fluid are followed by weaker inward motions of colder fluid. The two regions are separated by a rapid hot-to-cold transition in the temperature field and by a saddle point in the velocity field. The correlation between the streamwise and lateral velocity fluctuations is largest in the centerplane of the horseshoe-like structures. Thus, Grant's mixing jets and double roller structures are different aspects of the same structure, a horseshoe shaped vortex.

Acknowledgments

This work was financially supported by DGICYT project PB91-0551 and NATO Collaborative Research Grant 960142. The hardware and a portion of the software were supported by PB93-0656-C02-01. Computer support was granted by the Servei de Tecnologia Química of the Universitat Rovira i Virgili. G. A. Kopp was financially supported by NSERC Canada and the Universitat Rovira i Virgili.

References

- Antonia, R. A., Browne, L. W. B., Bisset, D. K., and Fulachier, L., 1987, "A Description of the Organized Motion in the Turbulent far Wake of a Cylinder at low Reynolds Number," *Journal of Fluid Mechanics*, Vol. 184, pp. 423-444.
- Fabris, G., 1979, "Conditional Sampling Study of the Turbulent Wake of a Cylinder. Part 1," *Journal of Fluid Mechanics*, Vol. 94, pp. 673-709.
- Fabris, G., 1983, "Third-Order Conditional Transport Correlations in the Two-Dimensional Turbulent Wake," *Physics of Fluids*, Vol. 26, pp. 422-428.
- Ferré, J. A., and Giralt, F., 1989a, "Pattern-Recognition Analysis of the Velocity Field in Plane Turbulent Wakes," *Journal of Fluid Mechanics*, Vol. 198, pp. 27-64.

Ferré, J. A., and Giralt, F., 1989b, "Some Topological Features of the Entrainment Process in a Heated Turbulent Wake," *Journal of Fluid Mechanics*, Vol. 198, pp. 65-77.

Giralt, F., and Ferré, J. A., 1993, "Structure and Flow Patterns in Turbulent Wakes," *Physics of Fluids A*, Vol. 5, pp. 1783-1789.

Grant, H. L., 1958, "The Large Eddies of Turbulent Motion," *Journal of Fluid Mechanics*, Vol. 4, pp. 149-190.

Kopp, G. A., Ferré, J. A., and Giralt, F., 1997, "The Use of Pattern Recognition and Proper Orthogonal Decomposition in Identifying the Structure of Fully-Developed Free Turbulence," *ASME JOURNAL OF FLUIDS ENGINEERING*, Vol. 119, published in this issue pp. 289-296.

LaRue, J. C., and Libby, P. A., 1974, "Temperature Fluctuations in the Plane Turbulent Wake," *Physics of Fluids*, Vol. 17, pp. 1956-1967.

Mumford, J. C., 1983, "The Structure of the Large Eddies in Fully Developed Turbulent Shear Flow. Part 2. The Plane Wake," *Journal of Fluid Mechanics*, Vol. 137, pp. 447-456.

Perry, A. E., and Chong, M. S., 1987, "A Description of Eddy Motions and Flow Patterns Using Critical Points," *Annual Review of Fluid Mechanics*, Vol. 19, pp. 125-155.

Theodorsen, T., 1952, "Mechanism of Turbulence," *Proceedings of the 2nd Midwestern Conference of Fluid Mechanics*, Ohio State Univ., Columbus.

Townsend, A. A., 1956, *The Structure of Turbulent Shear Flow*, Cambridge University Press, Cambridge.

The Response of a Turbulent Boundary Layer to a Square Groove

B. R. Pearson,¹ R. Elavarasan,¹ and R. A. Antonia¹

1 Introduction

The d-type rough surface, which is characterized by equally spaced transverse square grooves, has attracted a fair amount of attention recently because of the possibility that a zero pressure gradient boundary layer can be exactly self-preserving on this surface (Rotta, 1962). In such a boundary layer, the magnitude of the skin friction coefficient is independent of x , the streamwise distance. It has been suggested that the use of sparsely spaced square grooves could result in an overall reduction in the total turbulent skin friction drag compared to the smooth wall equivalent (Tani et al., 1988). The current investigation focuses on the effect of just one square groove, on a turbulent boundary layer, with a view to study the interaction between the groove flow and the boundary layer, as well as the way the boundary layer relaxes downstream of the groove. The laser doppler velocimetry (LDV) technique is used for velocity measurements. Accurate measurements of the near-wall mean velocity profile are used to determine the skin friction, c_f . The laser induced fluorescence (LIF) technique is used for visualizing the flow over, and within, the groove.

2 Experimental Setup

The experiments are conducted in a closed circuit constant-head vertical water tunnel. A description of the facility is available in Zhou and Antonia (1992). The test section of the tunnel is made of clear acrylic and is 2 m long and 250 mm square. The single groove (width w = height k = 5 mm) geometry is

¹ Postgraduate Student, Postdoctoral Research Fellow, and Professor, respectively, Department of Mechanical Engineering, University of Newcastle, N. S. W. 2308, Australia.

Contributed by the Fluids Engineering Division of THE AMERICAN SOCIETY OF MECHANICAL ENGINEERS. Manuscript received by the Fluids Engineering Division April 10, 1996; revised manuscript received February 11, 1997. Associate Technical Editor: F. Hussain.

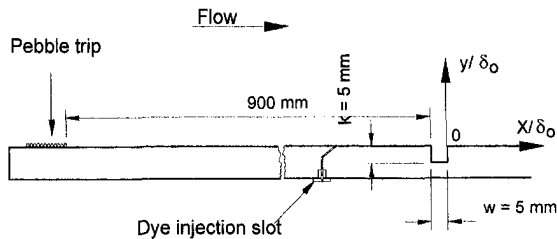


Fig. 1 A schematic of the wall geometry showing the square groove and dye-slot

shown in Fig. 1. A fibre-optic LDV DANTEC system is used in forward scatter mode. Only one-component (green, 514.5 nm wavelength) measurements are made. The LIF technique is used to visualize the near-wall region of the flow over the square groove. The sodium fluorescein solution is injected through a slot, of opening 0.25 mm, located $18w$ distance upstream of the groove (Fig. 1). A light sheet of thickness 0.4 mm, generated from the Ar-ion laser highlights the plane to be viewed. The flow visualizations are filmed with a CCD video camera (25 fps). Further details of the measurement and flow visualization techniques can be obtained from Pearson et al. (1995) and Ching et al. (1995a), respectively.

3 Results

3.1 Flow Visualization Observations. A prominent feature of the flow visualizations ($R_\theta = 700$) is the recirculation of fluid within the groove. There is a significant communication between the flow within the groove and the outer flow (flow above the groove) by means of frequent, though random, outflows from the groove (Fig. 2(a)). The outflow is supplemented by an inflow of fluid from the outer flow region into the groove (Fig. 2(b)) and there are periods where the outer flow skims over

the groove without disturbing the recirculation region inside the groove. The occurrence of outflows and inflows is believed to reflect the response of the groove to large-scale organized motions which are convected in the streamwise direction (Haugen and Dhanak, 1966). These observations support the suggestion of Townes and Sabersky (1966); the initiating mechanism for the outflows and inflows resides within the boundary layer rather than within the groove. An earlier study on a d-type rough surface (Ching et al., 1995a) indicates that the passage of quasi-streamwise vortices is responsible for the interaction of the groove and the outer flow. In order to verify this, the flow is observed in the spanwise ($x - z$) plane. The spanwise view obtained at this location is shown in Fig. 2(c). The figure indicates the presence of low-speed streaks similar in appearance to those over a smooth wall or d-type rough boundary layer (Liu et al., 1966). If the low-speed streaks are formed by the quasi-streamwise vortices, it is plausible that they are responsible for the outflows. Support for the quasi-streamwise vortices is obtained by viewing the flow at 45 deg to the upstream direction (Fig. 2(d)). The mushroom-like structure, which represents the cross-section of the streak in the viewing plane, can be interpreted as the signature of the quasi-streamwise vortices. Ching et al. (1995a) provided some flow visualization evidence in support of this for a d-type rough wall. In their study, rhodamine was injected locally into the groove, while sodium fluorescein was injected just upstream of the groove along a spanwise slot. The passage of the vortices, accompanied by low-speed streaks over the groove, coincided with the rhodamine escaping from the groove.

3.2 LDV Results. The LDV data are taken for $R_\theta = 1320$ at a distance of $10w$ upstream of the groove leading edge; at this station the boundary layer thickness, δ_0 , is 30 mm. The square groove width (w/δ_0) is 0.17. In the near-wall region the LDV traversing system allows \bar{U} to be measured in steps of 0.025 mm. The error in the location of the origin is estimated to be no worse than ± 0.5 wall units. Approximately 5 data

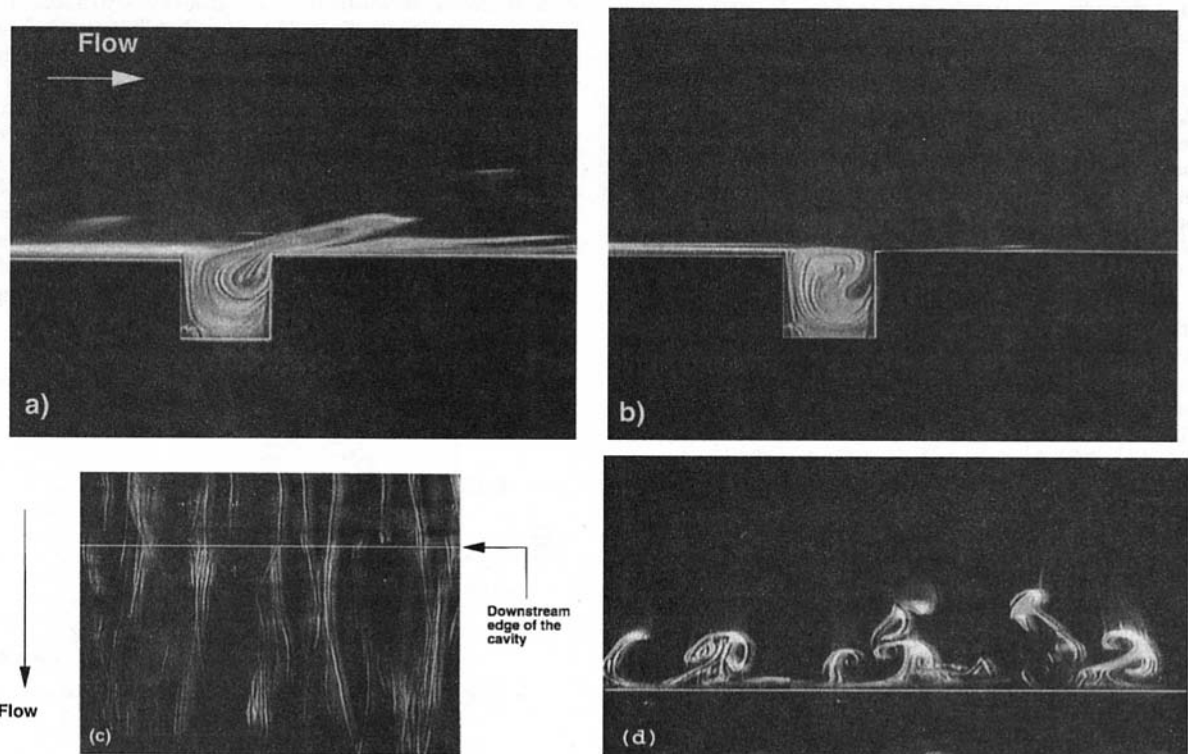


Fig. 2 (a) Typical outflow, (b) typical inflow, (c) view in the ($x - z$) plane showing the low-speed streaks downstream of the groove, (d) view in the ($x - z$) plane at 45 deg to the upstream direction. The mushroom-like structures are interpreted as signatures of the quasi-streamwise vortices. The smearing above each of these structures is interpreted as a low-speed streak. $R_\theta = 700$.

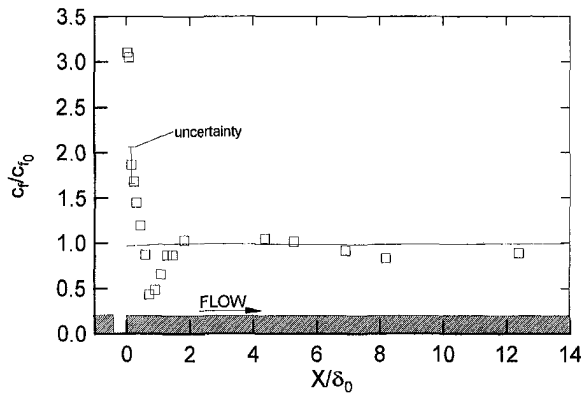


Fig. 3 Streamwise development of the skin friction ratio, c_f/c_{f0} , $R_\theta = 1320$ (\square , LDV; —, $R_\theta \approx 1500$, Choi and Fujisawa, 1993; maximum, $\pm 10\%$ at 95% confidence)

points are available to resolve the viscous sublayer to give a good estimate of $\partial \bar{U} / \partial y$ (typically, the correlation coefficient is 0.999 for 95 percent confidence) at the wall. The skin friction, $c_f (= 2u_\tau^2 / \bar{U}_1)$, is inferred from $\partial \bar{U}' / y \approx u_\tau^2 / \nu$; this approximation applies in the range $y^+ \leq 5$.

The variation of c_f is shown in Fig. 3. Also included are the data of Choi and Fujisawa (1993) for a similar R_θ (≈ 1500). As in the laminar case (Pearson et al., 1995), a sharp rise in c_f is observed at the downstream edge and it is attributed to the local intense favorable pressure gradient that emanates from the downstream stagnation edge of the groove. This sharp rise is followed by a sudden decrease and, unlike the laminar case, there is an undershoot in c_f/c_{f0} at about $x/\delta_0 \approx 1$. Following this undershoot, c_f/c_{f0} slowly relaxes back toward the non-perturbed value in an oscillatory manner. A qualitatively similar behavior is also observed for a turbulent boundary layer subjected to a small rate of suction through a slot (Merigaud, 1995) or through a short porous strip (Antonia et al., 1995). The reason for the undershoot is not known at this stage. The undershoot in c_f/c_{f0} is not apparent in the results of Choi and Fujisawa (1993). Their data exhibit none of the features displayed in the present data. It is most probably due to their use of the Clauser-chart method for estimating c_f . For $R_\theta = 1500$, the Reynolds number is sufficiently small to question the existence of a log region in the mean velocity profile and the Clauser-chart technique is therefore inaccurate for determining the wall shear stress. Evidence for the lack of a substantial log-region, and hence poor accuracy in using the Clauser-chart for estimating c_f , is the absence of a plateau region when $y^+ d\bar{U}^+ / dy^+$ is plotted against y^+ (Ching et al., 1995b) for $R_\theta = 1316$. Also for this type of flow, the inner region is recovering from the wall perturbation and the assumption of equilibrium, especially in the near-wall region, is questionable.

Figure 4 shows the distribution of the mean velocity at various downstream locations. The profiles have been nondimensionalized by the local value of the friction velocity (u_τ) and length (ν/u_τ). The figure includes a smooth wall experimental reference from the same facility for the same flow conditions ($R_\theta = 1316$; Ching et al., 1995b). Relative to the reference smooth wall profile, there is a noticeable downward shift in the mean velocity profiles at values of x for which c_f/c_{f0} overshoots (for example, $x/\delta_0 = 0.13$). The downstream relaxation of the mean velocity profile is unlikely to be complete by the last measurement station ($x/\delta_0 = 6.33$).

Figure 5 shows the development of the longitudinal rms turbulence intensity, u' . The intensity has been nondimensionalized with the free-stream velocity \bar{U}_1 to avoid any misinterpretation of the data due to the lack of near-wall equilibrium. Included is a smooth wall reference from the experiment of Ching et al. (1995b, $R_\theta = 1316$). For the u' profile immediately downstream of the groove, the peak value of u' is increased

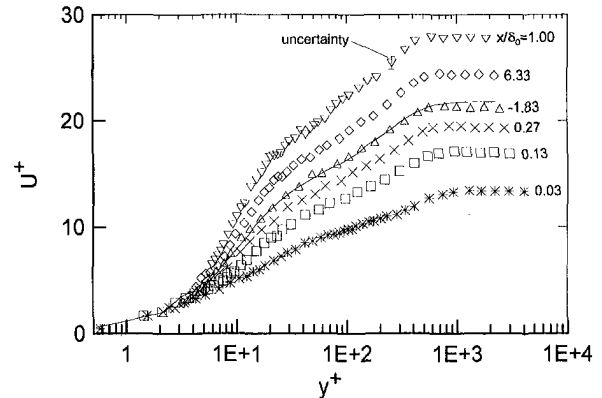


Fig. 4 Effect of the groove on the mean streamwise velocity, \bar{U} , $R_\theta = 1320$ (Δ , $x/\delta_0 = -1.83$; $*$, $x/\delta_0 = 0.03$; \square , $x/\delta_0 = 0.13$; \times , $x/\delta_0 = 0.27$; ∇ , $x/\delta_0 = 1.00$; \diamond , $x/\delta_0 = 6.33$; —, LDV $R_\theta = 1316$, Ching et al., 1995b; $\pm 2\%$ at 95% confidence)

and is located further from the wall compared to the undisturbed smooth wall value (for example, $x/\delta_0 = 0.07$). In the region where c_f/c_{f0} is smaller than unity (for example, $x/\delta_0 = 1.00$), the peak value of u' is decreased compared to the undisturbed smooth wall value. The effect of the groove is confined to the near-wall region ($y/\delta_0 < 0.1$). This is not surprising since $w/\delta_0 = 0.17$. For the outer layer to be affected, or for the outer layer to affect the near-wall region, w/δ_0 should be ≈ 1.0 (Haugen and Dhanak, 1966). Downstream, the u' distribution returns slowly to the smooth wall profile.

4 Concluding Remarks

The effect of the square groove on a turbulent boundary layer is to impulsively perturb the no-slip boundary condition at the wall. The wall shear stress is reliably inferred from LDV near-wall mean velocity measurements. There is a sharp rise in c_f/c_{f0} immediately downstream of the groove due to a local intense favorable pressure gradient. The c_f/c_{f0} distribution subsequently falls below unity before slowly relaxing to the non-perturbed state in an oscillatory manner.

Momentum exchange ensures a fuller and almost uniform turbulent mean velocity profile compared to a laminar profile. To reduce the skin friction drag in a turbulent boundary layer, a modification of the processes that lead to momentum exchange is required. Quasi-streamwise vortices are assumed responsible for the near-wall activities that cause the production of the Reynolds shear stress. In fact, it is accepted that regions of high skin friction are associated with sweeps and the splatting due

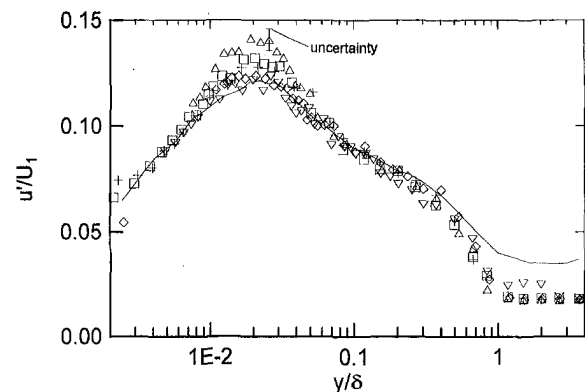


Fig. 5 Effect of the groove on u' / \bar{U}_1 , (Δ , $x/\delta_0 = 0.07$; \square , $x/\delta_0 = 0.13$; \times , $x/\delta_0 = 0.27$; ∇ , $x/\delta_0 = 1.00$; \diamond , $x/\delta_0 = 11.33$; —, LDV $R_\theta = 1316$, Ching et al., 1995b; $\pm 3\%$ at 95% confidence)

to the downwash of the quasi-streamwise vortices. These vortices are also responsible for the lifting of the low-speed streaks away from the wall (Robinson, 1991).

Flow visualizations confirm that there exists an important communication via out-flows and inflows between the groove and the overlying shear layer. When an outflow occurs from the groove, and with it a corresponding inflow along the span of the groove, the turbulent structures are modified to some extent. The strength of these vortices do not need to be changed, only their relative locations and interaction with the wall need to be modified. This, in turn, temporarily suspends the production of new quasi-streamwise vortices and the near-wall activity, which leads to momentum exchange, is diminished relative to the nonperturbed smooth wall. Consequently, the ratio c_f/c_{f0} falls below unity.

Acknowledgment

The support of the Australian Research Council is gratefully acknowledged.

References

- Antonia, R. A., Zhu, Y., and Sokolov, M., 1995, "Effect of Concentrated Wall Suction on a Turbulent Boundary Layer," *Physics of Fluids*, Vol. 7, pp. 2465–2474.
- Ching, C. Y., Elavarasan, R., and Antonia, R. A., 1995a, "Visualization of Near-Wall Region in a Turbulent Boundary Layer Over a d-Type Roughness," J. Crowder, ed., *Flow Visualization VII*, New York, Begell House, pp. 398–401.
- Ching, C. Y., Djenidi, L., and Antonia, R. A., 1995b, "Low Reynolds Number Effects in a Turbulent Boundary Layer," *Experiments in Fluids*, Vol. 19, pp. 61–68.
- Choi, K.-S. and Fujisawa, N., 1993, "Possibility of Drag Reduction Using d-Type Roughness," K. Krishna Prasad, ed., *Further Developments in Turbulence Management*, Dordrecht, Kluwer Academic Publishers, pp. 315–324.
- Haugen, R. L., and Dhanak, A. M., 1966, "Momentum Transfer in Turbulent Separated Flow Past a Rectangular Cavity," *ASME Journal of Applied Mechanics*, Vol. 33, pp. 641–646.
- Liu, C. K., Kline, S. J., and Johnston, J. P., 1966, "An Experimental Study of Turbulent Boundary Layers on Rough Walls," Report No. MD-15, Thermoscience Division, Department of Mechanical Engineering, Stanford University.
- Merigaud, E., "Structure de la couche limite turbulente en presence d'aspiration parietale localisee," Ph.D. thesis, Institut de Mecanique Statistique de la Turbulence, Marseille.
- Pearson, B. R., Elavarasan, R., and Antonia, R. A., 1995, "The Effect of a Square Groove on a Boundary Layer," *Proceedings 12th Australasian Fluid Mechanics Conference*, Sydney, pp. 477–480.
- Robinson, S. K., 1991, "The Kinematics of Turbulent Boundary Layer Structure," Report TM 103859, NASA-Langley.
- Rotta, J. C., 1962, "The Turbulent Boundary Layer in Incompressible Flow," A. Ferrie, D. Kucheman and L. H. G. Stone, eds., *Progress in Aeronautical Science*, Oxford, Pergamon Press, pp. 1–220.
- Tani, I., Munakata, H., Matsumoto, A., and Abe, K., 1988, "Turbulence Management by Groove Roughness," H. W. Liepmann and R. Narasimha, eds., *Turbulence Management and Relaminarisation*, Berlin, Springer-Verlag, pp. 161–172.
- Townes, H. W., and Sabersky, R. H., 1966, "Experiments on the Flow Over a Rough Surface," *International Journal of Heat and Mass Transfer*, Vol. 9, pp. 729–738.
- Zhou, Y., and Antonia, R. A., 1992, "Convection Velocity Measurements in a Cylinder Wake," *Experiments in Fluids*, Vol. 13, pp. 63–70.

Effect of Roughness Aspect Ratio on the "Bursting" Period in a Fully Turbulent Channel Flow

L. Labraga,¹ A. Mazouz,¹ S. Demare,¹ and C. Tournier¹

Introduction

Much attention has been given to the structure of the turbulent boundary layer over a smooth wall. By contrast, the turbulent

¹ Lecturer, Lecturer, Doctorate Student and Professor, respectively, Laboratoire de Mecanique des Fluides, Universite' de Valenciennes, 59326 Valenciennes Cedex, France.

Contributed by the Fluids Engineering Division of THE AMERICAN SOCIETY OF MECHANICAL ENGINEERS. Manuscript received by the Fluids Engineering Division April 8, 1996; revised manuscript received February 25, 1997. Associate Technical Editor: P. R. Bandyopadhyay.

boundary layer over a rough wall has received far less attention because of the complexity of its boundary conditions. Raupach et al. (1991) tackled the general problem raised by the structure of turbulence over rough walls. They underlined the necessity of taking into account some important variables that influence the structure of rough wall turbulent flows such as the roughness element aspect ratios and the roughness density. In particular, Bandyopadhyay and Watson (1988) showed the importance of the spanwise aspect ratio λ_z (span/height) of roughness elements on near-wall turbulence structure. They showed that the near wall turbulence structure varies with λ_z .

Manifestations of organized motions have been detected and studied by many authors (Hussain, 1986; Fiedler 1987). Grass (1971) obtained a visual and quantitative description on a free surface channel flow for smooth and rough walls. He showed that the 'bursting' process identified for smooth wall turbulent flows is also present on rough walls, but noted differences in this process between these two types of flows. In smooth walls, inner layer low-speed streaks are cyclically formed and ejected into the overlying flow. The 'bursting process' is likely to be connected to the existence of low speed streaks observed on smooth wall and on a 'd-type' rough wall as it has been pointed out by Liu et al. (1966). For a 'k-type' rough wall, the relatively large spacing between the roughness elements reduces the ability of the streaky pattern, associated with near wall structures, to form and to be ejected.

It would be interesting to study the frequency of occurrence of these events for different spanwise aspect ratios of the roughness elements. The ejections of the fluid from the rough wall, characterized by high values of λ_z , are expected to be infrequent because of the difficulty for the previously mentioned streaks to form when the spacing between the roughnesses is not large enough; in contrast, the less severe boundary condition, characterized by low values of λ_z , should generate more frequent ejections, the upper limit of λ_z being obtained for two-dimensional bars, and the lower limit being represented by the smooth wall.

The aim of this study is to quantify the influence of the spanwise aspect ratio λ_z on the "bursting" period in a smooth and rough-wall turbulent channel flow. The quadrant analysis method has been used to detect these events.

Experimental Details

The experiments were made in an air-channel at a distance of $x/h = 80$ from the entrance, where $h = 25$ mm is the channel half-height. The test section was 2 m long. The transition was triggered at the exit of the contraction using a strip of sandpaper and a thin rod that spanned the test section, on both upper and lower surfaces. The surface was made rough using grooves perpendicular to the direction of the mean flow. The roughness height k was 2 mm and the longitudinal spacing p was 10 mm (Fig 1). The roughness elements had a square section. The distance between the tops of the roughness elements of the upper and lower surfaces is $2h$.

Measurements were carried out at the section where third and fourth statistical moments of the velocity components are independent of the downstream distance, so that the turbulent flow may be considered as fully developed. The Reynolds number based on the centreline velocity U_0 and channel height $2h$ is 113300. Further details of the flow facility are given in Ma-

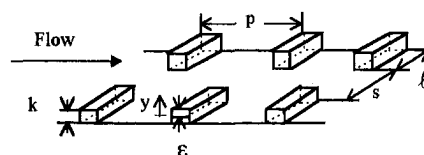


Fig. 1 Definition sketch of a grooved surface

to the downwash of the quasi-streamwise vortices. These vortices are also responsible for the lifting of the low-speed streaks away from the wall (Robinson, 1991).

Flow visualizations confirm that there exists an important communication via out-flows and inflows between the groove and the overlying shear layer. When an outflow occurs from the groove, and with it a corresponding inflow along the span of the groove, the turbulent structures are modified to some extent. The strength of these vortices do not need to be changed, only their relative locations and interaction with the wall need to be modified. This, in turn, temporarily suspends the production of new quasi-streamwise vortices and the near-wall activity, which leads to momentum exchange, is diminished relative to the nonperturbed smooth wall. Consequently, the ratio c_f/c_{f0} falls below unity.

Acknowledgment

The support of the Australian Research Council is gratefully acknowledged.

References

- Antonia, R. A., Zhu, Y., and Sokolov, M., 1995, "Effect of Concentrated Wall Suction on a Turbulent Boundary Layer," *Physics of Fluids*, Vol. 7, pp. 2465–2474.
- Ching, C. Y., Elavarasan, R., and Antonia, R. A., 1995a, "Visualization of Near-Wall Region in a Turbulent Boundary Layer Over a d-Type Roughness," J. Crowder, ed., *Flow Visualization VII*, New York, Begell House, pp. 398–401.
- Ching, C. Y., Djenidi, L., and Antonia, R. A., 1995b, "Low Reynolds Number Effects in a Turbulent Boundary Layer," *Experiments in Fluids*, Vol. 19, pp. 61–68.
- Choi, K.-S. and Fujisawa, N., 1993, "Possibility of Drag Reduction Using d-Type Roughness," K. Krishna Prasad, ed., *Further Developments in Turbulence Management*, Dordrecht, Kluwer Academic Publishers, pp. 315–324.
- Haugen, R. L., and Dhanak, A. M., 1966, "Momentum Transfer in Turbulent Separated Flow Past a Rectangular Cavity," *ASME Journal of Applied Mechanics*, Vol. 33, pp. 641–646.
- Liu, C. K., Kline, S. J., and Johnston, J. P., 1966, "An Experimental Study of Turbulent Boundary Layers on Rough Walls," Report No. MD-15, Thermoscience Division, Department of Mechanical Engineering, Stanford University.
- Merigaud, E., "Structure de la couche limite turbulente en presence d'aspiration parietale localisee," Ph.D. thesis, Institut de Mecanique Statistique de la Turbulence, Marseille.
- Pearson, B. R., Elavarasan, R., and Antonia, R. A., 1995, "The Effect of a Square Groove on a Boundary Layer," *Proceedings 12th Australasian Fluid Mechanics Conference*, Sydney, pp. 477–480.
- Robinson, S. K., 1991, "The Kinematics of Turbulent Boundary Layer Structure," Report TM 103859, NASA-Langley.
- Rotta, J. C., 1962, "The Turbulent Boundary Layer in Incompressible Flow," A. Ferrie, D. Kucheman and L. H. G. Stone, eds., *Progress in Aeronautical Science*, Oxford, Pergamon Press, pp. 1–220.
- Tani, I., Munakata, H., Matsumoto, A., and Abe, K., 1988, "Turbulence Management by Groove Roughness," H. W. Liepmann and R. Narasimha, eds., *Turbulence Management and Relaminarisation*, Berlin, Springer-Verlag, pp. 161–172.
- Townes, H. W., and Sabersky, R. H., 1966, "Experiments on the Flow Over a Rough Surface," *International Journal of Heat and Mass Transfer*, Vol. 9, pp. 729–738.
- Zhou, Y., and Antonia, R. A., 1992, "Convection Velocity Measurements in a Cylinder Wake," *Experiments in Fluids*, Vol. 13, pp. 63–70.

Effect of Roughness Aspect Ratio on the "Bursting" Period in a Fully Turbulent Channel Flow

L. Labraga,¹ A. Mazouz,¹ S. Demare,¹ and C. Tournier¹

Introduction

Much attention has been given to the structure of the turbulent boundary layer over a smooth wall. By contrast, the turbulent

¹ Lecturer, Lecturer, Doctorate Student and Professor, respectively, Laboratoire de Mecanique des Fluides, Universite' de Valenciennes, 59326 Valenciennes Cedex, France.

Contributed by the Fluids Engineering Division of THE AMERICAN SOCIETY OF MECHANICAL ENGINEERS. Manuscript received by the Fluids Engineering Division April 8, 1996; revised manuscript received February 25, 1997. Associate Technical Editor: P. R. Bandyopadhyay.

boundary layer over a rough wall has received far less attention because of the complexity of its boundary conditions. Raupach et al. (1991) tackled the general problem raised by the structure of turbulence over rough walls. They underlined the necessity of taking into account some important variables that influence the structure of rough wall turbulent flows such as the roughness element aspect ratios and the roughness density. In particular, Bandyopadhyay and Watson (1988) showed the importance of the spanwise aspect ratio λ_z (span/height) of roughness elements on near-wall turbulence structure. They showed that the near wall turbulence structure varies with λ_z .

Manifestations of organized motions have been detected and studied by many authors (Hussain, 1986; Fiedler 1987). Grass (1971) obtained a visual and quantitative description on a free surface channel flow for smooth and rough walls. He showed that the 'bursting' process identified for smooth wall turbulent flows is also present on rough walls, but noted differences in this process between these two types of flows. In smooth walls, inner layer low-speed streaks are cyclically formed and ejected into the overlying flow. The 'bursting process' is likely to be connected to the existence of low speed streaks observed on smooth wall and on a 'd-type' rough wall as it has been pointed out by Liu et al. (1966). For a 'k-type' rough wall, the relatively large spacing between the roughness elements reduces the ability of the streaky pattern, associated with near wall structures, to form and to be ejected.

It would be interesting to study the frequency of occurrence of these events for different spanwise aspect ratios of the roughness elements. The ejections of the fluid from the rough wall, characterized by high values of λ_z , are expected to be infrequent because of the difficulty for the previously mentioned streaks to form when the spacing between the roughnesses is not large enough; in contrast, the less severe boundary condition, characterized by low values of λ_z , should generate more frequent ejections, the upper limit of λ_z being obtained for two-dimensional bars, and the lower limit being represented by the smooth wall.

The aim of this study is to quantify the influence of the spanwise aspect ratio λ_z on the "bursting" period in a smooth and rough-wall turbulent channel flow. The quadrant analysis method has been used to detect these events.

Experimental Details

The experiments were made in an air-channel at a distance of $x/h = 80$ from the entrance, where $h = 25$ mm is the channel half-height. The test section was 2 m long. The transition was triggered at the exit of the contraction using a strip of sandpaper and a thin rod that spanned the test section, on both upper and lower surfaces. The surface was made rough using grooves perpendicular to the direction of the mean flow. The roughness height k was 2 mm and the longitudinal spacing p was 10 mm (Fig 1). The roughness elements had a square section. The distance between the tops of the roughness elements of the upper and lower surfaces is $2h$.

Measurements were carried out at the section where third and fourth statistical moments of the velocity components are independent of the downstream distance, so that the turbulent flow may be considered as fully developed. The Reynolds number based on the centreline velocity U_0 and channel height $2h$ is 113300. Further details of the flow facility are given in Ma-

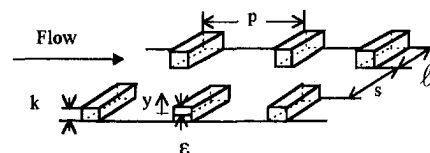


Fig. 1 Definition sketch of a grooved surface

Table 1 Parameters of the turbulent channel flow

	smooth	$\lambda_z = 1$	$\lambda_z = 5$	$\lambda_z = 7$	$\lambda_z = 400$
s (mm)	-----	14	6	2	0
ℓ (mm)	-----	2	10	14	800
θ (mm)	2.43	2.8	3.13	3.20	3.12
R_θ	5300	6160	6890	7040	6864
u_τ (m/s) $\pm 2\%$	1.25	1.70	2.00	2.42	2.51
ku_τ/ν	-----	227	267	323	335

zouz et al. (1994). The most important parameters are shown in Table 1.

Measurements of the longitudinal (u) and normal (v) fluctuating velocity components were performed using X-wire probes. The hot wires were run by constant temperature anemometers whose outputs were linearized and digitized at a sampling rate of 30 kHz.

Results and Discussion

The value of the friction velocity is obtained from static pressure measurements on both smooth and rough surfaces. It is then possible to overcome the difficult task of determining the shift in origin ϵ and the roughness function for the rough surfaces by matching the mean velocity data to a log law distribution. The mean shift obtained from this method is given by: $\epsilon/k = 0.29$. The values of the skin friction velocity are reported in Table 1.

For a turbulent channel flow, the \overline{uv} -distribution is given by: $-\overline{uv}/u_\tau^2 = 1 - y/h - dU^+/dy^+$ where $U^+ = U/u_\tau$; $y^+ = yu_\tau/\nu$, U being the mean longitudinal velocity and ν is the kinematic viscosity.

Fig. 2 Reynolds Stress Distribution

Figure 2 shows good agreement for a smooth wall between the measured uv and the above theoretical relationship; however the uv values measured for a rough wall are somewhat lower (10%). It is likely to be due to an insufficient angular response of the X-wire probes as it has been pointed out by Perry et al. (1987).

The uv -quadrant method is used here to identify ejections (Q_2) and sweeps (Q_4). Q_2 event is detected when $u < 0, v > 0$ and $|uv| > Hu'v'$ (a prime denotes a rms value); Q_4 event is detected when $u > 0$ and $v < 0$ and $|uv| > Hu'v'$, where H is a given threshold (Lu and Willmarth, 1973). Our previous studies have shown that ejection and sweep events remain significant contributors to uv for a threshold value between 2 and 4, for a large distance from the wall. To obtain a value of the mean time interval between events, we used at first the threshold $H = 2$, for which sweeps still make a significant contribution

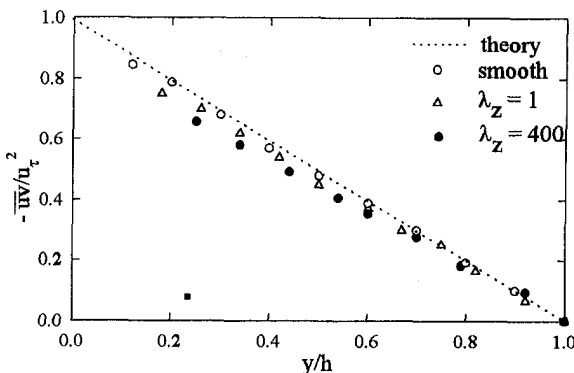


Fig. 2 Reynolds stress distribution

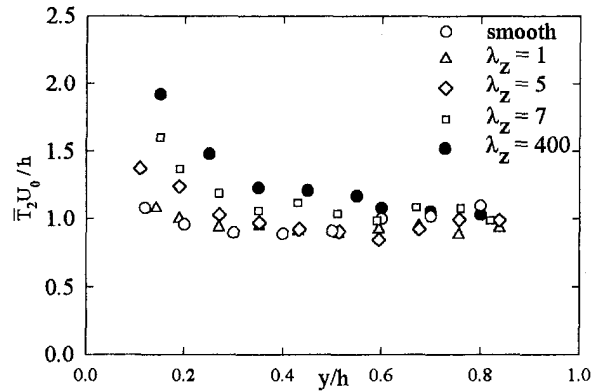


Fig. 3 Average time between ejections ($H = 2$) (Uncertainty in $T_2 U_0/h = \pm 2$ percent)

to the Reynolds stress in the inner layer. Threshold $H = 4$ has been chosen because only ejections contribute to the Reynolds stress in this case. The choice of these thresholds is also due to the fact that they were largely used in the literature. In this way, comparisons with other results are possible if the detection method are identical. The average period \overline{T} is scaled using the velocity U_0 and the channel half-height h .

Figure 3 clearly shows that the average period depends strongly on the aspect ratio λ_z for a threshold $H = 2$. Only results for $y/h < 0.9$ are reported, so no correction due to the opposite wall effect is needed.

Figure 3 indicates that the period of occurrence of ejections increases with λ_z , especially in the inner region. In the outer turbulent flow region ejection-type motions, due to the break-up of streak filaments, lead to lower values of \overline{T}_2 for the different cases (Bogard and Tiederman, 1986).

Figure 4 shows the average time between sweeps for $H = 2$. These results indicate that sweep events depend on the nature of the surface. The relatively rare ejections near the wall confirm the dominance of sweeps in this region. Indeed, sweeps occur more frequently when the distance from the wall decreases. Figures 3 and 4 show that the upper limit of the mean time between events is reached when $\lambda_z = 400$, corresponding to a two-dimensional roughness; the lower limit is observed for a smooth wall flow. For the other values of λ_z , the mean times between events have intermediate distributions.

Let us note that making the period between events dimensionless by using the wall units, emphasizes the differences between the different cases.

The distributions of the mean period of strong ejections for $H = 4$ are reported on Fig. 5. These distributions are similar to

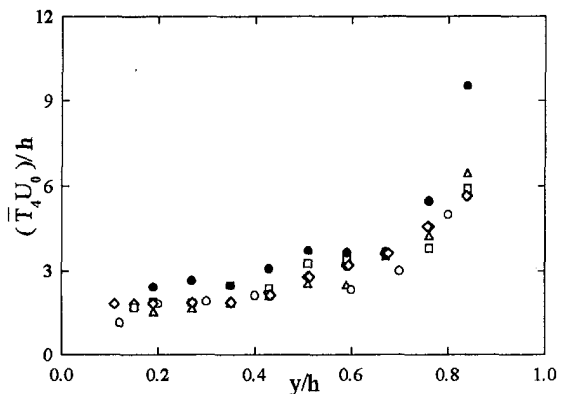


Fig. 4 Average time between sweeps ($H = 2$) (Uncertainty in $T_4 U_0/h = \pm 2$ percent); symbols are as in Fig. 3

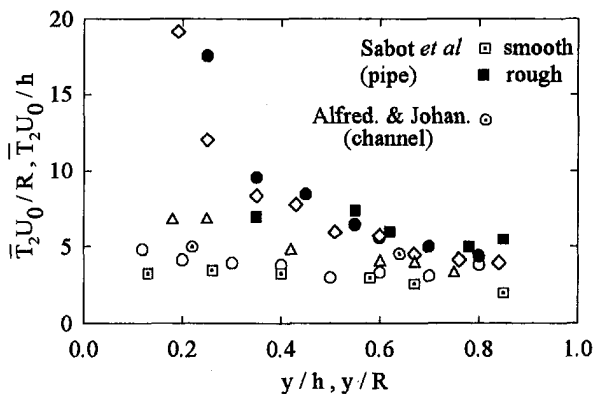


Fig. 5 Average time between ejections ($H = 4$) R : pipe radius

those obtained for $H = 2$, and show that violent ejections also occur more frequently on a smooth wall than on a rough wall. These results are consistent with those of Sabot et al. (1977), whose experiments have been carried out for fully developed smooth and rough pipe flow (Fig. 5). The roughness element used by these authors is ring-shaped. Results obtained by Alfredsson and Johansson (1984) in a turbulent channel flow, contained in this figure, support the values of the mean time period of ejections obtained in the present study on smooth walls, for $y/h \approx 0.2$. The distributions of \bar{T}_4 for $H = 4$ are not reported here because of the wide scatter in the results due to the scarcity of sweep events.

Bogard and Tiederman (1986) underlined the discrepancies when comparing the results obtained from the different techniques in making the measurements of \bar{T} . For the present study, exact numerical values of \bar{T} may be questionable, but the qualitative trends near the wall seem to be significant.

Conclusion

In this work, the structure of turbulent channel flow in smooth and various types of rough surfaces has been studied for varying aspect ratios of the roughness elements in a fully turbulent duct flow. The most important results are as follows:

The frequency of occurrence of both sweeps and ejections, normalized with the outer parameters, depends on the spanwise aspect ratio of a roughness element.

When the values of the spanwise aspect ratio decrease, the frequency of occurrence of ejection and sweep events increases and tends to follow the values obtained on a smooth surface.

When the values of the spanwise aspect ratio increase, the frequency of occurrence of these events decreases and tends to follow the values found on a two-dimensional roughness. This difference is probably due to the existence of low-speed streaks, the formation of which depends on the nature of the surface.

References

- Alfredsson, P. H., Johansson, A. V., 1984, "On the Detection of Turbulence-Generating Events," *Journal of Fluid Mechanics*, Vol. 139, pp. 325–345.
- Antonia, R. A., Krogstad, P. A., 1993, "Scaling of Bursting Period in Turbulent Rough Wall Boundary Layers," *Experiments in Fluids*, Vol. 15, pp. 82–84.
- Bandyopadhyay, P. R., Watson, R. D., 1988, "Structure of Rough-Wall Turbulent Boundary Layers," *Physics of Fluids*, Vol. 31, pp. 1877–1883.
- Bogard, D. G., Tiederman, W. G., 1986, "Burst Detection with Single-Point Velocity Measurements," *Journal of Fluid Mechanics*, Vol. 162, pp. 389–413.
- Fiedler, H., 1987, "Coherent Structures," *Advances in Turbulence*, Comte-Bellot G. and Mathieu J., eds. Springer, New York, 320–336.
- Grass, A. J., 1971, "Structural Features of Turbulent Flow over Smooth and Rough Boundaries," *Journal of Fluid Mechanics*, Vol. 50, 233–255.
- Hussain, A. K. M. F., 1986, "Coherent Structures and Turbulence," *Journal of Fluid Mechanics*, Vol. 173, pp. 303–356.
- Krogstad, P. A., Antonia, R. A., Browne, L. W. B., 1992, "Comparison between Rough and Smooth Wall Turbulent Boundary Layers," *Journal of Fluid Mechanics*, Vol. 245, pp. 599–617.

Liu, C. K., Kline, S. J., and Johnston, J. 1966, "An Experimental Study of Turbulent Boundary Layers on Rough Walls," Report MD-15, Department of Mechanical Engineering, Stanford University.

Lu, S. S., and Willmarth, W. W., 1973 "Measurements of the Structure of the Reynolds Stress in a Turbulent Boundary Layer," *Journal of Fluid Mechanics*, Vol. 60, part. 3, pp. 481–511.

Mazouz, A., Labraga, L., Tournier, C., 1994, "Behaviour of Reynolds Stress on Rough Wall," *Experiments in Fluids*, Vol. 1, pp. 39–44.

Perry, A. E., Lim, K. L., Henbest, S. M., 1987, "An Experimental Study of the Turbulence Structures in Smooth-and-Rough-Wall Boundary Layers," *Journal of Fluid Mechanics*, Vol. 177, pp. 437–466.

Raupach, M. R., 1981, "Conditional Statistics of Reynolds Stress in Rough-Wall and Smooth-Wall Turbulent Boundary Layers," *Journal of Fluid Mechanics*, Vol. 108, pp. 363–382.

Raupach, M. R., Antonia, R. A., Rajagopalan, S., 1991, "Rough-Wall Turbulent Boundary Layers," *Applied Mechanics Review*, Vol. 44, pp. 1–25.

Sabot, J., Saleh, I., Comte-Bellot, G., 1977, "Effect of Roughness on the Intermittent Maintenance of Reynolds Shear Stress in Pipe Flow," *Physics of Fluids*, Vol. 20, pp. 150–155.

The Effect of Induced Swirl on Mixing

D. W. Guillaume¹ and J. C. LaRue¹

Introduction

Swirling jets have received considerable attention both because of their occurrence in nature in the form of tornadoes and waterspouts and in devices of technological interest such as gas turbine combustors. Swirl is especially useful in gas turbine combustors as it provides a means to both effectively mix the fuel and air and also stabilize the reaction. Typically, the swirl is produced by means of high pressure air that is passed through swirl vanes that are coannular with the fuel jet (cf. Brum, 1983). In some cases, the increased mixing has been shown to lead to both a reduction in NO_x production and also an increase in combustion efficiency (cf. Takagi et al., 1981; Gupta et al., 1992; and Tangirala and Driscoll, 1988). In addition, swirl can be used to create a more stable and shorter reaction zone, which can be adjusted to burn leaner with a reduced risk of blow out (cf. Driscoll et al., 1992). However, Ho (1990) has shown that high levels of swirl can lead to blow-out due to excessive entrainment of air and recirculation of combustion products.

Due to the lack of high pressure air, the beneficial effects of swirl have not been applied in many combustion devices. Examples where the benefits of swirl stabilized combustion are not available include domestic hot water heaters, dryers, and furnaces. In addition, the increased mixing associated with swirl would be of benefit in cold air HVAC systems where the cold air must be mixed more efficiently than is possible using conventional diffusers (cf. Dorgan and Elleson, 1987), and in electronic cooling applications (cf. Steinberg, 1991).

One method to produce swirl without high pressure air has been discussed by Glassman (1991) who pointed out that swirl can be induced as a nonrotating jet exits through a plane surface into a larger diameter shroud which is equipped with tangential passages for the entrained air. The rotation of the entrained air causes the central jet to rotate after it exits through the exit plane.

¹Research Assistant and Associate Professor, respectively, Department of Mechanical and Aerospace Engineering, University of California, Irvine, CA 92697-3975.

Contributed by the Fluids Engineering Division of THE AMERICAN SOCIETY OF MECHANICAL ENGINEERS. Manuscript received by the Fluids Engineering Division May 9, 1996; revised manuscript received February 12, 1997. Associate Technical Editor: J. A. C. Humphrey.

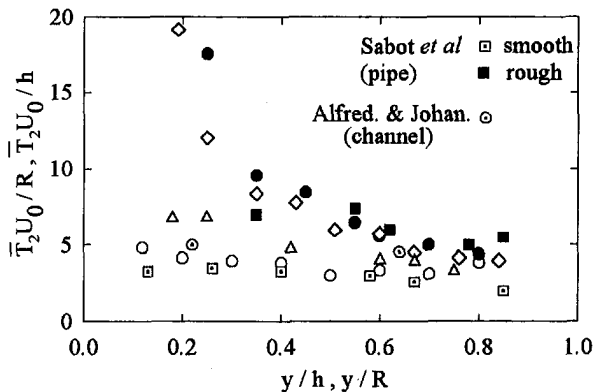


Fig. 5 Average time between ejections ($H = 4$) R : pipe radius

those obtained for $H = 2$, and show that violent ejections also occur more frequently on a smooth wall than on a rough wall. These results are consistent with those of Sabot et al. (1977), whose experiments have been carried out for fully developed smooth and rough pipe flow (Fig. 5). The roughness element used by these authors is ring-shaped. Results obtained by Alfredsson and Johansson (1984) in a turbulent channel flow, contained in this figure, support the values of the mean time period of ejections obtained in the present study on smooth walls, for $y/h \approx 0.2$. The distributions of \bar{T}_4 for $H = 4$ are not reported here because of the wide scatter in the results due to the scarcity of sweep events.

Bogard and Tiederman (1986) underlined the discrepancies when comparing the results obtained from the different techniques in making the measurements of \bar{T} . For the present study, exact numerical values of \bar{T} may be questionable, but the qualitative trends near the wall seem to be significant.

Conclusion

In this work, the structure of turbulent channel flow in smooth and various types of rough surfaces has been studied for varying aspect ratios of the roughness elements in a fully turbulent duct flow. The most important results are as follows:

The frequency of occurrence of both sweeps and ejections, normalized with the outer parameters, depends on the spanwise aspect ratio of a roughness element.

When the values of the spanwise aspect ratio decrease, the frequency of occurrence of ejection and sweep events increases and tends to follow the values obtained on a smooth surface.

When the values of the spanwise aspect ratio increase, the frequency of occurrence of these events decreases and tends to follow the values found on a two-dimensional roughness. This difference is probably due to the existence of low-speed streaks, the formation of which depends on the nature of the surface.

References

- Alfredsson, P. H., Johansson, A. V., 1984, "On the Detection of Turbulence-Generating Events," *Journal of Fluid Mechanics*, Vol. 139, pp. 325–345.
- Antonia, R. A., Krogstad, P. A., 1993, "Scaling of Bursting Period in Turbulent Rough Wall Boundary Layers," *Experiments in Fluids*, Vol. 15, pp. 82–84.
- Bandyopadhyay, P. R., Watson, R. D., 1988, "Structure of Rough-Wall Turbulent Boundary Layers," *Physics of Fluids*, Vol. 31, pp. 1877–1883.
- Bogard, D. G., Tiederman, W. G., 1986, "Burst Detection with Single-Point Velocity Measurements," *Journal of Fluid Mechanics*, Vol. 162, pp. 389–413.
- Fiedler, H., 1987, "Coherent Structures," *Advances in Turbulence*, Comte-Bellot G. and Mathieu J., eds. Springer, New York, 320–336.
- Grass, A. J., 1971, "Structural Features of Turbulent Flow over Smooth and Rough Boundaries," *Journal of Fluid Mechanics*, Vol. 50, 233–255.
- Hussain, A. K. M. F., 1986, "Coherent Structures and Turbulence," *Journal of Fluid Mechanics*, Vol. 173, pp. 303–356.
- Krogstad, P. A., Antonia, R. A., Browne, L. W. B., 1992, "Comparison between Rough and Smooth Wall Turbulent Boundary Layers," *Journal of Fluid Mechanics*, Vol. 245, pp. 599–617.

Liu, C. K., Kline, S. J., and Johnston, J. 1966, "An Experimental Study of Turbulent Boundary Layers on Rough Walls," Report MD-15, Department of Mechanical Engineering, Stanford University.

Lu, S. S., and Willmarth, W. W., 1973 "Measurements of the Structure of the Reynolds Stress in a Turbulent Boundary Layer," *Journal of Fluid Mechanics*, Vol. 60, part. 3, pp. 481–511.

Mazouz, A., Labraga, L., Tournier, C., 1994, "Behaviour of Reynolds Stress on Rough Wall," *Experiments in Fluids*, Vol. 1, pp. 39–44.

Perry, A. E., Lim, K. L., Henbest, S. M., 1987, "An Experimental Study of the Turbulence Structures in Smooth-and-Rough-Wall Boundary Layers," *Journal of Fluid Mechanics*, Vol. 177, pp. 437–466.

Raupach, M. R., 1981, "Conditional Statistics of Reynolds Stress in Rough-Wall and Smooth-Wall Turbulent Boundary Layers," *Journal of Fluid Mechanics*, Vol. 108, pp. 363–382.

Raupach, M. R., Antonia, R. A., Rajagopalan, S., 1991, "Rough-Wall Turbulent Boundary Layers," *Applied Mechanics Review*, Vol. 44, pp. 1–25.

Sabot, J., Saleh, I., Comte-Bellot, G., 1977, "Effect of Roughness on the Intermittent Maintenance of Reynolds Shear Stress in Pipe Flow," *Physics of Fluids*, Vol. 20, pp. 150–155.

The Effect of Induced Swirl on Mixing

D. W. Guillaume¹ and J. C. LaRue¹

Introduction

Swirling jets have received considerable attention both because of their occurrence in nature in the form of tornadoes and waterspouts and in devices of technological interest such as gas turbine combustors. Swirl is especially useful in gas turbine combustors as it provides a means to both effectively mix the fuel and air and also stabilize the reaction. Typically, the swirl is produced by means of high pressure air that is passed through swirl vanes that are coannular with the fuel jet (cf. Brum, 1983). In some cases, the increased mixing has been shown to lead to both a reduction in NO_x production and also an increase in combustion efficiency (cf. Takagi et al., 1981; Gupta et al., 1992; and Tangirala and Driscoll, 1988). In addition, swirl can be used to create a more stable and shorter reaction zone, which can be adjusted to burn leaner with a reduced risk of blow out (cf. Driscoll et al., 1992). However, Ho (1990) has shown that high levels of swirl can lead to blow-out due to excessive entrainment of air and recirculation of combustion products.

Due to the lack of high pressure air, the beneficial effects of swirl have not been applied in many combustion devices. Examples where the benefits of swirl stabilized combustion are not available include domestic hot water heaters, dryers, and furnaces. In addition, the increased mixing associated with swirl would be of benefit in cold air HVAC systems where the cold air must be mixed more efficiently than is possible using conventional diffusers (cf. Dorgan and Elleson, 1987), and in electronic cooling applications (cf. Steinberg, 1991).

One method to produce swirl without high pressure air has been discussed by Glassman (1991) who pointed out that swirl can be induced as a nonrotating jet exits through a plane surface into a larger diameter shroud which is equipped with tangential passages for the entrained air. The rotation of the entrained air causes the central jet to rotate after it exits through the exit plane.

¹Research Assistant and Associate Professor, respectively, Department of Mechanical and Aerospace Engineering, University of California, Irvine, CA 92697-3975.

Contributed by the Fluids Engineering Division of THE AMERICAN SOCIETY OF MECHANICAL ENGINEERS. Manuscript received by the Fluids Engineering Division May 9, 1996; revised manuscript received February 12, 1997. Associate Technical Editor: J. A. C. Humphrey.

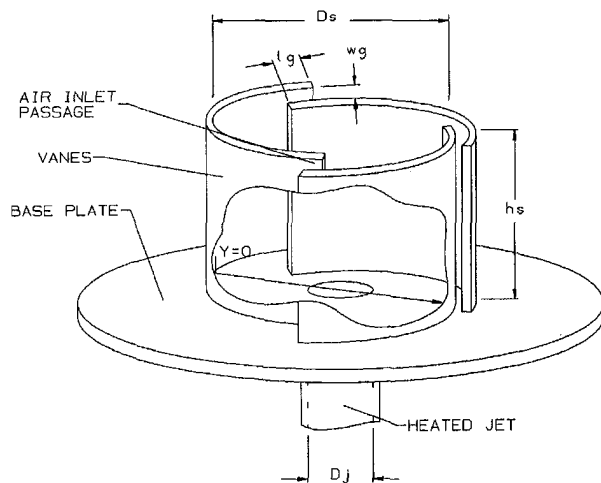


Fig. 1 Schematic of flow facility showing the concentric placement of the vanes and identifying the necessary variables

Induced swirl has been qualitatively shown to be an effective mixing enhancement tool in a simple combustion system. Guillaume and LaRue (1995) visually studied a natural gas reaction with and without induced swirl. The induced swirl case clearly produced a bluer flame which indicated improved mixing prior to combustion. The goal of the present study is to quantify the effect of induced swirl on the mixing of a hot air jet with air at ambient temperature and to provide a preliminary assessment of the flow structure.

For this preliminary study, the geometry of the swirl generator is made as simple as possible. The flow facility, shown in Fig. 1, consists of a jet of 1.27 cm diameter with a contoured nozzle that exits through a plane surface. Three overlapping curved vanes, which are concentric with the jet axis, are placed on the surface that forms the jet exit plane and are separated by a distance, w_g , of 0.25 cm with an overlap, l_g , of 2 cm. The vanes are fabricated by attaching a clear sheet of 0.0254 cm mylar to hardware cloth formed to a nominal radius of 10 cm. The height of the vanes is 46 cm and the joints formed by the vanes and plane surface are sealed to prevent air from flowing under the vanes.

Table 1 shows the flow characteristics and geometric parameters used in this study. The jet flow is provided by means of a high pressure regulated air supply which is passed through an electric heater. The jet flow is maintained at a velocity of 5 m/s and a temperature of 25°C above ambient. The jet exit velocity and temperature are maintained constant to within 0.05 m/s and 0.3°C, respectively.

Flow visualization, using smoke which is illuminated with a light sheet, is used to determine the qualitative flow characteristics. Photographs of the smoke are taken in both horizontal and vertical planes. For the horizontal plane measurements, the smoke is generated by means of an electric heater which vaporizes mineral oil. A very low air flow passes through the vaporizer and entrains the vapor which is passed through a tube and injected into the flow. For the vertical plane visualization, a smoke wire is used. For these studies, a slide projector with

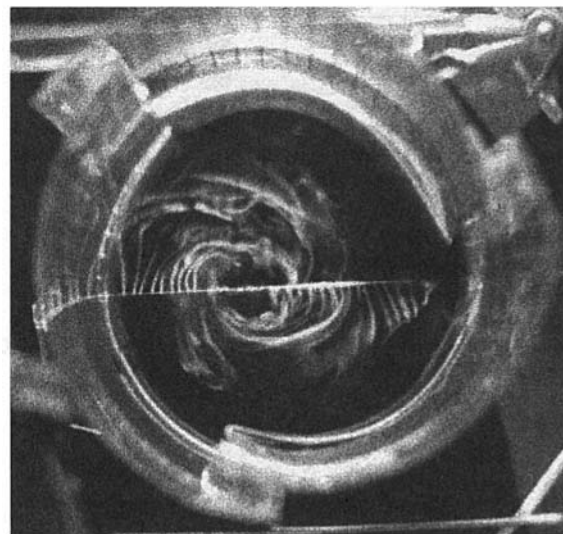


Fig. 2 Photograph showing that the swirling flow corresponds to the clockwise vane orientation. Wire is positioned at $X/D_j = 12$.

appropriate lenses and masks is used to produce the light sheet. The light sheet has a thickness of about 0.25 cm and is always maintained parallel to the plane of interest. Photographs are taken using film with an ASA speed of 400 and a 35 mm camera set to automatically adjust the f stop while maintaining a shutter speed of 1/250 s.

The photograph shown in Fig. 2 corresponds to this vane orientation with the smoke wire positioned at $X/D_j = 12$. Clearly, swirling flow is created in the clockwise direction. Although this photograph shows that swirl can be induced by a jet enclosed by a set of overlapping vanes, the presence of swirl alone, however, is not adequate to ensure improved mixing. As shown by Gupta (1984), weak swirl may lead to a long spiral flow that simply transports the gases out of the shroud in a spiraling manner. Accordingly, a stronger swirl will produce a reduced pressure region along the flow centerline that causes a recirculation zone. The recirculation zone created by the higher swirl leads to enhanced mixing of jet fluid with entrained air.

In order to further characterize the swirl flow produced by the shroud, a small tube issuing smoke at a low velocity is placed at the top on the shroud near the centerline. Figure 3 shows the smoke being drawn down the centerline, and hence, verifies the existence of a recirculation zone and infers that mixing can be enhanced by induced swirl.

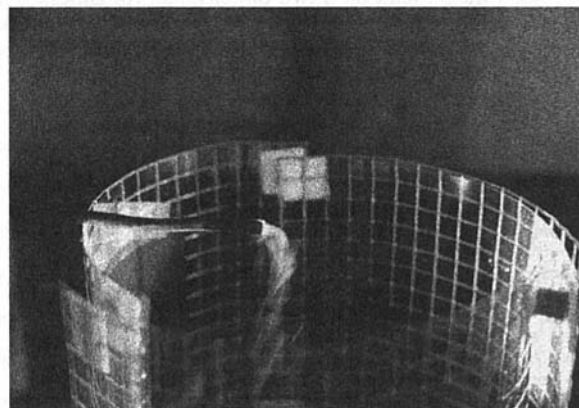


Fig. 3 Photograph showing that smoke injected at the shroud's exit is drawn down the centerline of the shroud verifying the existence of recirculation

Table 1 Flow and geometric parameters

Jet velocity	U_j	5 m/s
Maximum temperature difference	$T_j - T_a$	25°C
Jet diameter	D_j	1.28 cm
Height of shroud	h_s	46 cm
Length of gap overlap	l_g	2 cm
Width of gap	w_g	0.25 cm
Shroud diameter	D_s	16 cm

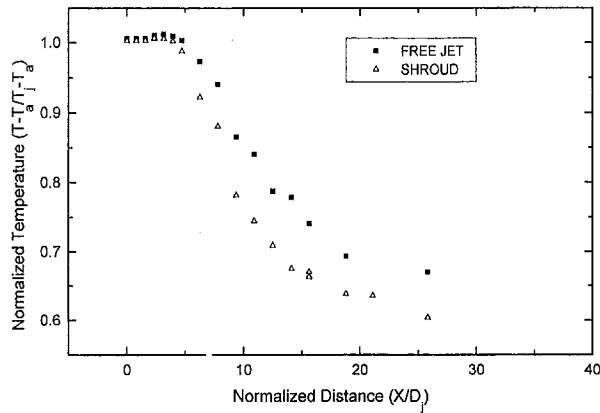


Fig. 4 Comparison of the downstream variation of mean centerline temperature between a shroud with a 0.25 cm gap and the no shroud (free jet) conditions

A quantitative study using temperature as a scalar, is used to verify observations based on the visualization studies. Specifically, temperature measurements of the degree of mixing are obtained using 28 gage type K thermocouples which are monitored by means of an ADAC analog to digital converter that is equipped with cold junction compensation. The resolution of the temperature recording system is $\pm 0.1^\circ\text{C}$. The uncertainties of the temperature measurements were estimated to the 95 percent confidence using the techniques of Kline and McClintock (1953). Based on comparison to a calibrated platinum resistance thermometer, the thermocouples were found to have an uncertainty of $\pm 0.219^\circ\text{C}$. At each location, the thermocouples are sampled at a rate of 60 samples/s for a duration of a least 180 seconds. However, at some positions, data are recorded for a duration of 300 seconds. The thermocouple probe that is used to obtain temperature measurements in the shroud is positioned with its active junction 1.0 cm from the end of a 60 cm long, 0.6 cm diameter support tube. The support tube is mounted on a three-dimensional traverse with a resolution of 0.1 mm. For these measurements, the probe is oriented vertically. Other thermocouples are positioned to monitor both the jet exit and entrained air temperatures. These temperatures are recorded simultaneously with the temperature from the sensor that is used to measure the temperature in the flow.

The temperature studies are performed while keeping the difference between the heated jet and the ambient air at approximately 25°C . Figure 4 shows the effect of a shroud with a 0.25 cm gap on the downstream centerline decay on the mean temperature. Starting at about $X/D_j = 5$, the mean centerline temperature with the shroud in place decreases faster than for the no shroud case.

In conclusion, preliminary qualitative and quantitative methods have been used to show that induced swirl can be generated and has the strength necessary to produce the required recirculation zone that is essential to enhance mixing. Smoke wire visualization has clearly demonstrated that, 1) swirl exists, 2) the swirl is dependent on the shroud configuration, and 3) flow reversal on the centerline occurs.

Thermocouple measurements support these findings. The axial decay in mean centerline temperature with the shroud is significantly greater than without the shroud. For example, at $X/D_j = 15$, the mean temperature is reduced by about 12 percent. This implies mixing is enhanced.

References

Brum, R. D., 1983, "Evaluation of a Candidate Model Complex Flow Combustor Using Instantaneous Two-Color Laser Anemometry," Ph.D. dissertation, University of California, Irvine.

Dorgan, J. F., Elleson, J. S., 1987, "Field Evaluation of Cold Air Distribution Systems," EPRI Report EM-5447, Palo Alto Calif., Electric Power Research Institute.

Driscoll, J. F., Chen, R., and Yoon, Y., 1992, "Nitric Oxide Levels of Turbulent Jet Diffusion Flames: Effects of Residence Time and Damkohler Number," *Comb. and Flame*, Vol. 88.

Glassman, I., 1991, Private communication.

Guillaume, D. W., LaRue, J. C., 1995, Combustion Enhancement Using Induced Swirl," *Experiments in Fluids*, Vol. 20, pp. 59–60.

Gupta, A. K., Lilley, D. G., and Syred, N., 1984, *Swirl Flows*, Kent: Abacus Press.

Gupta, A., Ramavajjala, M., and Taha, M., 1992, "The Effect of Swirl and Nozzle Geometry on the Structure of Flames and NO_x Emission," AIAA Thirtieth Aerospace Sciences Meeting and Exhibit, Reno, Nevada.

Ho, W., Yang, S., Yang, R., 1990, "The Advanced Burner Design Project. The Fourteenth Annual Conference on Theoretical and Applied Mechanics," Chung Li, Taiwan, R.O.C.

Keller, J. J., Egli, W., Althaus, R., 1988, "Vortex Breakdown as a Fundamental Element of Vortex Dynamics," *Zeitschrift für Physik*, 39, 404–440.

Kline, S. J., McClintock F. A., 1953, "Describing Uncertainties in Single-Sample Experiments," *Mechanical Engineering*, Vol. 75, pp. 3–9.

Steinberg, D. S., 1991, *Cooling Techniques for Electronic Equipment*, Wiley, NY.

Tangirala, V., and Driscoll, J. F., 1988, "Temperatures Within Non-Premixed Flames: Effects of Rapid Mixing Due to Swirl," *Combustion Science and Technology*, Vol. 69, pp. 143–162.

Talagi, T., and Okamoto, T., 1981, "Characteristics of Combustion and Pollutant Formation in Swirling Flames," *Combustion and Flame*, Vol. 43, pp. 69–79.

Air Venting in Pressure Die Casting

G. Bar-Meir,^{1,2} E. R. G. Eckert,¹ and R. J. Goldstein¹

Nomenclature

- A = vent cross-sectional area
- A_c = critical vent cross-sectional area which makes $(t_{\max}/t_c) = 1$
- c = speed of sound
- D = hydraulic diameter of vent
- f = friction factor in duct
- k = ratio of constant pressure to constant volume specific heats
- L = length or equivalent length of vent
- L_{\max} = maximum length in which flow is unchoked
- \bar{M} = Mach numbers ratio, $M_{in}(t)/M_{\max}$
- M_{exit} = Mach number at duct exit
- M_{in} = Mach number at duct entrance
- M_{\max} = maximum possible Mach number at duct entrance
- m = residual air mass in cylinder
- \bar{m} = residual mass fraction of air in cylinder, $m(t)/m(0)$
- \dot{m}_{in} = air mass flow rate into duct or out of cylinder
- \dot{m}_{in}^* = approximate air mass flow rate into duct when flow is first choked and pressure and temperature remain at their initial values, Eq. (11)
- P = air pressure in cylinder (unfilled shot sleeve, runner, and die cavity)
- \bar{P} = pressure ratio, $P(t)/P(0)$
- P_{exit} = pressure at duct exit
- P_0 = total or stagnation pressure

¹ Postdoctorate, Regents Professor Emeritus, and Regents Professor, respectively, Department of Mechanical Engineering, University of Minnesota, Minneapolis, MN 55455.

² Present address: Minnesota Supercomputer Institute, Minneapolis, MN 55415. Contributed by the Fluids Engineering Division of THE AMERICAN SOCIETY OF MECHANICAL ENGINEERS. Manuscript received by the Fluids Engineering Division February 21, 1996; revised manuscript received April 16, 1996. Associate Technical Editor: D. P. Telionis.

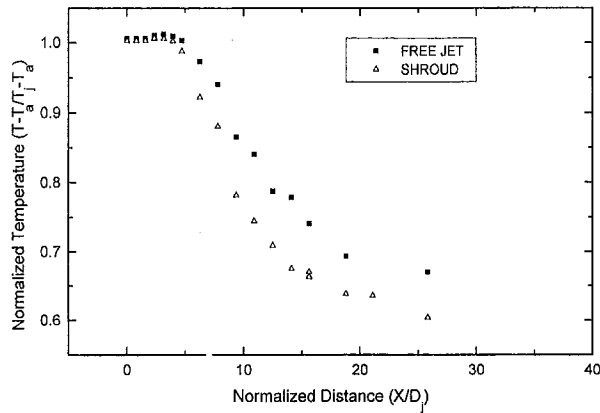


Fig. 4 Comparison of the downstream variation of mean centerline temperature between a shroud with a 0.25 cm gap and the no shroud (free jet) conditions

A quantitative study using temperature as a scalar, is used to verify observations based on the visualization studies. Specifically, temperature measurements of the degree of mixing are obtained using 28 gage type K thermocouples which are monitored by means of an ADAC analog to digital converter that is equipped with cold junction compensation. The resolution of the temperature recording system is $\pm 0.1^\circ\text{C}$. The uncertainties of the temperature measurements were estimated to the 95 percent confidence using the techniques of Kline and McClintock (1953). Based on comparison to a calibrated platinum resistance thermometer, the thermocouples were found to have an uncertainty of $\pm 0.219^\circ\text{C}$. At each location, the thermocouples are sampled at a rate of 60 samples/s for a duration of a least 180 seconds. However, at some positions, data are recorded for a duration of 300 seconds. The thermocouple probe that is used to obtain temperature measurements in the shroud is positioned with its active junction 1.0 cm from the end of a 60 cm long, 0.6 cm diameter support tube. The support tube is mounted on a three-dimensional traverse with a resolution of 0.1 mm. For these measurements, the probe is oriented vertically. Other thermocouples are positioned to monitor both the jet exit and entrained air temperatures. These temperatures are recorded simultaneously with the temperature from the sensor that is used to measure the temperature in the flow.

The temperature studies are performed while keeping the difference between the heated jet and the ambient air at approximately 25°C . Figure 4 shows the effect of a shroud with a 0.25 cm gap on the downstream centerline decay on the mean temperature. Starting at about $X/D_j = 5$, the mean centerline temperature with the shroud in place decreases faster than for the no shroud case.

In conclusion, preliminary qualitative and quantitative methods have been used to show that induced swirl can be generated and has the strength necessary to produce the required recirculation zone that is essential to enhance mixing. Smoke wire visualization has clearly demonstrated that, 1) swirl exists, 2) the swirl is dependent on the shroud configuration, and 3) flow reversal on the centerline occurs.

Thermocouple measurements support these findings. The axial decay in mean centerline temperature with the shroud is significantly greater than without the shroud. For example, at $X/D_j = 15$, the mean temperature is reduced by about 12 percent. This implies mixing is enhanced.

References

Brum, R. D., 1983, "Evaluation of a Candidate Model Complex Flow Combustor Using Instantaneous Two-Color Laser Anemometry," Ph.D. dissertation, University of California, Irvine.

Dorgan, J. F., Elleson, J. S., 1987, "Field Evaluation of Cold Air Distribution Systems," EPRI Report EM-5447, Palo Alto Calif., Electric Power Research Institute.

Driscoll, J. F., Chen, R., and Yoon, Y., 1992, "Nitric Oxide Levels of Turbulent Jet Diffusion Flames: Effects of Residence Time and Damkohler Number," *Comb. and Flame*, Vol. 88.

Glassman, I., 1991, Private communication.

Guillaume, D. W., LaRue, J. C., 1995, Combustion Enhancement Using Induced Swirl," *Experiments in Fluids*, Vol. 20, pp. 59–60.

Gupta, A. K., Lilley, D. G., and Syred, N., 1984, *Swirl Flows*, Kent: Abacus Press.

Gupta, A., Ramavajjala, M., and Taha, M., 1992, "The Effect of Swirl and Nozzle Geometry on the Structure of Flames and NO_x Emission," AIAA Thirtieth Aerospace Sciences Meeting and Exhibit, Reno, Nevada.

Ho, W., Yang, S., Yang, R., 1990, "The Advanced Burner Design Project. The Fourteenth Annual Conference on Theoretical and Applied Mechanics," Chung Li, Taiwan, R.O.C.

Keller, J. J., Egli, W., Althaus, R., 1988, "Vortex Breakdown as a Fundamental Element of Vortex Dynamics," *Zeitschrift für Physik*, 39, 404–440.

Kline, S. J., McClintock F. A., 1953, "Describing Uncertainties in Single-Sample Experiments," *Mechanical Engineering*, Vol. 75, pp. 3–9.

Steinberg, D. S., 1991, *Cooling Techniques for Electronic Equipment*, Wiley, NY.

Tangirala, V., and Driscoll, J. F., 1988, "Temperatures Within Non-Premixed Flames: Effects of Rapid Mixing Due to Swirl," *Combustion Science and Technology*, Vol. 69, pp. 143–162.

Talagi, T., and Okamoto, T., 1981, "Characteristics of Combustion and Pollutant Formation in Swirling Flames," *Combustion and Flame*, Vol. 43, pp. 69–79.

Air Venting in Pressure Die Casting

G. Bar-Meir,^{1,2} E. R. G. Eckert,¹
and R. J. Goldstein¹

Nomenclature

- A = vent cross-sectional area
- A_c = critical vent cross-sectional area which makes $(t_{\max}/t_c) = 1$
- c = speed of sound
- D = hydraulic diameter of vent
- f = friction factor in duct
- k = ratio of constant pressure to constant volume specific heats
- L = length or equivalent length of vent
- L_{\max} = maximum length in which flow is unchoked
- \bar{M} = Mach numbers ratio, $M_m(t)/M_{\max}$
- M_{exit} = Mach number at duct exit
- M_{in} = Mach number at duct entrance
- M_{\max} = maximum possible Mach number at duct entrance
- m = residual air mass in cylinder
- \bar{m} = residual mass fraction of air in cylinder, $m(t)/m(0)$
- \dot{m}_{in} = air mass flow rate into duct or out of cylinder
- \dot{m}_{in}^* = approximate air mass flow rate into duct when flow is first choked and pressure and temperature remain at their initial values, Eq. (11)
- P = air pressure in cylinder (unfilled shot sleeve, runner, and die cavity)
- \bar{P} = pressure ratio, $P(t)/P(0)$
- P_{exit} = pressure at duct exit
- P_0 = total or stagnation pressure

¹ Postdoctorate, Regents Professor Emeritus, and Regents Professor, respectively, Department of Mechanical Engineering, University of Minnesota, Minneapolis, MN 55455.

² Present address: Minnesota Supercomputer Institute, Minneapolis, MN 55415. Contributed by the Fluids Engineering Division of THE AMERICAN SOCIETY OF MECHANICAL ENGINEERS. Manuscript received by the Fluids Engineering Division February 21, 1996; revised manuscript received April 16, 1996. Associate Technical Editor: D. P. Telonis.

- R = universal gas constant
- T = air temperature in cylinder
- T_0 = total or stagnation temperature
- t = time measured from blockage of pouring hole to end of process, $0 \leq t \leq t_{\max}$
- \bar{t} = dimensionless time, also fraction of cylinder volume, t/t_{\max}
- t_c = evacuation time, characteristic time to evacuate cylinder, Eq. (10)
- t_{\max} = filling time, time for liquid metal to reach vent
- V = air volume in cylinder (unfilled shot sleeve, runner, and die cavity)
- 0 = signifies initial time, ($t = 0$)

1 Introduction

Porosity, a major production problem in many die casting products, results from shrinkage (difference between liquid density and solid density) and gas entrapment (gases entrapped in the liquid metal). The porosity due to entrapped gases constitutes a large portion of the total porosity especially when the cast walls are very thin (the shrinkage porosity is proportional to the cast thickness (Bar-Meir, 1995a)). The main causes for high porosity are insufficient vent area, lubricant evaporation (reaction processes), incorrect placement of the vents, and mixing processes during the filling time.

Discussions on these causes, except for an insufficient vent area, can be found elsewhere (Bar-Meir, Eckert and Goldstein, 1996) and (Bar-Meir, 1995b). The most widely used casting method opens the vent to the atmosphere. It is referred to herein as air venting. When the results for air venting are poor other methods such as vacuum venting, Pore Free Technique (in zinc and aluminum casting) or squeeze casting are used. The present work considers the influence of vent area in air venting on the gas remaining in the die at the end of the flow injection process.

The best ventilation is achieved for a die with a large vent area. However, to minimize the secondary machining such as trimming and to insure freezing of the liquid metal in the mold, the gates and vents have to be very narrow. A typical size of the vents and gate thicknesses is in the range of 1 to 2 mm. The conflicting requirements on the vent area suggest an optimum area, which is also indicated by experimental studies. Prior models (Sachs, 1952; Draper, 1967; Veinik, 1962; Lindsey and Wallace, 1972) in predicting optimum vent area do not consider the resistance in the venting system. The vent design in a commercial system includes at least an exit, several ducts, and several abrupt expansions/contractions in which the resistance coefficient $4fL/D$ (Shapiro, 1953) is of the order of 3 to 7 or more. In this case, the pressure ratio for the choking condition is at least 3 (Bar-Meir, Eckert and Goldstein, 1996) and the pressure ratio reaches this value only after about $\frac{1}{2}$ to $\frac{2}{3}$ of the piston stroke has elapsed.

Analysis of the air venting yields a solution for the critical/optimum vent area and finding this area in a simple form is one of the objectives of this study. The second objective is to provide a tool to "combine" the actual vent area with the resistance in the vent to the air flow, thus eliminating the need for calculating the gas flow in the vent. Hu et al. (1992) and others have shown that the air pressure is practically uniform in the system. Hence this analysis can also provide the average air pressure.

2 The Model

The derivation of the governing equations is given elsewhere (Bar-Meir, Eckert and Goldstein, 1996); only a short summary is presented herein. Figure 1 is a schematic of a die casting system with an air vent. The following model is proposed for the analysis. The main resistance to the air flow is assumed to

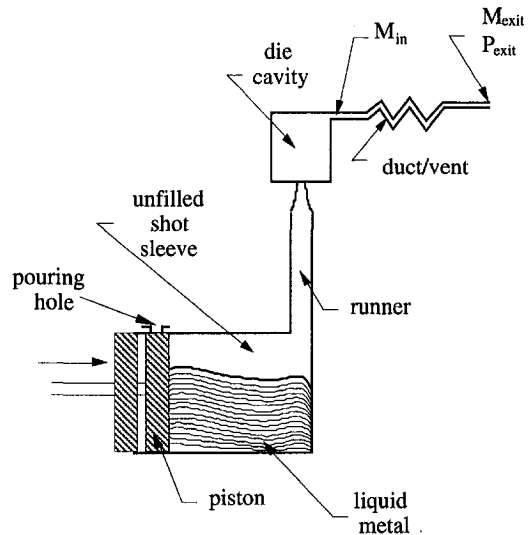


Fig. 1 A schematic of air venting in pressure die casting

be in the venting system. The unfilled shot sleeve and the die cavity with the runner are combined and called the cylinder. A piston, assumed moving with a constant known velocity, pushes the liquid metal, and both of them propel the air through a long straight duct as shown in Fig. 2.

In the cylinder we assume one-dimensional flow of an ideal gas undergoing an isentropic process. Two equations must be solved for the Mach numbers at the duct entrance and exit when the flow is un-choked. They are combinations of the momentum and energy equations in terms of the Mach numbers. The equations, characteristic of Fanno flow (Shapiro, 1953), are

$$\frac{4fL}{D} = \left[\frac{4fL_{\max}}{D} \right]_{M_{in}} - \left[\frac{4fL_{\max}}{D} \right]_{M_{exit}} \quad (1)$$

and

$$\frac{P_{exit}}{P_0(t)} = \left[1 + \frac{k-1}{2} M_{exit}^2 \right]^{k/(1-k)} \times \frac{M_{in}}{M_{exit}} \sqrt{\frac{1 + \frac{k-1}{2} M_{exit}^2}{1 + \frac{k-1}{2} M_{in}^2}}^{(k+1/k-1)} \quad (2)$$

where $4fL/D$ is defined by Bar-Meir et al. (1996).

The solution of Eqs. (1) and (2) for given $4fL/D$ and $P_{exit}/P_0(t)$ yields the entrance and exit Mach numbers. The term $4fL/D$ is very large for small values of the entrance Mach number which requires keeping many digits in the calculation. For small values of the Mach numbers, Eq. (1) can be approximated as

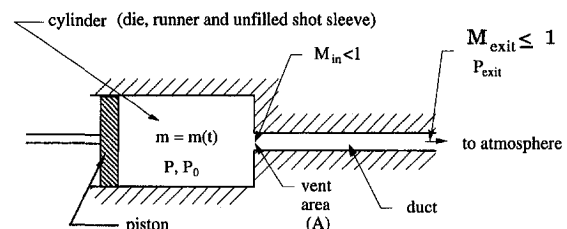


Fig. 2 A simplified model for air venting

$$\frac{4fL}{D} = \frac{1}{k} \frac{M_{\text{exit}}^2 - M_{\text{in}}^2}{M_{\text{exit}} M_{\text{in}}^2} \quad (3)$$

and Eq. (2) as

$$\frac{P_{\text{exit}}}{P_0(t)} = \frac{M_{\text{in}}}{M_{\text{exit}}} \quad (4)$$

The solution of the last two equations yields

$$M_{\text{in}} = \sqrt{\frac{1 - \left[\frac{P_{\text{exit}}}{P_0(t)} \right]^2}{k \frac{4fL}{D}}} \quad (5)$$

This solution is used only for $M_{\text{in}} < 0.00286$; otherwise Eqs. (1) and (2) must be solved.

The mass flow rate can be written

$$\dot{m}_{\text{in}} = P_0(0) A M_{\text{max}} \frac{M_{\text{in}}(t)}{M_{\text{max}}} \left(\frac{P_0(0)}{P_0(t)} \right)^{k+1/2k} \times \sqrt{\frac{k}{RT_0(0)}} f[M_{\text{in}}(t)] \quad (6)$$

where

$$f[M_{\text{in}}(t)] = \left[1 + \frac{k-1}{2} (M_{\text{in}}(t))^2 \right]^{-(k+1)/(2(k-1))} \quad (7)$$

and where M_{max} is the maximum entrance Mach number for a specific duct, determined from $4fL/D$.

The mass balance of the air in the piston and the cavity yields

$$\frac{dm}{dt} + \dot{m}_{\text{in}} = 0 \quad (8)$$

3 The Solution

For the ideal gas model and constant piston velocity, substituting Eq. (6) into Eq. (8) yields

$$\left[\bar{P} \right]^{1/k} \left\{ \frac{1}{k} \frac{V(t)}{\bar{P}} \frac{d\bar{P}}{dt} + \frac{dV(t)}{dt} \right\} + \frac{V(0)}{t_c} \bar{M} f(M) [\bar{P}]^{k+1/2k} = 0 \quad (9)$$

where

$$t_c \approx \frac{m(0)}{\dot{m}_{\text{in}}^*}, \quad \text{and} \quad (10)$$

$$\dot{m}_{\text{in}}^* = A M_{\text{max}} P_0(0) \sqrt{\frac{k}{RT_0(0)}} \quad (11)$$

Note, $m(0)$ is the initial mass of the air in the cylinder and \dot{m}_{in}^* is the mass flow rate when the flow is choked and the pressure and temperature remain at their initial values.

Equation (9) is an ordinary differential equation and can be rearranged as follows

$$\frac{d\bar{P}}{d\bar{t}} = \frac{k \left(1 - \frac{t_{\text{max}}}{t_c} \bar{M} f(M_{\text{in}}) \bar{P}^{k-1/2k} \right)}{1 - \bar{t}} \bar{P}; \quad \bar{P}(0) = 1 \quad (12)$$

The solution of Eq. (12) can be obtained by numerical integration. The residual mass fraction in the cavity as a function of time is then determined using the ideal gas assumption.

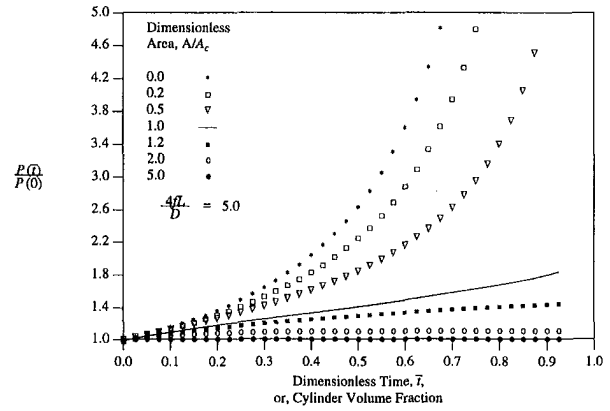


Fig. 3 The pressure ratio as a function of the dimensionless time

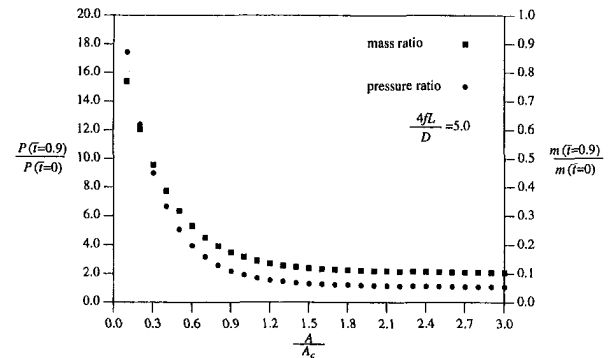


Fig. 4 The pressure ratio at 90 percent of the piston stroke

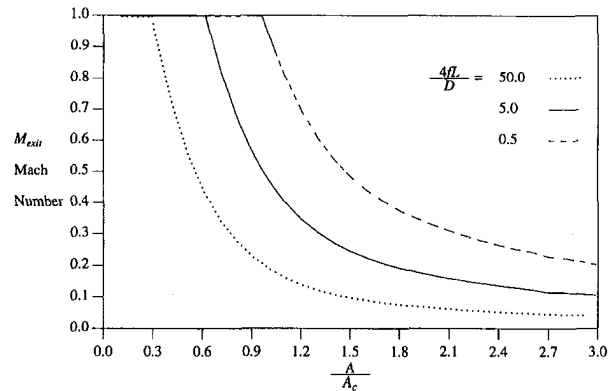


Fig. 5 The exit Mach number at 90 percent of the piston stroke

4 Results and Discussion

The results of a numerical evaluation of the equations in the preceding section are presented in Figs. 3 through 5. Figure 3 illustrates the variations of the pressure \bar{P} in the cylinder with dimensionless time, Fig. 4 exhibits the final pressure and the residual mass fraction when 90 percent of the stroke has elapsed as a function of A/A_c . (The critical area A_c is the area that makes the time ratio, t_{max}/t_c , equal to one. It is given by Eq. (14).) Figure 5 shows the variation of the exit Mach number, M_{exit} , as a function of the dimensionless vent area.

Parameters influencing the process are the area ratio, A/A_c , and the friction parameter, $4fL/D$. Detailed calculations (Bar-Meir, 1995a) show that the influence of the parameter $4fL/D$ on the pressure development in the cylinder is quite small; its influence is also small on the residual air mass in the cylinder

but larger on the Mach number, M_{exit} . The effects of the area ratio, A/A_C , are studied here since it is the dominant parameter.

It is important to point out the significance of the t_{max}/t_c . This parameter represents the ratio between the filling time and the evacuating time, the time which would be required to evacuate the cylinder for constant mass flow rate at the maximum Mach number when the gas temperature and pressure remain in their initial values. This parameter also represents the dimensionless area, A/A_C , according to the following equation

$$\frac{t_{\text{max}}}{t_c} = \frac{A}{A_C}, \quad (13)$$

Figure 3 describes the pressure as a function of the dimensionless time for various values of A/A_C . The line that represents $A/A_C = 1$ is almost straight. For large values of A/A_C the pressure increases with the volume flow of air until a quasi-steady state is reached. This quasi-steady state is achieved when the volumetric air flow rate out is equal to the volume pushed by the piston. The pressure and the mass flow rate are maintained constant after this state is reached. The pressure in this quasi-steady state is a function of A/A_C . For small values of A/A_C there is no steady-state stage. When A/A_C is greater than one the pressure curve is concave upwards and when A/A_C is less than one the pressure curve is concave downwards as shown in Fig. 3, which was obtained by an integration of Eq. (12).

This result is in contrast to Sachs (1952), Draper (1967), Veinik (1962), and Lindsey and Wallace (1972) where models assumed that the pressure and mass flow rate remain constant and are attained instantaneously.

To refer to the stroke completion (100 percent of the stroke) is meaningless since 1) no gas mass is left in the cylinder and thus no pressure can be measured, and 2) the vent can be blocked partially or totally at that the end of the stroke. Thus, the position when 90 percent of the stroke is completed will be used to describe the situation near the end of the process. Figure 4 presents the final pressure ratio as a function A/A_C for $4fL/D = 5$. The final pressure (really pressure ratio) depends strongly on A/A_C as is described in Fig. 4. The pressure in the die cavity increases by about 85 percent of its initial value when $A/A_C = 1$. The pressure remains almost constant after A/A_C reaches the value of 1.2. This implies that the vent area is sufficiently large when $A/A_C = 1.2$. The same can be observed from the line of the residual mass fraction.

Figure 5 describes the Mach number at the exit of the vent as a function of the dimensionless area for three values of $4fL/D$. The flow is choked only for a small dimensionless area, $A/A_C < 1$. For large $4fL/D$ the flow is not choked even for small A/A_C as sufficient pressure difference would not be available. The change from choked flow to a low exit Mach number occurs within a small range of vent area. Thus, the choking condition which was assumed by the previous studies (Sachs 1952; Draper 1967; Veinik 1962; Lindsey and Wallace 1972) is correct only for small $4fL/D$ and A/A_C . The desired situation is when A/A_C is large and only $4fL/D$ is small.

Typical values for $4fL/D$ can range between 0.5 and 50 with corresponding values of the M_{max} of 0.57 and ~ 0.11 , respectively. A simplified equation can be obtained for the critical vent area, valid for essentially any real system, by equating the time ratio t_{max}/t_c to one and using Eq. (10) to yield

$$A_c = \frac{V(0)}{c t_{\text{max}} M_{\text{max}}}, \quad (14)$$

where c is the speed of sound at the initial condition inside the cylinder (ambient condition).

5 Summary

The analysis indicates there is a critical vent area below which the ventilation is poor and above which the resistance to

air flow is minimal. This critical area depends on the geometry and the filling time. The critical area also provides a mean to "combine" the actual vent area with the vent resistance for numerical simulations of the cavity filling, taking into account the compressibility of the gas flow.

Acknowledgment

We would like to thank Hartzell Manufacturing for their support and discussions on this topic, the Productivity Center (CAMDAC) of the University of Minnesota for financial support, Professor S. Ramalingam for stimulating much of our work on die casting, and Mr. Barry Rackner for helping optimize the code. These calculations were carried out at the Minnesota Supercomputer Institute.

References

- Bar-Meir, G., 1995a, "On Gas/Air Porosity in Pressure Die Casting," PhD thesis, University of Minnesota.
- Bar-Meir, G., 1995b, "Analysis of Mass Transfer Processes in the Pore Free Technique," *ASME Journal of Engineering Materials and Technology*, Vol. 117, pp. 215–219.
- Bar-Meir, G., Eckert, E., and Goldstein, R. J., 1996, "Pressure Die Casting: A Model of Vacuum Pumping," *ASME Journal of Engineering for Industry*, Vol. 118, pp. 001–007.
- Draper, A. B., 1967, "Effect of Vent and Gate Areas on the Porosity of Die Casting," *Transactions of American Foundrymen's Society*, Vol. 75, pp. 727–734.
- Hu, J., Ramalingam, S., Meyerson, G., Eckert, E., and Goldstein, R. J., 1992, "Experiment and Computer Modeling of the Flows in Pressure Die Casting Casings," *ASME/CIE Design*, San Francisco, CA.
- Lindsey, D., and Wallace, J. F., 1972, "Effect of Vent Size and Design, Lubrication Practice, Metal Degassing, Die Texturing and Filling of Shot Sleeve on Die Casting Soundness," *Transactions 7th SDCE International Die Casting Congress*, Chicago, paper 10372.
- Sachs, B., 1952, "An Analytical Study of the Die Casting Process," PhD thesis, Columbia University.
- Shapiro, A. H., 1953, *The Dynamics and Thermodynamics of Compressible Fluid Flow*, Vol. I, Wiley, New York.
- Veinik, A. I., 1962, *Theory of Special Casting Method*, ASME, New York.

Stability of Various Molecular Dynamics Algorithms

Akira Satoh¹

Nomenclature

- E_{TOT} = total energy of system
- f_i = force vector of molecule i
- h = time interval
- k = Boltzmann's constant
- m = mass of molecule
- N = number of molecules
- n = molecular number density
- r_i = position vector of molecule i
- T = temperature
- t = time
- t_{div} = divergence time
- u = Lennard-Jones potential
- V = volume of system

¹ Department of Mechanical Engineering, Faculty of Engineering, Chiba University, 1-33, Yayoi-cho, Inage-ku, Chiba 263, Japan.

Contributed by the Fluids Engineering Division of THE AMERICAN SOCIETY OF MECHANICAL ENGINEERS. Manuscript received by the Fluids Engineering Division June 25, 1996; revised manuscript received February 11, 1997. Associate Technical Editor: F. Giralt.

but larger on the Mach number, M_{exit} . The effects of the area ratio, A/A_C , are studied here since it is the dominant parameter.

It is important to point out the significance of the t_{max}/t_c . This parameter represents the ratio between the filling time and the evacuating time, the time which would be required to evacuate the cylinder for constant mass flow rate at the maximum Mach number when the gas temperature and pressure remain in their initial values. This parameter also represents the dimensionless area, A/A_C , according to the following equation

$$\frac{t_{\text{max}}}{t_c} = \frac{A}{A_C}, \quad (13)$$

Figure 3 describes the pressure as a function of the dimensionless time for various values of A/A_C . The line that represents $A/A_C = 1$ is almost straight. For large values of A/A_C the pressure increases with the volume flow of air until a quasi-steady state is reached. This quasi-steady state is achieved when the volumetric air flow rate out is equal to the volume pushed by the piston. The pressure and the mass flow rate are maintained constant after this state is reached. The pressure in this quasi-steady state is a function of A/A_C . For small values of A/A_C there is no steady-state stage. When A/A_C is greater than one the pressure curve is concave upwards and when A/A_C is less than one the pressure curve is concave downwards as shown in Fig. 3, which was obtained by an integration of Eq. (12).

This result is in contrast to Sachs (1952), Draper (1967), Veinik (1962), and Lindsey and Wallace (1972) where models assumed that the pressure and mass flow rate remain constant and are attained instantaneously.

To refer to the stroke completion (100 percent of the stroke) is meaningless since 1) no gas mass is left in the cylinder and thus no pressure can be measured, and 2) the vent can be blocked partially or totally at that the end of the stroke. Thus, the position when 90 percent of the stroke is completed will be used to describe the situation near the end of the process. Figure 4 presents the final pressure ratio as a function A/A_C for $4fL/D = 5$. The final pressure (really pressure ratio) depends strongly on A/A_C as is described in Fig. 4. The pressure in the die cavity increases by about 85 percent of its initial value when $A/A_C = 1$. The pressure remains almost constant after A/A_C reaches the value of 1.2. This implies that the vent area is sufficiently large when $A/A_C = 1.2$. The same can be observed from the line of the residual mass fraction.

Figure 5 describes the Mach number at the exit of the vent as a function of the dimensionless area for three values of $4fL/D$. The flow is choked only for a small dimensionless area, $A/A_C < 1$. For large $4fL/D$ the flow is not choked even for small A/A_C as sufficient pressure difference would not be available. The change from choked flow to a low exit Mach number occurs within a small range of vent area. Thus, the choking condition which was assumed by the previous studies (Sachs 1952; Draper 1967; Veinik 1962; Lindsey and Wallace 1972) is correct only for small $4fL/D$ and A/A_C . The desired situation is when A/A_C is large and only $4fL/D$ is small.

Typical values for $4fL/D$ can range between 0.5 and 50 with corresponding values of the M_{max} of 0.57 and ~ 0.11 , respectively. A simplified equation can be obtained for the critical vent area, valid for essentially any real system, by equating the time ratio t_{max}/t_c to one and using Eq. (10) to yield

$$A_c = \frac{V(0)}{c t_{\text{max}} M_{\text{max}}}, \quad (14)$$

where c is the speed of sound at the initial condition inside the cylinder (ambient condition).

5 Summary

The analysis indicates there is a critical vent area below which the ventilation is poor and above which the resistance to

air flow is minimal. This critical area depends on the geometry and the filling time. The critical area also provides a mean to "combine" the actual vent area with the vent resistance for numerical simulations of the cavity filling, taking into account the compressibility of the gas flow.

Acknowledgment

We would like to thank Hartzell Manufacturing for their support and discussions on this topic, the Productivity Center (CAMDAC) of the University of Minnesota for financial support, Professor S. Ramalingam for stimulating much of our work on die casting, and Mr. Barry Rackner for helping optimize the code. These calculations were carried out at the Minnesota Supercomputer Institute.

References

- Bar-Meir, G., 1995a, "On Gas/Air Porosity in Pressure Die Casting," PhD thesis, University of Minnesota.
- Bar-Meir, G., 1995b, "Analysis of Mass Transfer Processes in the Pore Free Technique," *ASME Journal of Engineering Materials and Technology*, Vol. 117, pp. 215–219.
- Bar-Meir, G., Eckert, E., and Goldstein, R. J., 1996, "Pressure Die Casting: A Model of Vacuum Pumping," *ASME Journal of Engineering for Industry*, Vol. 118, pp. 001–007.
- Draper, A. B., 1967, "Effect of Vent and Gate Areas on the Porosity of Die Casting," *Transactions of American Foundrymen's Society*, Vol. 75, pp. 727–734.
- Hu, J., Ramalingam, S., Meyerson, G., Eckert, E., and Goldstein, R. J., 1992, "Experiment and Computer Modeling of the Flows in Pressure Die Casting Casings," *ASME/CIE Design*, San Francisco, CA.
- Lindsey, D., and Wallace, J. F., 1972, "Effect of Vent Size and Design, Lubrication Practice, Metal Degassing, Die Texturing and Filling of Shot Sleeve on Die Casting Soundness," *Transactions 7th SDCE International Die Casting Congress*, Chicago, paper 10372.
- Sachs, B., 1952, "An Analytical Study of the Die Casting Process," PhD thesis, Columbia University.
- Shapiro, A. H., 1953, *The Dynamics and Thermodynamics of Compressible Fluid Flow*, Vol. I, Wiley, New York.
- Veinik, A. I., 1962, *Theory of Special Casting Method*, ASME, New York.

Stability of Various Molecular Dynamics Algorithms

Akira Satoh¹

Nomenclature

- E_{TOT} = total energy of system
- f_i = force vector of molecule i
- h = time interval
- k = Boltzmann's constant
- m = mass of molecule
- N = number of molecules
- n = molecular number density
- r_i = position vector of molecule i
- T = temperature
- t = time
- t_{div} = divergence time
- u = Lennard-Jones potential
- V = volume of system

¹ Department of Mechanical Engineering, Faculty of Engineering, Chiba University, 1-33, Yayoi-cho, Inage-ku, Chiba 263, Japan.

Contributed by the Fluids Engineering Division of THE AMERICAN SOCIETY OF MECHANICAL ENGINEERS. Manuscript received by the Fluids Engineering Division June 25, 1996; revised manuscript received February 11, 1997. Associate Technical Editor: F. Giralt.

v_i = velocity vector of molecule i
 ϵ, σ = constants of Lennard-Jones potential
 $\langle \rangle$ = ensemble average

Superscripts

$*$ = nondimensional quantities
 n = time step

1 Introduction

Molecular dynamics (MD) is a molecular simulation method and a powerful tool for investigating physical phenomena from a microscopic point of view (Heermann, 1990; Allen and Tildesley, 1987). The recent appearance of supercomputers stimulates the application of MD methods to fluids engineering fields: for example, internal structures of shock waves in liquids (Holian, 1988; Tsai and Trevino, 1981; Satoh, 1995a), a flow around a sphere (Satoh, 1993a), a flow around a cylinder (Rapaport, 1987; Satoh, 1993b), Bénard cell problems (Mareschal et al., 1988), etc.

MD simulations for flow problems require much more computation time than for thermodynamic equilibrium, since the simulations cannot dispense with a large molecular system (more than about 100,000 molecules) that is several order of magnitude larger than that of the usual equilibrium investigation (usually 500 ~ 5,000 molecules). In this situation, the method of trial-and-error cannot efficiently be used to determine a suitable time interval. Hence, we need a useful criterion for the choice of an appropriate time interval. Even rough criterion data seem to be very useful for actual molecular simulation researchers who attempt to apply MD methods to engineering fields.

The previous paper (Satoh, 1995b) concentrated on the velocity Verlet algorithm, which is frequently used in simulations, and clarified the relationships between divergence processes and time intervals. The present paper extends these studies to other MD algorithms such as leapfrog, Beeman, Gear algorithms, etc.

2 Various Microcanonical Ensemble Molecular Dynamics Algorithms

2.1 Lennard-Jones System. We consider a model system with number density n and volume V , for the Lennard-Jones molecule. The potential of a pair of Lennard-Jones molecules, $u(r)$, is expressed as $u(r) = 4\epsilon\{(\sigma/r)^{12} - (\sigma/r)^6\}$, in which σ is the effective molecular diameter, ϵ the depth of potential curve, and r the distance between molecules. For Lennard-Jones systems, it is very convenient for each quantity to be normalized by the following representative values. The length is σ , the energy ϵ , the force ϵ/σ , the velocity $(\epsilon/m)^{1/2}$, the time $\sigma(m/\epsilon)^{1/2}$, the temperature ϵ/k , the number density $1/\sigma^3$, and the density m/σ^3 , where m is the molecular mass, and k is Boltzmann's constant. Nondimensional quantities will be described by the superscript $*$.

2.2 Velocity Verlet, Beeman, and Leapfrog Algorithms. If denoting the time interval by h^* and the time step by the superscript n , the following expressions may be derived from the Taylor series expansions:

$$r_i^{*n+1} = r_i^{*n} + h^*v_i^{*n} + \frac{h^{*2}}{2}f_i^{*n} + \frac{h^{*3}}{6} \cdot \frac{df_i^{*n}}{dt^*} + O(h^{*4}), \quad (1)$$

$$v_i^{*n+1} = v_i^{*n} + h^*f_i^{*n} + \frac{h^{*2}}{2} \cdot \frac{df_i^{*n}}{dt^*} + O(h^{*3}), \quad (2)$$

in which r_i^* is the molecular position vector expressed as (x_i^*, y_i^*, z_i^*) , v_i^* is the molecular velocity vector expressed as $(v_{xi}^*, v_{yi}^*, v_{zi}^*)$, f_i^* is the force acting the molecule i from the ambient molecules expressed as $(f_{xi}^*, f_{yi}^*, f_{zi}^*)$.

The use of different finite difference approximations for the first order differential terms in Eqs. (1) and (2) leads to different molecular dynamics algorithms. We show the final expressions in the following.

Velocity Verlet algorithm is:

$$r_i^{*n+1} = r_i^{*n} + h^*v_i^{*n} + \frac{h^{*2}}{2}f_i^{*n} + O(h^{*3}), \quad (3)$$

$$v_i^{*n+1} = v_i^{*n} + h^*\{f_i^{*n+1} + f_i^{*n}\}/2 + O(h^{*3}). \quad (4)$$

Beeman algorithm is:

$$r_i^{*n+1} = r_i^{*n} + h^*v_i^{*n} + \frac{h^{*2}}{6}(4f_i^{*n} - f_i^{*n-1}) + O(h^{*4}). \quad (5)$$

$$v_i^{*n+1} = v_i^{*n} + h^*\{2f_i^{*n+1} + 5f_i^{*n} - f_i^{*n-1}\}/6 + O(h^{*3}). \quad (6)$$

Leapfrog algorithm is:

$$r_i^{*n+1} = r_i^{*n} + h^*v_i^{*n+(1/2)} + O(h^{*3}), \quad (7)$$

$$v_i^{*n+(1/2)} = v_i^{*n-(1/2)} + h^*f_i^{*n} + O(h^{*3}). \quad (8)$$

2.3 Gear Algorithm. This algorithm is one of predictor-corrector methods and the form of the equations depends on the number of physical quantities of interest. We therefore concentrate on the 4-value Gear algorithm in the present paper. The predictors are obtained from Taylor series expansions as,

$$\left. \begin{aligned} {}^p r_i^{*n+1} &= r_i^{*n} + h^*v_i^{*n} + \frac{h^{*2}}{2}f_i^{*n} \\ &\quad + \frac{h^{*3}}{6}b_i^{*n} + O(h^{*4}), \\ {}^p v_i^{*n+1} &= v_i^{*n} + h^*f_i^{*n} + \frac{h^{*2}}{2}b_i^{*n} + O(h^{*3}), \\ {}^p f_i^{*n+1} &= f_i^{*n} + h^*b_i^{*n} + O(h^{*2}), \\ {}^p b_i^{*n+1} &= b_i^{*n} + O(h^*). \end{aligned} \right\} \quad (9)$$

The correctors of forces, ${}^c f_i^{*n+1}$, can be calculated using the predictors of positions, ${}^p r_i^{*n+1}$. If denoting the difference by $\Delta f_i^* = {}^c f_i^{*n+1} - {}^p f_i^{*n+1}$, the correctors can be evaluated as follows:

$$\left. \begin{aligned} {}^c r_i^{*n+1} &= {}^p r_i^{*n+1} + c_0(h^{*2}/2)\Delta f_i^*, \\ {}^c v_i^{*n+1} &= {}^p v_i^{*n+1} + c_1(h^*/2)\Delta f_i^*, \\ {}^c f_i^{*n+1} &= {}^p f_i^{*n+1} + c_2\Delta f_i^*, \\ {}^c b_i^{*n+1} &= {}^p b_i^{*n+1} + c_3(3/h^*)\Delta f_i^*, \end{aligned} \right\} \quad (10)$$

where the constants are $c_0 = \frac{1}{6}$, $c_1 = \frac{5}{6}$, $c_2 = 1$, and $c_3 = \frac{1}{3}$.

2.4 Other Algorithms. Equations (5) and (4) may be used for positions and velocities. We call this algorithm "A algorithm."

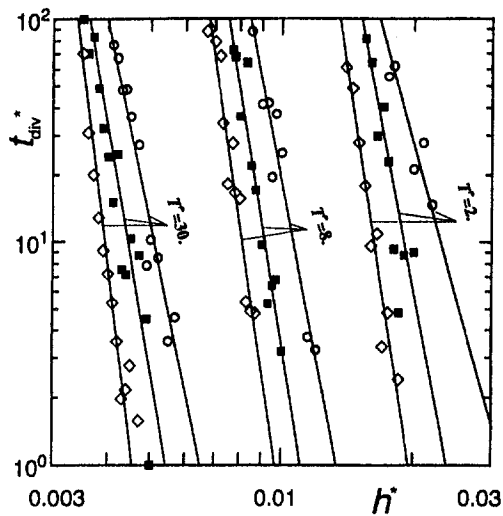


Fig. 1(a) Velocity Verlet

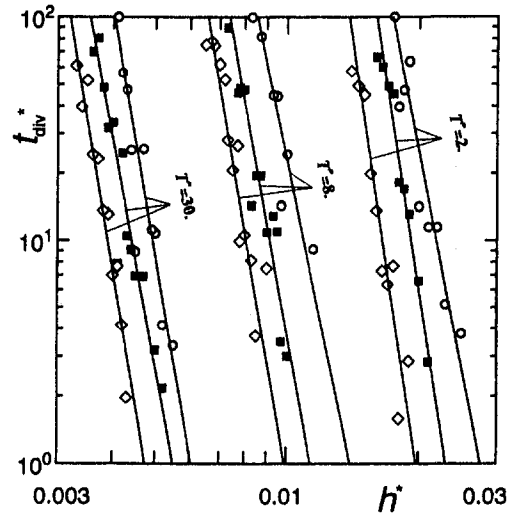


Fig. 1(b) Leapfrog

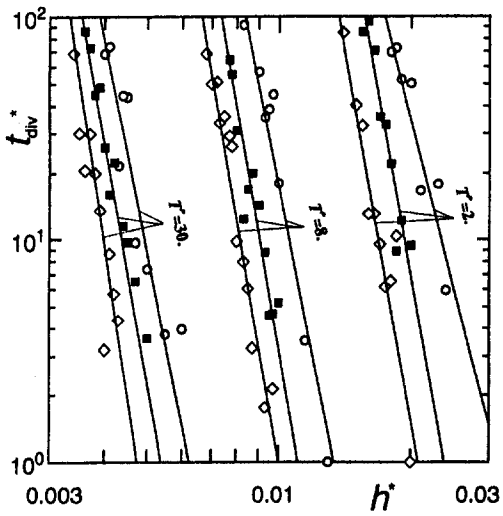


Fig. 1(c) Beeman

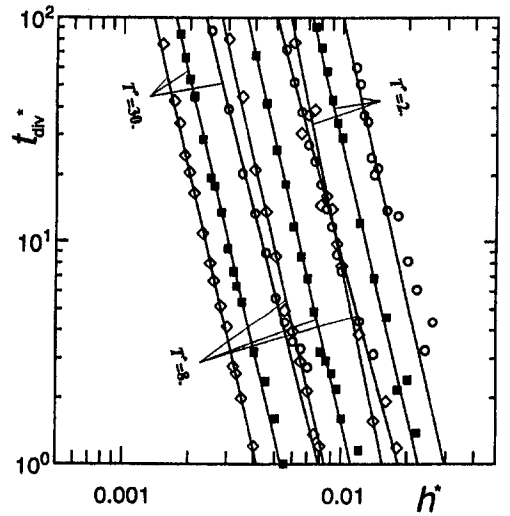


Fig. 1(d) 4-value Gear

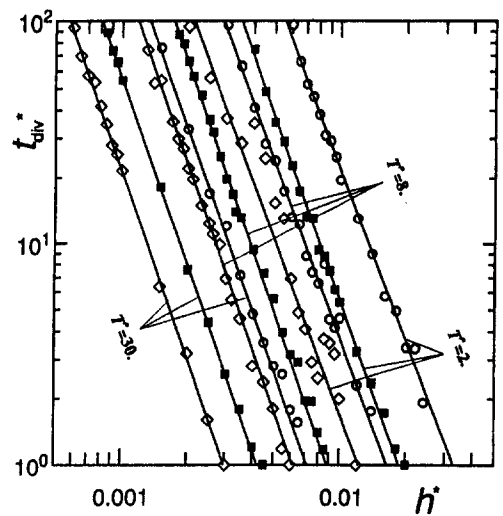


Fig. 1(e) A algorithm

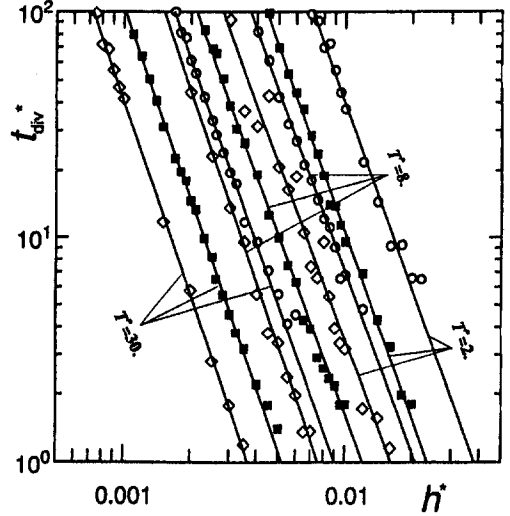


Fig. 1(f) B algorithm

Fig. 1 Relations between divergence times and time intervals; open circle, $n^* = 0.2$; solid square, $n^* = 0.6$; open rhombus, $n^* = 1.0$

If keeping the h^{*3} term in Eq. (2) and using the following relations:

$$\frac{df_i^{*n}}{dt^*} = \frac{f_i^{*(n+1)} - f_i^{*(n-1)}}{2h^*} + O(h^{*2}), \quad (11)$$

$$\frac{d^2f_i^{*n}}{dt^{*2}} = \frac{f_i^{*(n+1)} - 2f_i^{*n} + f_i^{*(n-1)}}{h^{*2}} + O(h^{*2}), \quad (12)$$

then the equation of velocities is obtained as

$$v_i^{*(n+1)} = v_i^{*n} + h^* \{5f_i^{*(n+1)} + 8f_i^{*n} - f_i^{*(n-1)}\} / 12 + O(h^{*4}). \quad (13)$$

We call the algorithm using Eqs. (5) and (13) "B algorithm."

3 Parameters for Simulations

The simulation region is taken as a cube, in which the molecules are initially placed on the sites of a close-packed lattice. The initial molecular velocities are given according to a Maxwellian distribution by using uniform random numbers. Equilibration procedures are carried out up to 1000 time steps using a set time interval in each run; the desired temperature can be obtained by scaling the molecular velocities every 0.2 nondimensional times. The number of molecules, N , is 108 and the cutoff radius r_c^* is 2.5 for $n^* = 0.2, 0.6$ and 2.38 for $n^* = 1.0$. In evaluating the energy conservation law, the simulations have been continued up to $t^* \doteq 100$ to obtain the averaged values of energy fluctuations.

4 Results and Discussion

4.1 Time Intervals and Divergence Times. Figure 1 shows the relationships between divergence times t_{div}^* and time intervals h^* for the above-mentioned algorithms. It was shown in the previous paper (Sato, 1995b) that, for the velocity Verlet algorithm, the instant temperature of a system gradually increases with time and then diverges exponentially at a certain time. This divergence process is common to the velocity Verlet, leapfrog, and Beeman algorithms, while the 4-value Gear, A, and B algorithms give an opposite divergence process, namely, the instant temperature gradually decreases with time. The divergence time is, therefore, defined as the time at which the instant temperature deviates from a prescribed temperature by 30 percent.

Figure 1 shows that these algorithms have the following common features. The relationship between the divergence times and the time intervals is well expressed as linear functions if the results are plotted on logarithmic scales. It is found that a system has a strong tendency to diverge with increasing number density and increasing temperature. This means that smaller time intervals have to be used for a system with a higher number density and/or higher temperature.

Figure 1 also shows the intrinsic features of each algorithm as follows. The velocity Verlet, leapfrog, and Beeman algorithms exhibit almost same characteristic concerning the relationships between the divergence times and the size of the time intervals. It is clear that these algorithms give larger divergence times for a same time interval than the 4-value Gear, A, and B algorithms. The A and B algorithm are seen to be clearly inferior to even the 4-value Gear algorithm. It is very interesting that the A algorithm is found to perform so poorly, since this algorithm is the combined form of the position equation of the Beeman algorithm and the velocity equation of the velocity Verlet algorithm. Since the 4-value Gear algorithm is a predictor-corrector method, this algorithm is theoretically an algorithm with higher accuracy than the velocity Verlet and leapfrog algorithms. The results show, however, that in practice there is no advantage in this respect. Similarly, the Beeman algorithm uses a more accu-

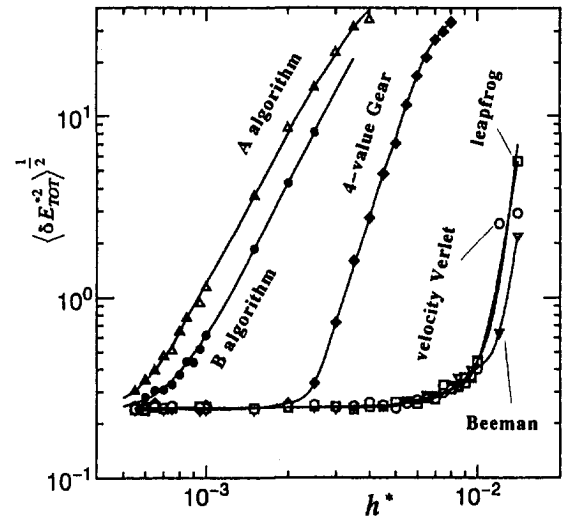


Fig. 2(a) $n^* = 0.6$ and $T^* = 2$

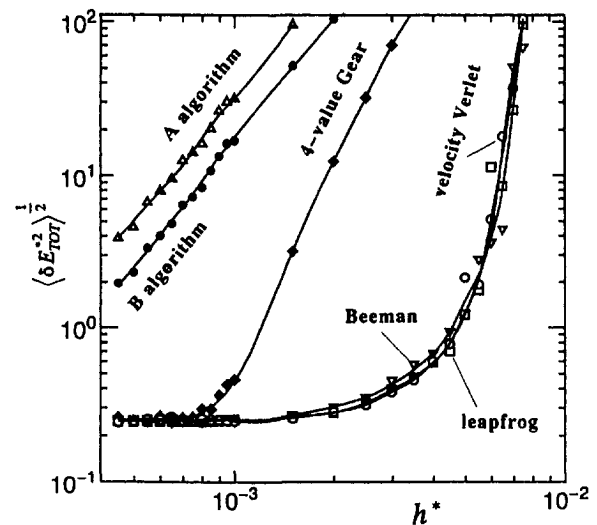


Fig. 2(b) $n^* = 0.6$ and $T^* = 8$

Fig. 2 Energy fluctuations; open circle, velocity Verlet; open square, leapfrog; open reverse triangle, Beeman; solid rhombus, 4-value Gear; open triangle, A algorithm; solid circle, B algorithm

rate expression than the velocity Verlet and leapfrog algorithms in the velocity equation, there appears to be no significant difference in their respective stability. This observation is also common to the A and B algorithms. We may conclude from these facts that a theoretically accurate form of molecular dynamics algorithm does not necessarily lead to a superior feature of the stability.

4.2 Fluctuations in Total Energy. All algorithms shown in Section 2 are for a microcanonical ensemble, so that the sum of kinetic and potential energies of a system, E_{TOT} , has to be conserved in a simulation process. We therefore consider the ensemble-average of the fluctuation in the total system energy, $\langle \delta E_{TOT}^2 \rangle^{1/2}$, in order to discuss the accuracy of the algorithms. The expression is written as

$$\langle \delta E_{TOT}^2 \rangle = \langle E_{TOT}^2 \rangle - \langle E_{TOT} \rangle^2, \quad (14)$$

in which $\langle E_{TOT} \rangle$ is the ensemble-averaged values of the total energy of a system.

Figure 2 shows the results of the energy fluctuation. It is clear from Figs. 2(a) and (b) that the velocity Verlet, leapfrog,

and Beeman algorithms also show a superior performance regarding the energy conservation. They maintain small energy fluctuations even for the larger values of h^* . On the other hand, although the 4-value Gear algorithm is a theoretically more accurate form than the above three algorithms, it does not exhibit smaller energy fluctuations under similar conditions. Again, these results clearly show that a theoretically more accurate molecular dynamics algorithm does not necessarily give rise to an improved performance for a multiparticle system. This is contrary to the results for a very simple case such as a harmonic oscillator (Berendsen and Gunsteren, 1986) and one-dimensional motion of two molecules (Haile, 1992). For these cases, a one order higher Gear algorithm produces a better performance of the energy conservation than the velocity Verlet and leapfrog algorithms. The A and B algorithms require approximately an order of magnitude smaller time interval in order to maintain an equivalent performance.

5 Concluding Remarks

Since molecular dynamics simulations of flow problems are generally a large-scale simulation, it is desirable to use an algorithm which allows as large a time interval as possible, and which also requires the minimum of computer memory. From this point of view, with the results shown in Sections 4.1 and 4.2, we may conclude that the most superior algorithm is the velocity Verlet, followed by the leapfrog, and then the Beeman. The 4-value Gear algorithm is inferior to these algorithms in that it is complicated and has a worse performance in terms of the stability and the energy fluctuation. The A and B algorithms

are found to perform less well than the 4-value Gear algorithm, and are not considered to be appropriate for the simulations of flow problems.

References

- Allen, M. P., and Tildesley, D. J., 1987, *Computer Simulation of Liquids*, Clarendon Press, Oxford.
- Berendsen, H. J. C., and Gunsteren, W. F., 1986, *Molecular-Dynamics Simulation of Statistical-Mechanical Systems*, Ciccoliti, G., and Hoover, W. G., eds, North-Holland Physics Publishing, p. 43.
- Haile, J. M., 1992, *Molecular Dynamics Simulation: Elementary Methods*, Wiley, New York.
- Heermann, D. W., 1990, *Computer Simulation Methods in Theoretical Physics*, 2nd Ed., Springer-Verlag, Berlin.
- Holian, B. L., 1988, "Modeling Shock-Wave Deformation via Molecular Dynamics," *Physical Review A*, Vol. 37, pp. 2562–2568.
- Mareschal, M., Mansour, M. M., Puhl, A., and Kestemont, E., 1988, "Molecular Dynamics versus Hydrodynamics in a Two-Dimensional Rayleigh-Bénard System," *Physical Review Letters*, Vol. 61, pp. 2550–2553.
- Rapaport, D. C., 1987, "Microscale Hydrodynamics (Discrete-Particle Simulation of Evolving Flow Patterns)," *Physical Review A*, Vol. 36, pp. 3288–3299.
- Satoh, A., 1993a, "Molecular Dynamics Simulation of a Subsonic Flow of a Rarefied Gas past a Sphere," *Advanced Powder Technology*, Vol. 4, pp. 59–70.
- Satoh, A., 1993b, "A New Outer Boundary Condition for Molecular Dynamics Simulations and Its Application to a Rarefied Gas Flow past a Cylinder (Periodic-Shell Boundary Condition)," *Advanced Powder Technology*, Vol. 5, pp. 105–117.
- Satoh, A., 1995a, "Molecular Dynamics Simulations on Internal Structures of Normal Shock Waves in Lennard-Jones Liquids," *ASME JOURNAL OF FLUIDS ENGINEERING*, Vol. 117, pp. 97–103.
- Satoh, A., 1995b, "Stability of Computational Algorithms used in Molecular Dynamics Simulations," *ASME JOURNAL OF FLUIDS ENGINEERING*, Vol. 117, pp. 531–534.
- Tsai, D. H., and Trevino, S. F., 1981, "Thermal Relaxation in a Dense Liquid under Shock Compression," *Physical Review A*, Vol. 24, pp. 2743–2757.

Flow Over Tube Banks— A Visualization Study

J. W. Hoyt¹ and R. H. J. Sellin²

Introduction

Rows or banks of tubes form the basis of many industrial heat transfer components such as boilers or heat exchangers. Crossflow over even a single circular cylinder is complex enough so that many heat-transfer and flow estimations are handled empirically. The much more complicated interaction between multiple tubes in crossflow occasionally results in unexpected and sometimes disaster-prone vibratory forces. Progress in understanding these flows has been hindered by lack of a means of tracing the effect of tube spacing and alignment on the flow path. A new tracer offers the possibility of obtaining greater understanding of the fluid mechanics involved in such flows.

A recently developed flow tracer comprised of shear-thickening and high extensional-viscosity fluids (Hoyt and Sellin, 1995) resists breakup in highly turbulent flows, and allows flow visualization at significantly higher Reynolds numbers than traditional dye-streak methods. It is used here to demonstrate aspects of flow around several circular-cylinder groupings re-

sembling tube banks, at Reynolds numbers ranging from 500 to 13,000.

The interaction and flow interference between just two cylinders has resulted in numerous studies, earlier summarized by Zdravkovich (1977). In the intervening twenty years, the flow around pairs of cylinders arranged side-by-side (Arie et al., 1983; Williamson, 1985) or staggered with respect to one another (Kiya et al., 1980) has been investigated with respect to pressure distributions over the cylinders, and their vortex shedding frequencies. Only at very low Reynolds numbers could the wake flow be visualized. At similarly low Reynolds numbers, Zdravkovich (1968) observed the wake flow from three cylinders in various arrangements. Visualization attempts at higher Reynolds numbers with flow around three cylinders provide little insight (Yao et al., 1989).

The flow around four cylinders in a square array is of interest as a model of ocean platform supports: papers by Sayers (1988), Lam and Lo (1992), and Lam and Fang (1995) indicate recent work.

Computational studies of flow around five cylinders in line, again at very low Reynolds numbers, have been made by Chang et al. (1989) and Zagar et al. (1992), among others. The experiments of Hetz et al. (1991) of five cylinders in line are very valuable in that by measuring frequencies, they were able to show the presence of various kinds of flow oscillations. These they classified into "cavity flow" where pairs of vortices simply rotate in the cavity between two in-line cylinders; "gap shedding", where vortices formed between the cylinders extend out beyond the in-line region; and "bluff-body shedding" where all the cylinders act as a single body, casting a large vortex wake. This nomenclature will be adopted in the discussion of the present results.

Aspects of flow-induced vibrations in cylinder arrays are well covered in the book by Blevins (1990) and the review by Moretti (1993). Pressure drop and heat transfer calculations seem to

¹ Professor Emeritus, Mechanical Engineering Department, San Diego State University, San Diego, CA 92182.

² Head, Civil Engineering Department, University of Bristol, Bristol, U.K.

Contributed by The Fluids Engineering Division of THE AMERICAN SOCIETY OF MECHANICAL ENGINEERS. Manuscript received by the Fluids Engineering Division October 10, 1996; revised manuscript received February 11, 1997. Associate Technical Editor: D. P. Telionis.

and Beeman algorithms also show a superior performance regarding the energy conservation. They maintain small energy fluctuations even for the larger values of h^* . On the other hand, although the 4-value Gear algorithm is a theoretically more accurate form than the above three algorithms, it does not exhibit smaller energy fluctuations under similar conditions. Again, these results clearly show that a theoretically more accurate molecular dynamics algorithm does not necessarily give rise to an improved performance for a multiparticle system. This is contrary to the results for a very simple case such as a harmonic oscillator (Berendsen and Gunsteren, 1986) and one-dimensional motion of two molecules (Haile, 1992). For these cases, a one order higher Gear algorithm produces a better performance of the energy conservation than the velocity Verlet and leapfrog algorithms. The A and B algorithms require approximately an order of magnitude smaller time interval in order to maintain an equivalent performance.

5 Concluding Remarks

Since molecular dynamics simulations of flow problems are generally a large-scale simulation, it is desirable to use an algorithm which allows as large a time interval as possible, and which also requires the minimum of computer memory. From this point of view, with the results shown in Sections 4.1 and 4.2, we may conclude that the most superior algorithm is the velocity Verlet, followed by the leapfrog, and then the Beeman. The 4-value Gear algorithm is inferior to these algorithms in that it is complicated and has a worse performance in terms of the stability and the energy fluctuation. The A and B algorithms

are found to perform less well than the 4-value Gear algorithm, and are not considered to be appropriate for the simulations of flow problems.

References

- Allen, M. P., and Tildesley, D. J., 1987, *Computer Simulation of Liquids*, Clarendon Press, Oxford.
- Berendsen, H. J. C., and Gunsteren, W. F., 1986, *Molecular-Dynamics Simulation of Statistical-Mechanical Systems*, Ciccotti, G., and Hoover, W. G., eds, North-Holland Physics Publishing, p. 43.
- Haile, J. M., 1992, *Molecular Dynamics Simulation: Elementary Methods*, Wiley, New York.
- Heermann, D. W., 1990, *Computer Simulation Methods in Theoretical Physics*, 2nd Ed., Springer-Verlag, Berlin.
- Holian, B. L., 1988, "Modeling Shock-Wave Deformation via Molecular Dynamics," *Physical Review A*, Vol. 37, pp. 2562–2568.
- Mareschal, M., Mansour, M. M., Puhl, A., and Kestemont, E., 1988, "Molecular Dynamics versus Hydrodynamics in a Two-Dimensional Rayleigh-Bénard System," *Physical Review Letters*, Vol. 61, pp. 2550–2553.
- Rapaport, D. C., 1987, "Microscale Hydrodynamics (Discrete-Particle Simulation of Evolving Flow Patterns)," *Physical Review A*, Vol. 36, pp. 3288–3299.
- Sato, A., 1993a, "Molecular Dynamics Simulation of a Subsonic Flow of a Rarefied Gas past a Sphere," *Advanced Powder Technology*, Vol. 4, pp. 59–70.
- Sato, A., 1993b, "A New Outer Boundary Condition for Molecular Dynamics Simulations and Its Application to a Rarefied Gas Flow past a Cylinder (Periodic-Shell Boundary Condition)," *Advanced Powder Technology*, Vol. 5, pp. 105–117.
- Sato, A., 1995a, "Molecular Dynamics Simulations on Internal Structures of Normal Shock Waves in Lennard-Jones Liquids," *ASME JOURNAL OF FLUIDS ENGINEERING*, Vol. 117, pp. 97–103.
- Sato, A., 1995b, "Stability of Computational Algorithms used in Molecular Dynamics Simulations," *ASME JOURNAL OF FLUIDS ENGINEERING*, Vol. 117, pp. 531–534.
- Tsai, D. H., and Trevino, S. F., 1981, "Thermal Relaxation in a Dense Liquid under Shock Compression," *Physical Review A*, Vol. 24, pp. 2743–2757.

Flow Over Tube Banks— A Visualization Study

J. W. Hoyt¹ and R. H. J. Sellin²

Introduction

Rows or banks of tubes form the basis of many industrial heat transfer components such as boilers or heat exchangers. Crossflow over even a single circular cylinder is complex enough so that many heat-transfer and flow estimations are handled empirically. The much more complicated interaction between multiple tubes in crossflow occasionally results in unexpected and sometimes disaster-prone vibratory forces. Progress in understanding these flows has been hindered by lack of a means of tracing the effect of tube spacing and alignment on the flow path. A new tracer offers the possibility of obtaining greater understanding of the fluid mechanics involved in such flows.

A recently developed flow tracer comprised of shear-thickening and high extensional-viscosity fluids (Hoyt and Sellin, 1995) resists breakup in highly turbulent flows, and allows flow visualization at significantly higher Reynolds numbers than traditional dye-streak methods. It is used here to demonstrate aspects of flow around several circular-cylinder groupings re-

sembling tube banks, at Reynolds numbers ranging from 500 to 13,000.

The interaction and flow interference between just two cylinders has resulted in numerous studies, earlier summarized by Zdravkovich (1977). In the intervening twenty years, the flow around pairs of cylinders arranged side-by-side (Arie et al., 1983; Williamson, 1985) or staggered with respect to one another (Kiya et al., 1980) has been investigated with respect to pressure distributions over the cylinders, and their vortex shedding frequencies. Only at very low Reynolds numbers could the wake flow be visualized. At similarly low Reynolds numbers, Zdravkovich (1968) observed the wake flow from three cylinders in various arrangements. Visualization attempts at higher Reynolds numbers with flow around three cylinders provide little insight (Yao et al., 1989).

The flow around four cylinders in a square array is of interest as a model of ocean platform supports: papers by Sayers (1988), Lam and Lo (1992), and Lam and Fang (1995) indicate recent work.

Computational studies of flow around five cylinders in line, again at very low Reynolds numbers, have been made by Chang et al. (1989) and Zagar et al. (1992), among others. The experiments of Hetz et al. (1991) of five cylinders in line are very valuable in that by measuring frequencies, they were able to show the presence of various kinds of flow oscillations. These they classified into "cavity flow" where pairs of vortices simply rotate in the cavity between two in-line cylinders; "gap shedding", where vortices formed between the cylinders extend out beyond the in-line region; and "bluff-body shedding" where all the cylinders act as a single body, casting a large vortex wake. This nomenclature will be adopted in the discussion of the present results.

Aspects of flow-induced vibrations in cylinder arrays are well covered in the book by Blevins (1990) and the review by Moretti (1993). Pressure drop and heat transfer calculations seem to

¹ Professor Emeritus, Mechanical Engineering Department, San Diego State University, San Diego, CA 92182.

² Head, Civil Engineering Department, University of Bristol, Bristol, U.K.
Contributed by the Fluids Engineering Division of THE AMERICAN SOCIETY OF MECHANICAL ENGINEERS. Manuscript received by the Fluids Engineering Division October 10, 1996; revised manuscript received February 11, 1997. Associate Technical Editor: D. P. Telionis.

be best handled by empirical means (i.e., Incropera and DeWitt, 1996).

Experimental

A small free-surface water channel at the University of Bristol was used for all tests. Stainless-steel tubes, 18.67 mm dia were fitted with spring wedges in their base, allowing them to be set in various tube-bank arrangements spanning the 10.2 cm width of the channel. Photo, video, and visual observations could thus be made through the glass wall of the channel; the opposite wall being matt black to enhance contrast. Screens and honeycomb were installed at the converging entrance to the test section of the channel; the turbulence level was not measured.

Both in-line and staggered tube banks, as well as other tube geometries could be simulated. Reynolds numbers for the inline arrangement were based on water velocities in the flow area between columns of tubes, and the tube diameter; for the staggered geometry, a similar calculation was used, except in cases where the minimum flow area occurred in the diagonal region between the staggered tubes. All Reynolds-number velocities were thus calculated to be substantially higher than the approach velocity.

The approach velocities to the tube banks were determined at the channel exit by catch-and-weigh volume measurement, using a stopwatch. Measurement of the water velocity and temperature, and the cylinder diameters, lead to an estimated uncertainty in the Reynolds number for a single cylinder placed in the flow of ± 2.3 percent. Spacing uncertainties bring the tube-bank Reynolds number estimation to ± 5 percent. Quoted Reynolds numbers have been rounded to the nearest hundred from the calculated value.

Spacings for the tube bank simulations were set at 3 and 6 cm (± 1 mm) in both axial (L) and transverse (T) directions, giving spacing ratios L/D and T/D of 1.61 and 3.21. Axial row spacing for the staggered arrangement was half these values. In all, eight different geometries were tested, each at two different Reynolds numbers. Additionally, a few tests were made with four cylinders set in a square pattern. Here the centerline spacing on each side of the square, (S), to diameter ratio was set at 3.02.

The flow tracer was a mixture of two percent cetyltrimethylammonium salicylate and one-half percent poly (ethylene oxide) solutions, colored by a small amount of white paint, and ejected from a rake of 1 mm dia hypodermic tubes, as shown in Fig. 1. Formulations of this type (Hoyt and Sellin, 1995) resist breakup under highly turbulent conditions, often fracturing into smaller threads which occasionally aid in the visualization. Non-Newtonian flow effects were avoided by discharging the channel into a very large reservoir where tracer degradation took place before recirculation.

The photos were taken using a 35 mm camera with ISO 1600 film at 1/250 sec exposure, with lighting from the top and sides of the channel; commercial color processing provided suitable prints. In addition, video records were made using a home-type camcorder.

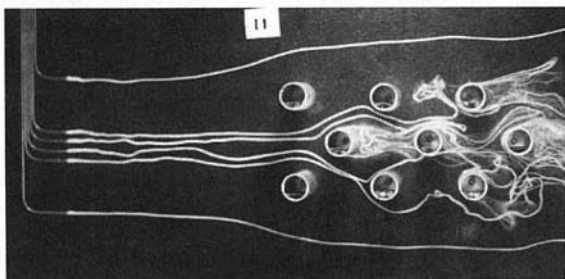


Fig. 1 Method of dispensing tracer from rake of hypodermic tubes

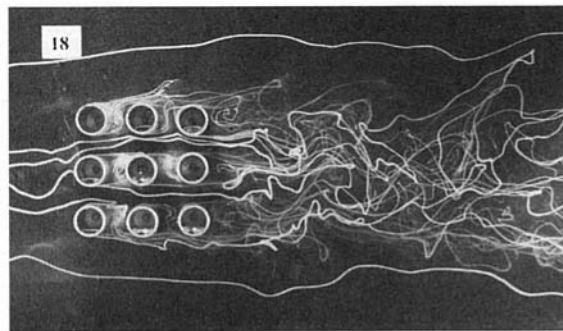


Fig. 2 In-line spacing; $L/D = T/D = 1.61$, $Re = 11,500$

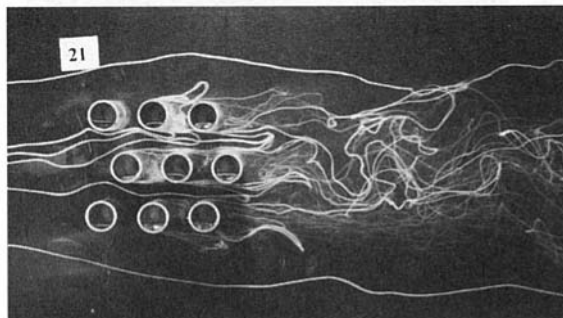


Fig. 3 Staggered spacing; $L/D = T/D = 1.61$, $Re = 9500$

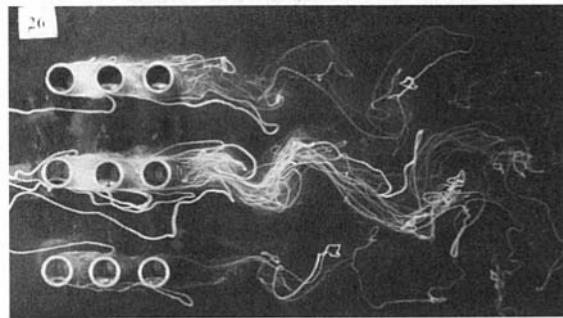


Fig. 4 In-line; $L/D = 1.61$, $T/D = 3.21$, $Re = 6600$

Results

Turning first to the tests with the smallest L/D and T/D (1.61), clear evidence of the “cavity flow” of Hetz et al. (1991) can be seen in the center row of cylinders, where most of the tracer was dispensed. For both the in-line (Fig. 2) and staggered (Fig. 3) arrangements, the cavity flow seems most significant; a hint of “bluff-body” wake appears behind the center row. With the same L/D , but expanding the T/D ratio to 3.21, the bluff-body wake dominates the flow picture, as seen in Figs. 4 and 5. The between-cylinder pattern is also prominent; the cavity vortices are especially clear in Fig. 5. These vortices are highly three-dimensional, as can be noticed in the photo taken at an angle to the array (Fig. 6).

With the larger L/D (3.21) and the same T/D , the cavity-type flow disappears, the flow between the cylinders becoming entirely the “gap-shedding” type in the nomenclature of Hetz, et al, (1991), as depicted in Figs. 7 and 8. The flow behind each cylinder differs from that found in the wake of an isolated cylinder; there is a distinct effect of the following cylinder on the between-cylinder flow. The combined wake of each column of cylinders tends to coalesce into a more intense activity resembling a bluff-body wake. Similar comments can be made regard-

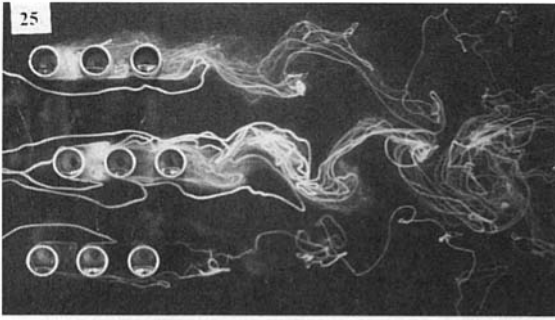


Fig. 5 Staggered; $L/D = 1.61$, $T/D = 3.21$, $Re = 5500$

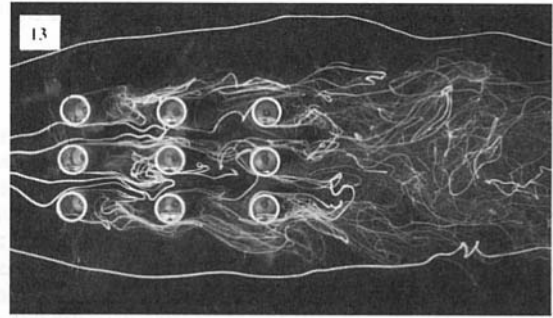


Fig. 9 In-line; $L/D = 3.21$, $T/D = 1.61$, $Re = 13,300$

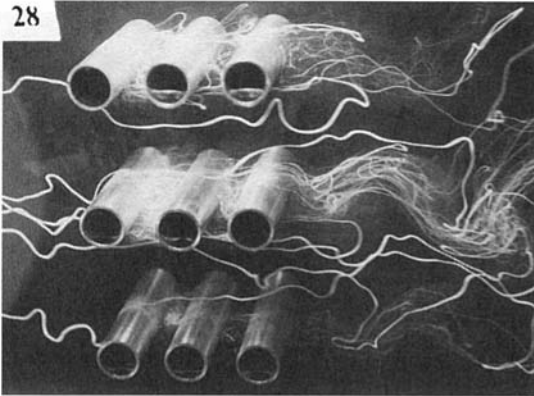


Fig. 6 View showing three-dimensional flow between cylinders; $L/D = 1.61$, $T/D = 3.21$, in-line arrangement, $Re = 6500$

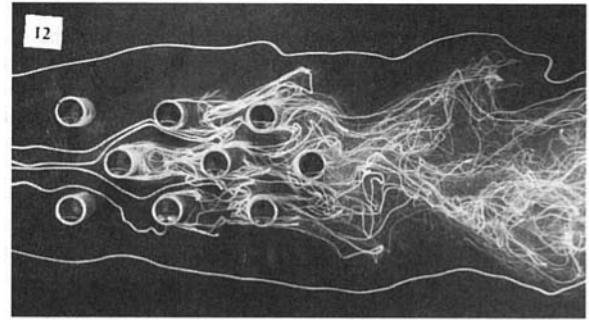


Fig. 10 Staggered; $L/D = 3.21$, $T/D = 1.61$, $Re = 6400$

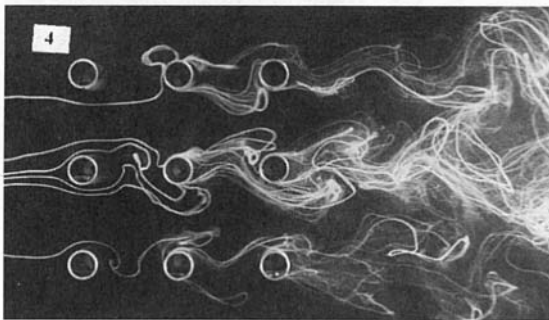


Fig. 7 In-line arrangement; $L/D = T/D = 3.21$, $Re = 9900$

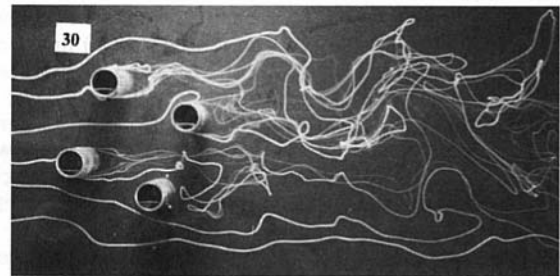


Fig. 11 Square arrangement with $S/D = 3.02$, rotated $22\frac{1}{2}^\circ$ from in-line position. Reynolds number, based on inflow velocity to leading cylinder, 6000.

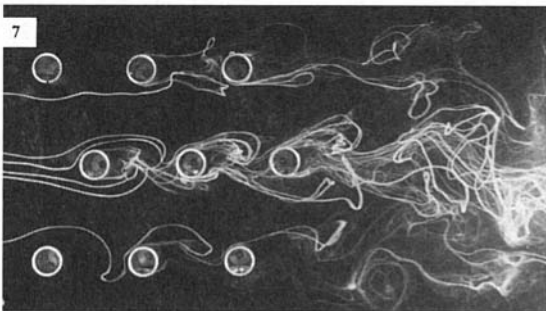


Fig. 8 Staggered arrangement; $L/D = T/D = 3.21$, $Re = 8300$

ing the pattern when the T/D ratio is reduced to 1.61. The gap-shedding tendency is less well defined; the entire array contributing to a large wake as shown in Figs. 9 and 10.

Each array was tested at two Reynolds numbers; these differed by around 40 percent. No effect of this change in Reynolds number could be discerned from the photos.

In tests with four cylinders arranged in a square, the pattern was very similar to that of the last four cylinders of Fig. 10 when the flow direction had the same orientation; rotating the array $22\frac{1}{2}^\circ$ as in Fig. 11 seems to indicate the wake of the upper two cylinders combines somewhat, while that of the lower two tends to cancel each other. Here the four cylinders (arranged in a square having center-to-center sides of 5.66 cm) act almost independently. Sayers (1987) indicates that in this arrangement the overall drag coefficient of the group is close to 1, i.e., the same as a single cylinder.

Discussion

The photos provide, in general, good visual confirmation of literature predictions regarding the effect of flow on heat transfer, pressure drop, and vibration aspects in tube banks. Incropera and DeWitt (1996) note that the heat transfer coefficient of the first row of tubes in a bank is about the same as that of a single isolated cylinder, while the heat transfer coefficient in the following rows increases, due to wake interactions acting

on those tubes. This point is beautifully illustrated by the photos, especially Figs. 7 and 8.

Blevins (1990) suggests that staggered tube arrays will generally have higher-amplitude turbulence-induced vibration than comparable in-line arrays. Comparing Figs. 9 and 10, we see that the staggered arrangement forms a much more organized wake than the in-line, together with more interaction between tubes in the transverse direction. To a lesser extent, we see this also in Figs. 2 and 3. Hence the photos imply that forces on such arrays seem more likely to be greater than the corresponding in-line arrangement. The greater wake may also contribute to a larger pressure drop in the staggered array, as indicated by Incropera and DeWitt (1996). However, at high transverse spacing, as shown in Figs. 4 and 5 and 7 and 8, there seems to be little difference between the wakes produced by the staggered or in-line arrangements.

Moretti (1993) has suggested that, in a single row of cylinders, two shedding frequencies would be observed at the transverse spacings used here. Our photos of flow through multiple rows indicates that many frequencies are involved, predominantly those of the bluff-body wake shedding frequency. In further work we hope to estimate frequencies by frame-by-frame examination of our video records of each array.

In addition to confirming some of the traditional ideas regarding flow through tube banks, some new information has emerged from this flow visualization study. First, if the transverse distance/diameter ratio (T/D) is around 3, the columns of tubes show no interaction with each other, and each column sheds a large bluff-body wake which may not be in phase with that of its neighbors. Similarly, the gap-shedding activity in the axial space between cylinders is not correlated from adjacent column to column, even for the in-line arrangement, when T/D is around 3, as can be seen in Fig. 7.

A remarkable feature found in many of the photos is the organization of the flow into a large bluff-body wake. A reviewer has commented that it is surprising that the many shear layers (often of alternate signs) contributing to the wake in a multiple-body flow can be organized into a single large oscillating wake. In certain geometries, the entire tube bank contributes to the large oscillating wake as in Fig. 10. Flow visualization thus plays a useful role in revealing unexpected flow characteristics.

Dedication

This paper is dedicated to the memory of Preston Lowrey, Chen Liang, and Constantinos Lyrintzis, engineering faculty

colleagues and friends at San Diego State University, murdered by a crazed graduate student, August 15, 1996.

Acknowledgments

The support of the University of Bristol and the U.S. National Science Foundation is very greatly appreciated. We especially wish to acknowledge the confidence in this work expressed by Dr. Michael Roco of the NSF, through grant no. CTS-9508409. We also wish to thank Mr. Philip Leonard for his skill in fabricating the test cylinders and assisting with the tests.

References

- Arie, M., M. Kiya, M. Moriya, and H. Mori, 1983, "Pressure Fluctuations on the Surface of Two Circular Cylinders in Tandem Arrangement," *ASME JOURNAL OF FLUIDS ENGINEERING*, Vol. 105, pp. 161-166.
- Blevins, R. D., 1990, "Flow-Induced Vibration," New York: Van Nostrand Reinhold, 2nd ed.
- Chang, Y., A. N. Beris, and E. E. Michaelides, 1989, "A Numerical Study of Heat and Momentum Transfer for Tube Bundles in Crossflow," *International Journal of Numerical Methods in Fluids*, Vol. 9, pp. 1381-1394.
- Hetz, A. A., M. N. Dhaubhadel, and D. P. Telionis, 1991, "Vortex Shedding over Five In-Line Cylinders," *Journal of Fluids & Structures*, Vol. 5, pp. 243-257.
- Hoyt, J. W. and R. H. J. Sellin, 1995, "A Turbulent-Flow Dye-Streak Technique," *Experiments in Fluids*, Vol. 20, pp. 38-41.
- Incropera, F. P. and D. P. DeWitt, "Introduction to Heat Transfer," New York: John Wiley & Sons, 3rd ed. 1996.
- Kiya, M., M. Arie, H. Tamura, and H. Mori, 1980, "Vortex Shedding from Two Circular Cylinders in Staggered Arrangement," *ASME JOURNAL OF FLUIDS ENGINEERING*, Vol. 102, pp. 166-171.
- Lam, K. and X. Fang, 1995, "The Effect of Interference of Four Equispaced Cylinders in Crossflow on Pressure and Force Coefficients," *Journal of Fluids & Structures*, Vol. 9, pp. 195-214.
- Lam, K. and S. C. Lo, 1992, "A Visualization Study of Cross-Flow around Four Cylinders in a Square Configuration," *Journal of Fluids & Structures*, Vol. 6, pp. 109-131.
- Moretti, P. M., 1993, "Flow-Induced Vibrations in Arrays of Cylinders," *Annual Review of Fluid Mechanics*, Vol. 25, pp. 99-114.
- Sayers, A. T., 1988, "Flow Interference between Four Equispaced Cylinders when Subjected to a Cross Flow," *Journal of Wind Engineering and Industrial Aerodynamics*, Vol. 31, pp. 9-28.
- Williamson, C. H. K., 1985, "Evolution of a Single Wake behind a Pair of Bluff Bodies," *Journal of Fluid Mechanics*, Vol. 159, pp. 1-18.
- Yao, M., M. Nakatani, and K. Suzuki, 1989, "Flow Visualization and Heat Transfer Experiments in a Duct with a Staggered Array of Cylinders," *Experimental Thermal & Fluid Sci.*, Vol. 2, pp. 193-200.
- Zagar, I., P. Skerget, A. Alujevic, and M. Hribersek, 1992, "Pressure Drop Calculations for Tube Bundles in Crossflow by the Boundary-Domain Integral Method," *ZAMM*, Vol. 72, pp. T395-T398.
- Zdravkovich, M. M., 1968, "Smoke Observations of the Wake of a Group of Three Cylinders at Low Reynolds Number," *Journal of Fluid Mechanics*, Vol. 32, pp. 339-351.
- Zdravkovich, M. M., 1977, "Review of Flow Interference between Two Circular Cylinders in Various Arrangements," *ASME JOURNAL OF FLUIDS ENGINEERING*, Vol. 99, pp. 618-633.